THE ELECTROCHEMISTRY OF SULPHUR AND ITS IONS IN MOLTEN HALIDES

A THESIS

submitted for the

DEGREE OF DOCTOR OF PHILOSOPHY

in the

UNIVERSITY OF LONDON

by

PETER GEORGE DUDLEY, M.Phil., DIC, B.Sc.(Eng.), ARSM

Department of Metallurgy and Materials Science

Royal School of Mines

Imperial College of Science and Technology

September 1982

ABSTRACT

The electrochemical behaviour of sulphur and its ions was examined in molten $PbCl_2$, $PbCl_2$-KCl and $PbCl_2$-KCl-NaCl solvents. In particular the electrooxidation of the sulphide ion, S^{2-}, was extensively studied at a variety of electrode substrates.

Electrochemical studies were carried out in the temperature range 410-550°C by linear sweep voltammetry, chronoamperometry, steady-state I-V relationships, chronopotentiometry, controlled potential electrolysis and open circuit decay techniques. The electrooxidation of PbS was primarily observed at planar vitreous carbon and graphite electrodes, although the behaviour at platinum and gold electrodes was investigated for comparison.

At vitreous carbon and graphite electrodes, two primary oxidation processes were observed corresponding to the reactions:

(1) $S^{2-} \rightarrow S^0 + 2\varepsilon'$ $\quad E \cong 0.45V$ wrt Ag/Ag^+

and

(2) $2S + 2Cl^- \rightarrow S_2Cl_2 + 2\varepsilon'$ $\quad E \cong 0.97V$ wrt Ag/Ag^+

The sulphur generated from reaction (1) under pulse conditions was shown to be reversible with respect to the electron transfer and to be diffusion controlled. However, at lower temperatures the oxidation process appears to be inhibited by the formation of a passive sulphur film. The nature and formation of sulphur films (at temperatures well below the boiling point of sulphur) on carbon, platinum and gold electrodes are discussed. Long time electrolysis of sulphide containing melts under both potentiostatic and galvanostatic conditions did not yield any insoluble anodic products.

Sodium polysulphide additions (Na_2S_2, Na_2S_4 and Na_2S_5) were found to be unstable in $PbCl_2$-KCl and $PbCl_2$-KCl-NaCl melts. Decomposition resulted in gaseous sulphur evolution. The resultant solutions were characterised by linear sweep voltammetry.

An attempt to quantitatively study the electroreduction of sulphur and its solubility in a $PbCl_2$-KCl-NaCl eutectic melt over the temperature range 420-500°C is reported and discussed.

Complementary studies include (a) the electrochemical characterisation of the solute species PbO, PbO_2 and $PbSO_4$ in a $PbCl_2$-KCl melt and 450°C and (b) contact angle measurements of $PbCl_2$ based molten salts on a variety of carbon substrates.

CONTENTS

	Page No.
CHAPTER 1	
Introduction	1
1.1 General Introduction	1
1.2 The Extraction of Metals from Sulphides	2
1.2.1 General	2
1.2.2 The Smelting of Metal Sulphides	2
1.2.2.1 Copper Smelting	3
1.2.2.2 Lead Smelting	4
1.2.3.3 Zinc Smelting	4
1.2.3 The Control of SO_2 Emissions	5
CHAPTER 2	
Electrochemical Techniques	8
2.1 Introduction	8
2.2 Cyclic Voltammetry	8
2.3 Chronopotentiometry	11
2.4 Chronoamperometry and Construction of Stationary Electrode Polarograms	13
CHAPTER 3	
Literature Survey	14
3.1 Introduction	14
3.2 Sulphur	14
3.2.1 Liquid Sulphur	14
3.2.2 Sulphur Vapour	15
3.3 Ionic Sulphides	16
3.3.1 Monosulphides	16
3.3.2 Polysulphides	16

Page No.

3.4 Metal Sulphides in General 17

3.4.1 Introduction 17

3.4.2 The Structure of Metal Sulphides 17

3.4.3 Electrical Properties of Metal Sulphides 23

3.5 Molten Salts 26

3.6 Identification of Sulphur Species in Molten Salts 28

3.7 The Solubility of Metal Sulphides in Molten Salts 30

3.8 Molten Mixtures of Halides and Chalcogenides 33

3.8.1 Introduction 33

3.8.2 Ag_2S - AgCℓ Mixtures 34

3.8.3 $PbCℓ_2$ - PbS Mixtures 35

3.8.4 Cu_2S-CuCℓ and FeS-$FeCℓ_2$ Mixtures 39

3.9 The Electrochemistry of Sulphur and Sulphur Species in Molten Salts 40

3.9.1 Introduction 40

3.9.2 The LiCℓ-KCℓ Eutectic Solvent 41

3.9.3 The $AlCℓ_3$-NaCℓ System 46

3.9.4 The $PbCℓ_2$-MCℓ System 51

3.10 Electrowinning from Metal Sulphide/Metal Chloride Solutions 55

3.11 Discussion 60

CHAPTER 4

Experimental 64

4.1 Apparatus 64

4.1.1 Furnace and Temperature Control 64

4.1.2 Electrochemical Cell 64

4.1.3 The Sulphur Gas Electrochemical Cell 67

4.1.4 Vacuum and Gas Supply Systems 69

4.1.5 Contact Angle Apparatus 71

Page No.

4.2 Electrodes 74

4.2.1 Micro-Electrodes 74

4.2.1.1 Gold Electrode 74

4.2.1.2 Platinum Electrode 74

4.2.1.3 Carbon Electrodes 76

4.2.2 Counter Electrode 78

4.2.3 Reference Electrode 80

4.3 Chemicals and Materials 80

4.4 Melt Purification 80

4.5 Experimental Procedure 86

4.5.1 Preparation of Electrochemical Apparatus 86

4.5.2 The Sulphur Electrochemical Cell 87

4.5.3 Contact Angle Measurements 89

4.5.4 Electrochemical Procedure 90

4.6 Sodium Polysulphide Preparation 96

CHAPTER 5

Electrochemical Behaviour of PbS in the Binary $PbCl_2$-KCl Eutectic Melt 98

5.1 Introduction 98

5.2 Results 101

5.2.1 Cyclic Voltammetry 101

5.2.2 Polarographic I-E Curves 126

5.2.3 Chronoamperometry (I-E Transients) 130

5.2.4 Steady-State I-E Relations 130

5.2.5 Controlled Potential Electrolysis 143

5.3 Discussion 144

Page No.

CHAPTER 6

Electrochemical Behaviour of PbS in the Ternary $PbCl_2$-KCl-NaCl Eutectic Melt 159

6.1 Introduction 159

6.2 Results: Vitreous Carbon and Graphite Electrodes 159

6.2.1 Cyclic Voltammetry 159

6.2.2 Chronoamperometry 175

6.2.3 Galvanostatic and Open Circuit Decay 178

6.3 Results: Gold Working Electrode 192

6.3.1 Cyclic Voltammetry 192

6.3.2 Chronoamperometry 212

6.4 Results: Platinum Electrode 214

6.4.1 Cyclic Voltammetry 214

6.4.2 Chronoamperometry 252

6.4.3 Chronopotentiometry 252

6.5 Discussion 258

CHAPTER 7

The Electrochemistry of Dissolved Sulphur Gas in the $PbCl_2$-KCl-NaCl Eutectic Melt 275

7.1 Introduction 275

7.2 Results 276

7.3 Discussion 289

CHAPTER 8

The Electrochemistry of Polysulphide Containing Solutions 294

8.1 Introduction 294

8.2 Results 295

8.2.1 Cyclic Voltammetry 295

8.2.2 Chronoamperometry 300

8.3 Discussion 304

Page No.

CHAPTER 9

Identification of Anionic Impurities in the $PbCl_2$-KCl Eutectic Melt 306

9.1 Introduction 306

9.2 PbO and PbO_2 Solute 306

9.2.1 Results 306

9.2.2 Discussion 310

9.3 $PbSO_4$ Solute 311

9.3.1 Results 311

9.3.2 Discussion 312

CHAPTER 10

Related Studies: Contact Angle Measurements 314

10.1 Introduction 314

10.2 Results 314

10.3 Discussion 320

CONCLUSIONS 324

APPENDIX 1 329

REFERENCES 330

ACKNOWLEDGEMENTS 351

CHAPTER 1

INTRODUCTION

1.1 General Introduction

The 'art' of extracting metals from their ores dates back to the dawn of human civilization. The first metals used by man were undoubtedly those of copper and gold which could be found in metallic form. Subsequently (4000 B.C.) man learned to produce copper and bronze by the smelting of copper and tin ores in a charcoal fire. Throughout history the progress made in extractive metallurgy have been one of trial and error and it is only relatively recently that the application of sound scientific priciples has enabled a detailed understanding of the complex systems involved.

The most common of the non-ferrous metals are those of copper, lead and zinc (the base metals) which are principally extracted from their sulphide ores. Metal sulphides are the most important group of minerals found in the earth's crust, constituting the raw materials from which most of the worlds supply of non-ferrous metals are obtained.

In addition, metal sulphides, particularly those obtained in a pure form and those synthesised with carefully controlled non-stoichiometry or impurity content have particular industrial application in the field of electronics. The unusual electrical and magnetic properties of metal chalcogenides have contributed significantly to the electronic revolution of today, through the fabrication of semiconductors and magnetic memory units etc.

1.2 The Extraction of Metals from Sulphides

1.2.1 General

Many text books (1)(2)(3), review articles (4)(5) and journals (6) are devoted to the general subject of extractive metallurgy. Here a brief description of the general processes employed in extracting the metals copper, lead and zinc will be given.

Prior to the extraction of any metal from its sulphide mineral a considerable number of stages are required to remove the large amounts of gangue material associated with the ore. In addition many valuable impurity minerals must also be separated and recovered; for example galena (PbS) ores contain profitable amounts of silver, antimony and bismuth. The benefication or concentration stages involve extensive crushing, grinding, flotation, thickening and drying processes before a suitable concentration of mineral is obtained for subsequent reduction to the metal. However, mineral ores are not always in the optimum chemical or physical state for conversion to metal; oxides are generally more conveniently reduced than are sulphides. The physical state of the concentrate may be too fine, and may require agglomeration by sintering prior to charging to a blast furnace.

1.2.2 The Smelting of Metal Sulphides

The roasting and smelting of concentrates is a process in which the sulphur is partially or completely removed from the metal as sulphur dioxide. A generalized reaction may be written as:

$$MS + O_2 = M + SO_2$$

with an equilibrium constant:

$$K = \frac{a_{M.}\ P_{SO_2}}{a_{MS} \cdot P_{O_2}}$$

Other reaction products may also be formed during the roasting operation which are largely dependant upon temperature and the oxygen potential. Thermodynamic plots of log P_{SO_2} versus log P_{O_2} clearly show the conditions of phase stability.

1.2.2.1 Copper Smelting

Copper smelting processes normally involve 2 or 3 steps to produce blister copper from sulphide ore concentrates. In the first step, a portion of the sulphur content of the concentrate is removed in a roaster; about 20-50% is removed at a concentration of less than 1% for conventional multiple hearth roasters, 6-10% for fluid bed roasters. The second operation involves smelting the roasted concentrate and fluxes in a reverberatory furnace to form slag and a copper-bearing matte. About 10-30% of the sulphur content of the ore is released in the smelting operation and approximately 20-40% is released in plants feeding the roasted concentrate to the smelter. The concentration of SO_2 in the off gas from the smelting furnace is in the range of less than 0.5-3%; the volume depending on the type of furnace used. The final pyrometallurgical step is oxidation of the matte to form blister copper in the convertor. Copper converting normally accounts for 40-50% of the sulphur released in the above 3-stage process. Sulphur dioxide is usually removed (50-90%) by the sulphuric acid plant; however weak SO_2-containing gases with ¼-1% SO_2 are released, untreated into the atmosphere at a rate of

170-340 NM^3h per ton of concentrate daily.

1.2.2.2. Lead Smelting

Lead is produced from sulphide ore concentrates in a 3-step operation. The concentrate (55-70% Pb, 13-19% S) is sintered to produce a lead oxide sinter and to eliminate sulphur as SO_2. The sinter machines may be operated with two off-gas streams, one rich (4-6% SO_2) and the other weak (0.5% SO_2). The sinter is fed to a blast furnace for reduction of oxide to molten bullion. Approximately 15% of the concentrate sulphur remains in the charge to the blast furnace and about 7% is released in the off-gas at less than 1% SO_2 concentration. The remaining sulphur is retained in the slag. The final step is the refining of the metal bullion i.e. to eliminate impurities such as antimony, gold and silver.

In the dual stream sinter machine operation, approximately 75% of SO_2 released is in the strong gas stream, accounting for about 25-50% of total gas volume and is easily handled by conventional sulphuric acid plants (7-11). To achieve a greater than 90% SO_2 removal from the various smelter off gases either the weak SO_2 containing streams must be treated or a more efficient SO_2 extraction plant installed. The weak gas streams are large in volume (1000-1300 NM^3h per ton Pb produced daily) containing 0.5% SO_2.

1.2.2.3 Zinc Smelting

Zinc is produced from sulphide ore concentrates (62% Zn, 32% S). The initial step in zinc smelting is roasting the concentrate to remove sulphur and to form a zinc oxide calcine. More than 90% of the SO_2 released in zinc smelting results from the roasting

step. Several different types of roasting systems are used, the Ropp roaster produces a gas of less than 1% SO_2; other processes (Multiple Hearth, fluid-bed etc) produce 5-14% SO_2 gas streams which can be fed to a conventional sulphuric acid plant. Sintering in the pyrometallurgical route accounts for the remaining sulphur in the off gas streams at concentrations of 0.2-0.05% SO_2 (7-11). With the exception of Ropp roasters, zinc smelters have been able to remove more than 90% SO_2 using conventional sulphuric acid plants.

It is evident from the above discussion that large quantities of SO_2-containing gases are generated during the pyrometallurgical treatment of sulphide ores; much of which is eliminated (via acid plants). However there remains significant amounts of SO_2 gases which are emitted, untreated into the atmosphere.

1.2.3 The Control of SO_2 Emissions

In these days of environmental awareness the non-ferrous metallurgical industry is under increasing pressure from Governmental Agencies to reduce atmospheric emissions of SO_2. At the present time most smelters have some degree of SO_2 control for their strong gas streams which generally reduce SO_2 emissions by 50-80%. However, further reductions of 90%+ are proposed; to achieve this aim existing smelters must either introduce "scrubbing" processes on the gas streams or install new, more efficient but more costly equipment.

During the past ten years (and undoubtedly the future) the control of sulphur oxide emissions has been a key factor in the economic performance of many smelting operations (12)(13).

The most widely used process to reduce atmospheric SO_2 pollution is via the sulphuric acid plant which may only be used for gases containing more than 3.5-4% SO_2 which is a major constraint in its application. An inherent problem with the production of sulphuric acid is its low market value and the difficulties involved in its transportation over long distances (smelters are usually sited in remote areas). Sulphuric acid cannot be easily disposed of without serious pollution.

Many alternative processes to the sulphuric acid plant have been investigated, these have included the major redesign of existing smelters and indeed the evolution of new processors which smelt the sulphide concentrates more efficiently and which produce a main off-gas stream of at least 5% SO_2. Such processes have included oxygen enrichment, fluid bed roasting, electric furnace and flash or continuous smelting. In the case of lead, continuous smelting techniques developed have included the Kivert, QSL (Queneau- Schuhman- Lurgi), Sirosmelt, and TRBC (Top Blown Rotary Converter processes (14,15). The Kivert process is the most developed and several installations are probable in the near future; this process produces lead by direct smelting of sulphide concentrates with simultaneous electrochemical production of zinc from the slag.

Other alternatives have included enriching the gas stream with further SO_2; the continued gas stream may then be handled by conventional means. The supplementary SO_2 is generally produced by burning sulphur or sulphur bearing minerals. This technique has been used on some molybdenum roasters in the U.S.A. (16).

The "Throwaway" system is becoming widespread, and popular for treating weak SO_2 containing gases for both smelters and other indus-

tries (16). The process involves the use of lime or limestone to scrub the SO_2 containing gas stream to produce a clean gas for release into the atmosphere and a calcium sulphate/sulphite slurry.

A process which is rapidly and successfully being employed in Japan involves the formation of gypsum, a valuable produce marketed at a profit (7-9).

From the above discussion it is clear that enormous effort and capital is being spent by the smelting operators to eliminate SO_2 gases in order to conform with the imposed environmental regulations. The quest for new, more efficient processes continues and many ingenious systems have been devised. An 'ideal' extraction system would facilitate the formation of a high purity liquid metal, suitable for further processing i.e. casting and the direct formation of elemental sulphur which could be readily marketed or disposed of readily. The process should be non-polluting, easy and clean and above all economically viable.

The electrowinning of sulphide-containing molten salt electrolytes offers such an 'ideal' process. The electrowinning of high purity lead from PbS - $PbCl_2$ mixtures has been shown to be viable and has been demonstrated up to pilot plant scale on several occasions at Halkyn (Wales), in Canada and at Port Pirie in Australia - the latter produced 1500 tons of 99.5% Pb per year. The use of electrowinning operations combined with molten salt systems possess many advantages over conventional pyrometallurgical routes and are discussed fully in section 3.10 .

It is the aim of this work to help elucidate the governing reaction mechanism(s) by which sulphur is generated at an anode during electrolysis operations at high temperatures.

CHAPTER 2

ELECTROCHEMICAL TECHNIQUES

2.1 Introduction

Characterisation of electrochemical oxidation and reduction processes may be achieved by the application of several techniques of which cyclic sweep voltammetry, chronopotentiometry and chronoamperometry are commonly used. Several books (17-19) and review articles (20-22) are available describing theoretical and experimental aspects.

2.2 Cyclic Voltammetry

Cyclic voltammetry is an electrochemical technique in which the potential of a stationary indicator or working electrode in an unstirred solution containing electroactive species is varied linearly with time. Assuming that the solution contains only the oxidized form (Ox), the potential sweep is started at some potential anodic of the standard potential of the redox couple (a potential at which there is zero current flow). As the standard potential is approached, species Ox will begin to be reduced. Species Ox will tend to diffuse towards the electrode because a concentration gradient is established between the bulk solution concentration and that at the electrode surface. As the potential is swept past the standard potential the current increases rapidly until a maximum is reached, and then the current decreases. This increase in current due to the electrode reaction is opposed by the depletion of the electroactive species at the electrode surface as a result of the

gradually increasing thickness of the diffusion layer. Depletion of electroactive species therefore causes the current to decay. Reversal of the direction of the potential sweep will lead to the reoxidation of the reduced species, resulting in an anodic peak. The current-potential curve (cyclic voltammogram) for a simple reversible reduction process is shown in Figure 2.1. with the measurable parameters obtained.

The peak current i_p for a simple reversible, diffusion controlled process is given by the Randles-Sevcik equation (17).

$$I_p = 0.452 \frac{(nF)^{\frac{3}{2}}}{(RT)^{\frac{1}{2}}} \cdot A.n.D^{\frac{1}{2}}.C.v^{\frac{1}{2}}$$

where I = the faradaic current (mA), n = the number of electrons involved in the electrode process, F = the Faraday (96,487 coulombs), R = the universal gas constant (8.315 joules/mole /degree), T = absolute tempearture (K), A = area of the working electrode (cm^2), D = the diffusion coefficient (cm^2/sec), C = bulk concentration of the reactant (mol/l), v = voltage scan rate (v/sec).

The peak potential Ep(v) for this process is independent of the concentration of the reactant and is related to the polarographic half-wave potential $E_{\frac{1}{2}}$ by the equation (17)

$$E_p = E_{\frac{1}{2}} - 1.11\ RT/nF$$

The value of $E_{\frac{1}{2}}$ may be estimated from a voltammogram of a simple reversible process as it occurs at the point corresponding to 0.85 i_p (23). The half-peak potential $E_{p/2}$ is a convenient reference point and is related to $E_{\frac{1}{2}}$ and $E_{p/2}$ by the equation (23).

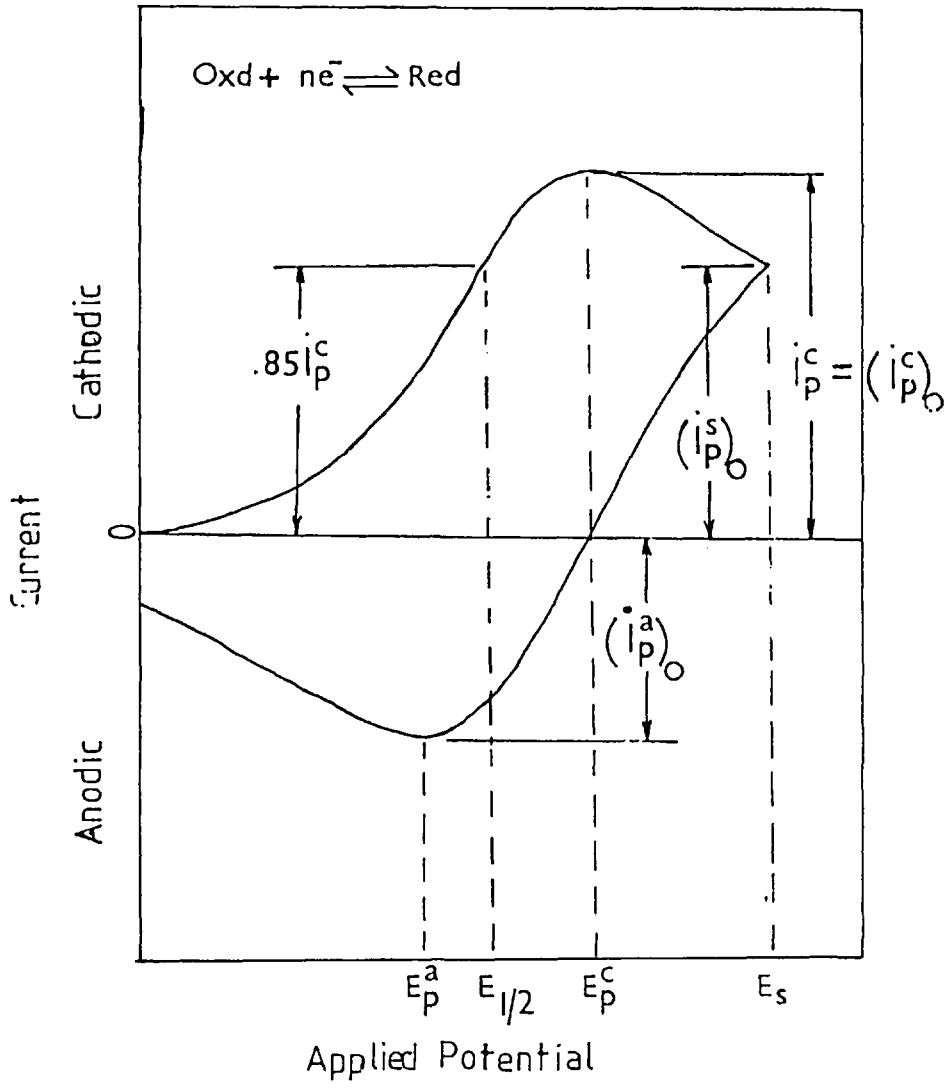


Fig 2.1. Cyclic voltammogram for the reversible reduction of a soluble product indicating the measurable parameters obtainable.

$$E_{p/2} = E_{\frac{1}{2}} + 1.09\ RT/nF$$

$$\Delta E = E_{p/2} - E_p = 2.20\ RT/nF$$

The above equations are only valid for a reversible electroreduction process where the product is soluble. Mamantov et al (24) have shown that in linear sweep voltammetry for the reversible process where both the reactant and product are soluble, a plot of log $(i_p - i)/i$ vs potential should be linear in the range 0.35 - 0.70 i_p with a slope of 0.58 (nF/RT).

The theory of linear sweep voltammetry has been extended to electrode processes involving irreversible electrode processes (17,23,25,26), chemical reactions couple to reversible or irreversible charge transfer (23,27-36), chemical reactions coupled between two charge transfers (27-29), multicharge transfer (37), adsorption of reactants or products (38), and several other mechanisms. In these theoretical treatments, convenient diagnostic criteria, such as variation of $i_p/v^{\frac{1}{2}}$, E_p and i_p^a/i_p^c with scan rate have been developed for both qualitative and quantitative characterization of unknown systems. A compilation of these is given by Dudley(39).

Linear sweep voltammetry has become a very powerful tool for the investigation of unknown systems.

2.3 Chronopotentiometry

Chronopotentiometry is an electrochemical technique characterized by the application of a controlled (usually constant) current between two electrodes in an unstirred solution containing an electroactive species; the resulting variations of potential of the working electrode are measured as a function of time. As the electrolysis,

proceeds, the concentration of the electroactive species near the electrode decreases until it is too small to sustain the imposed current; at this point the potential changes to some other value corresponding to another reaction (i.e. second charge transfer step or the decomposition of the solvent). The time elapsing between the sudden changes of potential is called the transition time τ.

For a reversible process the transition time is related to the current and concentration by the Sand equation (17):

$$\tau^{\frac{1}{2}} = \frac{\pi^{\frac{1}{2}} n F A D^{\frac{1}{2}} C}{2I}$$

The value of the transition time is controlled by the rate of diffusion and is independent of the rate of the electron transfer. However the shape of the potential-time curve (the chronopotentiogram) is dependent on the reversibility of the electrode process. For a reversible process $O + ne \rightleftharpoons R$, where both O and R are soluble in solution or in the electrode, the potential time relationship is given by the Karaoglanoff equation (17):

$$E = E_{\tau/4} + \frac{RT}{nF} \ln \frac{(\tau^{\frac{1}{2}} - t^{\frac{1}{2}})}{t^{\frac{1}{2}}}$$

where $E_{\tau/4}$ is equivalent to the polarographic half-wave potential $E_{\frac{1}{2}}$ (17). A plot of potential (E) vs log $(\tau^{\frac{1}{2}} - t^{\frac{1}{2}})/t^{\frac{1}{2}}$ for a reversible system, where both reactant and product are soluble in solution or in the electrode, yields a straight line with a slope of 2.3 RT/nF.

The theory and applications of chronopotentiometry have been received by Paunovic (20), Davis (40), Lingane (41), Adams (18) and Murray (42). This technique has been extended to irreversible

processes, consecutive and stepwise processes, kinetic processes, coupled chemical reactions and adsorption processes. Diagnostic criteria for different cases have been discussed and summarized by Reinmuth (21,43,44) and Adams (18).

2.4 Chronoamperometry and Construction of Stationary Electrode Polarograms.

Chronoamperometry is an electrochemical technique characterized by the application of a potential step to a stationary working electrode in an unstirred solution containing an electroactive species; the resulting current decay is measured as a function of time. For a reversible process the resulting current is governed by the rate of diffusion of the electroactive species from the bulk solution to the electrode surface. The relationship between current and time for a simple linear diffusion process is given by the Cottrell equation (17).

$$It^{\frac{1}{2}} = \frac{n\ F\ A\ D^{\frac{1}{2}}\ C}{\pi^{\frac{1}{2}}}$$

Applications of this technique have been reviewed by Adams (18) and Murray (42).

This technique has been used for the construction of polarograms from current-time curves (45)(46). The potential is stepped from a value at which no electrochemical reaction is taking place to some chosen value. The current is subsequently measured at time intervals ranging from a few m/sec to several seconds. The polarogram is constructed by plotting current values corresponding to a given time vs the applied potential steps. The analysis of these polarograms is analogous to that of conventional polarograms (47)(48)(49).

CHAPTER 3

LITERATURE SURVEY

3.1 Introduction

An 'in-depth' understanding of the process(es) of electrolysing molten sulphide/chloride solutions in particular with respect to the design of new processes, requires a knowledge of the physico-chemical properties of metal sulphide compounds, their solution in molten inorganic chlorides and the electrolysis products. Indeed many fundamental studies have been motivated from this point of view. It is therefore intended within this literature survey to review as briefly as possible the main areas of both applied and fundamental studies which relate to a greater understanding of molten sulphide/chloride electrolysis.

3.2. Sulphur

3.2.1 Liquid Sulphur

On melting sulphur (S_8) gives first a yellow, transparent, mobile liquid which becomes brown and increasingly viscous at temperatures above 160^{o}C. Both the viscosity and specific heat (50) reach a maximum at approximately 200^{o}C and decrease gradually as the temperature is raised to the boiling point (444.4^{o}C). Although S_8 rings persist in the liquid upto approximately 193^{o}C, the changes in viscosity are attributed to the ring cleavage and the formation of catenasulphur species, i.e. very long sulphur chains. At any temperature an equilibrium between chains and rings of varying lengths will be established. E.s.r studies have shown the presence of the radical ends of these chains in molten sulphur at temperatures

greater than 160°C. It is assumed that these chains reach their greatest average length (5-8 x 10^5 atoms) at 200°C at which the maximum in viscosity occurs. The colour change upon melting is due to an increase in the intensity and a shift of an adsorption band to the red. This is associated with the formation (T 250°C) of the red species S_3 and S_4 which comprise 1-3% of sulphur at its boiling point.

3.2.2 Sulphur Vapour

Saturated sulphur vapour is known to be composed mainly of molecules in the range S_2 - S_8, and like the other phases has a complex composition.

Several workers have determined the vapour pressure of sulphur (51)(52). Baker (53) found the overall vapour pressure, over the temperature range 340-1040°C to obey the relationship:-

$$\log P_{(atm)} = 6.00282 - 3584.42T^{-1} - 2.23934 \times 10^{-3} + 1.14662 \times 10^{-6}T^2$$

(T = K)

Below 340°C the data of West and Menzies (51) should be used. Berkowitz and Marquart (54) from mass spectrographic studies of the vapour, evaluated the composition of the saturated vapour upto the normal boiling point, and determined a set of six independent equations for the sulphur species. (see Appendix 1). Recent computations by Tegman and Eriksson (55) give the free energy change (ΔG^o) as a function of temperature for the reaction:-

$$\tfrac{1}{2} S_2 (g) \rightleftharpoons S_{(l)}$$

as

$$\Delta G^{o}\ J/mol = 44621 - 946.18T - 7.2029 \times 10^{-2}T^{2} - 1.2864 \times 10^{7}/T + 143.77T \ln T$$

For $(473 < T < 273K)$

The energy per bond in a molecule (assumed to be ring shaped) increases from S_2 (51.5 Kcal/mole) to S_3 (55.5), S_4(57.5), S_5(60.5) and then levels off at S_6(61.5), S_7(62), S_8(62.5), S_9(62) and S_{10}(62.5).

3.3 Ionic Sulphides

3.3.1 Monosulphides

The alkali and alkaline earth metal sulphides (the monosulphides) in their anhydrous form exhibit the antifluorite type structure. The cation is tetrahedrally coordinated whilst the sulphide ion (S^{2-}) is surrounded by eight nearest M^{+} neighbours forming a cube.

3.3.2 Polysulphides

In addition to the monosulphides (M_2S), the alkali metals form polysulphides of the general formulea M_2S_n. The following compounds are well established :-

Li_2S , Na_2S_n (n = 2,4,5), K_2S_n (n = 2-6), Rb_2S_n (n = 2,3,4) and Cs_2S_n (n = 2, 3, 4, 6).

Cleaver and co-workers (56,57) have measured a range of physical properties of molten polysulphides. A pure sodium polysulphide melt has been determined (58)(59) to consist of an equilibrium mixture of S_2^{2-}, S_3^{2-}, S_4^{2-}, S_5^{2-} and S_6^{2-}; the relative amounts of which being dependent upon both the temperature and overall composition.

3.4 Metal Sulphides in General

3.4.1 Introduction

Virtually all of the known metal elements react with sulphur in various proportions to form sulphides and polysulphides. In addition to laboratory produced compounds a whole range of mineral sulphides exist many of which are industrially important. Many books and review articles are available covering the many diverse properties of these compounds; including structure (60-62), structural classification (63), electrical properties (64,65), spectroscopic data (66) and thermochemistry (67).

Two particularly relevant areas of interest will be reviewed here a) structure and b) electrical properties.

3.4.2 The Structures of Metal Sulphides

A wide range of structures and stereochemistries are exhibited by metal sulphides. Generally many minerals are crystalline solids and may be represented using ionic models, in which the ions are considered to be charged spheres of definite radii.

The most common coordination polyhedra of metals in sulphides are tetrahedra and octahedra and distortions thereof. The cations Zn^{2+}, Ga^{3+}, As^{5+} and Sb^{5+} are nearly always tetrahedrally coordinated by sulphur whilst In^{3+} and Sn^{4+} may occur in either tetrahedral or octahedral environments.

Sulphide ions commonly prefer asymmetrical surroundings which leads to the marked structural differences between sulphides and the corresponding oxide system; the oxide ion being much less polarizable. The ability of sulphur atoms to form S-S bonds (as in pyrite) is much

less important in the oxide systems (but see Cu_2O , ZnO_2). Simple monosulphides with the sodium chloride (e.g. PbS) and zinc-blend (e.g. β-ZnS. CdS) structures are analogous to their oxides. In the case of the above groups, both cations and anions have octahedral and tetrahedral coordination and may be described as close-packing of sulphide ions with the cations situated in octahedral or tetrahedral interstices. Many other sulphides can be described in terms of the packing of sulphide ions. Wells (60) has classified the sulphide structures (Table 3.1) although more detailed classifications are available in the literature (see ref. 66).

The sodium cloride structure is perhaps the best known of all crystal structures (Fig. 3.1). Both lead sulphide (galena) and calcium sulphide exhibit this structure. The structure is based on cubic close packing of the anions in planes parallel to the (111) direction; both anions and cations are in regular octahedral six-fold coordination (68). The M-S distance in galena is 3.1Å. The homogeneity of PbS and its semiconducting properties have been studied in detail (69)(70). At a pressure of 25 K bars it undergoes a phase transition (71) and may possibly have the SnS structure. A large group of complex lead sulphide containing minerals of general composition $xPbS.\ yM^3_2\ S_3$ (M^2 = As, Sb, Bi for example) and their derivatives containing Cu or Ag exist and have been discussed (72).

The sphalerite (β- ZnS) structure is also one of the fundamental structure types. The structure was determined in the early X-ray diffraction experiments of Bragg, and consists of a unit cube with Zn atoms at the corners and face centres (Fig 3.2); the four sulphur atoms within each unit cell are coordinated such that each tetrahedron of zinc atoms and each Zn^{2+} ion at the centre of a regular

Table 3.1: The Crystal Structures of some Sulphides

Type of Structure	Coordination number of M and S	Name of Structure	Example
Infinite	4:8	Antifluorite	Li_2S, Na_2S, K_2S, Rb_2S
3-dimensional complexes	6:6	Rock Salt	MgS, CaS, BaS, MnS, PbS
	6:6	Nickel Arsenide	FeS, CoS, VS, FeS_2
	6:6	Pyrites or Marcasite	NiS_2, MnS_2, FeS_2, CoS_2
	4:4	Zinc-blend Wurtzite	BeS, ZnS, CdS, ZnS, CdS, MnS
	4:4	Cooperite	PtS
Layer structure	6:3	Cadmium Iodide	TiS_2, ZrS_2, SnS_2, PtS_2
	6:3	Molybdenum Sulphide	MoS_2, WS_2
Chain structure			Sb_2S_3, Bi_2S_3, SiS_2
Molecular structure			All sulphides consisting of finite molecules

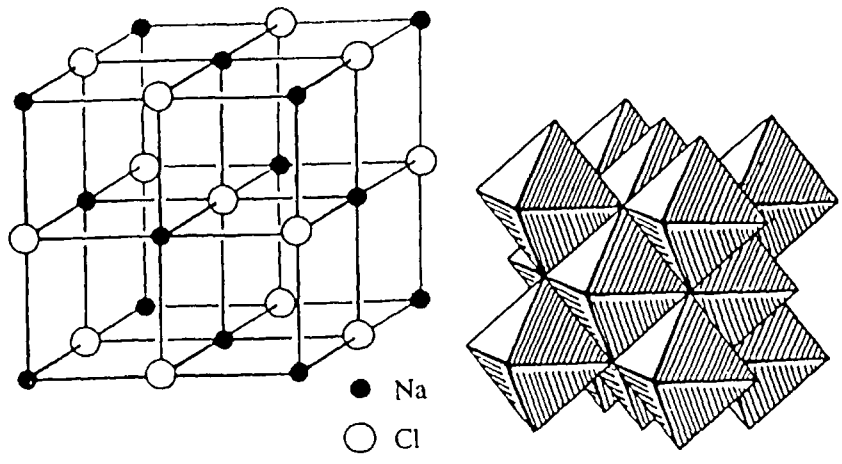


Fig. 3.1: The crystal structure of galena (PbS) or halite (NaCℓ) structure showing the coordination of ions and the linking of octahedral units.

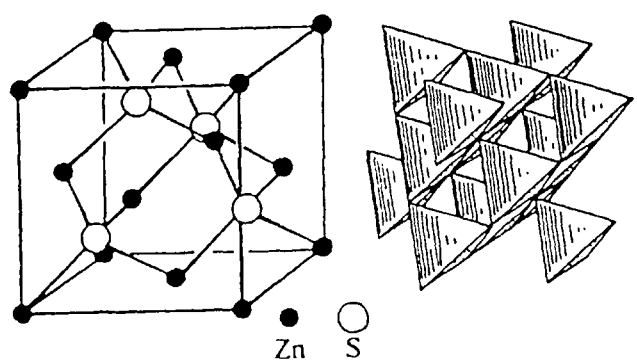


Fig. 3.2: The sphalerite (β-ZnS) structure showing the coordination of ions and the linking of tetrahedral units.

sulphur tetrahedron. Chalcopyrite ($CuFeS_2$), an important sulphide mineral exhibits this structure (73,74). The disulphides ZnS_2 and CdS_2 (with pyrite structure) have been prepared at high pressures (75), and both cations form amorphous polysulphides.

A closely related structure to that of sphalerite is the hexagonal α-ZnS or Wurtzite structure (77)(78). As in sphalerite each atom is tetrahedrally surrounded by four atoms of the other kind, but the arrangement of the tetrahedra is such that a lattice of hexagonal rather than cubic symmetry is formed.

The hexagonal NiAs structure is one of the most important structures in transition metal chemistry; indeed over 100 compounds crystallise with this structure (Fig. 3.3). The cations and anions lie respectively on interpenetrating simple hexagonal and close-packed hexagonal sublattices. The transition metal atoms occupy all octahedral holes in the close-packed hexagonal array of anions; the anions are surrounded by 6 transition metal atoms in the form of a trigonal prism. The NiAs structure has two important features:-

(a) the ability to accomodate additional transition metal atoms in the trigonal bipyramidal holes at a maximum composition of M_2X.

and (b) to omit metal atoms, either randomly or on planes perpendicular to the c-axis until the $Cd(OH)_2$-type structure is reached.

The true NiAs structure has been shown to be mainly a high temperature/high pressure phase (66) which is rarely retained at low temperatures; for example FeS, CoS and NiS have a true NiAs structure at high temperatures and a slightly distorted one at low temperatures.

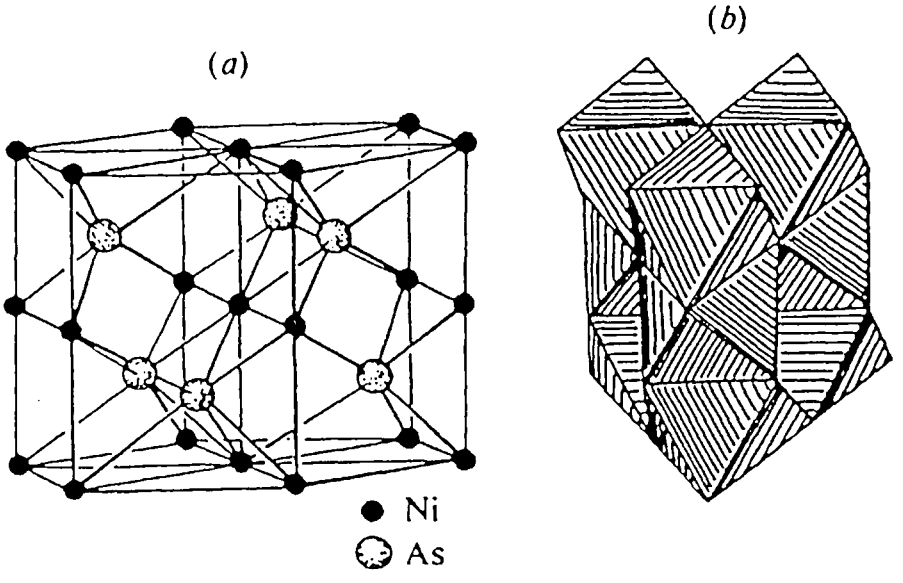


Fig. 3.3: The NiAs-type structure showing

(a) linkage of ions in a unit cell;

(b) stack ing of octahedral units

Probably FeS is one of the most important compounds exhibiting this structure and the metal-deficient iron sulphides which make up the pyrrhotite group. A comprehensive review of the NiAs and related phases has been published by Kjekshus and Pearson (79).

The $Cd(OH)_2$ structure type (also known as the $Mg(OH)_2$ or CdI_2 structure) occurs in many minerals e.g. MoS_2 (80) and Covellite (CuS). The latter contains layers which are nets of planar CuS_3 triangles (81).

Other important structure types are those of the metal-excess group in which a large number of unique crystal forms exhibiting M-M bonding; e.g. Ni_2S_2, AgS_2 and the copper sulphides Cu_2S, $Cu_{1.96}S$, $CuqS_5$ and Cu_5FeS_4 (66).

Non-stoichiometry in metal sulphides is particularly prevelant; the general theories of this phenomenon have been considered by Wadsley (82), Anderson (83) and Fender (84).

3.4.3 Electrical Properties of Metal Sulphides

The great diversity of electrical and magnetic properties exhibited by the metal sulphides has both scientific and practical application.

To the mineral technologist they offer methods for benefication and extraction of metals; whereas to the applied physicist they are a class of compounds important to the electronics industry.

As pointed out by Jellinek (72) all sulphides of main group (i.e. non-transition) including Zn,Cd, Hg are diamagnetic insulators or semiconductors; this is because the valence and conduction bands are respectively filled and empty and do not overlap. Galena (PbS)

and Sphalerite (ZnS) are the two most important examples of this group of sulphides. For the case of transition metal sulphides, the electronic structures and hence the magnetic and electrical properties are complicated by the presence of 'd' electrons (85).

Galena is a diamagnetic semiconductor, and its properties have been reviewed by Dalken (86). The forbidden energy gap of PbS at 300K is 0.41 eV (87). A simplistic representation of the type of band structure found in galena is shown in Fig. 3.4; although its structure is known in detail. The conduction mechanism and carrier concentrations (as in the case of all such compounds) are very sensitive to both precise stoichiometry and impurity levels. Thus, slightly metal rich PbS with n-type semiconductivity or sulphur rich (p-type) are readily synthesised. Most natural galenas exhibit n-type conductivity although carrier concentrations are strongly influenced by the presence of Ag, Bi and Sb (88).

Pure ZnS is a diamagnetic semiconductor although the band gap is sufficiently large that it is sometimes described as an insulator. The forbidden energy gap has been reported to be between 3.2-3.9 eV at 300K (89)(90). An increase in pressure has been found to decrease the forbidden energy gap (91) and also by the substitution by Cd or Ag ions. The mechanism of intrinsic semiconduction in ZnS may be p- or n-type depending upon the stoichiometry (92)(93); sphalerite exhibits p-type and wurtzite n-type. The effect of transition metal impurities upon the magnetic and electrical properties of ZnS has been examined extensively (94)(95). Probably the most important substitution is that of Fe in ZnS (natural ZnS may contain upto 20% Fe); addition of substituted Fe substantially reduces the forbidden

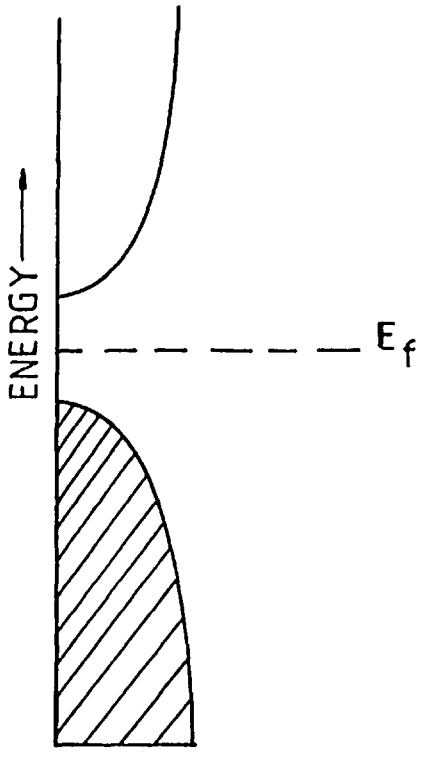


Fig. 3.4: A simplified band model for galena (PbS) is typical of an intrinsic semiconductor at 0K. Energy (E) is plotted versus the density of states. Occupied states shaded and empty states open. E_f = the Fermi level.

energy gap (96). The electrical and magnetic properties of many other sulphides are reported in the literature e.g. MnS_2 (97), FeS_2 (65), NiS_2 (98), Cu_2S (66), FeS (99) and NiS (100).

3.5 Molten Salts

The numerous aspects of molten salt chemistry have been discussed in several books and review articles (101, 102, 103-108, 112, 115, 117). The topics include the thermodynamic studies (101-112), transport properties (101, 102, 104, 105, 108, 109, 113, 114), spectroscopic studies (101, 102, 105, 115, 116), theoretical and structural studies (101-103), electrochemical studies (101, 102, 105, 109, 113, 117-125) and experimental techniques (106, 108, 126-128).

The term molten salts applies to a wide range of liquid compounds and covers a temperature range from about 100°C to over 2000°C. Three main categories may, however, be distinguished:

(a) simple ionic melts, such as the alkali halides,
(b) simple oxy-anionic melts, for example nitrates, and
(c) complex polymeric melts, such as phosphates and silicates.

Ionic melt systems are the most concentrated electrolytes available, which is reflected in the very large number of electrolytic investigations reported. The particular advantages of these electrolytes may be summarized by the following:

1. A wide range of electroinactivity, ie., a large decomposition voltage as compared with other solvent systems.

2. They are good ionic conductors of electricity.
3. Powerful solvents for inorganic materials.
4. Voltage losses due to polarization are small
5. Chemical and electrochemical reactions are generally fast due to the high operating temperatures.

Several fundamental ideas are important for an understanding of the interactions between solute species and the solvent composition. Complex ion formation and acid-base interactions, which may be further interpreted in terms of the S.H.A.B. concept.

The structure of molten ionic salts is one of interlocking anionic and cationic quasi lattices which satisfies the condition of local electrical neutrality. The liquid structure is therefore continuous, and the concept of complex ions in this medium cannot be interpreted in the dilute aqueous sense. Flengas and Kurcharski (129) discussed the difference between a complexed and non-complexed state containing cation M^{n+} and anion X^- as simply a 'shorter' bond distance MX* for the complexed state as compared with MX bond distance for the non-complexed state. Using this definition the continuous structure of the liquid is maintained. The interaction of a ligand X* in a complex MX_n^* with surrounding cations may be diagramatically represented by

$$X^- - A^+ - X^+ \text{——} \begin{matrix} X \\ | \\ M \\ | \\ X \end{matrix} \text{——} X^* - A^+ - X^-$$

where anion X is always a cation bridging species. Therefore the tendency to form complexes depends upon the size of the solvent cation.

The acid-base concept for molten salts was first introduced by Lux and Flood for the molten oxide containing systems (130,131):

$$\text{Acid} + O^{2-} \rightleftharpoons \text{Base}$$

and may be extended to the molten halide systems in the form

$$\text{Acid (acceptor)} + X^- \rightleftharpoons \text{Base (donor)}$$

An acid may be defined as a chloride ion acceptor and a base as a chloride ion donor in the modified Lewis sense. Furthermore, the acid-base theory may be extended to include the S.H.A.B. concept (132, 133), i.e. using the concepts of 'soft' and 'hard' acids and bases. Using this system for example, 'hard' acids are characterized by ions of small size and high positive oxidation state. Thus the effects of solvent cation composition may be explained in terms of a modification of the 'hardness' of 'softness' of the solvent anions.

3.6 Identification of Sulphur Species in Molten Salts.

A knowledge of the exact nature of sulphur species present in sulphur/sulphide containing molten salts is obviously a prerequisite to a quantitative understanding of their electrochemical properties. Thus, numerous investigations have been undertaken using a variety of spectroscopic and/or electrochemical techniques. Although it is the intention to review those studies concerning molten salt solutions, some evidence from aprotic solvents is given to provide a fuller description of the solvated sulphur species.

The characteristic blue colour of the molten potassium thiocyanate salt is a well known phenomenon and the absorption spectra has been

measured by several workers (134, 135). Greenberg et al (134) found that the same absorption peak occured with solutions of sulphur in KSCN, LiBr - KBr and LiCl - KCl, thus inferring that the same sulphur species was responsible for the blue colour. Both groups of early workers, Greenberg et al (134) and Lux and Anslinger (135) postulated a neutral sulphur species (S_2) to be responsible for the blue colouration. It has subsequently been shown, quite clearly, by Plambeck and Bodewig (136) that both sulphur and sulphide must be present before the blue colouration is observed. The same authors demonstrated that sulphur is quite insoluble in the molten LiCl - KCl eutectic melt (137). The extensive spectroscopic investigations by Giggenback (138, 139) in both aprotic (138) and molten salt systems (139) concluded the blue colour was due to the S_2^- ion. In alkali-halide and sulphate melts; the observed colour disappears below 400°C and was attributed to the dimerization reaction:

$$2S_2^- \rightleftharpoons S_4^{2-}$$

Recent investigations by Greun et al (140) found the species S_2^- and S_3^- predominate in equilibria in the LiCl - KCl melt at 600°C. For sulphur/sulphide solutions they propose the two equilibria between sulphur and sulphide as:-

$$2S^{2-} + 2S_2 \rightleftharpoons 4S_2^-$$

and

$$2S^{2-} + 5S_2 \rightleftharpoons 4S_3^-$$

The characteristic blue colour (600mm) was further concluded to be due to the S_3^- ion and the green colour to the S_2^- ion. In the aprotic solvent DMSO, Martin et al (141) have demonstrated using spectrophotometric and electrochemical evidence for various polysulphides in the above solvent that the S_3^- ion was responsible for the blue colouration. However, Giggenback (142) has attributed the blue colour to the S_2^- ion in both DMF and DMF-H_2O mixtures.

Mamantov et al (143) investigated the solution chemistry of sulphur in chloroaluminate melts using Raman spectroscopy. A single band at $218cm^{-1}$ was observed for sulphur in a 63 - 37% ($AlCl_3$ - NaCl) solution at 175^oC. Three further bands at 476, 215 and 149 cm^{-1} were observed upon increasing the temperature to 250^oC; they were not due to the solvent species $AlCl_4^-$ and $Al_2Cl_7^-$. The predominant sulphur species in solution was attributed to the S_8 molecule, the solubility of which increases with both temperature and the Lewis acidity of the solvent.

3.7 The Solubility of Metal Sulphides in Molten Salts.

Several recent studies have determined the solubilities of Li_2S and the solubility products of FeS_2 and PbS in the LiCl - KCl and LiCl - LiF eutectic mixtures. Potentiometric titrations were used.

Lo/ et al (144), using an Ni/NiS (1:1 mole ratio) electrode demonstrated that sulphide (S^{2-}) could be successfully generated (coulometrically) into a LiCl - KCl eutectic. The same authors further demonstrated the system Ni/NiS/S^{2-} cell to behave as an electrode of the second kind obeying the Nernst equation:-

$$E = E^{o}_{NiS-Ni} - \frac{RT}{2F} \ln a_{S2-}$$

The solubility product of NiS was calculated using the relation

$$E^{o}_{NiS-Ni} = E^{o}_{Ni(II)-Ni} + \frac{RT}{2F} \ln K_{SP}$$

The Ni/Ni electrode was successfully used by Lui et al (144) to measure the solubility of Li_2S over the temperature range 375-475^{o}C. The results for both NiS and Li_2S are shown in Table 3.2.

The solubility of Li_2S and the solubility product of FeS in the LiCl - KCl melt over the temperature range 673-773^{o}K has been determined (145). Potentiometric titration based on the reaction

$$Li_2S + FeCl_2 \rightarrow FeS(\downarrow) + 2LiCl$$

using the cell

$$Ag \mid AgCl - LiCl - KCl \parallel LiCl - KCl\ (eut) - FeCl_2 - Li_2S \mid Fe$$

was used. The results are shown in Table 3.2. Blander and co-workers (146) have subsequently measured the solubility product of PbS in the LiCl - KCl and the LiCl - LiF eutectic melts using the cell.

$$Ag \mid AgCl + Eut \parallel Eut + PbCl_2 + Li_2S \mid Pb(l)$$

The results of the above investigations are compiled in Table 3.2.

Cleaver et al (147) found Na_2S to be insoluble in the LiCl - KCl melt at 450^{o}C based upon the absence of any detectable voltammetric waves.

Table 3.2: Measured solubilities of Li_2S (Mole Fraction Basis), solubility products of PbS (Ion Fraction Basis) in the LiCℓ-KCℓ and LiCℓ-LiF Eutectics

(1) reference (145,146) (2) reference (144)

T,K	Li_2S(1)	Li_2S(2)	PbS(1)	Solvent
673	0.95×10^{-3}	0.67×10^{-3}	7.3×10^{-13}	LiCℓ-KCℓ
723	1.56×10^{-3}	1.3×10^{-3}	3.9×10^{-12}	"
773	2.5×10^{-3}	2.0×10^{-3}	2.2×10^{-11}	"
823	3.5×10^{-3}		1.0×10^{-10}	"
823	1.95×10^{-2}		6.8×10^{-11}	LiCℓ-LiF

Table 3.3: Calculated solubility products (Ion Fraction Basis) of some sulphides in the LiCℓ-KCℓ eutectic (from reference (146))

Metal	K_{SP}
Ag(1)	3.17×10^{-16}
Cu(1)	1.72×10^{-16}
Cr(11)	3.18×10^{-11}
Fe(11)	2.98×10^{-12}
Mg(11)	1.70×10^{-9}
Mn(11)	2.86×10^{-11}
Ni(11)	4.2×10^{-16}
Pb(11)	3.22×10^{-12}
Ti(11)	6.29×10^{-16}

Blander (146) has discussed in detail the steps involved in calculating the solubility products of metal sulphides in molten chloride solvents from thermodynamic principles using an exact cycle. The three main steps involved may be written as:-

1. $MS + 2LiCl\ (Eut) \rightleftharpoons MCl_{2(l)} + Li_2S_{(s)}$

2. $MCl_{2(l)} \rightleftharpoons MCl_2\ (\infty\ diln:\ Eut)$

3. $Li_2S_{(s)} \rightleftharpoons Li_2S\ (\infty\ diln:\ Eut)$

where M is a divalent metal.

The solubility product of the sulphide MS, is then given by the equation:-

$$-RT \ln K_{SP} = \Delta G_1 + \Delta G_2 + \Delta G_3$$

Using these principles Blander (146) has calculated the solubility product K_{SP} for many metal sulphides in the LiCl - KCl eutectic mixture, these are given in Table 3.3; similar reasoning was used to explain the solvent effect on solubility and solubility products.

3.8 Molten Mixtures of Halides and Chalcogenides.

3.8.1 Introduction

A knowledge of the solution chemistry of molten halide/chalcogenide mixtures is particularly pertinent to this work. A recent, comprehensive review by Brookes (148) is available, detailing the properties of a wide range of chaleogenide/halide mixtures with particular emphasis upon structural understanding. This section of the literature survey will, however be confined to a description of

the physical properties of molten metal sulphide-metal chloride systems with a common cation. In particular the molten mixtures Ag_2S - AgCl, PbS - $PbCl_2$, Cu_2S - CuCl and FeS - $FeCl_2$.

3.8.2 Ag_2S - AgCl Mixtures

The phase diagram for the Ag_2S - AgCl system has been determined by Flengas et al (149) using cooling curves, and by Blachnik and co-workers (150) using the D.T.A. method; both are in good agreement. The phase-diagram shows a single eutectic occuring at 35.8$^m/_o$ Ag_2S at a temperature of 377^{o}C. At approximately 50$^m/_o$ composition a weak, incongruently melting compound of unknown composition was found (149), however this has not been confirmed by subsequent investigations (150, 151). Dilute solutions of Ag_2S (8$^m/_o$) were found (from cryoscopic calculations (149), to be adequately described by the simple Temkin model for ionic liquids.

Solutions containing more than 8$^m/_o$ Ag_2S showed positive deviation from ideality. Silver sulphide rich solutions could not be described in terms of a simple, completely dissociated, ionic liquid and evidence for covalent association was inferred. The measured densities and calculated molar volume isotherms (149) indicated ideal behaviour (as do AgBr - Ag_2S mixtures (152), although negative deviations occured at temperatures greater than 750^{o}C. The activities of both AgCl and AgBr in molten Ag_2S, as determined by mass spectrometry indicated positive deviations from ideality (153).

Electrical conductivity measurements (154) have shown pure, liquid AgCl to be ionically conducting with a very low activation energy for conductance (1.35 at 500^{o}C). In the case of solutions containing more than 20$^m/_o$ Ag_2S the conductivity was found to rise

rapidly with both increasing temperature and increasing sulphide concentration; thus representing the onset of electronic conductivity. Above $50^{m}/_{o}$ Ag_2S an extreme increase in conductivity occurs due to structural changes in the melt markedly influencing the electron mobility.

3.8.3 $PbCl_2$ - PbS Mixtures

The phase relations, densities and conductances for the molten $PbC\ell_2$ - PbS mixtures were investigated by the Flengas group (155, 156).

The croscopic data obtained from cooling curves indicated pure molten PbS to be dissociated and that pure $PbCl_2$ contained ions other than Cl^- and Pb^{2+}. Dilute solutions of PbS in $PbCl_2$ (upto $12^{m}/_{o}$) were found to have positive deviations from ideality. Comparison with other reciprical $PbCl_2$ containing melts (i.e. $PbCl_2$ - NaF; $PbCl_2$ - KBr) and to systems with a common ion e.g. $PbCl_2$ - NaCl similarly showed positive deviation. The $PbCl_2$ - NaCl mixture was found to be virtually ideal. It was therefore concluded that the positive deviations were due to the tendency of $PbCl_2$ to associate in the liquid. Calculated molar volume isotherms also indicated slight positive deviation from ideality. Determination of the phase diagram (155) by the cooling curve method revealed a single, simple eutectic system; the eutectic occuring at $20^{m}/_{o}$ PbS at a temperature of $450^{o}C$. Pelton and Flengas (157) have similarly investigated the phase relations of lead sulphide - alkali chloride mixtures (MCl = NaCl, KCl, RbCl and CsCl). A large range of liquid immiscibility was found in all the systems; they behaved as quasi-binary solutions. Monoeutectic temperatures were found to be

independent of the PbS concentration and to occur within $1^{o}C$ of each other for the four alkali chlorides considered. The results of decantation and chemical analysis studies showed a distinct trend towards increasing PbS solubility as the alkali cation size increased i.e. from NaCl → CsCl, see Table 3.4. The measured solubilities were found to be relatively small and thus these solutions may be expected to be pure ionic conductors.

The electrical conductivities of PbS - $PbCl_2$ molten mixtures was measured by Flengas and Bell (156). Lead chloride rich solutions, at temperatures ranging from 500-860^{o}C showed a decrease in specific conductivity with increasing PbS concentration (Fig. 3.5a; reaching a minimum at approximately $40^{m}/_{o}$ PbS at all temperatures. A rapid increase in specific conductivity was found to occur at higher temperatures viz ~900^{o}C and at about 60-65$^{m}/o$ PbS (Fig. 3.5b; reaching values of 110 - 120 $ohm^{-1}cm^{-1}$ the value reported for pure molten PbS. All the PbS melts were found to have a positive temperature dependence of specific conductivity, unlike the Ag_2S - AgCl system which showed a typical metallic dependence for solutions containing more than $50^{m}/o$ Ag_2S. This difference between the two systems may be due to the greater ionic bonding of the PbS.

The measured conductivities for mixtures upto $36^{m}/o$ PbS may be described by the quadratic equation:-

$$K = a + b\ (T^{o}C - 500) - c\ (T^{o}C - 500)^{2}$$

In order to determine the effect of dissolved lead metal upon the electronic conductivity, initial solubility measurements were required (156). In pure $PbCl_2$ the solubility of Pb was very small

TABLE 3.4

Solubilities of PbS in various alkali-halides. The Effect of alkali cation and increasing temperature. Data evaluated from the results of Flengas and Pelton (157).

$T^{o}C$	Na^{+}	K^{+}	Rb^{+}	Cs^{+}
		molas / ℓ		
850	0.23	0.60	0.91	0.48
900	0.25	0.67	1.22	0.80
950	0.4	0.8	1.55	1.18
1000	0.65	1.2	1.86	1.79
1050	0.92	1.68	2.19	2.56
1100	1.20	2.22	2.50	3.36
1150	1.48	2.78	2.82	4.16

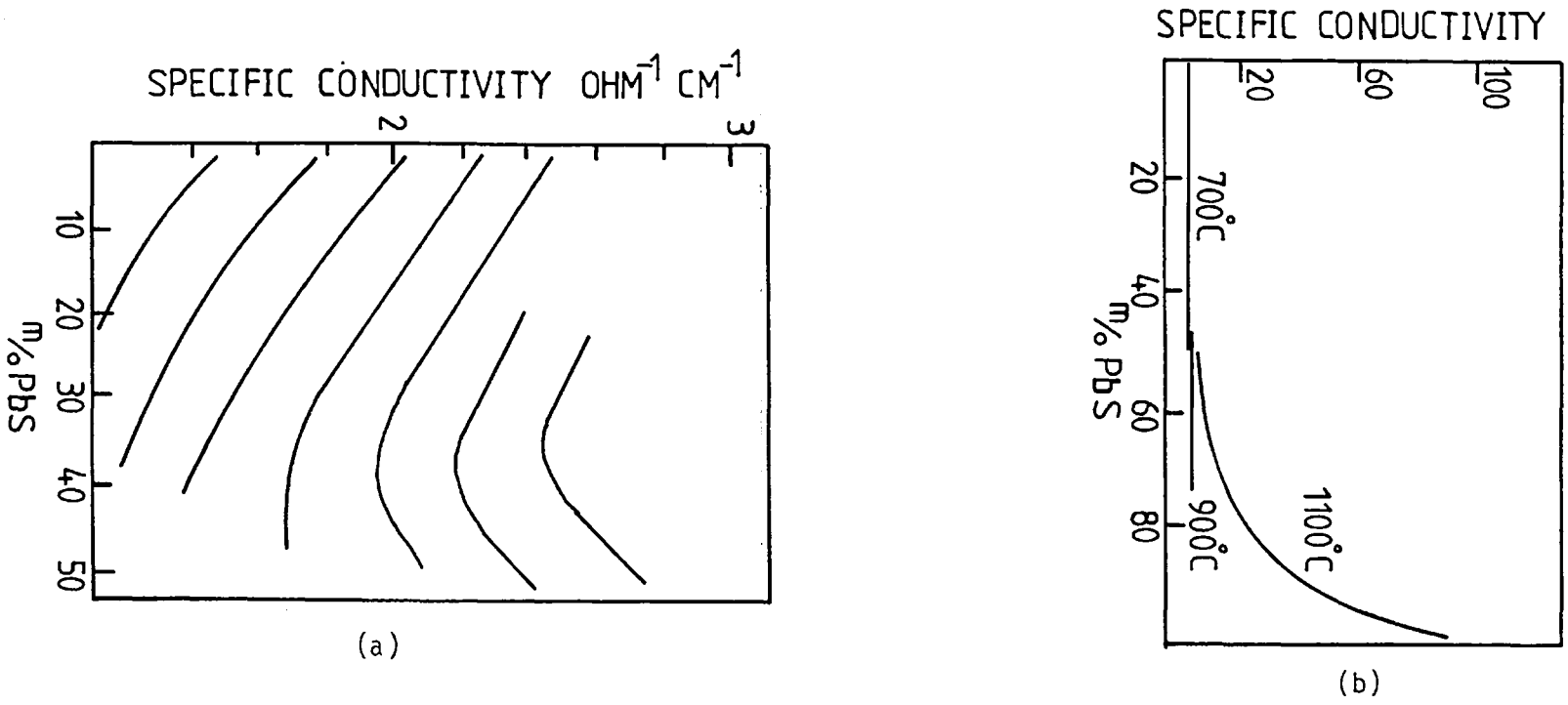


Fig. 3.5 (a), (b): The specific conductivity (ohm^{-1} cm^{-1}) as a function of $^{m}/_{o}$ PbS for the system PbS-$PbC\ell_2$ (from reference [156])

viz 0.008^{m}/o at 583^{o}C - 0.056^{m}/o at 886^{o}C. The effect of increasing temperature and/or lead sulphide concentration was to increase metal solubility, viz 0.65^{m}/o in 50^{m}/o PbS at 886^{o}C. Only a small increase in the electronic conductivity of PbS - $PbCl_2$ - Pb melts was observed; thus establishing that soluble lead was not acting as an electron donor to the system.

3.8.4 Cu_2S - CuCl and FeS - $FeCl_2$ Mixtures

Garbee and Flengas (158) have measured the density, molar volumes, phase relations and electrical conductivities of the molten mixtures Cu_2S - CuCl and FeS - $FeCl_2$.

The Cu_2S - CuCl phase diagram was found to be of the simple eutectic type; the eutectic occuring at 12.1^{m}/o Cu_2S and at a temperature of 389.5^{o}C. The measured liquidus was in poor agreement with previous workers (159) by some 60^{o}C.

A single eutectic occured in the FeS - $FeCl_2$ system (upto 40^{m}/o FeS) at 674^{o}C and at 2^{m}/o FeS. The solubility of FeS in $FeCl_2$ was found to be very limited as measured by decantation and chemical analysis methods, viz 0.032^{m}/o FeS at 697^{o}C - 0.138^{m}/o FeS at 898^{o}C.

Cryoscopic calculations on the copper system indicated positive deviations from ideality upon increasing Cu_2S concentrations. It was inferred, from the above calculations that $(Cu_2S)_2$ dimers were present in solution; and for mixtures upto 5^{m}/o Cu_2S it was estimated that 80% of the Cu_2S was present in this form. Molar volume isotherms for the copper system showed a prominent minimum to occur at approximately 30^{m}/o Cu_2S at 1000^{o}C and was found to shift to lower Cu_2S concentrations as the temperature decreased. The electrical conducti-

vity measurements of the Cu_2S - CuCl systems were found to be in excellent agreement with earlier workers (160, 161). A non-linear increase in the conductivity of pure CuCl, (reaching a maximum at 950^oC) with increasing temperature was observed. The magnitude of the conductivity was typical of an ionic conductor. For temperatures upto 700^oC, the addition of Cu_2S to liquid CuCl resulted in a decrease in the conductivity of the solution reaching a minimum and then rising significantly. A rapid increase in the specific conductivity was observed at high temperatures and when the sulphide content exceeded $30^m/o$ Cu_2S and represents the onset of electronic conductivity at 1000^oC. The composition found for the onset of electronic conductivity by Flengas and Garbee (158) is not in good agreement with the results of Derge and Pound (162). The latter workers considered mixtures below $50^m/o$ Cu_2S to be ionic conductors even at 1200^oC.

3.9 The Electrochemistry of Sulphur and Sulphur Species in Molten Salts

3.9.1 Introduction

The electrochemical behaviour of sulphur and sulphur species has been investigated using a variety of solvents, aqueous (163-166) and molten inorganic liquids including pure polysulphides melts (167 - 170), cyanide (147) and chloride based melts (171-177). A recent, comprehensive review by Ludwig and Tisher (170) describes the electrochemistry of sulphur species in non-aqueous media.

A brief review of the literature concerning halide solvents is given here; the reader is referred to those references above for details concerning other solvent systems.

3.9.2 The LiCl - KCl Eutectic Solvent

The early voltammetric studies of sulphide solutions in the LiCl - KCl eutectic melt made by Delarue (171), attributed the oxidation of sulphide to an anodic wave with a half wave potential $E_{\frac{1}{2}} = -0.45$ (vs Pt/Pt^{2+} 1M reference electrode). This has not been confirmed by more recent workers (see below) and may possibly be attributed to the 'poorly' purified melt used.

Voltammetric investigations by Bodewig and Plambeck (137) when sulphur only was present in the melt, found a single cathodic wave on graphite at -0.92V and an anodic wave at +0.03V (vs Pt/Pt^{2+} 1M). The anodic wave was suggested to be due to the formation of sulphur chloride via the reaction

$$2S + 2Cl^- \rightarrow S_2Cl_2 + 2e$$

Unfortunately, repeated attempts to collect the sulphur chloride product were unsuccessful. Sulphur/sulphide solutions (the sulphide being coulometrically generated from a sulphur pool) gave linear i-v relationships under stirred conditions. The slope of these lines gave a cell resistance of 10-15 chms. A single anodic chronopotentiogram was obtained in sulphide containing solutions at a gold electrode and was attributed to the reaction

$$S^{2-} \rightarrow S + 2e$$

Reasonable fit to the Sand's equation held and by further assuming an n = 2 reaction a diffusion coefficient of $D = 3.12 \times 10^{-6}$ cm^2 s^{-1} at 420^oC was obtained; a value much lower than is normally determined for species in molten salts. During their work both platinum and

tungsten electrodes were found to be unsatisfactory; for the case of platinum an insoluble PtS film was produced.

Adamo and Kennedy (172) studied the electro-reduction of sulphur using cyclic voltammetry and controlled potential coulometry at a gold electrode at 420°C. The sulphur was added to an isolated (fritted) working electrode compartment as pellets. Cyclic voltammetry showed two reduction waves to occur with peak potentials of -1.0V and -1.3V; upon reversing the scan direction two reoxidation waves were observed at -1.10 and -0.83V (vs S.M.P.E.). The processes were not found to be strictly reversible according to the peak seperation criteria (i.e. $\Delta E = E_p^c - E_p^a \neq 132/n$ at 420°C). Controlled potential electrolysis for each of the reduction waves resulted in an n = 1 value for both processes. Based upon the similarity with results obtained in the DMSO solvent, Kennedy and Adamo postulated a general reaction mechanism:

$$S_n \xrightarrow{+\ 1e^-} S_n^- \xrightarrow{1e^-} S_n^{2-}$$

where $n \lesssim 2$.

It is interesting to note that during both the voltammetric and constant potential electrolysis of the first reduction wave the characteristic blue colouration was observed in the solution immediately adjacent to the working electrode. The most likely reaction mechanism would be:-

$$S_4 + e^- \rightarrow S_4^-$$

$$S_4^- + 3e \rightarrow 2S_2^{2-}$$

The deep blue colour was found to disappear upon electrolysis at a potential corresponding to the more cathodic process; upon electrolysis at a potential of the first anodic wave the blue colour reappeared and upon further oxidation sulphur was formed.

Birk and Steunenberg (173) employed cyclic voltammetry to investigate the oxidation and re-reduction of Li_2S (0.002 - 0.065 $^m/_o$) in the LiCl - KCl eutectic. A graphite working electrode was used and the effect of increasing sweep rate (6.6 - 660mV s^{-1}), Li_2S concentration and temperature (410 - 462^oC) were obtained. In general two oxidation and three reduction waves were observed; the following corresponding reactions were proposed:-

Anodic

1. $2S^{2-} \rightarrow S_2^{2-} + 2e$
2. $S^{2-} \rightarrow 2S + 2e$

Cathodic

$$3S + S^{2-} \rightleftharpoons 2S_2^- \rightleftharpoons S_4^{2-}$$

1. $2S + 2e \rightarrow S_2^{2-}$
2. $S_2^- + e \rightarrow S_2^{2-}$
3. $S_2^{2-} + 2e \rightarrow S^{2-}$

Kam and Johnson (174) subsequently reinvestigated the oxidation of Li_2S packed into a hole in a carbon support at a temperature of 450^oC . The results obtained did not agree with those of Birk and Steunenberg (173); three oxidation waves were observed at -1.22, -0.91 and -0.41V vs SMPE via cyclic voltammetry. Repetitive cycling indicated a further oxidation process to occur at -1.45V. Assuming all the above processes to be simple diffusion controlled reactions an n = 1 for the processes at -0.91 and -0.4V and an n = 1-2 for the process

at -1.22V was calculated. The general reaction sequence was proposed.

$$2S^{2-} \rightleftharpoons S_2^{2-} + 2e$$

$$S_2^{2-} \rightleftharpoons S_2^{-} + e$$

$$S_2^{-} \rightleftharpoons 2S + e$$

The general morphology of the voltammograms was the same over the the temperature range 420 - 450^{o}C. The cyclic voltammetry results obtained by Raliegh et al (175) using both stationary and rotating graphite, Pt and Mo electrodes in a Li_2S saturated melt at 450^{o}C support the observations of Birk and Steunenberg, (173). It is interesting to note that the former authors consider all three electrodes to be suitable for the study of metal sulphide redox processes.

Bernard et al (176) employed both chronopotentiometry and adsorption spectroscopy to elucidate the electrochemical behaviour of CaS in the LiCl - KCl eutectic. Three oxidation processes were observed with quarter wave potentials of -0.2, -0.1 and +0.3V (vs. Ag/Ag^{+}) and a single reduction process at $E_{\frac{1}{4}}$ = -0.5V. The three oxidation products were attributed to the species, S^{-}, S_x and S^{+} with corresponding adsorption bands at 320, 390 and 590 nm.

Cleaver et al (147) have mainly investigated the electro-oxidation and reduction of alkali metal polysulphides in fused KSCN although some results were obtained using the LiCl - KCl eutectic. Platinum electrodes were generally found to be unsatisfactory due to the formation of a black PtS film; gold electrodes were preferred. The addition of anhydrous Na_2S was found to be

practically insoluble in this melt at 420°C, higher polysulphides were unstable resulting in the immediate evolution of gaseous sulphur. Addition of $Na_2S_{2.2}$ however formed solutions which were stable long enough to record cyclic voltammetric data. The lime-green solution gradually lost sulphur. Two oxidation and reduction waves were observed. A sharp sulphur deposition wave at +0.2V (w.r.t. Ag/Ag_2S) and a second wave at -0.2V. The first oxidation wave was assigned to the reaction

$$S_2^{2-} \rightarrow S_2^{-} + e$$

Both oxidation and reduction processes were found to be diffusion controlled (i_p vs $v^{\frac{1}{2}}$ criterion) and an apparent diffusion coefficient for the S^{2-} ion was calculated as 5.7×10^{-5} cm^2 s^{-1} assuming $n = 1$.

The chronopotentiometric oxidation and potentiometric behaviour of nominally Na_2S solutions in a LiCl - KCl eutectic at several electrode substrates (vitreous carbon, gold and platinum) was studied by Weaver and Inman (177).

The sodium sulphide was found to dissolve in the melt quite readily and well defined open-circuit potentials were obtained on all electrodes thus clearly indicating the presence of a redox couple. The yellow coloured solution probably indicates the presence of sulphur as an impurity element in the sodium sulphide. The potential was found to be linearly dependent with the nominal Na_2S concentration and a two electron (2.3 RT/2F) Nernst slope was determined. The Nernstian behaviour was interpreted in terms of the redox equilibrium $2S^{2-} \overset{-2e}{\rightleftharpoons} S_2^{2-}$.

Complex electrode behaviour was observed by Weaver and the chronopotentiometric data was interpreted in terms of sulphur film formation. The sulphur film was thought to back react with the sulphide ion to form a polysulphide S_x^{2-} which could subsequently diffuse into the bulk solution. A soluble product passivation model was involed to explain the constant $i\tau^{\frac{1}{2}}$ product at low current densities but with an increasing $i\tau$ at higher current densities. Good agreement with the Sand's equation was observed and a calculated diffusion coefficient of 3.4×10^{-5} cm^2 s^{-1} was obtained. Analysis of the potential-time plots generally indicated a two electron transfer process. Frequently, quite different anodic behaviour was observed which was attributed to changes in the form of the sulphur film which lead to the formation of species such as S_2^- via a one electron transfer reaction. The concept of the build up of an inhibiting film was further supported by the use of steady-state voltammetry, potential-time galvanostatic build up and open-circuit decay techniques.

3.9.3 The $AlCl_3$ - NaCl System

Many investigations have been concerned with the electrochemical characterization of sulphur and sulphur ions in chloroaluminate melts (183-187). It is well etsablished (178-182) that the acid-base properties of this melt near the 1:1 $AlCl_3$/NaCl mole ratio composition can be described by the equilibrium:-

$$2AlCl_4^- = Al_2Cl_7^- + Cl^-$$

and

$$K_M = [Al_2Cl_7^-]\,[Cl^-] \;/\; [AlCl_4^-]^2$$

The Lewis acidity of the solvent may be expressed in terms of the pCl (pCl = -log $[Cl^-]$). Thus the $Al_2Cl_7^-$ and the Cl^- ions are the dominant Lewis acid and base species respectively. The electrochemistry of sulphur and its ions are dependent to a large degree upon the acidity of the chloroaluminate solvent.

Sulphur solutions are generally a pale yellow colour (175-300^oC) both in the absence and presence of sulphide (S^{2-}) and would therefore tend to suggest that an equilibria producing anionic species such as S_3^- or S_2^- (the species responsible for the blue and green solutions respectively) is absent. Raman investigations (143) of sulphur solutions (see section 3.6) indicated a dominant S_8 species to be present and that the sulphur solubility increases with increasing temperature. The sulphur solubility (as S) in $AlCl_3$ - NaCl (sat) at 175^oC is reported to be less than 2.1 x 10^{-2} molal (186).

Marassi et al (183) studied the electro-oxidation and reduction of sulphur and selenium at a Pt electrode. A single oxidation and two reduction waves were observed; the oxidation wave was found to be quasi-reversible and to occur close to the anodic limit of the solvent. No interpretation was given for the results. The electro-oxidation of sulphur in the $AlCl_2$ - NaCl (63 - 37$^m/o$) solvent over the temperature range 150 - 200^oC was found to be complex (184). Cyclic voltammetry, chronoamperometry and controlled potential coulometry were employed to elucidate the mechanisms involved at Pt, W and vitreous carbon electrodes. Four oxidation processes with four corresponding reduction waves were observed, the voltammetric waves were clearly defined by the use of differential pulse voltammetry. The single reduction wave and its reoxidation process was attributed to the S^{2-}/S redox process; agreeing with the work of

Osteryoung et al (185). Although the first oxidation process could not be resolved easily the variation of the voltammetric parameters with sweep rate suggested a simple process to be involved. The apparent n value involved in this electron transfer step was found to be 0.125 and to be concentration dependent . A mechanism involving the formation of both S_8^+ and S_8^{2+} was involved; the likely reaction being formulated as:-

$$S_8 = S_8^+ + e$$

$$2S_8^+ \rightarrow S_{16}^{2+}$$

$$S_8^+ = S_8^{2+} + e$$

and

$$S_8 = S_8^{2+} + 2e$$

$$S_8^{2+} + S_8 = S_{16}^{2+}$$

The results of the voltammetric log plots giving an n = 1 value and additional spectroelectrochemical studies currently in progress favour the S_8^+ (S_{16}^{2+}) mechanism to be the most likely. The second oxidation process results in an S (1) product (from coulometry); the most probable overall reaction consistent with the electrochemical results in

$$S_8^+ + 8AlCl_4^- = 4S_2Cl^+ + 4Al_2Cl_7^- + 6e$$

The final oxidation process resulted in the formation of S(1V) species, which from Raman spectroscopy studies is believed to be the SCl_3^+ ion. Supporting evidence was obtained by the addition of SCl_3^+ $AlCl_4^-$ to the melt, the same electrochemistry resulted. The overall reaction:

$$S_2Cl^+ + 10AlCl_4^- \rightarrow 2SCl_3^+ + 5Al_2Cl_7^- + 6e$$

was proposed.

Mamantov et al (186) using a NaCl saturated chloroaluminate melt at 175°C containing 1.8×10^{-2} molal sulphur (as monomer) found a single oxidation and reduction wave; being independent of electrode substrate. The limiting current ratios of the oxidation wave to that of the reduction wave was found to be 0.5. The results obtained for sulphur only solutions were supported by those obtained for Na_2S containing melts. Two oxidation processes were observed for the S^{2-} ion and the simple reaction sequence postulated:-

$$S^{2-} \rightarrow S + 2e$$

$$S \rightarrow \tfrac{1}{2}S_2^{2+} + e$$

A generalised model consistent with overall variations of voltammetric parameters is illustrated below and which invokes the fragmentation of sulphur rings initiated thermally or by electron transfer.

$$2Sn \rightleftharpoons \underset{\text{chain}}{\text{Sulphur}} \rightleftharpoons nS_2 - 2e$$

$$2Sn \overset{-2e}{\rightleftharpoons} 2S_n^{+} \rightleftharpoons \underset{\text{chain}}{\text{sulphur}} \overset{nS_2^{2+}}{\underset{-e}{}}$$

Osteryoung et al (185) investigated the electrochemistry of sulphur as a function of melt acidity. The electroreduction of sulphur was found to be a two electron transfer process and to be independent of the solvent acidity. The coulometric titration of Cu(I) into sulphide containing solutions enabled the solubility product of Cu_2S to be determined; a value of 6.8×10^{-5} at 175°C in a basic melt was evaluated. No Cu_2S precipitation was observed in acidic melts, however upon addition of NaCl, Cu_2S precipitation readily occurred. Thus the sulphide activity in acid melts is much lower

than in the basic melts presumably due to the S^{2-} species being complexed in the acid melt. Similar results were obtained with silver. The sulphur/sulphide redox couple showed Nernstian behaviour in both acid and basic solutions giving a slope of RT/4F and was attributed to the couple

$$S_2 + 4e = 2S^{2-} \text{ (at constant pCl)}.$$

At low sulphur concentrations, values lower than the RT/4F line were obtained, an equilibrium with sulphur species containing more than two molecules was thus inferred. The potential of the S/S^{2-} couple was linearly dependent upon solvent acidity, a slope of 3RT/2F being obtained. The overall behaviour of the S/S^{2-} couple suggests the reaction

$$S_2 + 2AlCl_4^- + 4e = 2AlSCl + 6Cl^-$$

to be determining. Because of the change in the copper and silver solubilities with melt acidity, the free S^{2-} activity must be a function of melt acidity. Thus the change in sulphide activity is governed by a reaction of the form:-

$$AlSCl + 3Cl^- = S^{2-} + AlCl_4^-$$

with an equilibrium constant written as:-

$$K = [S^{2-}] [AlCl_4^-] / [AlSCl] [Cl^-]^3$$

Osteryoung et al (187) have subsequently extended their investigations of the acid-base dependence of anionic species to include the ions O^{2-}, S^{2-}, Se^{2-} and Te^{2-}. In general these ions were found to be trichloro bases in acidic melts, the determining equilibrium being

given by the reaction:

$$3Al_2Cl_7^- + X^{2-} \rightleftharpoons AlXCl + 5AlCl_4^-$$

However in basic melts 'these ions become dibases according to the equilibrium

$$2Al_2Cl_7^- + X^{2-} \rightleftharpoons AlCl_2^- + 3AlCl_4^-$$

The relative strengths of the tribases appear to be in the order Te^{2-}, $Se^{2-} < S^{2-} < O^{2-}$.

3.9.4. The $PbCl_2$ - MCl System

Here the electrochemical behaviour of lead sulphide in $PbCl_2$ - MCl (alkali-chloride) solvents, with particular reference to the anodic oxidation reactions will be given. The more applied investigations i.e. electrowinning studies are discussed in section 3.10.

Two oxidation processes (via chronopotentiometry) were observed by Welch and King (188) at a vitreous carbon electrode immersed in a quiescent solution of a molten $PbCl_2$ - NaCl eutectic containing lead sulphide ($6.8 - 41 \times 10^{-5}$ mole cm^{-3}) at 450^oC. The quarter wave potential of the first process was found to be approximately 0.5V w.r.t. a Pb/Pb^{2+} reference electrode, and attributed to the overall reaction

$$PbS \overset{n = 2}{\rightleftharpoons} Pb + \frac{1}{v} S_v \ (g)$$

The quarter wave potential for the second process being 1.05V and was thought to be the formation of sulphur chloride. The sulphur/ sulphide reaction was found to obey the Sand's equation upto a

PbS concentration of 4.1×10^{-4} mole cm^{-3} and is thus diffusion controlled. A diffusion coefficient of 1.13×10^{-4} cm^2 s^{-1} was calculated assuming n = 1 and 2.8×10^{-5} cm^2 s^{-1} for n = 2. Analysis of the E-t profile showed a linear relationship between the potential (E) and ln ($\tau^{\frac{1}{2}} - t^{\frac{1}{2}}$) with slopes ranging from RT/0.95F to RT/1.1F. Steady-state i-v measurements using both galvanostatic and slow potentiodynamic scans (200 mV/min) indicated Tafel behaviour, a limiting current was obtained at high potentials. A decrease in current noted at high overpotentials was attributed to the formation of a solid layer on the electrode surface which dissolved slowly in the melt. An average Tafal constant of RT/1.5F was determined. It is noteworthy that the solid film was not always observed but "required considerable electrolysis to bring about its formation". Galvanostatic electrolysis at 500°C using a melt almost saturated with PbS was conducted to identify the anodic, insoluble product. It was found that relatively high current densities were required to form a film whose morphology was dependent upon the applied current density. The product was found to be highly passivating; however its chemical composition could not be determined. The saturation solubility of anodically generated sulphur in a 7 m/o PbS - $PbCl_2$ - NaCl solution was determined; a value of 5×10^{-4} moles S cm^{-3} at 500°C was obtained. However several assumptions were required to obtain this value.

Recent chronopotentiometric investigations by Skyllas and Welch (189) confirmed the earlier work (188); the oxidation of PbS solutions ($PbCl_2$ - NaCl eutectic) was found to be diffusion controlled and to be described by the general scheme:-

$$A^{2-} \underset{k_b}{\overset{k_f}{\rightleftharpoons}} B + 2e$$

where k_f k_b, k_f and k_b being the forward and reverse rate constants. Detailed current reversal chronopotentiometric studies revealed two reduction transitions; the first reduction corresponded to the oxidation process and the second occurred at a potential of 0.13V positive of the lead reduction. The latter process was found to be independent of the oxidation process but dependent upon the presence of lead sulphide. The ratio of the reverse to forward transition times was found to be less than unity and to be independent upon current density. The increase in the ratio τ_f/t_f with t_f was diagnostic of the generalized reaction:

$$A^{X-} \rightleftharpoons B + ne \qquad B = \text{insoluble product}$$

$$A^{X-} + ZB \rightleftharpoons D$$

Increasing the temperature above the boiling point (444.4°C) did not alter the trend.

The use of an interupt period between the forward and reverse current pulses enabled the rate of the dissolution reaction (by comparison with theoretical relations) to be evaluated; assuming the rate of dissolution to be first order with respect to species A a value of $K = 8s^{-1}$ was obtained. The overall reaction was concluded to be:-

$$S^{2-} \overset{\text{slow}}{\rightleftharpoons} S + 2e$$

$$S + S^{2-} \xrightarrow{k = 8S^{-1}} S_2^{2-}$$

The reduction of sulphur and its solubility in the PbS - $PbCl_2$ - NaCl melt at 430^{o}C has been investigated, again using the chronopotiometric technique (190). The sulphur was generated by two means a) the 'in-situ' electrochemical generation via oxidation of PbS and b) the addition of sulphur pellets. Subsequent chronopotentiometric investigation (after galvanostatic electrolysis of 0.55 x 10^{-3} mole PbS cm^{-3} for 30 mins at 4mA/cm^2) failed to reveal a sulphur reduction process and was taken to confirm the idea of an insoluble sulphur product. However the observed increase in the transition time for the 'pre-lead' process inferred the reduction of polysulphide according to

$$S_{n+1}^{2-} + 2e \rightleftharpoons (n+1)S^{2-}$$

The presence of this process immediately after the addition of PbS to a fresh melt would seem to suggest sulphur impurity. Analysis of the E-t profile suggested the $(n+1)S^{2-}$ species to be present as a Pb containing solution revealed two reduction waves, the more anodic of which was attributed to the dissolution of sulphur. The saturation solubility of sulphur was assumed to be reached when the transition time for this reduction process became constant. Saturation solubilities of 5.4 x 10^{-5} mole S/cm^3 in a 1.2 x 10^{-3} mole PbS/cm^3 solution and 2.3 x 10^{-4} mole S/cm^3 upon increasing the PbS concentration to 2.4 x 10^{-3} mole PbS/cm^3. The investigations conducted by Plichon and co-workers into the electro-oxidation of PbS in the $PbCl_2$ - KCl (77 - 23^{m}/o) using the techniques of double step chronoamperometry (191), a.c. impedance measurements (192) and by controlled potential electrolysis coupled with visible adsorption spectrophotometry (193-194) are in 'broad' agreement with those of Welch and co-workers (188-189). The impedance studies did not, however, provide

any evidence for a passivation mechanism.

3.10 Electrowinning from Metal Sulphide/Metal Chloride Solutions

The electrowinning of liquid metals (Al, Mg, Pb and Zn) from molten chloride electrolytes, including metal sulphide containing salts has been the subject of a recent review by Skeaff (195). Particular emphasis was given to practical aspects including electrolyte composition, cell design and operating conditions with respect to current efficiencies and energy consumptions. Here, however a general discussion of the feasability of winning liquid metals and elemental sulphur by electrolytic techniques is presented.

The feasability of directly electrolysing metal sulphide containing molten salts has been demonstrated on numerous occasions for the systems Pb (199-208), Cu (209), Mo (210) and, Sb (211).

The electrolysis of lead sulphide (galena) dissolved in lead chloride was first proposed by Townsend (196) in 1906). A major patent was subsequently awarded to the National Smelting Company Limited in 1934 (197). The electrolytic processing of lead using molten salt electrolytes was developed to pilot plant scale on several occasions. The first plant was situated at Halkyn in Wales, which produced some 300 tons of lead per year and 40 tons of sulphur using a commercial galena concentrate as the cell feed. Unfortunately the plant was closed down during World War II. Since this time the name Halkyn has become synonymous with the molten salt electrowinning of lead from galena. Subsequent plants were built in Canada and at Port Pirie in Australia; the latter produced 1800 tons of lead per year.

Unfortunately little information is available concerning the operational conditions and parameters used for these plants. Although the lead was reported (198) to be of high purity (99.94%) and that a 'scum' (presumably gangue) developed on top of the electrolyte causing loss of solvent through entrapment during de-scumming. However an interim report by Gibson (199) at National Smelting describes the operation and difficulties encountered of a small scale (0.75 ton) unit cell. Evaluation of two 'brick' cell configurations was attempted viz cylindrical and horizontal types, each unit contained ten graphite electrodes arranged in the bi-polar fashion, thus facilitating internal heating. After prolonged electrolysis, lasting several days no sign of any significant wear of the electrodes was observed. Typically some 1500 lbs of lead could be produced during a $7\frac{1}{2}$ day run with an energy consumption of 777 k.W. Hrs per ton of Pb. Analysis of the electrolytic lead indicated 99.92 - 99.96% Pb. A sulphur condenser was employed on the cover of the cell from which several pounds of sulphur was collected during a run; during earlier experiments sulphur was allowed to burn at the electrolyte surface. Sulphur chloride evolution tended to occur when the operating temperature was less than $570^{o}C$ and upon partial exhaustion of the solute. It was stated that no contamination by sulphur chloride was obtained under 'normal' working conditions. Removal of the gangue material was required during extended electrolysis and various methods were investigated to recover the entrapped lead chloride. The distillation of $PbCl_2$ leaving a residue of ZnS, FeS and SiO_2 was found to be satisfactory; alternative processes were envisaged and the recovery of $PbCl_2$ was not considered a major obstacle. A marked decrease in both lead and sulphur yields were noted with increasing galena concentration viz upto $20^{m}/o$.

A concentration of 5% was recommended for efficient working of the cell. An optimum current density of 400-450 A/ft^2 was proposed by Gibson although higher current densities (660 - 700 A/ft^2) was used in the above studies. The liquid lead was easily and satisfactorily removed by a simple iron tube syphon.

Due to the promising results and the near commercial success of the pilot plant studies many subsequent current efficiency investigations have been conducted on a laboratory scale (200-206). More recent and extensive current efficiency studies have been conducted by Welch and co- workers (204-206). All of these studies were based soley upon cathodic yields and unfortunately corresponding sulphur yields have not been measured. The effect of melt composition, temperature and current density may be summarised:-

1. Improved cathodic yields are obtained at lower PbS concentrations (204).
2. For a given PbS concentration, higher current efficiencies are obtained with high current densities (204).
3. Although the influence of temperature and solvent have not been determined independently. The addition of an alkali chloride reduces the solvent melting point and generally increases the lead yield.
4. The influence of electrode arrangement has shown the incorporation of diaphrams between the electrodes to be beneficial (204).

The above observations are consistent with the concept of back reaction between the electro-generated sulphur and lead (205). The very low solubility of metallic lead in PbS - $PbCl_2$ solutions (198)

would not be an attributing factor. The influence of anionic impurities (207) e.g. SO_4^{2-} upon cathodic efficiency has also been reported.

A variation of the direct electrolytic route has been investigated by the U.S. Bureau of Mines (208) and successful recovery of lead and sulphur could be achieved by using a combined chlorination and electrolysis process utilizing a galena feed. Electrolysis of PbS in $PbCl_2$ - MCl (MCl = KCl, NaCl) melts at 600°C with an anodic current density of 13A/sq in showed the highest cathodic efficiencies (70%) to be obtained with the $PbCl_2$ - NaCl melt; the electrolysis of a pure $PbCl_2$ solvent was relatively straightforward. Maximum sulphur removal from the galena was achieved at 350°C, the incorperation of cold traps into the system enabled the sulphur and sulphur chloride products to be collected. Electrolysis of the lead chloride product was performed in large graphite containers which also acted as the cathode at 600 - 650°C. A cell potential of 11-12V was used with a current density of 12.5 A/cm^2. The lead produced during extended electrolysis (6 hrs) was >99% pure and contained Zn, Fe and Si as the major impurity elements. Current efficiencies were greater than those for electrolytes containing galena. Approximately 99% of the silver impurity could be recovered from the initial electrolysis product as a rich Ag-Pb alloy.

Hoar and Ward have demonstrated the feasibility of recovering liquid copper and gaseous sulphur by electrolysis of Cu_2S anode and cathodes in a $BaCl_2$ solvent at 1100°C (209). The cell may be represented in the form:-

$$Cu,\ Cu_2S \mid BaCl_2 \mid Cu_2S,\ S_2\ (g)$$

During electrolysis sulphur was found to evolve rapidly from the Cu_2S anode, a vigorous reaction with the carbon construction material resulting in the formation of carbon disulphide was observed. Cell modifications, i.e. removal of hot carbon surfaces enabled a pure sulphur product to be collected; no evidence for chlorine contamination (e.g. from Cl_2 or SCl_2) was found from the product analysis. Generally current efficiencies greater than 90% were achieved at current densities of 0.95 A/cm^2. Violent instability of the cell voltages at current densities >1Amp/cm^2 were attributed to the growth and seperation of gaseous sulphur bubbles. Sulphur efficiencies were virtually 100%. The overall electrode reactions may be written as:

Cathode: $2Cu_2S + 4e \rightarrow 4Cu + 2S^{2-}$

Anode : $2Cu_2S \rightarrow 4Cu^{2+} + S_2(g) + 4e$

Garbee and Flengas (158) have successfully electrolysed Cu_2S - CuCl electrolytes to yield copper metal with high current efficiencies. The selective leaching of FeS from FeS - Cu_2S matte in liquid CuCl was also demonstrated and was attributed to the reaction:

$$FeS_{(s)} + 2CuCl_{(l)} \rightarrow FeCl_{2(l)} + Cu_2S$$

which has a Gibbs free energy of ΔG^o = -4100 KJ/mole at 1000°C.

3.11 DISCUSSION

A potentially, viable and clean alternative to the melting of base metal sulphides is available via the molten salt electrowinning route. The usage of molten salt solvents combined with an electrolytic route offer many advantages which may be summarized:-

1. The selective solubility of metal sulphides in molten salts may be employed as a leaching process to further concentrate the required metal sulphide.

2. High purity (>99%) metal products are readily achieved with high current efficiencies. The use of a high operating temperature combined with the relatively low melting point of base metals enables the liquid product to be produced and to be easily removed from the cell for further direct processing e.g. casting. The major problems associated with solid deposits (211), i.e. entrapment of solidified salt and dendritic growths; are therefore eliminated.

3. Sulphur gas may be obtained directly at the anode and thus eliminates additional expensive processing of SO_2 emissions. Furthermore the solidified sulphur may readily be transported or easily and safely disposed of (i.e. buried) without being detrimental to the environment.

4. The inherent electronic conductivity of metal sulphides combined with their selective solubility in molten salts may be conveniently used to advantage. Thus molten (or solid) metal sulphide electrodes may directly be used with encouraging results (209).

The advantages and disadvantages of using molten salt systems has been discussed (212). Generally the combination of high operating temperatures; the corrosive nature of many molten inorganic liquids and the inherent difficulties in handling them (many salts are hygroscopic) has unfortunately prevented their greater usage . This is particularly true of the electrolytic production of refractory metals where molten salt processes (winning, refining and plating) may be used to great advantage (213)(214)(215). The problems associated with the drying and handling of molten ionic liquids has recently been extensively discussed (217). With particular reference to the anodic evolution of sulphur from sulphide solutions, the formation of insoluble polysulphides have been observed (188).

The recombination of sulphur gas with, for example electroreduced lead has been shown to reduce current efficiencies (205); recombination reactions are however an inherent problem with the formation of reactive gases (e.g. Mg production (218). However the use of suitable electrode seperators may significantly reduce this problem. The evolution of gaseous products do, under certain circumstances lead to the onset of the 'anode effect', again it is a general phenomenon, e.g. Al electrolysis (219-221). The well known intrinsic semiconducting properties of metal sulphides do not persist in dilute chloride solutions (153, 155, 157). The conductivity of, for example PbS-$PbCl_2$ solutions upto $50^m/o$ at 900^oC are 'purely' ionic; the onset of electronic conductivity occurs at higher metal sulphide concentrations. Thus electrolytic processes may be used at low sulphide concentrations, the onset of significant solution electronic conductivity is to substantially

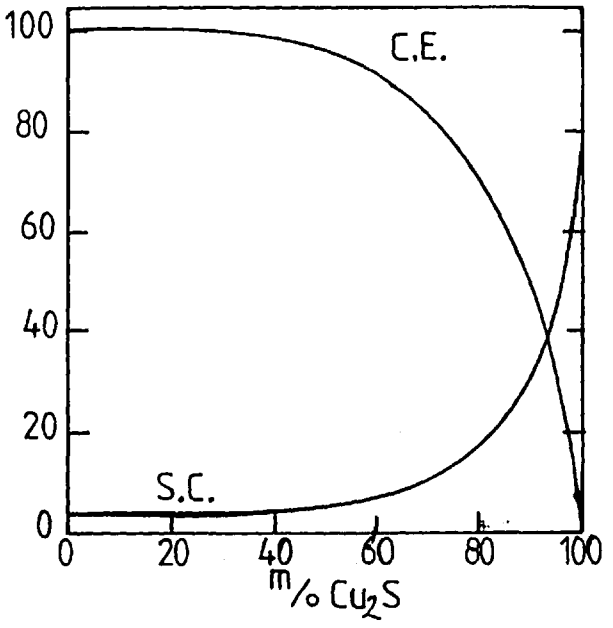


Fig. 3.6: Current Efficiency (C.E.) and Specific Conductance (S.C.) curves for various compositions of Cu_2S-CuCℓ mixtures (from reference [162])

reduce current efficiencies, see Figure 3.6.

It is interesting to note, that all commercially adopted molten salt electrowinning processes (e.g. Al, Mg, Na) produce as their products a liquid metal and an evolved gas. The 'near' success (in a commercial sense) of a similar process being adopted by industry for the extraction of metals from metal sulphides has clearly been demonstrated by the investment and operation of the pilot plants at Halkyn and those in Australia and Canada. However a complete understanding of the electrokinetics of anodically evolved sulphur remains elusive.

CHAPTER 4

EXPERIMENTAL

4.1. Apparatus

4.1.1. Furnace and Temperature Control

The furnace and temperature control were the same as that used by earlier workers in this laboratory. The vertical furnace consisted of a Kanthal wire (18 s.w.g.) wound silica tube with a maximum operating temperature of 950°C. An arrangement of pulleys and counterweights enabled the furnace to be raised and lowered about the clamped electrochemical cell. To minimise electrical noise, a Nimonic earth shield lined the inside of the furnace tube. The temperature was controlled by a P.I.D. 15 Eurotherm controller which monitored a Pt/Pt-13%Rh thermocouple located within the furnace tube. A temperature control of $\pm$ 1°C was maintained with this arrangement.

4.1.2. Electrochemical Cell

The electrochemical cell consisted of a round bottomed Pyrex or Silica envelope, 80mm diameter and 320mm long, capped by a water-cooled brass head. A pyrex pot, 65mm diameter and 70mm long was used to contain the molten salt. The crucible sat upon a bed of glass beads. For temperatures above 500°C a vitreous carbon crucible was employed. A vacuum tight seal was achieved between the brass cell head and the glass by means of an 'O' ring. Seven holes located within the brass cell head enabled the fixture of seven Quickfit SQ13 screw cap joints through which the cell components (electrodes, gas bubbler etc) were passed. A vacuum tight seal



Photo 4.1: The High Temperature Electrochemical Cell

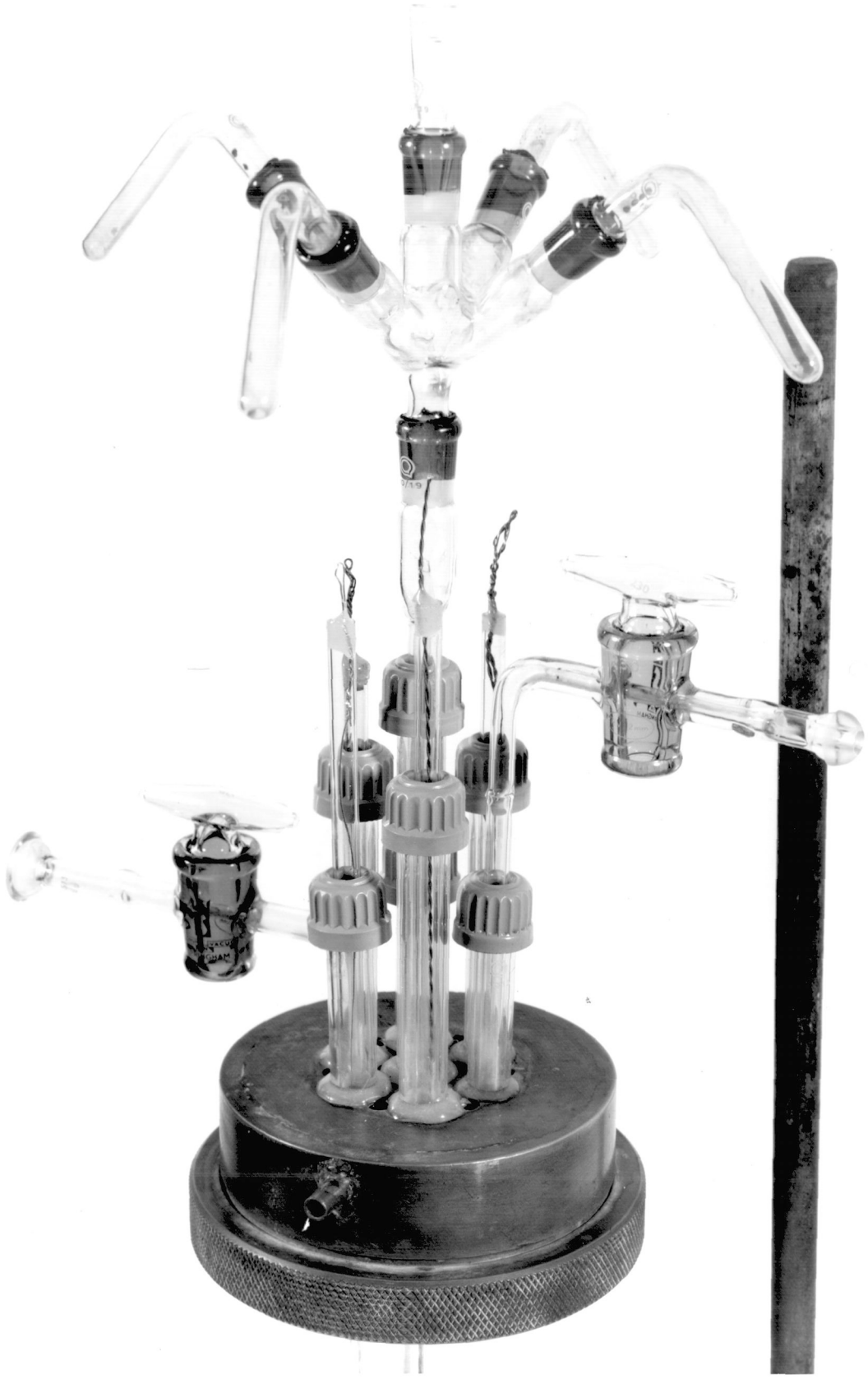


Photo 4.2: The electrochemical cell head showingthe solute addition assembly

was produced by compressing, by means of the screw cap a P.T.F.E. washer backed by a rubber sleeve. The cell arrangement is shown in Photo 4.1. Using this system the electrodes could be more readily raised and lowered than with previous simple 'O' ring designs. The cell components were made of 6mm o.d. pyrex tubes through which electrode contact wires could run; seals were made with epoxy resin.

With this system a vacuum of 5×10^{-3} Torr could be achieved. Solid materials were added to the cell by means of a special addition assembly (see Photo 4.2).

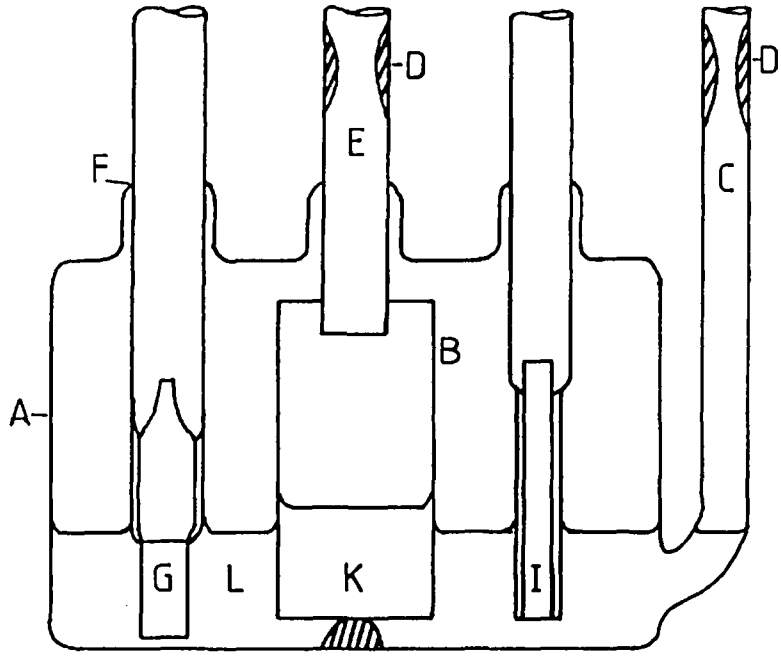
4.1.3. The Sulphur Gas Electrochemical Cell

The electrochemical cell used to determine the influence of sulphur gas upon the electrochemical characteristics of PbS containing melts is shown in Figure 4.1.

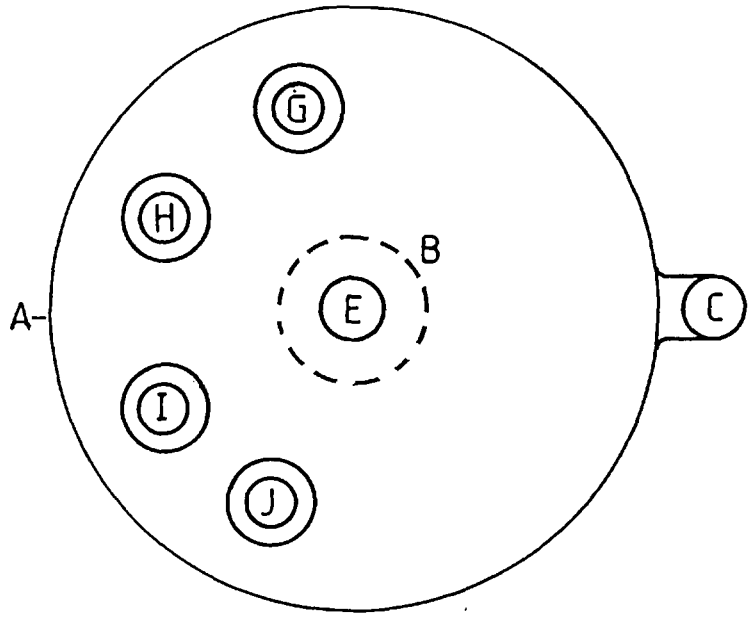
The cell was of an entirely closed design, the main chamber being 80mm high and 80mm in diameter. The whole assembly was made from pyrex glass and was therefore limited to a maximum working temperature of $550^{o}C$.

The liquid sulphur pool was held within a small (25mm diameter) pyrex beaker and was thus isolated from the solvent melt. The beaker was attached to the main cell by means of a glass bead. Thus by varying the temperature of the cell, the partial pressure of gaseous sulphur in equilibrium with the liquid sulphur could be varied. No liquid sulphur was therefore in contact with the melt.

The electrode system was the conventional 3 electrode system. The silver reference electrode consisted of a straight 10mm bore



Sectional View



Plan View

Fig. 4.1: A Diagramatic Representation of the Sulphur Electrochemical Cell

A, Pyrex Cell; B, Pyrex beaker containing liquid sulphur (K); C, Solvent addition tube; D, Sealing positions; E, Sulphur powder addition tube; F, Pyrex internal seals; G, Graphite counter electrode; H, Reference electrode; I, Working electrode; J, Thermocouple well; L, Molten Salt.

tube with a thin glass bulb blown on the end; inside the bulb a solution of AgCl-$PbCl_2$-NaCl-KCl was added in which a silver wire was immersed. The working electrode was a planar vitreous carbon electrode sealed into pyrex; the exposed surface was ground and polished as described in section 4.2.1.3. The counter electrode consisted of a 1cm diameter, high density graphite rod sealed into pyrex; a one centimeter length of graphite protruded from the seal. Electrical contact was provided by a copper wire and graphite powder. A closed end tube was incorporated into the cell in which a thermocouple was placed.

All the electrodes were incorporated into the cell by means of internal glass seals, the electrode surface was arranged to be 5mm from the bottom surface. The electrode tubes were extended well outside the furnace and electrical connections were made in the normal way.

The cell was designed so that the main chamber (A in Fig. 4.1) was wholly contained within the hot zone of the furnace.

4.1.4. Vacuum and Gas Supply Systems

Three vacuum and gas line assemblies were employed during these studies. A single line for the electrochemical studies and a further two separate purification vacuum lines enabled virtually continuous operation. All three systems were approximately the same although with minor variations. However, the principal and general construction were the same; thus only the line used for the electrochemical experiments will be described in detail.



Photo 4.3: Assembly for the purification of Cl_2 and HCl gases (a) HCl cylinder, (b) Cl_2 cylinder, (c) molecular sieve, (d) activated charcoal

The vacuum system consisted of an Edwards oil diffusion pump backed by an Edwards ED50 rotary pump, a liquid nitrogen cold trap was also incorporated in the system. With this arrangement cell pressures of 5×10^{-3} Torr could be achieved as measured by an Edwards G5 B2 Pirani Gauge. The cell could be filled with Argon by rotating a two-way stopcock from the vacuum line to the gas line; the flow of argon was regulated by a needle valve. Pressures inside the cell and gas lines were measured by a mercury manometer. High purity B.O.C. Argon was further purified by drying over magnesium perchlorate, residual oxygen was removed by passing over heated ($500^{o}C$) copper turnings. The whole apparatus was made of glass except for a small length of flexible copper tubing connecting the vacuum/gas line to the cell.

The vacuum lines employed for melt purification used much higher pumping rate vacuum pumps; typically ED200. The chlorine and hydrogen chloride gases used were further purified by passage through molecular sieve and through activated charcoal at $550^{o}C$ (see Photo 4.3).

4.1.5. Contact Angle Apparatus

The apparatus and experimental arrangement used for measuring contact angles via the sessile drop technique is shown in Photo 4.4. The apparatus consisted of a horizontal tube furnace through which high purity argon was continuously flushed. A platform situated within the furnace hot zone was attached by an arm to a stopper at one end of the furnace tube. The platform carried the carbon discs (1cm diameter, 2mm thick) which acted as the substrate for the sessile drop, see Fig. 4.2. A camera was set in horizontal alignment with the furnace tube and was used to obtain photographs of the drop profile.

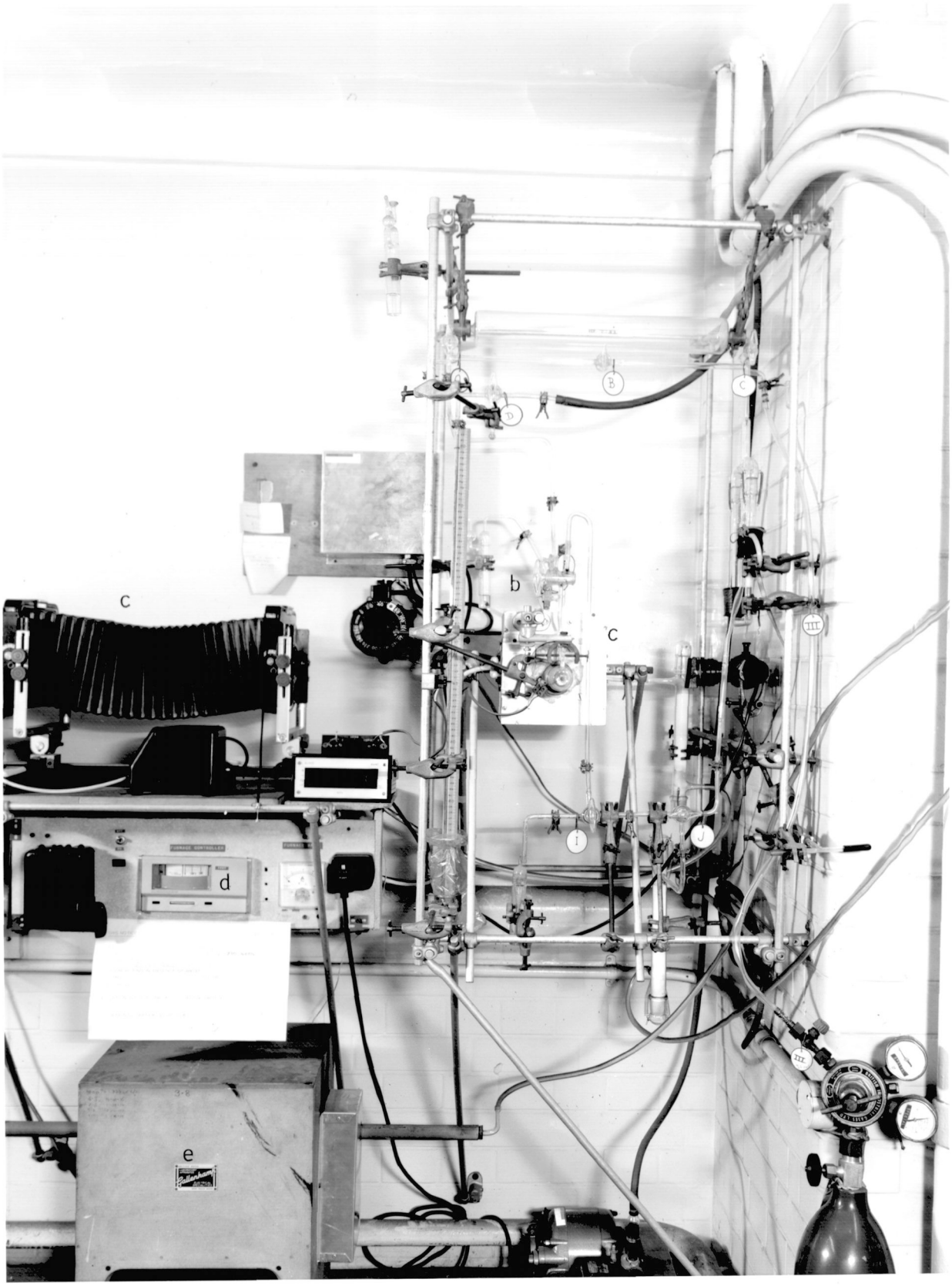


Photo 4.4: Contact angle apparatus
(a) furnace, (b) inert gas inlet, (c) bellows camera,
(d) temperature controller, (e) Ar purification

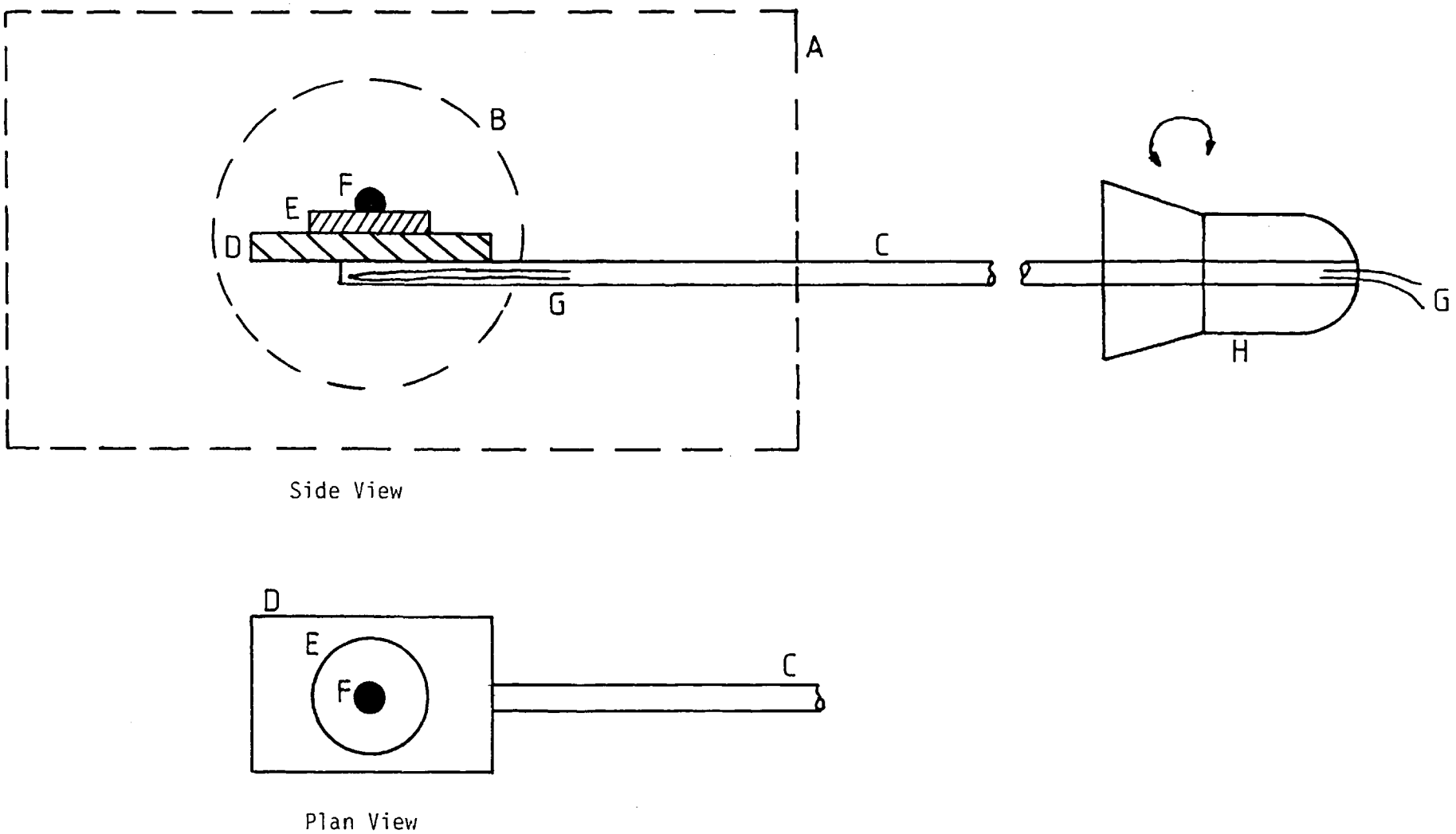


Fig. 4.2: A Diagrammatic Representation of the Contact Angle Apparatus
A furnace; B window; C Silica support tube; D silica support plate; E carbon substrate; F bead of molten salt; G thermocouple; H cone socket enabling alignment of sample.

The argon gas was purified by passing through molecular sieve and heated copper turnings at 500^{o}C. The furnace was regulated by means of a Eurotherm P.I.D. 15 temperature controller which monitored a Pt/Pt-13% Rh thermocouple within the furnace tube. A more accurate measure of the 'drop' temperature was obtained from a chromel/alumel thermocouple situated directly below the silica platform.

4.2. Electrodes

4.2.1. Micro Electrodes

4.2.1.1. Gold Electrodes

Two types of gold electrodes were used in these investigations, a flag type electrode and a small sphere electrode. The former electrode was found to be unreliable in its electrochemical performance. The small sphere electrode was made by using an all gold wire electrode (0.5mm dia) and melting one end in an oxy-gas flame until a sphere of approximately 2mm diameter was formed, Fig. 4.3b. The use of this electrode was restricted in its usage since the exact surface area was unknown. However it was found useful for comparative studies.

4.2.1.2. Platinum Electrodes

Platinum flag electrodes were cut from 0.125mm sheet giving a 2mm square edge, which was spot welded to 0.05mm diameter platinum wire, which in turn was spot welded to a copper lead (Fig. 4.3a). The surface of the electrode was flame polished by heating the platinum in a reducing flame until bright red and dipping into 12M HCl; the process was repeated several times after which the platinum was

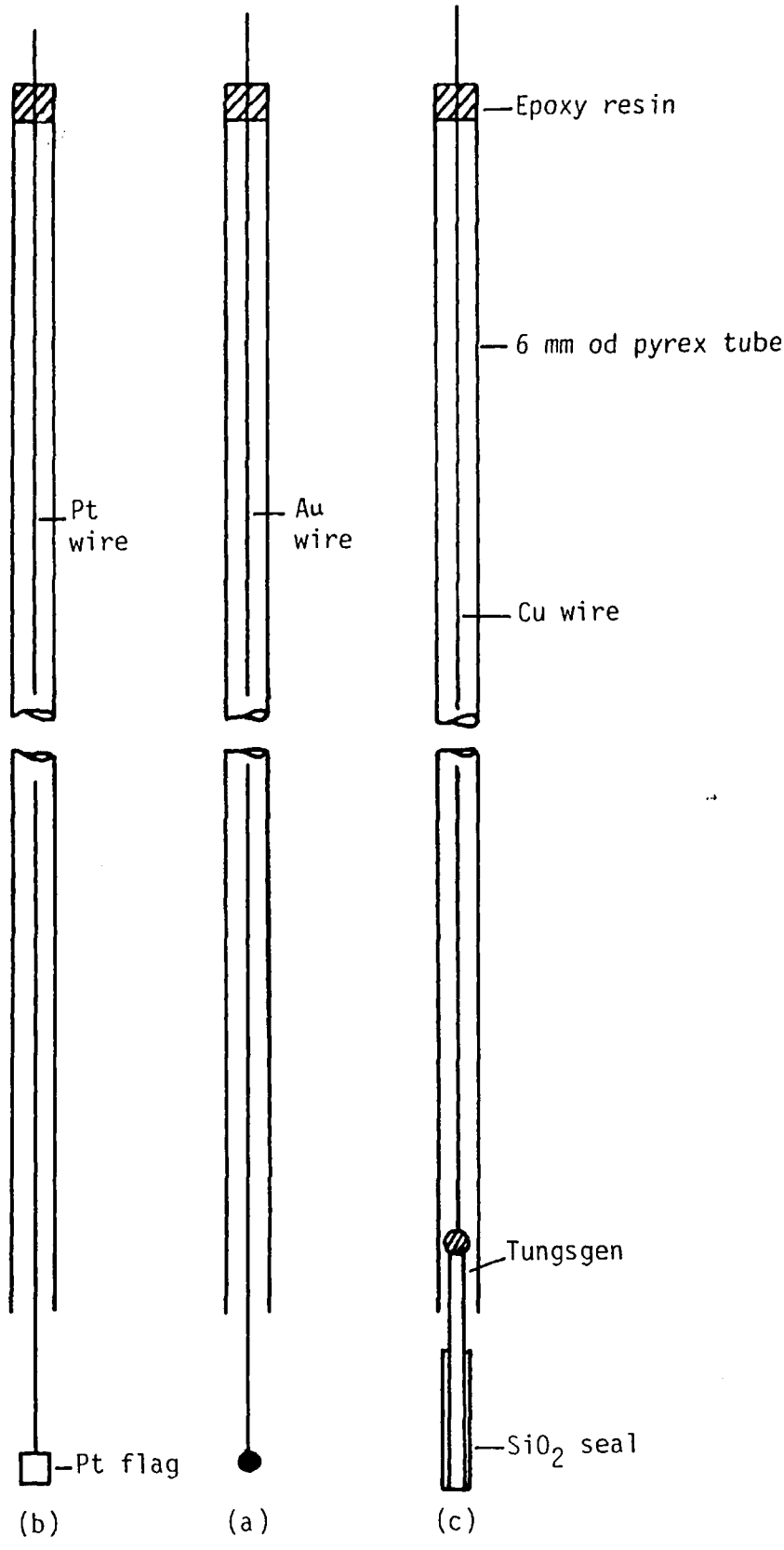


Fig. 4.3: (a) Gold sphere micro electrode
(b) Pt flag, micro electrode
(c) Tungsten micro electrode

finally washed with distilled water and acetone.

4.2.1.3. Carbon Electrodes

Several types of sealed carbon electrodes have been employed during the course of these experiments. In all cases the principle of electrode manufacture was the same. However, vitreous carbon electrodes required considerably more care and attention than those of the graphites in order to produce reliable seals.

A length of carbon (4cm) was placed in a 6mm diameter closed end pyrex tube and connected to a vacuum line by means of an adaptor. The tubing was then evacuated to 5×10^{-3} Torr for several hours at room temperature. The end requiring the seal was placed in a small vertical wire wound furnace, and the temperature slowly increased (3 hrs) to red heat by an 8-amp Variac Controller. The assembly was at this point closely observed. The pyrex glass gradually collapsed around the carbon and slowly extended upwards. When the seal was approximately 1cm from the top of the carbon rod, the power was switched off and the furnace slowly cooled to room temperature. In the case of the vitreous carbon electrodes, a further heat treatment ($500^{o}C$, in air) for 20 hrs was found to be beneficial in removing residual stresses within the seal. The pyrex covering the carbon end was carefully removed by grinding using silicon carbide powder. The grinding stage was the most critical period when the seal was likely to fracture. Successful electrodes were subsequently polished on 3μ and 1μ diamond wheels to produce a 'mirror-like' finish. The electrodes were then cleaned with distilled water, acetone and vacuum dried. The vacuum drying operation was found necessary particularly for the porous graphite electrodes. Electrical

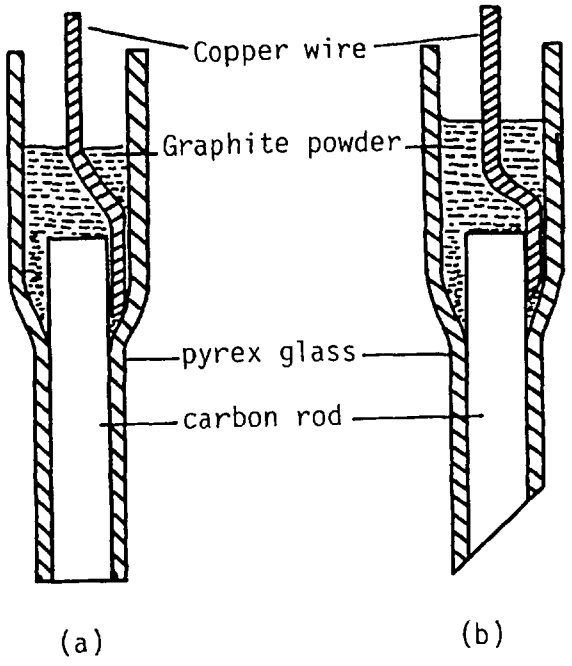


Fig. 4.4: Carbon Electrodes sealed into Pyrex Glass

contact to the carbon was made by inserting a length of copper wire and ensuring close contact by pushing the wire between the carbon and the glass; fine powdered graphite was added to further ensure good contact (Figs. 4.4a and 4.4b). The copper wire was sealed into the glass with epoxy-resin. The resistances of all electrodes was measured prior to use, and were typically of the order 0.01 - 0.1Ω. Using this type of electrode assembly good seals could be made which lasted for several 'runs' before any deterioration could be detected; usually melt seepage within the seal. Alternative methods have been proposed for making good, reproducible vitreous carbon/pyrex seals (284,285); however these techniques were not attempted.

4.2.2. Counter Electrode

The counter electrode consisted of a ¼" diameter graphite rod connected to a stainless steel rod which was sealed into 6mm Pyrex tubing. The graphite was contained in a fritted compartment using a No. 0 pyrex frit. The use of this compartment was found to be essential in order to prevent loose carbon particles from 'contaminating' the electrolyte, i.e. providing an alternative current pathway. During the course of the experiments it was also found necessary to add a small amount of electrolyte to the counter compartment to aid wetting of the frit. Failure to do so generally resulted in a non-wetted frit and thus an isolated compartment finally requiring termination of the experiment. Consistent results were obtained using the number 0 porosity frit. Figure 4.5a illustrates the arrangement used.

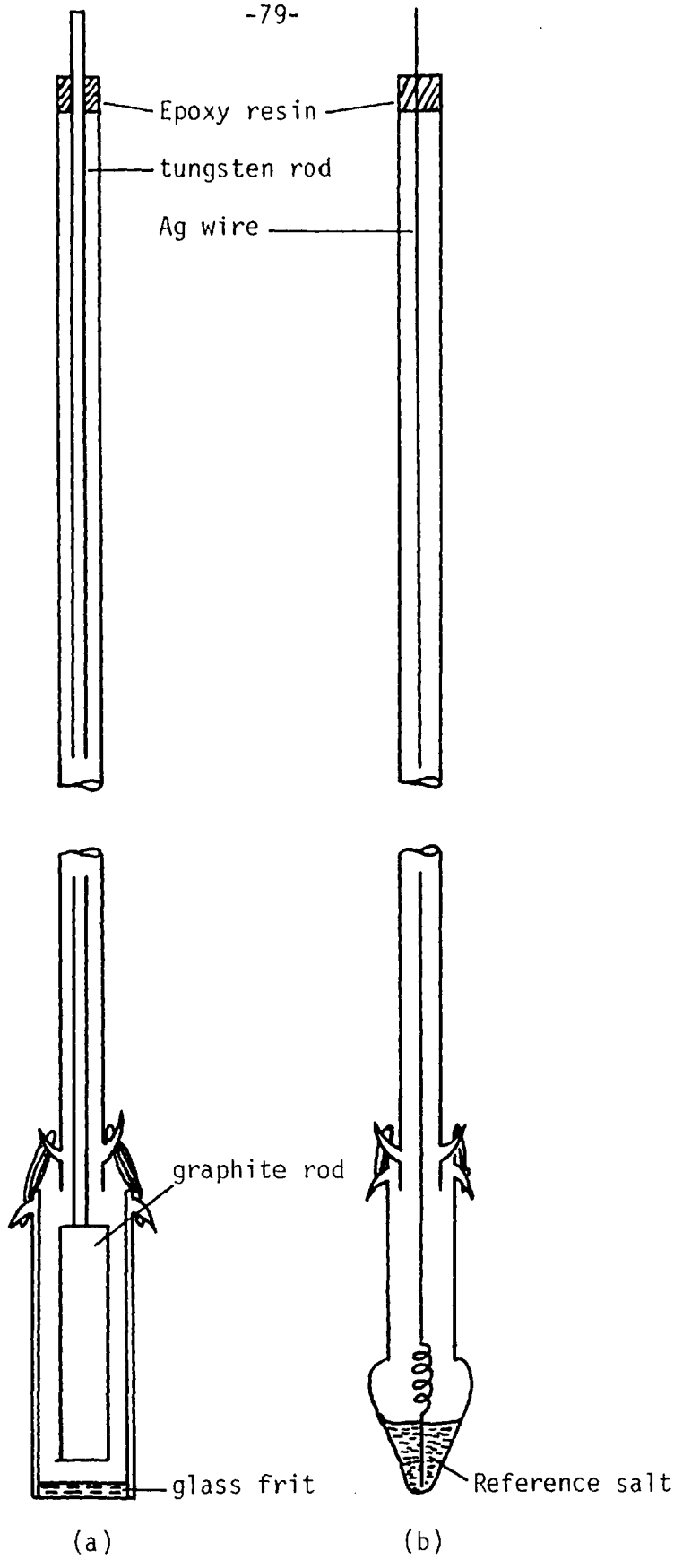


Fig. 4.5: (a) Counter Electrode
(b) Reference Electrode

4.2.3. Reference Electrode

The silver-silver ion couple was used for the reference electrode. The solution of silver chloride in the electrolyte (either $PbCl_2$ - KCl; $PbCl_2$ - KCl - NaCl, or $PbCl_2$ depending upon the experiment) was contained in a pear-shaped pyrex bulb with a very thin end; a silver wire was immersed into the solution (Fig. 4.5b).

This type of reference electrode arrangement was first developed by Inman (286) for use in chloride melts and has subsequently become a standard arrangement for use in halide melts.

The silver ion solution o(0.5m) were prepared by adding the appropriate amount of silverchloride to a pre-purified melt. After cooling, the mixture was transferred to a dry box where the solidified melt was crushed and stored in a desiccator. A single batch of 100gm of each electrolyte lasted for a whole experimental period.

4.3. Chemicals and Materials

The grades and suppliers of the chemicals and materials used for these experiments are shown in Table 4.1.

4.4. Melt Purification

Two types of purification procedure were employed during the course of these experiments. Normally a vacuum drying and melting coupled with bubbling of the melt with HCl gas and filtration were used. An alternative method simply employed slow vacuum drying, melting and filtration Photo 4.5. The former method employed both pyrex apparatus (for the electrolytes $PbCl_2$ - KCl and $PbCl_2$ - KCl - NaCl) and silica apparatus for the $PbCl_2$ melt. The relatively

TABLE 4.1

The grade and supplier of chemicals and materials used.

Chemical or Materials	Grade	Supplier
$PbCl_2$	Puriss	Koch-Ligh Laboratories Limited.
KCl	Analar	B.D.H. Chemicals Ltd.,
NaCl	Analar	B.D.H. Chemicals Ltd.,
PbS	99.9%	Alpha Chemicals Ltd.,
	Reagent	B.D.H. Chemicals Ltd.,
$Na_2S \cdot 9H_2O$	Analar	Hopkins and Williams.
S	Optran	B.D.H. Chemicals Ltd.,
PbO	Analar	Hopkins and Williams
PbO_2	Analar	Hopkins and Williams
$PbSO_4$	Analar	Hopkins and Williams
Pt wire/sheet	Spec Pure	Engelhard Limited.
Au wire	Spec Pure	Johnson Matthey.
Vitreous Carbon	-	Fluorocarbon Limited
Graphite rod	Spec Pure	Johnson Matthey
Other graphite rods	EYA9,EYA110,EYA9	Morganite Sepcial Carbons Limited.
Graphite Powder	Spec Pure	Johson Matthey
Argon	High purity	B.O.C.

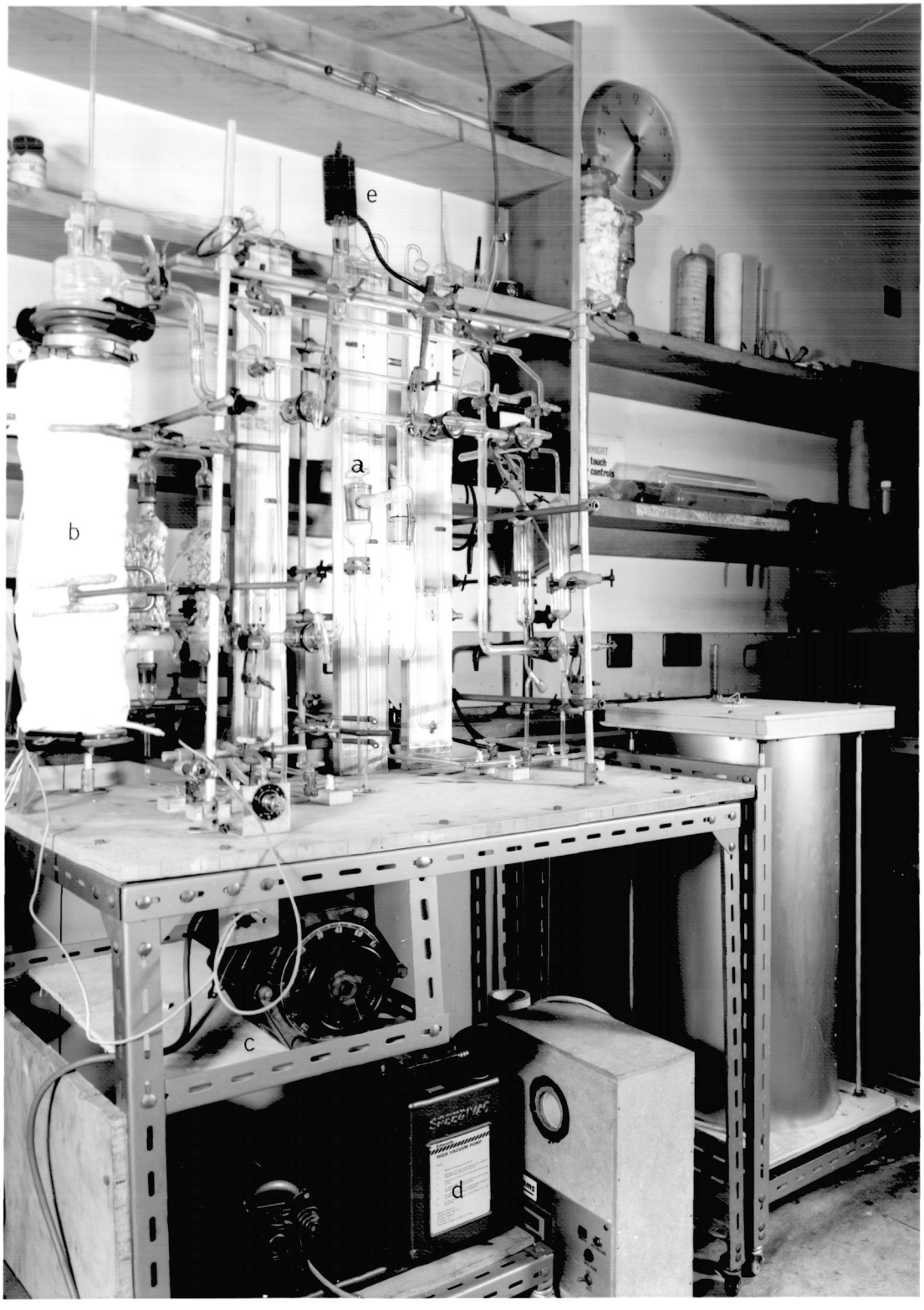


Photo 4.5: Simple vacuum drying apparatus
(a) glass vacuum line, (b) drying furnace,
(c) controlling variac, (d) vacuum pump,
(e) vacuum gauge

simple 'Non-HCl' melt employed an all pyrex apparatus and was used for the eutectic mixtures only.

Two sets of apparatus were employed, their design and experimental operation being essentially the same and thus only the 'HCl' procedure will be discussed in detail.

The purification apparatus and arrangement is shown in Fig. 5 and Photo 4.6. All glassware in contact with the melt, i.e. melt receiver, filter tubes and container etc. were soaked in a 1:1 sulphuric/nitric acid bath for 12-24 hours, washed with distilled water and acetone and dried at 200^{o}C in an air oven. Particular attention was given to cleaning the glass frit. The filter tube was lowered into the main assembly and sealed by a 'O' ring. The melt receiver was placed underneath the filter tube and held in position with an 'O' ring-sealed brass cooling plate. The eutectic mixture was weighed and thoroughly mixed, added to the melt container and inserted into the filter tube. The gass cell head, containing the gas bubbler, outlet, and breaker was quickly fitted and sealed with an 'O' ring; the head was also directly connected to the vacuum line by means of a ball and socket arrangement.

The whole apparatus was slowly evacuated, initially through the lower entrance and finally through both. A pressure of less than 10μ was generally achieved and maintained for at least two days before slowly heating the cell to 300^{o}C. This temperature was maintained overnight. The mixture was then melted under vacuum at 450^{o}C for $PbCl_2$ - KCl - NaCl (480^{o}C for $PbCl_2$ - KCl and 530^{o}C for the $PbCl_2$-melt) and the pressure allowed to fall to its original value. The apparatus was then 'let-down' to atmospheric pressure

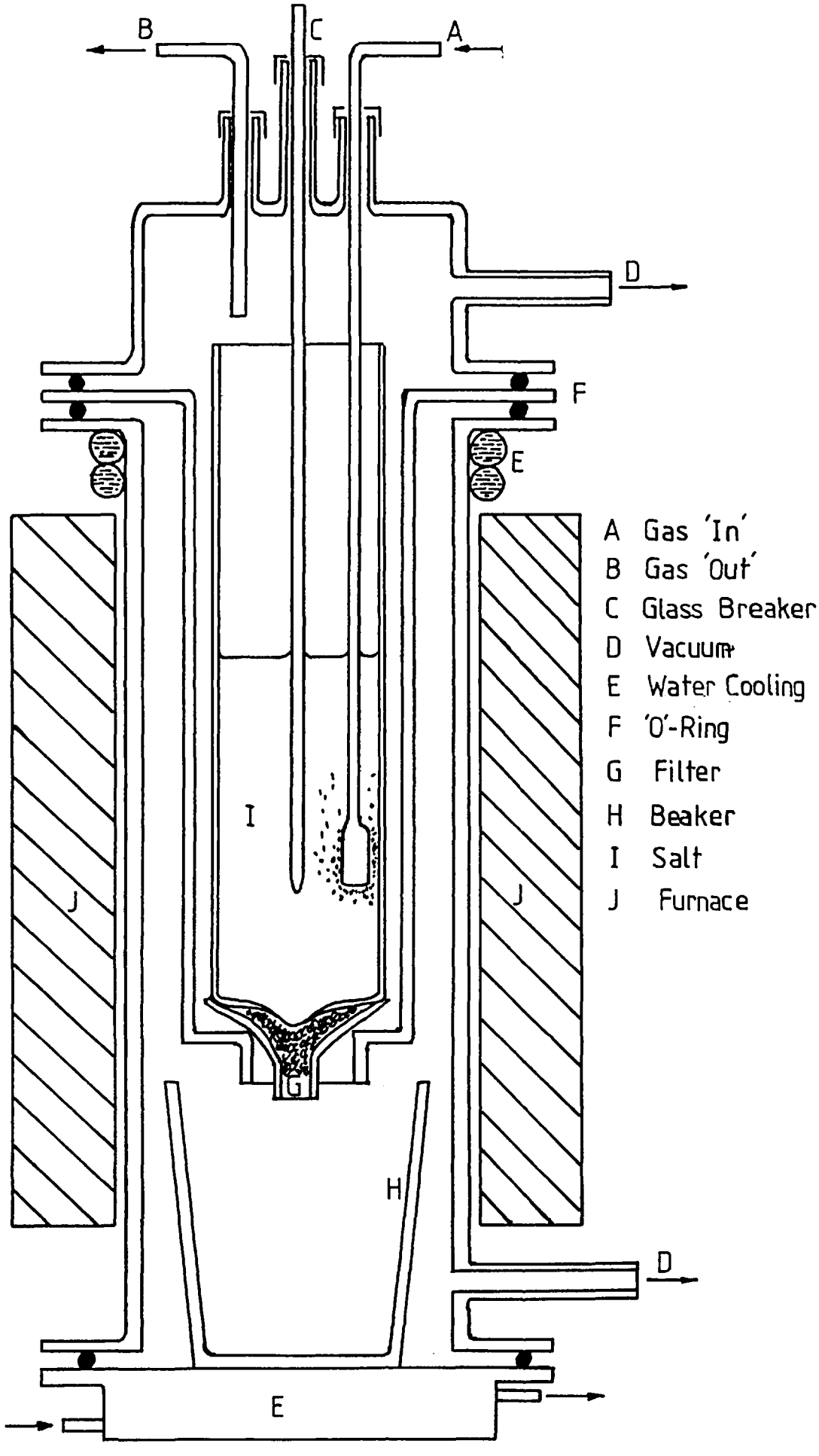


Fig. 5 Schematic Representation of Purification Apparatus

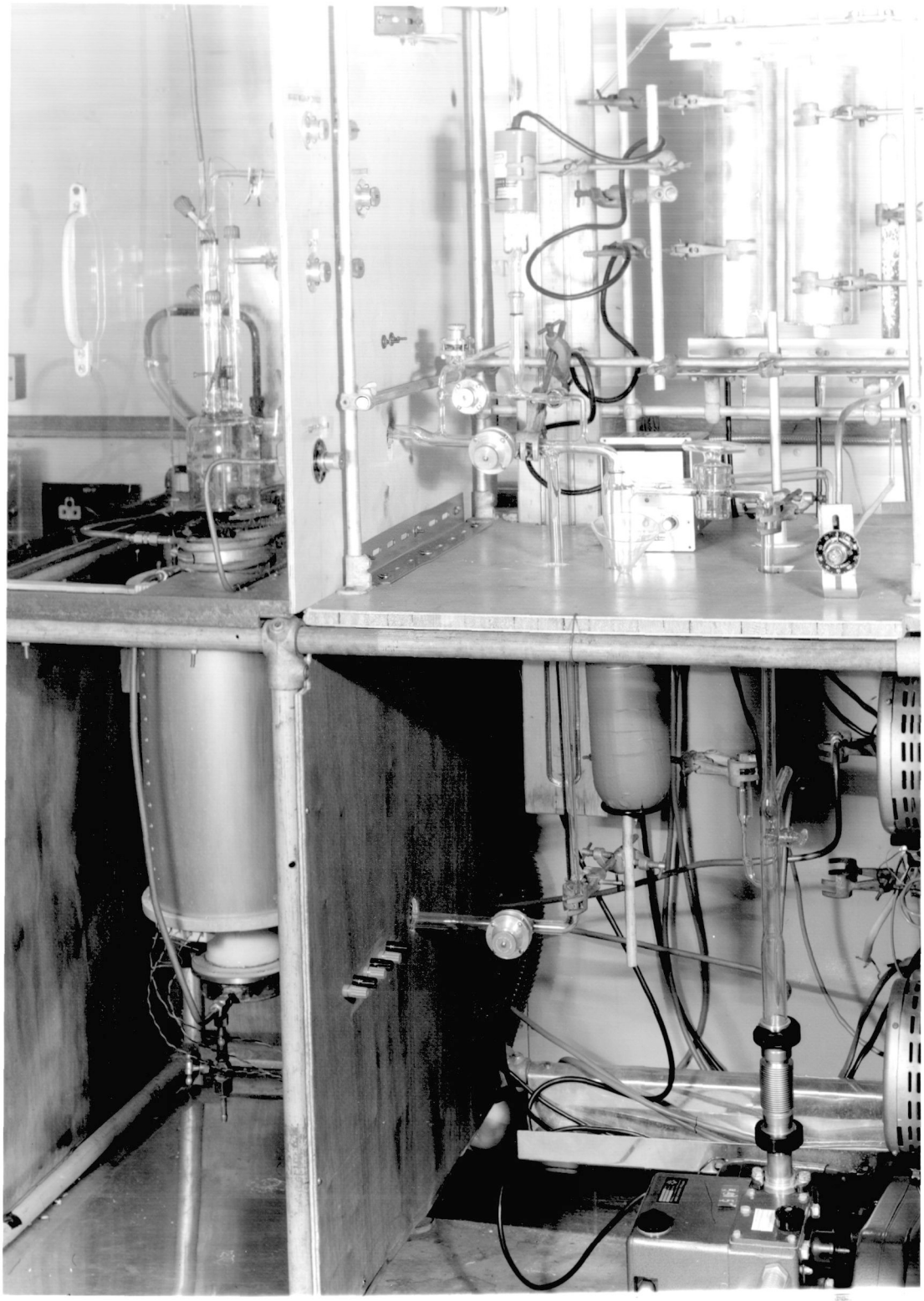


Photo 4.6: Purification Apparatus

by leaking purified high purity Argon into the system. Dry hydrogen chloride gas was then slowly introduced into the system, and subsequently bubbled through the melt for one hour. Residual HCl was then removed by purging with argon and finally evacuating the assembly. The thin glass bulb on the filter tube was then broken by the glass breaker and the melt allowed to run onto the glass frit (No.4 pososity). A slight pressure of argon was then introduced into the upper part of the cell, whilst a vacuum was pulled from the bottom, this enabled filtration of the molten salt which was suitably collected. In the case of the higher temperature $PbCl_2$ system SiO_2 wool was employed as the filter which was tightly packed into a special container through which the melt was vacuum filtered.

The whole apparatus was finally cooled under vacuum overnight. The purified melt was transferred to the dry box by using the argon filled polythene bag.

Using this procedure, approximately 600 gms of salt could be purified in one batch from which four runs could be obtained. All melts were checked for electrochemical purity by cyclic voltammetry, and those which were not satisfactory were disgarded.

4.5. Experimental Procedure

4.5.1. Preparation of Electrochemical Apparatus

All glassware and all components i.e. crucible, reference bulb, gas bubbler etc., which contacted the melt were soaked for 24 hours in a 1:1 concentration sulphuric/nitric acid.bath. They were then thoroughly washed with distilled water and acetone.

Electrodes were cleaned as mentioned before and new electrodes were used for each experiment. The brass cell head was polished

with a commercial polishing compound to produce a mirror like surface for the 'O' ring seating. The p.t.f.e. washers and silicone rubber sleeves used to 'seal in' the electrodes were thoroughly cleaned with chloroform.

After assembly of the cell, it was placed in the furnace support stand and connected to the vacuum line and evacuated to 10μ. The whole assembly was thus checked for vacuum tightness. The cell was then removed and the purified melt added (typically 150 gms) and the reference bulb filled. The closed cell was then reconnected to the system and evacuated overnight as before. Argon was then introduced into the cell, providing a small flow at a slight positive pressure before melting the salt . The argon outlet stream was passed through dibutylphalate which acted as an indicator of the gas flowrate and also prevented back diffusion of air into the system.

After melting, the electrodes were then lowered into the melt and allowed to equilibriate for approximately one hour. The electrolyte was then checked for electrochemical purity by cyclic voltammetry prior to the addition of solute ions. All solid additions were added as pellets made in the dry box with a small hand press (Gallenkamp).

The whole electrochemical and assembly apparatus is shown in Photo 4.7.

4.5.2. The Sulphur Electrochemical Cell

Initially sulphur powder was added via the addition tube to the small beaker contained within the cell; the addition tube was then sealed. The powdered, pre-purified solvent was then carefully added through the side arm addition tube. The cell was then connected to

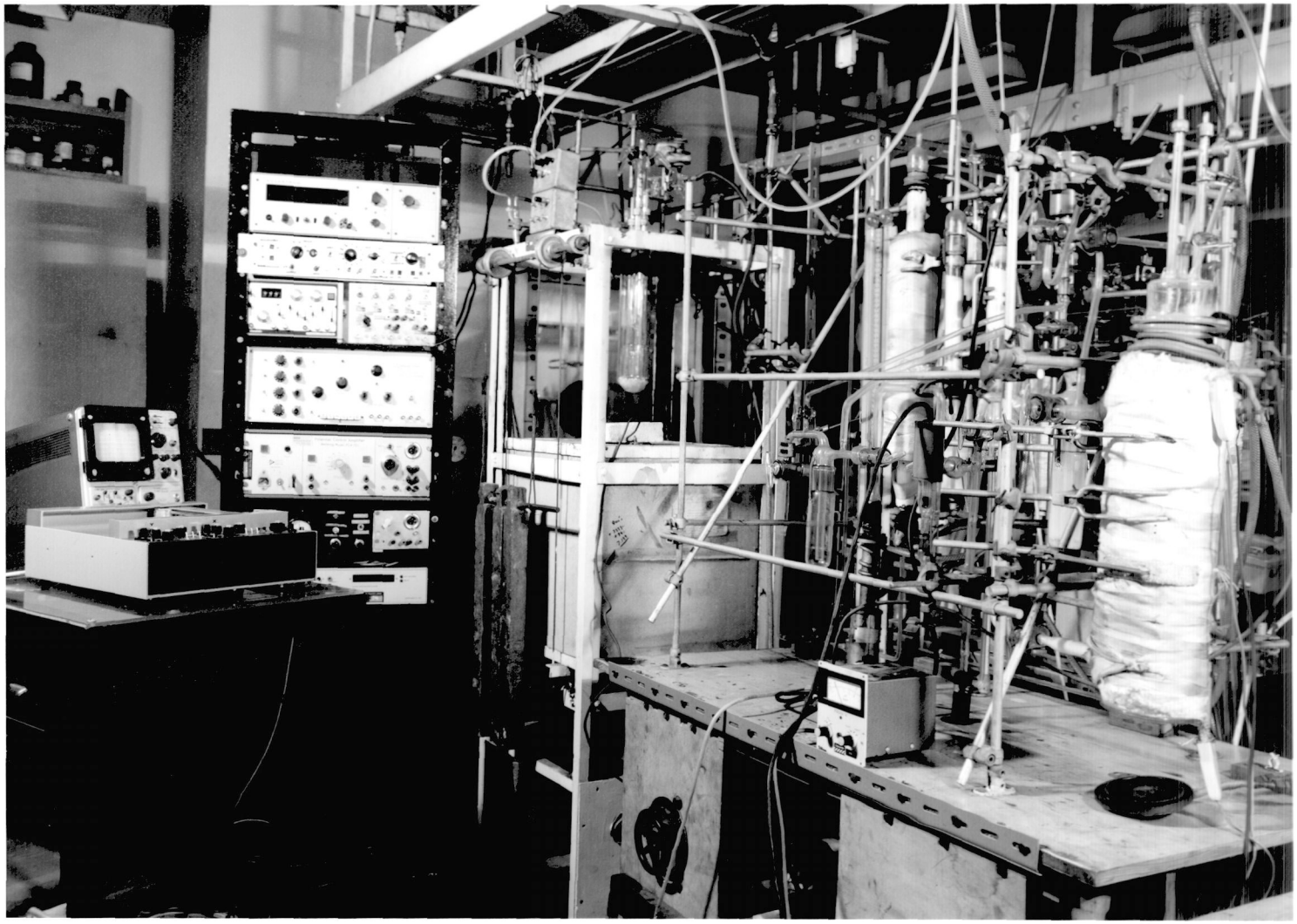


Fig. 4.7: The Experimental Arrangement showing the vacuum line, furnace, electrochemical cell and the electrochemical instrumentation

the vacuum line and evacuated overnight; a vacuum of 10μ was achieved. The following day the side arm was sealed. The electrode wire connectors were then carefully inserted as described previously and sealed with epoxy-resin. The cell was initially placed into a cold furnace and rested upon a bed of 'safron' blanket. The cell and furnace was slowly heated to the operating temperature. Once the solvent awas molten, the system was allowed to come to equilibrium overnight.

4.5.3. Contact Angle Measurements

The solvents employed for the contact angle studies were purified in the normal manner (see section 4.4). The required PbS solutions were made by vacuum melting followed by argon bubbling to ensure homogeneity. The carbon discs used were carefully 'parted' from stock material in a lathe to ensure parallel faces. The discs were subsequently polished on diamond wheels (3μ and 1μ) and finally washed with acetone and vacuum dried. All discs and solvent materials were kept in a desiccator. The carbon disc was placed on the SiO_2 platform onto which a small piece of salt (0.5 cm edge cube) was placed; the whole arrangement was then inserted into the cold furnace and carefully aligned. Purified argon was continuously flushed through the system and the furnace gradually heated to just below the melting point of the salt. The cell was allowed to come to an equilibrium temperature for 20 minutes before slowly melting the salt. The temperature of the platform was then measured and a photograph of the drop profile taken. A melting/cooling cycle was repeated several times. The furnace was allowed to cool to

room temperature during which time the plate film was processed according to the manufacturer's instructions. The contact angle Θ was measured by scribing a tangent at the appropriate point on the emulsion of the photograph using a sharp point. The angle was measured with a protractor (see Chap.10 for a discussion on this method).

4.5.4. Electrochemical Procedure

Cyclic voltammograms were obtained by applying a linearly varying potential ramp to the electrode and measuring the resultant current flowing between the working and counter electrode as a function of potential ramp. The range of sweep rates employed varied between 0.02 - 20 V/S. A schematic diagram of the applied signal and response is shown in Fig. 4.6a, a block circuit diagram in Fig. 4.7. Potential scans were started at initial potentials at which essentially no current was observed to flow.

Steady-state current-voltage relationships were obtained by using a sweep rate of 1mV/s, thus the experimental arrangement was exactly the same as that used for cyclic voltammetry.

Current-time transients (chronoamperometry) were obtained by stepping a voltage from an initial potential at which no current flows to a predetermined voltage which was held constant for a pre-determined time before stepping back to the original value. Thus both the magnitude of the applied potential step and its time of duration may be varied over a considerable range using the voltage pulse generator. The current-time profiles were recorded on a Transient Recorder. A schematic diagram of the applied signal and response is shown in Fig. 4.6b and the circuit diagram

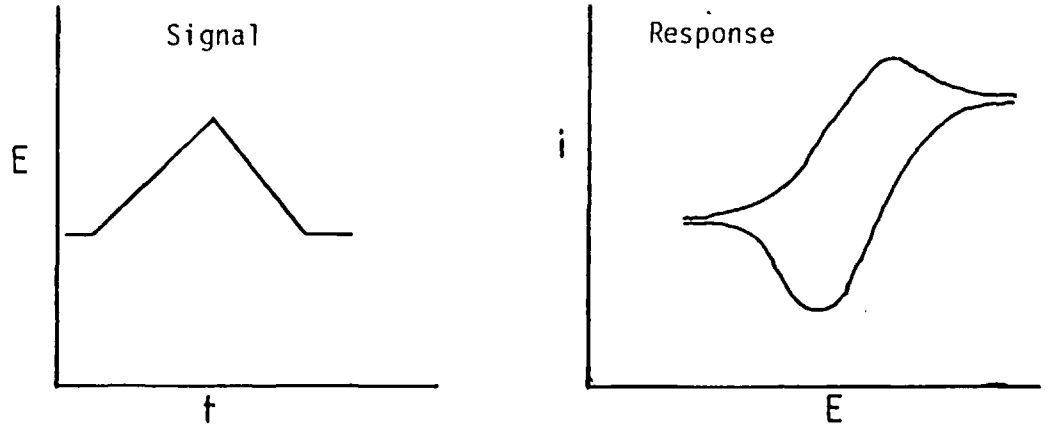


Fig. 4.6a: Signal and Response for Cyclic Voltammetry

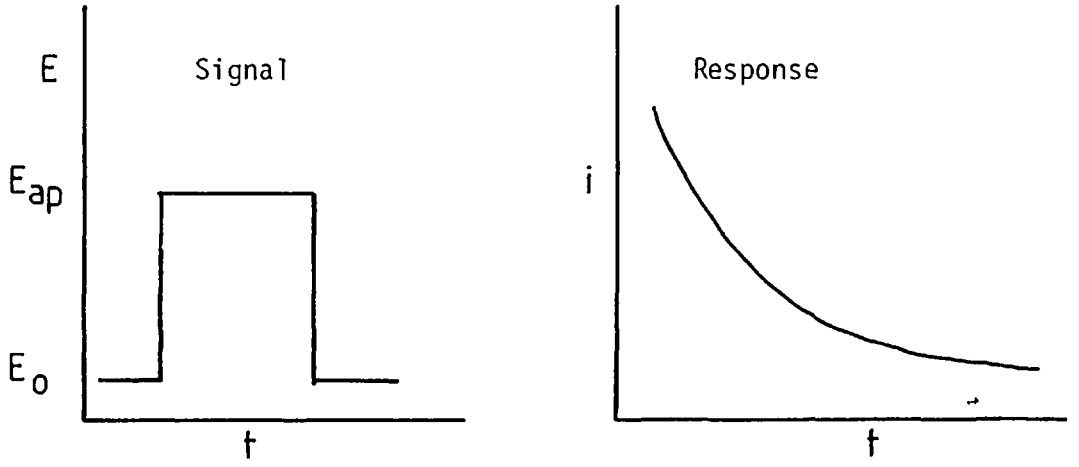


Fig. 4.6b: Signal and Response for Chronoamperometry

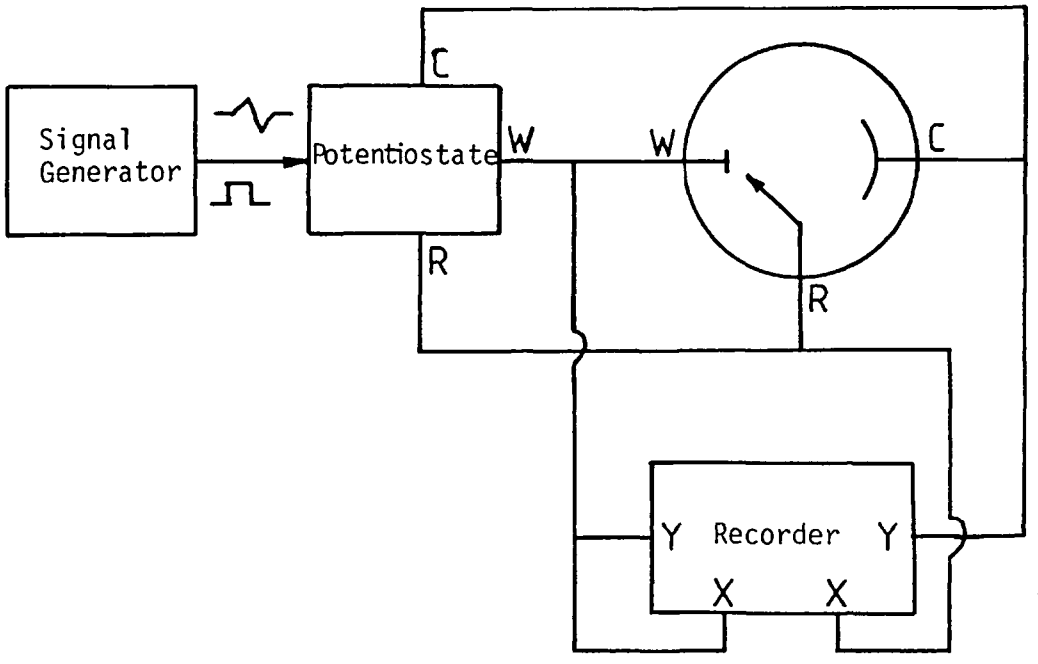


Fig. 4.7: A Block Diagram showing the Electrochemical Arrangement for Potentiostatic Techniques

in Fig. 4.7.

Chronopotentiometry (E-t transients) was accomplished by employing a potentiostat operating in the galvanostatic mode . The current pulses were a direct result of varying the potential step from the pulse generator and the value of the external resistor according to Ohm's law. In principle a range of currents may be generated ranging from 1.10^{-6} to 1A. The resistors used were either 5 or 10 watt wire wound and their exact resistance was measured prior to use. The schematic signal and response is shown in Fig. 4.8a. and the block circuit diagram in Fig. 4.9. The potential between the working and reference electrodes was recorded on either a Transient recorder or directly on the storage oscilloscope. In both cases it was necessary for the voltage to be 'buffered', that is the voltage must be measured by a floating input device. In the case of the transient recorder and the oscilloscope inputs one side of the potential must be earthed. Therefore a high input and low output impedance buffer was built to counter this difficulty. The circuit diagram of this unit is shown in Fig. 4.10. Prior to use, the buffer unit was checked for unity gain and linearity.

Open circuit decay measurements, as a result of a constant current pulse, employed the same circuitry as that described above for chronopotentiometry.

The electrochemical instrument 'rig' is shown in Photo 4.8 and comprised of the following:-
EG and G Parc Model 175 Universal Programmer, Wenking Potentiostat Model PCA 72L, Datalab Transient Recorder Model DL 905, Solartron Digital Voltmeter LM 1420.2, Bryants 29000 X-Y(t) recorder, and a

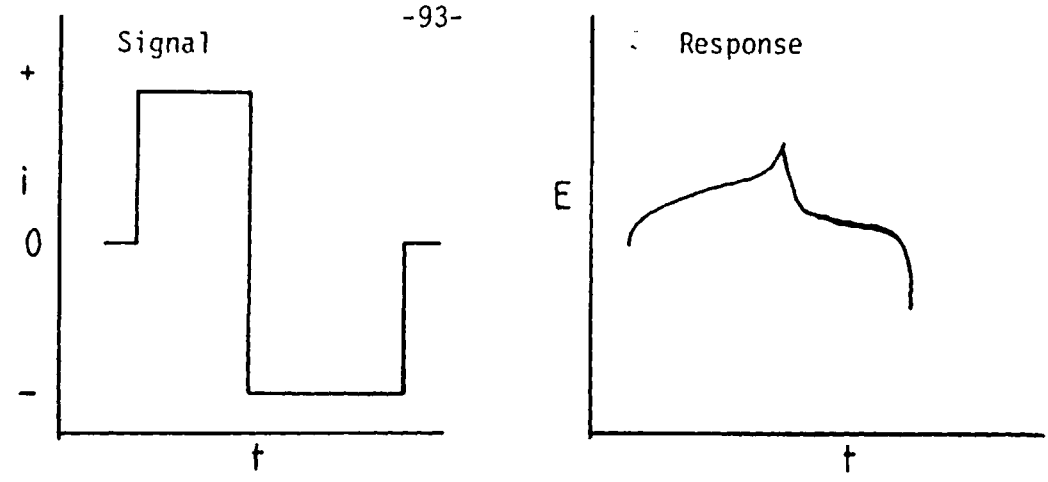


Fig. 4.8a: Signal and Response for Chronopotentiometry

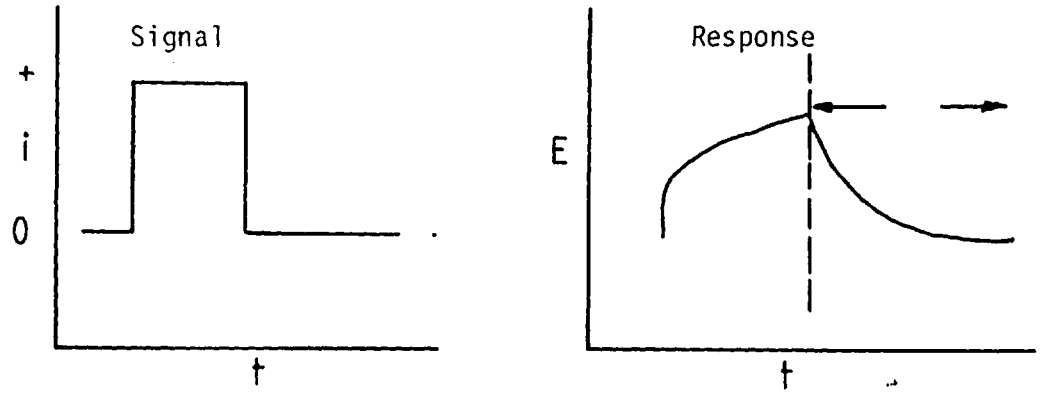


Fig. 4.8b: Signal and Response for Open Circuit Decay

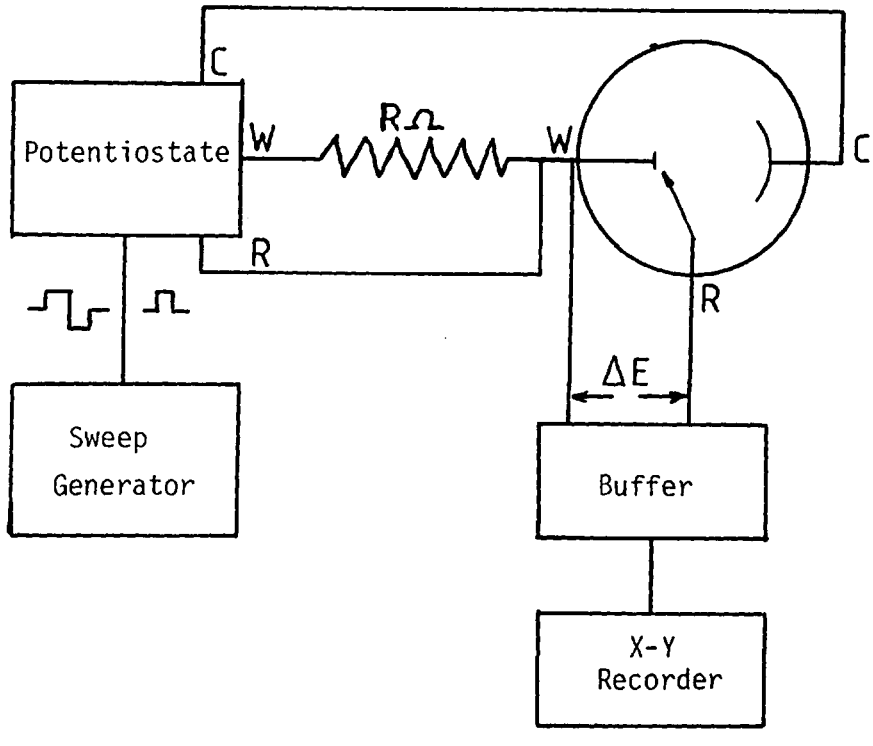


Fig. 4.9: A Block Diagram for the Galvanostatic Techniques

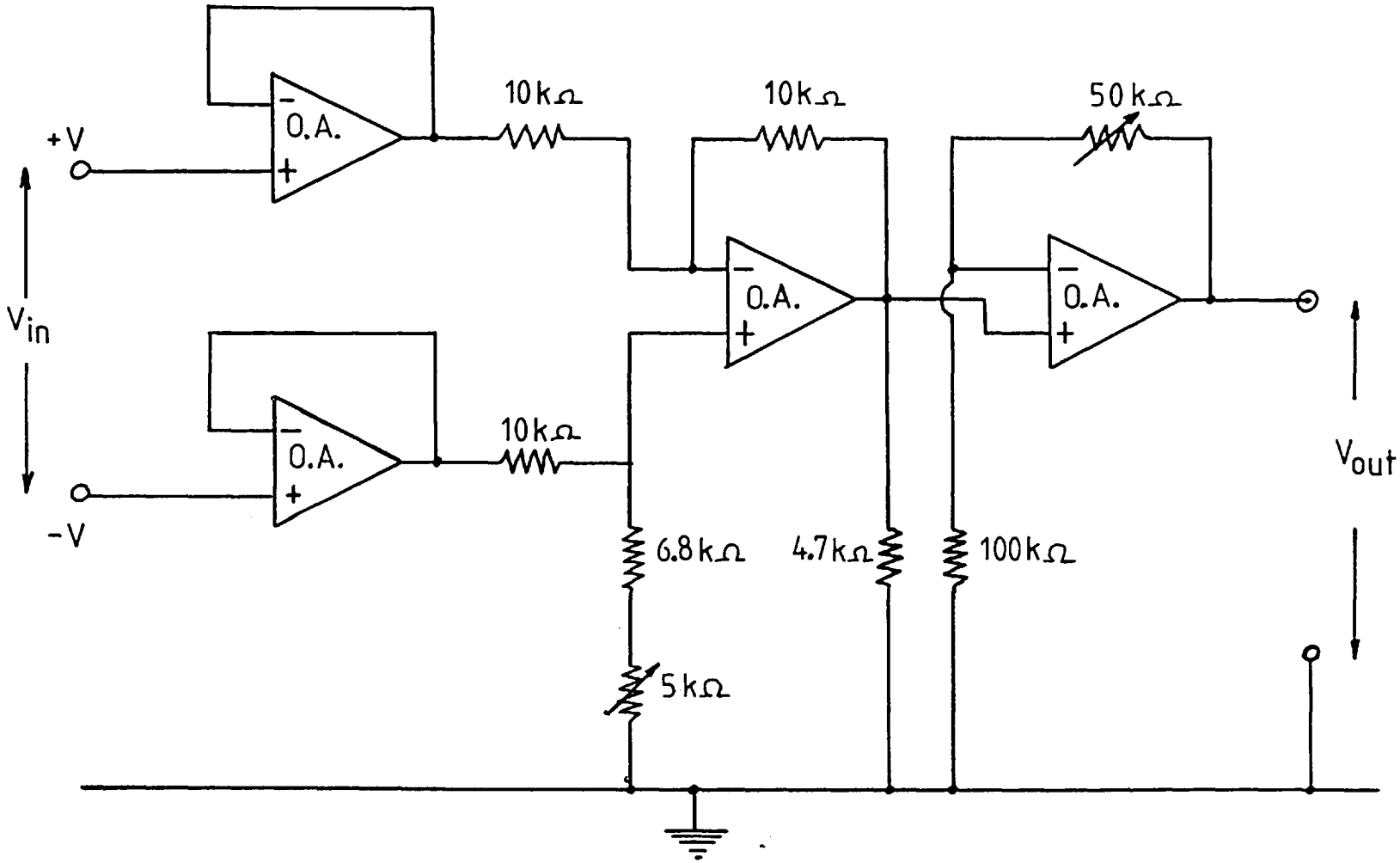


Fig. 4.10: Circuit Diagram for the Buffer Unit

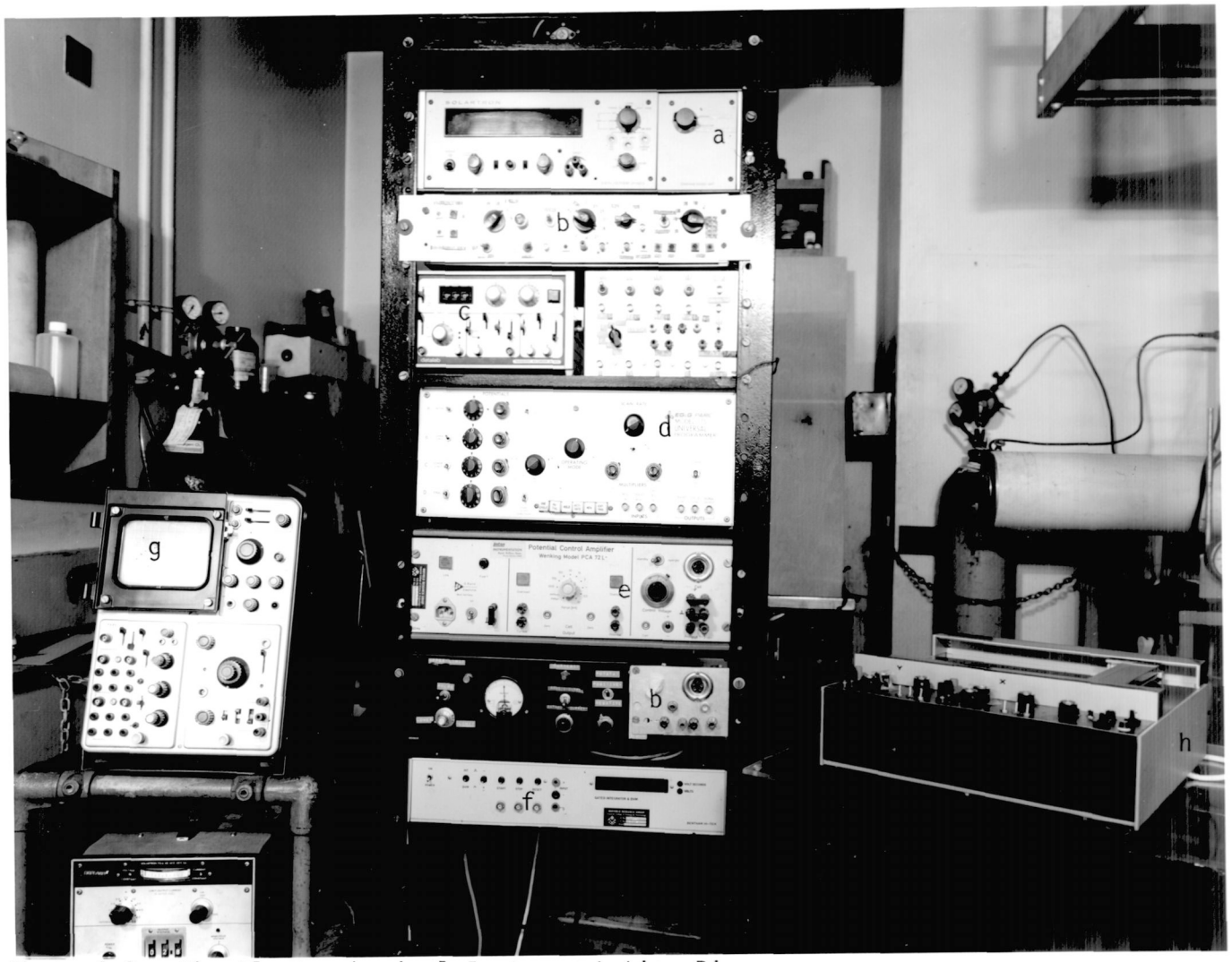


Photo 4.8: The Electrochemical Instrumentation Rig.
(a) DVM, (b) Home-made chronopotentiometry units, (c) Transient Recorder, (d) Sweep Generator, (e) Potentiostate, (f) DVM/Integrator, (g) Oscilloscope, (h) X-Y Recorder

Tektronix Type 564 Storage Oscilloscope with Type 3A8 plug in unit and a Type 2B67 time base.

4.6. Sodium-Polysulphide Preparation

The sodium polysulphides Na_2S_2, Na_2S_4 and Na_2S_5 were prepared by the reaction between an Anhydrous Na_2S and elemental sulphur, according to the reaction:

$$Na_2S + nS = Na_2S_{n+1} \ (s,l)$$

Anhydrous Na_2S was initially prepared from $Na_2S \cdot 9H_2O$ which involved prolonged vacuum pumping at room temperature for many days followed by slow heating to 300°C, which was maintained for 24 hours. The Na_2S was then transferred to the dry box and finely ground, and subsequently dried at 700°C. under vacuum. The dehydrated Na_2S was a very white colour which may itself be a strong indication of the high purity of the product; contamination by as little as 0.1% polysulphide gives a faint but distinct colouration to the material.

Stoichiometric amounts of Na_2S and sulphur were then weighed and carefully mixed by grinding and then put into pyrex tubes (previously flamed under vacuum), evacuated and sealed.

The reaction proceeded through three stages:

a) Reaction at 200-230°C for 12 hours.
   This is a solid state reaction during which 80-90% conversion takes place.

b) Liquid reaction at 300-500°C for ½ hour. Complete reaction occurs.

c) Tempering at 200-220°C for 12 hours.

During this period well crystallized phases may be obtained.

The reaction tube was furnace cooled, transferred to the dry box and the content removed. The ground samples were then stored in a dessicator within the dry box. The sodium polysulphide products were subsequently analysed by X-ray diffraction and compared with the data of Tegman (287).

CHAPTER 5

ELECTROCHEMICAL BEHAVIOUR OF PbS IN THE BINARY $PbCl_2$-KCl EUTECTIC MELT

5.1 Introduction

The $PbCl_2$-KCl (77-23 m/o) eutectic system was initially selected as the solvent for an 'in-depth' electrochemical characterisation study of lead sulphide solutions. The addition of KCl to $PbCl_2$ results in the following:

(a) a decrease in the liquidus temperature to a range (430°C +) in which standard pyrex apparatus may be used;

(b) an increase in the conductivity of the melt, and

(c) a significant decrease in the $PbCl_2$ vapour pressure.

At a temperature of 450°C, for example, $PbCl_2$-KCl melts are liquid within the composition range 15-55 m/o KCl; pure $PbCl_2$ melts at 501°C. Furthermore the eutectic composition 77-23 m/o ($PbCl_2$-KCl) was particularly chosen because it corresponds to the composition of maximum PbS solubility (20·1).

Characterisation of PbS-$PbCl_2$-KCl solutions were undertaken using primarily the technique of cyclic voltammetry. Additional and supplementary information was gained from steady-state I-E curves, polarographic I-E relations, I-t transients and controlled potential electrolyis. Electrochemical data were obtained as functions of the bulk PbS concentration, temperature and electrode structure.

Two principal types of carbon electrodes were used, these being vitreous carbon and spec-pure graphite; all the carbon electrodes were sealed into pyrex glass. The vitreous carbon substrate presents an electrode

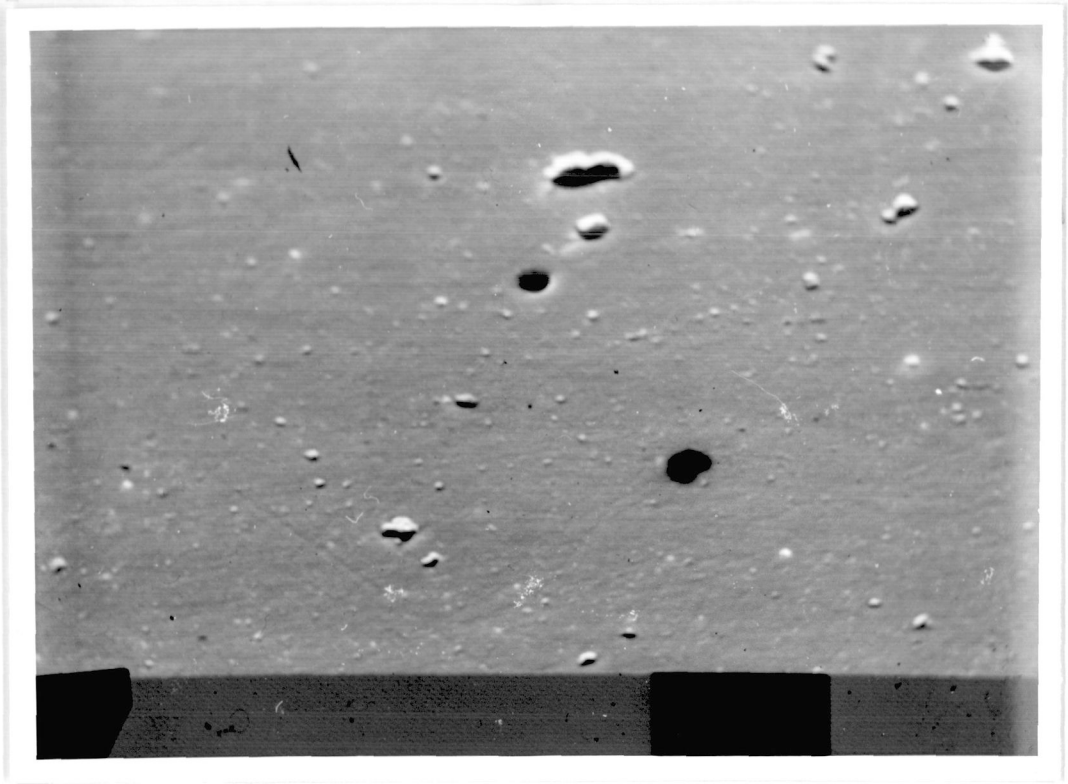


Photo 5.1: A stereomicrograph of the surface of polished vitreous carbon

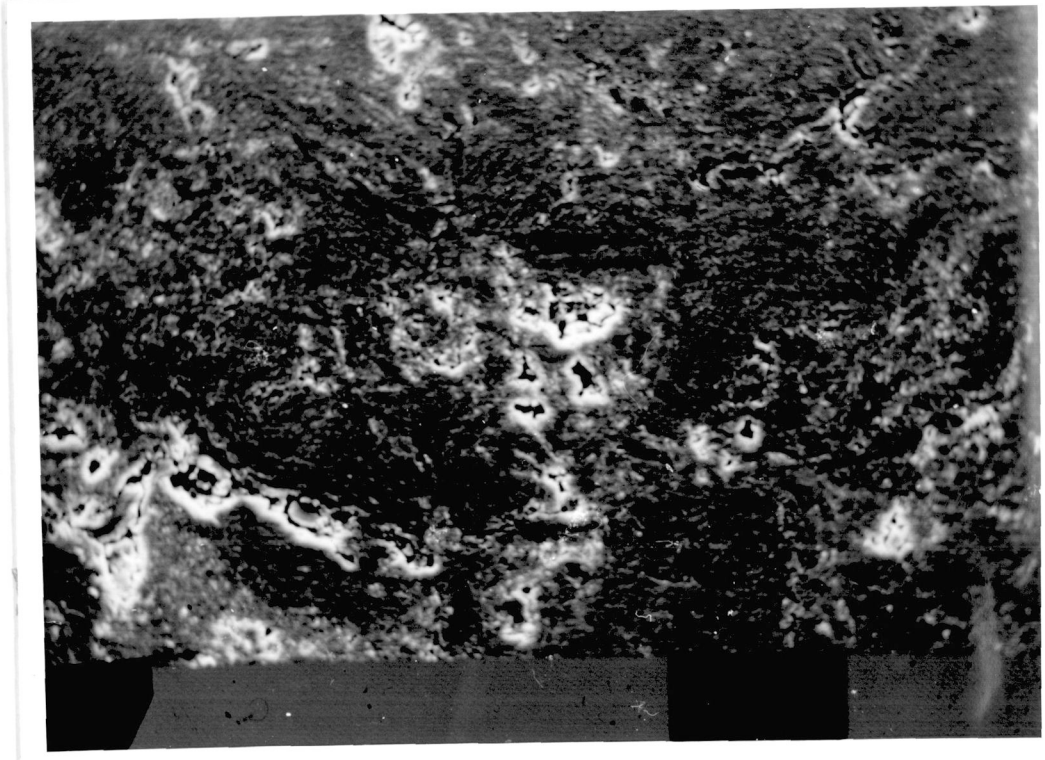


Photo 5.2: A stereomicrograph of the surface of a polished spec-pure graphite rod

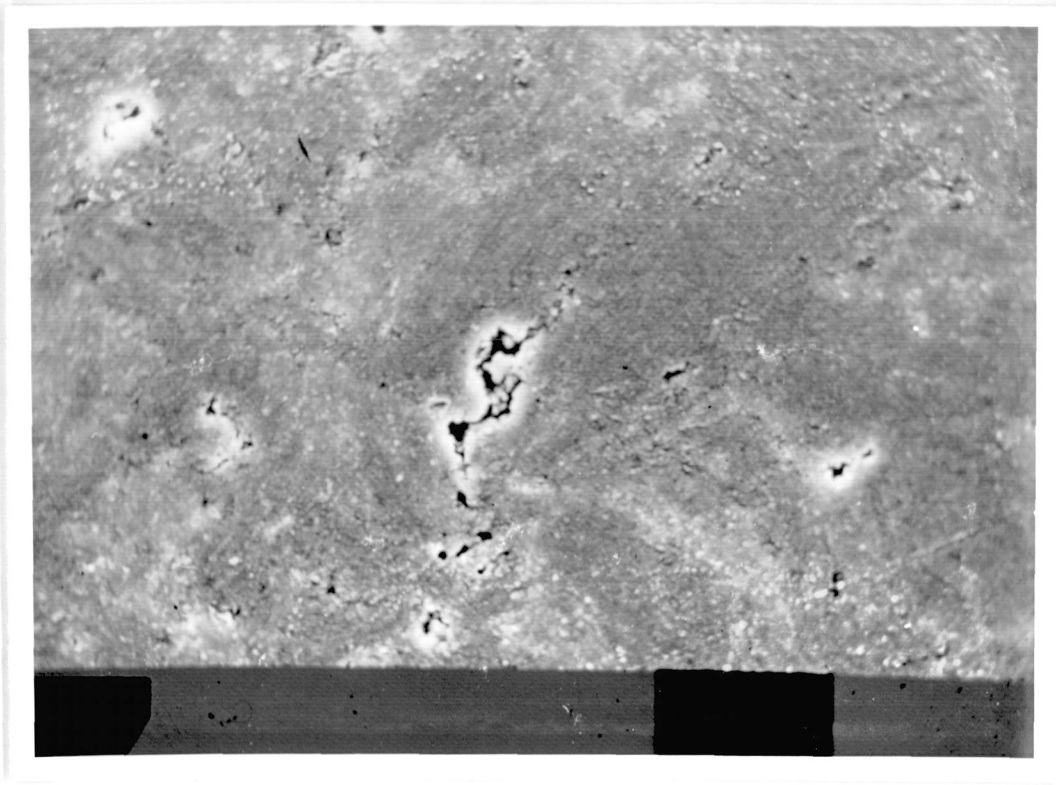


Photo 5.3: A stereomicrograph of the surface of a polished EYA110 graphite rod

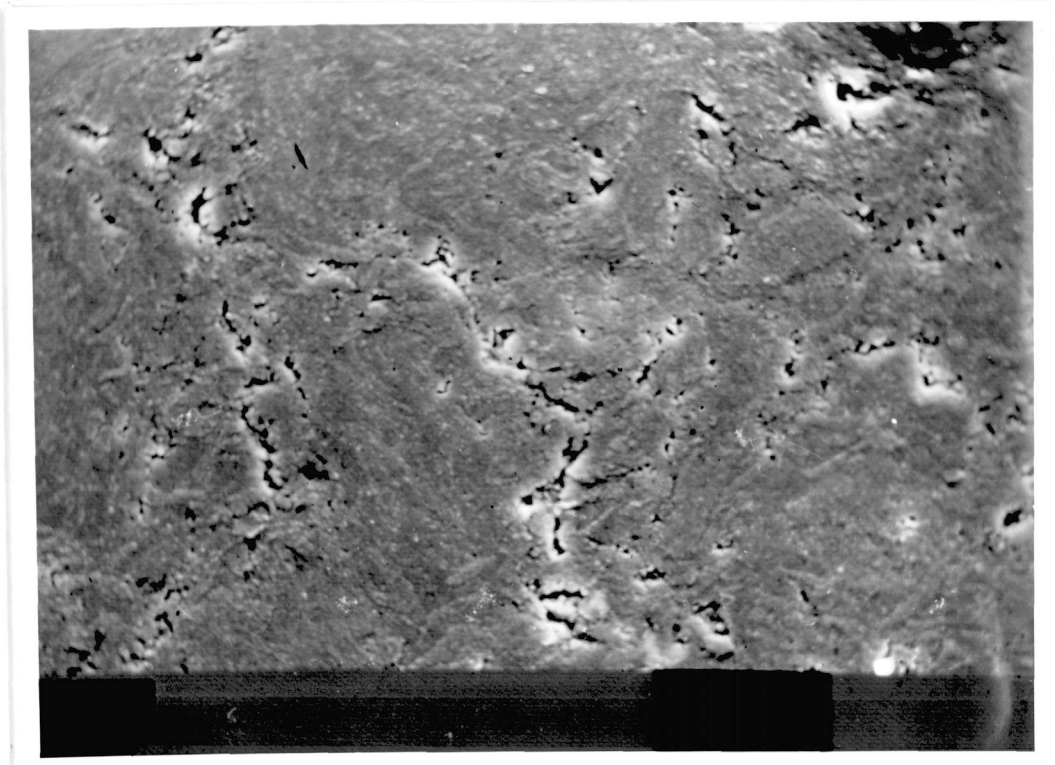


Photo 5.4: A stereomicrograph of the surface of a polished EYA9 graphite rod

surface which is smooth and of theoretical density, the graphite electrode on the other hand may be viewed as a porous electrode. Photographs 5.1 and 5.2 show scanning electron micrographs of the surfaces of polished vitreous carbon and graphite respectively. The structures typify the surfaces of the electrodes as used in this study. Photographs 5.3 and 5.4 show for comparison the surfaces of two commercially available graphites, one of which, EYA 110, is used as an anode material in aqueous electrolysis processes. The high degree of porosity of the graphites (10-20%) thus represents an electrode surface with a high roughness factor as compared to the vitreous carbon.

A comparison of the electrochemical properties of sulphide oxidation/reduction processes on the two electrodes is thus of both fundamental and applied interest.

5.2 Results

5.2.1 Cyclic Voltammetry

Fig. 5.1 shows a typical cyclic voltammogram obtained within the available 'potential window' and thus describes the system. The rapid increases in current at potentials > 1.1V wrt Ag^+/Ag corresponds to the chlorine evolution reaction and hence the anodic limit of the solvent. Two primary oxidation processes occur, the first at ∿0.45V and the second at ∿0.9V. A possible further oxidation process may be observed as an ill-defined shoulder or inflection on the first process. A single reduction wave corresponding to the first process occurs at ∿0.35V. No further reduction processes were observed up to the limiting Pb^{2+} reduction potential.

The absence of any polysulphide or sulphur impurities was further confirmed by the floating open circuit potential of the electrodes which was monitored after each successive PbS addition.

Fig. 5.2 shows the two primary oxidation processes in greater detail; in this figure the pre-wave is shown to be more prominent than

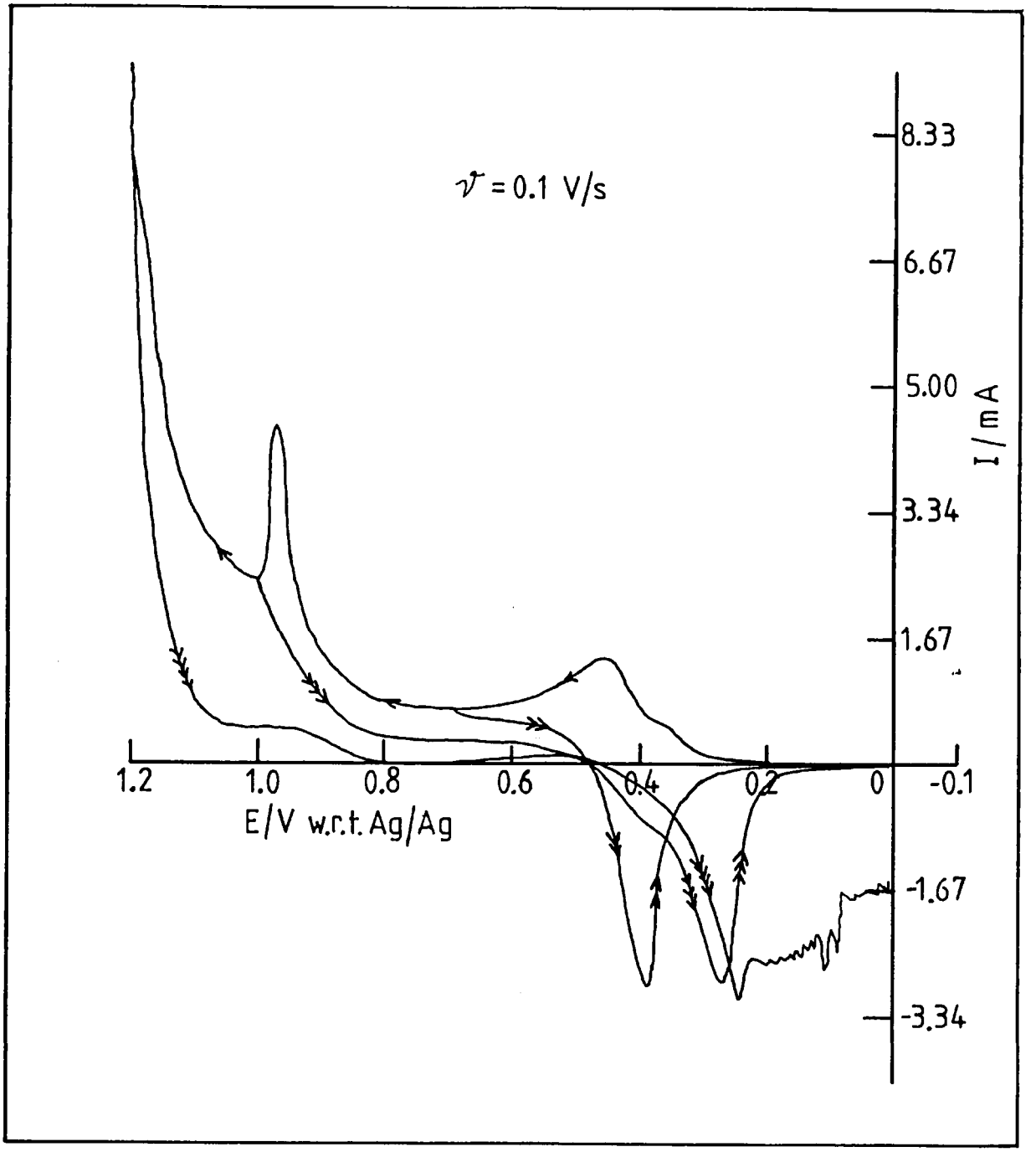


Fig. 5.1: A cyclic voltammogram obtained at a vitreous carbon electrode in a PbS-$PbC\ell_2$ - $KC\ell$ melt up to the anodic solvent limit. [Pbs] = 4.511×10^{-5} mole/cm^3; T = 457°C. Electrode area = 0.08553 cm^2; Solvent = $PbC\ell_2$ - $KC\ell$ (77.23 m/o).

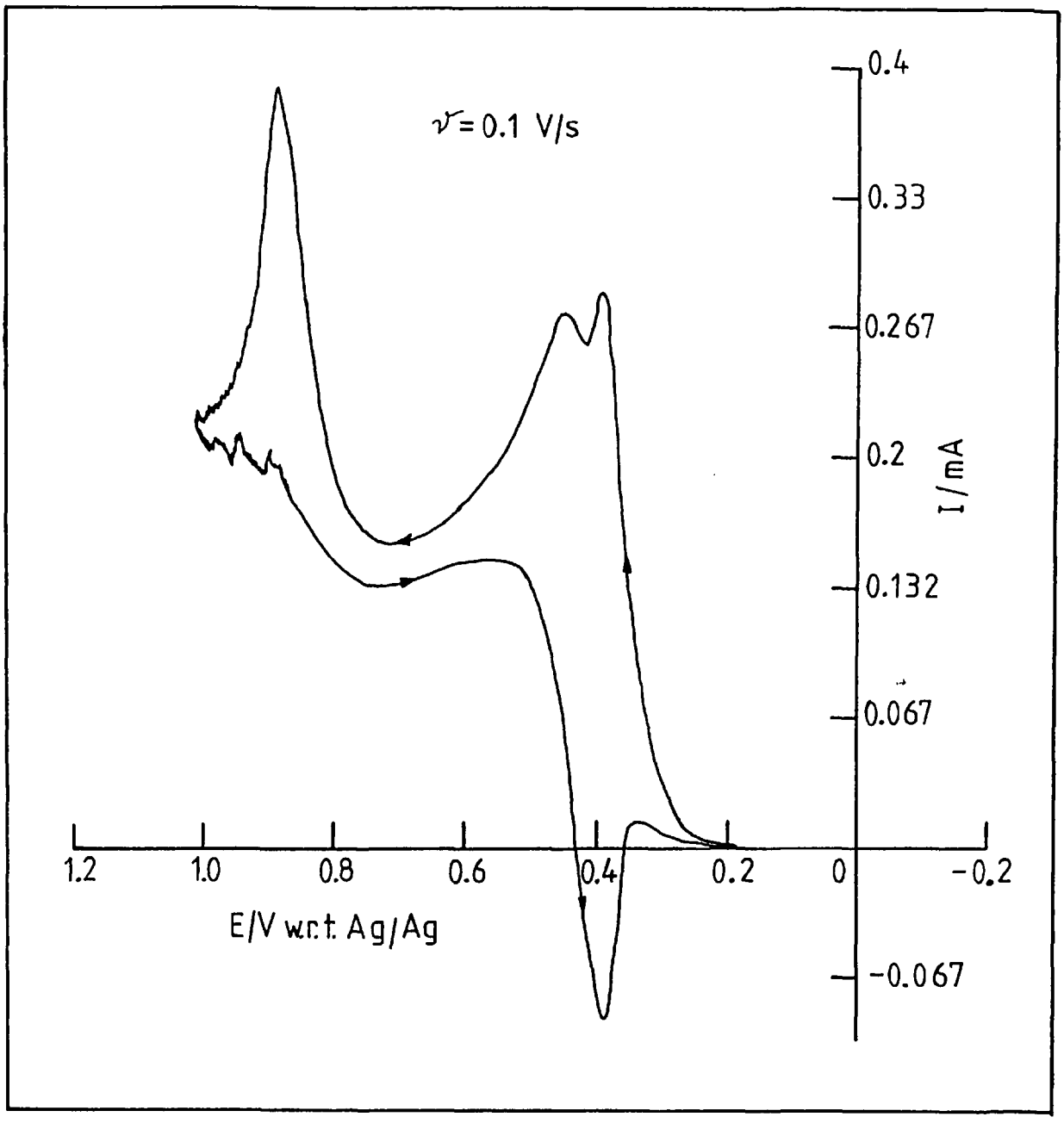


Fig. 5.2: A cyclic voltammogram showing the two anodic processes for the oxidation of PbS containing melts at carbon based electrodes [PbS = 1.573×10^{-4} mole/cm^3; T = 460°C; Electrode = vitreous carbon (0.08553 cm^3): Solvent = $PbCl_2$ - KCl (77-23 m/o).

was usually obtained. Detailed electrochemical investigations were confined to the first anodic process, i.e. sulphur formation. The more anodic process most probably corresponds to that of sulphur chloride formation according to the reaction (136):

$$2S + 2C\ell^- \rightarrow S_2C\ell_2 + 2e'$$

The pre-wave was observed primarily at the vitreous carbon electrode and was indeed found to occur in all the experiments undertaken. The wave could not be resolved sufficiently to yield any worthwhile analytical data either by varying the sweep rate, PbS concentration or temperature. The occurrence of the wave could not be attributed to any impurity of either the bulk solvent or to the type of lead sulphide employed. The only observation that could be made was that it occurred mainly at the highly polished vitreous carbon electrode rather than the 'rough' graphite electrode and would, therefore, indicate a possible surface induced phenomenon. However, no statistically meaningful results were obtained by varying the surface roughness or cleaning procedure of the vitreous carbon.

The effect of increasing sweep rate (typically ν = 0.02 - 20 V/s) (see Figs. 5.3 and 5.4) upon the various voltammetric parameters obtained at vitreous carbon and spec-pure graphite electrodes are given in Tables 5.1 and 5.2 respectively.

Fig. 5.5 shows that the anodic peak current I_p^a increases linearly with increasing (sweep rate)$^{\frac{1}{2}}$ at all concentrations (4.5×10^{-2} - 1.573×10^{-1} mole/l). The results of linear regression analysis gave correlations of > 0.995. At the higher PbS concentrations used, slight positive I intercepts were obtained rather than the zero intercept as would be expected on the basis of Randles Sevcik equation. Similar relationships were obtained at the graphite electrode, indeed no deviation from the I_p^a-$\nu^{\frac{1}{2}}$ dependency was obtained in any of the numerous experiments undertaken.

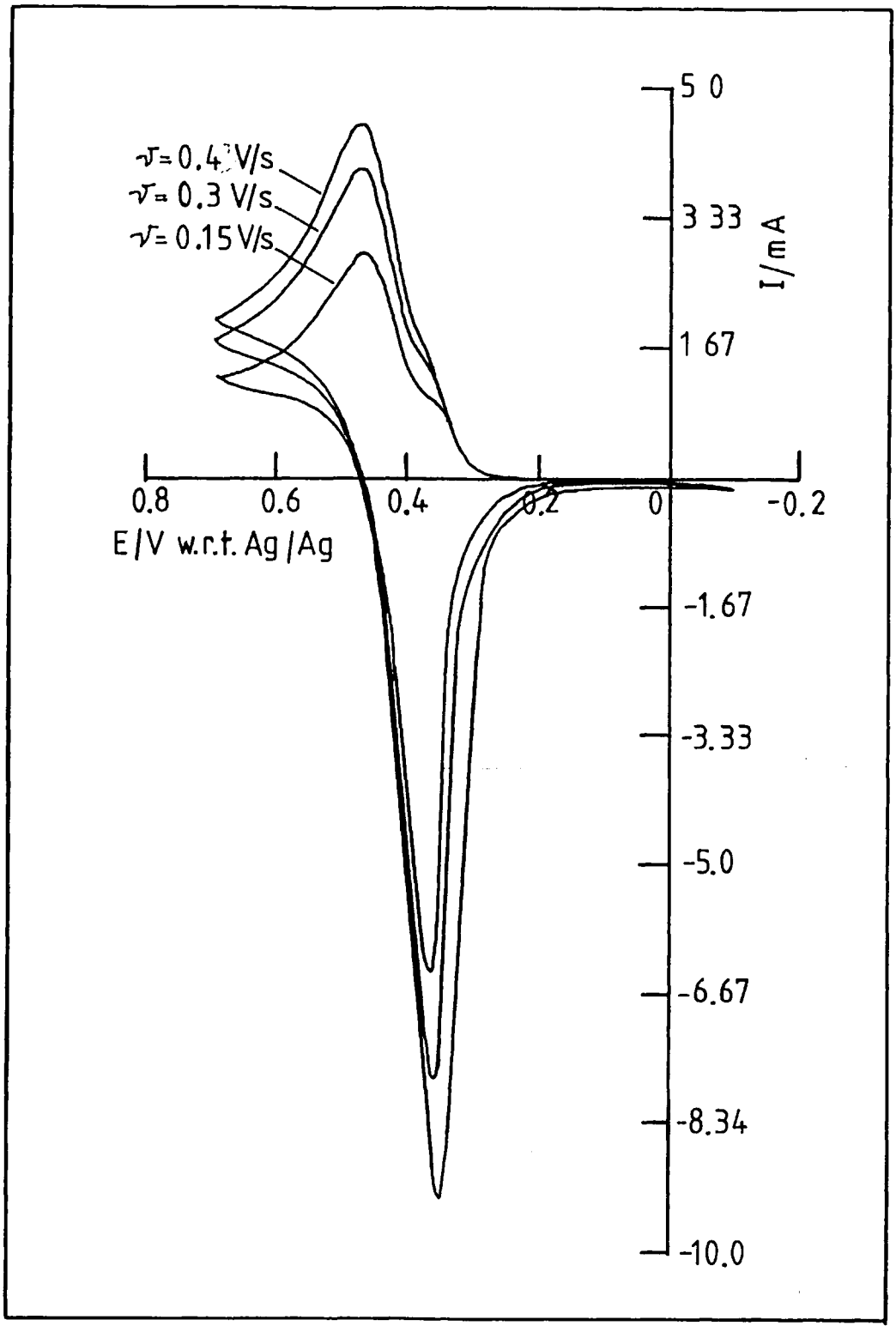


Fig. 5.3: The effect of sweep rate upon the I-E curve for the S^{2-}/S oxidation/reduction process [PbS] = 8.754×10^{-5} mole/cm^3; T = 457°C; Electrode = vitreous carbon (area = 0.0855 cm^2): Solvent = $PbCl_2$ - KCl (77-23 m/o).

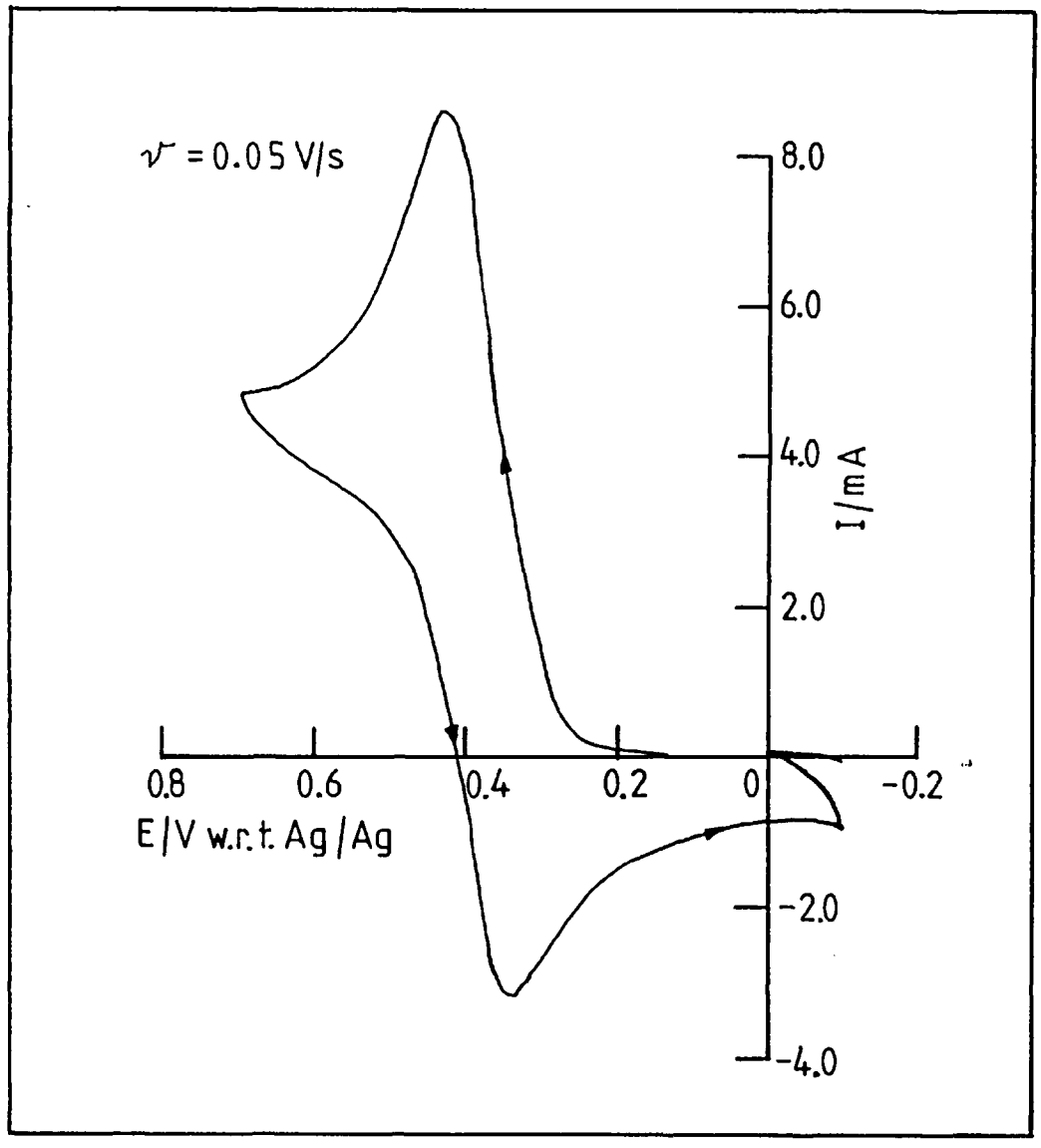


Fig. 5.4: A typical voltammogram obtained at a spec-pure graphite electrode for the oxidation of PbS containing melts over the voltage range 0 - 0.7V wrt Ag^{+}/Ag^{o}. [PbS] = 1.577 x 10^{-4} mole/cm^3; T = 445°C; Area = 0.0707 cm^2: Solvent = $PbC\ell_2$ - $KC\ell$ (77-23 m/o).

TABLE 5.1

Effect of increasing sweep rate (V) upon the cyclic voltammetric parameters for the oxidation of S^{2-} ion at a vitreous carbon electrode. T = 457°C; PbS = 4.511×10^{-5} mole/cm^3; Electrode = vitreous carbon; Area = 0.0855 cm^2.

V v/s	Ip^a mA	$Ip^a/v^{\frac{1}{2}}$	Ip^c/Ip^a	Ep^a *	Ep^c *	E mV
0.02	0.667	4.717	1.901	450	390	60
0.05	1.10	4.919	2.108	475	395	80
0.1	1.40	4.43	2.351	474	400	75
0.2	1.917	4.29	2.317	485	400	85
0.3	2.292	4.18	2.296	490	395	95
0.4	2.58	4.08	2.304	490	390	100
0.5	2.83	4.0	2.344	480	395	85
1.0	4.0	4.0	2.224	483	375	108
2.0	5.7	4.03	7.044	488	365	123
5.0	9.0	4.03	1.773	499	357	142
10.0	12.25	3.87	1.710	513	335	178
20.0	16.5	3.69	1.652	533	316	219

* E/mV w.r.t. Ag^+/Ag

TABLE 5.2

Effect of increasing sweep rate (V) upon the cyclic voltammetric parameter for the oxidation of S^{2-} ion at a planar spec pure carbon electrode.
$T = 440^{o}C$; PbS = 8.068×10^{-5} mole/cm^3; Area = 0.707 cm^2

V v/s	Ip^a mA	$Ip^a/v^{\frac{1}{2}}$	Ip^c/Ip^a	Ep^a	Ep^c	ΔE mV	Ep^a-Ep/2 mV
0.02	1.583	11.19	0.833	0.45	0.355	90	75
0.05	2.4	10.73	0.764	0.45	0.355	95	75
0.10	3.3	10.44	0.906	0.45	0.380	70	75
0.15	4.0	10.33	1.026	0.455	0.375	80	80
0.20	4.5	10.06	1.133	0.455	0.370	85	80
0.25	5.0	10.0	1.203	0.46	0.370	90	80
0.30	5.33	9.732	1.273	0.465	0.370	95	80
0.35	5.75	9.72	1.295	0.465	0.360	105	80
0.40	6.08	9.61	1.324	0.460	0.350	105	80
0.50	7.0	9.90	1.337	0.453	0.360	93	80
0.60	7.625	9.84	1.382	0.457	0.358	99	-
0.80	8.625	9.64	1.404	0.461	0.344	117	-
1.0	9.375	9.38	1.438	0.475	0.320	155	-
2.0	12.75	9.02	1.430	0.495	0.30	195	-
3.0	15.375	8.877	1.415	0.503	0.289	214	-
4.0	17.5	8.75	1.420	0.510	0.279	231	-
5.0	19.5	8.72	1.385	0.523	0.278	245	-
6.0	21.125	8.63	1.388	0.526	0.274	252	-

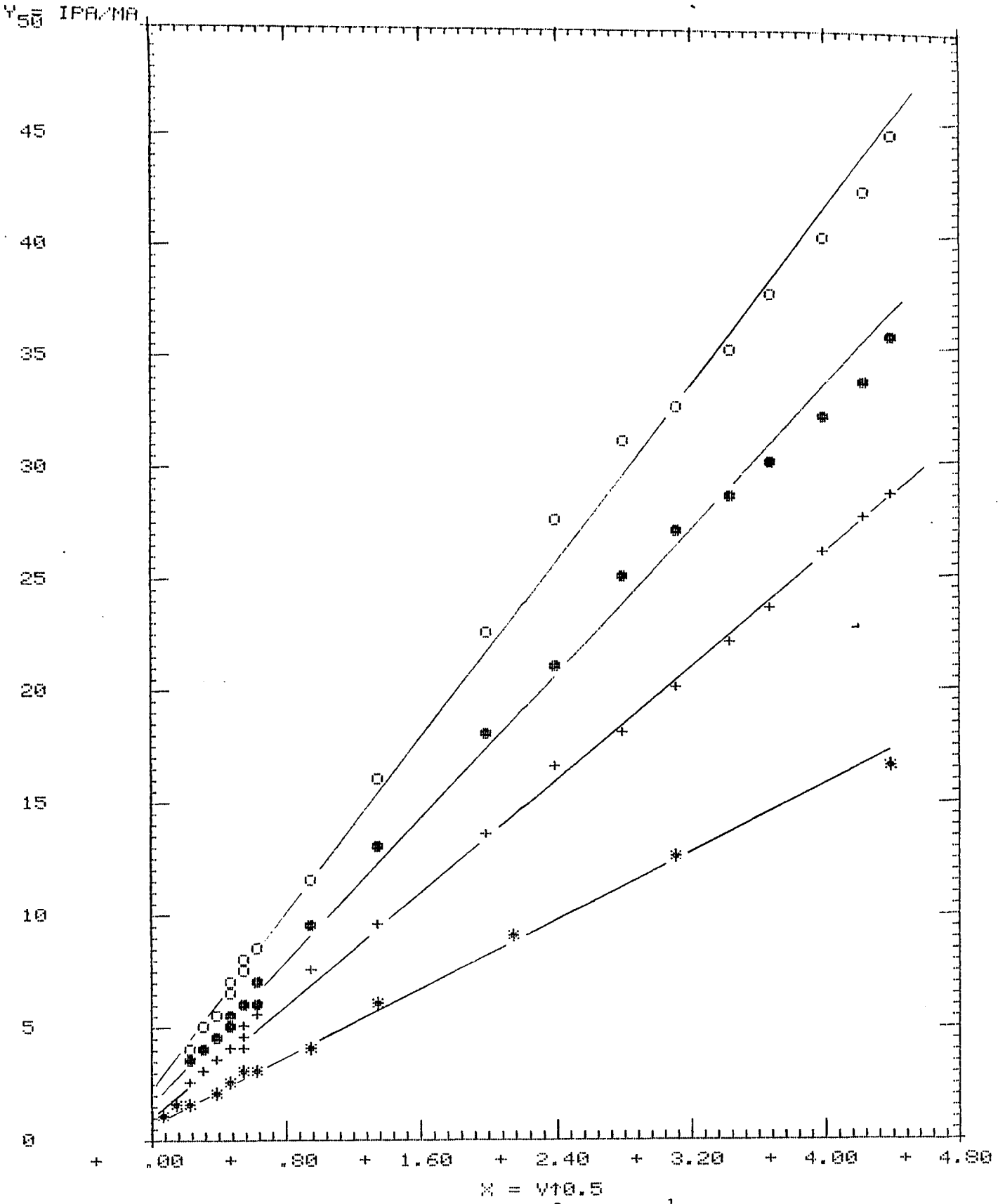


FIGURE NUMBER : 5.5: A plot of I_p^a versus $v^{\frac{1}{2}}$ for various PbS concentrations. Electrode = vitreous carbon (area = 0.0855 cm^2; T = 457°C; Solvent = $PbCl_2$ - KCl (77-23 m/o). PbS concentrations: O = 1.573×10^{-4}; ● = 1.235×10^{-4}; + = 8.75×10^{-5}; * = 4.511×10^{-5} mole/cm^3.

Values of the diffusion coefficient calculated at different PbS concentrations for both types of electrodes are shown in Table 5.3. The calculations were based on the value of $dI_p^a/dv^{\frac{1}{2}}$ obtained by linear regression analysis. Table 5.3 further provides values calculated for n = 1 and n =2 processes using the relevant formulas for soluble and insoluble products. The results from two independent experiments show the diffusion coefficient values to decrease with increasing concentration. These values were independent of the type of electrode used and the type of calculation performed. Assuming an n = 2 value the D values for both soluble and insoluble calculations are very low, i.e. 10^{-6} cm^2/s as compared to normal diffusion coefficient values obtained in molten salt media, i.e. 10^{-5} cm^2/s. However, assuming n = 1, more reasonable D values were obtained.

The more sensitive current plot of $I_p^2/v^{\frac{1}{2}}$ versus v, Fig. 5.6, shows $I_p^a/v^{\frac{1}{2}}$ to be virtually independent of sweep rate at low PbS concentrations but gradually to decrease with increasing v at high PbS concentrations. The dependency of the parameter I_p^c/I_p^a with increasing sweep rate is a particularly interesting one. The ratio may be considered as a collection efficiency parameter and thus may be used to distinguish between those systems in which coupled chemical reactions to the electron transfer reaction take place. Low I_p^c/I_p^a ratios may occur as the direct result of the physical removal of the product, e.g. as in the case of gas evolution reactions. The I_p^c/I_p^a ratios were calculated from the modified Nicholson empirical formula (18):

$$\frac{I_p^c}{I_p^a} = \frac{(I_p^c)_o}{(I_p^a)_o} + \frac{0.45\ (I_{SW})_o}{(I_p^a)_o} + 0.086$$

Fig. 5.7 shows the variation of I_p^c/I_p^a obtained at a vitreous carbon electrode with increasing sweep rate, and various PbS concentrations and which typifies the behaviour of systems at temperatures $< \sim 470°C$. At low sweep rates the

TABLE 5.3

Values of the diffusion coefficients obtained at VC and SPG electrodes as a function of the PbS concentration. VC = 457°C; SPG = 440°C. The values are calculated from the Randles Sevcik equation for soluble and insoluble products and for n = 1 and n = 2.

Vitreous Carbon

PbS	Soluble Product		Insoluble Product	
mole/l	n = 1	n = 2	n = 1	n = 2
4.51×10^{-2}	3.06×10^{-5}	3.83×10^{-6}	1.68×10^{-5}	2.1×10^{-6}
8.754×10^{-2}	2.30×10^{-5}	2.88×10^{-6}	1.27×10^{-5}	1.58×10^{-6}
1.235×10^{-1}	1.82×10^{-5}	2.28×10^{-6}	1.0×10^{-5}	1.25×10^{-6}
1.573×10^{-1}	1.74×10^{-5}	2.20×10^{-6}	0.95×10^{-5}	1.19×10^{-6}

Spec Pure Graphite (SPG)

8.068×10^{-2}	7.02×10^{-5}	8.76×10^{-6}	3.85×10^{-5}	4.82×10^{-6}
1.351×10^{-1}	5.97×10^{-5}	7.46×10^{-6}	3.27×10^{-5}	4.09×10^{-6}
2.151×10^{-1}	5.95×10^{-5}	7.43×10^{-6}	3.26×10^{-5}	4.08×10^{-6}
2.553×10^{-1}	5.65×10^{-5}	7.07×10^{-6}	3.11×10^{-5}	3.88×10^{-6}

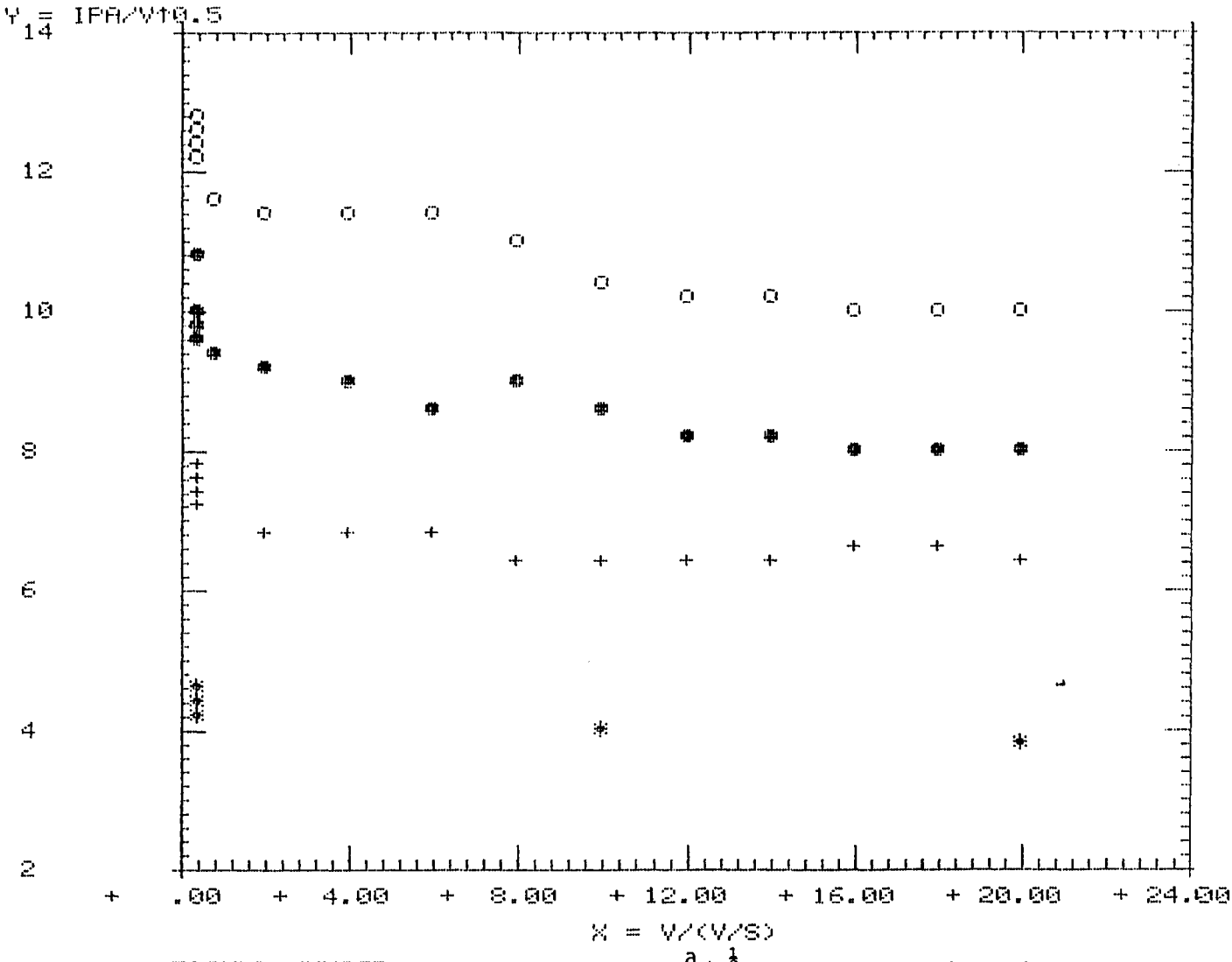


FIGURE NUMBER 5.6: A plot of $I_p^a/\nu^{\frac{1}{2}}$ versus ν for the oxidation of PbS containing solutions at vitreous carbon Area = 0.0855 cm^2; T = 457°C; Solvent = $PbC\ell_2$-KCℓ (77-23 m/o) PbS concentrations; O = 1.573×10^{-4}; ● = 1.235×10^{-4}; + = 8.754×10^{-5}; * = 4.511×10^{-5} mole/cm^3.

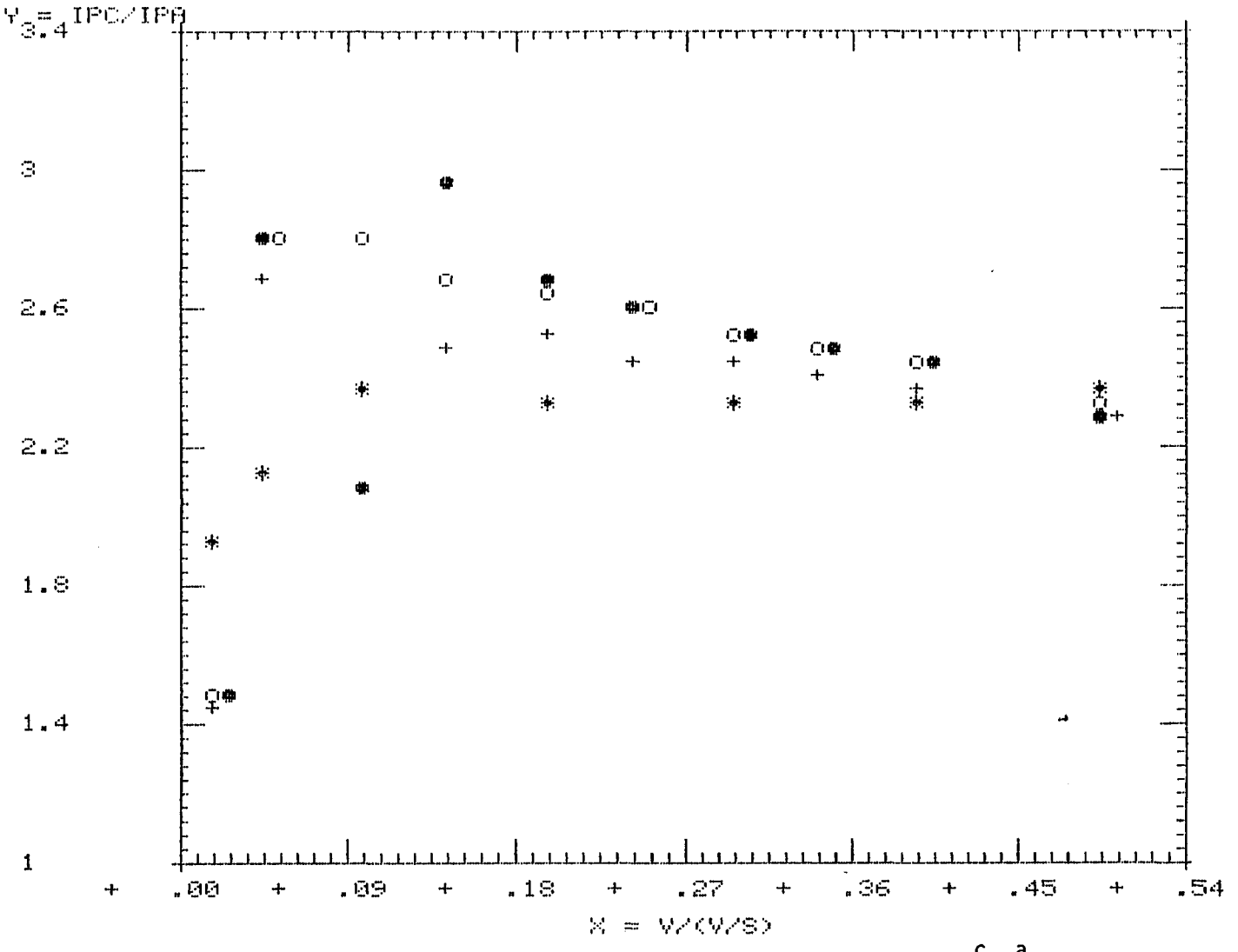


FIGURE NUMBER 5.7: A plot of the current function I_p^c/I_p^a versus ν
Electrode = vitreous carbon (area = 0.0855 cm^2);
T = 457°C; Solvent = $PbC\ell_2$ - $KC\ell$ (77-23 m/o);
PbS concentration: O = 1.573×10^{-4};
● = 1.235×10^{-4}; + = 8.754×10^{-5};
⋆ = 4.511×10^{-5} mole/cm^3.

current ratio increases with increasing sweep rate until either a plateau is reached or a maximum is reached after which the ratio gradually decreases. It is noted that typical I_p^c/I_p^a ratios vary (for $T \leq \sim 470°$) from 1.4 - 3; this hence infers the formation and subsequent stripping of an insoluble product.

Similar behaviour was observed at the graphite electrode although the initial increase in I_p^c/I_p^a occurred over a wider range of sweep rates and culimated in a plateau.

The variation of the potential peak values E_p^a and E_p^c and in particular the ΔE value with increasing sweep rate may provide both qualitative and quantitative information concerning the reversibility of the system. At the vitreous carbon electrode and particularly for those solutions at temperatures < 470°C, the oxidation peak potential E_p^a remains essentially constant at low sweep rates, i.e. $<\sim$1V/s. A further increase in ν causes the E_p^a to shift anodically and that of E_p^c cathodically. Figs. 5.8 and 5.9 show the shift of E_p^a to be linearly dependent on log ν. The peak separation value ΔE shows a similar trend with increasing ν, Figs. 5.10 and 5.11. At low sweep rates $\Delta E \cong 80$ mV and increases to $\sim$150 mV at 10V/s. Plots of E_p^a vs log ν may yield several useful kinetic parameters, namely the value of αn_a which may be obtained from the value of $dE/d\log\nu$ and secondly the critical sweep rate at which the transition from reversible to irreversible behaviour occurs, i.e. $\log\nu_c$. The electrochemical rate constant k may be obtained from a knowledge of $\log\nu_c$. Table 5.4 shows typical values of αn_a, $\log\nu_c$ and k which were either measured or calculated from E_p^a-logν plots obtained at various PbS concentrations. At high temperatures, two linear sections of $dE/d\log\nu \neq 0$ were obtained and thus values of $\log\nu_c$ could not be obtained. Typical E_p^a - log plots obtained at the graphite electrode are shown in Fig. 5.12. Two linearly dependent E_p^a-logν sections are obtained corresponding to low and high potential scan rate regions. Typical values of the slopes and

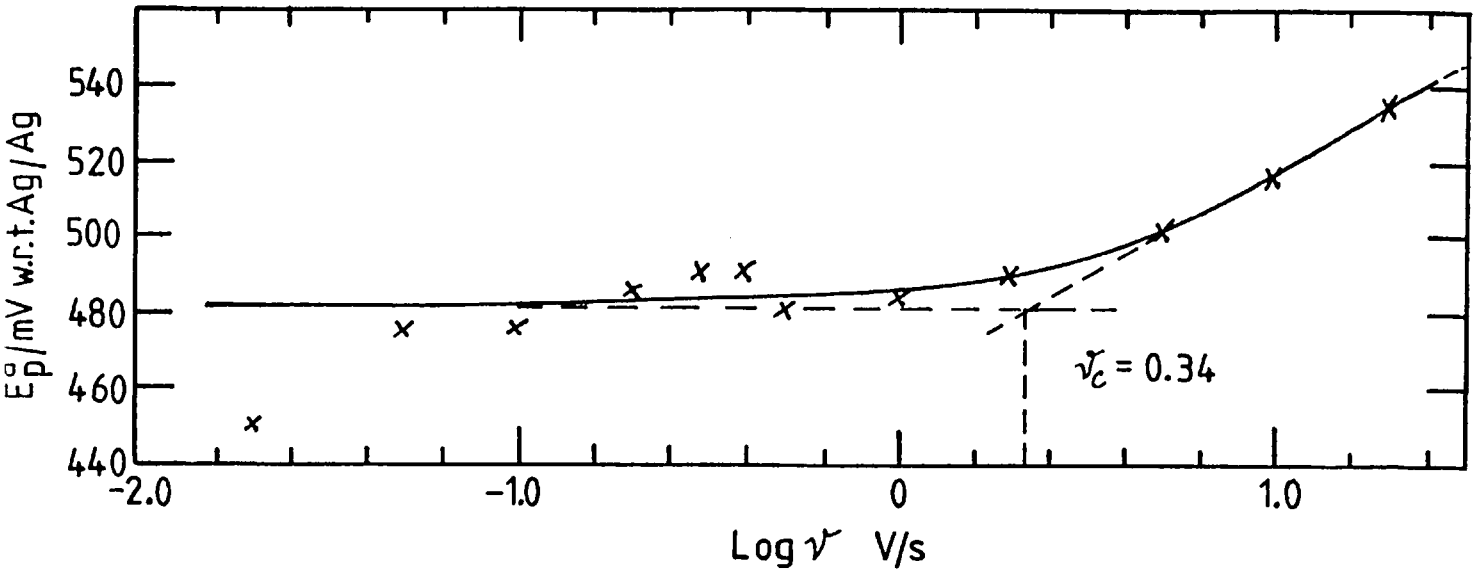


Fig. 5.8: The variation of the peak potential E_p^a with increasing log ν at a PbS concentration of 4.511×10^{-5} mole/cm^3. T = 457°C; electrode = vitreous carbon; area = 0.0855 cm^2.

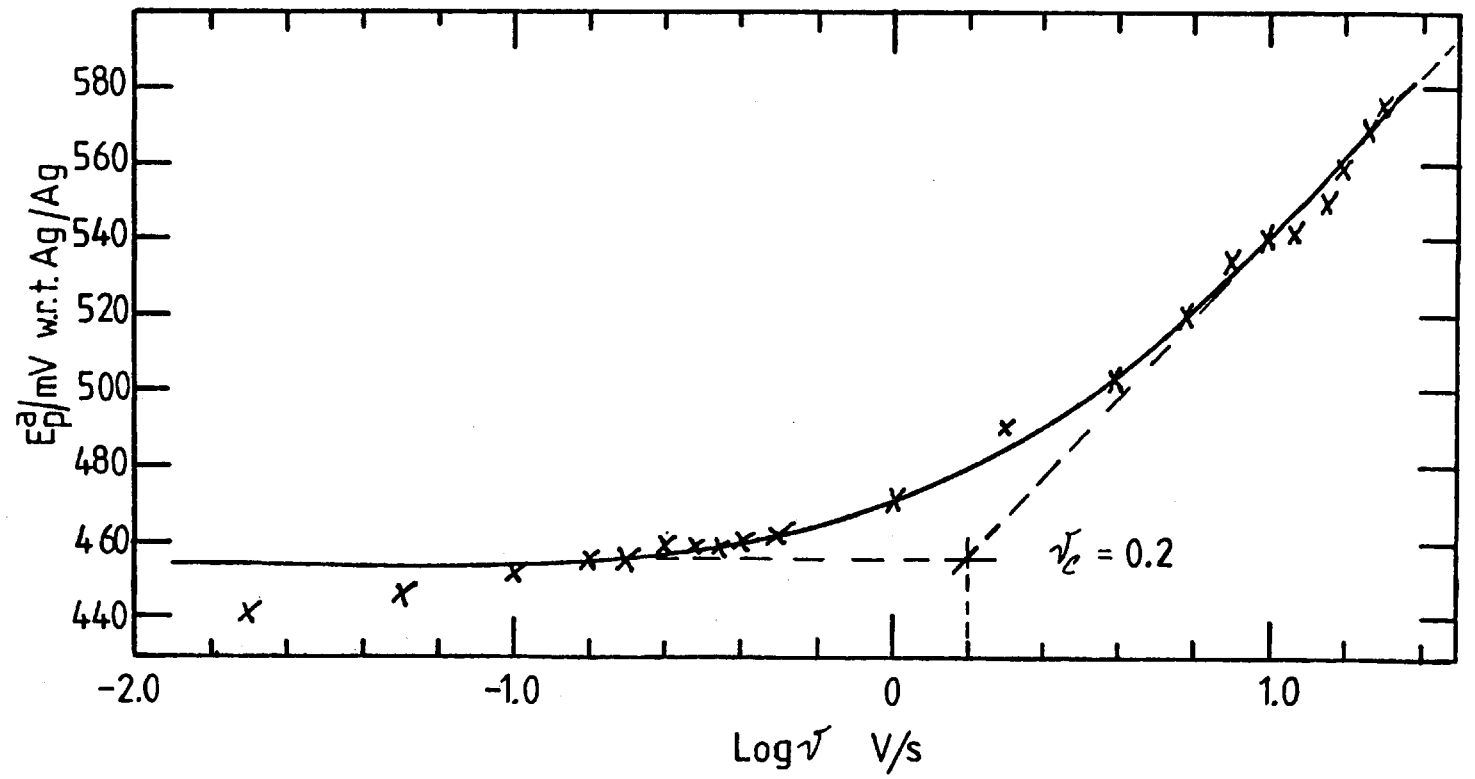
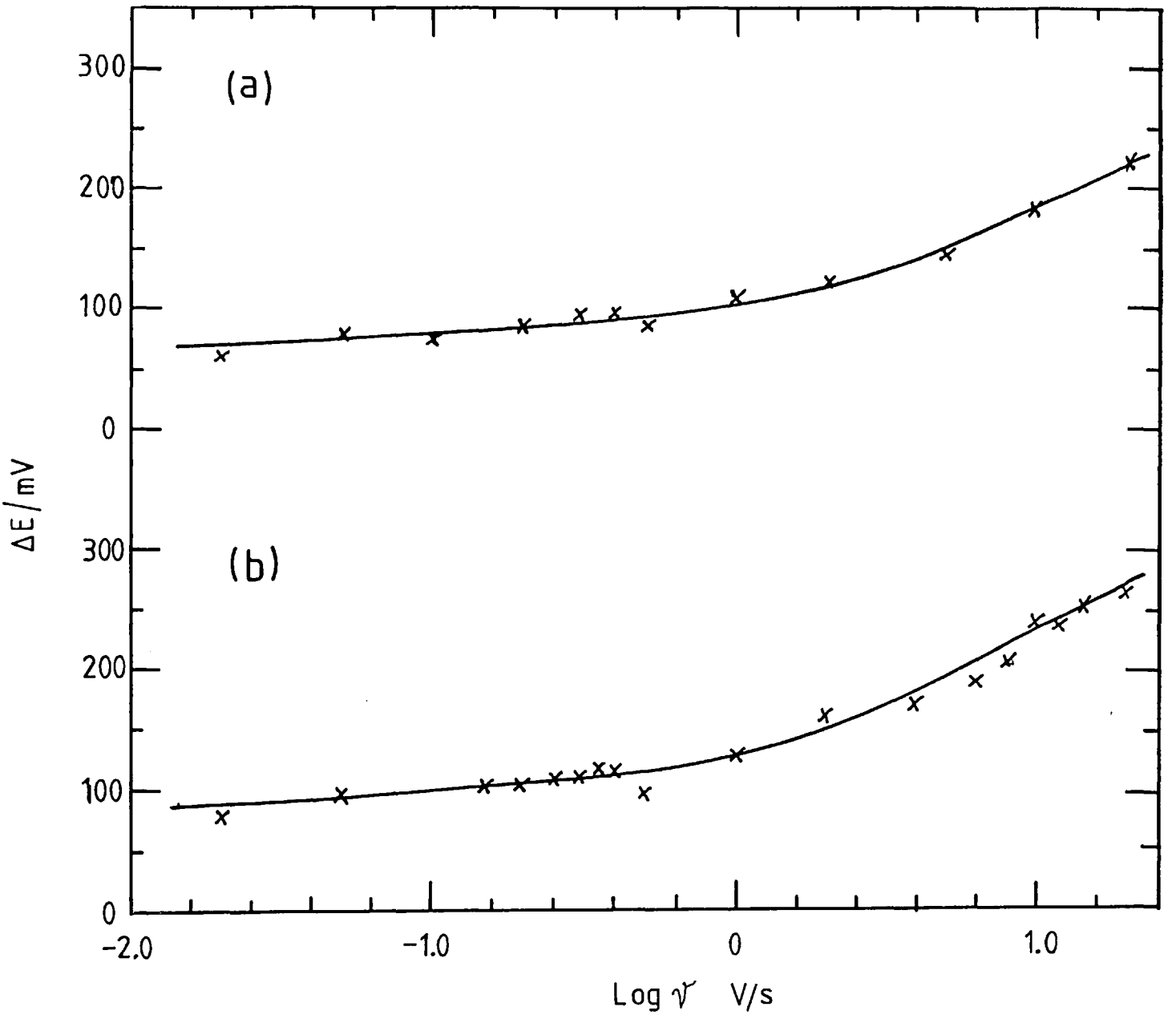


Fig. 5.9: The variation of the peak potential E_p^a with increaing log ν at a PbS concentration of 1.573×10^{-4} mole/cm^3. T = 457°C; electrode = vitreous carbon; area = 0.0855 cm^2.



Figs. 5.10 and 5.11: The variation of the peak separation voltage ΔE (= $E_p^a - E_p^c$) with increasing log ν.

(a) [PbS] = 4.511×10^{-5} mole/cm^3

(b) [PbS] = 8.754×10^{-5} mole/cm^3

T = 457°C; Electrode = vitreous carbon (area = 0.855 cm^2).

TABLE 5.4.

Values of the critical sweep rate for the oxidation of PbS and derived parameters obtained at a vitreous carbon electrode at 457°C.

PbS mole	log v_c	k s^{-1}	dE/d log v	αn_a
4.511×10^{-5}	0.34	7.0×10^{-3}	0.046	3.15
8.754×10^{-5}	0.32	1.04×10^{-2}	0.074	1.96
1.235×10^{-4}	0.32	1.14×10^{-2}	0.089	1.63
1.573×10^{-4}	0.20	1.04×10^{-2}	0.104	1.39

Note R, the rate constant was calculated assuming a soluble reactant and product scheme.

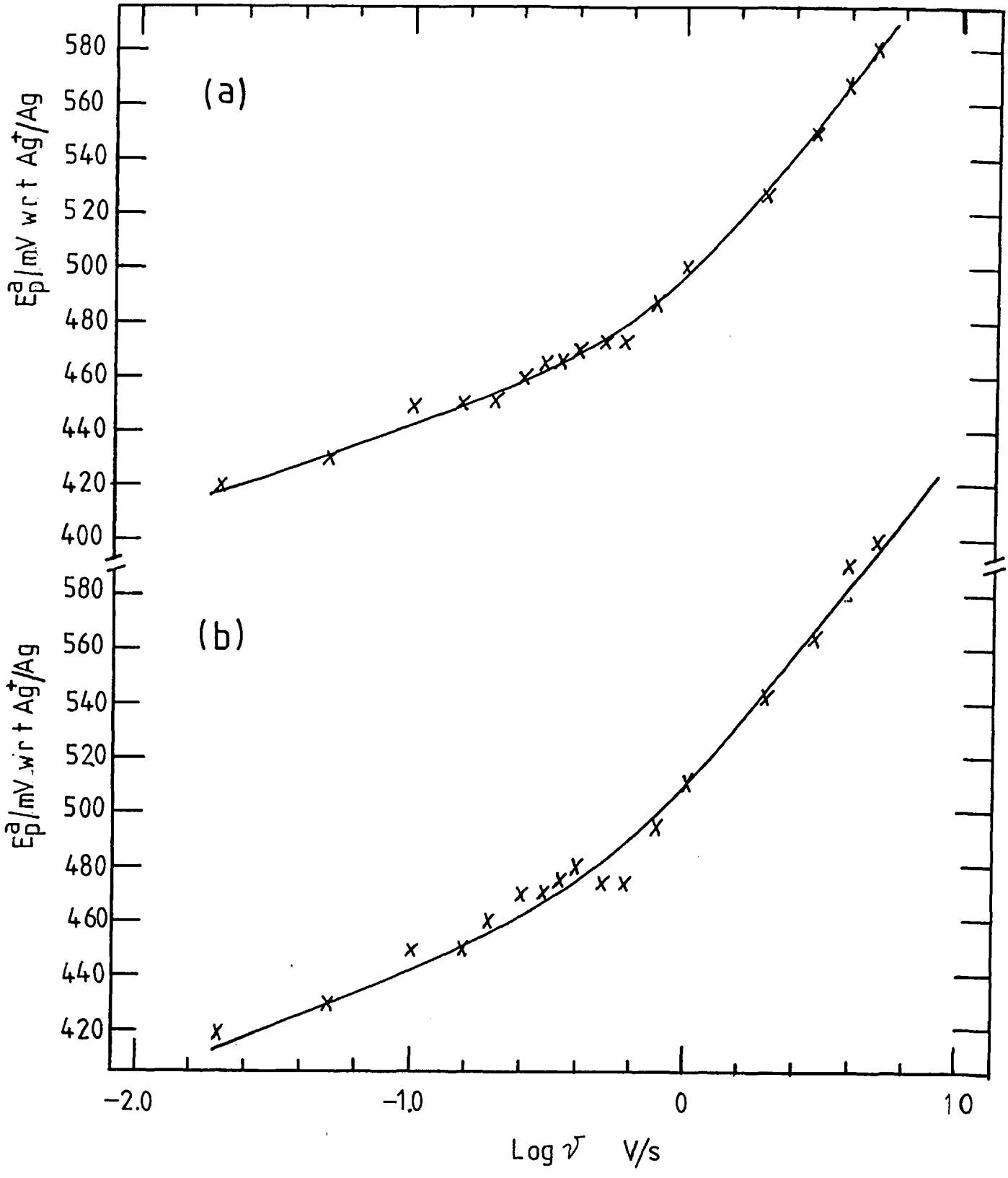


Fig. 5.12: The effect of PbS concentration upon the shift of the peak potential E_p^a with increasing log ν at a spec-pure graphite electrode.

(a) PbS = 2.151×10^{-4} mole/cm^3

(b) PbS = 2.553×10^{-4} mole/cm^3

T = 440°C; Area = 0.707 cm^2

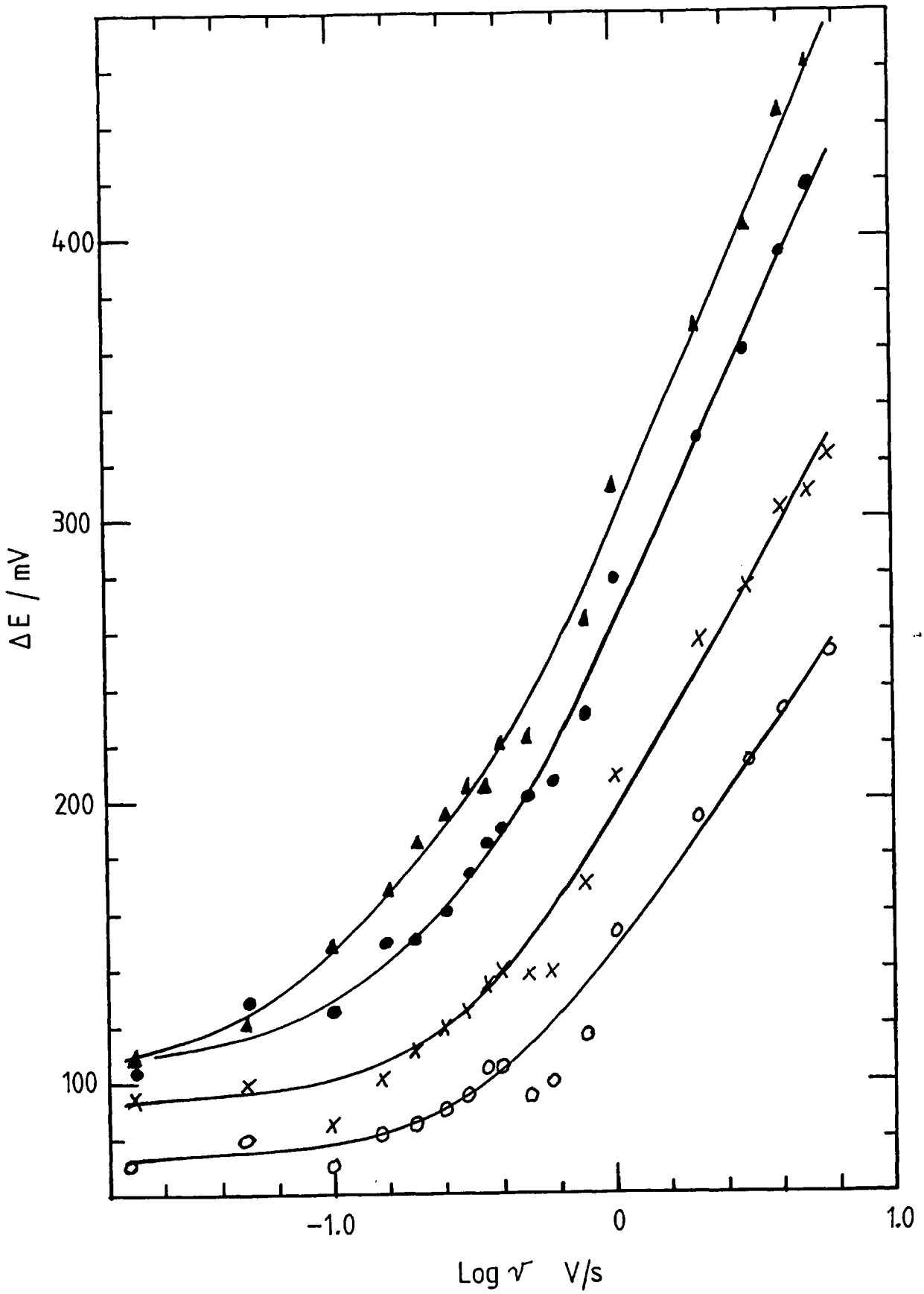


Fig. 5.13: The effect of increaisng PbS concentration upon the peak separation value ΔE (= $E_p^a - E_p^c$) with increasing log ν.
[PbS] mole/cm^3; O = 8.07 x 10^{-5};
X = 1.35 x 10^{-4}; ● = 2.151 x 10^{-4}; ▲ = 2.553 x 10^{-4}
Electrode = spec-pure graphite (area = 0.707 cm^2); T = 440°C

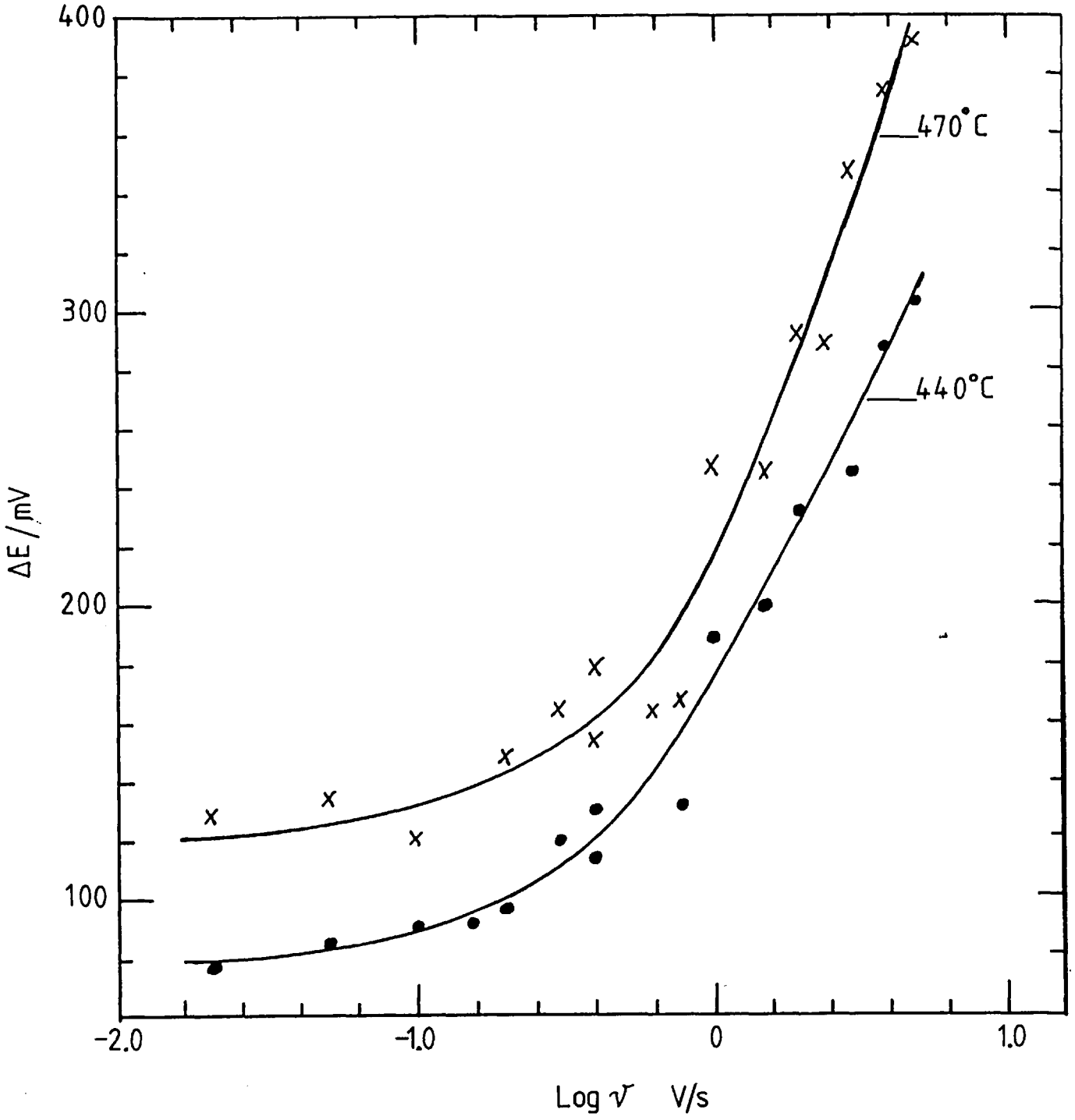


Fig. 5.14: The effect of increasing temperature upon the peak separation value ΔE versus log ν plot.
[PbS] = 1.572×10^{-4} mole/cm^3; electrode = vitreous carbon (area = 0.707 cm^2).

TABLE 5.5

The influence of increasing temperature upon the cyclic voltammetric parameters of the oxidation of the S^{2-} ion at a vitreous carbon electrode.

PbS = 1.573×10^{-4} mole/cm^3; Sweep rate = 0.2 v/s; Switching potential (Eλ) = 0.8V; Vitreous Carbon electrode Area = $0.0855\,cm^2$

T ^oC	$1/T.10^3$ K	Ip^a mV	log Ip^a	Ip^c/Ip^a	Q^a mC	Q^c mC	Q^c/Q^a	Ep^a *	Ep^c *	E mV
432	4.18	5.125	0.71	3.276	9.0	7.5	0.833	425	285	140
445	1.392	5.375	0.730	3.080	9.75	7.625	0.782	445	305	140
468	1.349	5.75	0.760	2.971	10.875	7.625	0.701	470	330	140
491	1.309	6.50	0.813	2.618	12.875	7.25	0.620	490	350	140
513	1.272	7.50	0.875	2.411	15.375	8.25	0.550	510	365	145
538	1.233	9.125	0.910	2.201	17.0	8.5	0.500	535	395	140
560	1200	9.625	0.983	1.895	20.625	8.125	0.394	555	415	140

* E/mV w.r.t. Ag^+/Ag

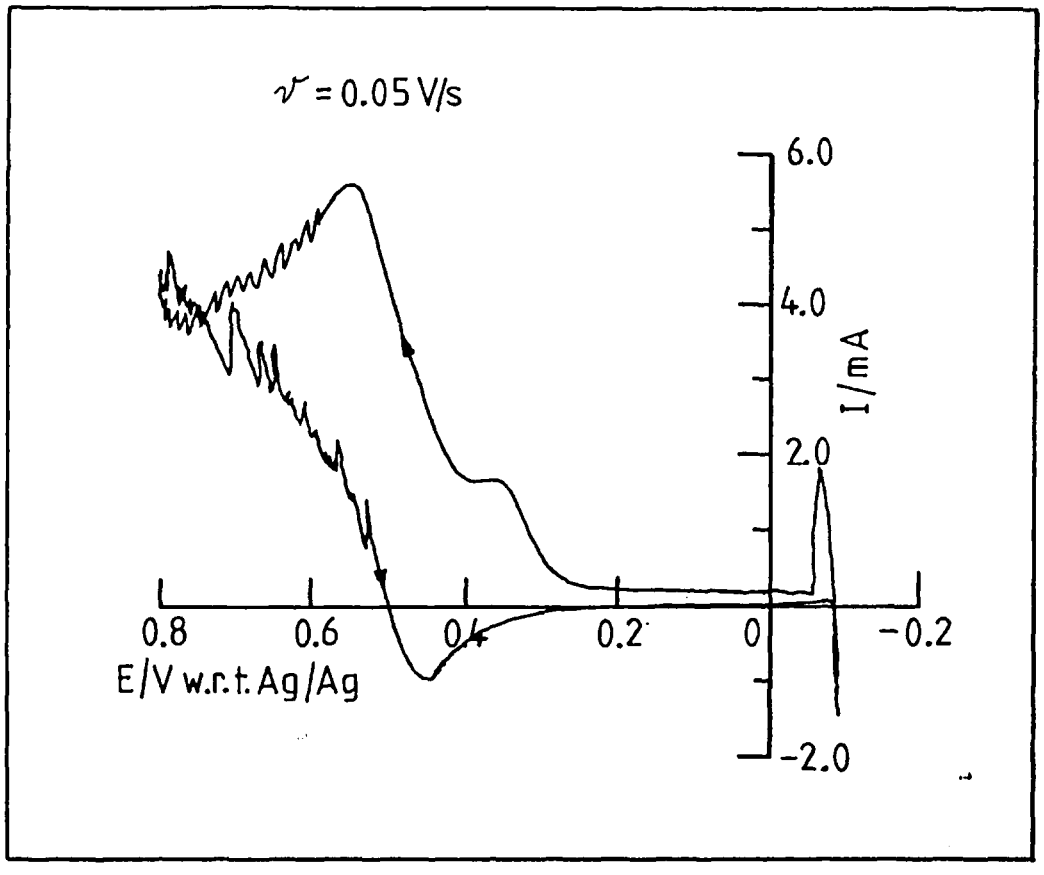


Fig. 5.15: A typical voltammogram obtained at a vitreous carbon electrode at higher temperature (538°C) for the oxidation of PbS containing melts. [Pbs] = 1.573×10^{-4} mole/cm^3; ARea = 0.0855 cm^2.

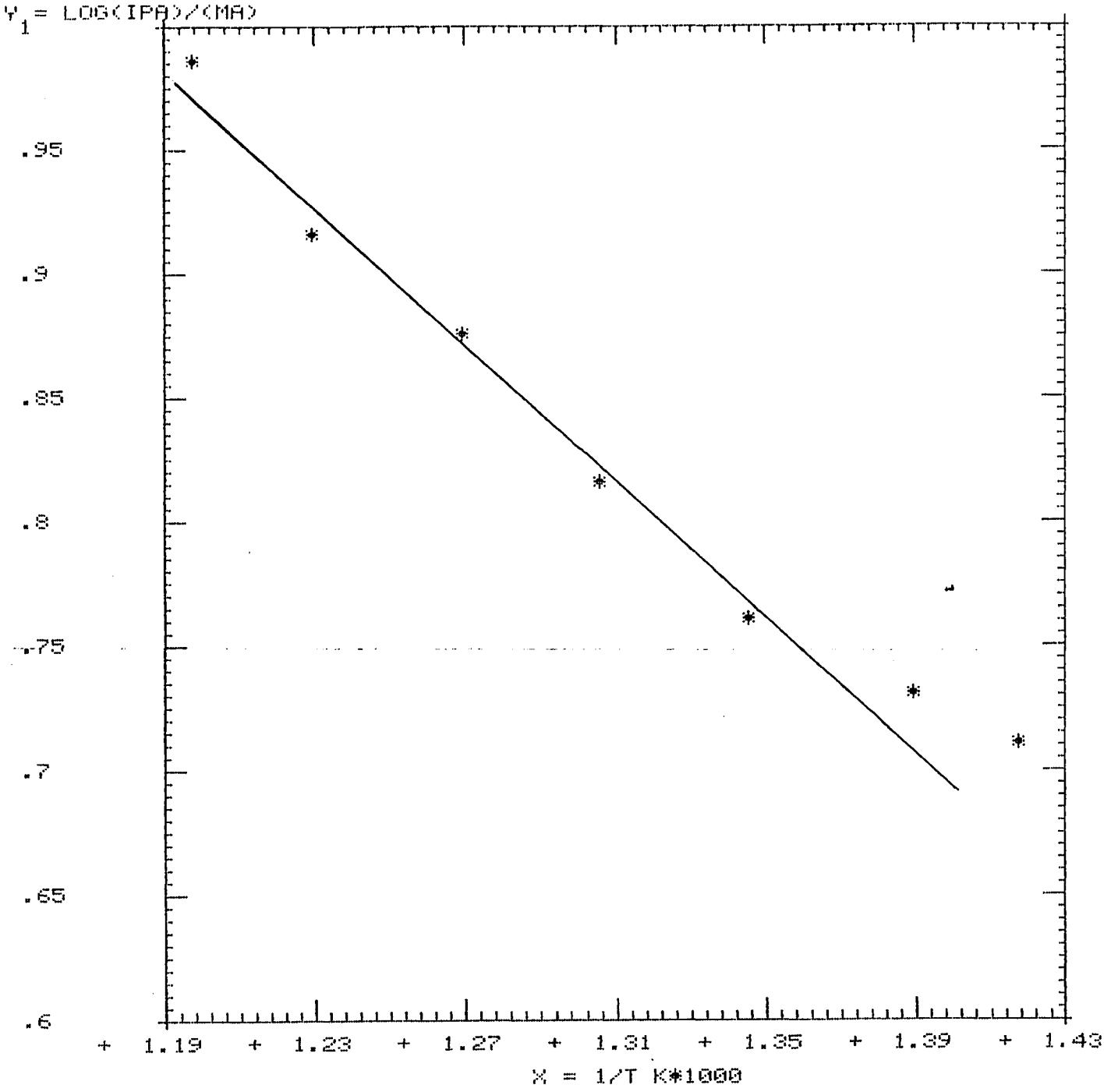


FIGURE NUMBER 5.16: An Arrhenius type plot (log I_p^a versus 1/T°K) for the oxidation of PbS containing solutions
[PbS] = 1.573×10^{-4} mole/cm^3
Electrode = vitreous carbon (area = 0.0855 cm^2)
sweep rate = 0.2 v/s

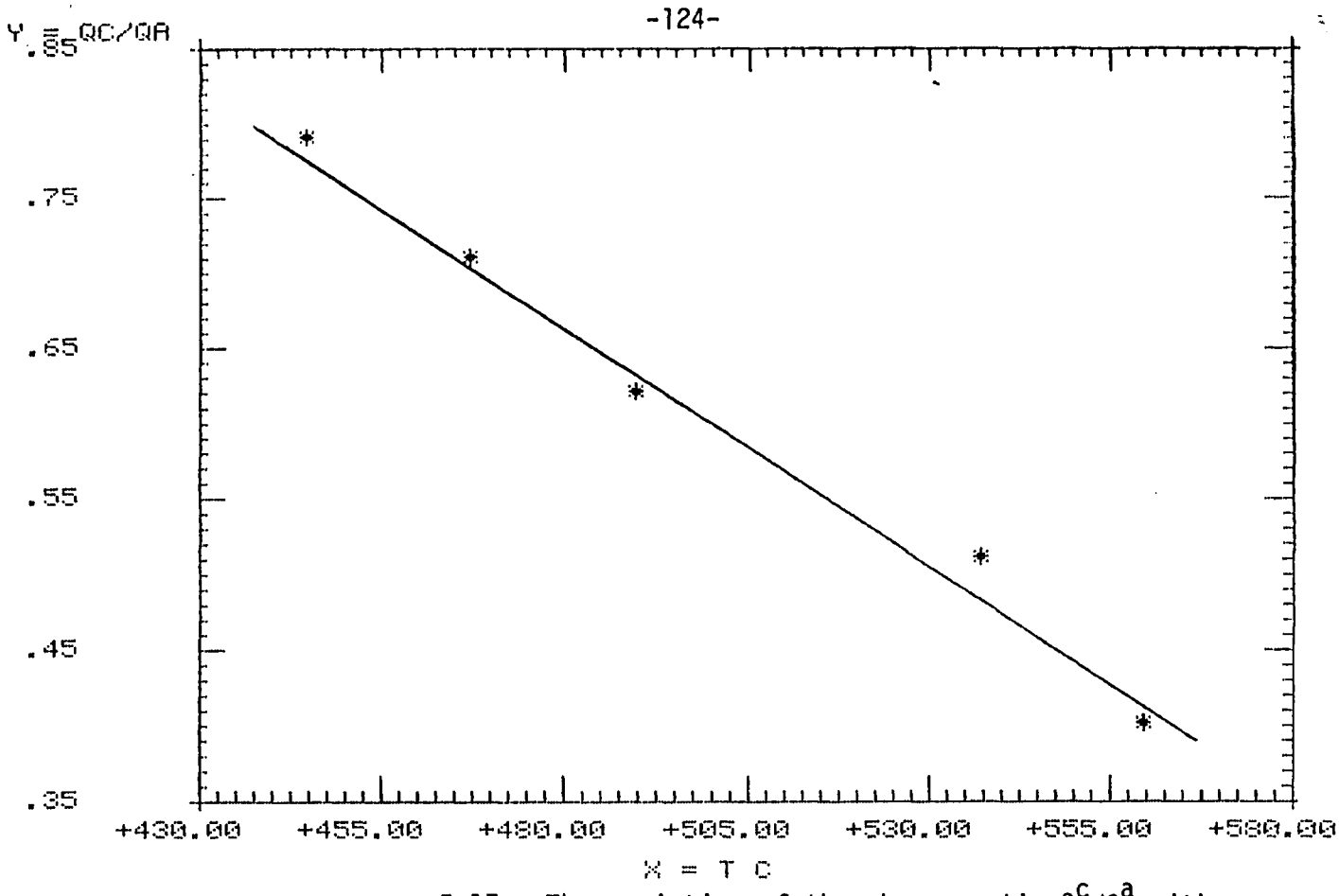


FIGURE NUMBER 5.17: The variation of the charge ratio Q^c/Q^a with increasing temperature. [PbS] = 1.573 x 10^{-4} mole/cm^3 Electrode = vitreous carbon (area = 0.0855 cm^2)

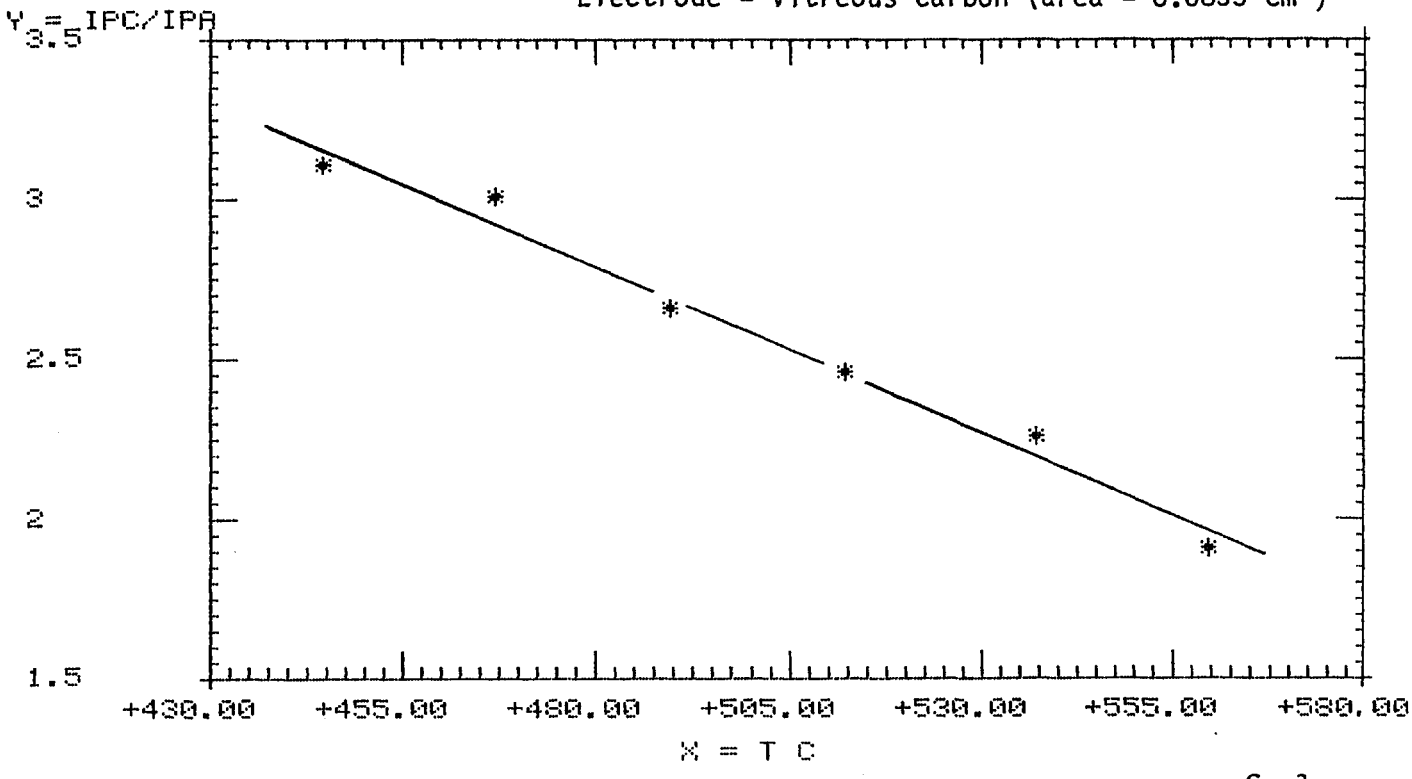


FIGURE NUMBER 5.18: The variation of the peak current ratio I_{p-4}^c/I_p^a with increasing temperature. [PbS] = 1.573 x 10^{-4} mole/cm^3 Electrode = vitreous carbon (area = 0.0855 cm^2)

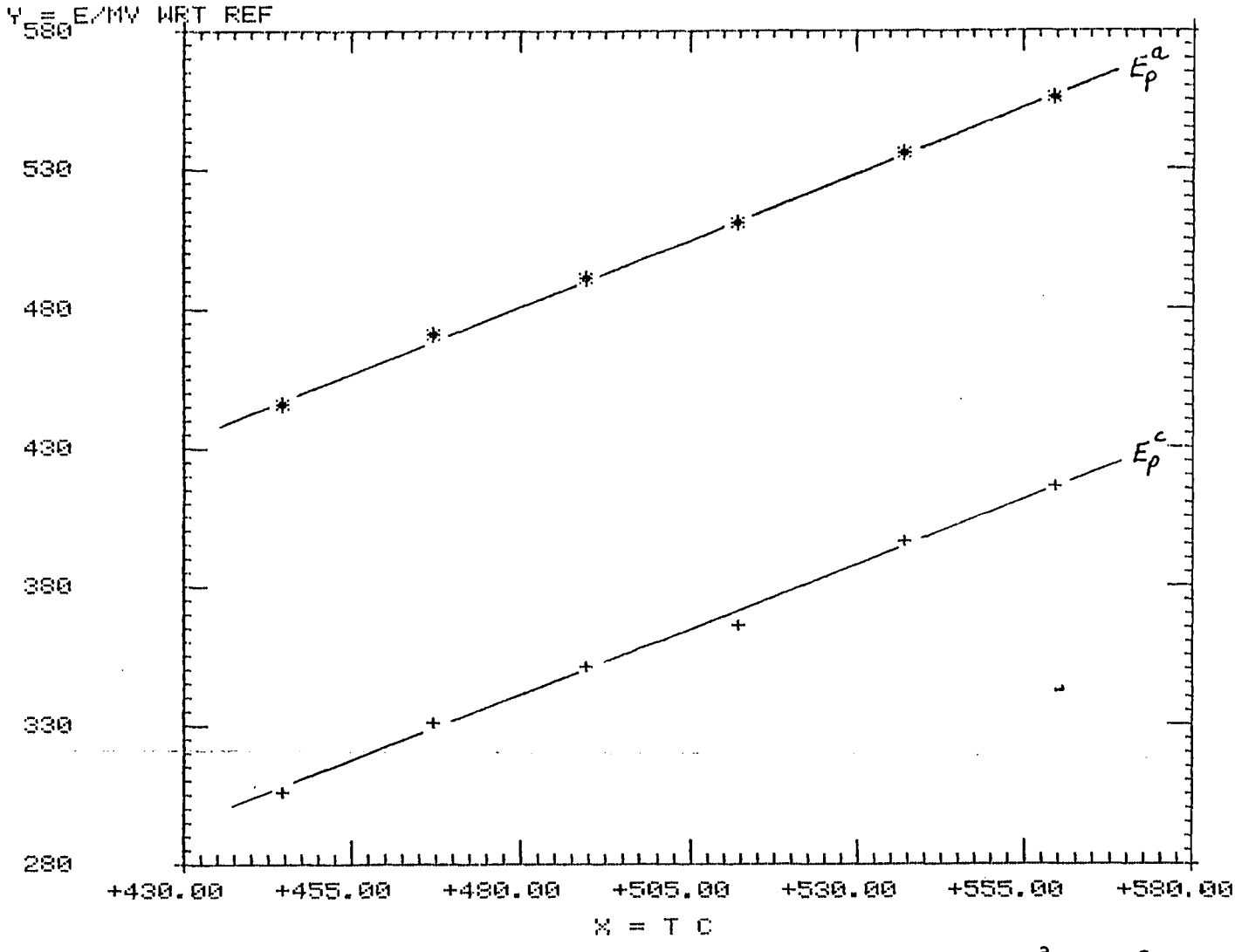


FIGURE NUMBER 5.19: The variation of the peak potentials E_p^a and E_p^c with increasing temperature. [PbS] = 1.573 x 10^{-4} mole/cm^3. Electrode = vitreous carbon (area = 0.0855 cm^2).

of the calculated αn_a values are 0.044 for ν = 0.02-0.8 V/s and 0.118 for ν = 1.0 - 20V/s. Fig. 5.12 shows that the electrochemical oxidation of sulphide at the graphite substrate does not behave as reversibly at low sweep rates as on the vitreous carbon electrode. Plots of ΔE versus $\log\nu$ show the effect of PbS concentration (Fig. 5.13) and temperature (Fig. 5.14). An increase in either the PbS concentration and/or temperature results in an increase in the irreversibility of the process.

The influence of increasing temperature (440-550°C) upon the cyclic voltammetric parameters at the vitreous carbon electrode are shown in Table 5.5. Fig. 5.15 shows a typical voltammogram obtained at the higher temperatures. Two observations may be made, firstly the currents at potentials greater than E_p^a exhibit vigorous fluctuations and upon reversing the scan direction, hysteresis occurs. Secondly, the corresponding reduction wave was drastically smaller than that obtained at lower temperatures. Both phenomena may be directly attributed to the evolution of sulphur gas.

A typical Arrhenius plot for the oxidation process, i.e. log I_p^a versus 1/T°K is shown in Fig. 5.16, a straight line is obtained and on the basis of a linear regression analysis an activation energy of 23.62 Kj/mole was calculated. Figs. 5.17 and 5.18 show that both the Q^a/Q^c and I^c/I^a ratios decrease with increasing temperature. The peak potentials E_p^a and E_p^c shift linearly towards more anodic potentials; the ΔE value remaining constant (Fig. 5.19).

5.2.2 Polarographic I-E Curves

Polarographic I-E curves were constructed from I-t transients as a result of various pre-determined potential pulses, and are shown in Figs. 5.20 and 5.21.

The polarograms clearly show the current to rise and reach a diffusion limiting current plateau, only one oxidation process was observed up to the anodic limit, viz. 1.2V. Fig. 5.20 shows the effect of temperature.

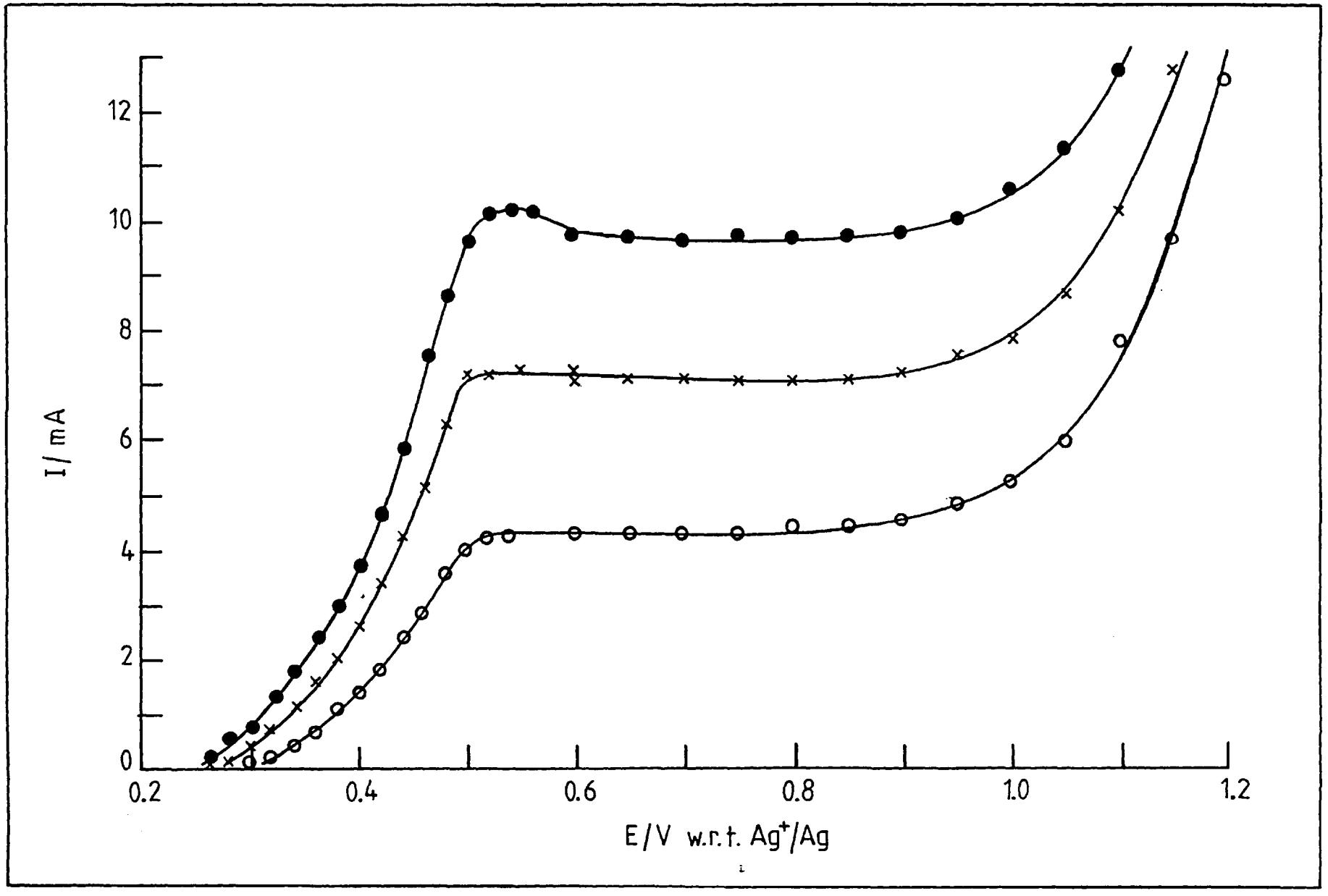


Fig. 5:21: The effect of PbS concentration upon the polarographic I-E curves constructed from I-t transients (t = 95 ms). T = 450°C; electrode = vitreous carbon (area = 0.0855 cm^2). [PbS] mole/cm^3:- O = 5.331×10^{-5}; X = 9.58×10^{-5}; ● = 1.523×10^{-4}.

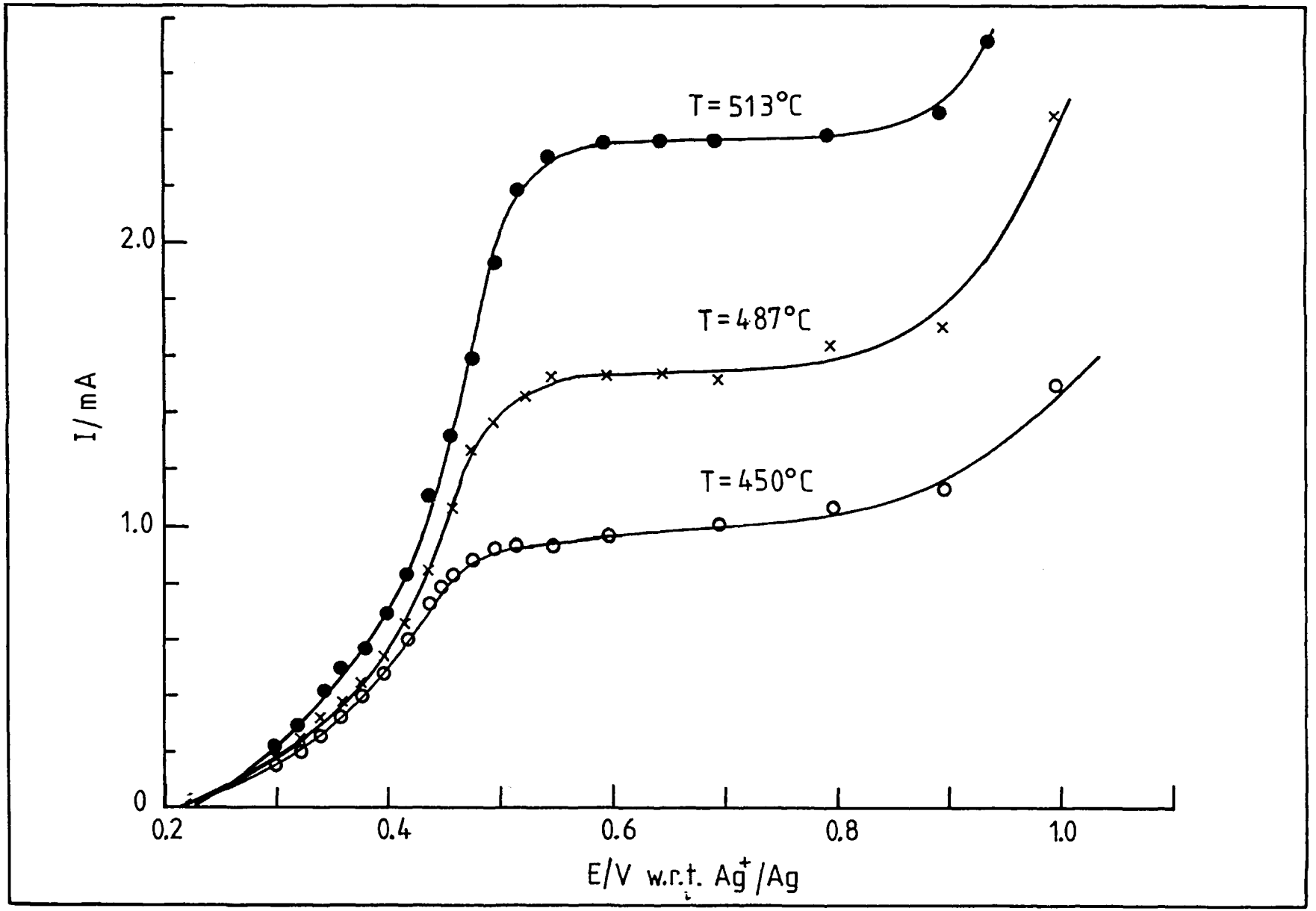


Fig. 5.20: The effect of temperature upon the polarographic I-E curves constructed from I-t plots (t = 1.9s). [PbS] = 9.780 x 10^{-5} mole/cm^3. Electrode = vitreous carbon (area = 0.855 cm^2).

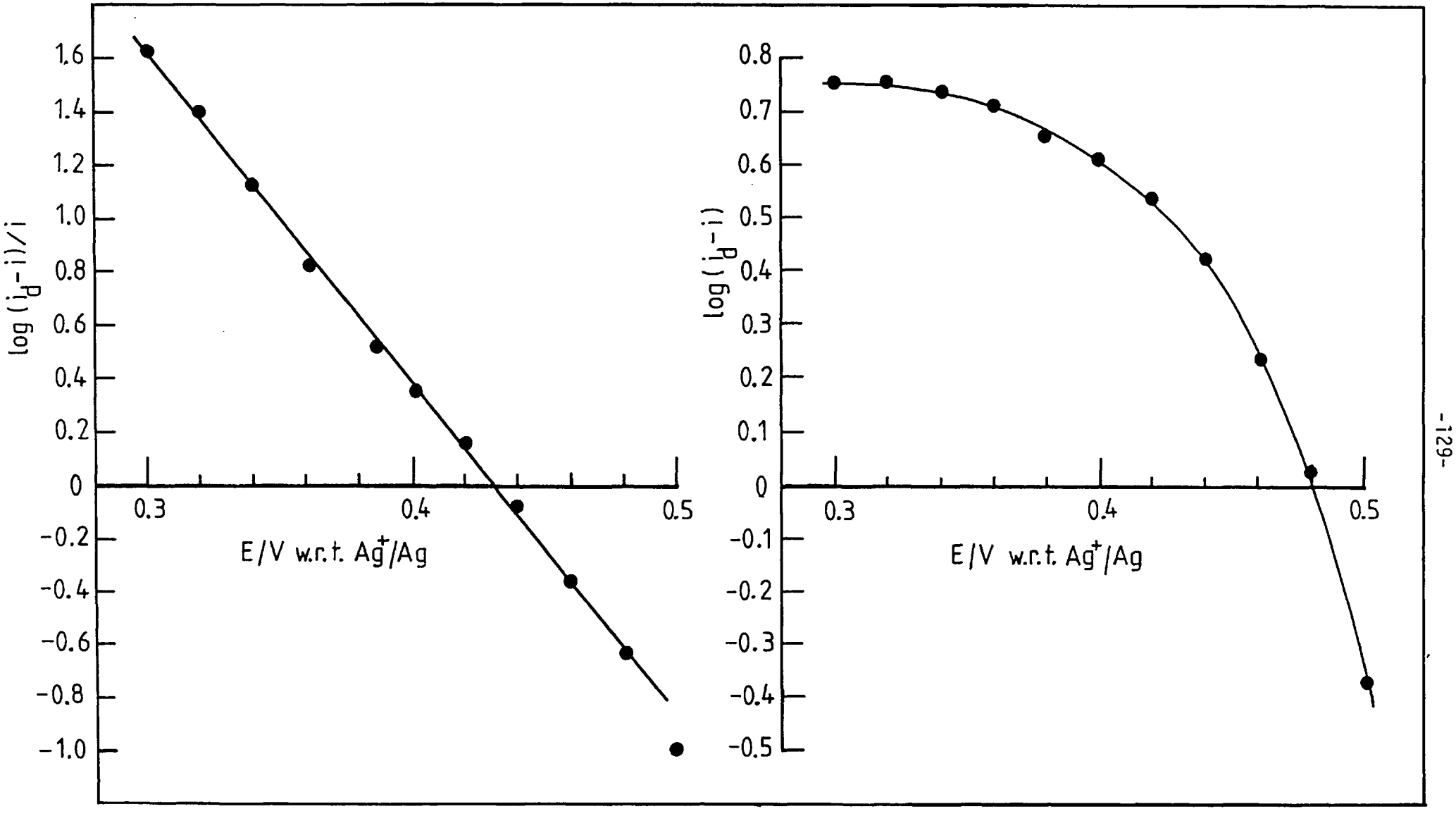


Fig. 5.22: Analysis of the polarographic I-E curves according to the relations log (i_d-i/i) vs. E and log (i_d-i) vs. E. [Pbs] = 5.331 x 10^{-5} mole/cm^3. Electrode = vitreous carbon (area = 0.0855 cm^2).

Analysis of the rising current portion of the I-E curve according to standard polarographic procedures, viz. plots of log (i_d-i) and log (i_d-i/i) versus E, show that the latter plot yields a linear relation whilst the former yields a curve, Fig. 5.22. No significant difference was obtained by constructing the polarograms from current values at either short (10 ms) or long (2s) times.

5.2.3 Chronoamperometry (I-t Transients)

Typical anodic I-t transients obtained from the oxidation of PbS containing solutions are shown in Fig. 5.23 for various applied potentials. It is noteworthy that during these experiments no peaks were observed at any potential or time span ($\sim$10 ms $\rightarrow$ 100 s). Fig. 5.23 shows the currents to decay with time, the decay being linearly dependent upon $t^{-\frac{1}{2}}$, Fig. 5.24. The reverse I-t profiles showed unusual behaviour. At short times the reverse current remained virtually constant for a certain period before rapidly falling to zero current. To clearly show this effect Fig. 5.25 shows a plot of I^c/I^a versus θ where θ is dimensionless time parameter, i.e. $\theta = (t-\tau)/\tau$ where τ is the time of the forward pulse. At short times, e.g. 10 ms the current extends to $\sim 0.3\theta$ before rapidly decreasing. As the pulse length (τ) increases the current plateau dissapears and the point at which the rapid decrease occurs moves towards lower θ values. Fig. 5.26 shows a similar plot illustrating the effect of PbS concentration.

5.2.4 Steady-State I-E Relations

Steady-state I-E curves were obtained using slow potentiodynamic sweeps, i.e. 1 mV/s and two different methods were used to record the response:

(a) An integral I-E plot obtained to produce the overall I-E curve, and

(b) A much more accurate current measurement was made by initially potentiostating the electrode at a

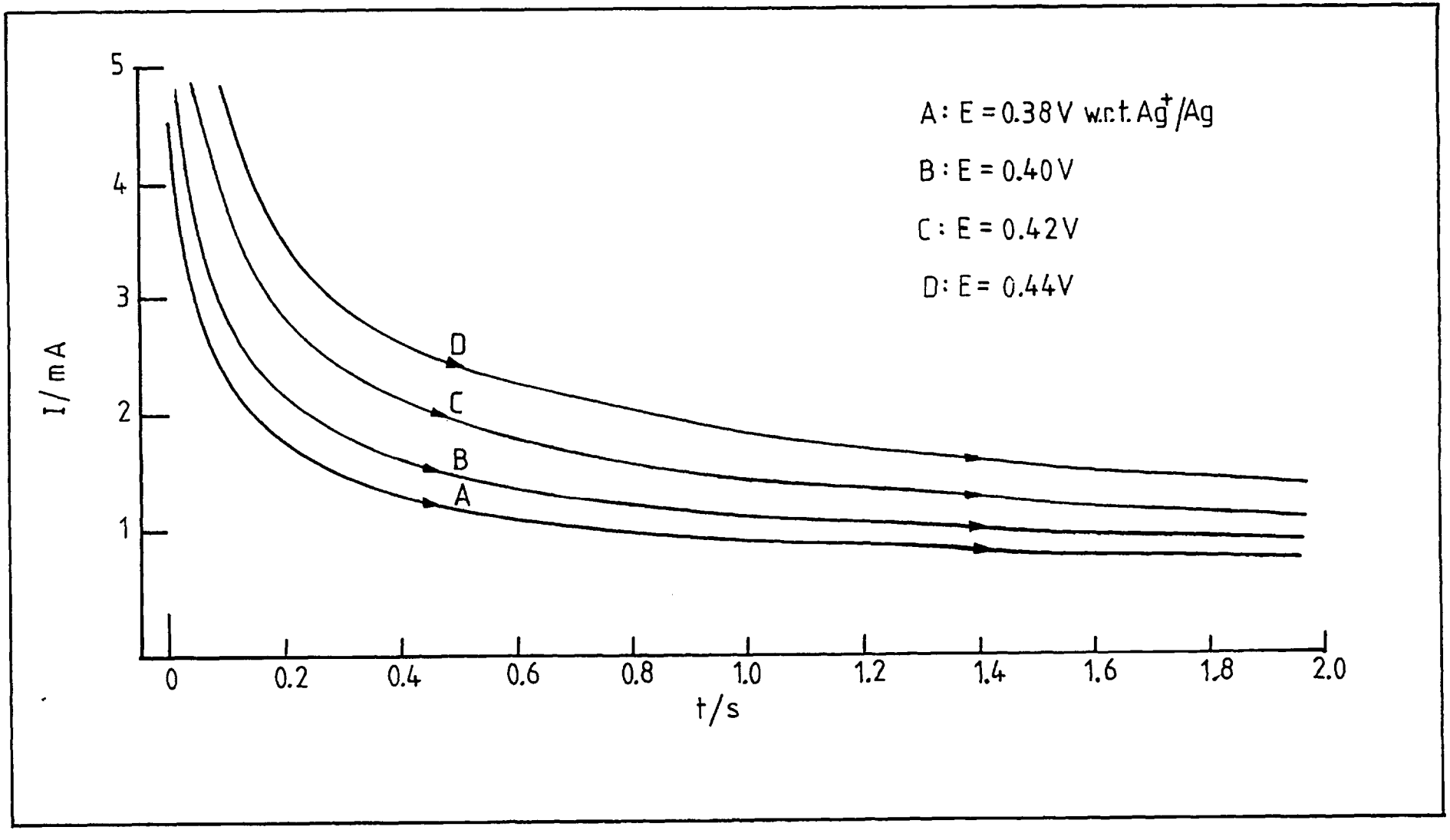


Fig. 5.23: Typical I-t transients obtained at a vitreous carbon electrode for the oxidation of PbS containing solutions. T = 450°C: [PbS] = 9.780×10^{-5} mole/cm^3. Area = 0.0855 cm^2.

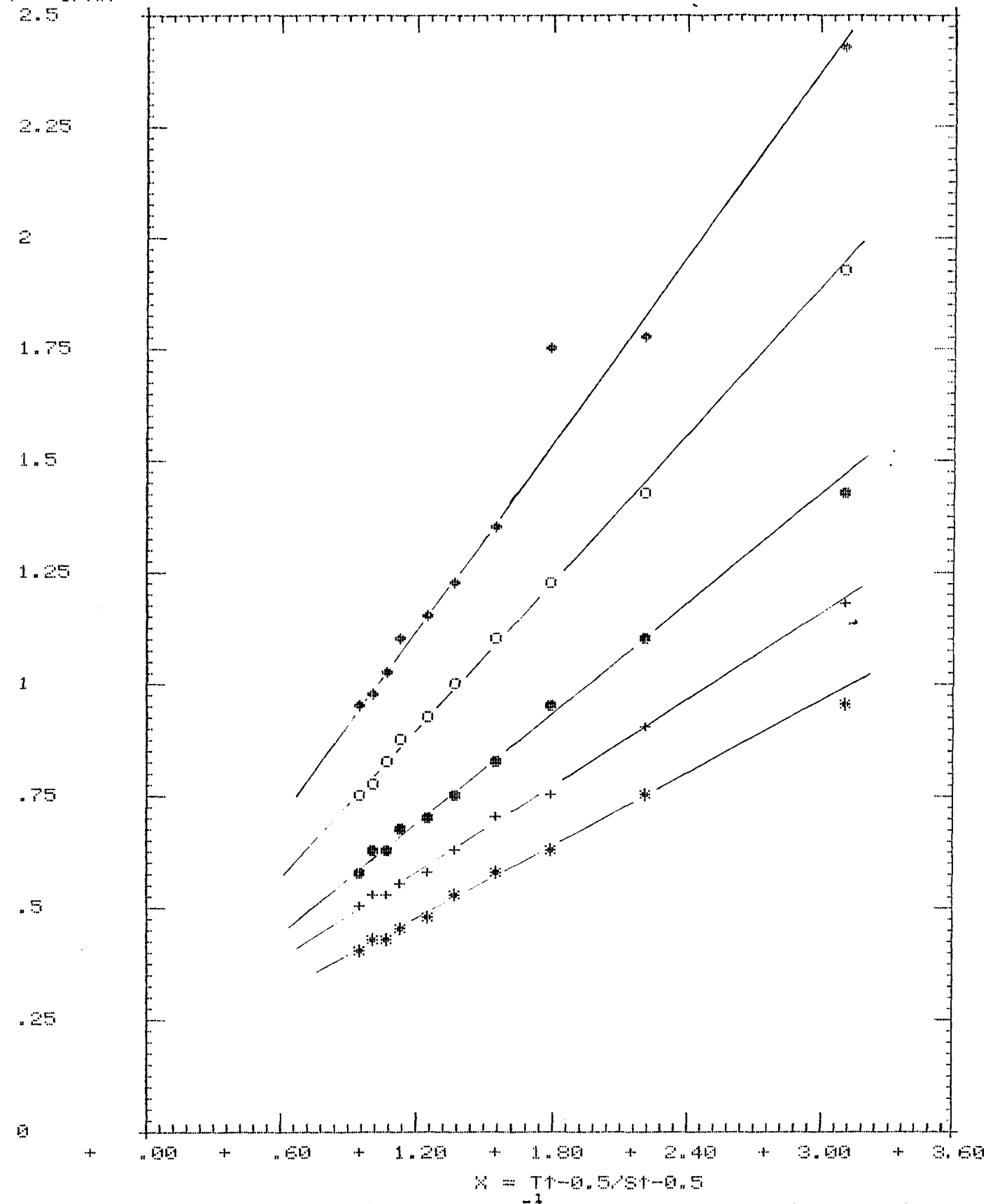


FIGURE NUMBER 5.24: I versus $t^{-\frac{1}{2}}$;ots for various applied potentials. Electrode = vitreous carbon (area = 0.0855 cm^2): T = 450°C [Pb] = 9.780 x 10^{-5} mole/cm^3. Applied potentials E (wrt $Ag^+/Ag°$):- * 360 mV; + 380 mV; ● 400 mV; 0 420 mV; ▲ = 440 mV.

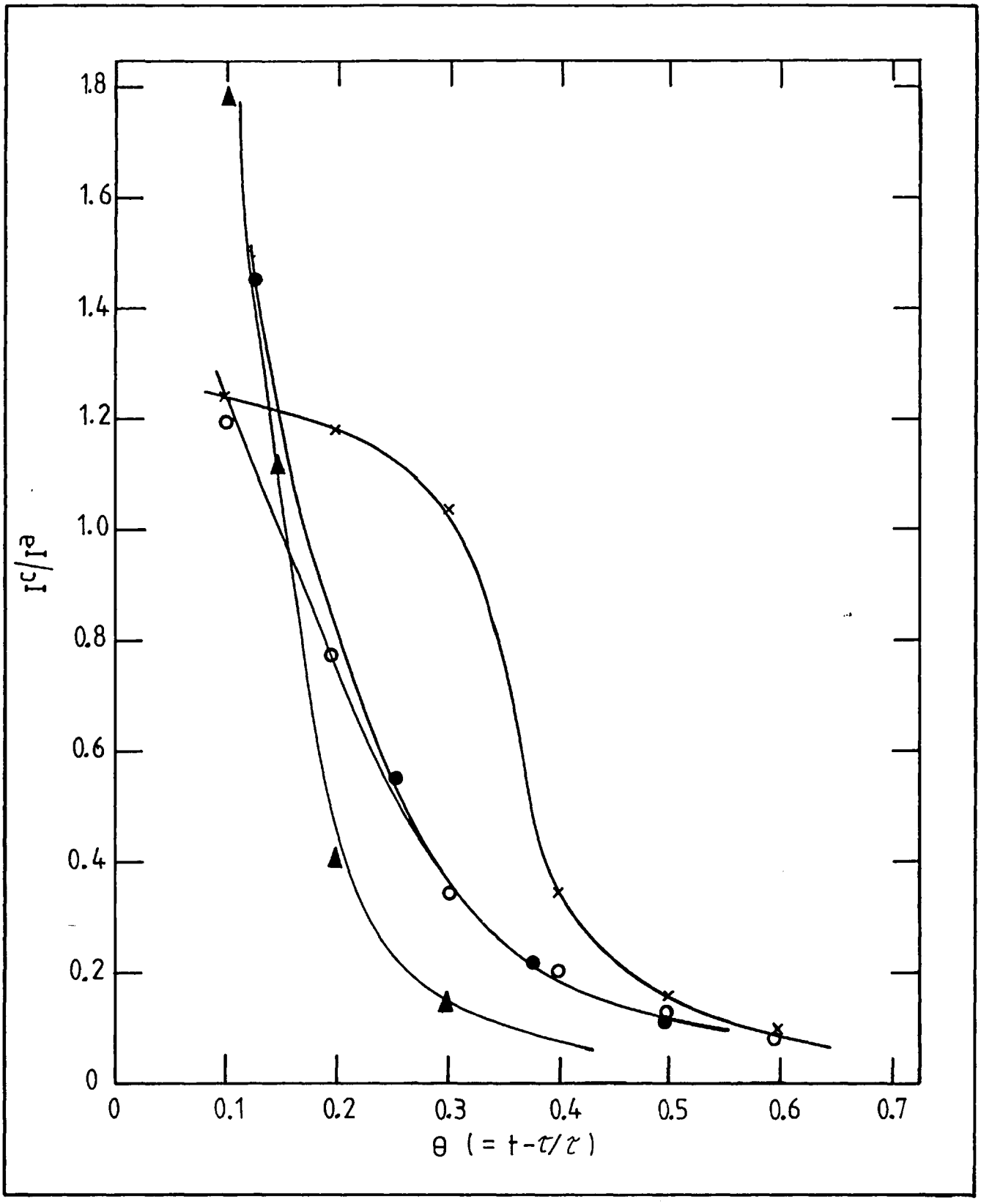


Fig. 5.25: A plot of I^c/I^a versus θ (= $t-\tau/\tau$) from the double potential step technique: showing the effect of the forward pulse length time. Electrode = vitreous carbon (area = 0.0855 cm^2); T = 470°C; [PbS] = 2.138 x 10^{-4} mole/cm^2; Anodic pulse length:- X 10 ms; O 50 ms; ● 0.2s; ▲ 0.5s.

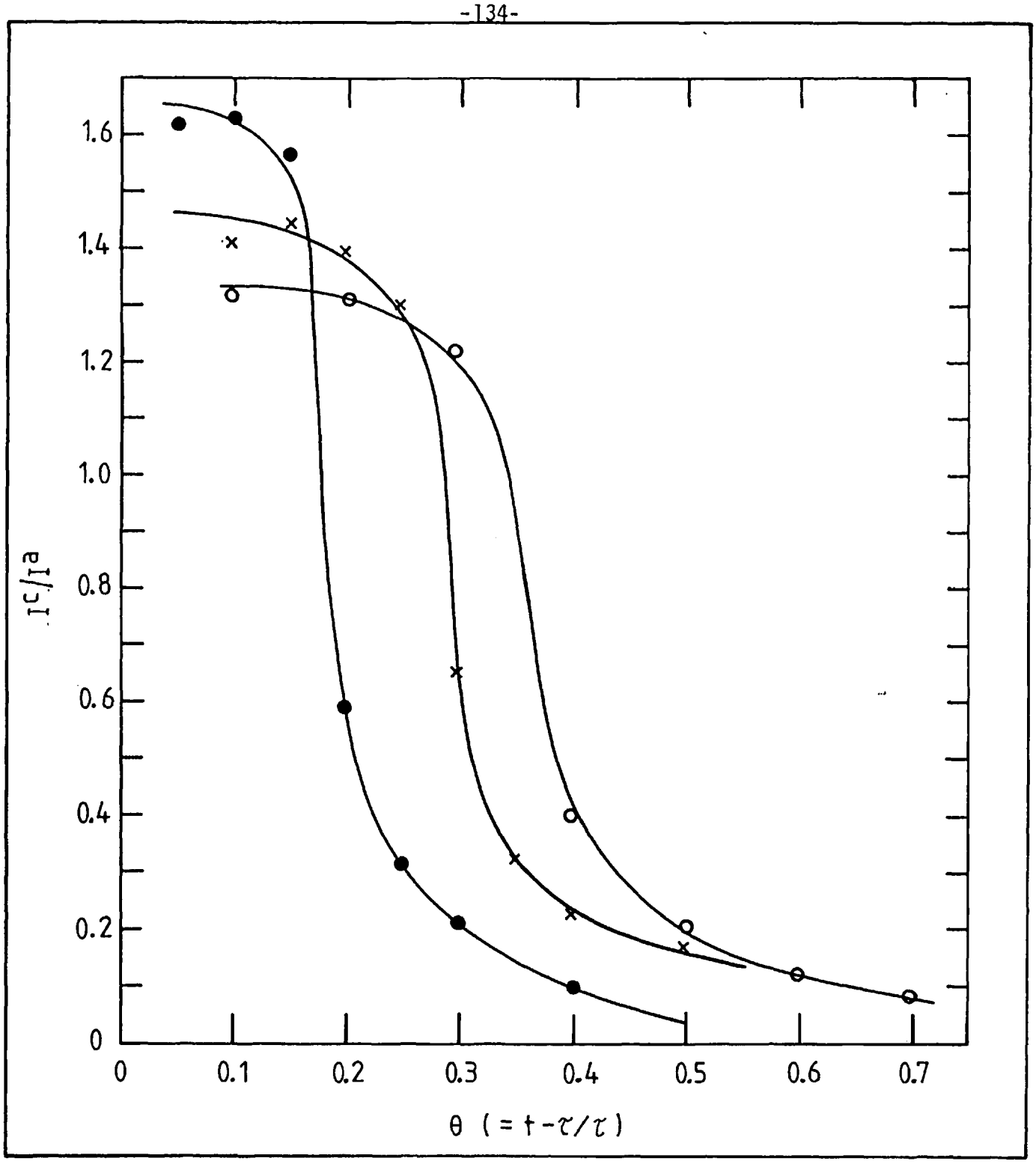


Fig. 5.26: A plot of I^c/I^a versus θ (= t - τ/τ) obtained from the double potential step technique; the effect of PbS concentration. Eledtrode = vitreous carbon (area = 0.0855 cm^2); T = 470°C; Anodic pulse length = 50 ms; [PbS] mole/cm^3:- O 9.19 x 10^{-5}; X 1.544 x 10^{-4}; ● 2.138 x 10^{-4}.

potential at which zero current flowed using
the most sensitive current range available.

The I-E curve was measured on an X-Y recorder and as the sweep progressed the current scale was changed periodically to give the most accurate current measurement. The high accuracy particularly in the low current region is particuarly necessary because it is in this region, i.e. $i/i_d < \sim 0.05$ that activation control and therefore Tafel behaviour occurs.

During the many experiments and measurements undertaken a few I-E curves similar to that shown in Fig. 5.27 were recorded. However the conditions under which this type of behaviour occurred could not be quantified and indeed seemed to be a random phenomenon. Fig. 5.27 shows that upon increasing the potential the current rises to reach a peak value and then rapidly falls to a very low current value which was maintained for several hundred millivolts before again increasing at a potential corresponding to the anodic limit. Although,as explained above,this type of behaviour was infrequently obtained it is an important observation and is discussed fully in section 5.3.

Tafel plots, i.e. E-logi were constructed from the precision I-E curves at both low and high potentials using both types of electrodes and various PbS concentrations and temperatures. The current at high potentials usually resulted in the expected limiting diffusion current although sometimes a broad current peak was obtained after which the current decreased.

At the vitreous carbon electrode and in solutions at temperatures < 470°C two Tafel regions were observed, see Fig. 5.28. The low Tafel region extended over ∿100-200 mV whilst that of the upper region extended over a 200-300 mV range. At higher temperatures the transition between the two Tafel regions becomes more pronounced and the upper Tafel region more difficult to discern (Fig. 5.29). The Tafel slopes (b) obtained at a vitreous carbon electrode are shown in Table 5.6, as a function of PbS

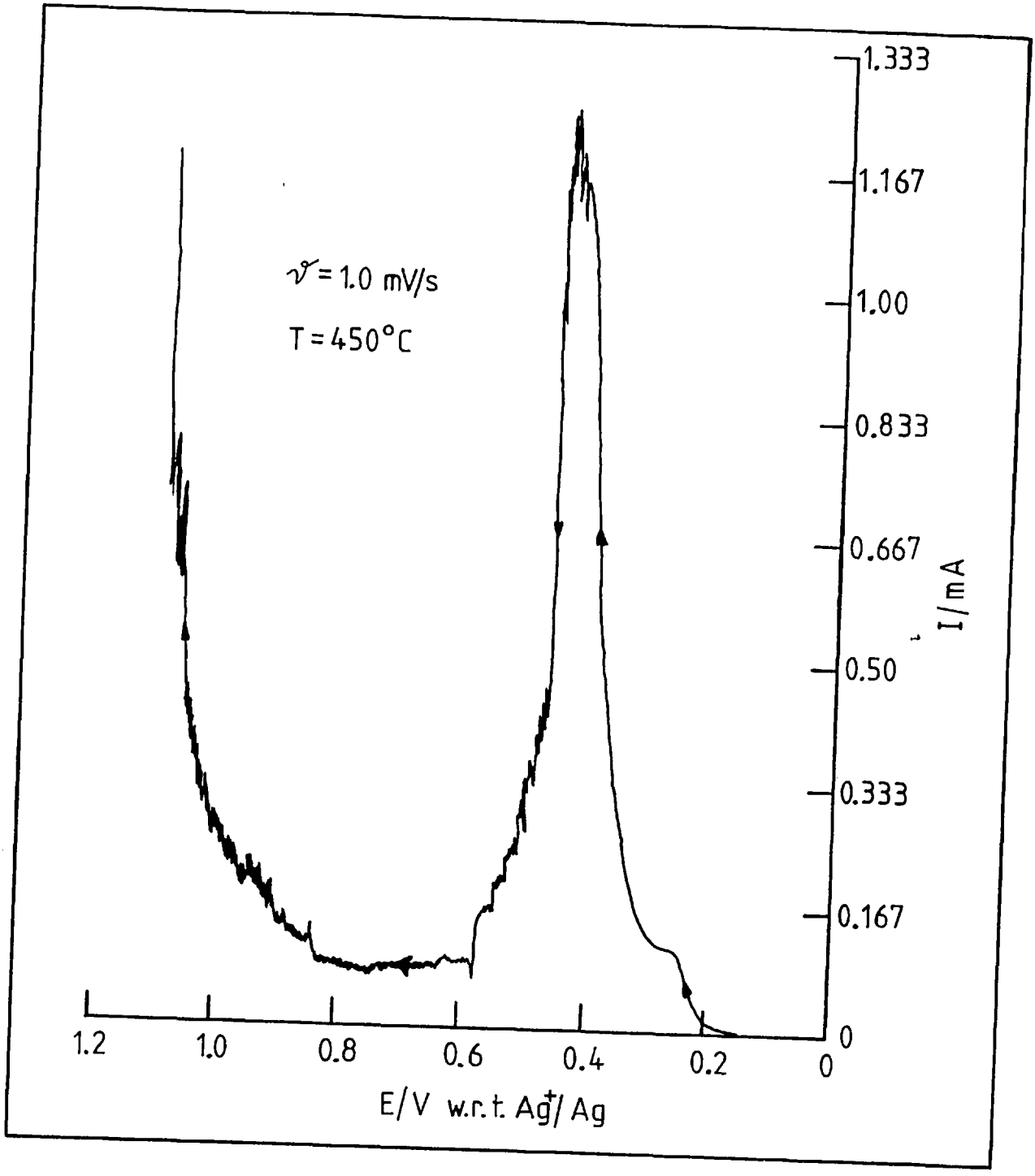


Fig. 5.27: A slow (1 mV/s) potentiodynamic scan obtained for the oxidation of PbS containing solutions at a vitreous carbon electrode [Pb] = 2.429×10^{-4} mole/cm^3. T = 450°C; Area = 0.0855 cm^2.

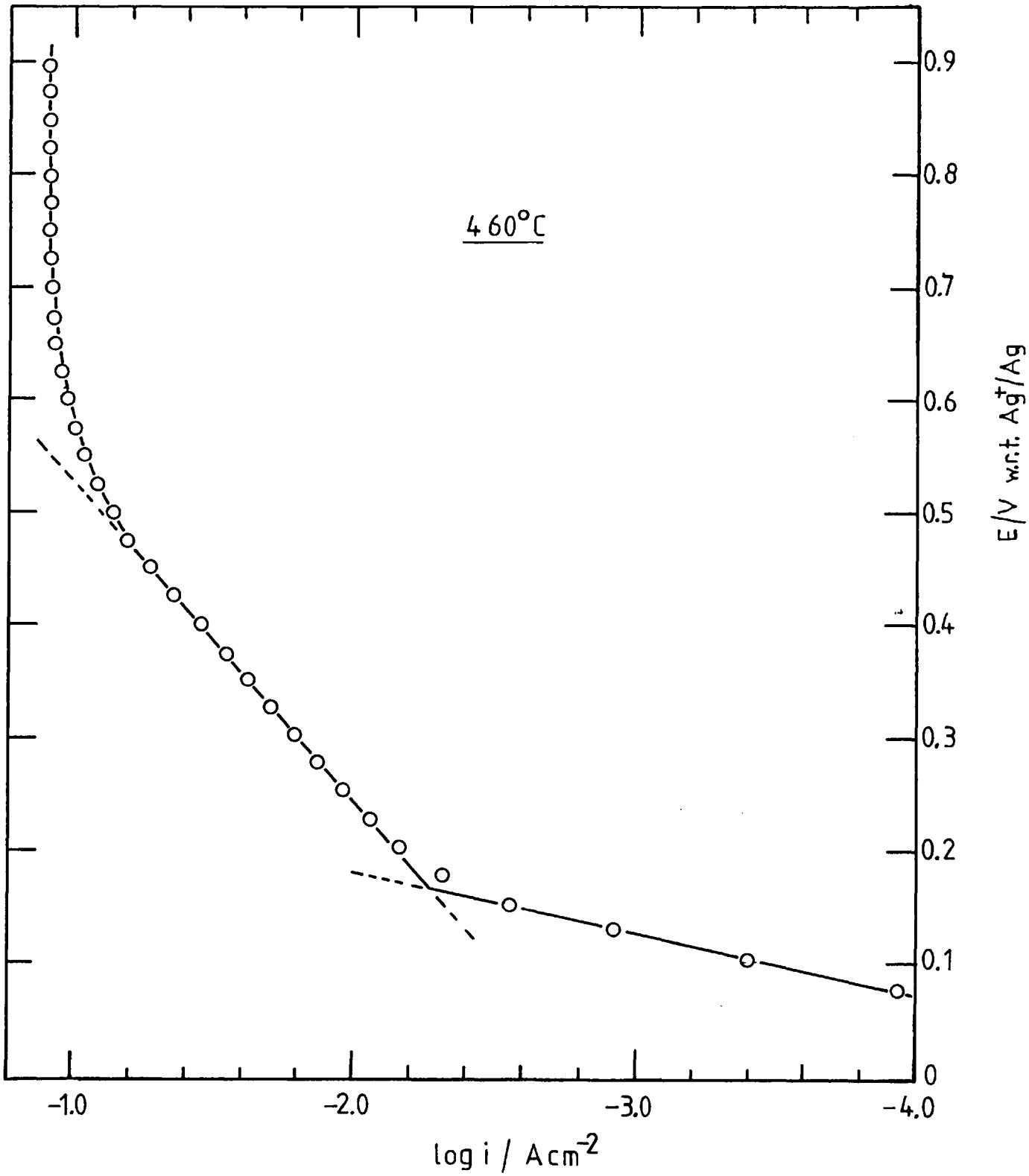


Fig. 5.28: A Tafel Plot (E vs. log i) for the oxidation of a PbS containing solution at a vitreous carbon electrode at 460°C.
[PbS] = 1.520×10^{-3} mole/cm^3. Electrode area = 0.0855 cm^2.

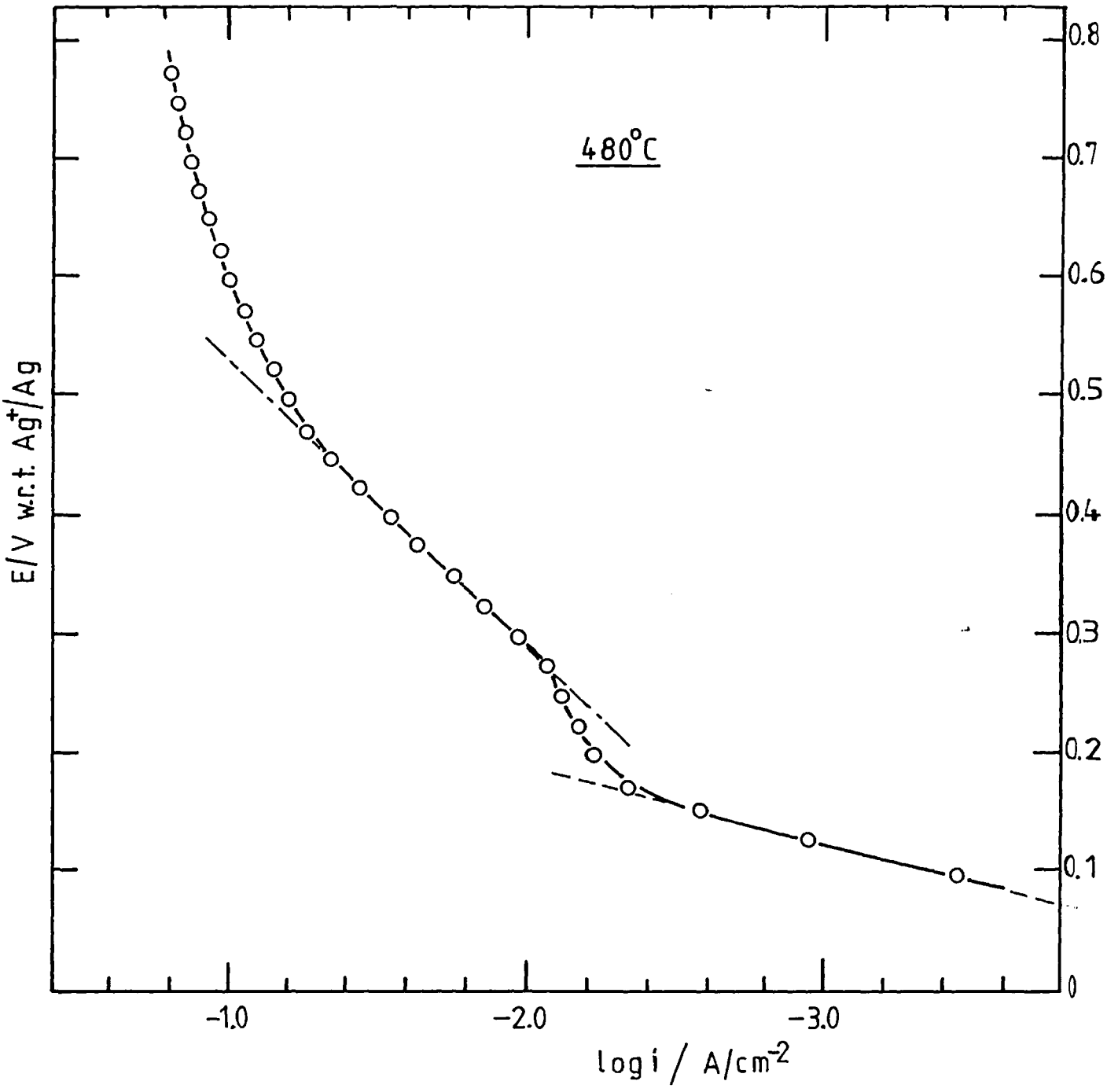


Fig. 5.29: A Tafel Plot (E vs. log i) for the oxidation of a PbS containing solution at a vitreous carbon electrode at 506°C. [PbS] = 1.883 x 10^{-3} mole/cm^3. Electrode area = 0.0855 cm^2.

TABLE 5.6

Values of the Tafel Slope obtained at a vitreous carbon electrode for various PbS concentrations at 460°C

[PbS] mole/l	Low E		High E	
	dE/d log i	Correlation	dE/d log i	Correlation
1.140	0.0469	0.996	0.589	0.995
1.327	0.0540	0.995	0.224	0.999
1.502	0.0538	0.996	0.291	0.999
1.695	0.0542	0.995	0.252	0.998
1.883	0.0533	0.997	0.311	0.998

TABLE 5.7

Values of the Tafel Slope obtained at a vitreous carbon electrode for various temperatures at a [PbS] = 1.883 mole/l.

T°K	Low E		High E	
	dE/d log i	Correlation	dE/d log i	Correlation
718	0.0512	0.996	0.270	0.995
725	0.0490	0.995	0.229	0.998
733	0.0532	0.997	0.310	0.998
753	0.0570	0.995	0.227	0.999
779	0.065	0.988	0.2401	0.999

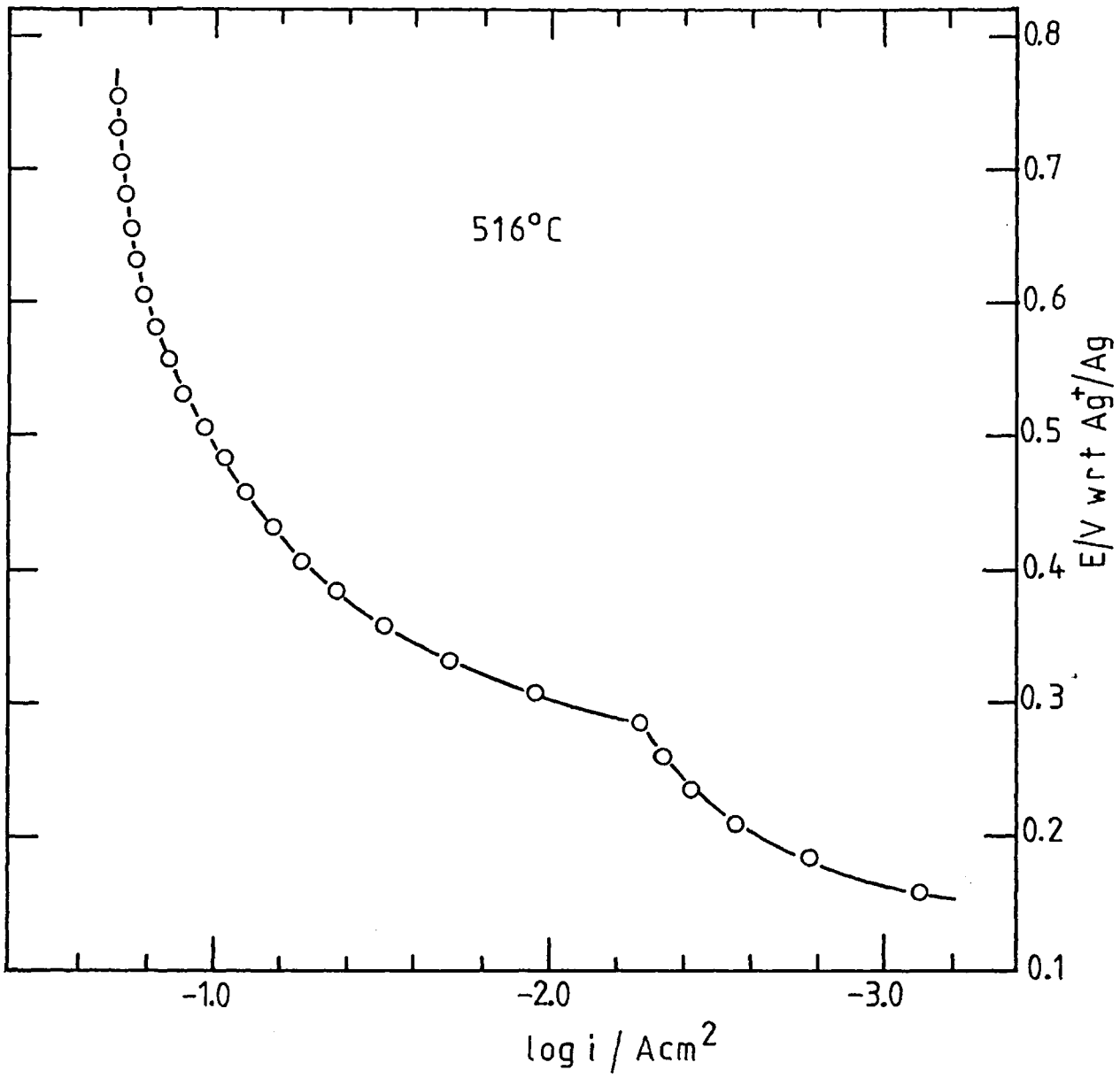


Fig. 5.30: A Tafel Plot (E vs. log i) for the oxidation of a PbS containing solution at a spec-pure graphite electrode at 516°C. [PbS] = 1.229×10^{-3} mole/cm^3. Electrode area = 0.0707 cm^2.

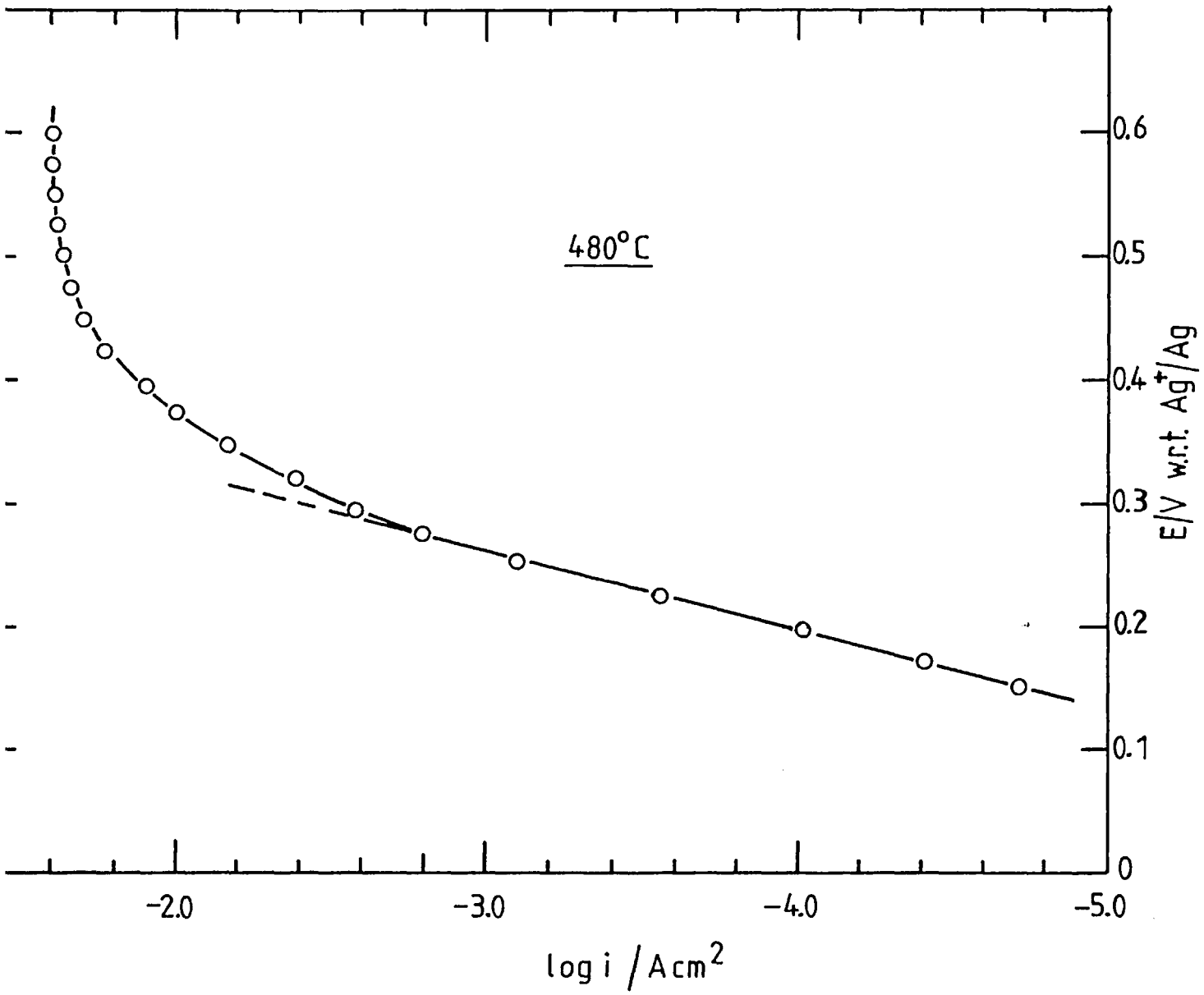


Fig. 5.31: A Tafel Plot (E vs. log i) for the oxidation of a PbS containing solution at a spec-pure graphite electrode at 480°C. [PbS] = 9.525×10^{-4} mole/cm^3. Electrode area = 0.0707 cm^2.

TABLE 5.8

Values of the Tafel Slope obtained at a graphite electrode for various PbS concentrations at 480°C

[PbS] x 10^1 mole/l	dE/d log i
1.747	0.0604
3.747	0.0556
6.338	0.0806
7.65	0.0937
9.425	0.0635

concentration and in Table 5.7 as a function of increasing temperature. The Tafel values were obtained from a linear regression analysis which gave correlations of linearity > 0.995.

The logi-E plots obtained at the graphite electrode did not usually show well defined Tafel regions, see Fig. 5.30 for example. Even so, two regions may be distinguished, the transition between the two occurring at the same potential as was observed at the vitreous carbon electrodes. However low overpotential Tafel behaviour could sometimes be observed, see Fig. 5.31, and Table 5.8 gives the values of b obtained from linear regression analysis as a function of PbS concentration at 480°C. The values obtained show significant scatter, although no obvious trend is noted.

No discernible influence upon the Tafel behaviour was caused by stirring the solution.

5.2.5 Controlled Potential Electrolysis

A value for the overall number of electrons involved in the oxidation of PbS containing solutions corresponding to the first anodic process was obtained by exhaustive constant potential electrolysis. The electrolysis employed a large graphite working electrode and the solution was stirred by Ar gas bubbling to increase the rate of mass transfer. Prior to electrolysis voltammograms were obtained before and after the addition of PbS, and from the latter the exact potential for electrolysis was selected. During electrolysis the current was integrated digitally and electrolysis was continue until a low current was attained. Voltammograms obtained after electrolysis were similar to that of the bulk solution thus indicating that all electroactive species were removed during the electrolysis. Exhaustive electrolysis was carried out at potentials of +0.45, +0.5 and +0.6V at solution temperatures of 460 and 490°C. An n = 2 value was calculated using Faraday's Law and assuming 100% efficiency. After

dismantling the cell, yellow sulphur powder had formed on the cold brass cell head.

5.3 Discussion

The cyclic sweep voltammograms for the oxidation of PbS-$PbCl_2$-KCl solutions at both vitreous carbon and graphite electrodes have clearly shown that two oxidation processes occur at peak potentials of 0.45 and 0.95V wrt Ag(I)/Ag reference electrode (Figs. 5.1 and 5.2). The chlorine reaction occurs at ∿1.15V. The exhaustive controlled potential electrolysis studies have shown that the first anodic process corresponds to a two electron transfer reaction and that a gaseous sulphur product is produced and which condenses upon the cooler regions of the electrochemical cell. A voltammetric examination of the electrolyte after the complete electrolysis at potentials corresponding to the first wave did not reveal the presence of any electroactive species. Thus the two oxidation processes must correspond to a consecutive electron transfer scheme. The overall reaction for the first anodic process may be represented by:

$$S^{2-}_{(soln)} \rightleftharpoons \tfrac{1}{2}S_2 + e \qquad E = 0.45V$$

The more anodic process did not show any reverse wave and most probably corresponds to the sulphur chloride formation reaction as first proposed by Plambeck (136):

$$2S + 2Cl^- \longrightarrow S_2Cl_2(g) + 2e$$

No further electrochemical data was obtained for this reaction. De Guibert et al [191] have however investigated the sulphur chloride reaction in more depth using the chronoamperometric technique.

The single reduction wave with a peak potential of 0.3V corresponds to the reduction of sulphur to form the sulphide ion. The absence of any further reduction waves signifies that the sulphide ion is not further

reducible and that reducible polysulphide ions of the form S_x^{2-} (x = 2-6) are not formed. The observed electroreduction behaviour of sulphur is further confirmed by the reduction of dissolved sulphur, see Chapter 7. The above behaviour is in complete contrast to the reduction of sulphur in, for example, the LiCℓ-KCℓ melt where according to Adamo and Kennedy [172] two reduction waves occur. The observed voltammetric reduction of sulphur obtained in this work and that of de Guibert et al [193] do not agree with that of Skyllas and Welch [189]. The latter authors employing the $PbCℓ_2$-NaCℓ eutectic melt found chronopotentiometric evidence for a further reduction wave some 100 mV positive to the lead deposition potential and ascribed it to the reduction of the polysulphide ion S_2^{2-}. The latter ion was supposedly formed by reaction of the electrogenerated sulphur and the sulphide ion according to

$$S^{2-} \rightleftharpoons S + 2e$$
$$S + S^{2-} \longrightarrow S_2^{2-}$$

The presence of a single reduction wave for sulphur in the $PbCℓ_2$-KCℓ melt must imply that the sulphide ion is stabilised in this melt more strongly than in either the $PbCℓ_2$-NaCℓ or the LiCℓ-KCℓ melts. The addition of sodium polysulphides (Na_2S_x, x = 2,4,5) to the melt and also to a $PbCℓ_2$ - KCℓ-NaCℓ melt were found to decompose yielding solutions containing only the sulphide ion, see Chapter 8.

Although the short time scale electrolysis of PbS solutions, i.e. via cyclic voltammetry have not shown any evidence for polysulphide formation the long time potentiostatic electrolysis coupled with 'in-situ' spectroscopy has provided some indication that a further intermediate species is formed (194). Thus Plichon et al (194) found that the optical density of a PbS-$PbCℓ_2$-KCℓ solution (at λ = 500 nm) remained virtually constant during prolonged electrolysis at 440°C. After an exchange of $\sim$1.3 moles of electrons

a rapid decrease in optical density occurs to a value corresponding to the pure $PbCl_2$-KCl melt after an exchange of 2 moles of electrons. It was further established that this behaviour was independent of the melt composition. The authors explained this in terms of the formation of a low degree polysulphide.

The overall morphology of the cyclic voltammograms obtained in this work and in particular their position upon the potential axis are in very good agreement with the data of Plichon and de Guibert (193), as are the electrolysis studies. Unfortunately the same authors have not provided any further electrochemical information with which to compare and contrast the present results.

The voltammograms obtained at the vitreous carbon electrode for the sulphur evolution reaction further reveal a possible additional oxidation process (Fig. 5.3). The latter is exhibited as a pre-wave or shoulder to the main anodic wave; however it could not be resolved sufficiently to provide any useful electroanalytical information. It is notable that the pre-wave was not observed at the graphite electrode.

The overall sulphide oxidation process has been shown to be diffusion-controlled. This is substantiated from the linear I_p^a versus $\nu^{\frac{1}{2}}$ plots (Fig. 5.5) with corresponding zero intercepts over the concentration range 4.511×10^{-5} - 1.573×10^{-5} mole PbS/cm^3 and hence obeys the Randles Sevcik equation (17). Further evidence for diffusion control is given by the linear $I\text{-}t^{-\frac{1}{2}}$ chronoamperometric plots (Fig. 5.24) and the observed diffusion limiting current plateaux obtained from the polarographic I-E plots (Figs. 5.20 and 5.21). The gradual decrease in the current function $I_p^a/\nu^{\frac{1}{2}}$ with increasing sweep rate at higher concentrations may however suggest further kinetic or chemical complications. As to the nature of the anodic product, i.e. suluble or insoluble, the results obtained are in conflict. On the one hand the $I_p^c/I_p^a > 1$ criteria obtained at both carbon electrodes in the medium sweep rate range and at lower

temperatures ($< \sim 460°C$) suggest an insoluble product, some further evidence is given from the reduction I-t transients (see below). However the independence of the peak potential E_p^a with the bulk PbS concentration and the linear log i_p-i/i versus E polarographic plots (Fig. 5.22) suggest a soluble product. Linear log i_p-i/i versus E plots are predicted for the case where both the products and reactant are soluble according to the equation (47):

$$E = E_{\frac{1}{2}} + \frac{RT}{nF} \ln \frac{i_d - i}{i}$$

the same result is expected for an irreversible reaction in which case a slope of $\alpha n_a F/2.303RT$ is predicted (47). The presence of a reverse wave clearly shows the process to be reversible and hence the latter criterion is not applicable. The slope of the log i_p-i/i versus E plot (Fig. 5.22) yielded a slope of 12.5 from which an n = 1.8 was calculated and hence substantiates the n = 2 process. For the case of the reversible deposition of an insoluble product, the Kothoff and Lingane equation (47) applies, i.e.

$$E = E_{\frac{1}{2}} + \frac{RT}{nF} \ln(i_d - i)$$

Fig. 5.22 clearly shows that this equation does not apply.

The variation of the peak current ratio I_p^c/I_p^a (as calculated from the modified Nicholson equation (17)) with increasing sweep rate (Fig. 5.7) clearly shows that at low sweep rates the sulphur product is removed from the vicinity of the electrode and hence less product is available for reduction. This is typical behaviour predicted for the case of a post chemical reaction (39). However in the present case sulphur vaporisation and physical dissolution into the melt are the most probable reasons for this. For the particular case of the graphite electrode the increase in I_p^c/I_p^a with increasing sweep rate to form a plateau is consistent with this simple mechanism. In the case of the vitreous carbon

electrode the initial low I_p^c/I_p^a values at low sweep rates and the gradual increase with increasing sweep rate is also consistent. However the formation of a peak in the I_p^c/I_p^a versus $\sqrt{\nu}$ plot with a subsequent gradual decrease in I_p^c/I_p^a is consistent with the results obtained at carbon and metal electrodes in the lower temperatures (see Chapter 6) and which is consistent with the formation of an insoluble film followed by a dissolution process.

The diffusion coefficient calculated from the Randles Sevcik equation from a knowledge of the $dI_p^a/d\nu^{\frac{1}{2}}$ values, shows the diffusion coefficient to decrease with increasing PbS concentration. This behaviour was confirmed at both types of carbon electrodes and indeed was consistent between experiments. Thus it must be inferred that a more complex and less mobile species is formed in solution at the higher PbS concentrations. It is tentatively suggested that PbS dimers of the form $(PbS)_2$ are produced; some cryoscopic evidence has been given for the formation of CuS dimers in the CuS-$CuCl_2$ system (158). However similar cryoscopic studies on the $PbCl_2$-PbS system do not evidence dimer formation (155). The diffusion coefficients calculated for an n = 2 process using both the soluble and insoluble criteria yield values of $D \sim 10^{-6}$ cm^2/s, a value much lower than is normally found in molten salt media although it is consistent with the value obtained by Plichon and de Guibert from their chronoamperometric studies (191). The reduction I-t transient of electrogenerated sulphur shows unusual behaviour at temperatures $< \sim 460°C$. The I-t behaviour does not show any diffusion contribution as one would expect for a soluble product species. Instead a virtually constant current plateau is produced and is maintained for a certain time before rapidly falling to zero current. The effect is particularly prominent at low time scales. Fig. 5.25 shows the relation of the reverse current to that of the forward current as a function of a dimensionless time parameter $\theta = t - \tau/\tau$. Exactly the same behaviour was obtained in the studies of Plichon and de Guibert (191) who

further showed that similar behaviour occurs for the oxidation of an electroreduced Ni film. The same authors also determined that the anodic change in the I-t transient reached a peak with increasing electrolysis time after which the charge decreased before finally becoming constant. The maximum charge value corresponded to a sulphur deposit of 0.23μ thick. The value of Q_{max} was found to decrease with increasing temperature.

The independence of both the anodic and cathodic peak potentials (E_p^a and E_p^c) with increasing sweep rate up to ~1V/s indicates the electron transfer reaction to be reversible (Figs. 5.8 and 5.9). As the sweep rate is further increased both peak potentials shift, the anodic peak potential being linear with $\ell n\nu$. The latter behaviour is consistent with the onset of irreversible conditions, the dependency of the peak potential with sweep rate being given by (19):

$$E_p = E_{\frac{1}{2}} - b[0.52 - \tfrac{1}{2}\log\left(\frac{b}{D}\right) - \log k + \tfrac{1}{2}\log\nu\ ]$$

where k is the specific rate constant and b the Tafel slope ($2.3\ RT/\alpha n_a F$). The transformation from reversible to irreversible behaviour is an indication of the departure of the system from equilibrium and occurs at a characteristic sweep rate ν_c which depends primarily on the value k and to a lesser extent on D and b. Table 5.4 shows that the value of $\log\nu_c$ remains virtually constant with increasing PbS concentration. The value of the rate constant k, may be obtained from the value of $\log\nu_c$ using the relation

$$E_{\frac{1}{2}} - 1.1\,\frac{RT}{nF} = E_{\frac{1}{2}} - b[0.52 - \tfrac{1}{2}\log\left(\frac{b}{D}\right) - \log k + \tfrac{1}{2}\log\nu_c]$$

The above equation is only valid for a soluble product and indeed only for first order charge transfer reactions with no ~~kinectic~~ kinetic or catalytic complications.

The E_p^a versus logν plots obtained at the graphite electrode (Fig. 5.12) did not show reversible behaviour in the slow sweep rate region, thus signifying the electron transfer reaction to be less reversible on this electrode. Using the variation of the peak separation, ΔE, ($= E_p^a - E_p^c$) as a criterion of irreversibility, Figs. 5.13 and 5.14 show that a greater degree of irreversibility occurrs with increasing concentration and temperature. Conway et al (222) have shown how the potentiodynamic sweep method (in particular E versus logν plots) can provide quantitative kinetic information and reversibility parameters for surface processes.

The cyclic voltammetric results at temperatures $>\sim 470°C$ clearly show that gas evolution occurs which is inferred from the current oscillations and the expected low I_p^c values. The oxidation process was found to obey a simple Arrhenius type relation (Fig. 5.16) from which an activation enthalpy of 23.62kj/mole was calculated. The analysis of the slow sweep potentiodynamic I-E curves has clearly shown linear regions in the transcribed E versus logi plots (Figs. 5.28 - 5.31) and thus may be analysed according to the Tafel equation (223):

$$\eta = a + B \ln i$$

At the graphite electrode a single low overpotential Tafel region was observed (Fig. 5.31), the slope of which was calculated to vary between 2.303RT/2.7F - 2.303RT/1.6F over the concentration range 0.175-0.9425 mole PbS/ℓ at 480°C. At the vitreous carbon electrode two Tafel regions were shown to occur (Figs. 5.28 and 5.29), the slope of the low overpotential region was calculated as 2.303 RT/3.0F - 2.303RT/2.5F at a single temperature of 460°C and over the concentration range 1.14-1.88 mole PbS/ℓ. At a concentration of 1.883 mole PbS/ℓ and over the temperature range 718-779K the low overpotential Tafel slopes varied between 2.303RT/3.0F - 2.303RT/2.5F. The slope of the high overpotential Tafel region varied between

2.30RT/0.7F - 2.303RT/0.47F.

The value of the Tafel slope may be used to distinguish between various kinetic schemes and is indeed a powerful approach. The value of the intercept a (the exchange current density i_0) may further be used, however the values of the Tafel slope obtained in this work are considered to be more accurate and reproducible and hence of greater use.

The most likely kinetic scheme that describes sulphur gas evolution may in the first instance be approached in an analogous manner to that used to describe $C\ell_2$, H_2 and O_2 evolution (224, 225, 226). Thus it has been shown from the electrolysis studies that the overall reaction may be given as

$$2S^{2-}_{(soln)} \rightleftharpoons S_2(g) + 4e'$$

The above reaction may be composed of three simple reaction steps:

(1) The discharge reaction:

$$S^{2-} \rightleftharpoons S_{(ads)} + 2e$$

(2) The combination reaction:

$$S_{(ads)} + S_{(ads)} \rightleftharpoons S_2(g)$$

(3) The ion and atom reaction:

$$S^{2-} + S_{(ads)} \rightleftharpoons S_2(g) + 2e$$

The above reactions may be combined to form two possible reaction pathways:

(a) Reaction 1 followed by reaction 2, or

(b) reaction 1 followed by reaction 3.

Thus following the derivation given by Bockris (226) for the anodic evolution of O_2 from water then:

(1) If the S^{2-} discharge reaction is rate determining and surface coverage is small then

$$\vec{V}_1 = k_1 a_{S^{2-}} \exp(2\alpha\Delta\phi F/RT)$$

and thus

$$\vec{i} = 2F k_1 a_{S^{2-}} \exp(2\alpha\Delta\phi F/RT)$$

(2) If the combination reaction is rate determining and if the surface coverage of the adsorbed species is given by $\theta_{(MS)_{ads}} = k' a_{MS}$ (MS refers to the adsorbed state of sulphur atom and does not imply a chemical species MS) then

$$\vec{V} = k_1 a_{S^{2-}} (1-\theta_{MS}) \exp(2\alpha\Delta\phi F/R)$$

at low overpotential, $\Delta\phi$, i.e. $a_{MS} << 1$

then

$$\vec{i} = 4FK_1^2 k_2 a^2_{S^{2-}} \exp(4\Delta\phi F/RT)$$

where $K_1 = k_1/k_{-1}$

at high overpotential, $\Delta\phi$ $a_{MS} = a_{MS(sat)}$

then

$$\vec{i} = 4F \frac{k_2}{k'} a_{MS(sat)}$$

(3) If the ion + atom reaction is rate determining and the surface coverage given by $\theta_{MS} = k' a_{MS}$ then

$$\vec{V}_1 = k_1 a_{S^{2-}} (1-\theta_{MS}) \exp(2\alpha\Delta\phi F/RT)$$

and for small

$$\vec{i} = 4FK_1k_2 a^2_{S^{2-}} \exp[2(1 + \alpha)\, \Delta\phi F/RT]$$

and for large

$$\vec{i} = 4F \frac{k_2}{k_T} \exp 2\alpha\Delta\phi F/RT$$

The Tafel slopes predicted for the above mechanisms assuming $\alpha = 0.5$ yield:

	Tafel Slope 2.303 RT/F	
Ion discharge		
Ion discharge + combination reaction	2.303 RT/4F	$a_{MS} \rightarrow 0$
	i_L	$a_{MS} \rightarrow 1$
Ion discharge + ion/atom reaction	2.303 RT/3F	$\Delta\phi$ small
	2.303 RT/F	$\Delta\phi$ large

The above analysis is quite a simple one and more complex adsorption isotherms may be used, i.e. Temkin or Langmuir either activated or non-activated (227). However, from the above analysis the results obtained at the vitreous carbon electrode are in reasonable agreement with the mechanism of ion discharge followed by ion-atom combination. The presence of any adsorbed species has not been confirmed by the cyclic voltammetry results using sweep rates 0.02-20V/s. Further evidence to distinguish between the kinetic schemes may be obtained from the value of the stoichiometry number ν' from the equations:

$$i = i_o \exp \alpha(\frac{n}{\nu'}) F/RT \qquad \text{at high } \Delta\phi$$

and

$$i = i_o(\frac{n}{\nu'}) F/RT \qquad \text{at low } \Delta\phi$$

However to obtain ν' a knowledge of i_o is required. The i_o values

obtainable from the E-logi plots in this work are not considered to be analytically useful since a the true value of the overpotential ($\eta = E-E_{S^{2-}/S}$) is not known. Thus further analysis based upon the stochiometric number is not possible.

The single Tafel region obtained at the graphite electrode of slope 2.303RT/2.7F - 2.303RT/1.6F is more difficult to explain. It must be noted, however, that Tafel behaviour was not generally observed at the graphite electrode and thus further experiments should be conducted to determine if the above values are really true. A single Tafel region was also obtained by King and Welch (188) for the oxidation of PbS-$PbC\ell_2$-NaCℓ melts at a graphite electrode with Tafel slopes of RT/1.2F-RT/1.7F. Again Tafel behaviour was found to be irreproducible, and limiting currents were obtained at high overpotentials. The same authors explained their results on the basis of a one electron transfer mechanism:

$$AS_x + AS^- \rightleftharpoons S_{(ads)} + A_2S_{(melt)} + e$$

$$m\ S_{(ads)} \rightleftharpoons S_n\ (gas)$$

where AS^- represents the dissolved sulphide ion and AS is a sulphur product of fixed activity, i.e. a heterogeneous phase on the electrode surface. Assuming the electron discharge reaction to be rate determining then a Tafel slope of $RT/(1 + \alpha)F$ is predicted and thus corresponds to their Tafel slope.

The combined electrolysis and optical experiments undertaken by King and Welch (204) have clearly demonstrated that sulphur evolution occurs, in particular that evolution continues to occur even after the current is switched off. The latter phenomenon is usually referred to as residual gas evolution (r.g.e.) and may be indicative of Volmer-Heyrovsky type reaction mechanisms, e.g. ion discharge + ion/atom combination.

Jansenn and Hoogland (228) have investigated the r.g.e. phenomenon in depth for the evolution of chlorine from aqueous electrolytes. The difference between Tafel behaviour at the vitreous carbon electrode and graphite electrodes may be attributed to the structural difference between the two substrates. Thus Tunold et al (229) have shown that significantly different Tafel slopes may be obtained for the chlorine evolution reaction from molten chloride media at different carbon substrates and indeed at different crystal faces. Higher Tafel slopes at graphite may, for example, be due to ohmic voltage drop or a change in the transport process in the pores. A further contribution may be caused by variation in the active surface area due to bubbles adhering to the electrode (230,231).

The slow potentiodynamic I-E curves have shown that the 'anode effect' (A.E.) may occur during the sulphur evolution reaction (Fig. 5.27). However the onset of the A.E. was quite irreproducible and no information concerning critical current densities or potentials could be obtained. In general diffusion limiting currents were observed. This is in complete contrast to the highly reproducible A.E. obtained for chlorine or fluorine evolution in either aqueous or molten salt media (220,223). The A.E. is however a complex process and many theories have been proposed in an attempt to fully understand this phenomenon. One of the theories considers the formation of a film or a compound on the electrode surface. The electrode then becomes non-conducting or the interfacial energy is decreased such that the electrode is not wetted by the melt (232,233). For example, intercalation compounds detected by observed increase in lattice parameter have been found in both the fluoride and chloride electrolysis (234-236). However the formation of an insoluble film during sulphur evaluation has not been observed during this work, either under prolonged potentiostatic or galvanostatic conditions. The same conclusion has been reached by Plichon and du Guibert (194) during their prolonged electrolysis studies, impedance

studies by the same authors (192) do not indicate an increase in the resistance of the electrode. The above results are in complete contrast to the earlier electrolysis studies of Welch and King (188) who found insoluble films to build up during electrolysis of PbS-$PbC\ell_2$-NaCℓ electrolytes, the morphology of the film being dependent upon the applied current density.

A further cause of the A.E. is via a pure bubble phenomenon and may be directly compared to the case of nucleate boilding heat transfer processes. The nucleation and growth of gas bubbles at an electrode is only possible if the electrolyte in the vicinity of the electrode is supersaturated with dissolved gas. The results of Shibata (237) for the case of H_2 evolution have shown that the gas concentration in the electrolyte at zero distance from the electrode may reach 160-fold the saturation value. The degree of supersaturation depends upon the current density and on the number of bubble nuclei at the surface and hence upon the surface condition of the electrode. An increase in the surface roughness of the electrode results in lower supersaturation values (238). Vogt (239) has given a detailed but generalised account of the supersaturation of gases in the concentration boundary layer of gas evolving electrodes and has shown the degree of supersaturation ($c' c_s$) to be dependent upon the current density through the relation:

$$c' - c_s = i^{0.25}$$

Thus on the basis of the above, bubble nucleation and growth of sulphur should be more favourable on the rough graphite electrodes.

The A.E. as caused by a pure bubble effect is obtained as a consequence of a change in the morphology of the growth and separation of the gas bubbles. At low current densities the gas evolves in the form of separate bubbles (nucleate boiling) and it is in this region that bubble size increases with increasing current density. A transition period is

then reached in which coalescence of the bubbles occurs and the electrode becomes covered with an irregular gaseous blanket in violent motion. Under the latter conditions there occurs a drop in the current density and an increase in the electrode potential. Finally the A.E. occurs when the electrode becomes enclosed with a permanent, continuous gaseous envelope. Mazza et al have given a detailed description of the hydrodynamic instabilities in electrolytic gas evolution (240). The same authors have shown that the critical current density for A.E. is given by

$$i_{crit} = nF \frac{\psi_g}{Mg} \left(\frac{N}{\psi_L} \frac{\Delta C}{\psi_g}\right)^x . R_c$$

where x = 0.25 (for chlorine and oxygen evolution), M = the molecular weight, N = equivalent concentration, C = supersaturation of gas and R_c is the critical gas evolution rate which is dependent upon the type of gas flow conditions prevailing. A description of the A.E. is further complicated by the effects of a change in the interfacial tension of the three phase boundary during electrolysis. Gesler has stated that the chemical factors affecting the interfacial energy can only increase or decrease the probability of the A.E. and that a certain amount of electrical energy is necessary for neutralising the wetting (241). Drossbach (242,231) has suggested that the A.E. is the result of gas bubbles being pressed against the anode surface by an electrostatic field. The most significant effect of the change in potential is upon the bubble contact angle, ϕ, as was first shown by Lipmann (243) and has been further demonstrated by the experiments of Möeler (244). For the specific case of sulphur it has been shown that the contact angle of a droplet of liquid sulphur upon a vitreous carbon electrode may be significantly changed by a change in potential (245).

The oscillations obtained on the I-E curves in this study clearly indicate gas bubble formation. The oscillations arise from a change in the active electrode area during bubble growth and break off. A measure of the break off diameter of bubbles in a quiescent liquid is given by the equation (246):

$$d = 0.837\ \theta\left[\frac{2\gamma}{g(\psi_L - \psi_g)}\right]^{0.5}$$

where g = acceleration of gravity, θ the contact angle, γ the interfacial tension and ψ the density. A very comprehensive and mathematical account of mass transfer to gas evolving electrodes has been given by Stephan and Vogt (247).

From the above brief discussion it is evident the A.E. is a complex phenomenon involving the 'interplay' of several effects. It is thus impossible to draw any definite conclusions as to why the A.E. is so irreproducible for sulphur evolution.

CHAPTER 6

ELECTROCHEMICAL BEHAVIOUR OF PbS IN THE TERNARY $PbCl_2$-KCl-NaCl EUTECTIC MELT

6.1 Introduction

The study of the electrochemical behaviour of lead sulphide solutions using the $PbCl_2$-KCl-NaCl (48-35-17 m/o) ternary eutectic melt was undertaken in an attempt to understand better the formation of insoluble sulphur or sulphide films on the electrode surface(s). The lower operating temperature available (∿410°C) using this melt system (MPt = 399°C) should facilitate film formation. Two fundamentally different electrode systems were employed:

(1) 'Inert' carbon based electrodes, e.g. vitreous carbon and spec-pure graphite planar electrodes.

(2) 'Reactive' metal electrodes, e.g. platinum and gold.

The results obtained using these electrodes are presented individually and compared and contrasted in the discussion section (6.5).

6.2 Results: Vitreous Carbon and Graphite Electrodes

6.2.1 Cyclic Voltammetry

The effects of increasing sweep rate (0.01-0.4 V/s) and PbS bulk concentration (1.08×10^{-2} - 7.335×10^{-2} M) upon the voltammetric parameters for the initial oxidation of PbS and subsequent reduction were studied at a single temperature of 417°C. Generally, two distinct morphological types of voltammetric waves were obtained. At low concentrations, i.e. 1.08×10^{-2} M), see Fig. 6.2.1; a single, well-defined oxidation wave was obtained up to a potential of 0.6V vs Ref.

A slight inflection on the forward wave generally occurred at approximately +0.25V; it was not possible to resolve further this wave by a change of sweep rate or PbS concentration. A single reduction process corresponding to that of the main oxidation wave was observed up to the limiting Pb^{2+} reduction potential.

Upon increasing the bulk PbS concentration the oxidation wave was observed to broaden significantly; this broadening was further enhanced by an increase in sweep rate (see Fig. 6.2.2). A similar effect upon the reduction wave is apparent. The above behaviour was confirmed during many separate experiments using freshly made electrodes.

The effect of increasing sweep rate upon the voltammetric parameters may be presented in terms of (i) current and (ii) potential dependent functions.

Fig. 6.2.3 illustrates the effect of increasing sweep rate at a PbS concentration of 1.08×10^{-2}M and Table 6.2.1. lists the values of the voltammetric parameters. The anodic peak current (I_p^a) increases linearly with increasing $(\text{sweep rate})^{\frac{1}{2}}$, Fig. 6.2.4; for all concentrations used. A zero intercept was obtained at the lowest concentration used; as the concentration increases a progressively larger current intercept was obtained. The results of a linear regression analysis (using the Randles Sevcik equation and assuming n = 2) are given in Table 6.2.2. The sweep rate range that could be usefully employed at high concentrations was severely limited by the appreciable anodic shift in peak potential. The more sensitive plots of $I_p^a/\nu^{\frac{1}{2}}$ vs ν exhibits a virtually constant value at low concentrations (Fig. 6.2.5) but shows a significant decrease at low sweep rates with increasing concentration. A useful analytical tool is the variation of the I_p^c/I_p^a ratio as a function of both sweep rate and concentration. Fig. 6.2.6, shows the variation of the I_p^c/I_p^a ratio (as calculated by the Nicholson's empirical formula (19)) as a function of sweep

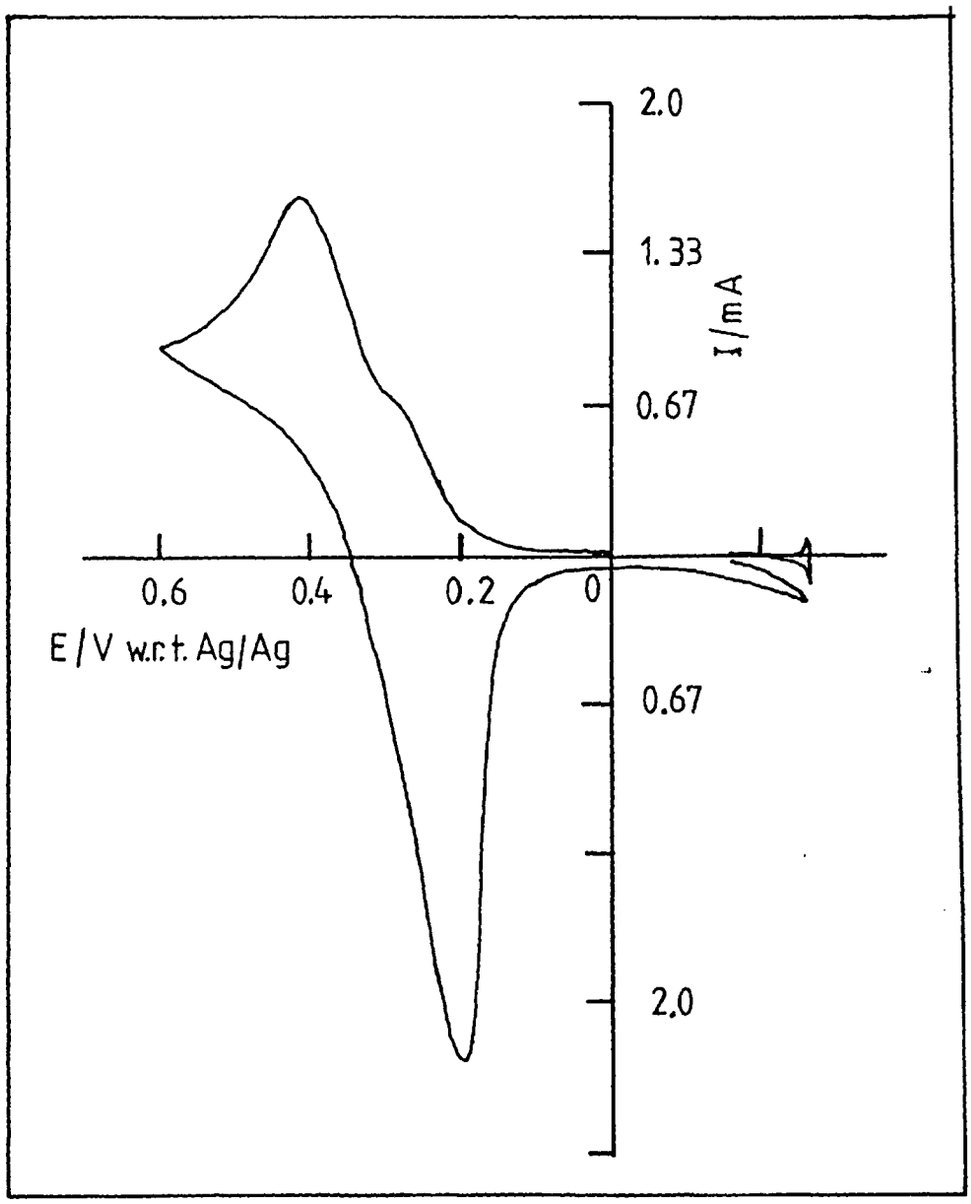


Fig. 6.2.1: A typical cyclic voltammogram obtained at a vitreous carbon electrode for the oxidation of PbS containing solutions over the voltage range 0 → 0.6V w.r.t. Ag^{+}/Ag°.
[PbS] = 1.077×10^{-2}M, electrode area = 0.0855 cm^2; sweep rate = 0.25 V/s; T = 417°C.

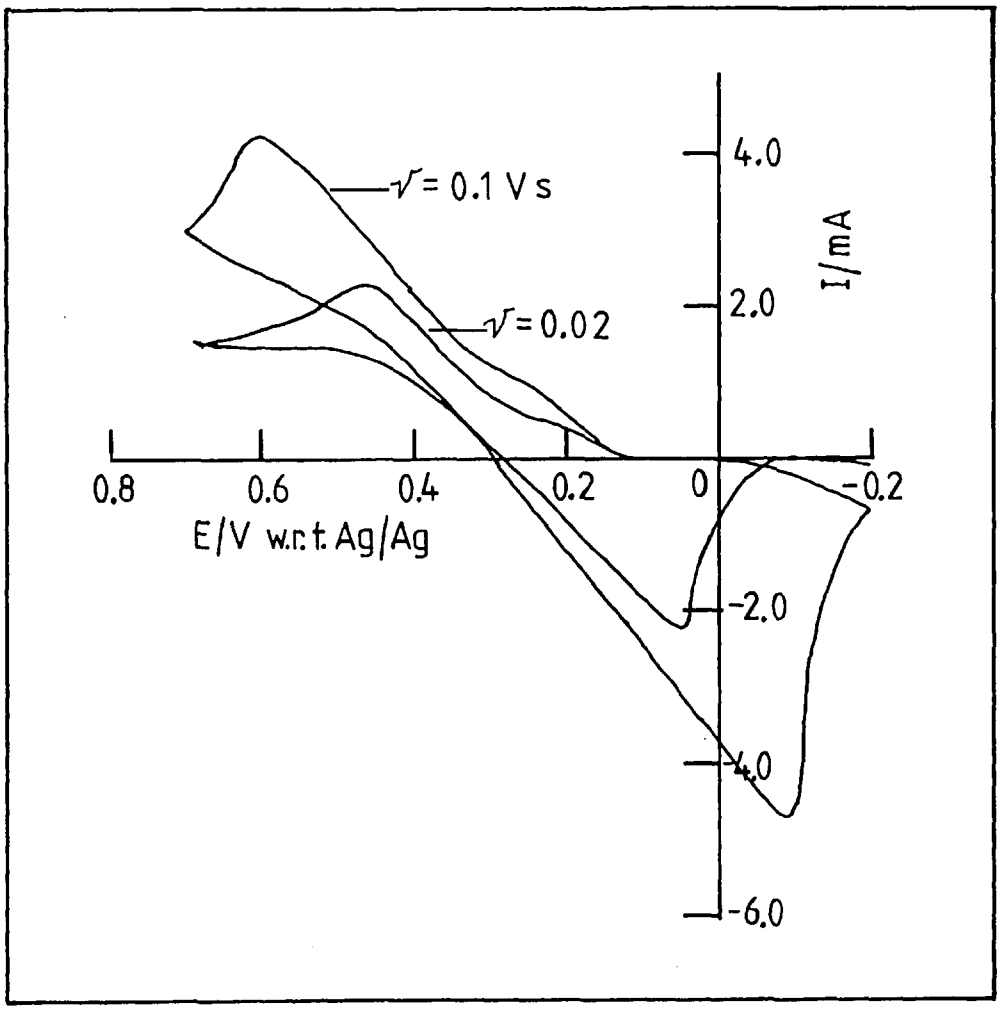


Fig. 6.2.2: The effect of increasing sweep rate at 'high' PbS concentrations (5.352×10^{-2}M) upon the cyclic voltammetric response.
Electrode: vitreous carbon (area 0.0855 cm^2):
T = 417°C.

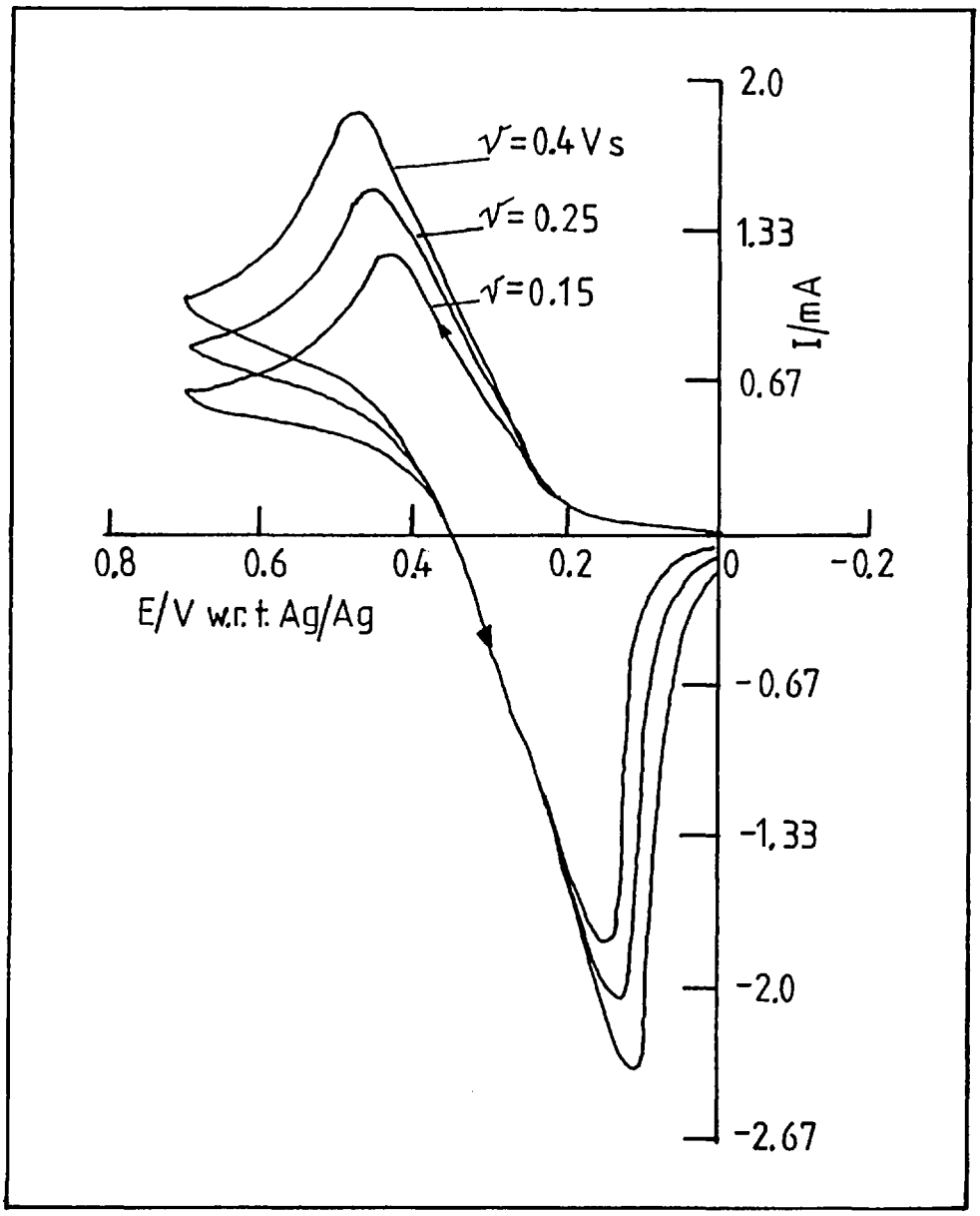


Fig. 6.2.3: The effect of increasing sweep rate upon the voltammetric response at 'lower' concentrations (1.077×10^{-2}M).
Electrode: vitreous carbon (area 0.0855 cm^2);
T = 417°C.

TABLE 6.2.1.

The effect of increasing sweep rate upon the cyclic voltammetric parameters for the oxidation of PbS at a vitreous carbon electrode. Melt: $PbCl_2$-KCl-NaCl: T = 417°C, PbS = 1.08×10^{-2} mole/Kg, Electrode Area = 0.0855 cm^2.

V v/s	$V^{\frac{1}{2}}$ $(v/s)^{\frac{1}{2}}$	Ip^a mA	$Ip^a/V^{\frac{1}{2}}$	Ip^c/Ip^a	Ep^a mV	Ep^c mV	ΔE mV	$Ep^a-Ep/2^a$ mV
0.01	0.1	3.67	3.667	2.006	375	225	150	80
0.02	0.1414	0.467	3.30	2.236	375	205	170	90
0.04	0.2	0.633	3.167	2.30	385	180	205	90
0.06	0.245	0.75	3.062	2.21	400	180	220	100
0.08	0.283	0.825	2.917	2.188	405	170	235	105
0.1	0.316	0.916	2.899	2.087	410	170	240	105
0.15	0.387	1.223	3.184	1.807	435	155	280	120
0.2	0.447	1.367	3.056	1.760	440	145	295	125
0.25	0.5	1.533	3.067	1.470	450	140	310	130
0.3	0.548	1.633	2.982	1.680	460	130	330	135
0.35	0.592	1.767	2.986	1.634	470	125	345	140
0.4	0.632	1.867	2.951	1.613	475	120	355	150

TABLE 6.2.2

Analytical data obtained from the Ip^a versus $v^{\frac{1}{2}}$ plot for the oxidation of S^{2-} at a vitreous carbon electrode T = 417°C, Area = 0.0855 cm^2.

PbS x 10^2M	$Ip^a/v^{\frac{1}{2}}$	ImA intercept	Corr
1.08	2.9006	0.05	0.998
2.52	5.273	0.42	0.998
3.918	7.878	0.68	0.999
5.35	10.446	0.86	0.999
7.335	11.351	1.51	0.999

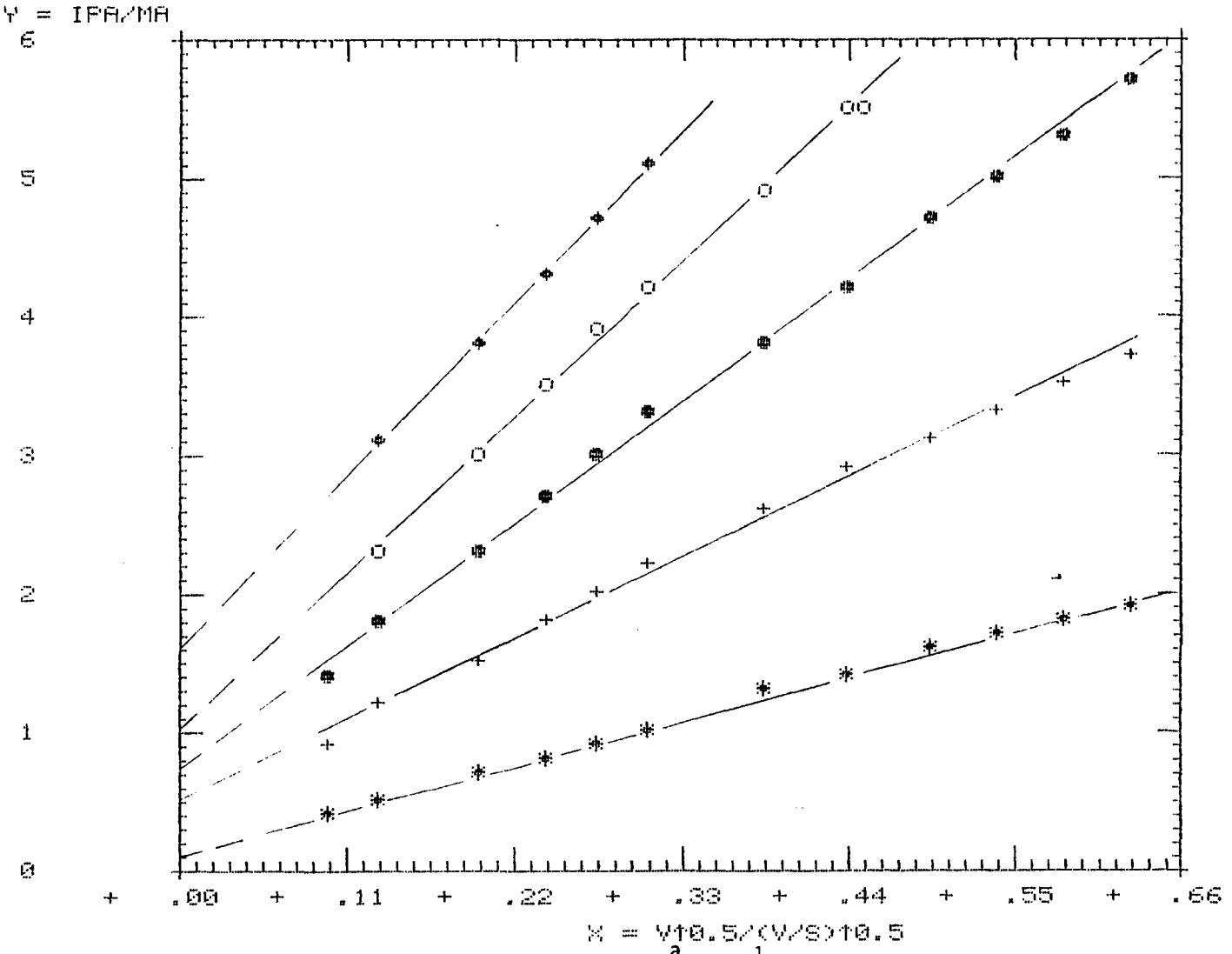


FIGURE NUMBER 6.2.4: A plot of I_p^a vs $\theta^{\frac{1}{2}}$ for the oxidation of PbS in the ternary $PbCl_2$-KCl-NaCl eutectic melt at 417°C. Electrode vitreous carbon (area = 0.0855 cm^2); [PbS]M:- * 1.08×10^{-2}; + 2.52×10^{-2}; ● 3.918×10^{-2}; O 5.35×10^{-2}; ▲ 7.335×10^{-2}.

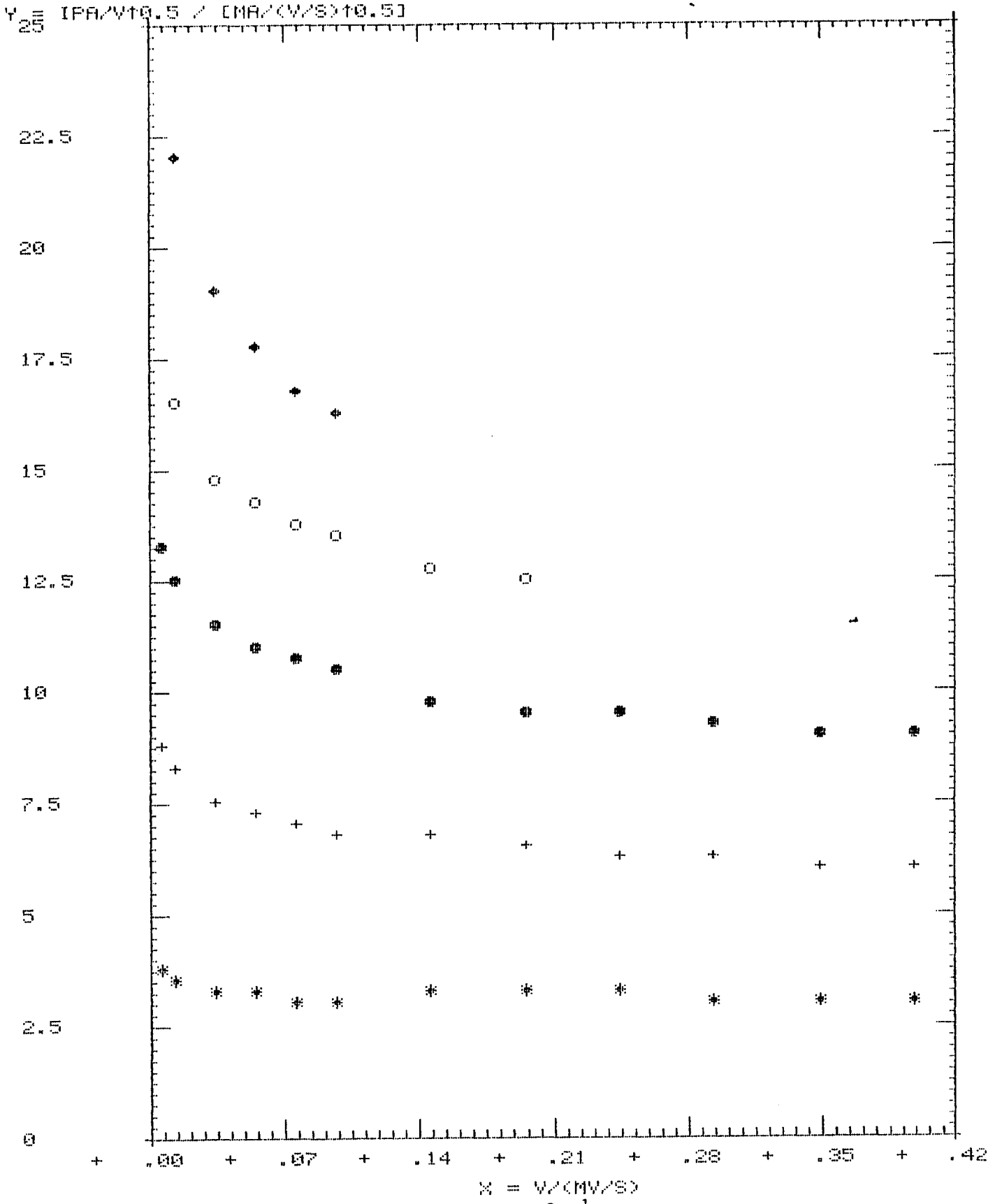


FIGURE NUMBER 6.2.5: A plot of $I_p^a/\nu^{\frac{1}{2}}$ vs ν for the oxidation of PbS in the ternary $PbCl_2$-KCl-NaCl eutectic melt at 417°C. Electrode: vitreous carbon (area = 0.0855 cm^2) [PbS]M:- *1.08x10^{-2}; + 2.52x10^{-2}; ● 3.918x10^{-2}; O 5.35 x 10^{-2}; ▲ 7.335x10^{-2}.

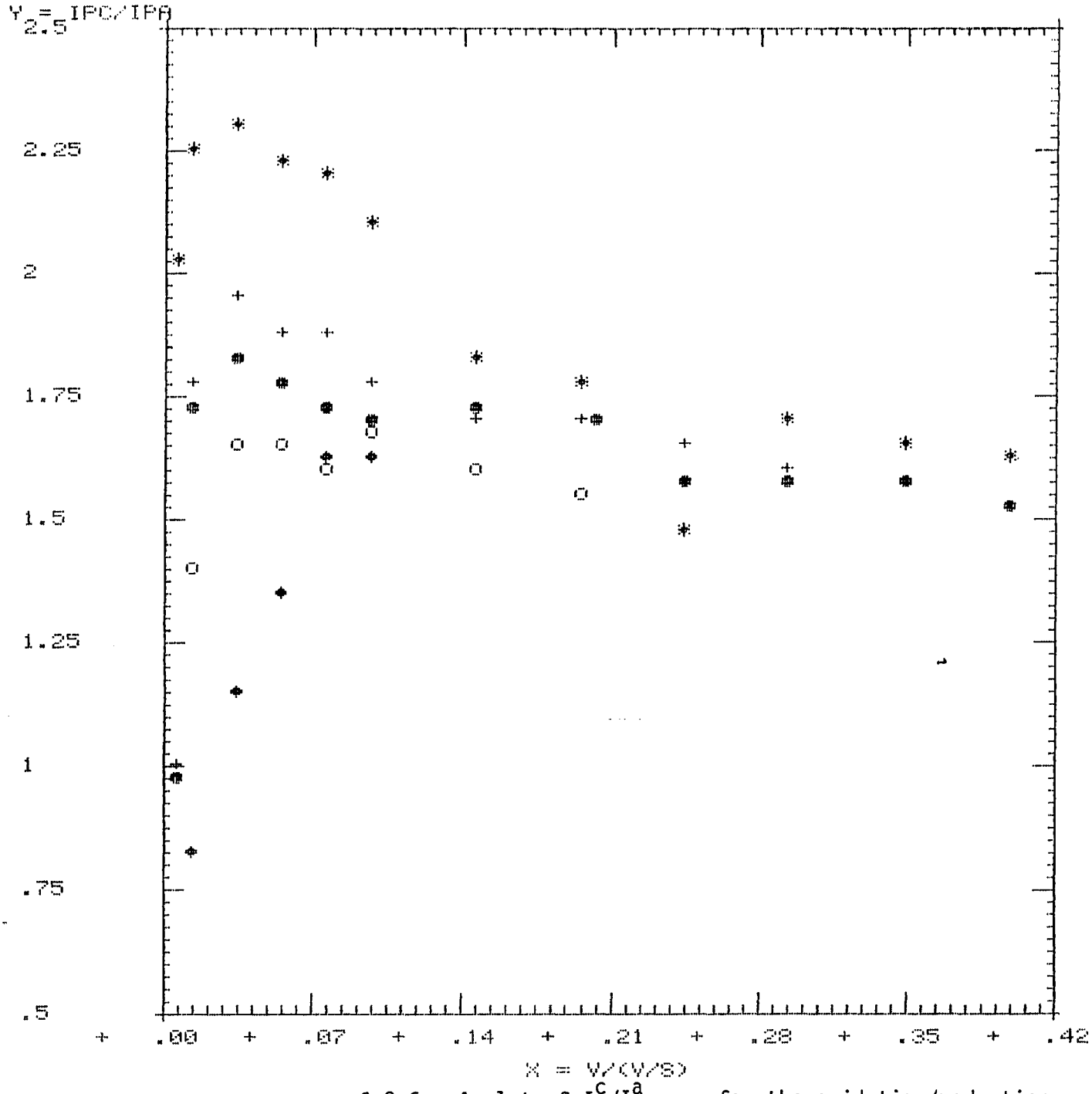


FIGURE NUMBER 6.2.6: A plot of I_p^c/I_p^a vs ν for the oxidation/reduction of PbS in the ternary $PbC\ell_2$-KCℓ-NaCℓ eutectic melt at 417°C. Electrode: vitreous carbon (area = 0.0855 cm^2). [PbS]M = $*1.08x10^{-2}$; + $2.52x10^{-2}$; ● $3.918x10^{-2}$; 0 $5.35x10^{-2}$; ▲ $7.335x10^{-2}$.

rate and concentration. A general feature observed at all concentrations is a rapid rise in the current ratio at low sweep-rates, culminating in a maximum at $\nu \sim$ 40-60 mV/s, the current ratio finally becoming virtually independent of sweep rate as the latter is increased. The observed maximum appears to be dependent upon concentration. A more interesting plot is that for the corresponding charges ratio Q^c/Q_T^a with increasing sweep rate. Fig. 6.2.7 shows this relationship for two lead sulphide concentrations from which a similar trend to that obtained with the current ratio can be seen, although a sharp maximum is not obtained. It is further noted that $Q^c/Q_T^a \rightarrow 1$ as the lead sulphide concentration is increased. The measured anodic charge Q^a increases linearly with increasing (sweep rate)$^{-\frac{1}{2}}$ (Fig. 6.2.8) with zero intercept.

The effect of increasing sweep rate upon the potential functions E_p^a, ΔE (= $E_p^a - E_p^c$) and $E_p^a - E_{p/2}^a$ was significant. Fig. 6.2.9 shows quite clearly a linear anodic shift of the E_p^a value with increasing $\nu^{\frac{1}{2}}$; the rate of increase, i.e. $\partial E_p^a/\partial\nu^{\frac{1}{2}}$ increasing with increasing concentration. A non-linear trend is noted at the highest lead sulphide concentration used. The results of a linear regression analysis are given below (Table 6.2.3).

Table 6.2.3: Linear regression analysis of voltammetric potential/sweep rate relations with increasing PbS concentration

[PbS] x 10^2M	$\partial E_p^a/\partial\nu^{\frac{1}{2}}$	Corr	$\partial(E_p^a - E_{p/2}^a)/\partial\nu^{\frac{1}{2}}$	Corr
1.08	0.202	0.995	0.124	0.994
2.52	0.370	0.998	0.209	0.997
3.918	0.461	0.899	0.306	0.998
5.35	0.698	0.999	0.427	0.996

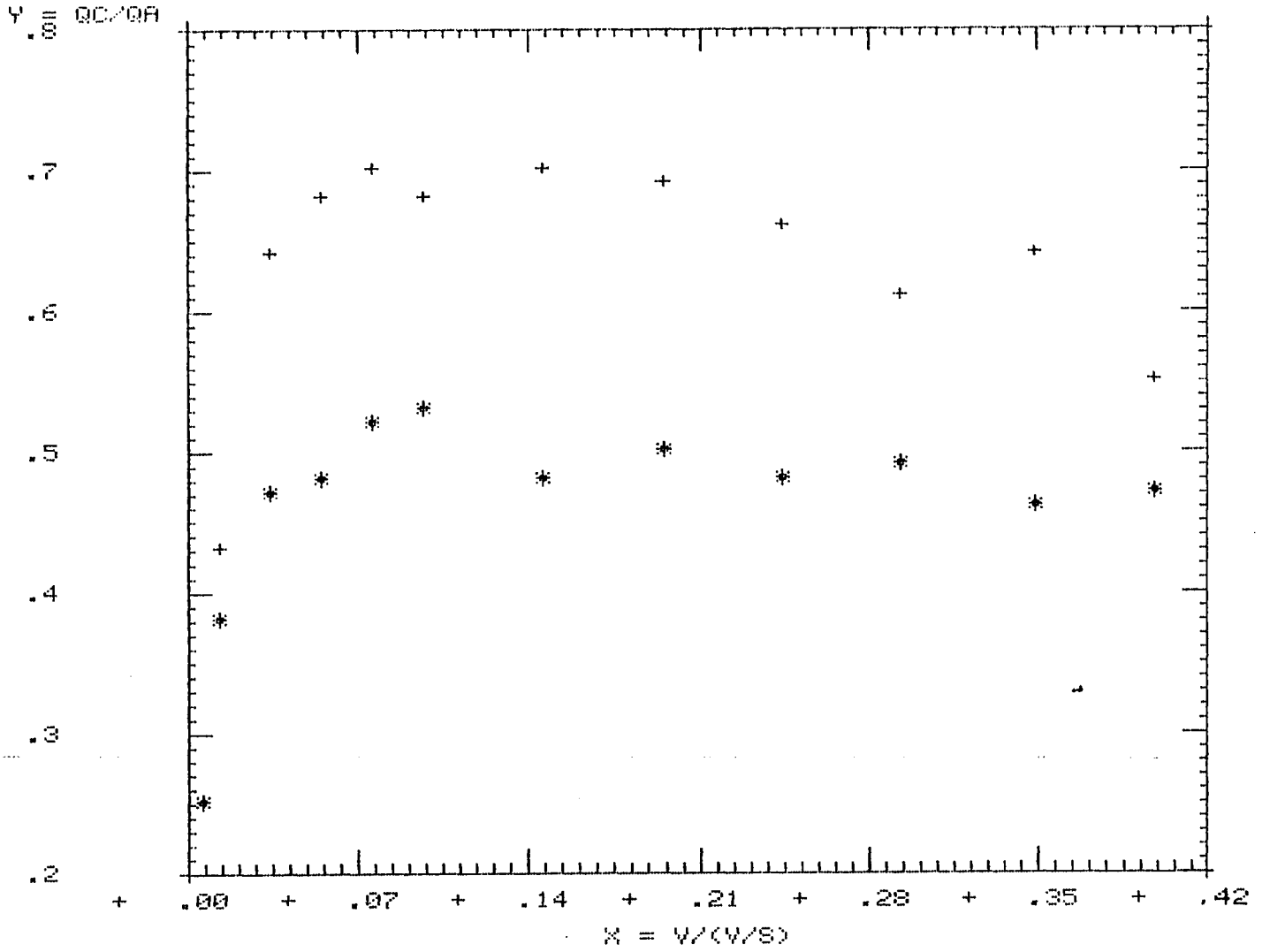


FIGURE NUMBER 6.2.7: A plot of Q^c/Q_T^a vs ν for the oxidation/reduction of PbS in the ternary $PbCl_2$-KCl-NaCl eutectic melt at 417°C. Electrode: vitreous carbon (area = 0.0855 cm^2). [PbS]M: ⋆ 1.08×10^{-2}; + 3.918×10^{-2}.

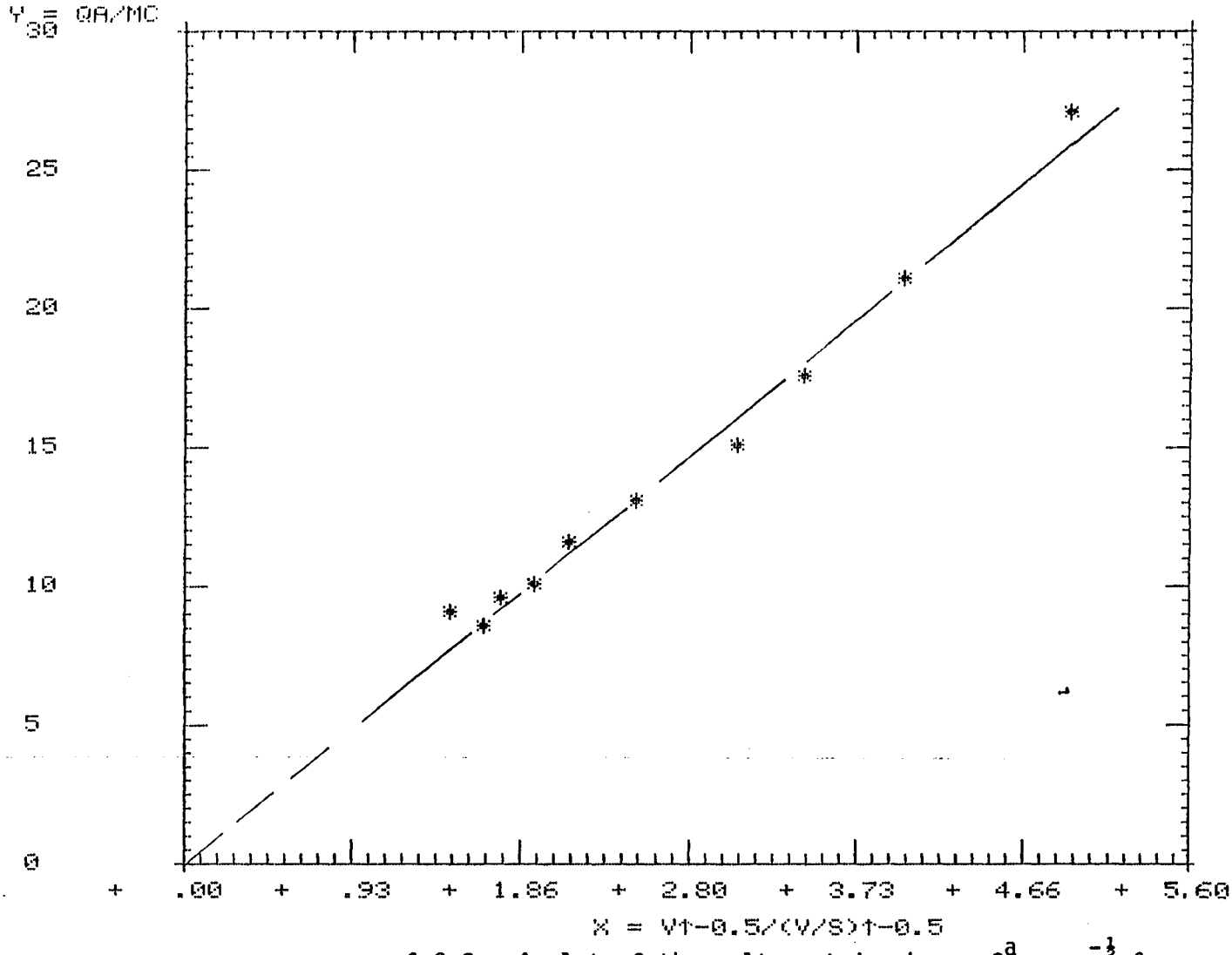


FIGURE NUMBER 6.2.8: A plot of the voltammetric charge Q^a vs $\nu^{-\frac{1}{2}}$ for the oxidation of PbS (3.918×10^{-2} M) at a vitreous carbon electrode (0.0855 cm^2) at 417°C.
Solvent: $PbCl_2$-KCl-NaCl ternary melt.

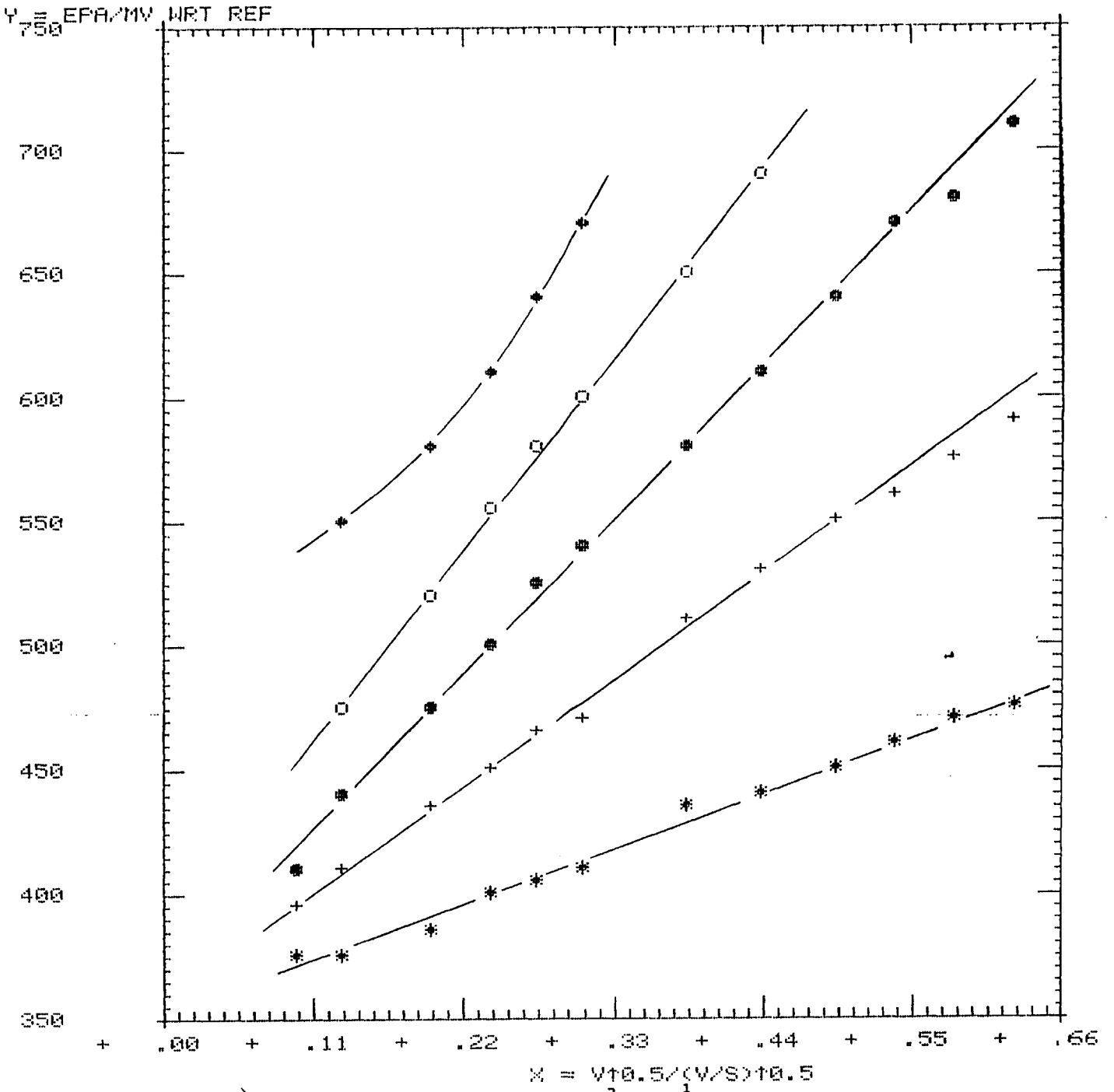


FIGURE NUMBER 6.2.9: A plot of E_p^a vs $\nu^{\frac{1}{2}}$ for the oxidation of PbS in the ternary $PbCl_2$-KCl-NaCl eutectic melt at 417°C. Electrode = vitreous carbon (0.0855 cm^2). [PbS]M:- * 1.077×10^{-2}; + 2.52×10^{-2}; ● 3.918×10^{-2}; O 5.352×10^{-2}; ▲ 7.335×10^{-2}.

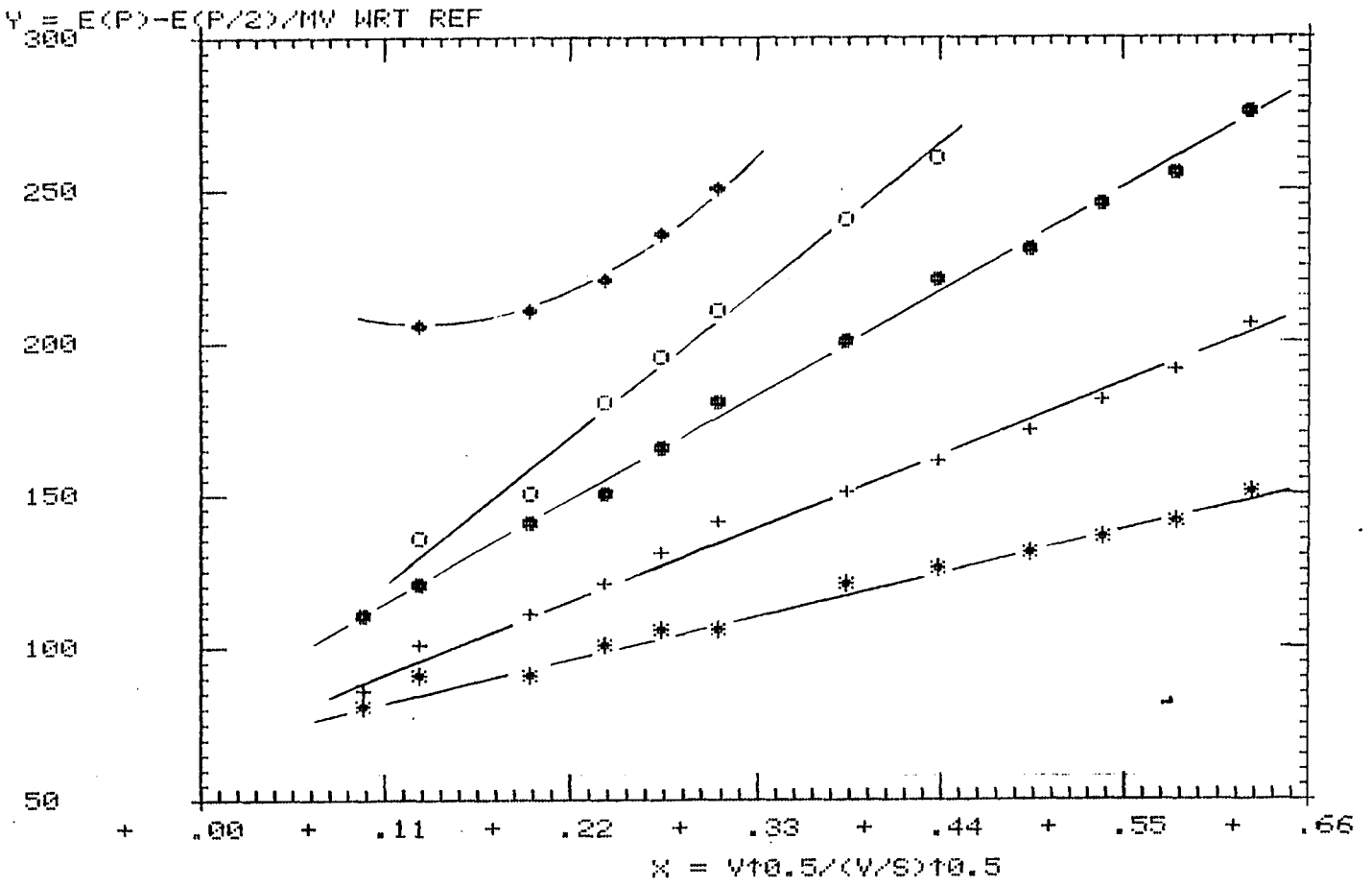


FIGURE NUMBER 6.2.10: A plot of the voltammetric half peak width ($E_p^a - E_{p/2}$) vs $s^{\frac{1}{2}}$ for the oxidation of PbS in the PbC_2-KC -NaC ternary eutectic melt at 417°C. Electrode: vitreous carbon (area = 0.0855 cm^2). [PbS]M: * 1.077×10^{-2}; + 2.52×10^{-2}; ● 3.918×10^{-2}; O 5.352×10^{-2}; ▲ 7.335×10^{-2}.

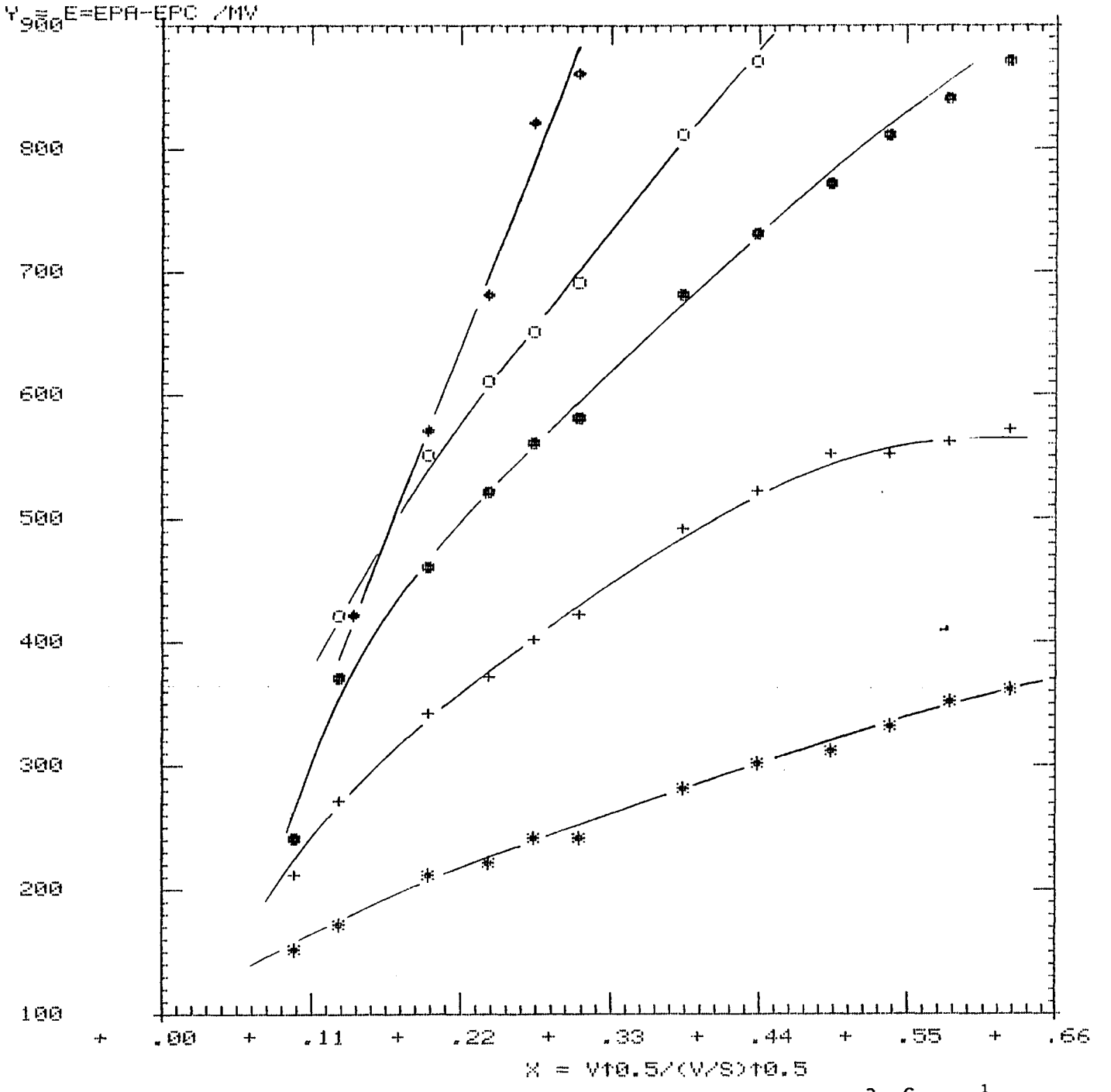


FIGURE NUMBER 6.2.11: A plot of the peak separation $E_p^a - E_p^c$ vs $\nu^{\frac{1}{2}}$ for the oxidation/reduction of PbS in the $PbCl_2$-KCl-NaCl ternary eutectic melt at 417°C. Electrode: vitreous carbon (area = 0.0855 cm^2). [PbS]M: * 1.077×10^{-2}; + 2.52×10^{-2}; ● 3.918×10^{-2}; O 5.352×10^{-2}; ◆ 7.335×10^{-2}.

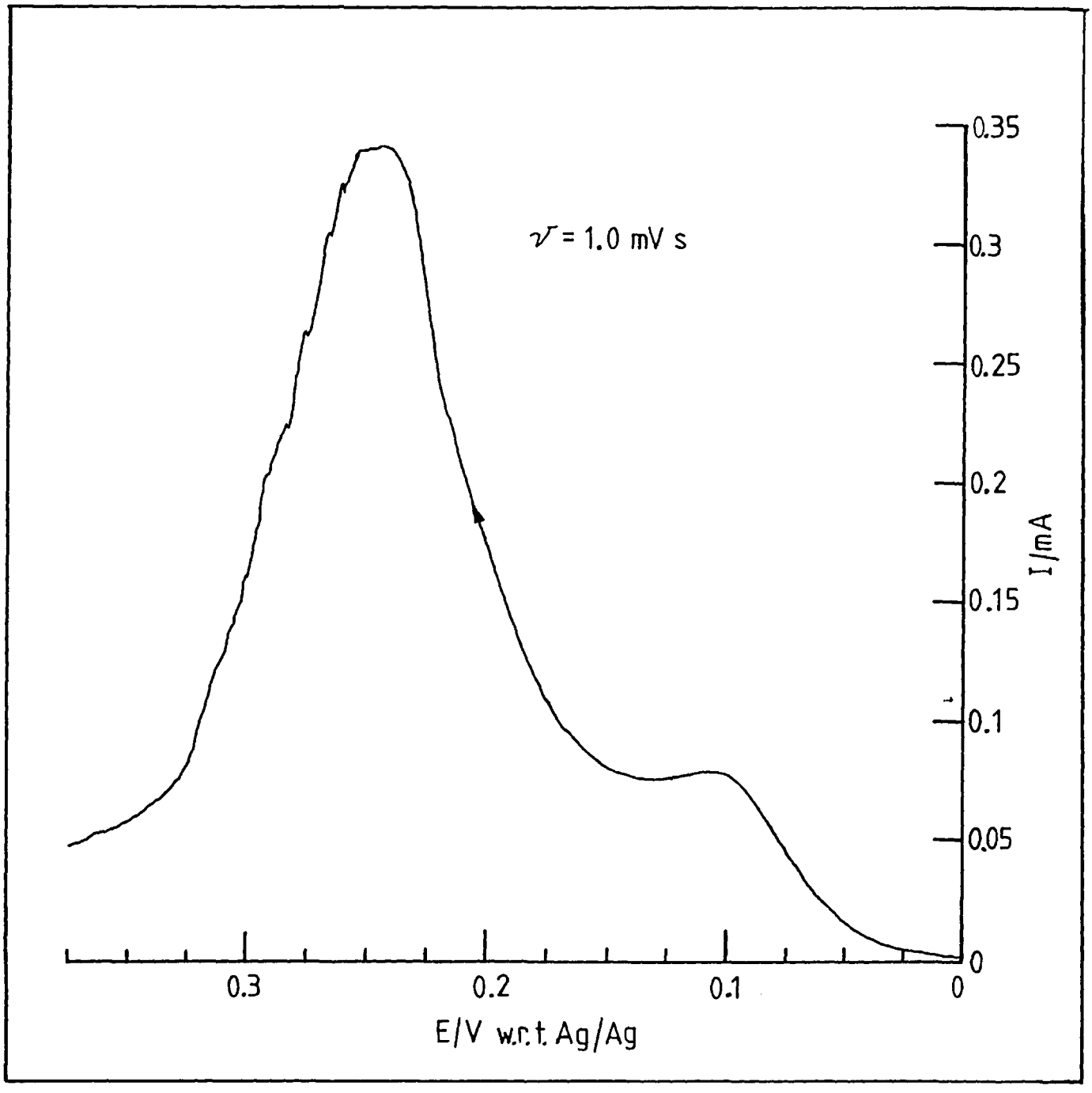


Fig. 6.2.12: A slow potentiodynamic (1m V/s) I-E curve obtained at a vitreous carbon electrode in a PbS-$CbC\ell_2$-$KC\ell$-$NaC\ell$ melt at 417°C. [PbS] = 2.624 x 10^{-2}M; electrode area = 0.0855 cm^2.

A similar relationship was obtained for the value of the half-peak width ($E_p^a - E_{p/2}^a$), see Fig. 6.2.10 and Table 6.2.3. The peak separation function ΔE ($= E_p^c - E_p^a$) does not however show a linear variation with increasing $\nu^{\frac{1}{2}}$ (see Fig. 6.2.11). Although the cathodic peak potential shifts cathodically with increasing sweep rate, the rate of shift decreases upon increasing the sweep rate (see Table 6.2.1) as inferred by the trend in ΔE.

Pseudo steady-state I-E relationships, obtained using slow (1 mV/s) potentiodynamic sweeps did not show diffusion limiting current plateaux as would be expected under pure diffusion control of, say, a soluble product. Fig. 6.2.12 shows two noteable features. Firstly the pre-wave or inflection has been resolved and exhibits a peak and secondly a decrease in current very low values occurs for the major oxidation process as the potential is further increased. The steady-state voltammograms were quite reproducible between different experiments.

6.2.2 Chronoamperometry

The measured current-time transients as a result of an applied potential pulse clearly show diffusion controlled behaviour, i.e. linear $I\text{-}E^{-\frac{1}{2}}$ relationship, see Fig. 6.2.13. No peaks or increases in current with time were observed at any potential or pulse length (10 ms-10s) were obtained. Unusual reverse I-t transients were observed as may be seen in Fig. 6.2.13. Upon returning the potential pulse to zero the resultant I-t transient did not decay as would be expected for a soluble product. A large current is maintained for a period of time before rapidly falling to zero. The time at which this rapid decrease occurs was dependent upon the time of the forward pulse as can be seen from Figs. 6.2.13 and 6.2.14. The ratio of the respective charges, i.e. Q^c/Q^a was virtually constant at 0.7-0.8. The relationship between the transients for the forward and reverse processes are shown in Fig. 6.2.14 as a plot of the current function

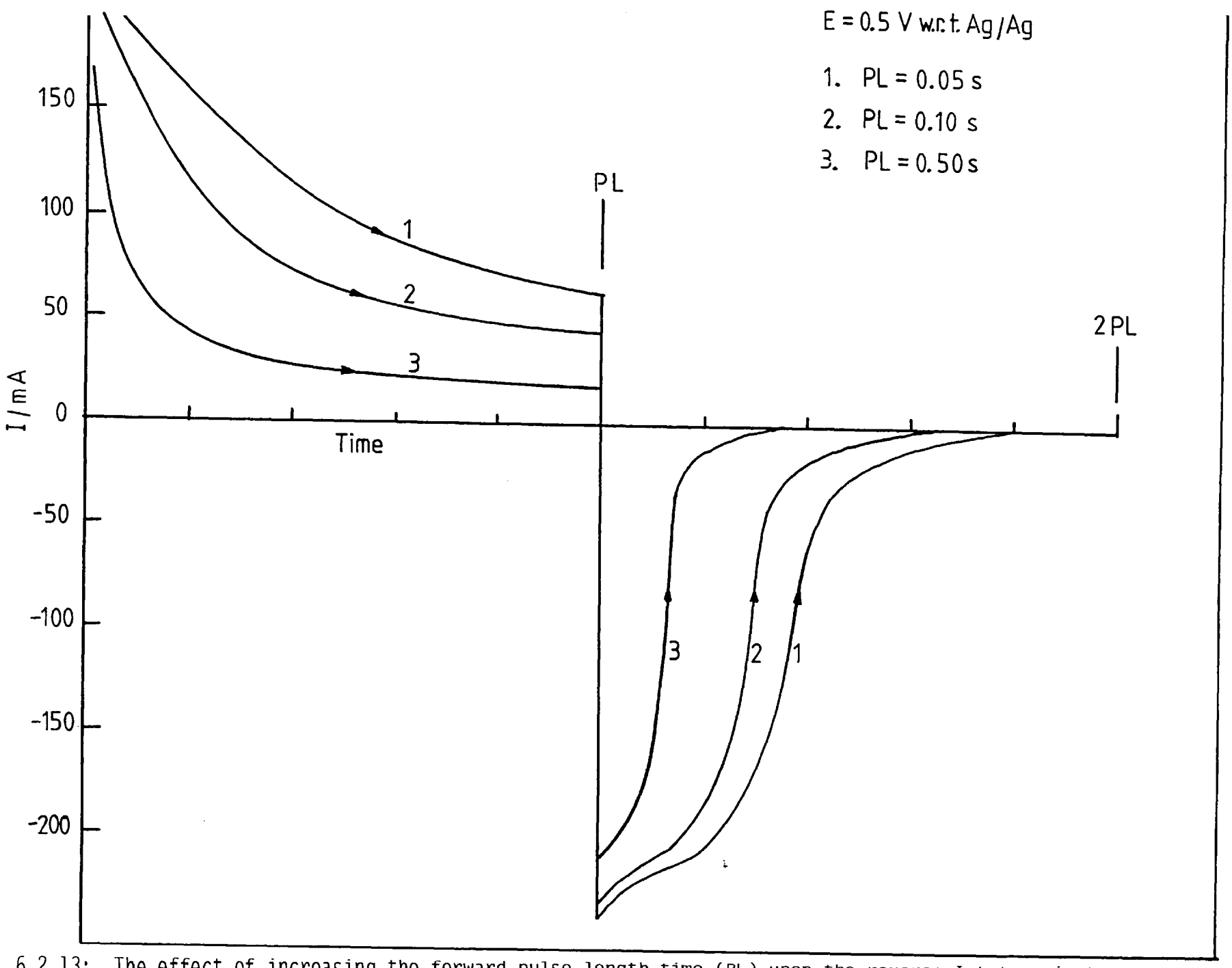


Fig. 6.2.13: The effect of increasing the forward pulse length time (PL) upon the reverse I-t transient [PbS] = 7.335×10^{-2}M: T = 417°C; electrode: vitreous carbon (area = 0.0855 cm^2)

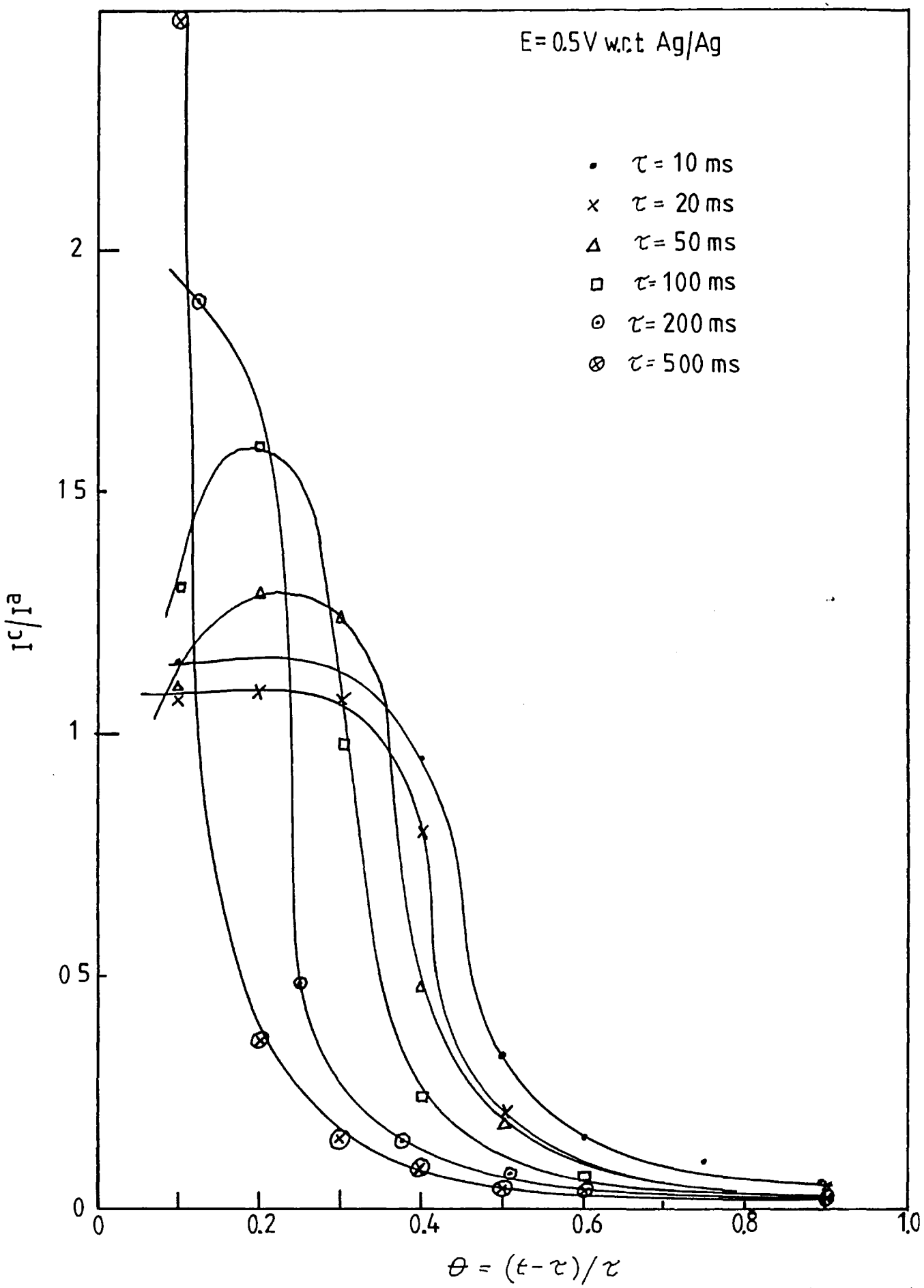


Fig. 6.2.14: The effect of increasing the forward switching time τ upon the current ratio I^c/I^a. [PbS] = 7.335 x 10^{-2}M; T = 417°C; electrode = vitreous carbon (area = 0.0855 cm^2).

I_p^c/I_p^a as a function of the dimensionless parameter θ, where $\theta = (t-\tau)/\tau$ and τ = switching time or pulse length.

6.2.3 Galvanostatic and Open Circuit Decay

Additional information concerning the electrochemical oxidation of S^{2-} at both vitreous carbon and spec-pure graphite electrodes and the possible formation of insoluble sulphur films was obtained using the galvanostatic charging technique and open circuit E-t profiles. The lead sulphide concentration was varied over the range 1.119×10^{-2} - 6.944×10^{-2}M. The purity of the solvent melt was initially checked using linear sweep voltammetry. During the galvanostatic regime and prior to the application of a current pulse the open circuit potential was monitored. In all cases a random emf was obtained thus indicating an absence of any potential-poising redox systems.

The forward E-t transients obtained using both forms of carbon electrodes were well defined and quite reproducible. The influence of current density upon the transition time (τ) was obtained as a function of lead sulphide concentration. The transition time was measured according to the method of Reinmuth (248).

The relationship between current density and transition time for a PbS concentration of 1.119×10^{-2}M at a vitreous carbon electrode is given in Table 6.2.4. Fig. 6.2.15 shows the traditional Sands plot, i.e. $\tau^{\frac{1}{2}}$ vs 1/I for the four concentrations studied using a vitreous carbon electrode. A linear increase in $\tau^{\frac{1}{2}}$ occurs with increasing 1/I and the extrapolated intercept was zero. The more sensitive plot of $i\tau$ vs $\tau^{\frac{1}{2}}$ (Fig. 6.2.16) similarly shows a linear relationhip with extrapolated zero intercepts. Similar results were obtained with a spec-pure graphite electrode, although a greater scatter of results is noted, see Figs. 6.2.17 and 6.2.18.

TABLE 6.2.4.

Chronopotentiometric data obtained for the oxidation of S^{2-} at a vitreous carbon electrode. Solvent = $PbCl_2$-KCl-NaCl: PbS = 1.119×10^{-2}M: Electrode Area = 0.0855 cm^2: T = 417°C

i $mAcm^{-2}$	$\frac{1}{i}$	τ (s)	$\tau^{\frac{1}{2}}$	$i\tau$ $mCcm^{-2}$	$i\tau^{\frac{1}{2}}$
6.893	.1450	1.290	1.1357	8.8925	7.8294
8.042	0.1243	1.00	1.00	8.0423	8.0423
9.191	0.1087	0.72	0.8485	6.618	7.799
10.34	0.0967	0.59	0.7681	6.101	7.9424
11.49	0.087	0.49	0.70	5.6296	8.0423
12.638	0.0791	0.40	0.6324	5.055	7.993
13.787	0.0725	0.343	0.585	4.722	8.069
14.936	0.0669	0.2925	0.541	4.369	8.078
16.085	0.0621	0.260	0.5099	4.182	8.202
17.234	0.058	0.230	0.4795	3.964	8.265
18.383	0.054	0.205	0.453	3.768	8.323
20.680	0.0483	0.1625	0.403	3.361	8.337
22.978	0.0435	0.130	0.3605	2.9871	8.285

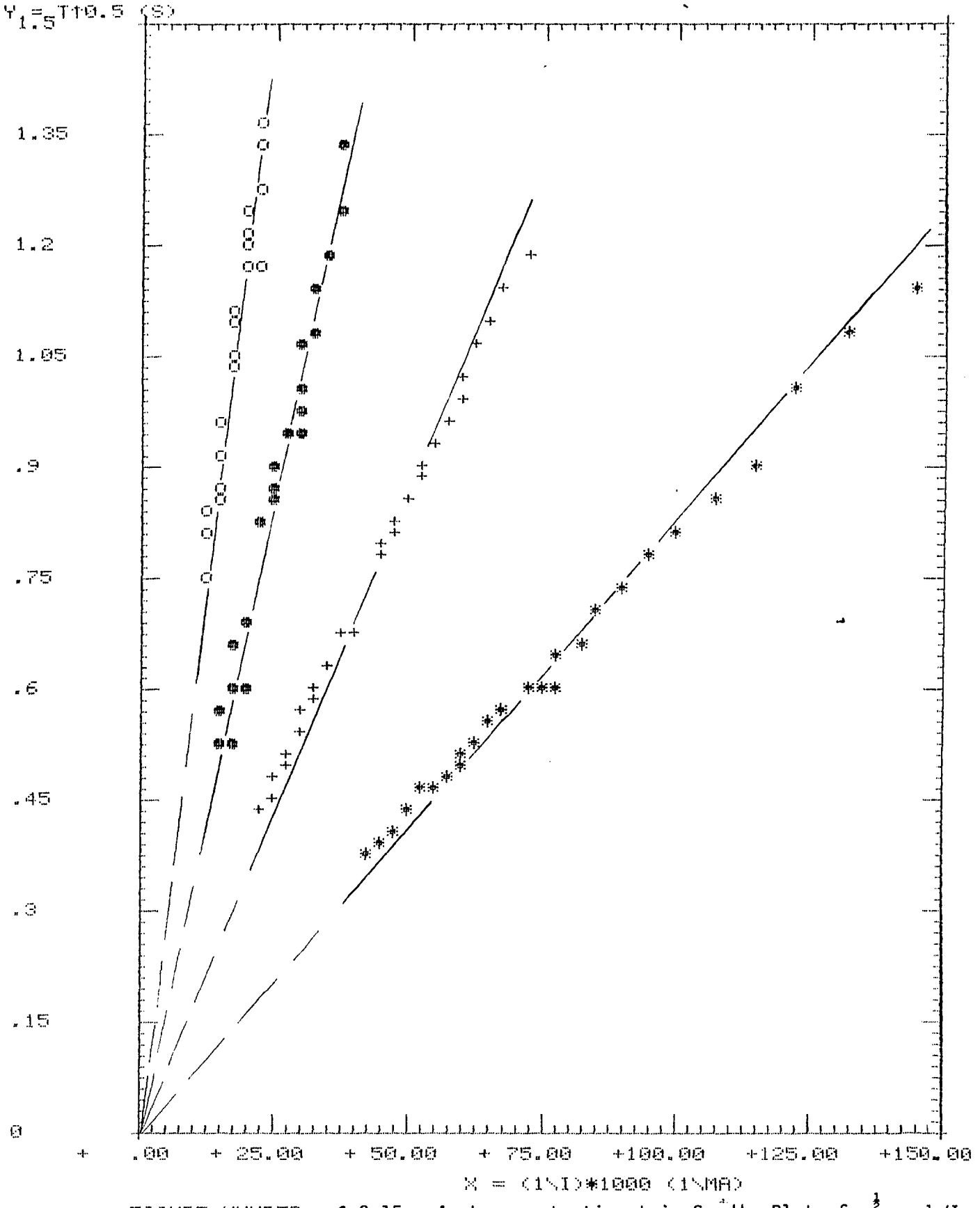


FIGURE NUMBER 6.2.15: A chronopotentiometric Sand's Plot of $\tau^{\frac{1}{2}}$ vs 1/I for the oxidation of various PbS containing solutions at a vitreous carbon electrode.
T = 417°C; area = 0.0855 cm^2. [PbS] M: 0 = 6.944 x 10^{-2}; ● 4.472x10^{-2}; + 2.472x10^{-2} * 1.119x10^{-2}

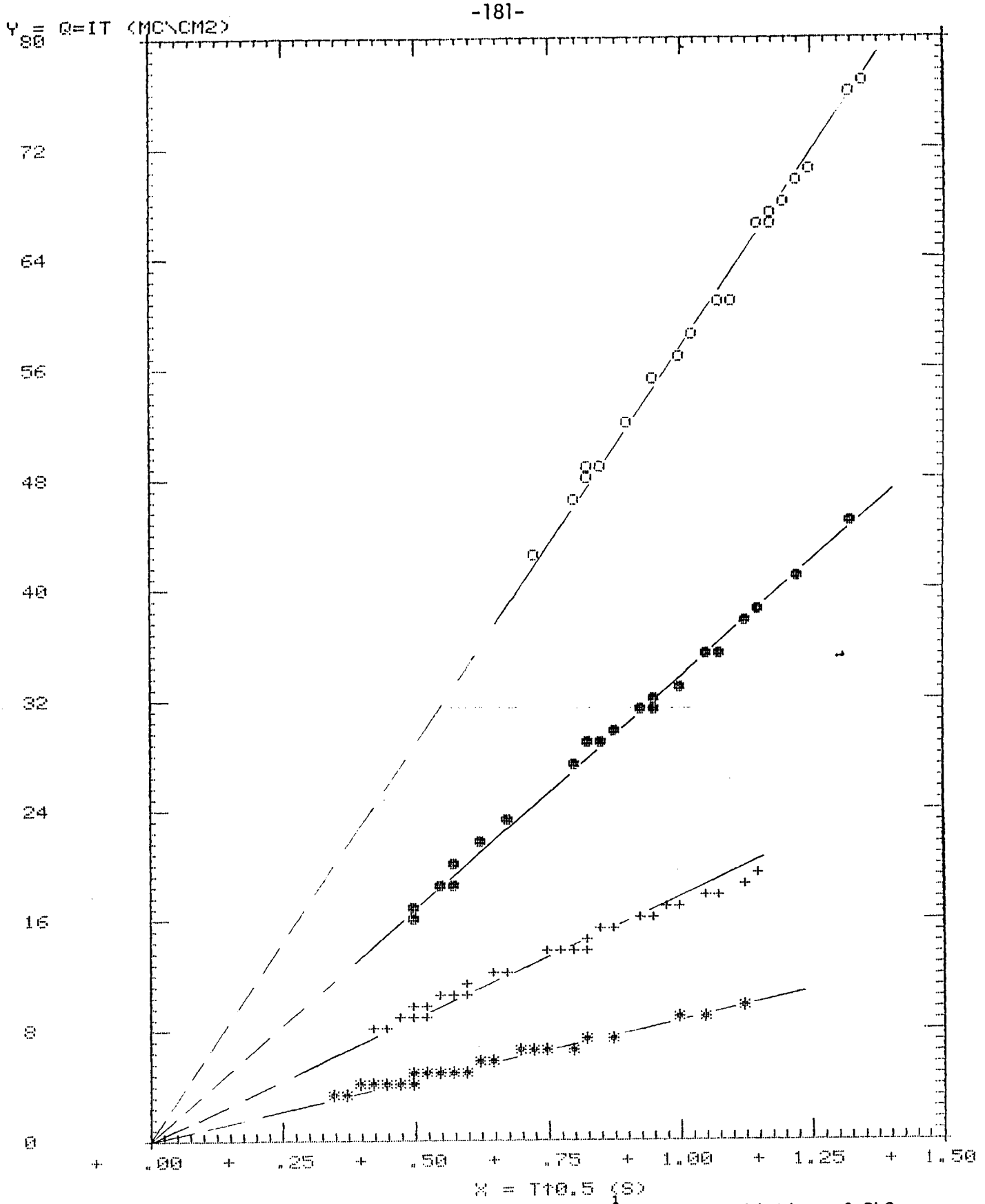


FIGURE NUMBER 6.2.16: A plot of $I\tau$ vs $\tau^{\frac{1}{2}}$ for the oxidation of PbS containing solutions at a vitreous carbon electrode. T = 417°c; area = 0.0855 cm^2. [PbS] M: 0 6.944×10^{-2}; ● 4.472×10^{-2}; + 2.472×10^{-2}; * 1.119×10^{-2}.

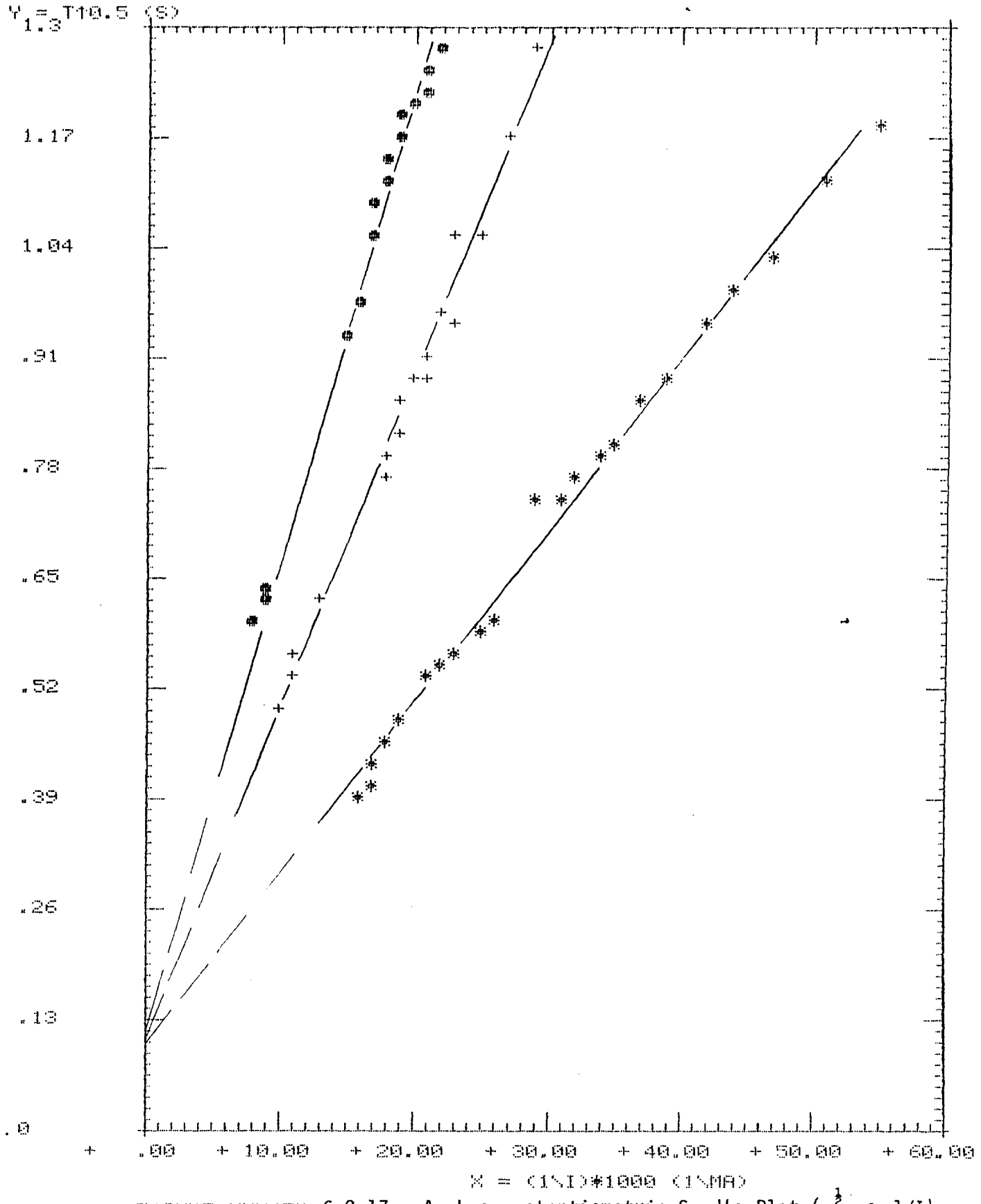


FIGURE NUMBER 6.2.17: A chronopotentiometric Sand's Plot ($\tau^{\frac{1}{2}}$ vs 1/I) for the oxidation of PbS containing solutions at a graphite electrode. T = 417°C; area = 0.0707 cm^2. [PbS]M: ● 4.472 x 10^{-2}; + 2.472 x 10^{-2}; * 1.119 x 10^{-2}.

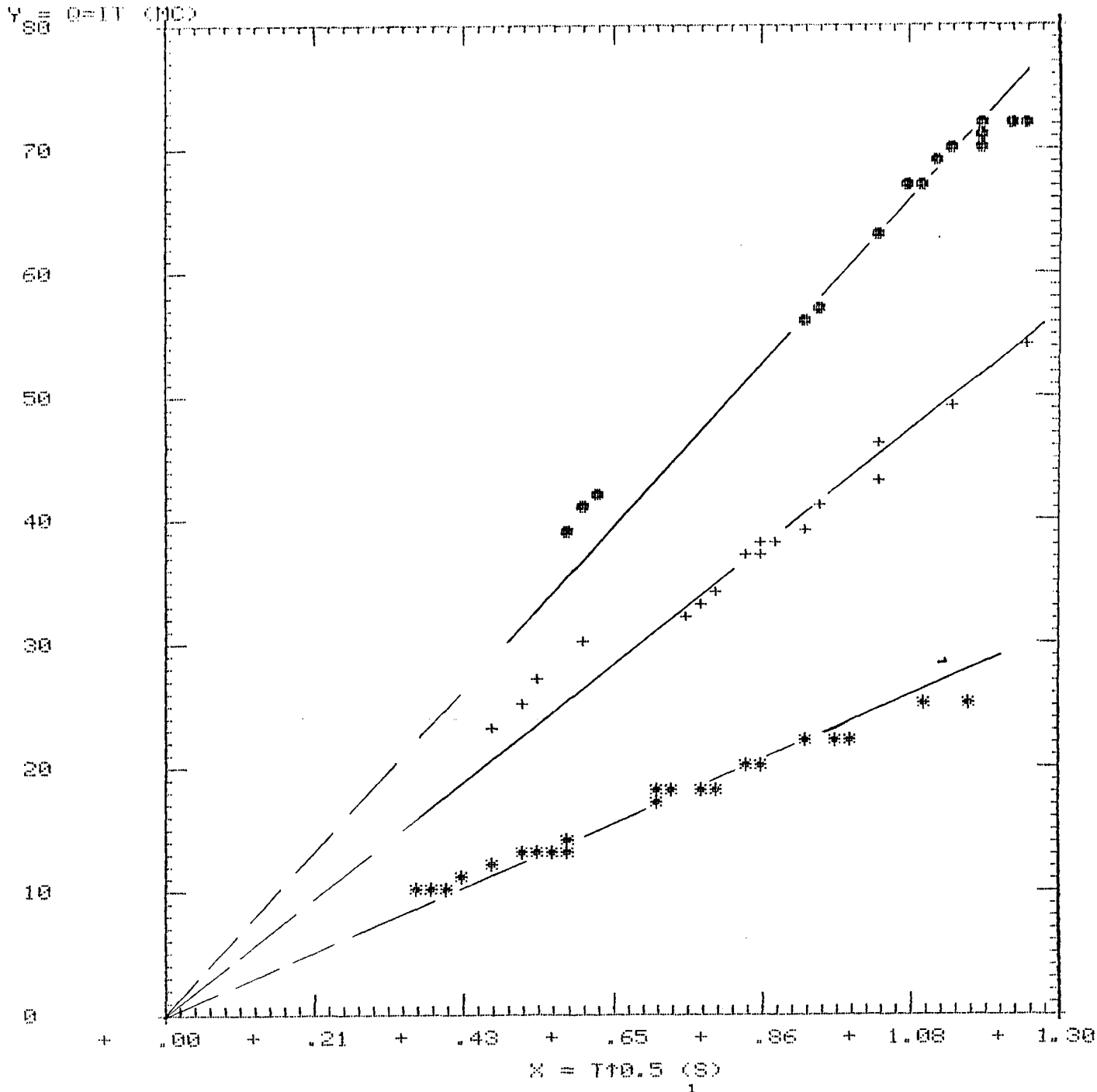


FIGURE NUMBER 6.2.18: A plot of $I\tau$ vs $\tau^{\frac{1}{2}}$ for the oxidation of PbS containing solutions at a graphite electrode. T = 417°C; area = 0.0707 cm^2. [PbS]M: ● 4.472 x 10^{-2}; + 2.427 x 10^{-2}; ⋆1.119 x 10^{-2}.

During the chronopotentiometric studies at low current densities, and in particular when a vitreous carbon electrode was used, a constant dE/dt portion was noted after the initial rapid rise in potential as a result of charging the electrode. Fig. 6.2.19 clearly shows this phenomenon. The influence of current density upon this initial dE/dt is shown in Fig. 6.2.20 in which the pseudo-capitance i/(dE/dt) is plotted against i, from which the capacitance is observed to decrease with increasing current density. A notable feature of the constant dE/dt section of the chronopotentiogram was its dependence upon the initial surface state of the electrode. The influence of surface state was obtained by consecutive anodic charging of an initially 'electrochemically clean' surface, and interposing between pulses an open circuit decay regime. The resultant E-t profile is shown in Fig. 6.2.21. The E-t transient obtained at the initially clean electrode exhibits the constant dE/dt section whereas that corresponding to a partially covered electrode does not show any initial region of constant dE/dt. The graphite electrodes did not show the above behaviour, Fig. 6.2.22.

The open circuit decay response, as a result of galvanostatic charging, showed two distinct trends which were dependent upon overpotential, see Fig. 6.2.23. Decay from low overpotentials ($\sim$ < 360 mV vs Ref) exhibited a linear decrease in potential with the logarithm of the decay time, Fig. 6.2.24. The slopes of these plots, i.e. E(decay) vs logt(decay), as obtained from a linear regression analysis, were linearly dependent upon the initial overpotential although approximately independent of lead sulphide concentration, see Fig. 6.2.25. As the overpotential was increased an initial constant dE/dt transient was observed during the initial decay period after which the 'normal' logarithmic decay occurred The dependence of dE/dt upon overpotential is shown in Table 6.2.5 below. A linear regression analysis provides a high correlation (0.98) between

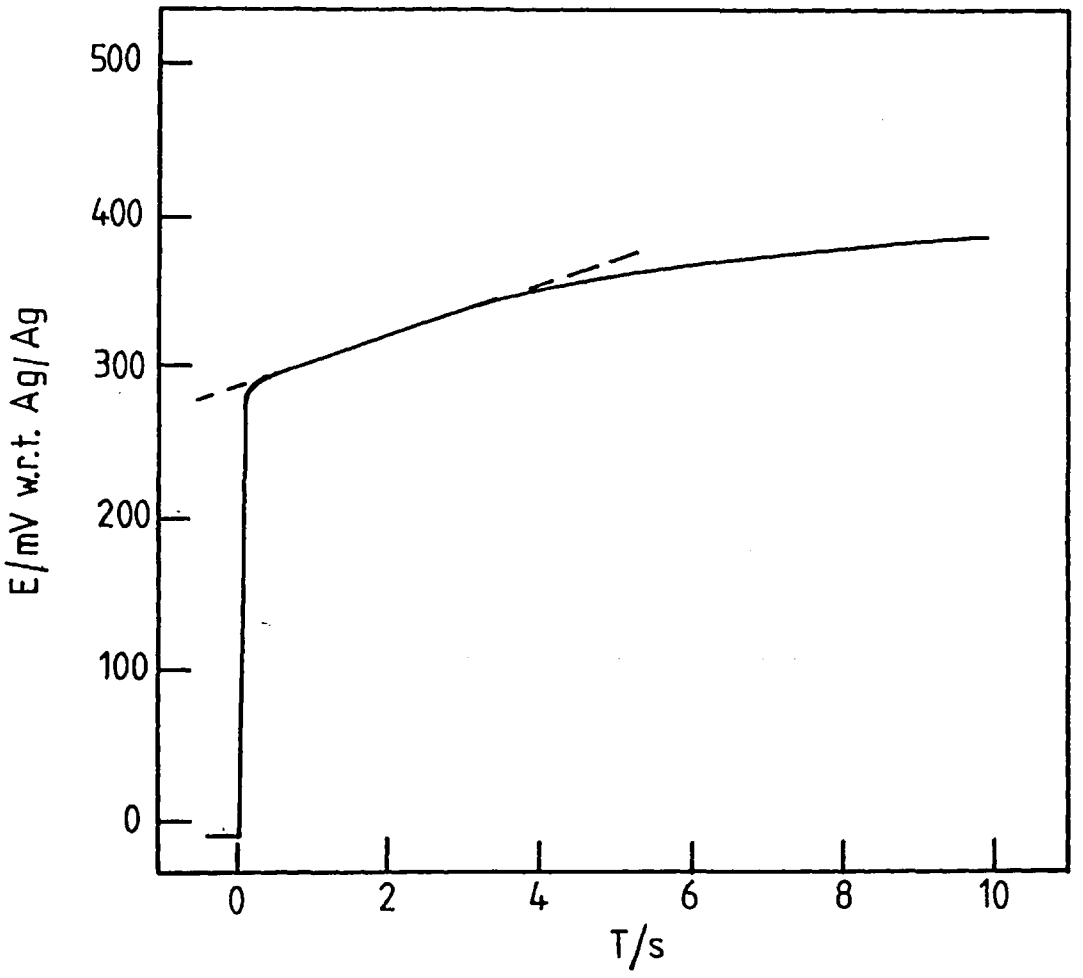


Fig. 6.2.19: A typical E-t transient obtained for the oxidation of low concentrations of PbS in the $PbCl_2$-KCl-NaCl melt at a vitreous carbon electrode. I = 1.474×10^{-4}A; electrode area = 0.0855 cm^2; T = 417°C; [PbS)M = 1.119×10^{-2}M.

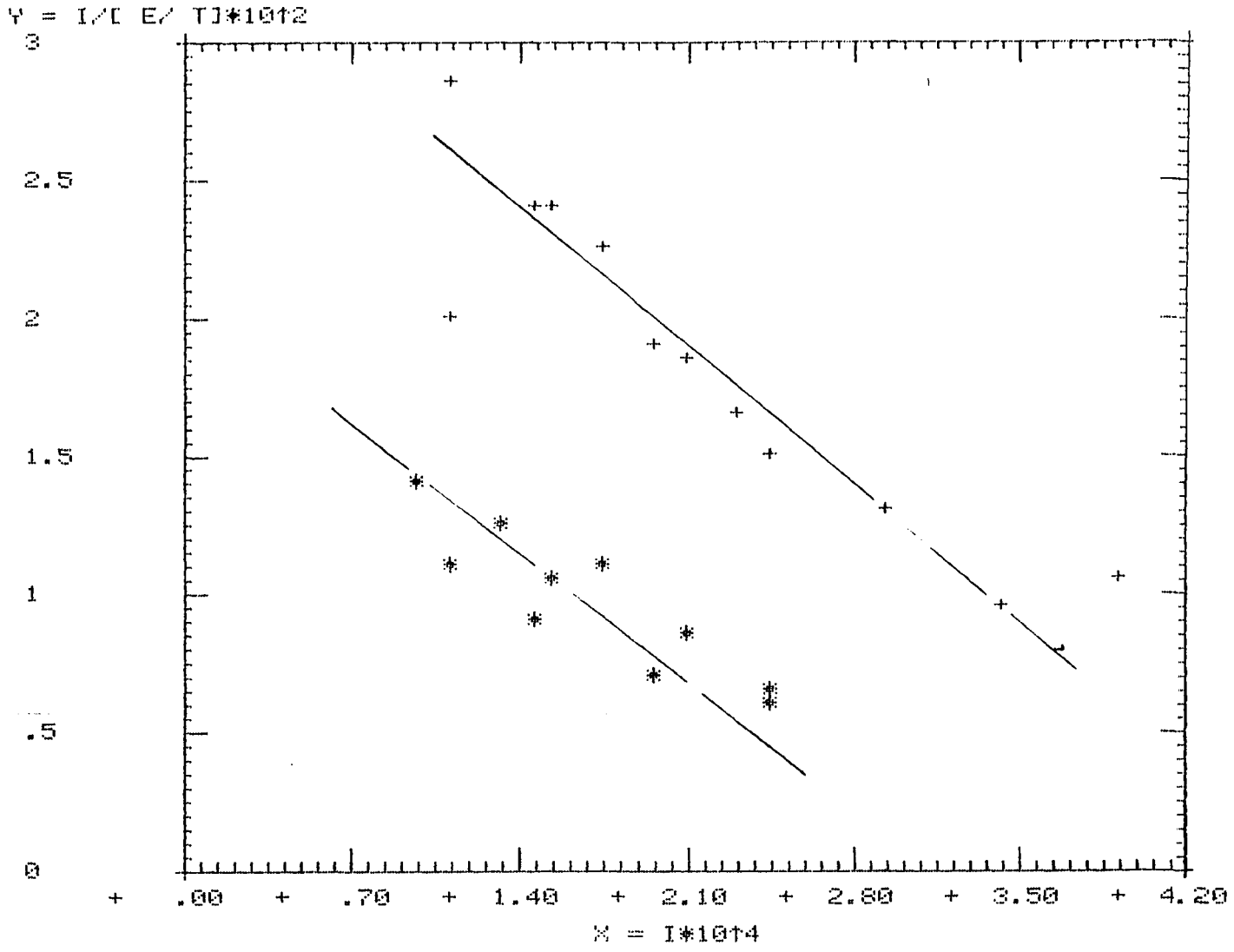


FIGURE NUMBER 6.2.20: A plot of the pseudo-capacitance (I/dE/dt) vs I for the oxidation of PbS containing solutions at a vitreous carbon electrode. Electrode area = 0.0855 cm^2; T = 417°C; [PbS]M: + 2.472 x 10^{-2}; *1.119 x 10^{-2}.

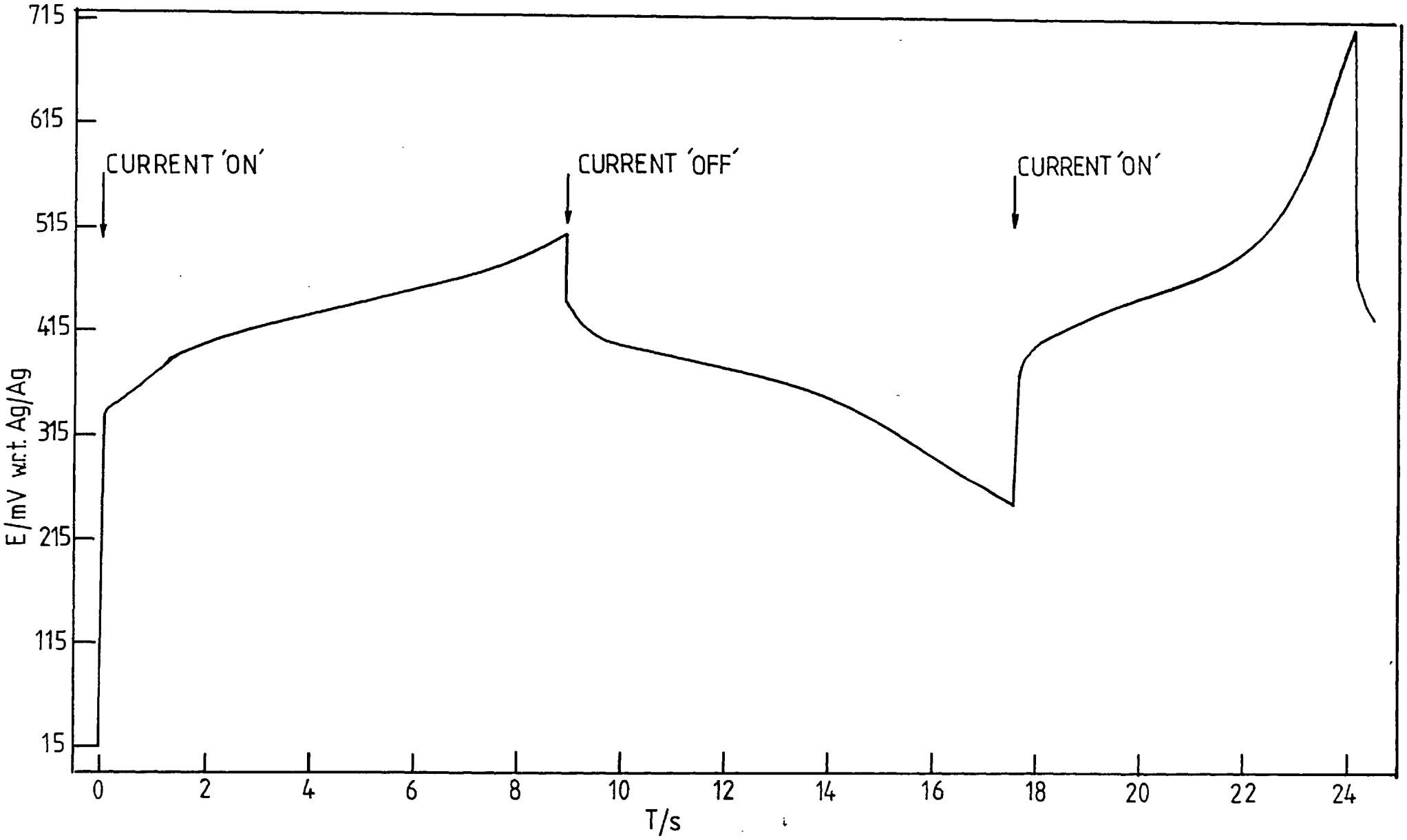


Fig. 6.2.21: The effect of electrode's surface state upon the anodic E/t transient during oxidation of PbS containing solutions at a vitreous carbon electrode. I = 2.456 x 10^{-4}A; electrode area = 0.0855 cm^2; T = 417°C; [Pbs] = 1.119 x 10^{-2}M.

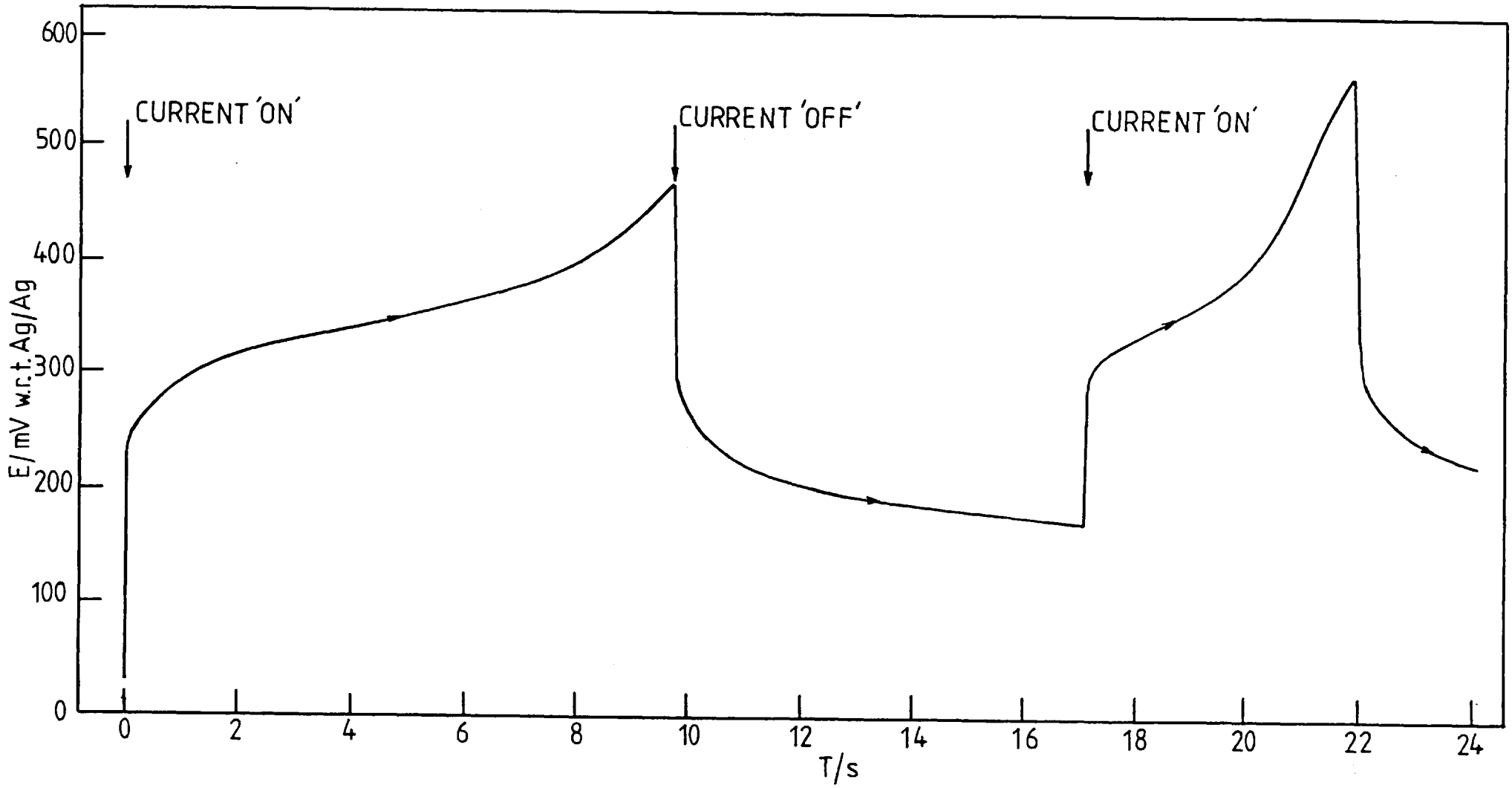


Fig. 6.2.22: The effect of the electrode's surface state upon the anodic E/t transient during the oxidation of PbS containing solutions at a graphite electrode. I = 6.876×10^{-4}A; area = 0.0707 cm^2; T = 417°C; [PbS] = 1.119×10^{-2}M.

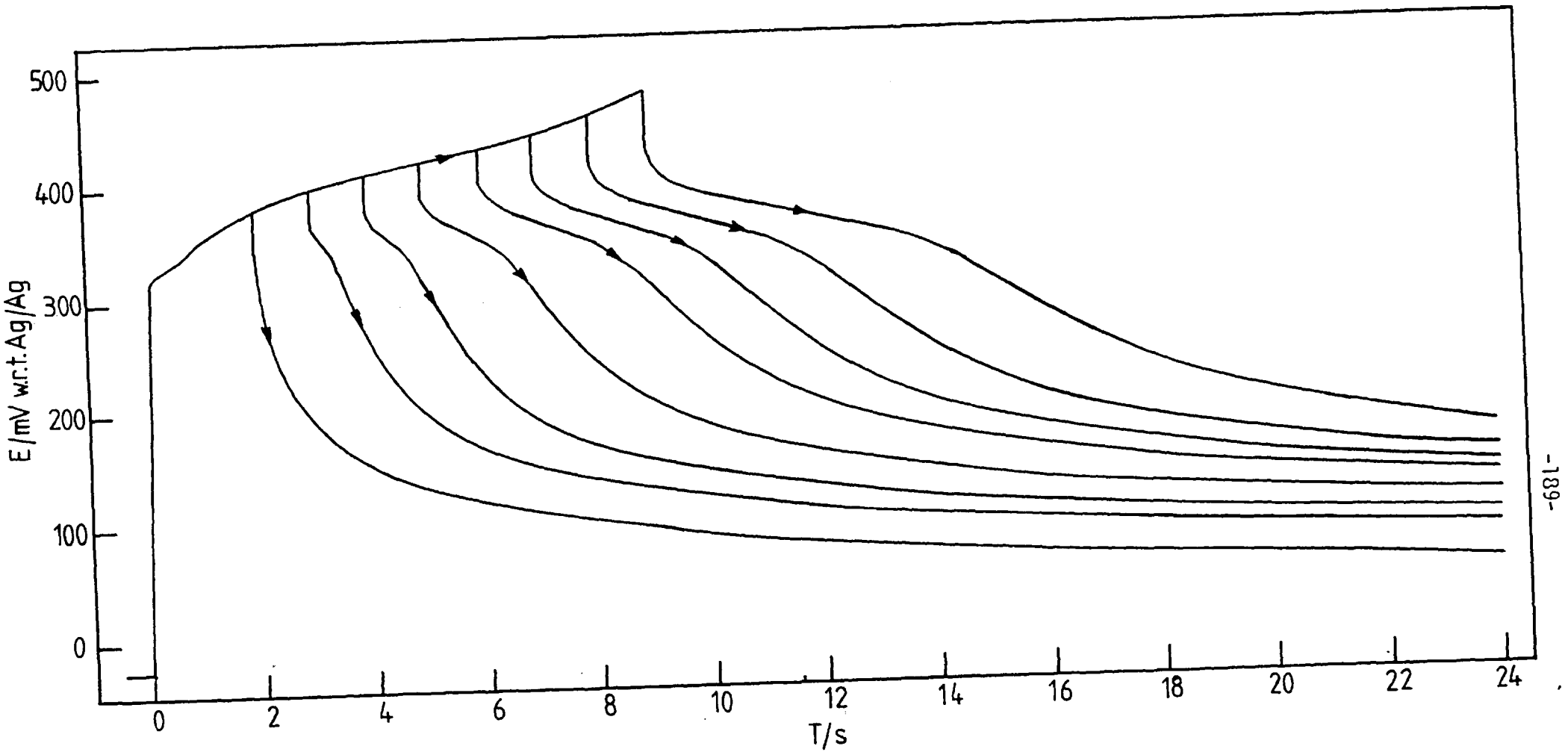


Fig. 6.2.23: The effect of the oxidation potential upon the open-circuit decay of a vitreous carbon electrode. $I = 2.456 \times 10^{-4}$A; electrode area = 0.0855 cm^2; T = 417°C; [PbS]M = 1.119×10^{-2}.

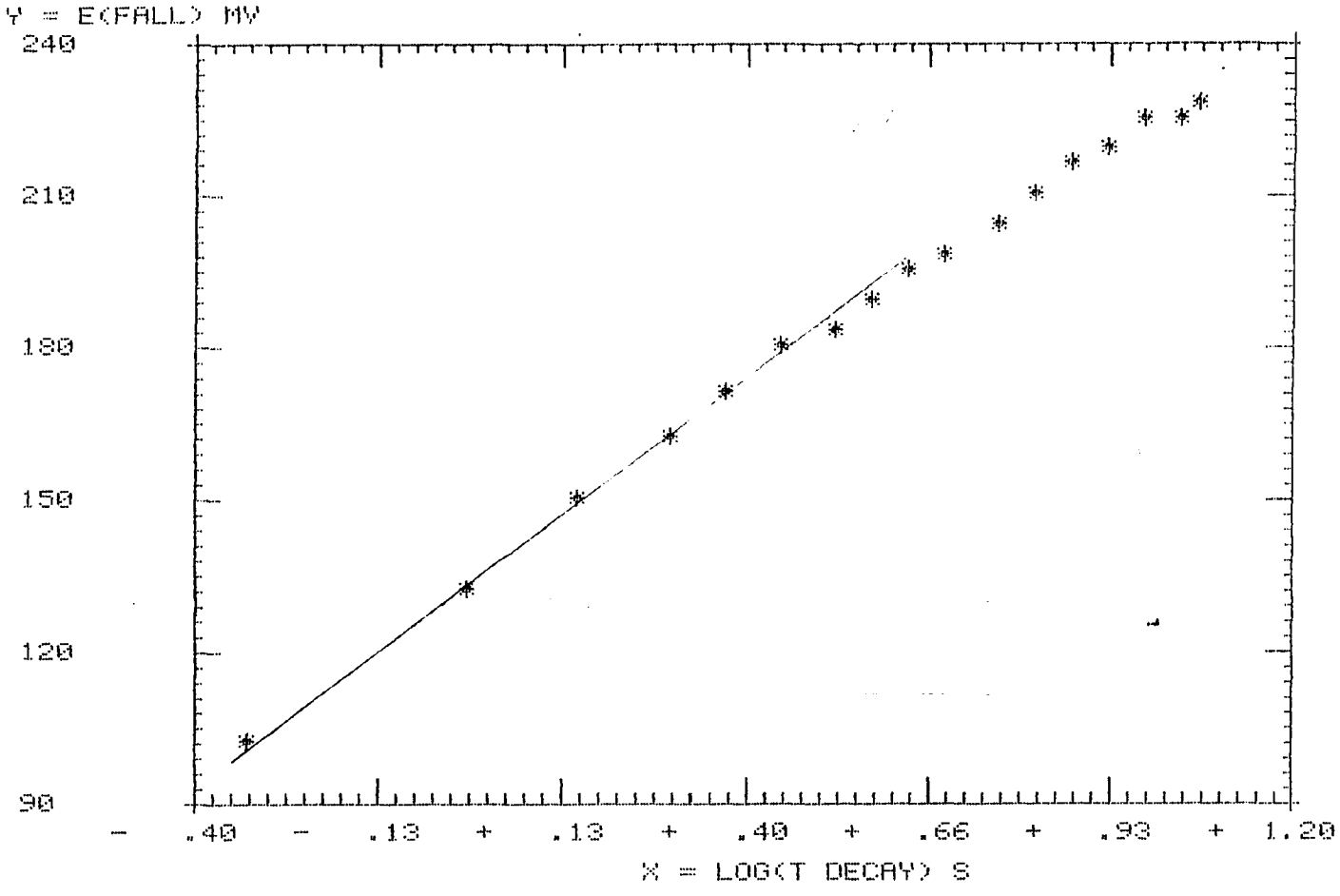


FIGURE NUMBER 6.2.24: A plot of E(fall) vs log(t decay) from $E = 0.362V$ vs Ag^{+}/Ag during open-circuit conditions.
Electrode = vitreous carbon (area = 0.0855 cm^2);
T = 417°C; [PbS]M = 1.119×10^{-2}.

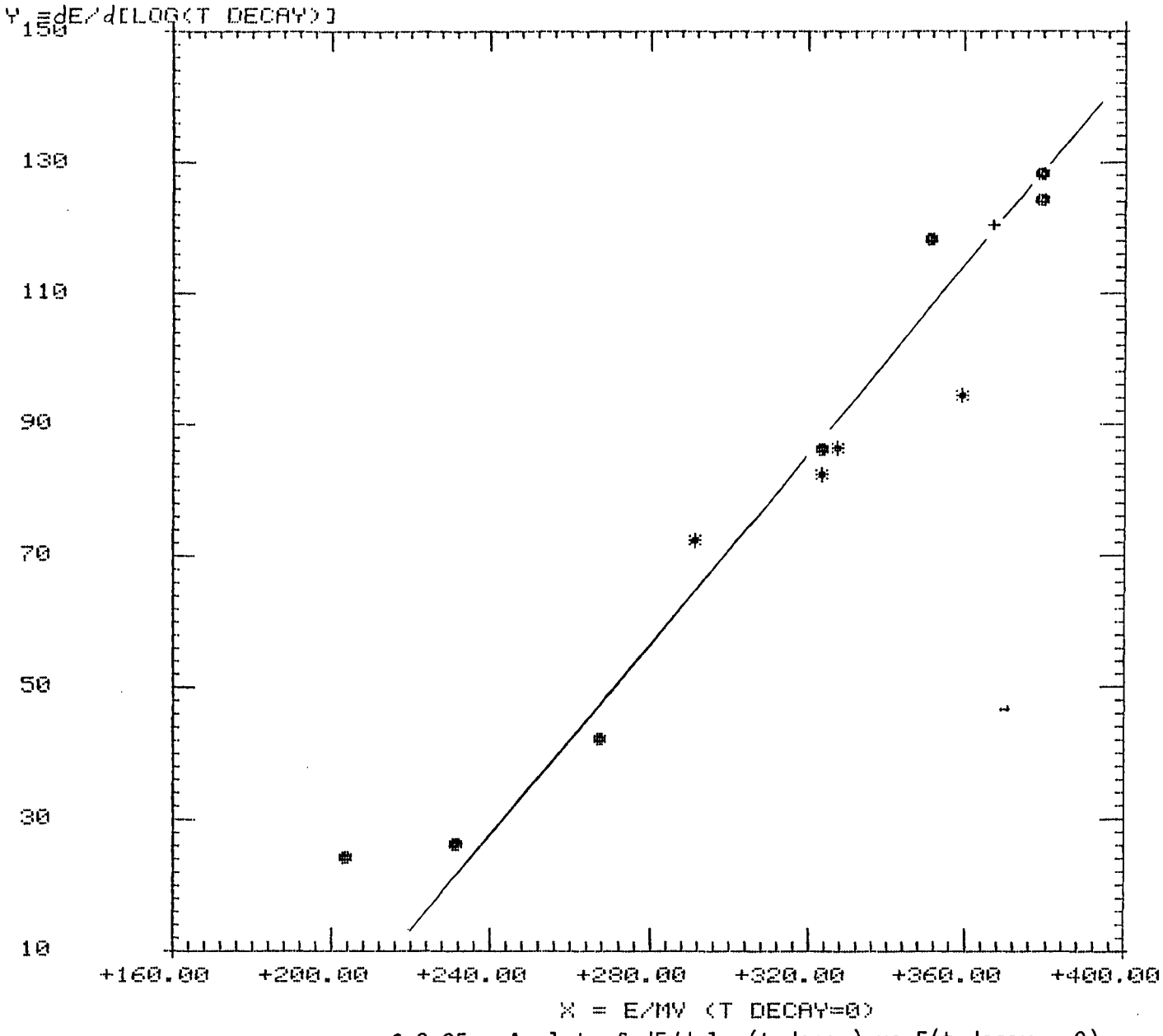


FIGURE NUMBER 6.2.25: A plot of dE/d log(t decay) vs E(t decay = 0) obtained at a vitreous carbon electrode after galvanostatic charging for various PbS containing solutions.
Electrode = vitreous carbon (area = 0.0855 cm^2);
T = 417°C; [PbS]M: ● 4.472 x 10^{-2}; + 2.472 x 10^{-2}; *1.119 x 10^{-2}.

dE/dt and 1/E(decay = 0); the derived relationship was:

$$dE/dt = 400 + 499/E(decay = 0)$$

The above behaviour was quite reproducible.

Table 6.2.5: The effect of overpotential upon the rate of open-circuit decay

E(fall) mV w.r.t. Ref	Decay Slope -dE/dt mV/s
414	76.92
426.5	45.45
439	26.32
449	18.18
459	16.67
469	14.77
494	11.20

6.3 Results: Gold Working Electrode

6.3.1 Cyclic Voltammetry

The electrochemical oxidation and reduction of the sulphide ion was also investigated using a gold sphere electrode. The results were obtained primarily as a comparison to those obtained at a platinum electrode; thus an extensive electroanalytical programme was not involved. The results presented are those obtained using potentiodynamic sweep techniques on a melt system at 417°C only; the normal effect of increasing sweep rate and bulk PbS concentration are given. The use of a gold sphere type electrode, in terms of implicit values of current and charge function is obviously limited due to an inexact knowledge of the electrode surface area.

A typical cyclic voltammogram obtained for the oxidation of sulphide and its subsequent reduction is shown in Fig. 6.3.1. Within the anodic potential window of 0 → 0.5V w.r.t. Ref two anodic processes may be discerned; an initial 'pre-wave' occurring at a potential of 0.23V and a main wave at ∿0.35V. The latter wave exhibits a very sharp rise in current over a small potential range, i.e. small half-peak width which is generally typical of what one might expect for the deposition of an insoluble product. A single very narrow and sharp reduction wave corresponding to that of the more anodic process was observed, typical of the stripping of an insoluble product. No further reduction processes whether as a result of the oxidation process or for the reduction of the initial S^{2-} ion were detected within the cathodic potential range available.

The resolution of the anodic pre-wave was found to be variable between experiments and no statistically meaningful information was gained concerning the initial surface state, i.e. roughness and the pre-wave. Fig. 6.3.1 shows the wave to occur as a limiting current plateau rather than a separate peak; however in depth analysis of this wave (see below) was obtained from voltammograms in which the pre-wave was 'fully' resolved. No corresponding reduction wave was associated with this process.

The effect of increasing scan rate (0.02 - 0.4V/s) for each of the five concentrations (1.077×10^{-2} - 7.335×10^{-2}M) upon the main oxidation and reduction process is given in Table 6.3.1. Fig. 6.3.2 shows that the anodic peak current (I_p^a) increases linearly with (sweep-rate)$^{\frac{1}{2}}$, zero current intercepts was obtained at the lowest concentration whilst slight positive intercepts were obtained using higher lead sulphide concentrations. A linear regression analysis of the data from Fig. 6.3.2 is shown in Table 6.3.2 below.

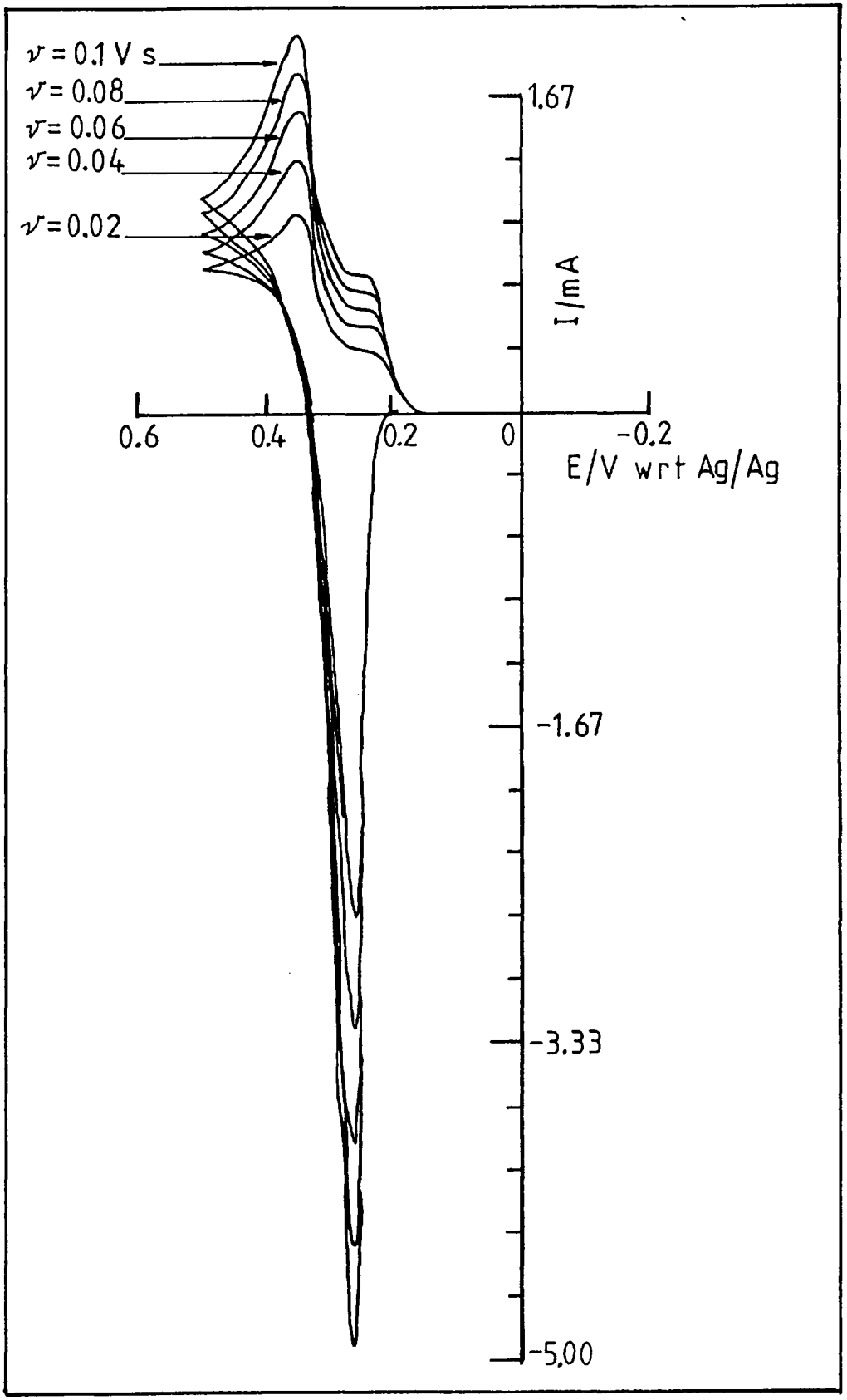


Fig. 6.3.1: Typical I-E curves obtained under voltammetric conditions for the oxidation and reduction of PbS at a gold sphere electrode.
T = 417°C; [PbS]M = 1.077×10^{-2}. Au electrode ∿ 2mm dia.

TABLE 6.3.1.

The effect of increasing scan rate upon the various voltammetric parameters for the oxidation of S^{2-} at a gold sphere electrode in the $PbCl_2$-KCl-NaCl ternary eutectic melt at 417°C. PbS = 1.077×10^{-2}M.

V v/s	$V^{\frac{1}{2}}$	Ip^a mA	$Ip^a/V^{\frac{1}{2}}$	Ip^c/Ip^a	Ep^a	Ep^c	ΔE mV
0.02	0.1414	1.05	7.425	2.98	350	280	70
0.04	0.2	1.33	6.667	2.845	350	280	70
0.06	0.245	1.6	6.532	2.582	350	280	70
0.08	0.283	1.8	6.364	2.822	350	280	70
0.1	0.316	2.0	6.325	2.814	350	280	70
0.15	0.387	2.417	6.24	2.767	350	280	70
0.2	0.447	2.792	6.242	2.735	350	270	80
0.25	0.5	3.083	6.167	2.727	350	270	80
0.3	0.548	3.416	6.238	2.73	350	270	80
0.35	0.592	3.75	6.339	2.60	350	270	80
0.4	0.632	3.917	6.193	2.53	350	270	80

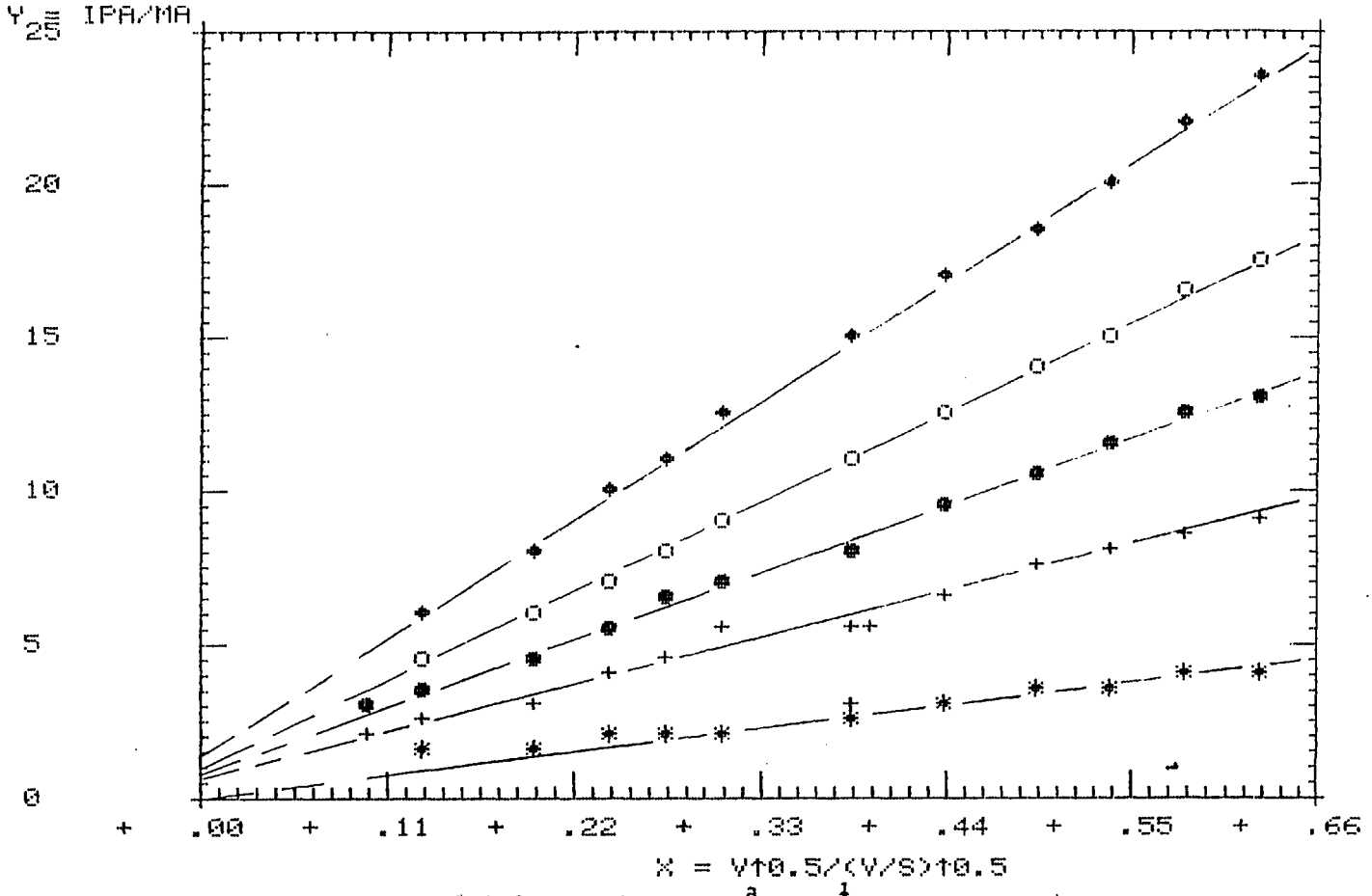


FIGURE NUMBER 6.3.2: A plot of I_p^a vs $\nu^{\frac{1}{2}}$ for the oxidation of various PbS containing solutions at a gold electrode.

T = 417°C; [PbS]M: ♦ 7.335×10^{-2};
O 5.35×10^{-2}; ● 3.918×10^{-2};
+ 2.52×10^{-2}; * 1.077×10^{-2}.

Table 6.3.2: Linear regression analysis of the I_p^a-$\nu^{\frac{1}{2}}$ plots for the oxidation of PbS at a gold sphere electrode

[PbS] x 10^2M	$\partial I_p^a/\partial\nu^{\frac{1}{2}}$	I(mA) intercept	Corr
1.077	5.9751	0.137	0.999
2.52	13.475	0.183	0.942
3.918	19.625	0.527	0.999
5.35	26.960	0.414	0.999
7.335	34.755	1.130	0.999

The $I_p^a/\nu^{\frac{1}{2}}$ current function was independent of sweep rate at high sweep rates, e.g. > 0.1V/s. The current function decreases as the scan rate increases at low scan rates and was dependent upon concentration (Fig. 6.3.3). The evaluated I_p^c/I_p^a ratio exhibits several types of behaviour with increasing scan rate and lead sulphide concentration (Fig. 6.3.4). At low concentrations, e.g. 1.077 x 10^{-2} and 2.52 x 10^{-2}M, a non-linear decrease in I_p^c/I_p^a occurs with increasing scan rate. At higher concentrations the I_p^c/I_p^a function initially increases to a maximum and then decreases with increasing sweep rate. No regular trend in terms of the position of the peak maximum with sulphide concentration was observed.

The potential functions E_p^a and E_p^c were independent of sweep rate, see Table 6.3.1. The small peak separation $\Delta E \sim$ 70-80 mV suggests the process to be highly reversible. The concentration dependency of various potentials obtained from the cyclic voltammograms is of interest. Fig. 6.3.5 shows a diagrammatic voltammogram which further defines these potentials. All the potentials considered vary in the Nernstian manner, i.e. E vs log [Pbs] and all have essentially the same slope, Fig. 6.3.6. Table 6.3.3 gives the slopes of these functions as obtained from a linear regression analysis.

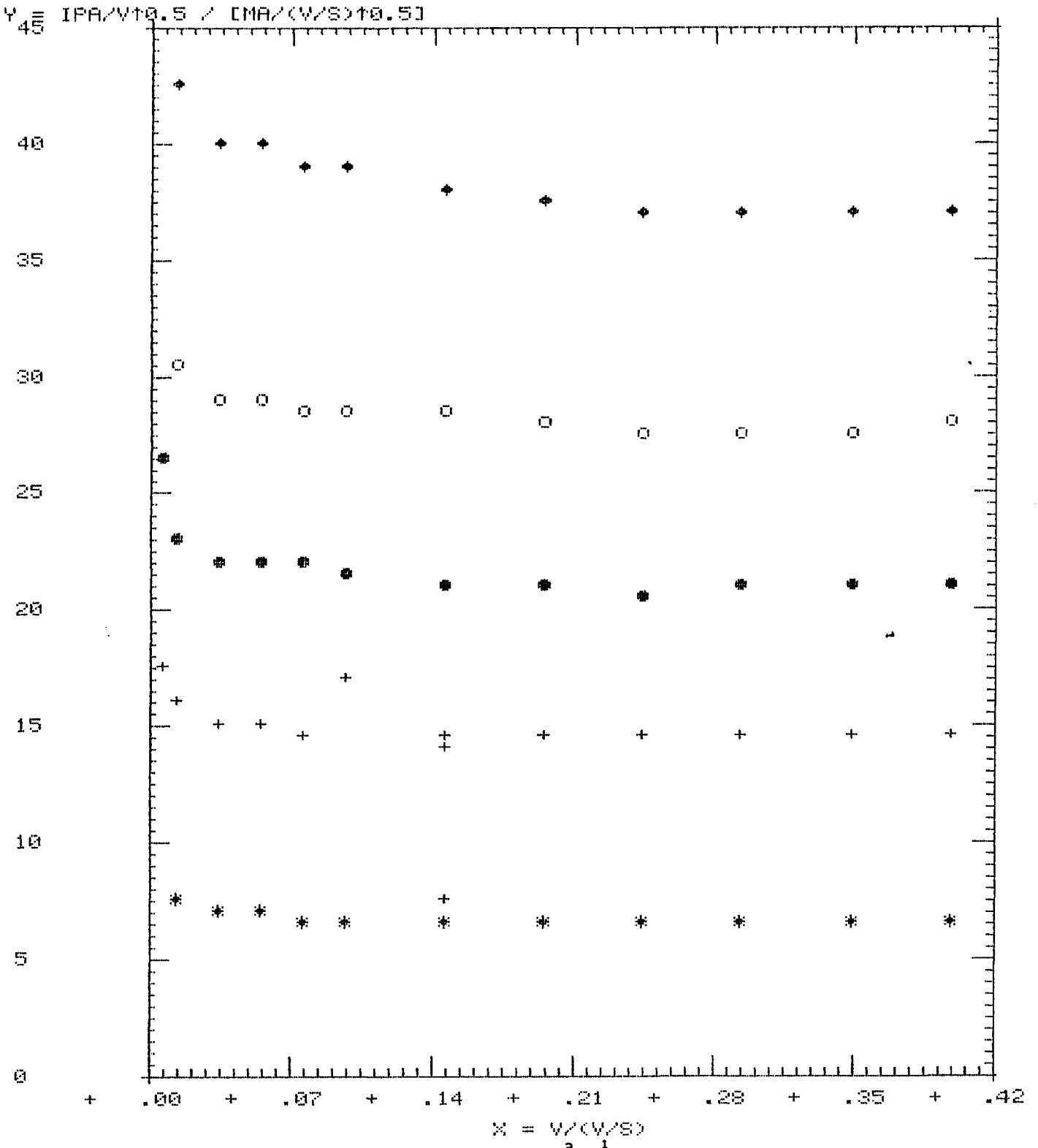


FIGURE NUMBER 6.3.3: A plot of $I_p^a/\nu^{\frac{1}{2}}$ vs ν for the oxidation of PbS containing solutions at a gold electrode. T = 417°C; [PbS]M:

♦ 7.335×10^{-2}; o 5.35×10^{-2};
● 3.918×10^{-2}; + 2.52×10^{-2};
* 1.077×10^{-2}

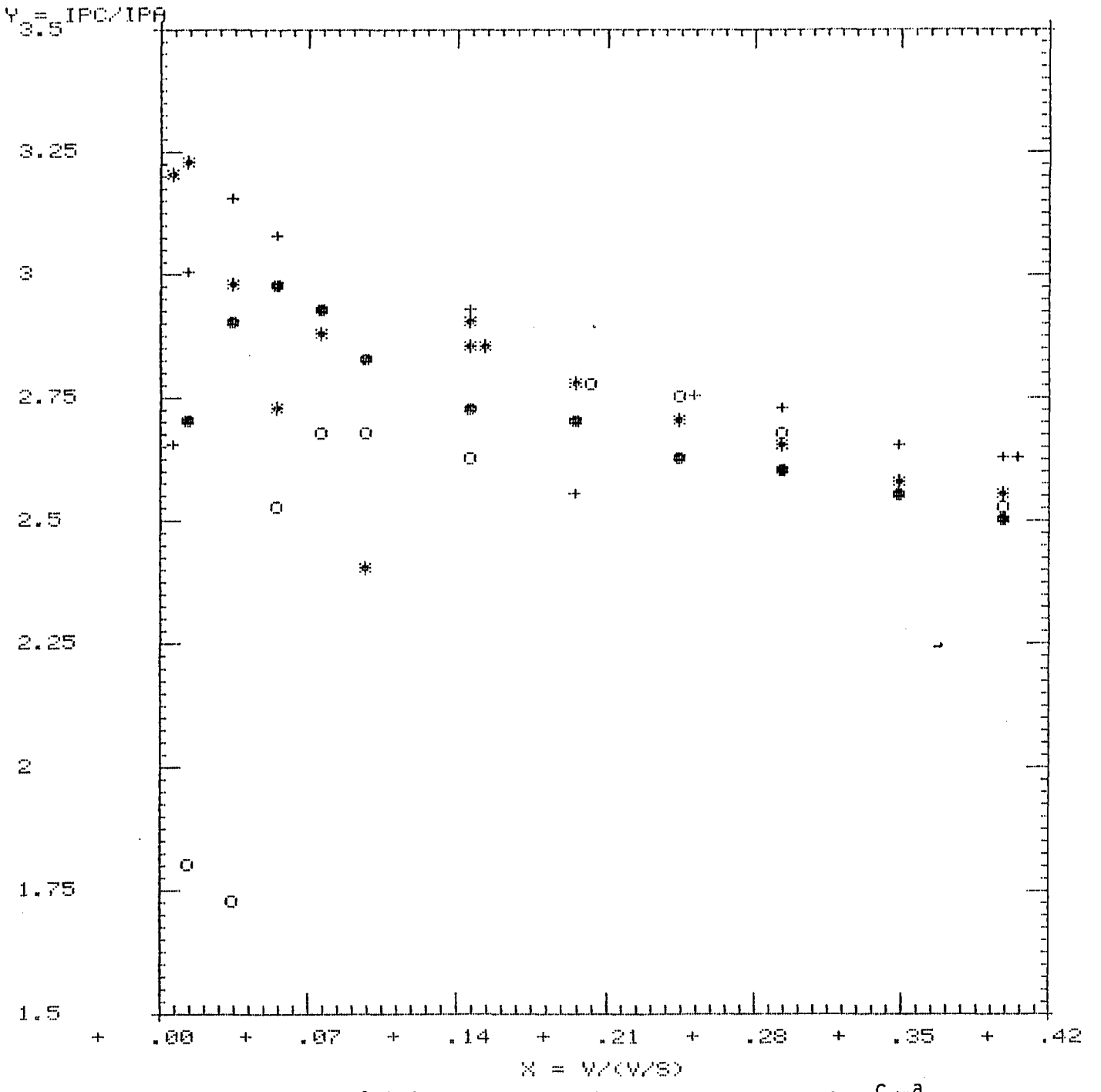


FIGURE NUMBER 6.3.4: A plot of the peak current ratio I_p^c/I_p^a vs ν for the oxidation and reduction of sulphide at a gold electrode.

T = 417°C; [PbS]M :

♦ 7.335×10^{-2}; O 5.35×10^{-2};

● 3.918×10^{-2}; + 2.52×10^{-2};

* 1.077×10^{-2}.

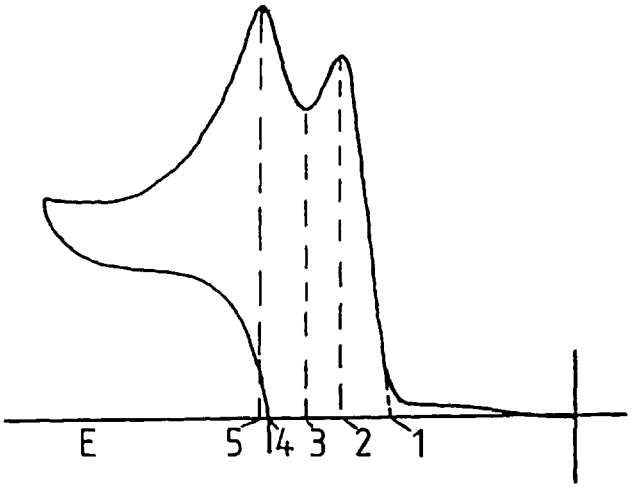


Fig. 6.3.5: A schematic anodic voltammogram defining the various potentials measured during the oxidation of PbS solutions at Pt and Au electrodes.

1. η_1 the nucleation potential
2. η_2 the peak potential for process A (the pre-wave)
3. η_3 the potential corresponding to the current minimum between the two anodic processes
4. η_4 the peak potential for process B
5. η_{-4} the potential at which reduction commences

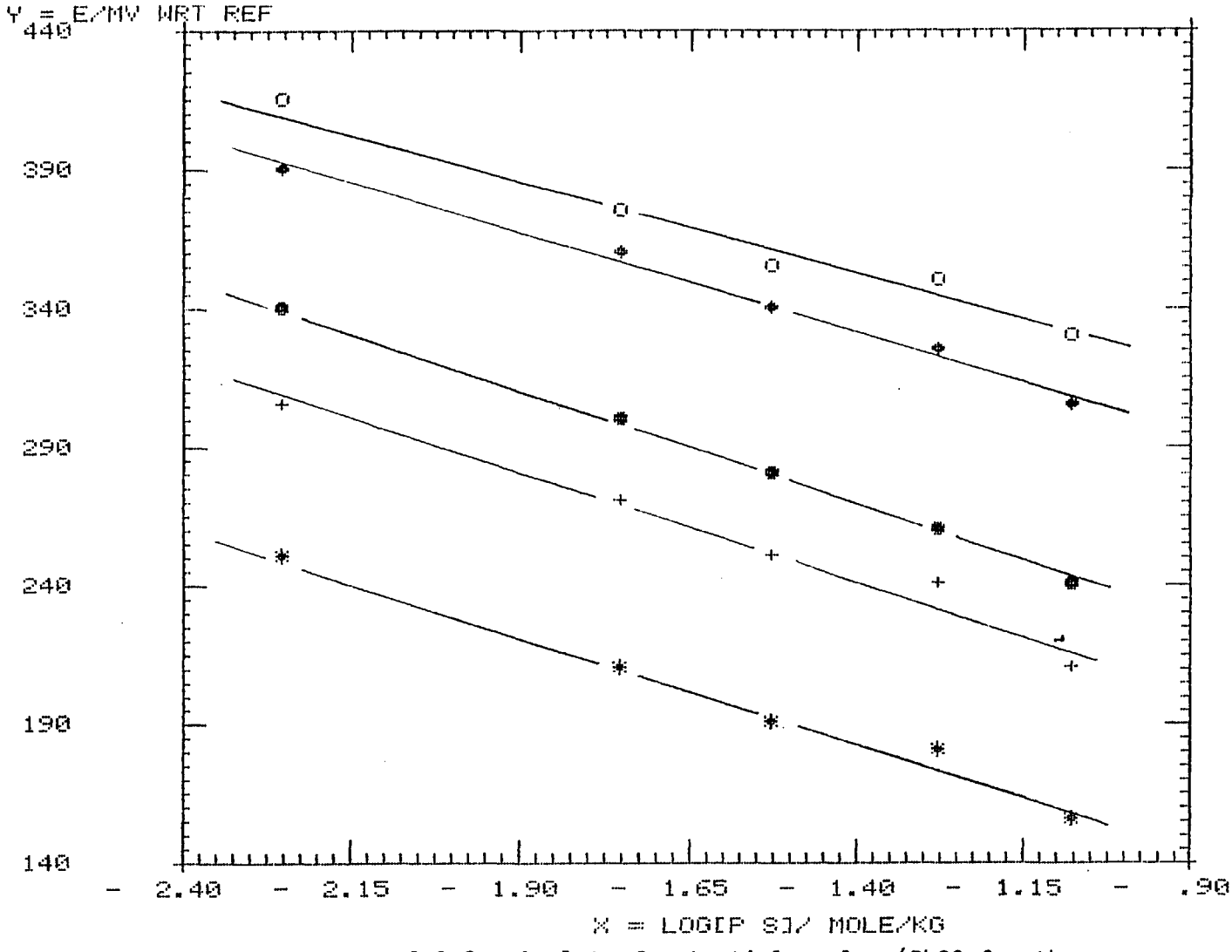


FIGURE NUMBER 6.3.6: A plot of potential vs log (PbS9 for the voltammetric potentials η_1(*); η_2(+); η_3(●); η_4(0) and η_{-4}(▲), see Fig. 6.3.5 for definition.
T = 417°C; Au sphere electrode.

Table 6.3.3: The concentration dependency of various voltammetric potentials obtained at a gold sphere electrode

Potential Function	dE/d(log[PbS]	Correlation
η_1	-0.07844	0.996
η_2	-0.07747	0.991
η_3	-0.08504	0.999
η_4	-0.0705	0.990
η_{-4}	-0.07206	0.996

Subsequent to obtaining general information concerning the electrochemical oxidation of the sulphide ion additional 'in-depth' experiments were undertaken to obtain electrochemical details of the 'pre-wave' and its relationship to the main oxidation wave.

The results presented here correspond to those voltammetric experiments in which the pre-wave was found to be highly resolved, i.e. to be well defined and exhibit a separate peak. The definition of the pre-wave is considered to be dependent upon the condition and presumably initial preparation of the electrode. Unfortunately no quantitative information could be discerned with regard to the initial preparation of the electrode.

The effect of increasing sweep rate upon the pre-wave was determined by reversing the sweep at a potential just beyond the corresponding peak and before the onset of the main oxidation process. Fig. 6.3.7 illustrates several typical I-E curves obtained employing scan rates between 40-250 mV/s. It is immediately evident that no corresponding reduction wave is associated with this process. Table 6.3.4 shows the effect of scan rate upon the voltammetric parameters for this process.

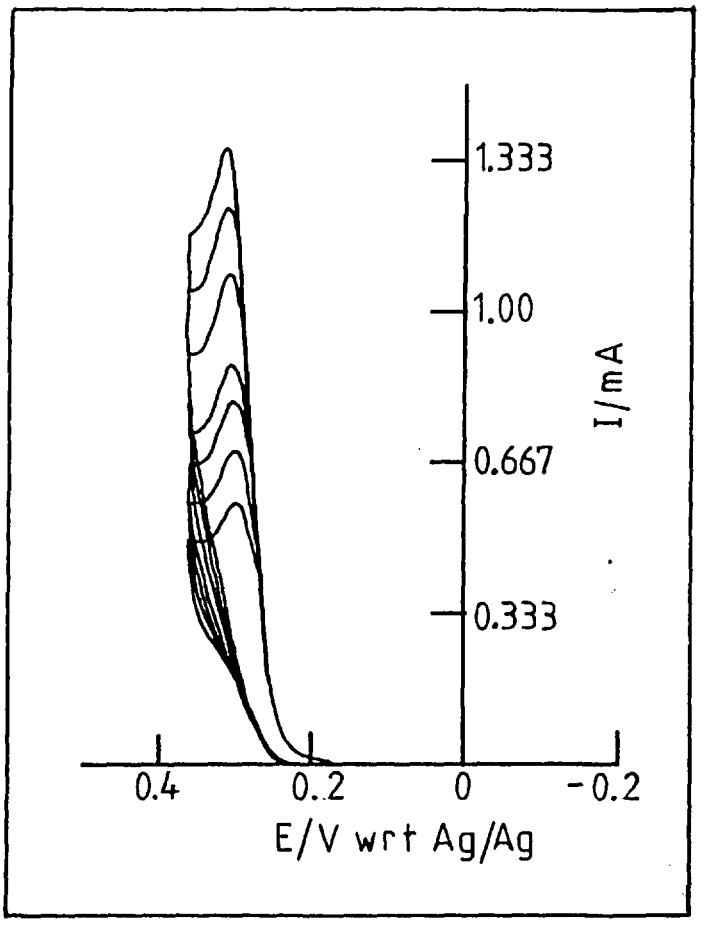


Fig. 6.3.7: The effect of increasing sweep rate upon the 'pre-wave' obtained at a Au sphere electrode.

ν = 0.04, 0.06, 0.08, 0.1, 0.15, 0.2 and 0.25 V/s.

T = 417°C; [PbS]M = 5.814×10^{-3}.

Table 6.3.4: The effect of increasing scan-rate upon the 'pre-wave' observed during the oxidation of S^{2-} ion at a Au sphere electrode in the $PbCl_2$-KCl-NaCl ternary solvent melt at 417°C.

ν V/s	I_p^a mA	Q^a mC	E_p^a mV	$E_p^a - E_{p/2}^a$ mV
0.01	0.333	1.667	145	35
0.02	0.425	1.002	145	30
0.04	0.583	0.625	145	30
0.06	0.700	0.486	150	30
0.08	0.800	0.406	150	30
0.10	0.883	0.350	150	30
0.15	1.083	0.295	150	30
0.20	1.234	0.246	150	30
0.25	1.367	0.213	150	30

Fig. 6.3.8 shows that the 'pre-wave' peak current increases linearly with increasing (sweep rate)$^{\frac{1}{2}}$ with a corresponding slope of 2.6164 mA/(V/s)$^{\frac{1}{2}}$ and an intercept of 0.062 mA; a linear correlation of 0.999 was obtained from a linear regression analysis. The measured charge Q^a for the process decreased exponentially with increasing sweep rate reaching a virtually constant value at $\nu > \sim 150$ mV, see Fig. 6.3.9. Both the peak potential E_p^a and the half-peak width remained constant (within experimental accuracy) at 145-150 mV wrt Ag^+/Ag and 30 mV respectively.

The effect of increasing switching potential (E_λ) upon the reduction process is illustrated by the I-E curve given in Fig. 6.3.10 and the results obtained in Table 6.3.5. The composite I-E curve was constructed by allowing a 'settling' period of 5 minutes between each scan. Fig. 6.3.10 clearly demonstrates the good reproducibility of the system and further

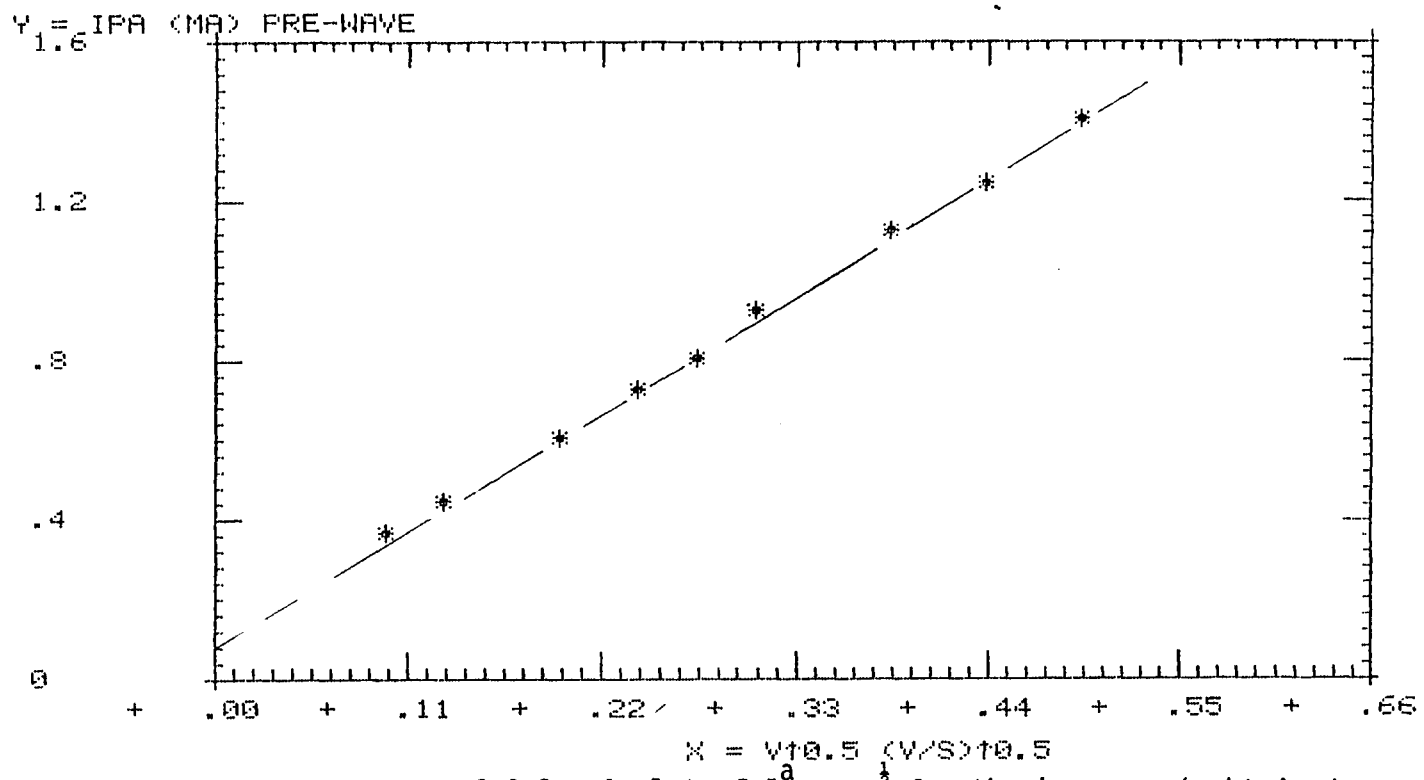


FIGURE NUMBER 6.3.8: A plot of I_p^a vs $\nu^{\frac{1}{2}}$ for the 'pre-wave' obtained at a gold sphere electrode.
T = 417°C; [PbS]M = 5.814×10^{-3}.

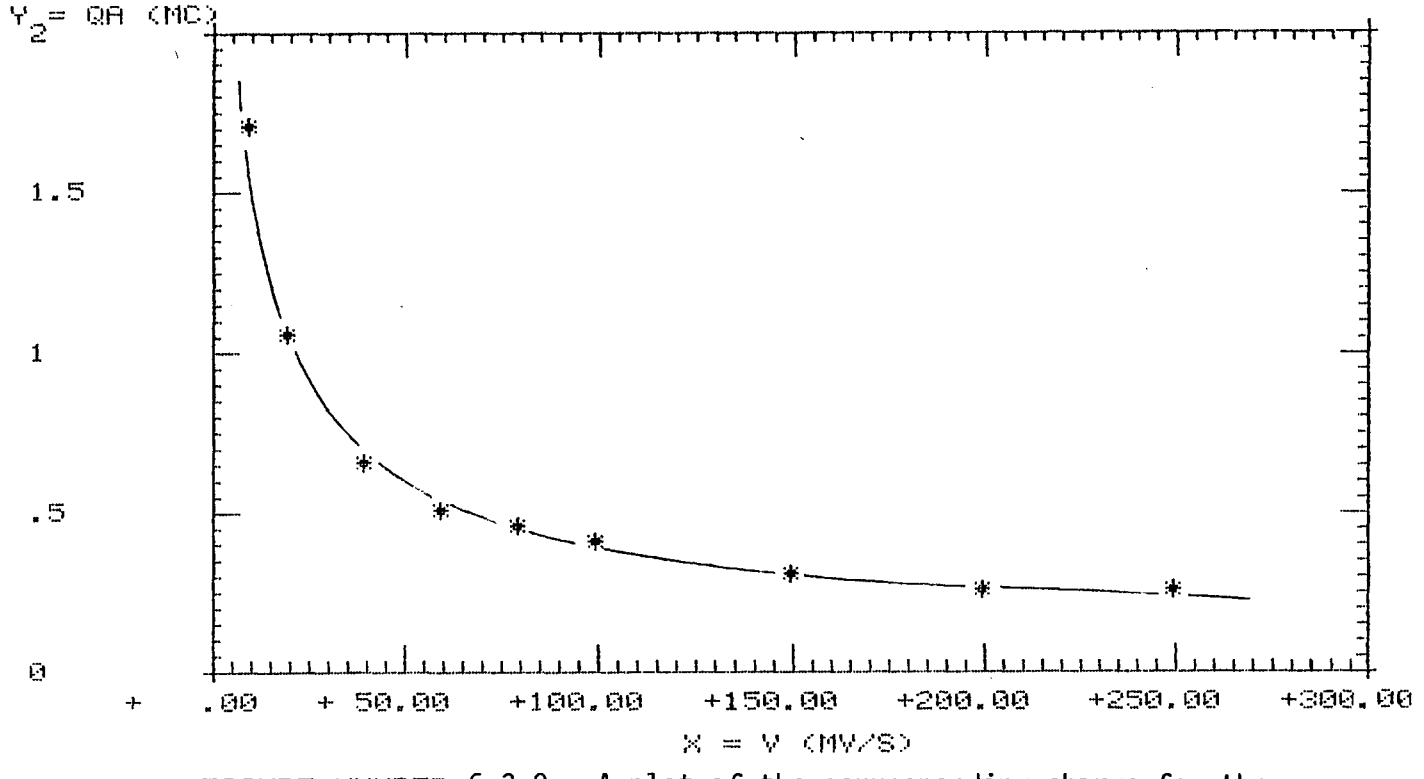


FIGURE NUMBER 6.3.9: A plot of the corresponding charge for the 'pre-wave' as a function of increasing sweep rate.
T = 417°C; [PbS] = 5.814×10^{-3}.

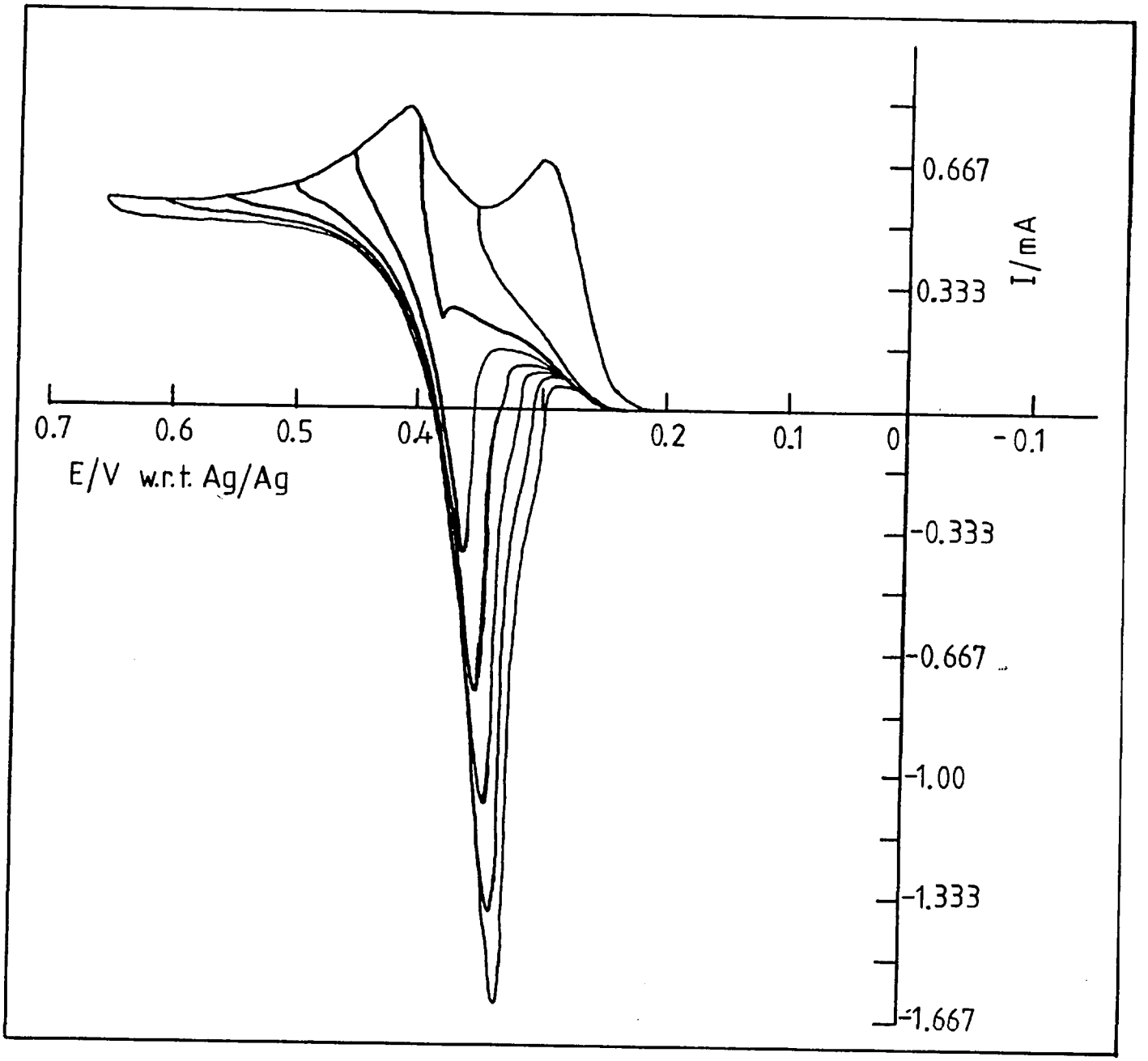


Fig. 6.3.10: The effect of increasing the switching potential upon the reduction wave obtained at a gold sphere electrode.

T = 417°C; [PbS]M = 5.814×10^{-3}; sweep rate = 0.05 V/s.

Table 6.3.5: The Effect of the Anodic Switching Potential E_λ^a upon the Voltametric Parameters for the oxidation/reduction of PbS at a Au sphere. Electrode T = 417°C, ν = 50 mV/s; Solvent = $PbCl_2$-KCl-NaCl; [PbS]M = 5.814×10^{-3}

E_λ^a mV	Q_T^A mC	I_p^c mA	E_p^c mV	Q^c mC
450	3.183	0.383	363	0.150
500	4.233	0.767	352	0.417
550	4.750	1.07	350	0.700
600	5.150	1.367	340	1.00
650	5.583	1.617	335	1.30

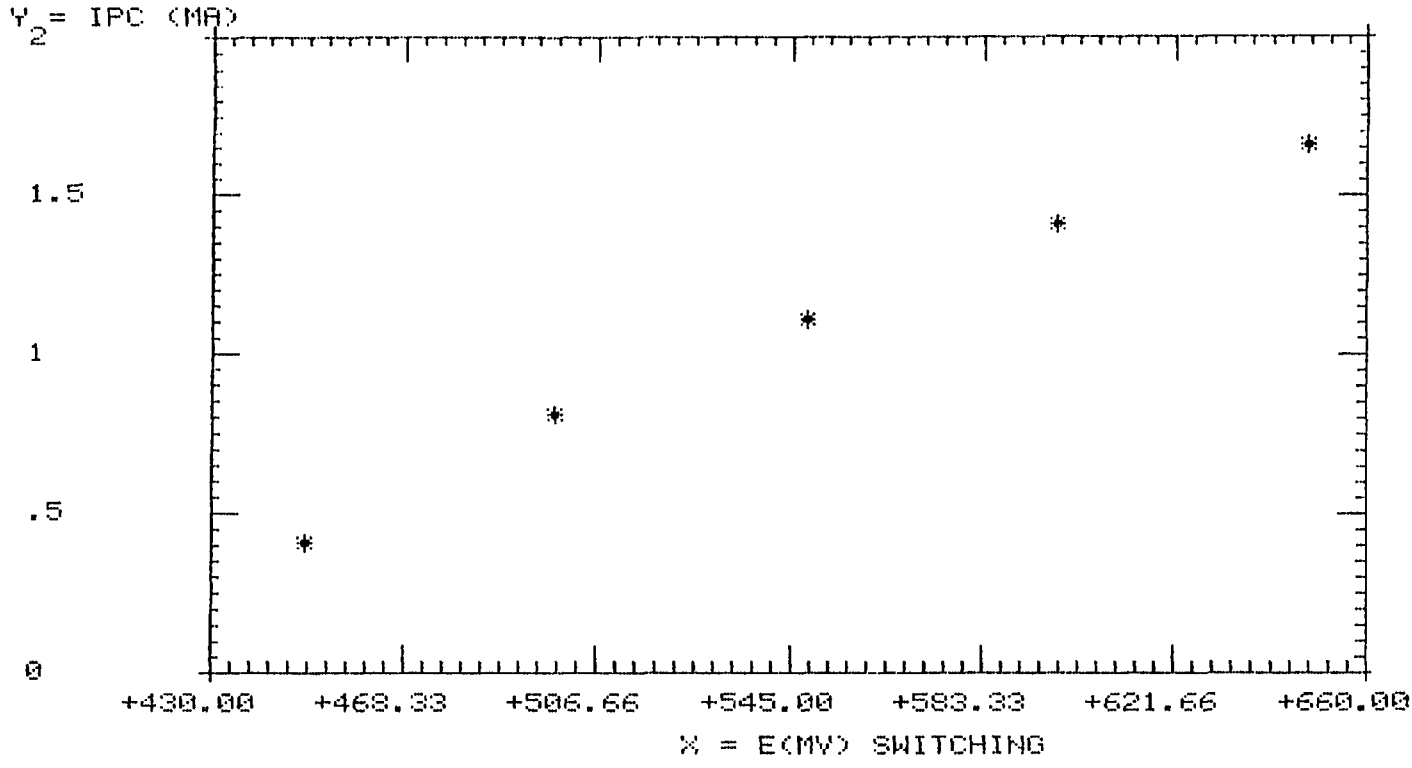


FIGURE NUMBER 6.3.11: The effect of increasing switching potential (E) upon the reduction peak current $I_{p'}^{c}$ T = 417°C; [PbS]M = 5.814 x 10^{-3}. Au sphere electrode.

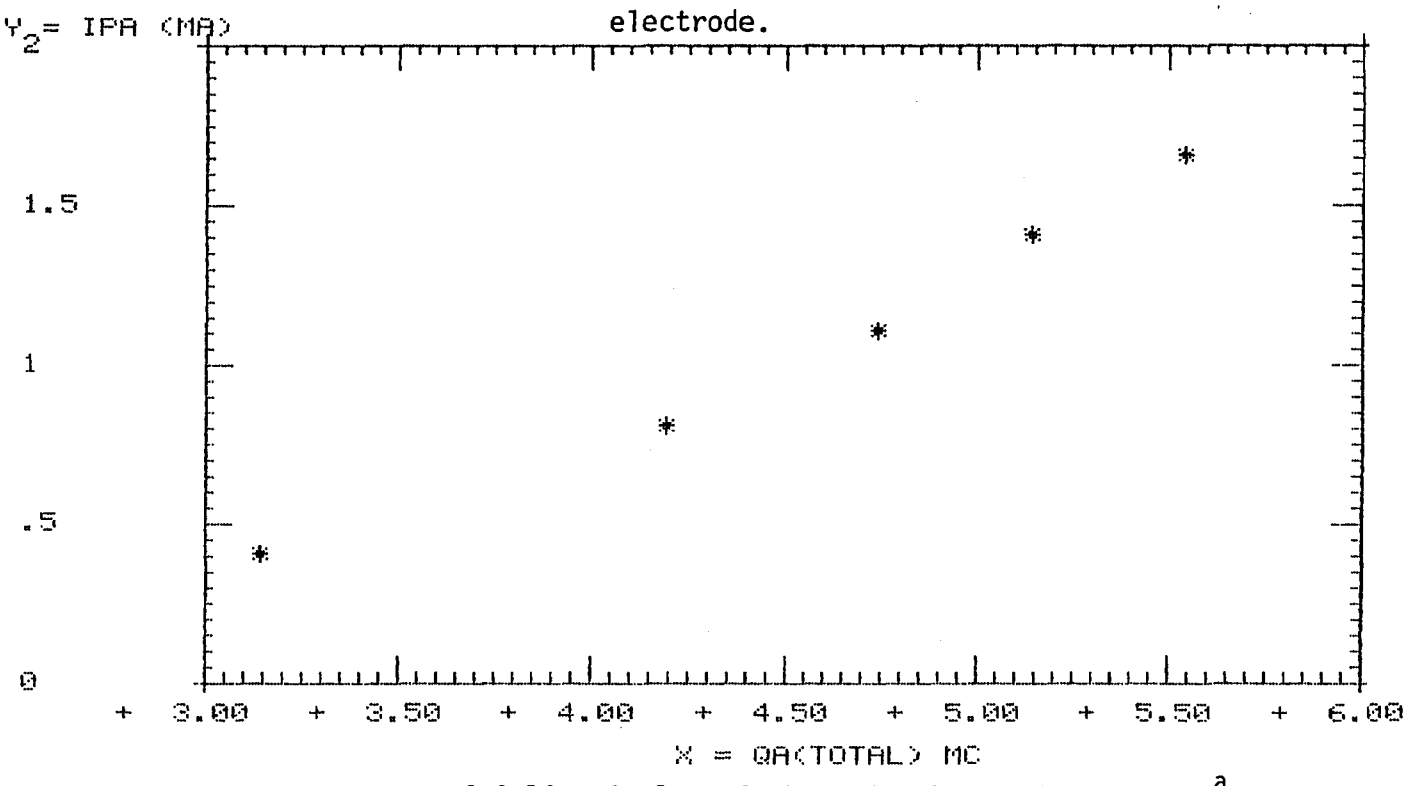


FIGURE NUMBER 6.3.12: A plot of the reduction peak current I_{p}^{a} as a function of the total anodic charge Q^{a}. T = 417°C; [PbS]M = 5.814 x 10^{-3}. Au sphere electrode.

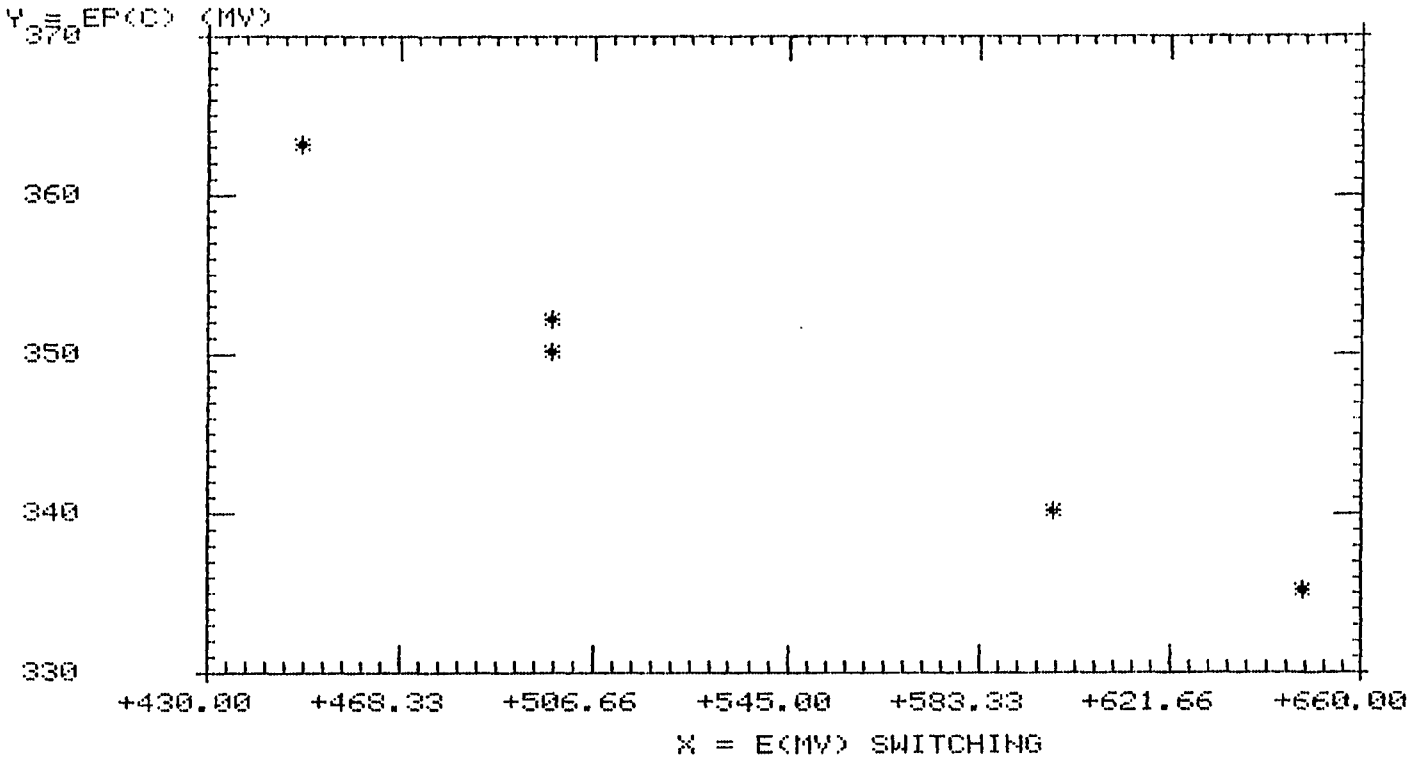


FIGURE NUMBER 6.3.13: The effect of increasing anodic switching potential upon the reduction peak potential E_p^c.

T = 417°C; [PbS]M = 5.814×10^{-3}.

Au sphere electrode.

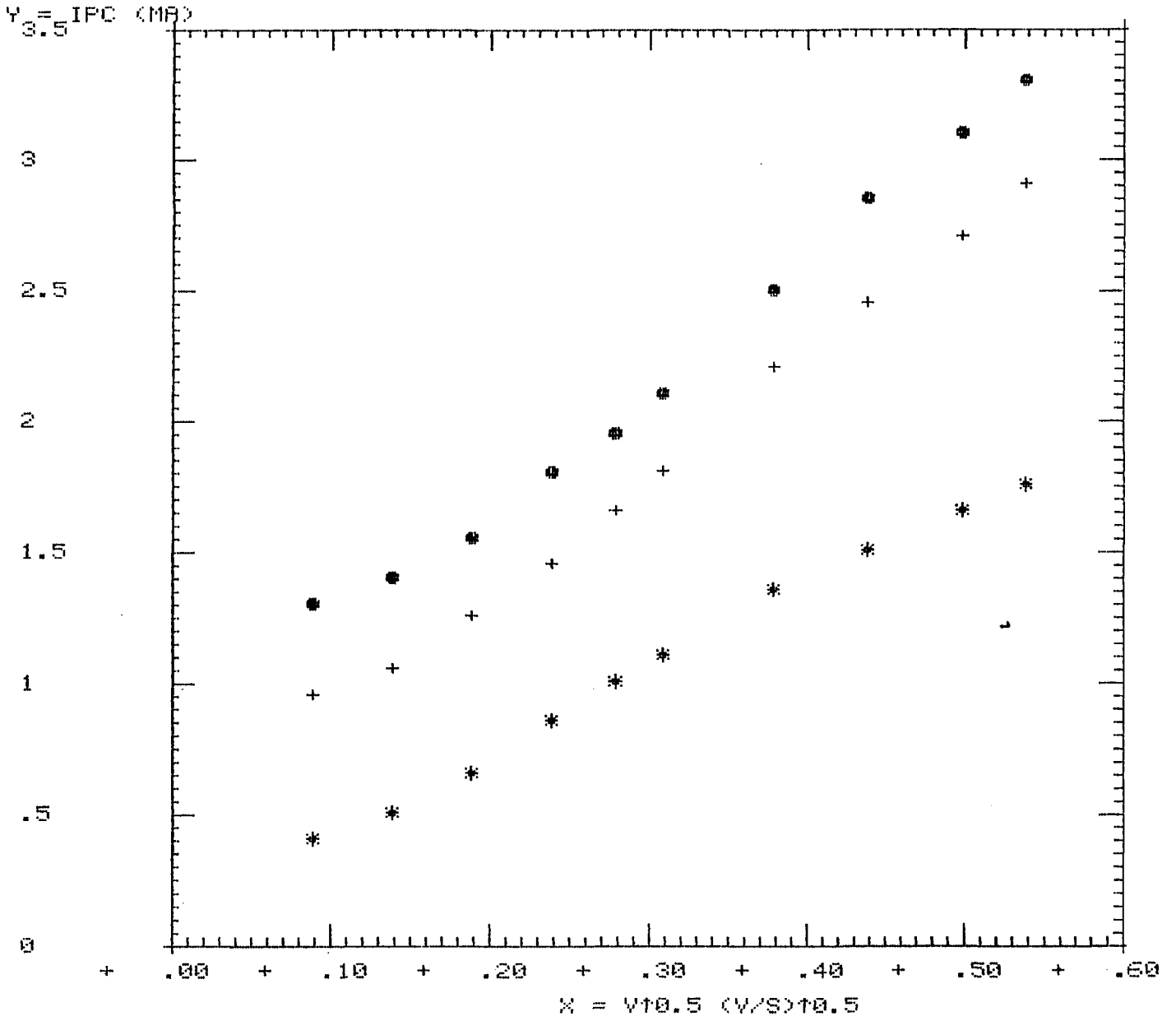


FIGURE NUMBER 6.3.14: The effect of the anodic switching potential upon the I_p^c vs $\nu^{\frac{1}{2}}$ relation.

E_λ^a: ⋆ 0.5V; + 0.6V; ● 0.7V wrt $Ag^+/Ag°$

T = 417°C; [PbS]M = 5.814 x 10^{-3}.Au sphere electrode.

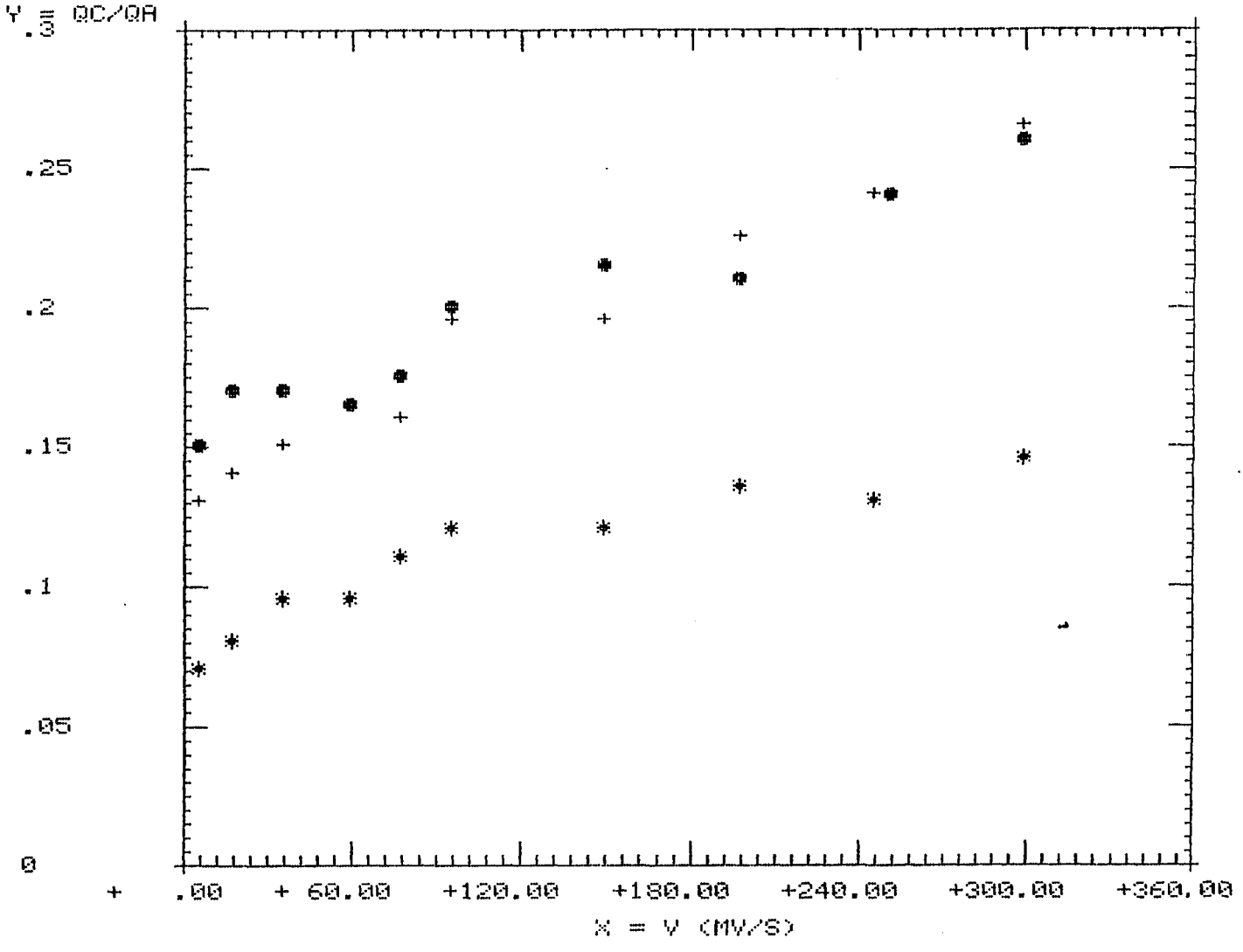


FIGURE NUMBER 6.3.15: The effect of the anodic switching potential (E^a_λ) upon the charge ratio Q^c/Q^a vs ν relation.
E^a_λ : * 0.5V; + 0.6V; ● 0.7V wrt $Ag^+/Ag°$
T = 417°C; [PbS]M = 5.814 x 10^{-3}. Au sphere electrode.

indicates that both oxidation waves are independent of 'history' and cycling. It is observed that the reduction process does not begin to occur until anodic potentials greater than the E_p^a value of the main oxidation process are obtained. It is further noted that the potential corresponding to the onset of reduction is independent of the anodic switching potential. After the peak reduction potential has been reached the current decreases rapidly,crosses the zero current line and forms an anodic current loop. The charge within this loop and the potential at which i = 0 is crossed is sensitive to E_λ.

Figs. 6.3.11 or 6.3.12 show that the reduction peak current is not linearly dependent upon either the switching potential or the total anodic charge. The peak potential is observed to shift cathodically with increasing E_λ, Fig. 6.3.13.

The effect of increasing sweep upon the reduction peak current and the charge ratio Q^c/Q_T^a as a function of E_λ^a is shown in Figs. 6.3.14 and 6.3.15 respectively. Fig. 6.3.14 shows the reduction peak current I_p^c to increase linearly with $\nu^{\frac{1}{2}}$ although a non-zero intercept is obtained which increases with increasing E_λ^a. The charge ratio Q^c/Q_T^a increases with increasing sweep rate, although not in a linear manner, Fig. 6.3.15. The ratios are noted to be quite low thus indicating that the recovery of material is low and that the ratio is dependent upon E_λ^a.

6.3.2 Chronoamperometry

Several I-t transients as a result of a preselected potential pulse were recorded primarily to verify the voltammetric studies. The potentials employed were confined to those corresponding to the 'pre-wave' and main wave potentials, e.g. +300, 340 and +420 and 450 mV wrt Ag^+/Ag respectively. Fig. 6.3.16 shows that the current for each process decreases linearly with $t^{-\frac{1}{2}}$ in a typical diffusion-controlled manner. Surprisingly, during this work no peaks were observed in the I-t transient at any potential (0→+500 mV) and at any time scale between 10 ms and 100 s which could be attributed to

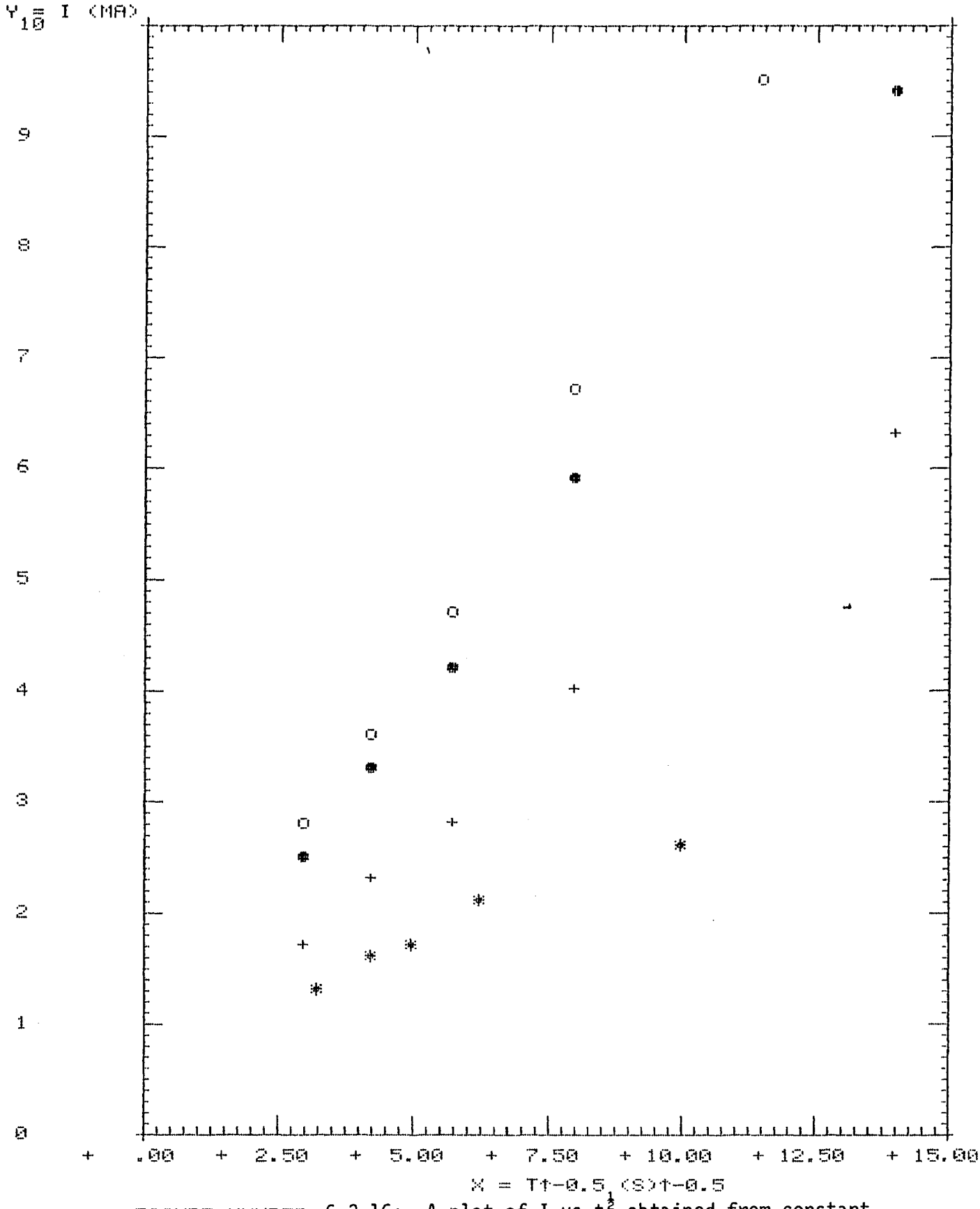


FIGURE NUMBER 6.3.16: A plot of I vs $t^{\frac{1}{2}}$ obtained from constant potential I-t transients for the oxidation of PbS at a gold sphere electrode. Applied potential: ⋆0.3V, + 0.34V; ● 0.42V and O 0.45V wrt $Ag^{+}/Ag°$. T = 417°C; [PbS]M = 5.814 x 10^{-3}.

nucleation and growth phenomenon.

6.4 Results: Platinum Electrode

The oxidation of PbS-containing solutions at a Pt flag electrode were investigated using the technique of cyclic voltammetry, chrono-amperametry, chronopotentiometry and open-circuit potential decay transients.

6.4.1 Cyclic Voltammetry

Cyclic voltammetric studies were undertaken to determine the effect of increasing sweep rate, PbS concentration and temperature upon both the oxidation and reduction behaviour. Fig. 6.4.1 shows a typical voltammogram obtained at a concentration of 1.077×10^{-2}M at 417°C. Two oxidation (labelled A and B) and three reduction waves (A', B' and C') were obtained. The reduction wave A' corresponds to the oxidation process A and that of B' to B. The third very cathodic reduction wave was ill-defined and rarely observed and thus no quantitative data were obtained. The general morphology of the main oxidation and reduction waves B and B' is typical of that expected for the deposition and stripping of an insoluble product. The analysis of the voltammograms may be divided into the following:

(a) the behaviour of the main process B/B';

(b) the formation of process A;

(c) the effect of increasing anodic switching potential (E_λ^a) upon processes A and B and their interrelation.

The above factors are evaluated as a function of increasing sweep rate, PbS concentration and temperature. The voltammetric results for process B will be presented first.

Table 6.4.1 summarises the effect of increasing sweep rate upon the voltammetric parameters obtained in a 1.077×10^{-2}M PbS solution at 417°C. Fig. 6.4.2 shows that the peak current I_p^a increases linearly with increasing $(\text{sweep rate})^{\frac{1}{2}}$ at all five concentrations. The slopes of these plots together with their intercepts and correlation values,as calculated from linear regression analysis, are given in Table 6.4.2.

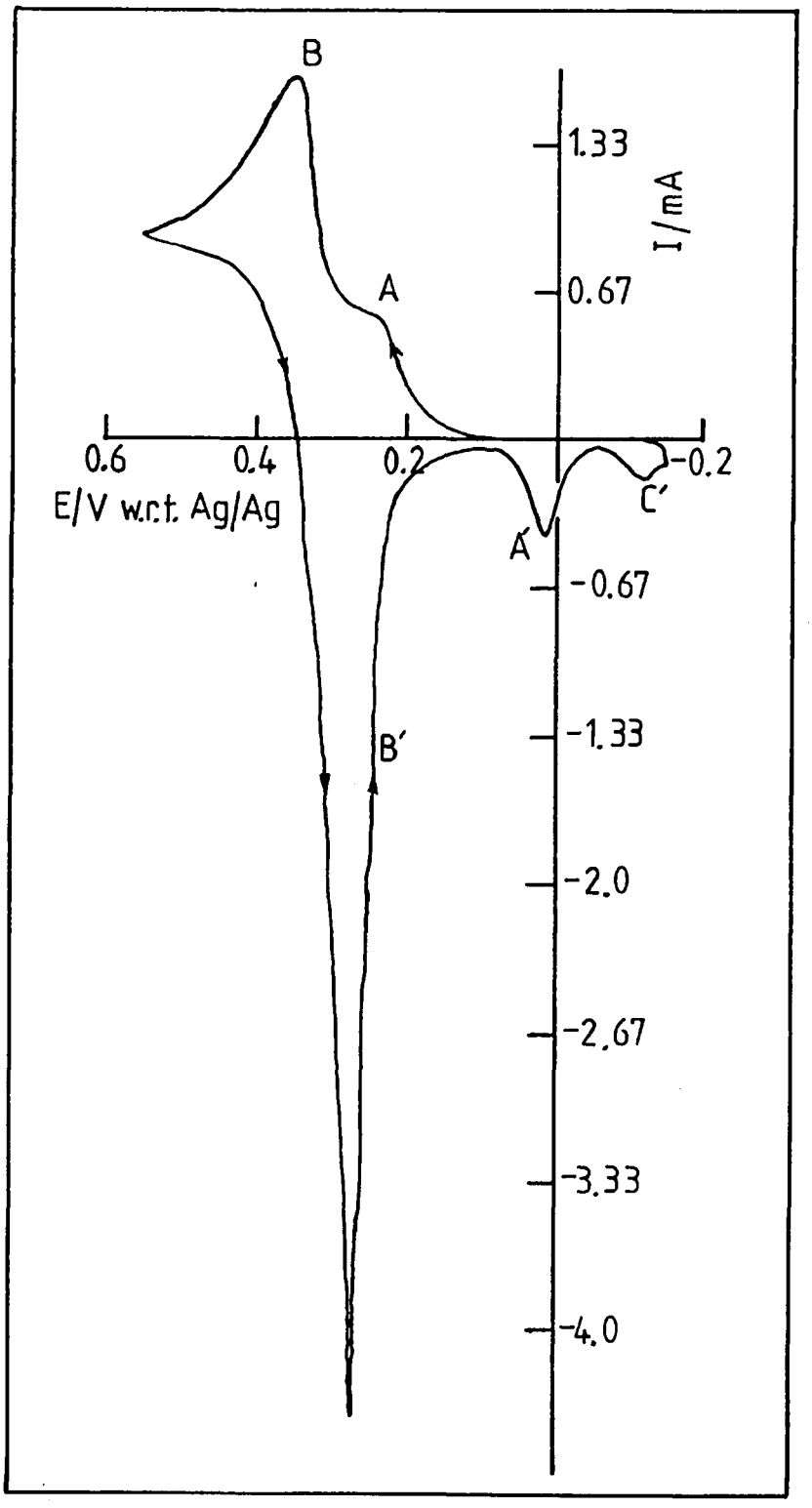


Fig. 6.4.1: A cyclic voltammogram obtained for the oxidation of PbS containing solutions at a Pt flag electrode. [PbS]M = 1.077×10^{-2}; electrode area =

TABLE 6.4.1.

The effect of increasing sweep rate upon the voltammetric parameters for the main oxidation wave obtained at a Pt electrode. Electrode Area = ;
PbS = 1.077×10^{-2} M; Melt = $PbCl_2$/KCl/NaCl Ternary Eutectic; T = 417°C.

V v/s	$V^{\frac{1}{2}}$	Ip^a	$Ip^a/V^{\frac{1}{2}}$	Ip^c/Ip^a	Ep^a	Ep^c	E
0.02	0.1414	1.667	11.785	2.437	345	280	65
0.04	0.20	2.233	11.167	-	345	-	-
0.06	0.245	2.667	10.89	-	350	-	-
0.08	0.283	3.067	10.84	-	350	-	-
0.10	0.316	3.40	10.75	-	350	-	-
0.10	0.316	3.45	10.91	2.607	355	280	75
0.15	0.387	4.15	10.715	2.560	355	280	75
0.20	0.447	4.75	10.62	2.510	355	280	75
0.25	0.5	5.30	10.60	2.455	355	280	75
0.30	0.548	5.90	10.77	2.374	355	280	75
0.35	0.592	6.30	10.65	2.260	355	280	75
0.4	0.632	6.75	10.67	2.175	355	280	75

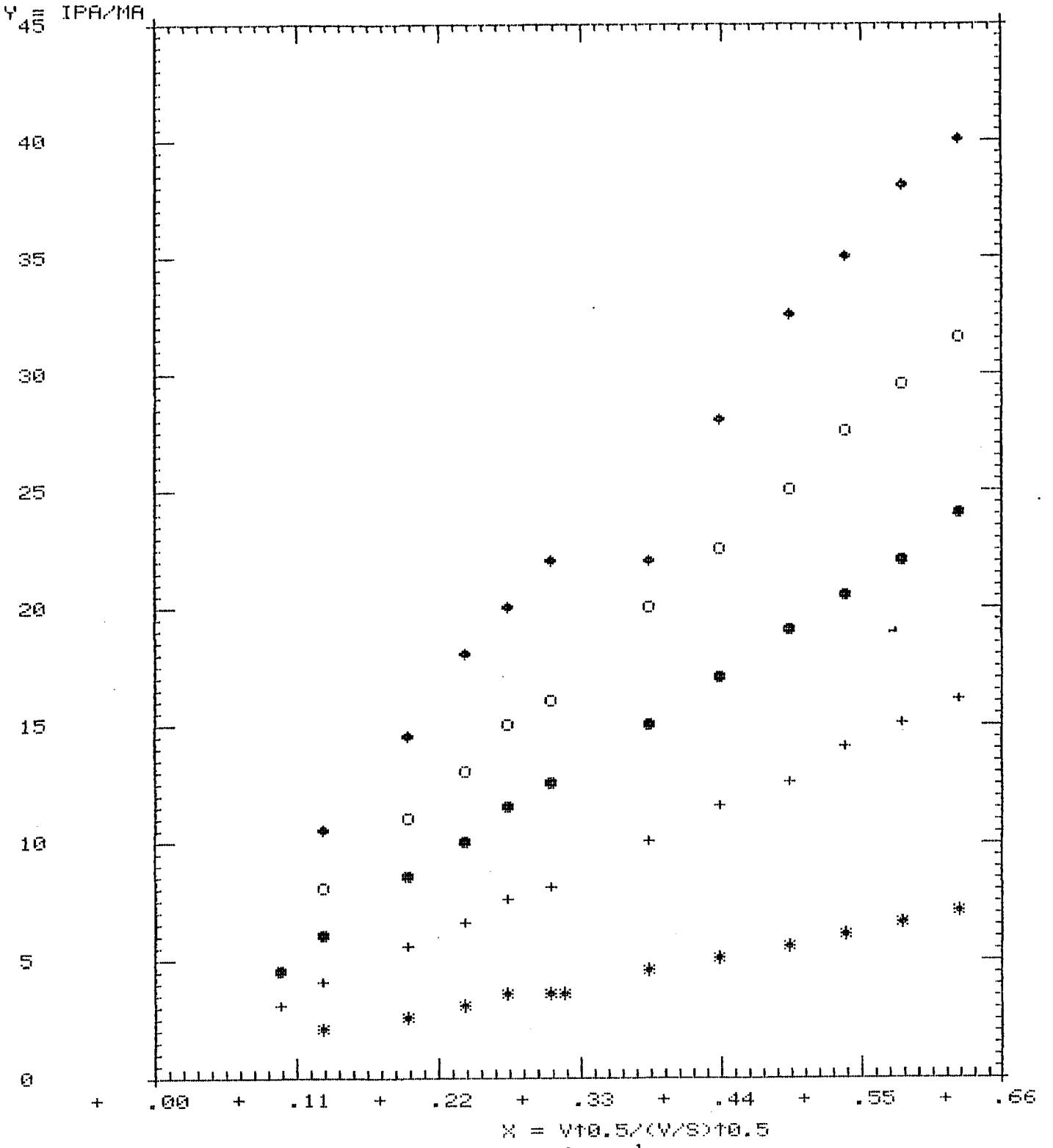


FIGURE NUMBER 6.4.2: A plot of I_p^a vs $\nu^{\frac{1}{2}}$ for process B. Pt flag electrode; area =
T ° 417°C; [PbS]M: ⋆1.077 x 10^{-2};
+ 2.52 x 10^{-2}; ● 3.918 x 10^{-2};
O 5.352 x 10^{-2}; ▲ 7.335 x 10^{-2}.

Table 6.4.2: Linear regression analysis of I_p^a vs $\nu^{\frac{1}{2}}$ plots for the oxidation of S^{2-} at a Pt electrode for various PbS concentrations

[PbS] x 10^2M	d $I_p^a/d\nu^{\frac{1}{2}}$ mA/(V/s)$^{\frac{1}{2}}$	Intercept mA	Correlation
1.077	10.448	0.117	0.999
2.52	24.541	0.280	0.999
3.918	35.750	0.859	0.999
5.352	47.907	1.030	0.999
7.335	59.174	2.294	0.992

The more sensitive current function $I_p^a/\nu^{\frac{1}{2}}$ is shown in Fig. 6.4.3 to be virtually independent of sweep rate at low PbS concentrations. At higher concentrations an initial decrease in the current function occurs at low ν values, and becomes virtually independent at high ν. Table 6.4.3 further indicates the potential functions E_p^a, E_p^c and ΔE to be approximately constant with increasing scan rate with values of +0.35V, 0.28V and 75 mV respectively. The concentration dependence of the various potentials defined previously (see Fig. 6.3.5) shows a linear relation with log(PbS), Fig. 6.44. The slopes dE/d(log[PbS]) and correlations are given in Table 6.4.3 below.

Table 6.4.3: A linear regression analysis of voltammetric potential parameters with increasing PbS concentration

Potential	dE/d(log[Pbs])	Correlation
η_1	-0.0612	0.989
η_2	-0.0732	0.992
η_3	-0.0731	0.984
η_4	-0.0489	0.989

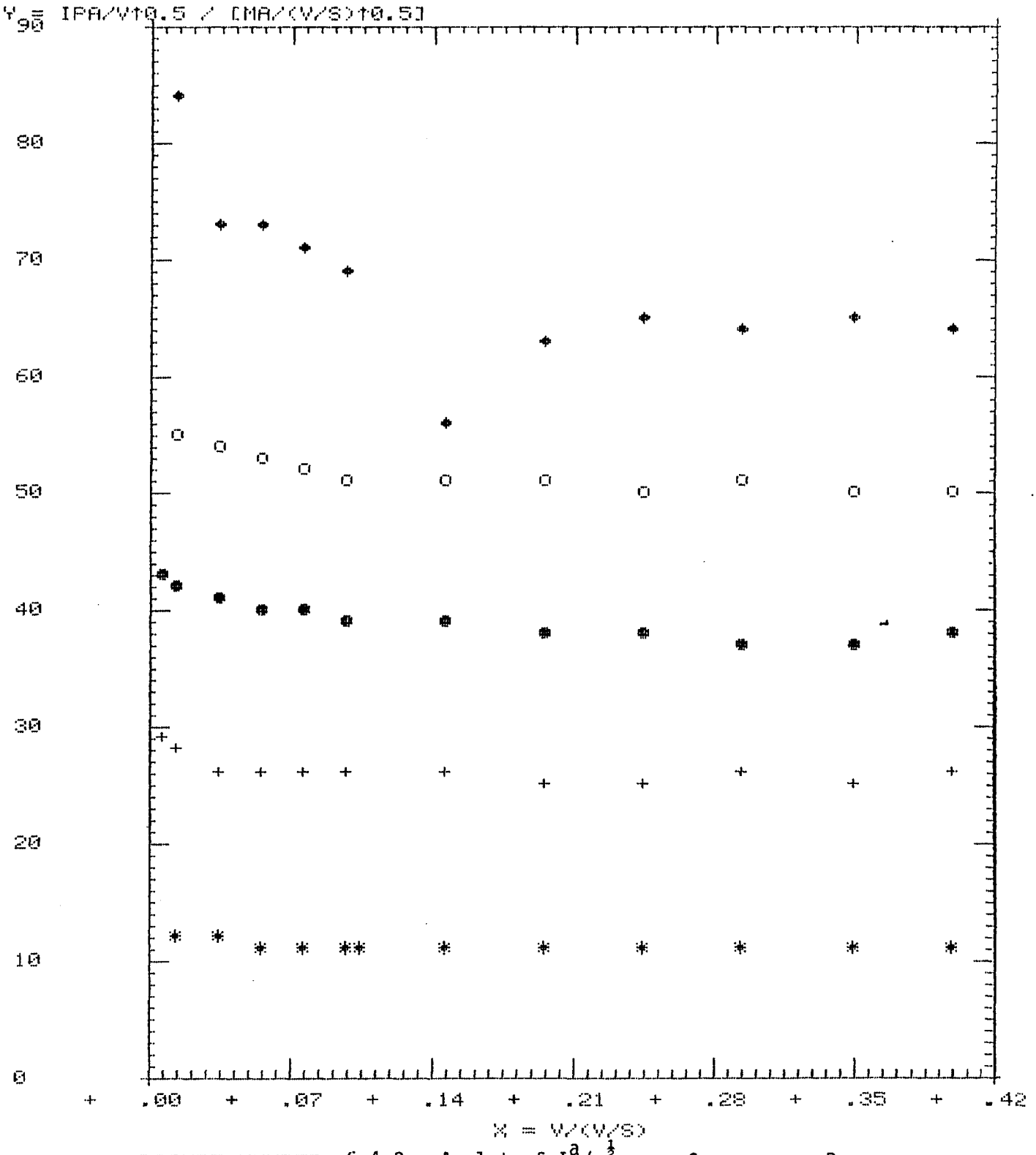


FIGURE NUMBER 6.4.3: A plot of $I_p^a/\nu^{\frac{1}{2}}$ vs ν for process B. Pt flag electrode, area = T = 417°C; [PbS]M: ⋆1.077 x 10^{-2}; + 2.52 x 10^{-2}; ● 3.198 x 10^{-2}; O 5.352 x 10^{-2}; ▲ 7.335 x 10^{-2}.

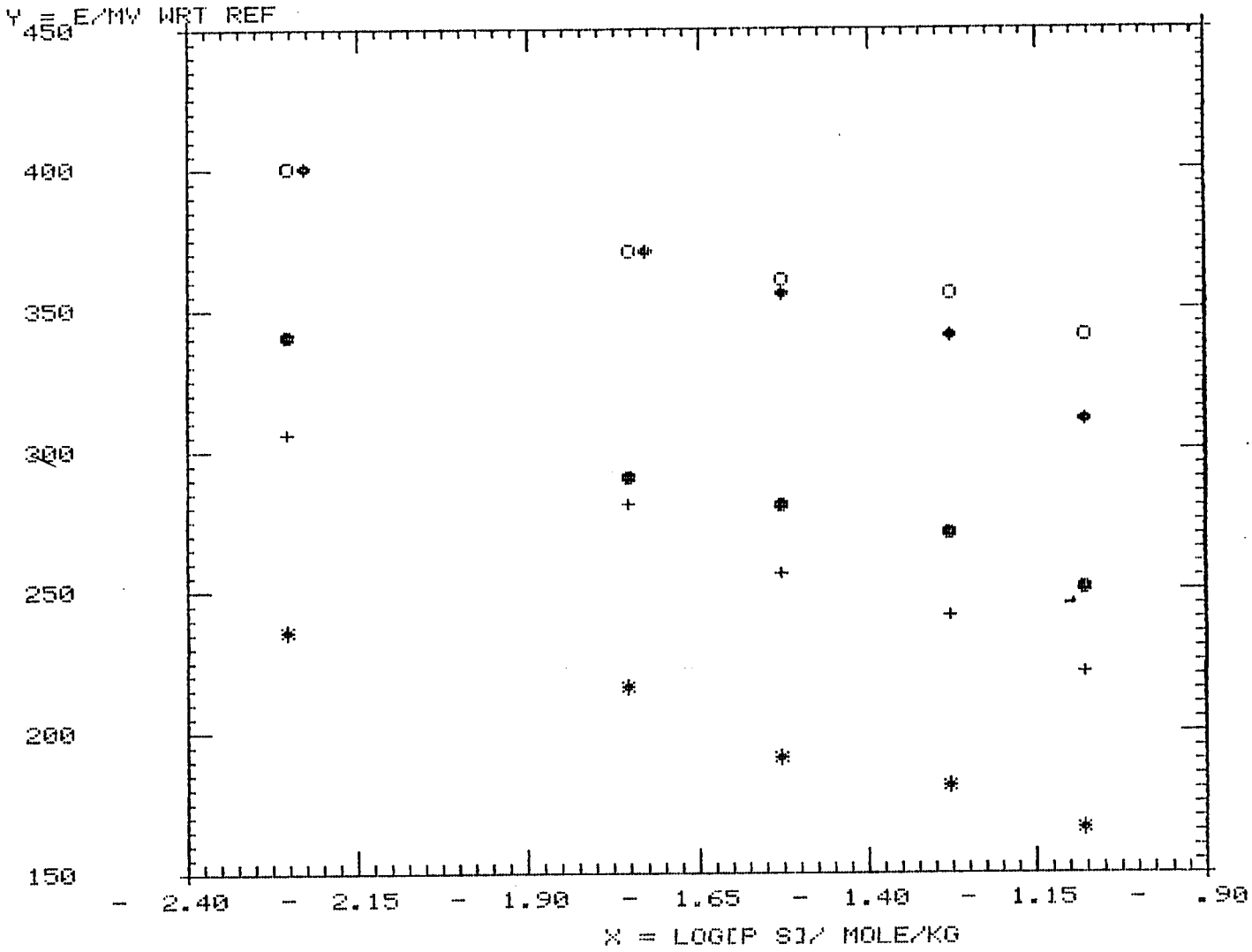


FIGURE NUMBER 6..4.4: A plot of potential vs log(PbS) for the voltammetric potentials η_1(*); η_2(+); η_3(●); η_4(0) and η_{-4}(▲), see Fig. 6.3.5 for definition T = 417°C; Pt flag electrode.

The Voltammetric Formation of Peak A/A'

The gradual formation of the anodic product corresponding to reaction A and its subsequent reduction process (A') was investigated by the gradual increase in E_λ^a. The anodic switching potential (E_λ^a) was stepped in 20 mV increments from potentials corresponding to the foot of the wave (i.e. + 260 mV) to a potential at which the second oxidation process may be discerned to be occurring, i.e. +400 mV. Fig. 6.4.5 shows the influence of E^a upon the subsequent reduction wave and Table 6.4.4 the numerical parameters obtained.

Table 6.4.4: The effect of increasing switching potential, limited to the potential range 0.26 - 0.4V upon the reduction wave A'. [PbS]= 5.814 x 10^{-3}M; sweep rate = 0.2V/s; electrode area = 0.2 cm^2; E_λ^a, E_p^c w.r.t. Ag^+/Ag

E_λ^a mV	E_p^c mV	I_p^c mA	Q^c mC
260	90	0.392	0.4167
280	85	0.508	0.4167
300	77	0.592	0.375
320	73	0.667	0.375
340	67	0.717	0.4167
360	64	0.767	0.4167
380	60	0.80	0.5418
400	55	0.833	0.6251

It is clear from Fig. 6.4.5 that as a consequence of an increase in E_λ^a the peak current for reduction increases and that the whole wave shifts towards more cathodic potentials. Fig. 6.4.6 shows that the reduction peak current I_p^c does not increase linearly with E_λ^a; the corresponding change Q^c remaining constant up to E_λ^a = 0.36 - 0.38V after which a rapid increase

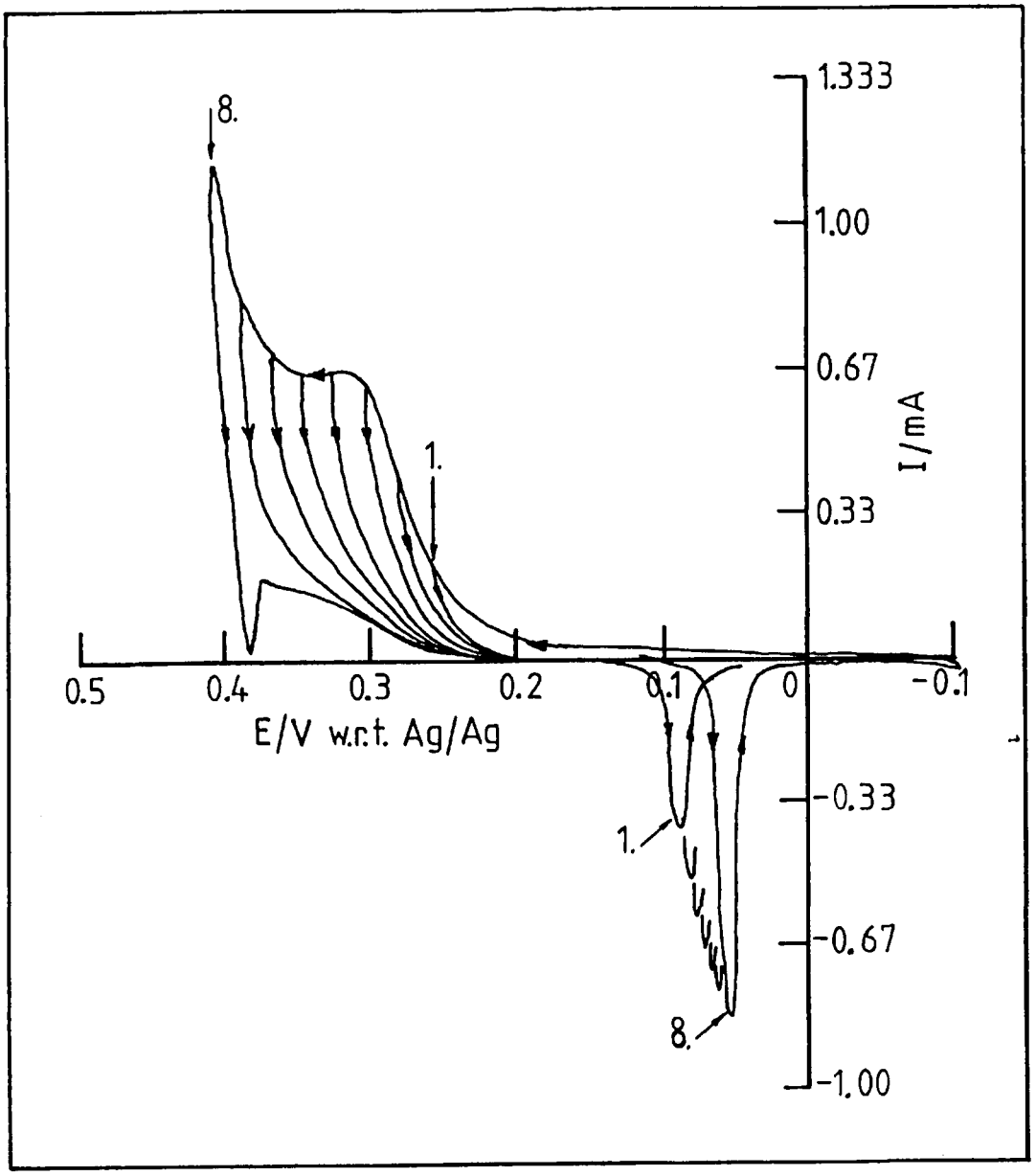


Fig. 6.4.5: The effect of increasing the anodic switching potential E_λ^a upon the voltammetric response for process A. Pt flag electrode; area = 0.2 cm^2. [PbS]M = 5.814 x 10^{-3}; sweep rate = 0.2 V/s.

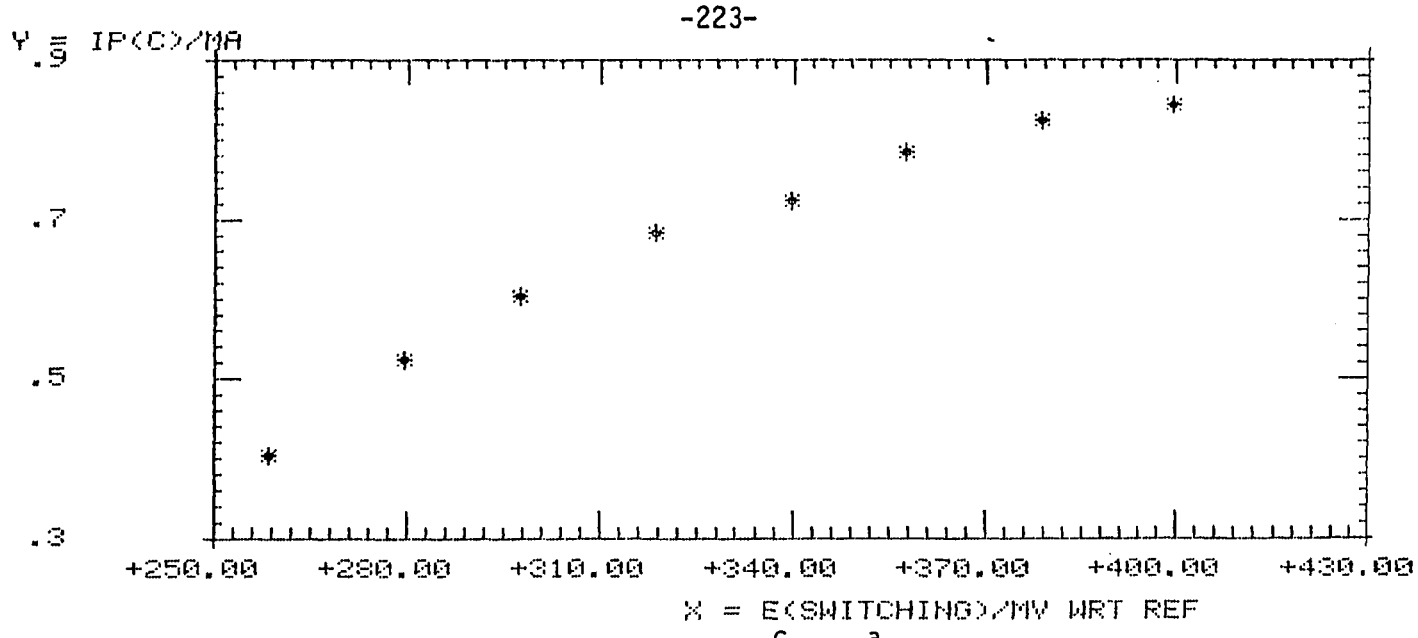


FIGURE NUMBER 6.4.6: A plot of I_p^c vs E_λ^a for process A. Pt flag electrode (0.2 cm^2). [PbS]M = 5.8141 x 10^{-3}.

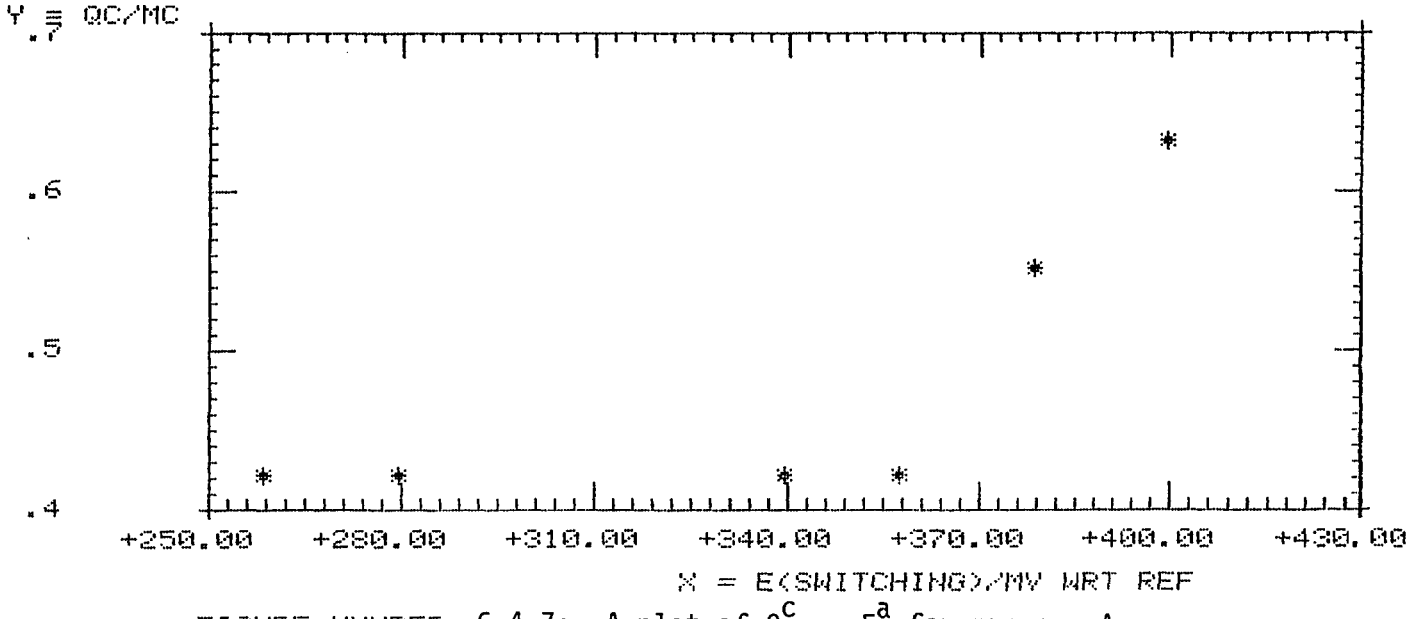


FIGURE NUMBER 6.4.7: A plot of Q^c vs E_λ^a for process A. Pt flag electrode (0.2 cm^2). [PbS]M = 5.8141 x 10^{-3}.

is obsered with a further increase in E_λ^a, Fig. 6.4.7. The peak potential E_p^c shifts linearly with increasing E_λ by a factor of $dE_p^c/dE_\lambda = -0.247$ (correlation = 0.994), Fig. 6.4.8.

The effect of increasing scan rate and to a limit extent PbS concentration upon the overall process, A, was obtained by switching the potential at a value intermediate between the peak potentials of processes A and B. The resolution of the oxidation wave and in particular that of reduction was best observed in very dilute solutions and the concentration effect was limited to two concentrations of 5.814×10^{-3} and 1.4213×10^{-2}M. Fig. 6.4.9 clearly shows the influence of increasing scan rate upon the oxidation and reduction peaks for process A; the results are tabulated in Table 6.4.5.

Table 6.4.5: The effect of increasing sweep rate upon the voltammetric parameters for process A: $E_\lambda^a = 0.35$V. [PbS] = 5.8141×10^{-2}M; electrode area = 0.2 cm^2. E values w.r.t. Ag^+/Ag.

ν V/s	I_p^a mA	I_p^c mA	Q_T^A mC	Q^C mC	E_p^a V	E_p^c V
0.01	0.5	0.417	6.168	0.667	0.31	0.065
0.02	0.717	0.73	4.0	0.708	0.315	0.065
0.04	1.017	1.217	2.667	0.625	0.32	0.065
0.06	1.4	1.10	2.331	0.5	0.32	0.075
0.08	1.6	1.467	1.956	0.5	0.325	0.073
0.10	1.867	1.75	1.798	0.5	0.33	0.071
0.12	2.033	2.033	1.554	0.458	0.33	0.070
0.14	2.20	2.30	1.403	0.476	0.33	0.070

Both peak currents, i.e. I_p^a and I_p^c for process A increase linearly with increasing $(\text{sweep rate})^{\frac{1}{2}}$ with a zero intercept (Fig. 6.4.10). It is noteworthy that the I_p^a/I_p^c ratio $\cong$ 1. The ratio of the corresponding

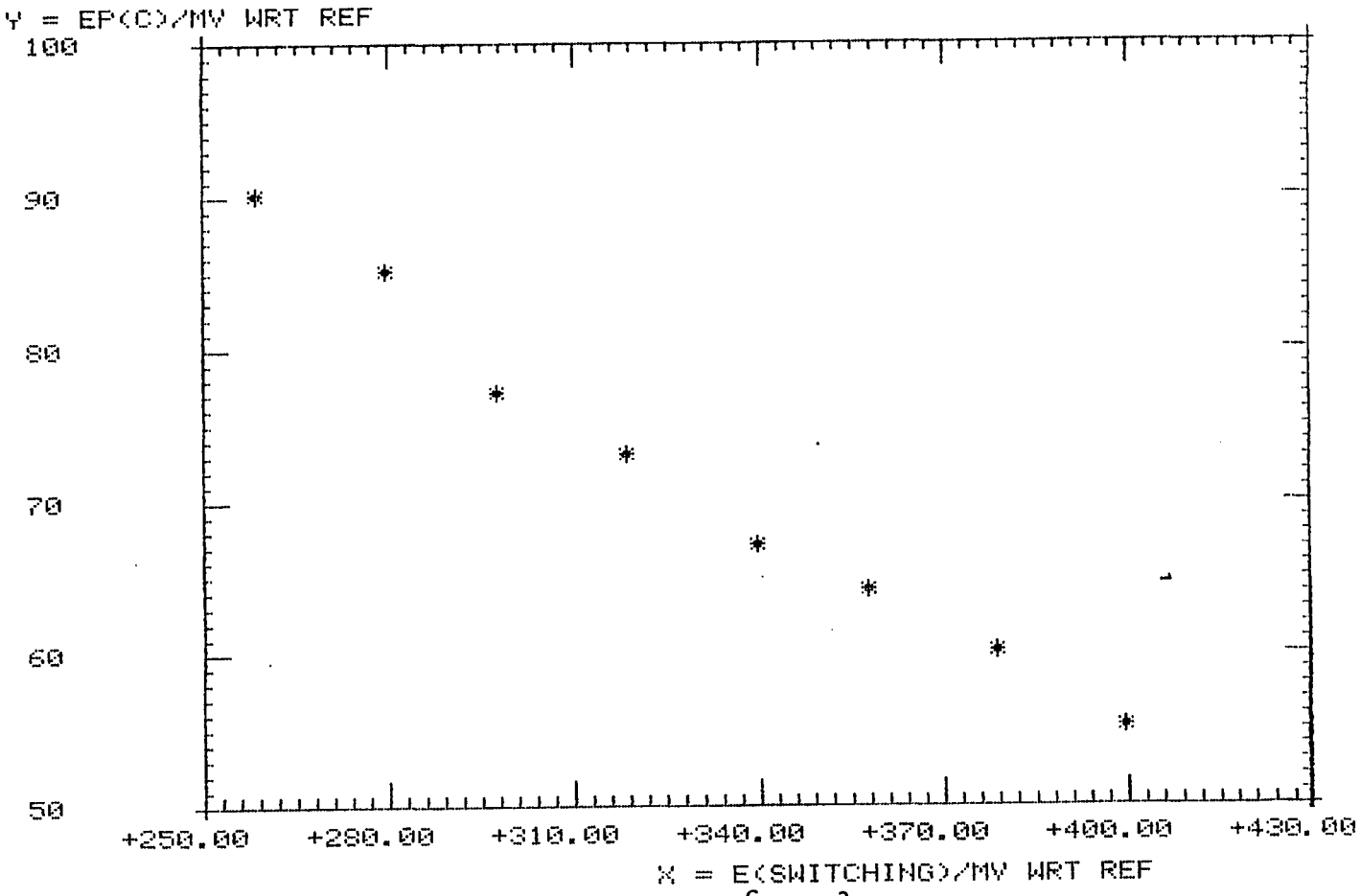


FIGURE NUMBER 6.4.8: A plot of E_p^c vs E_λ^a for process A.
Pt flag electrode (0.2 cm^2).
[PbS]M = 5.8141 x 10^{-3}.

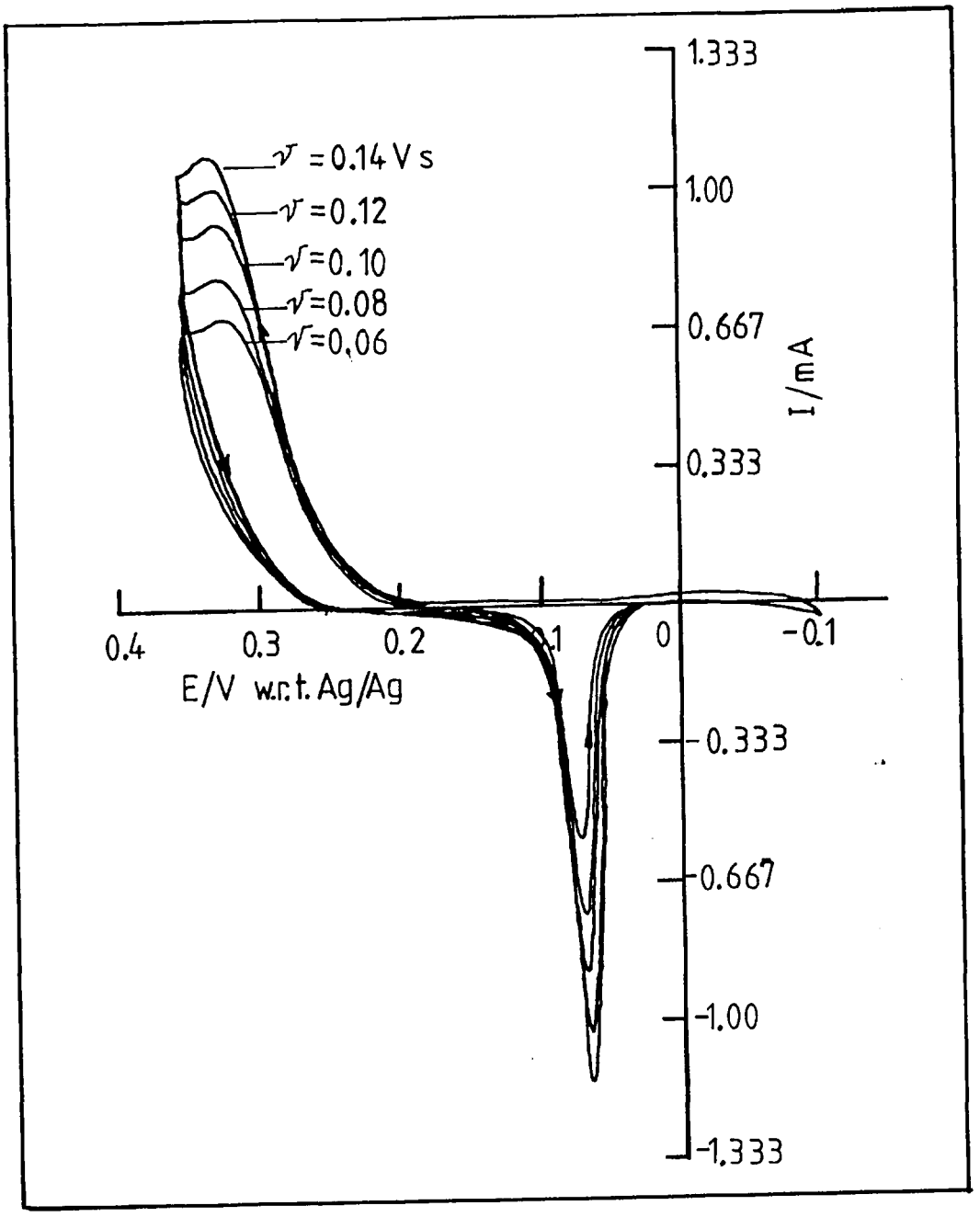


Fig. 6.4.9: The effect of increaing sweep rate upon the voltammetric response for process A.
Pt flag electrode (0.2 cm^2).
T = 417°C; [PbS]M = 5.8141 x 10^{-2}.

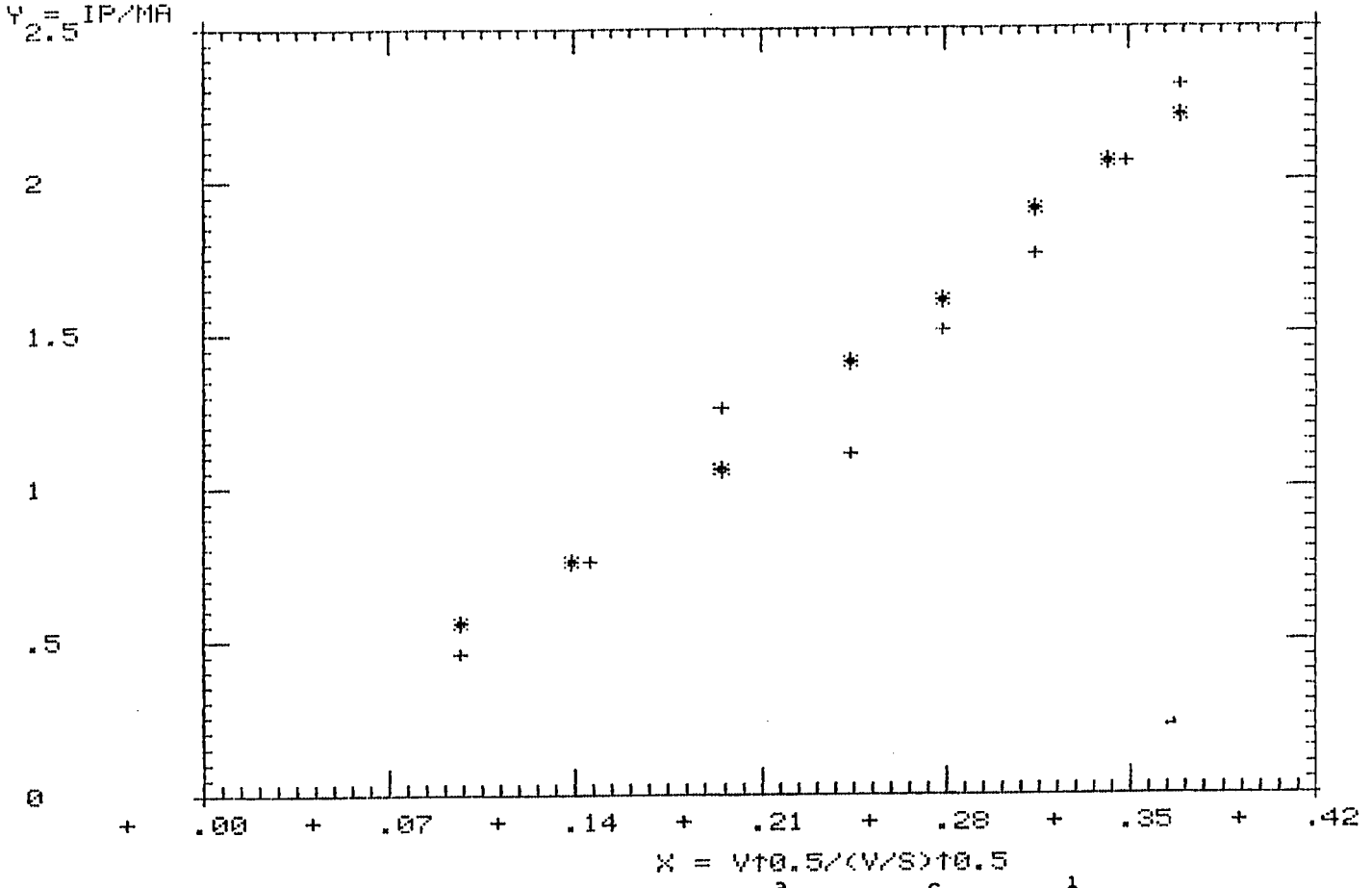


FIGURE NUMBER 6.4.10: A plot of I_p^a(*) and I_p^c(+) vs $\nu^{\frac{1}{2}}$ for process A.
Pt flag electrode (0.2 cm^2).
T = 417°C; [PbS]M = 5.8141 x 10^{-2}.

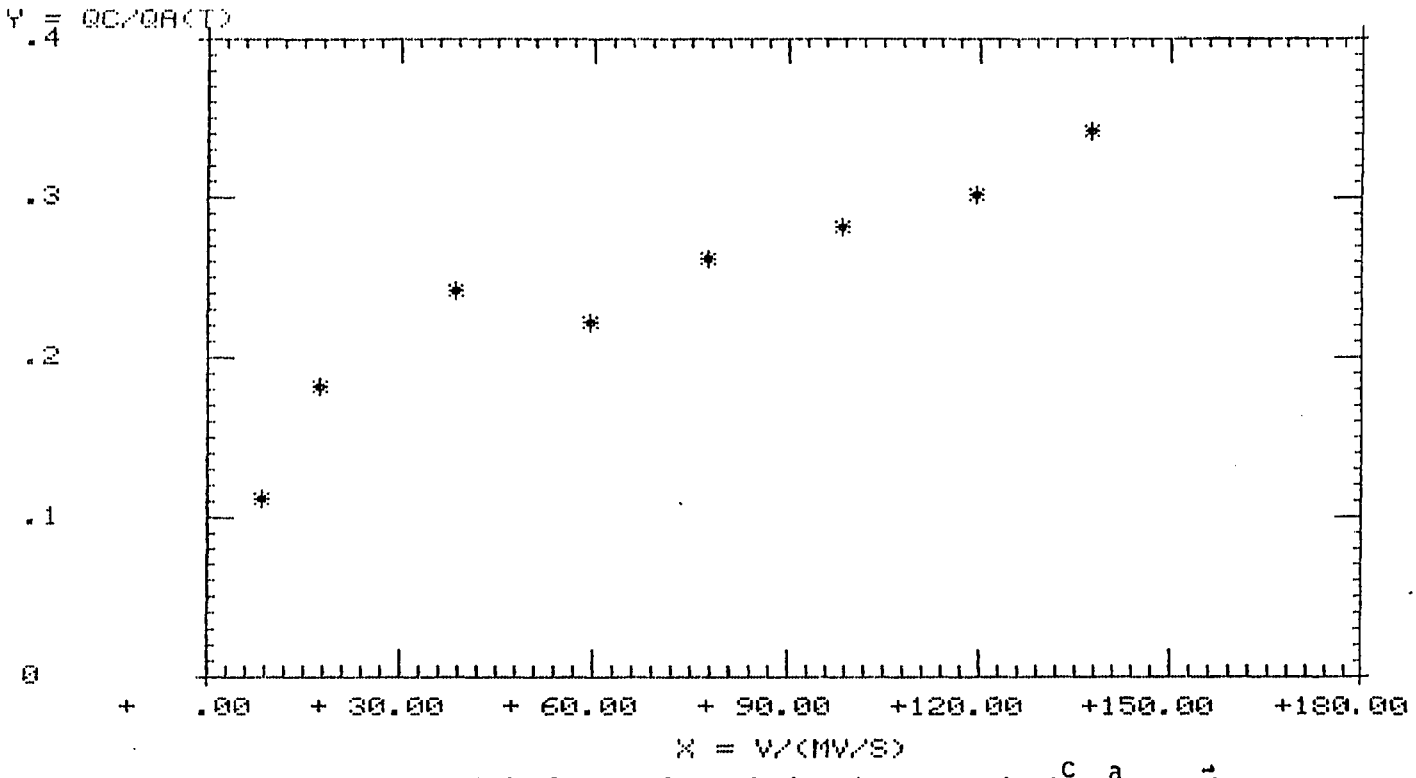


FIGURE NUMBER 6.4.11: A plot of the charge ratio Q^c/Q_T^a vs $\nu^{\rightarrow}$ for process A. Pt flag electrode (0.2 cm^2). T = 417°C; [PbS]M = 5.8141 x 10^{-2}.

charges Q^c/Q_T^a is shown in Fig. 6.4.11, from which it can be seen that the charge ratio increases from ∿0.1 at 10 mV/s to ∿0.35 at 140 mV/s. The anodic peak potential shifts slightly positive with increasing sweep rate although the reduction peak potential remains essentially constant.

The effect of concentration upon the current and charge ratios was evaluated at two concentrations, 5.8141×10^{-3}M and 1.4213×10^{-2}M. Although ideally detailed information would have been preferred for a larger number of PbS concentrations, well defined and therefore analytically useful data were only obtained at the above concentrations. Fig. 6.4.12 shows the anodic peak current to be linearly dependent upon $\nu^{\frac{1}{2}}$ for both concentrations. The slopes, i.e. $dI_p^a/d\nu^{\frac{1}{2}}$ were 6.158 and 11.854 mA $V^{-\frac{1}{2}}S^{-\frac{1}{2}}$ for the two concentrations respectively. The stability of the product formed by this oxidation process was evaluated by a constant potential electrolysis at + 0.3V followed by a reverse voltammetric scan. The charge Q^a of the forward electrolysis and that of the reduction peak were recorded. The waveform used is illustrated below:

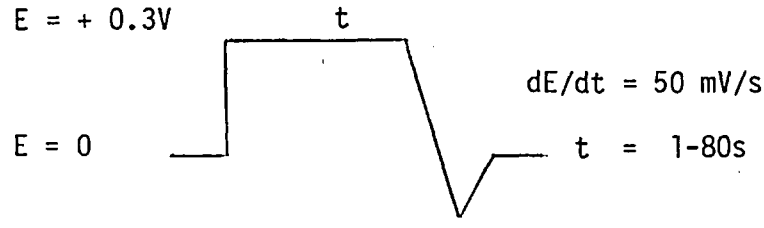


Table 6.4.6 shows the results obtained, from which it can be seen that for electrolysis times up to ∿10s (or Q^a = 9.2 mC) the reverse charge Q^c remains constant at 0.65 mC. With increasing electrolysis time (and therefore charge) the value of Q^c decreases and was associated with a decrease in the reduction peak current. The decrease in Q^c was not a simple result of product stability either of a chemical or a physical nature. Fig. 6.4.13 shows three responses corresponding to electrolysis times of 1,20 and 80 seconds. The response at 1s clearly shows that a single

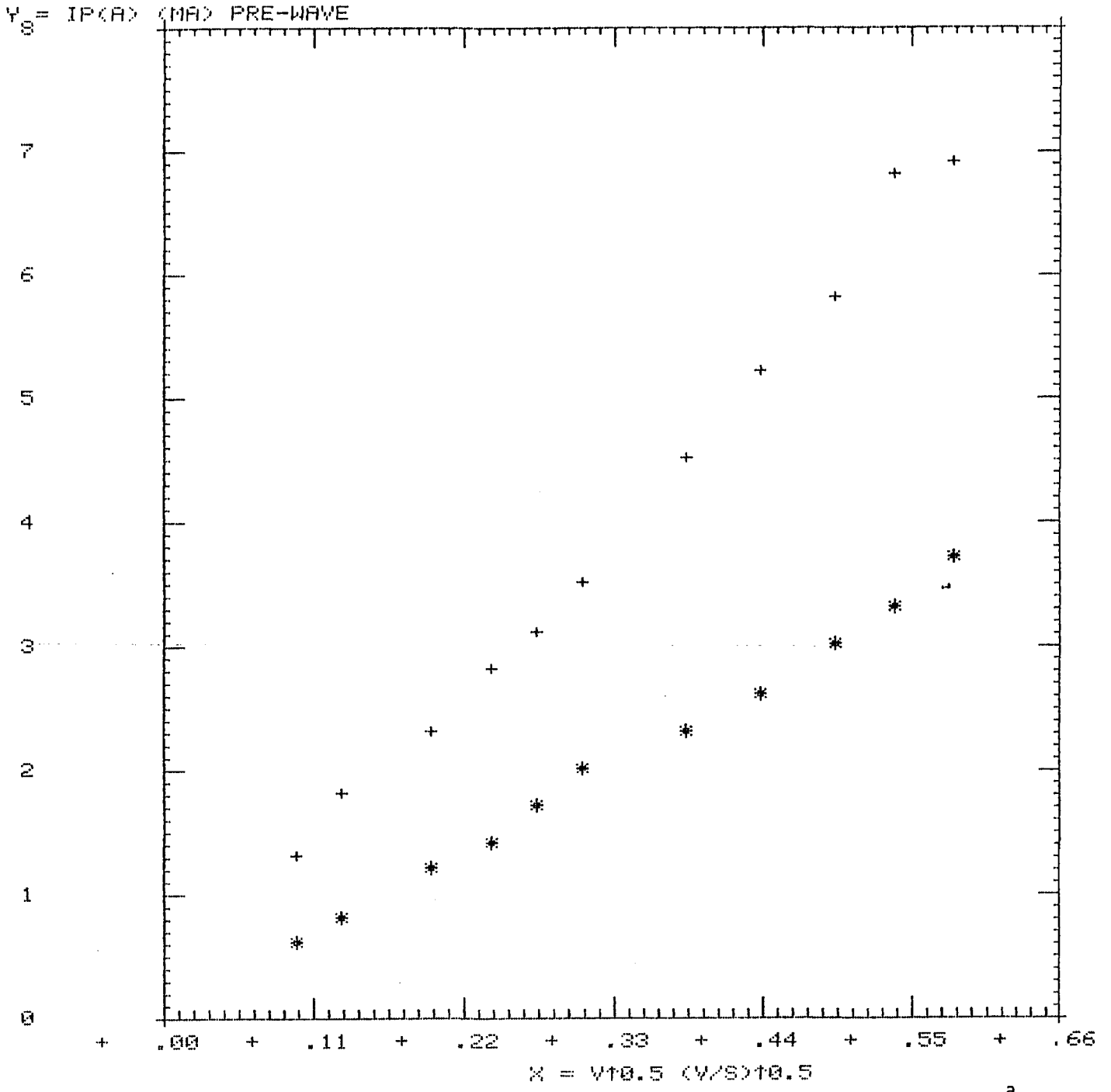


FIGURE NUMBER 6.4.12: The effect of PbS concentration upon the I_p^a vs $\nu^{\frac{1}{2}}$ relation for process A.
Pt flag electrode (0.2 cm^2).
T = 417°C; [PbS]: - * 5.814×10^{-3};
+ 1.4213×10^{-2}.

TABLE 6.4.6.

Constant potential Electrolysis at +0.3V at a Pt electrode.

Area = 0.70.

[PbS] = Electrolysis Time / s	Q^a / mC	Q^c / mC
1	3.949	0.65
2	5.083	0.65
4	6.712	0.65
6	7.826	0.65
8	8.294	0.65
10	9.208	0.65
20	14.44	0.55
30	20.51	0.50
40	22.62	0.45
50	26.53	0.40
80	38.37	0.35

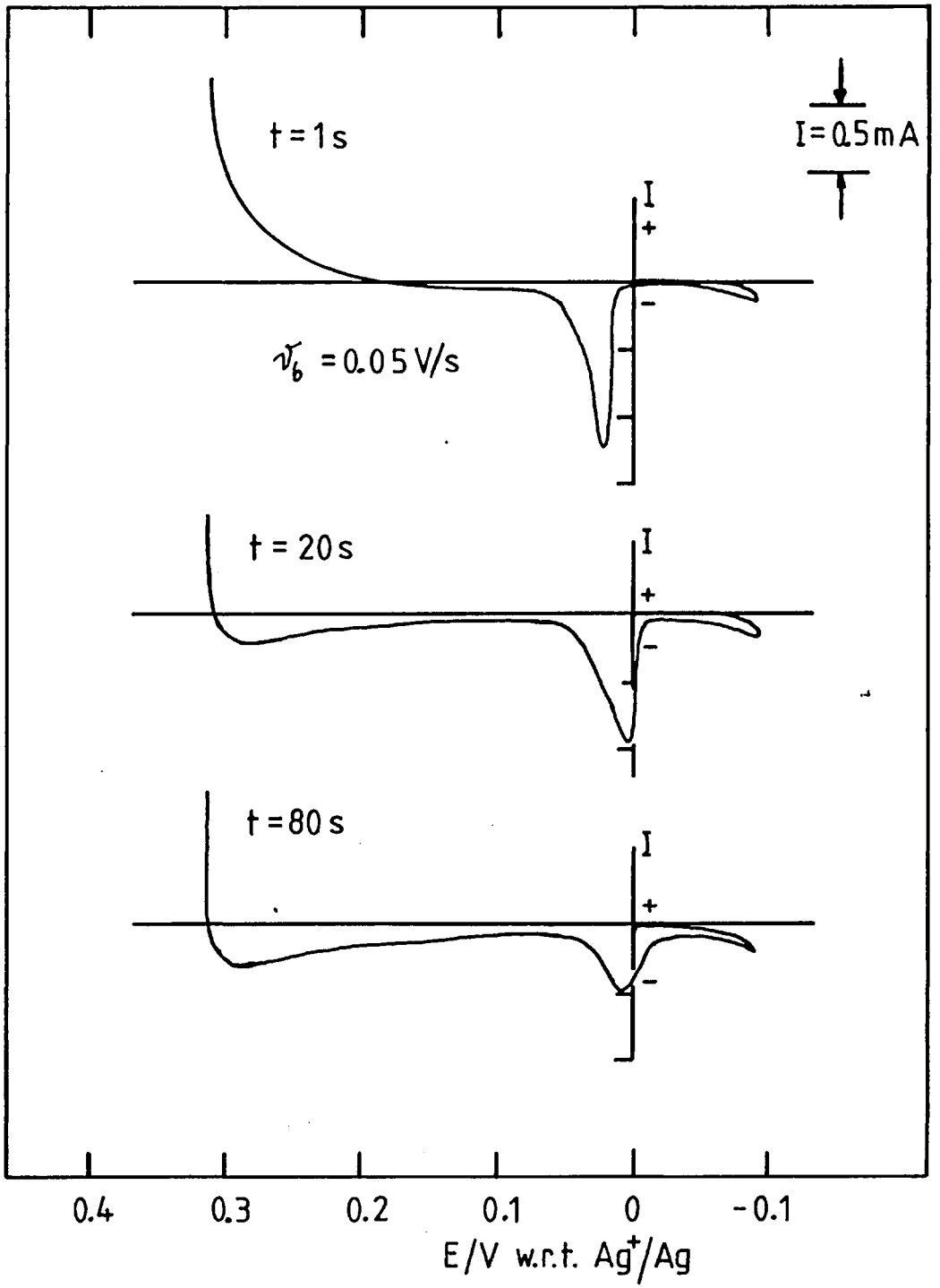


Fig. 6.4.13: The effect of an anodic, controlled potential electrolysis (0.3V) upon the reduction wave for process A. Pt flag electrode (0.2 cm^2). [PbS]M = 1.4213×10^{-2}; T = 417°C.

reduction process, i.e. A', is occurring. However as the electrolysis was continued at the same potential, some reduction product from process B becomes significant. Thus it may be inferred that the potential for the start of process B has shifted cathodic as a result of prolonged electrolysis of process A.

The influence (and interrelation between) of the oxidation process A upon B and vice versa for the reduction sequence may be conveniently studied by voltammetric methods. The effect of concentration and E_λ may be evaluated as functions of sweep rate.

The effect of concentration upon the two processes was evaluated at 5.8141×10^{-3}M and 1.4213×10^{-2}M using an E_λ^a of + 0.5V. Fig. 6.4.14 shows that the ratio of anodic charges $Q^a(A)/Q^a(B)$ increases steadily with increasing sweep rate, although at $\nu \geq 200$ mV/s at the higher concentration the ratio decreases and therefore $Q^a(B)$ becomes more predominant. The total cathodic to anodic charge Q_T^c/Q_T^a gradually increases with increasing sweep rate, the rate of increase being greater at low sweep rates (Fig. 6.4.15). A slightly lower ratio was obtained with increasing concentration. The ratio of the two cathodic charges tends to increase with increasing sweep rate, the rate of increase being greater at the lower concentration and hence $Q^c(A)$ predominates at lower concentrations (see Fig. 6.4.16). This relation is also confirmed by the ratio of the two cathodic current peaks $I_p^c(A)/I_p^c(B)$, Fig. 6.4.17, that is the peak current for process A is more significant and increases more rapidly than $I_p^c(B)$ at the lower concentration.

The influence of increasing E_λ^a upon both reduction processes at a given sweep rate (0.1V/s) is shown in Fig. 6.4.18 and Table 6.4.7. It is observed that upon increasing E_λ^a through the oxidation process B so that more of product B is being formed the reduction wave for process A increases slightly and gradually shifts towards more cathodic potentials. The relation between the total anodic charge Q^a and the individual cathodic charges $Q_c(A)$,

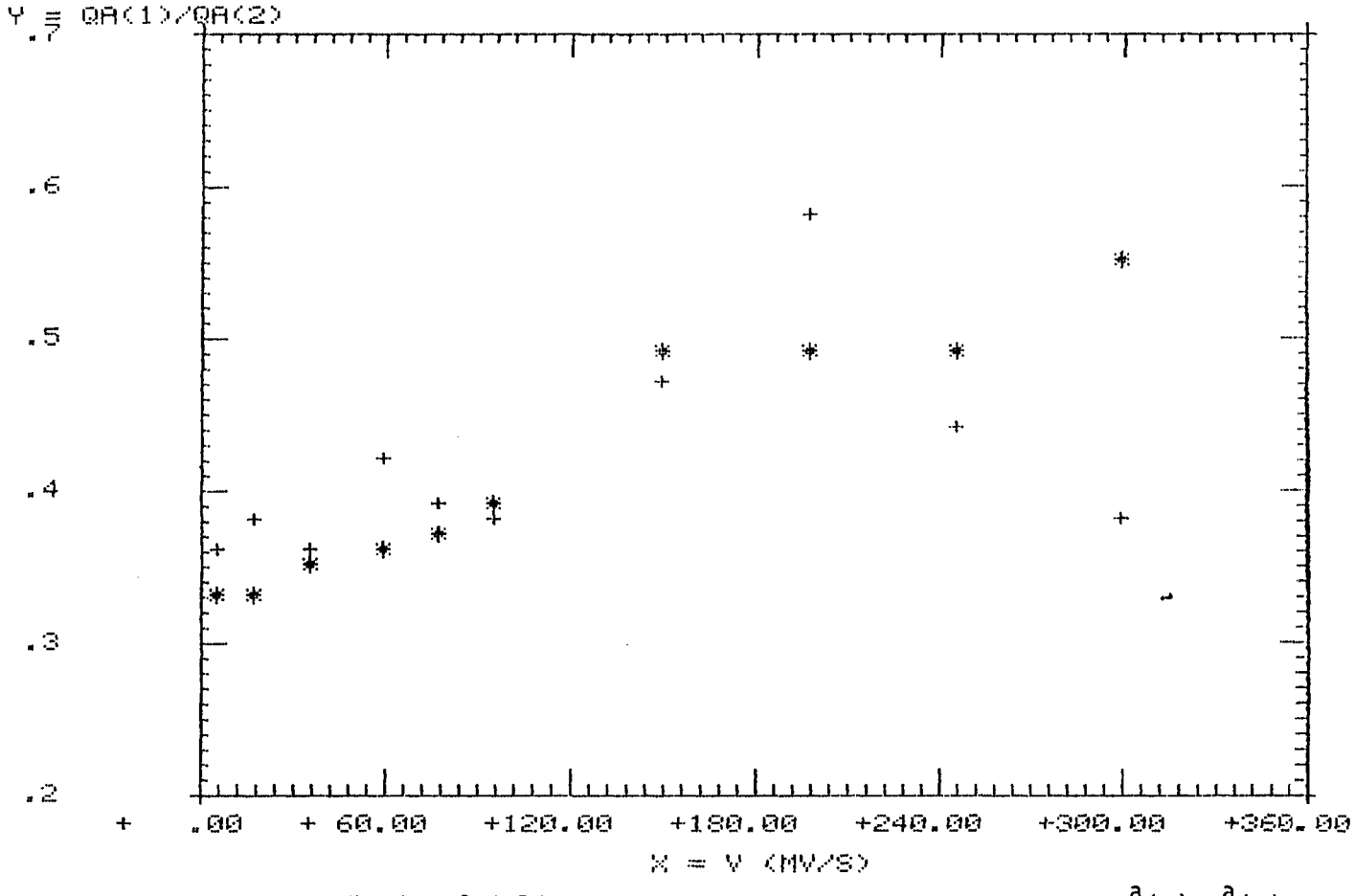


FIGURE NUMBER 6.4.14: A plot of the anodic charge ratio $Q^a(A)/Q^a(B)$ vs sweep rate at PbS concentrations of (*) 5.8141×10^{-3}M; + 1.4213×10^{-2}M. Pt flag electrode (0.2 cm^2). T = 417°C.

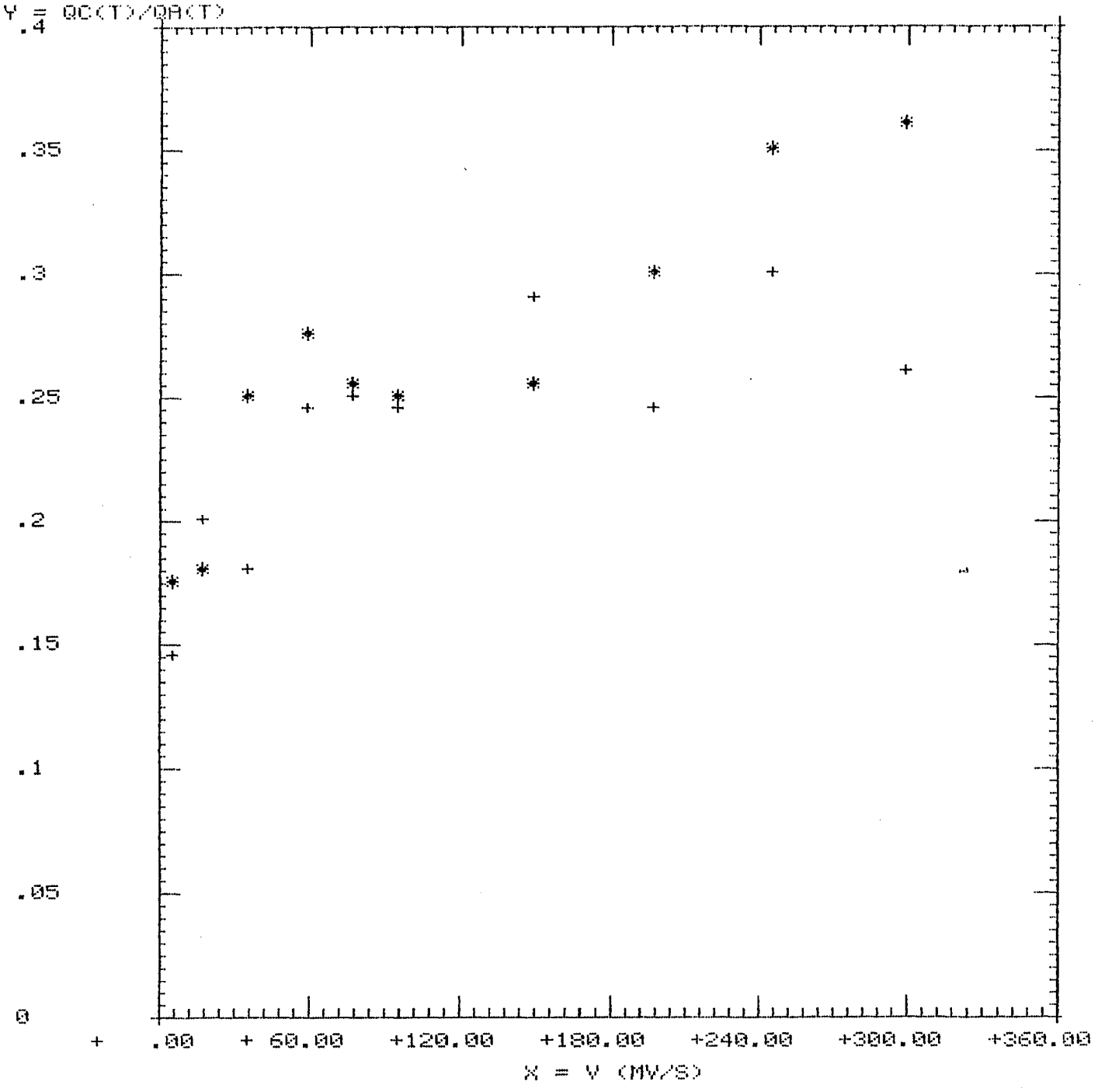


FIGURE NUMBER 6.4.15: A plot of the total cathodic to anodic charge ratio Q_T^c/Q_T^a vs ν at PbS concentrations of (*) 5.8141 x 10^{-2}M; (+) 1.4213 x 10^{-2}M. E_λ^a = 0.5V. Pt flag electrode (0.2 cm^2). T = 417°C.

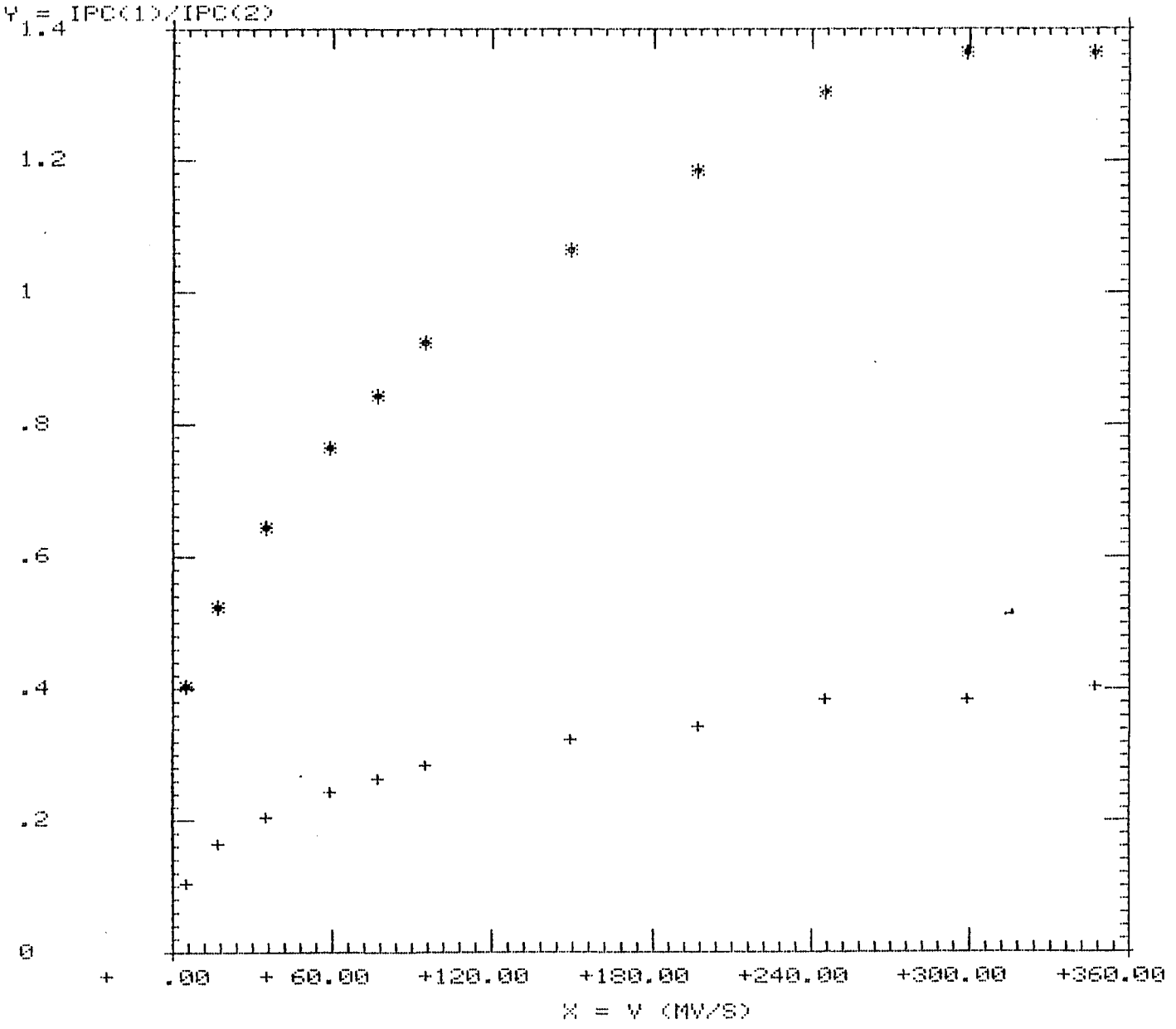


FIGURE NUMBER 6.4.17: A plot of the ratio of the two reduction peak currents $I_p^c(A)/I_p^c(B)$ vs sweep rate at the PbS concentrations of (*) 5.8141×10^{-2}M; (+) 1.4213×10^{-2}M. Pt flag electrode (0.2 cm^2). T = 417°C.

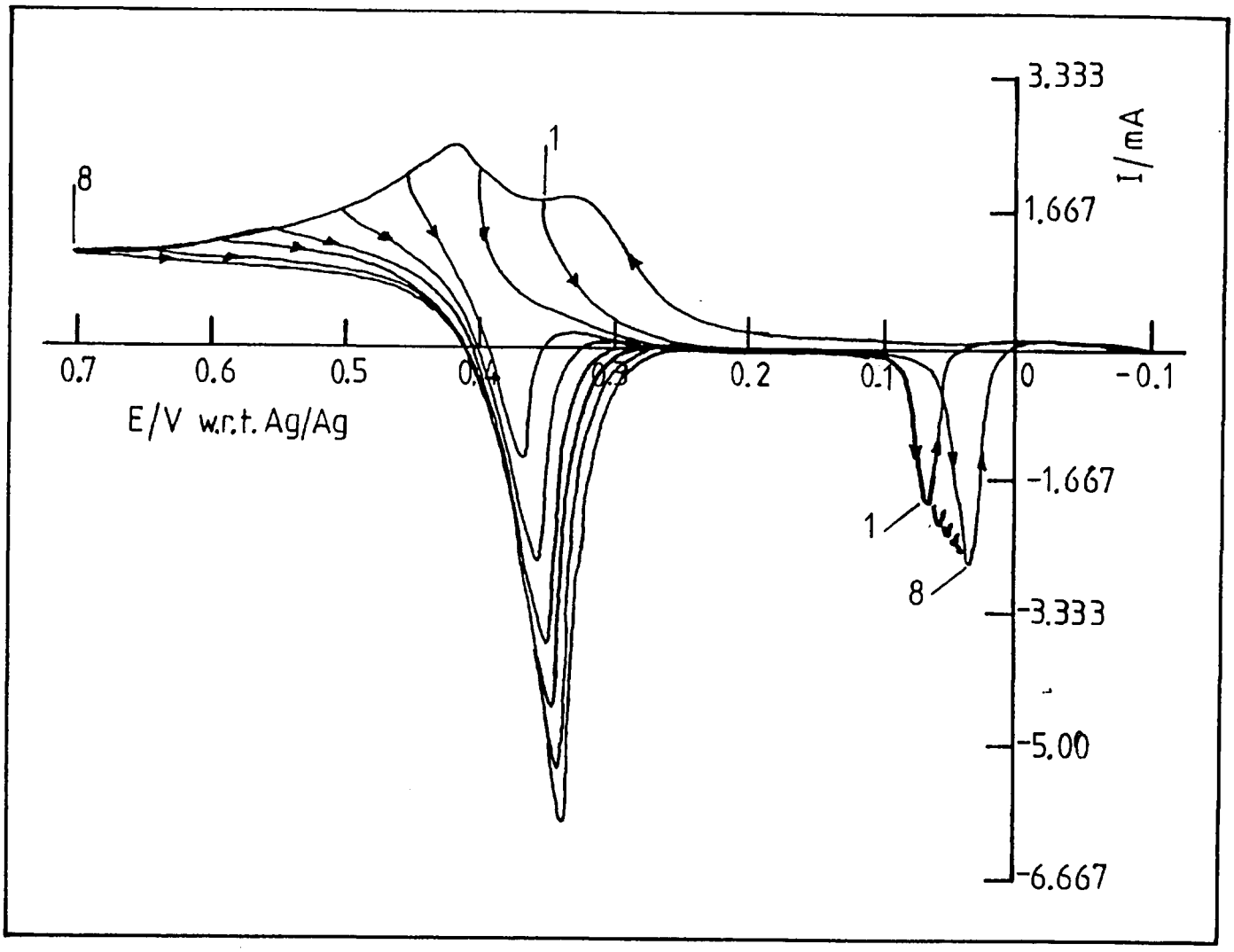


Fig. 6.4.18: The influence of increasing the anodic switching potential upon the reduction waves of process A and B at a sweep rate of 0.1V/s. Pt flag electrode (0.2 cm^2). T = 417°C; [PbS]M = 5.8141 x 10^{-2}.

$Q^c(B)$ and $Q^c(A) + Q^c(B)$ are shown in Fig. 6.4.19. The charge corresponding to $Q^c(A)$ remains virtually constant whereas $Q^c(B)$ increases much more rapidly. The total reduction charge $Q^c(A) + Q^c(B)$ is noted to be much less than Q_T^a the difference becoming larger as E_λ increases.

Table 6.4.7: The effect of the anodic switching potential upon the reduction of sulphur at a Pt electrode. Electrode area = 0.2 cm^2, [PbS] = 5.8141 x 10^{-2}M; T = 417°C.

E_λ V	Q_T^a mC	$I_o^c(A)$ mA	Q^c(A9 mC	$E_p^c(A)$ V	$I_p^c(B)$ mA	$Q^c(B)$ mC	$E_p^c(B)$ V
0.35	1.875	-	0.417	-	2.0	-	0.065
0.4	3.042	-	0.458	-	2.25	-	0.057
0.45	3.958	1.375	0.542	0.367	2.33	0.5	0.05
0.5	5.458	2.708	0.583	0.355	2.458	0.667	0.045
0.55	6.667	3.75	0.583	0.35	2.542	1.5	0.042
0.6	7.875	4.5	0.625	0.345	2.583	1.875	0.039
0.65	8.75	5.29	0.708	0.341	2.625	2.167	0.037
0.7	9.667	5.917	0.750	0.338	2.725	2.625	0.035

In addition to the effect of progressively increasing the anodic switching potential upon the voltammetric parameters at a constant sweep rate a series of experiments were undertaken to determine the overall effect of increasing sweep rate (0.02 - 0.4 V/s) at three different switching potentials, i.e. + 0.5, + 0.6 and + 0.7V. For this series of results the PbS concentration was 5.1814 x 10^{-3}M at 417°C.

Fig. 6.4.20 shows that the ratio of total cathodic to anodic charges Q_T^c/Q_T^a increases with increasing sweep rate and that higher values are obtained at the higher E_λ^a. The peak current for the reduction process A increases linearly with increasing (sweep rate)$^{\frac{1}{2}}$ but more importantly is virtually independent of E_λ^a (Fig. 6.4.21). The cathodic peak current for process B does not, however, increase linearly with $\nu^{\frac{1}{2}}$ and Fig. 6.4.22

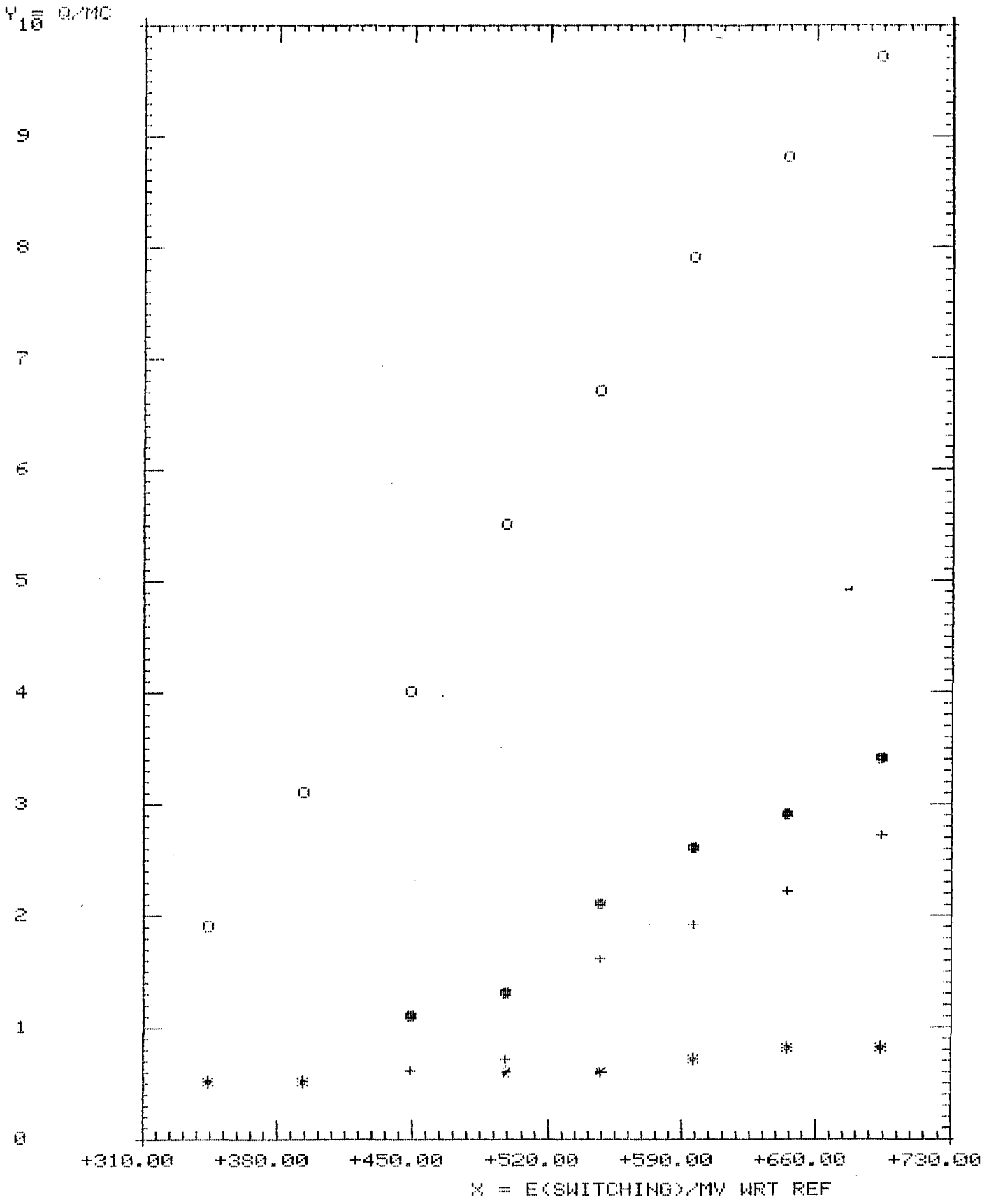


FIGURE NUMBER 6.5.19: A plot of the relation of the reduction charges for processes A (⋆) and B (+) and the total anodic charge Q_T^a(●) with increasing E_λ^a. O = Q^c(A) + Q^c(B). Pt flag electrode (0.2 cm^2); T = 417°C. [PbS]M = 5.8141 x 10^{-2}.

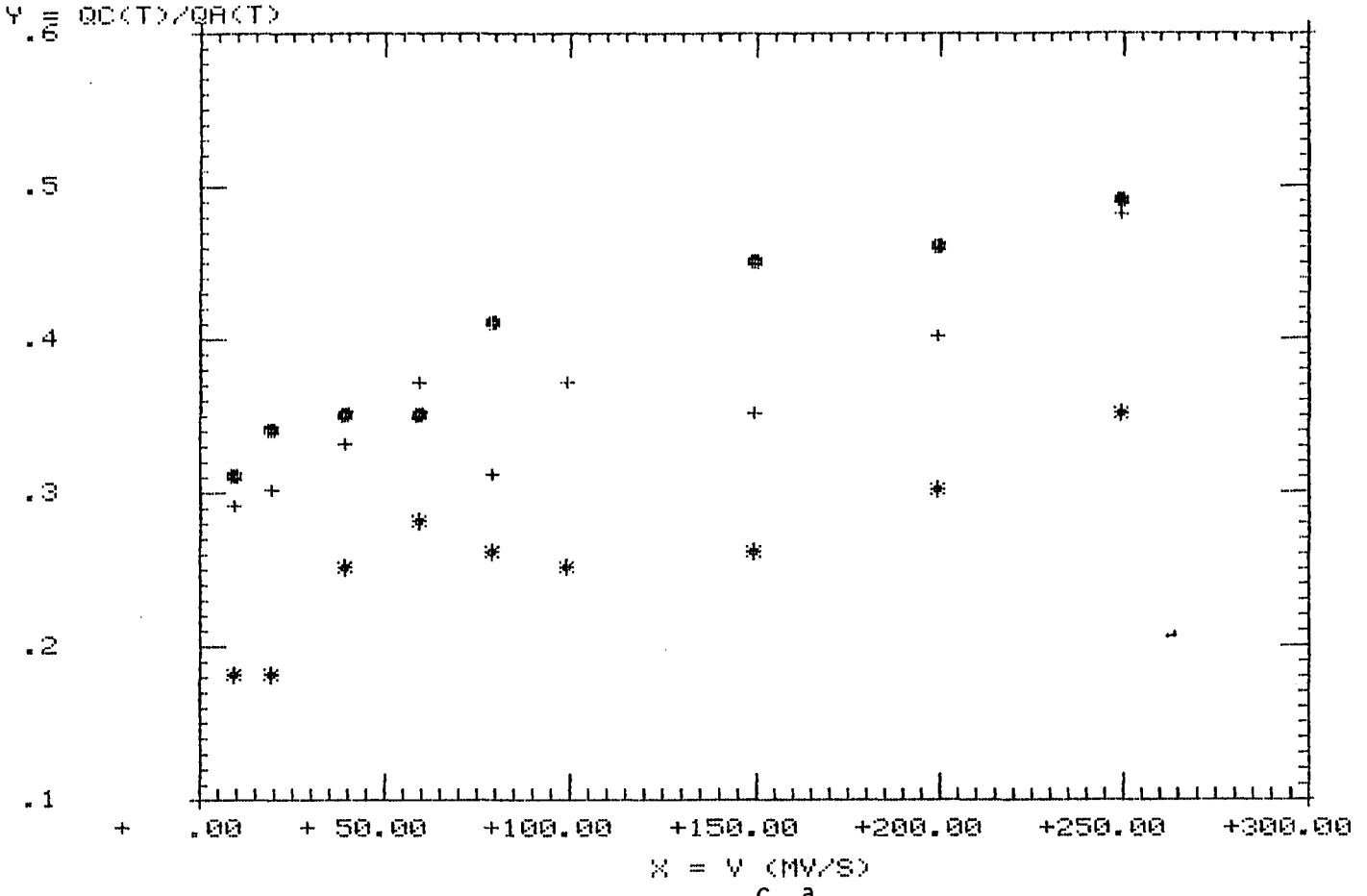


FIGURE NUMBER 6.4.20: A plot of Q_T^c/Q_T^a as a function of increasing sweep rate for various E_λ^a.
(*) 0.5V; (+) 0.6V and (●) 0.7V wrt Ag^+/Ag.
Pt flag electrode (0.2 cm^2). T = 417°C;
PbS = 5.8141 x 10^{-2}M.

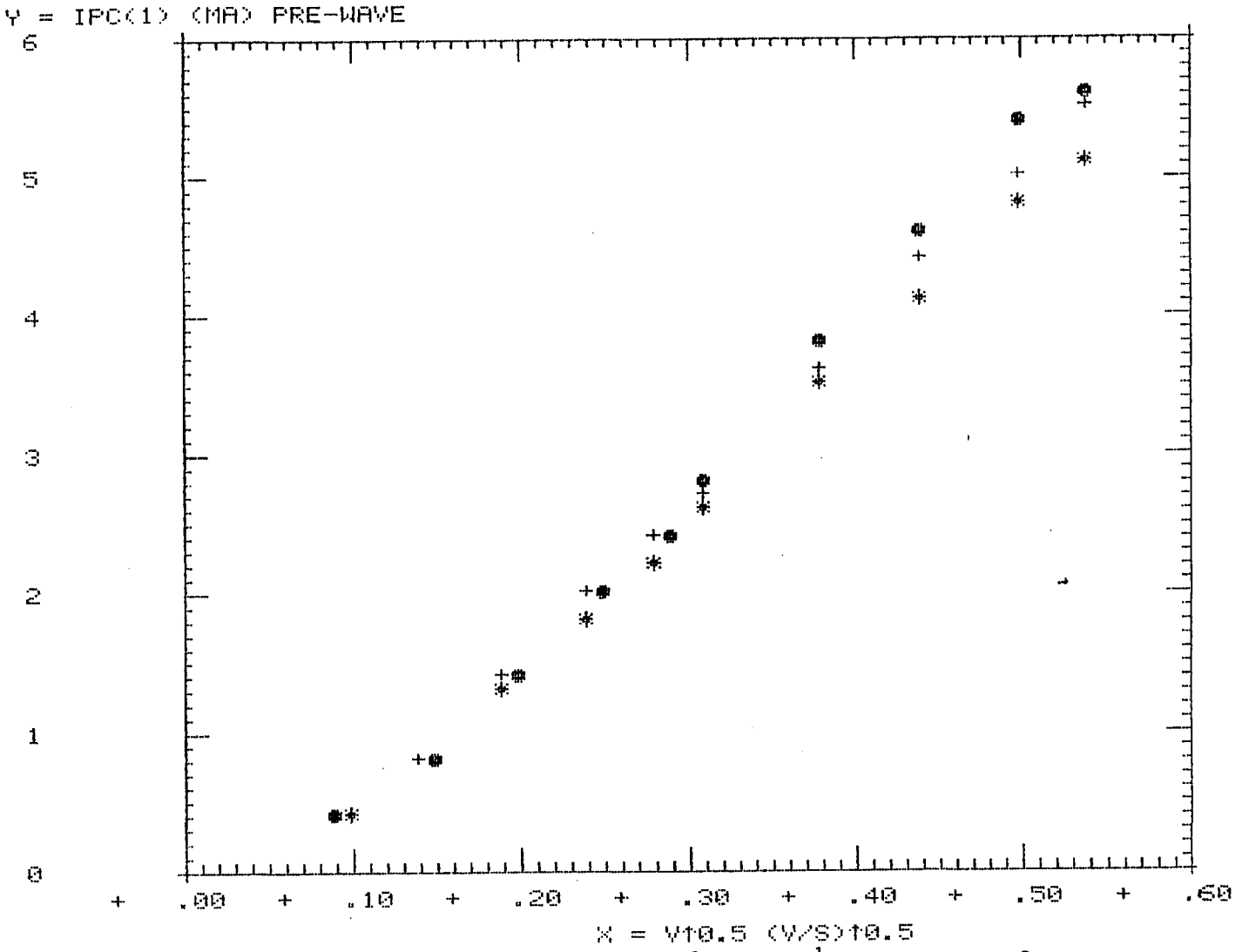


FIGURE NUMBER 6.4.21: A plot of $I_p^c(A)$ vs $\nu^{\frac{1}{2}}$ for various E_λ^a values (*) 0.5V; (+) 0.6V and (●) 0.7V wrt Ag^+/Ag. Pt flag electrode (0.2 cm^2). T = 417°C; [PbS]M = 5.8141 x 10^{-2}.

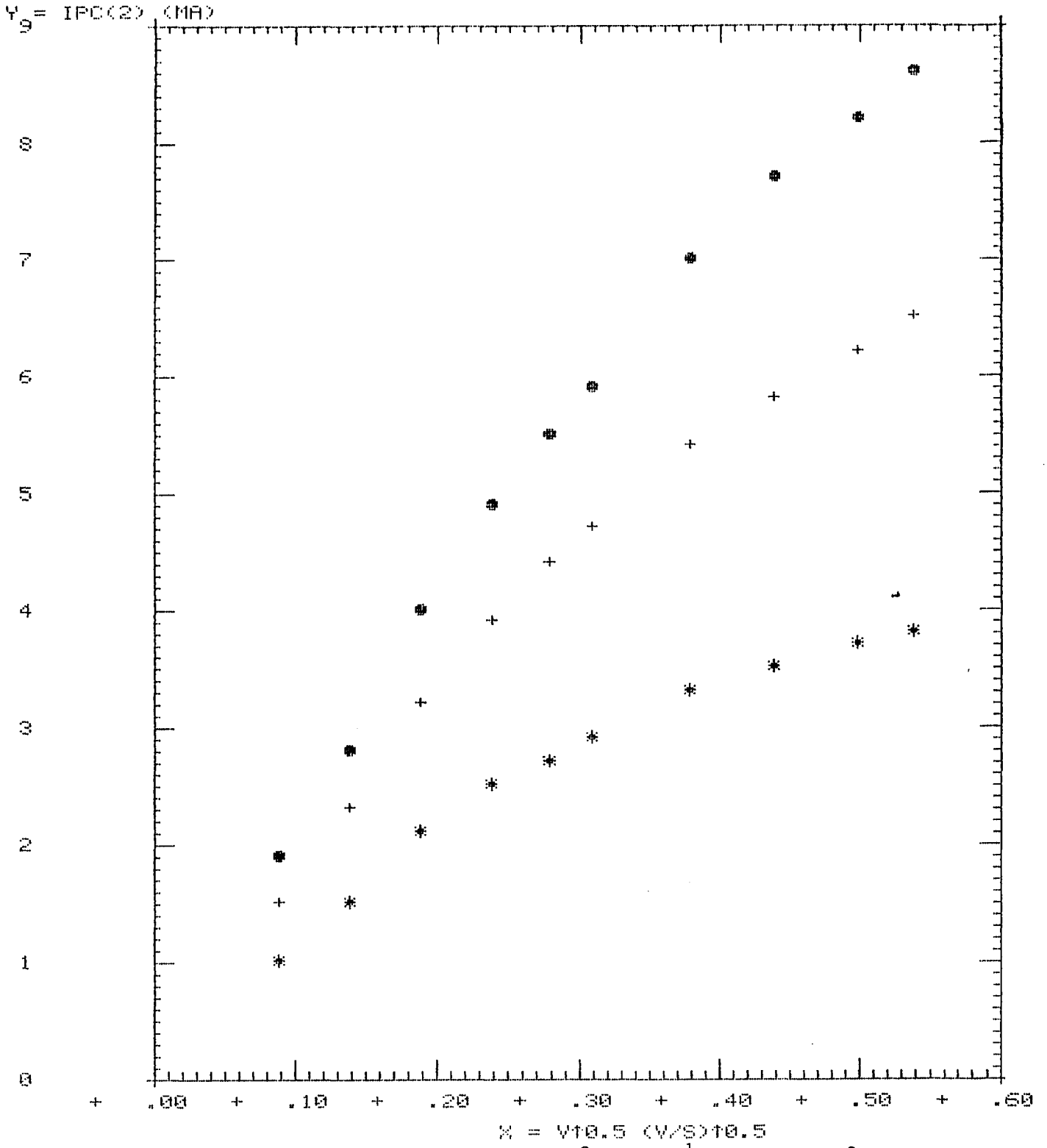


FIGURE NUMBER 6.4.22: A plot of $I_p^c(B)$ vs $\nu^{\frac{1}{2}}$ at various E_λ^a values (*) 0.5V; (+) 0.6V and (●) 0.7V wrt Ag^+/Ag. Pt flag electrode (0.2 cm^2). [PbS] = 5.8141 x 10^{-2}; T = 417°C.

shows that the $I_p^c(B)$ is very dependent upon the anodic switching potential. The combined effect upon both reduction currents is shown in Fig. 6.4.23 from which it is observed that the $I_p^c(A)$ is more prominent at the lower E_λ^a value. The ratio of the reduction charges $Q^c(A)/Q^c(B)$ shows a similar trend (see Fig. 6.4.24) to that of the current ratio.

The influence of temperature (414°C-523°C) upon the oxidation and reduction voltammetric parameters and their inter-relationship was also studied. A solution containing 1.20×10^{-2}M PbS was used. At temperatures greater than 424°C the reduction wave corresponding to process A was no longer observed and could not be re-established by returning the temperature to the lower value. Thus the results given here concern the temperature dependence of the two oxidation processes and the reduction process B. It is also notable that at temperatures $> \sim$430°C the oxidation wave A became less distinct and may be the cause of the scatter obtained at the higher temperatures.

Figs. 6.4.25 and 6.4.26 show that the $I_p^a - \nu^{\frac{1}{2}}$ relations for both oxidation waves is maintained with increasing temperature, and that an increase in I_p^a for a given sweep rate occurs. The reduction current $I_p^c(B)$ shows a decrease with increasing temperature, Fig. 6.4.27. Both oxidation processes show linear Arrhenius type, i.e. linear logI vs 1/T°K behaviour (Fig. 6.4.28). The activation energies for processes A and B were calculated to be 27.1kj/mole and 14.62kj/mole respectively. The influence of increasing temperature upon the charge values is shown in Fig. 6.4.29. Both the total anodic charge Q_T^a and the charge for process B, $Q^a(B)$ increase rapidly with increasing temperature whilst $Q^a(A)$ remains virtually c-nstant. The cathodic charge shows a rapid decline for temperatures 430°C. The effect of temperature upon the charge efficiency is shown in Fig. 6.4.30.

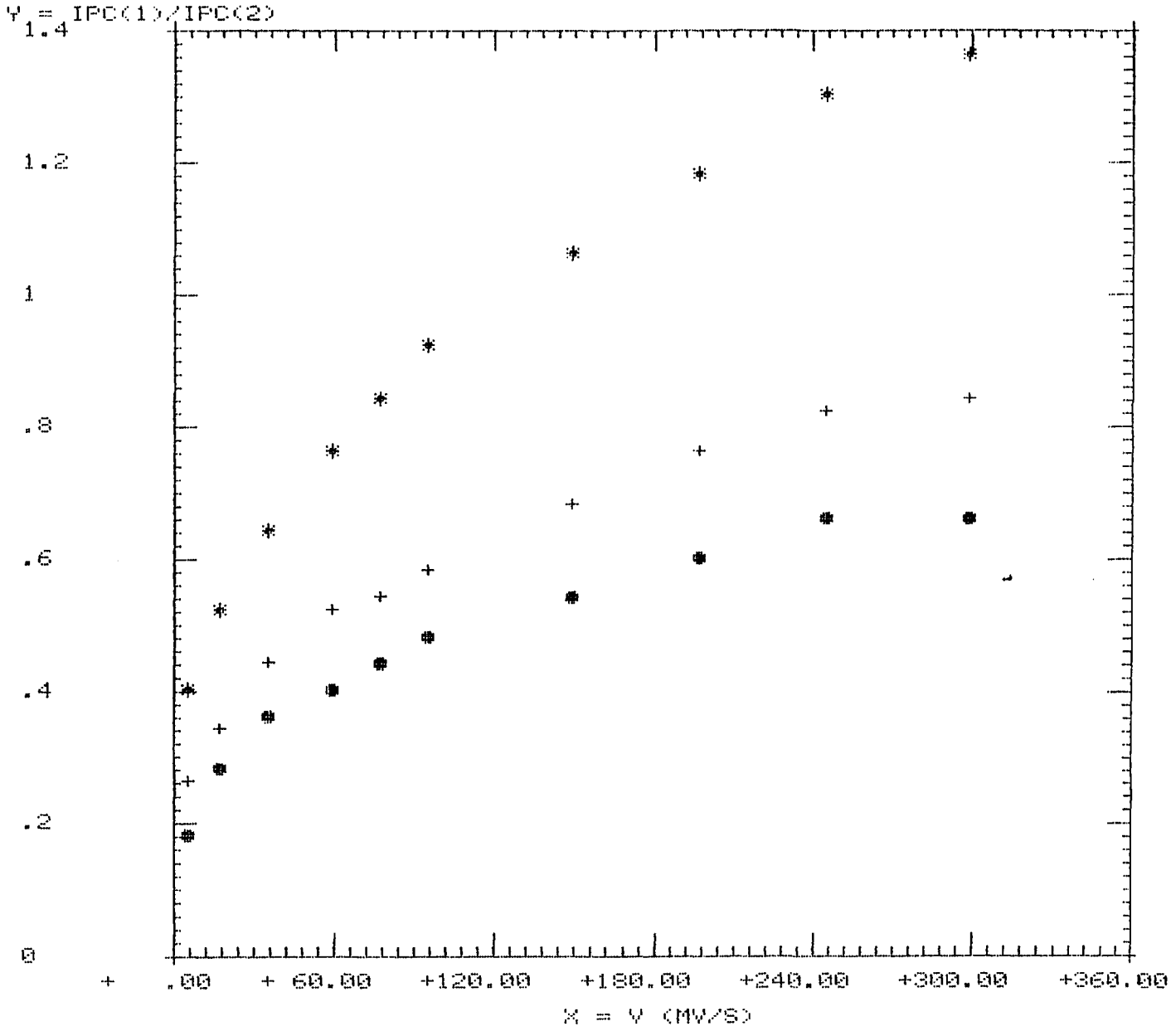


FIGURE NUMBER 6.4.23: The variation of the reduction current ratio $I_p^c(A)/I_p^c(B)$ vs sweep rate for various E_λ^a values (*) 0.5V; (+) 0.6V and (●) 0.7V wrt Ag^+/Ag. Pt flag electrode (0.2 cm^2). T = 417°C; [PbS]M = 5.8141×10^{-2}.

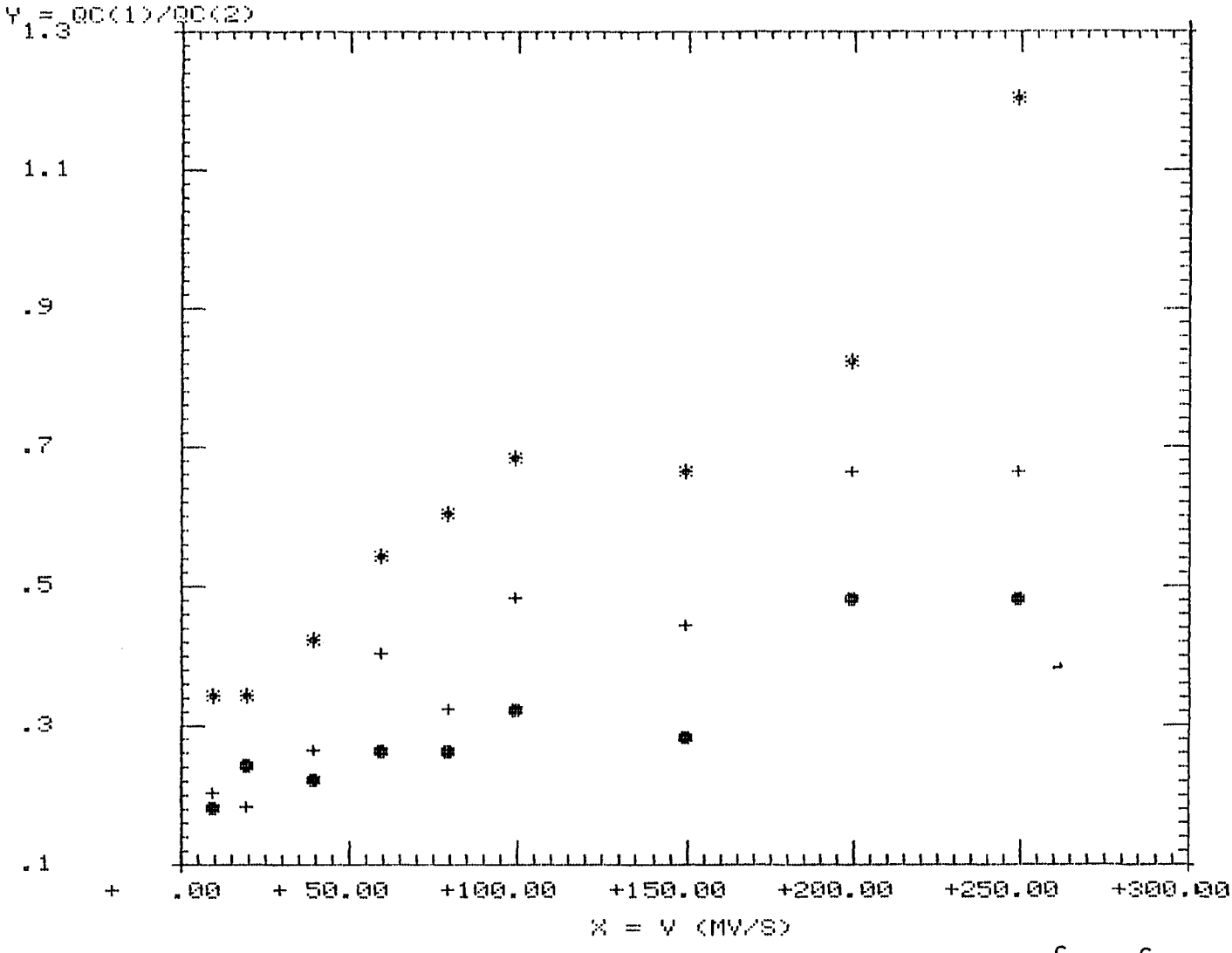


FIGURE NUMBER 6.2.24: A plot of the reduction charge ratio $Q^c(A)/Q^c(B)$ with increasing sweep rate for various E^a_λ values: (*) 0.5V; (+) 0.6V and (●) 0.7V wrt Ag^+/Ag. Pt flag electrode (0.2 cm^2). T = 417°C; [PbS]M = 5.8141×10^{-2}.

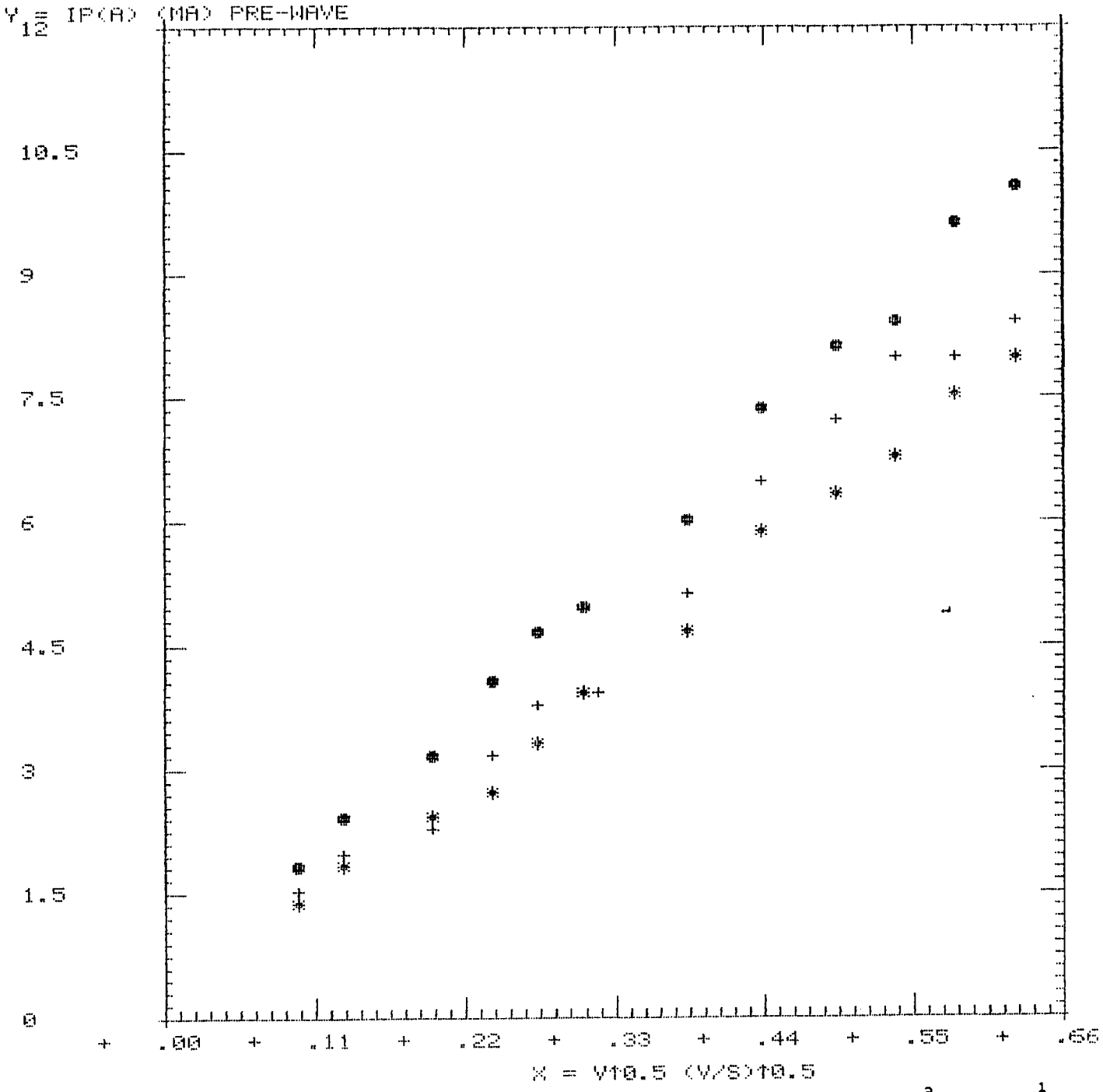


FIGURE NUMBER 6.4.25: The effect of temperature upon the I_p^a(A) vs $\nu^{\frac{1}{2}}$ relation: (*) 414°C; (+) 471°C and (●) 523°C. Pt flag electrode (0.28 cm^2). [PbS]M = 1200 x 10^{-2}.

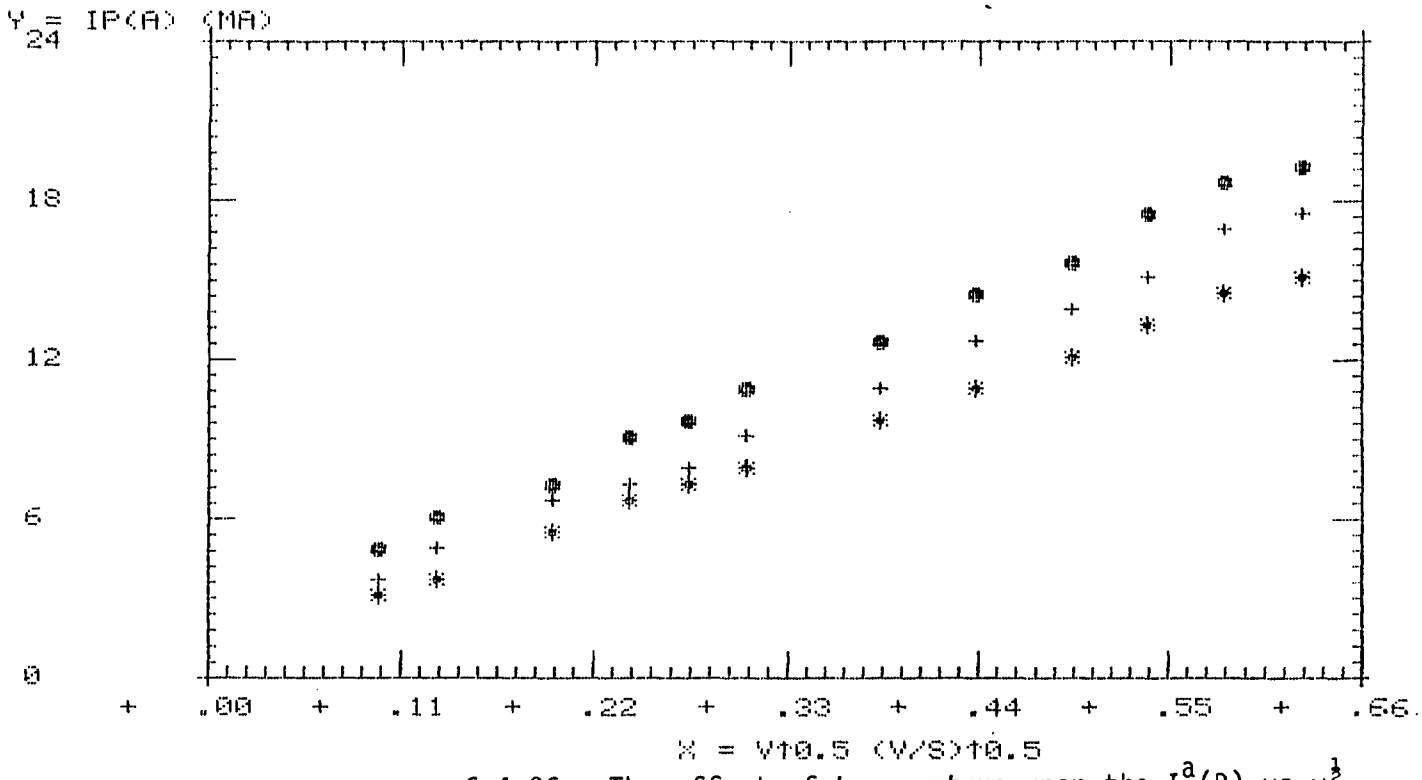


FIGURE NUMBER 6.4.26: The effect of temperature upon the $I_p^a(B)$ vs $\nu^{\frac{1}{2}}$ relation: (*) 414°C; (+) 471°C and (●) 523°C.

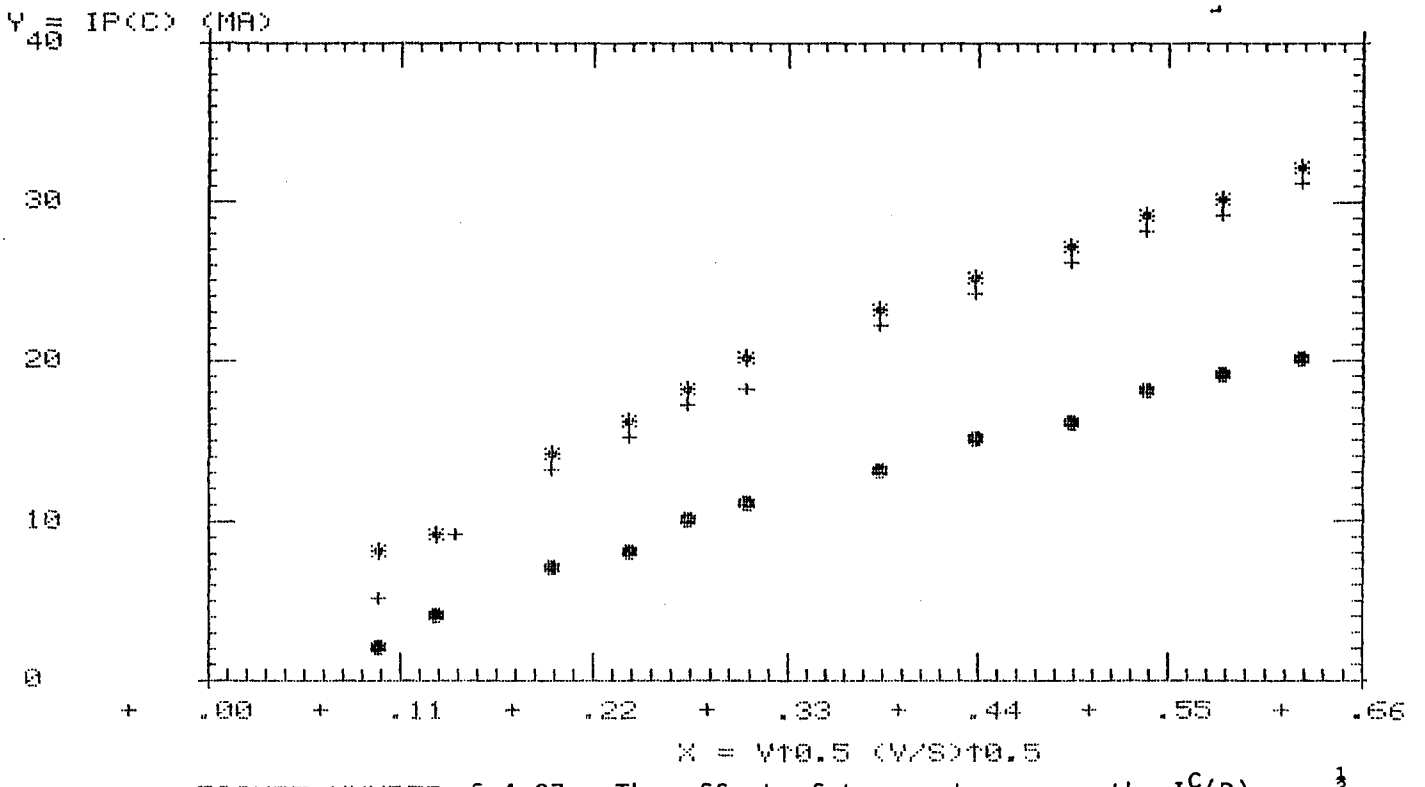


FIGURE NUMBER 6.4.27: The effect of temperature upon the $I_p^c(B)$ vs $\nu^{\frac{1}{2}}$ relation: (*) 414°C; (+) 471°C and (●) 523°C. Pt flag electrode (0.28 cm^2). [PbS]M = 1.200×10^{-2}.

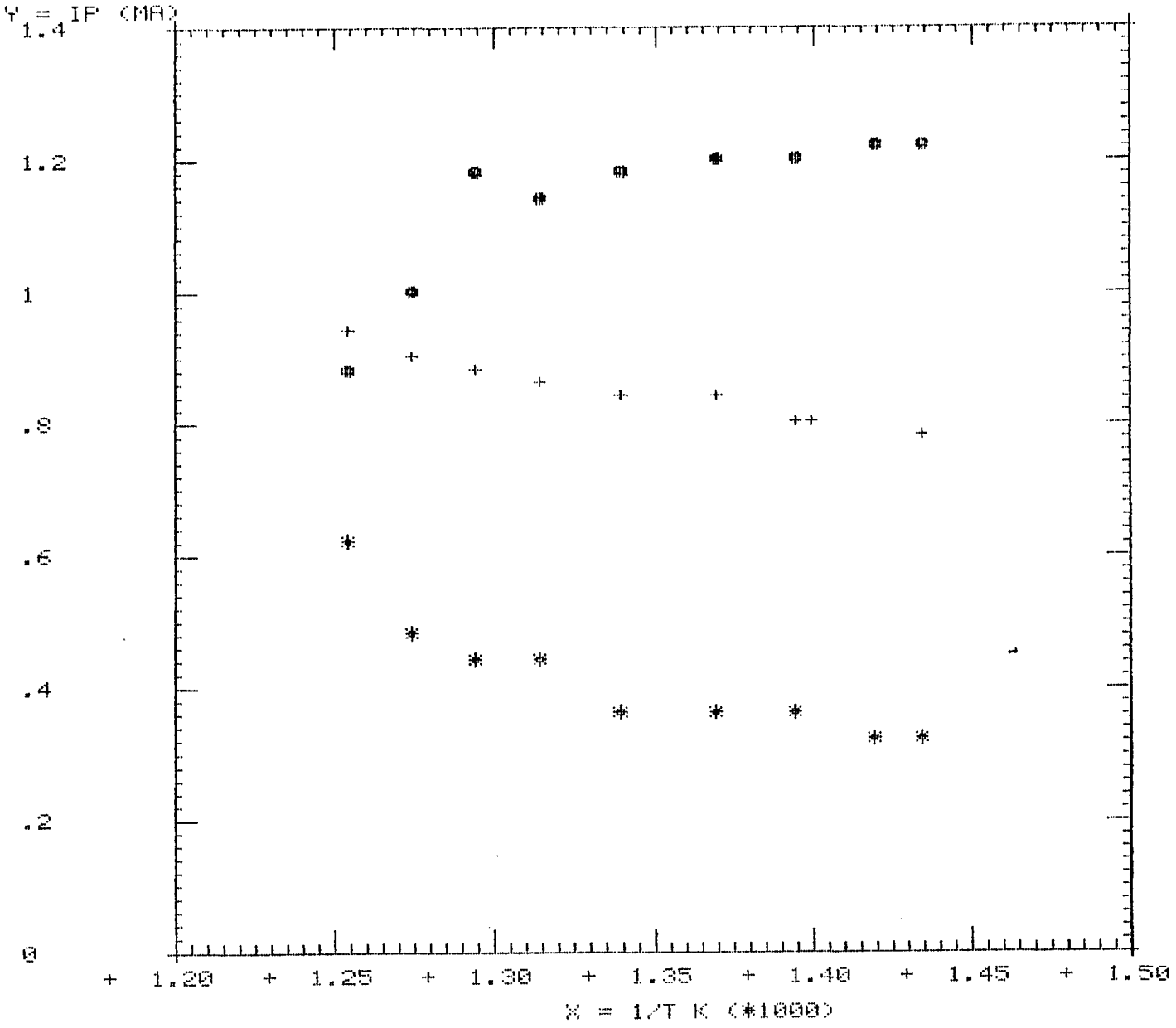


FIGURE NUMBER 6.4.28: An arrhenius plot for the peak currents I_p^a(A) *; I_p^a(B) + and I_p^c(B) ●. Pt flag electrode (0.28 cm^2). [PbS]M = 1.200 x 10^{-2}.

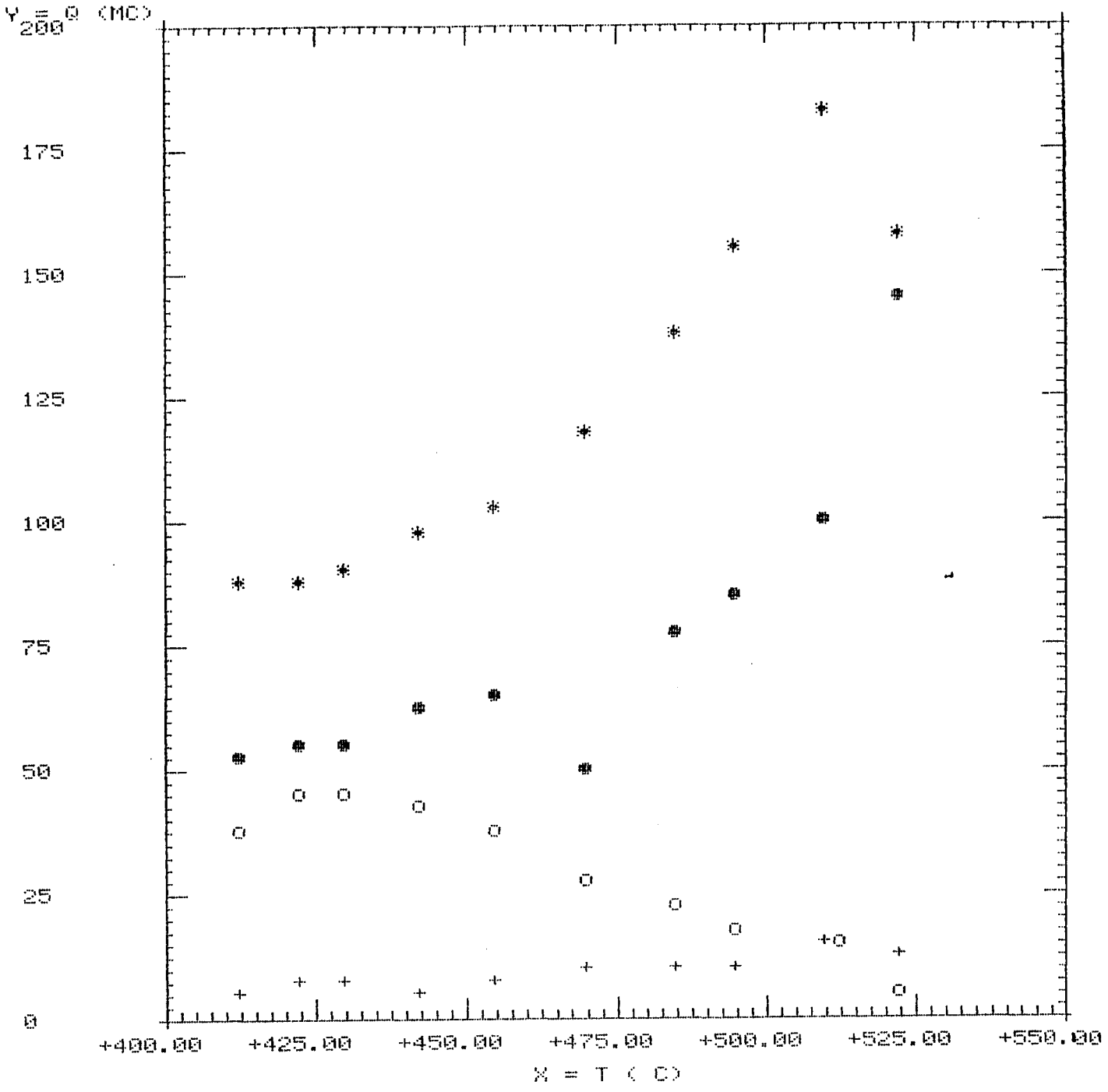


FIGURE NUMBER 6.4.29: A plot of the various voltammetric charges as a function of increasing temperature: (+) $Q^a(A)$; ● $Q^a(B)$; (*) Q_T^a; O $Q^c(B)$.

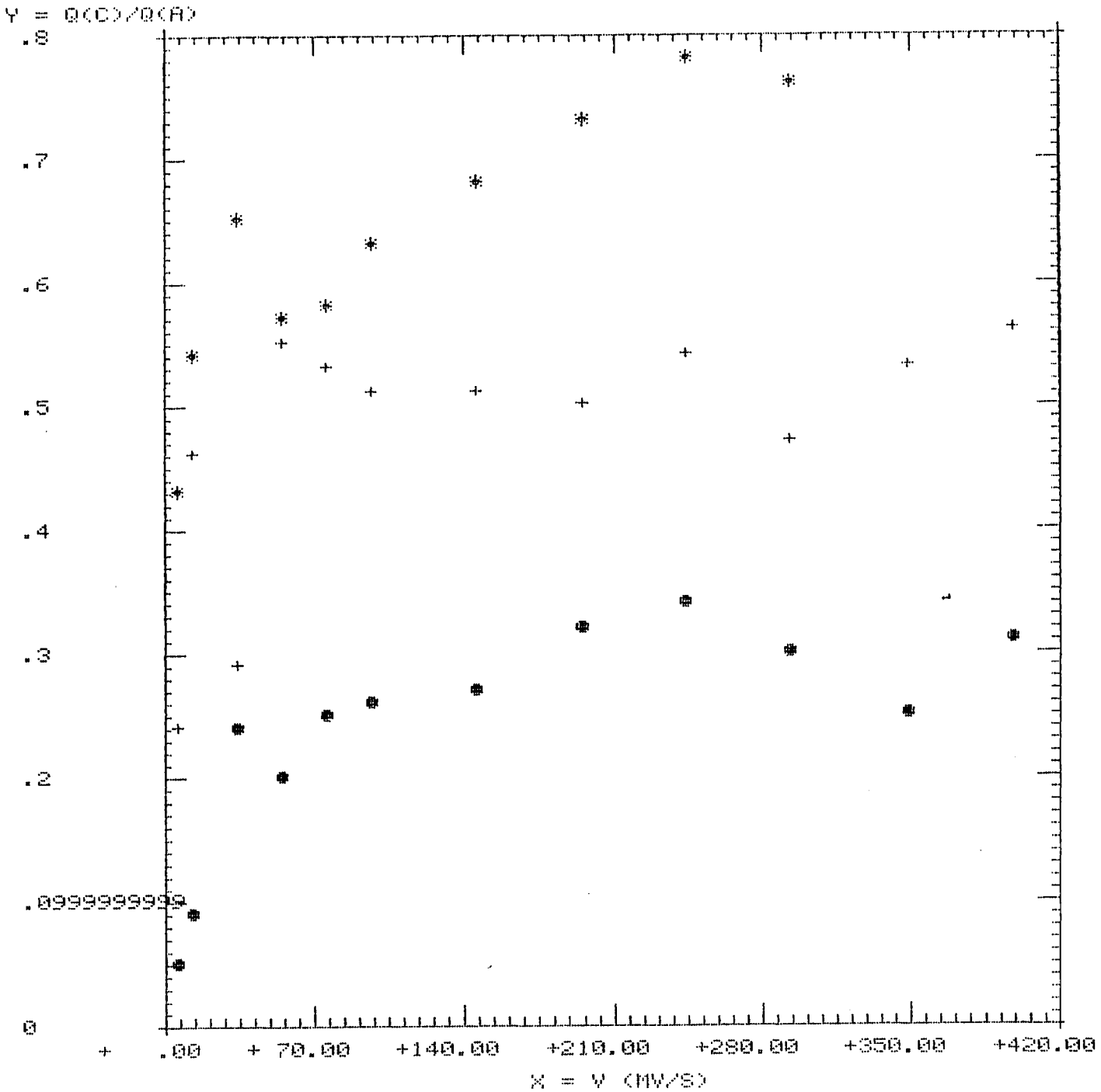


FIGURE NUMBER 6.4.30: The effect of increaisng temperature upon the charge efficiency Q_T^c/Q_T^a.
(*) 414°C; (+) 472°C; and (●) 523°C.

6.4.2 Chronoamperometry

The I-t transients obtained for both anodic processes exhibited typical diffusion-controlled behaviour, i.e. linear $I\text{-}t^{-\frac{1}{2}}$ plots, Fig. 6.4.31. Transients that could be attributed to nucleation and growth phenomenon were not obtained under any conditions of applied potential, time or temperature.

6.4.3 Chronopotentiometry

E-t transients were obtained to determine if any significant adsorption process(es) was occurring. Chronopotentiograms were recorded as a function of current density over the PbS concentration range 1.20 - 7.391×10^{-2}M and over the temperature range 410°C to 520°C. Fig. 6.4.32 shows a typical transient obtained in which two oxidation processes occur (see below). The influence of increasing current density upon the main transition time τ_2 and the effect of PbS concentration is shown in Fig. 6.4.33. It is observed that Sand's plot is linear with an extrapolated zero intercept. The more sensitive plot of $i\tau$ vs $\tau^{\frac{1}{2}}$ similarly exhibits a zero intercept at all PbS concentrations (Fig. 6.4.34) and temperatures (Fig. 6.4.35) employed.

Upon close inspection of the initial portion of the E-t transient, particularly those obtained at low current densities, i.e. τ, a further transition may be discerned (τ_1). Unfortunately analytically useful information for this wave and its relation to τ_2 with, for example, increasing current density was not observed due to its low resolution. The presence of τ_1 was, however, noted to be more prominent at the lowest concentration used. However an estimate of the relation between the two transition times was obtained, i.e. $\tau_2 = 7.375\tau_1$. A ratio of the two n values for the oxidation processes may be obtained from the relation (20):

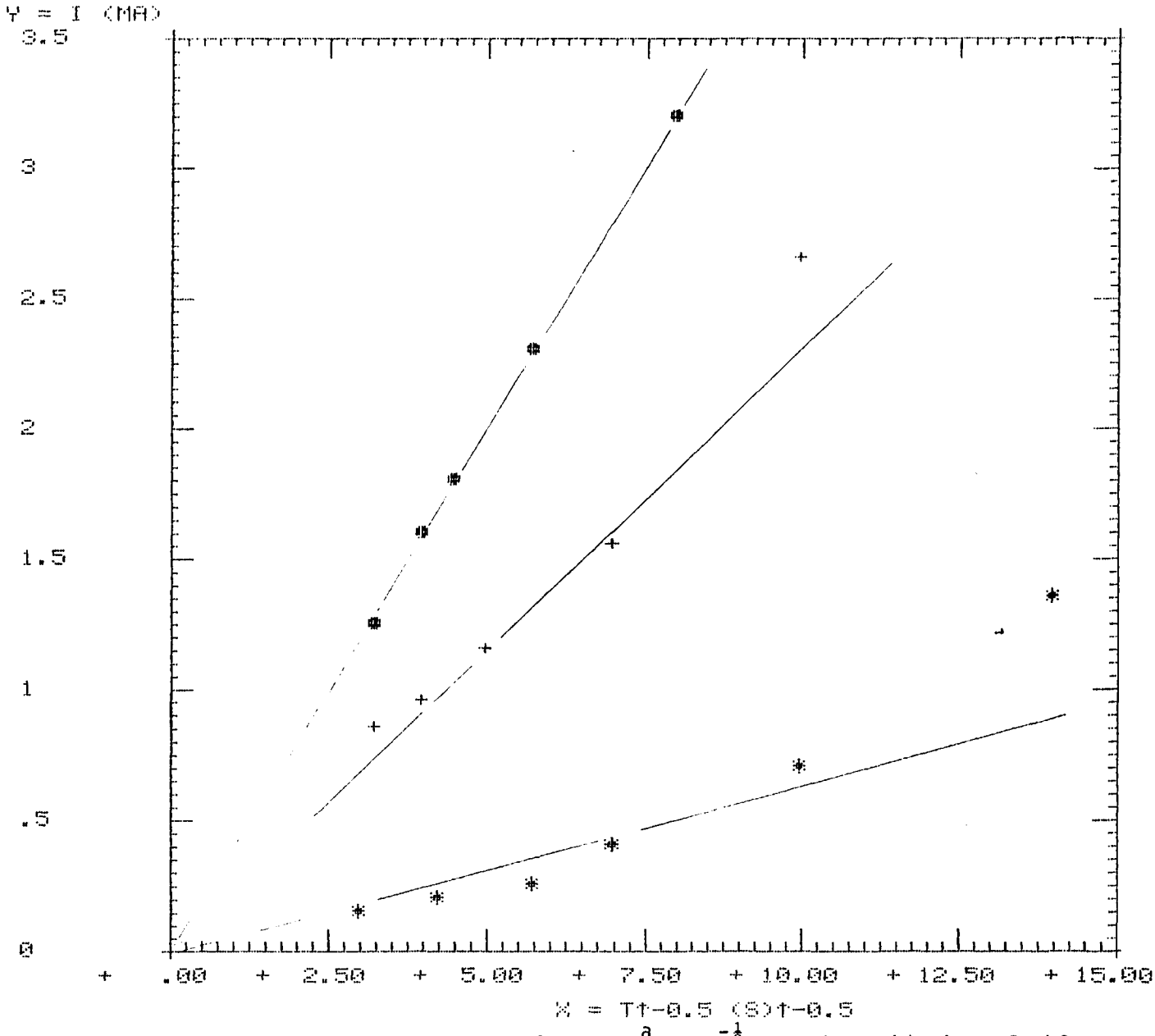


FIGURE NUMBER 6.4.31: A plot of I^a vs $t^{-\frac{1}{2}}$ for the oxidation of PbS at a Pt flag electrode.

* E = 0.2V; + E = 0.31V; ● E = 0.35V w.r.t. Ref.

Solvent $PbCl_2$-KCl-NaCl, T = 417°C; area = 0.72 cm^2. [PbS]M = 1.200 x 10^{-2}.

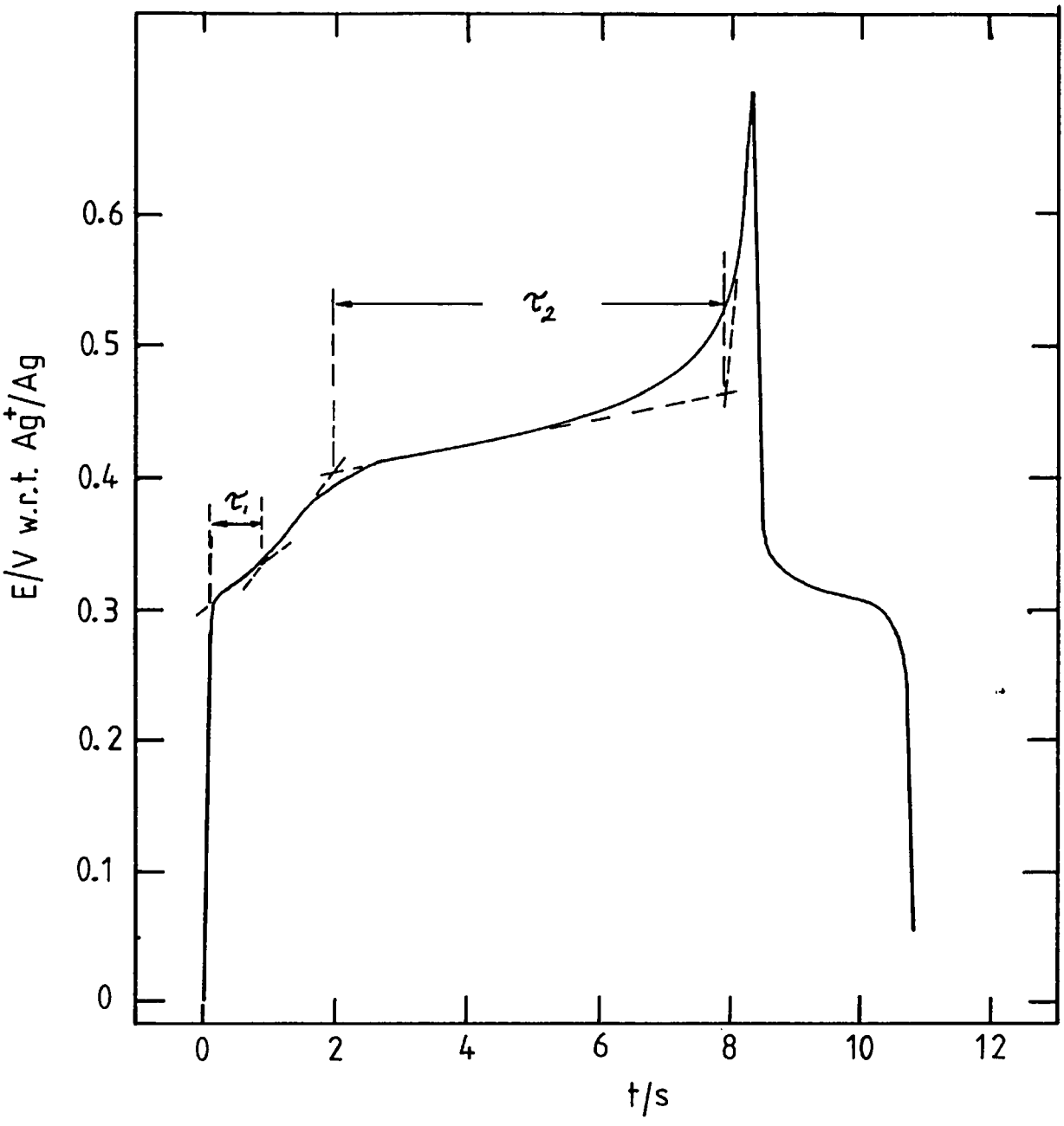


Fig. 6.4.32: A typical chronopotentiogram obtained for the oxidation of PbS in the $PbCl_2$-KCl-NaCl eutectic melt of 417°C. Electrode: Pt flag (area 0.72 cm^2). [Pbs]M = 1.200×10^{-2}; I = 2.95 mA.

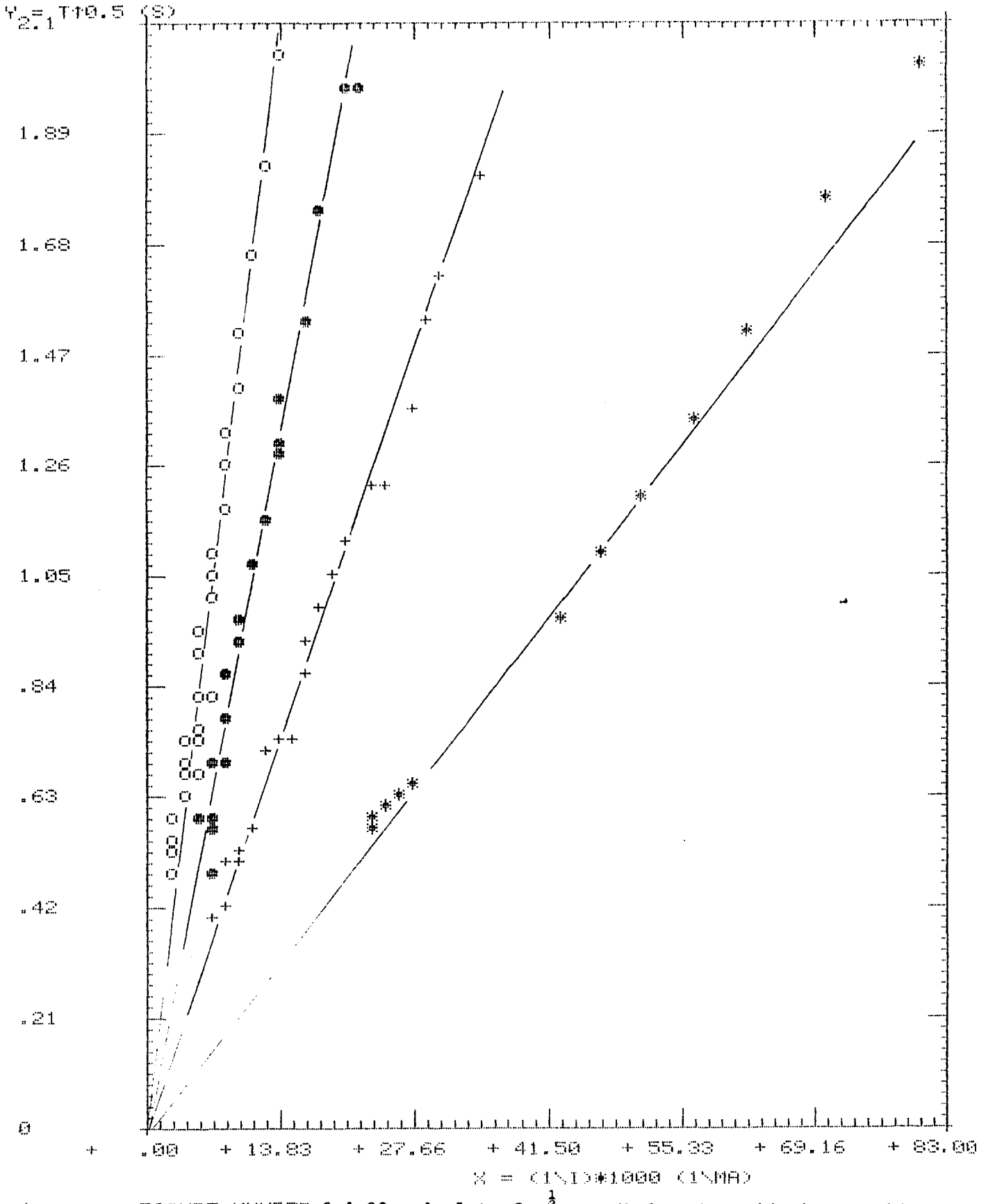


FIGURE NUMBER 6.4.33: A plot of $\tau^{\frac{1}{2}}$ vs I/I for the oxidation of PbS at a Pt electrode in the $PbCl_2$-KCl-NaCl eutectic at 417°C electrode area = 0.72 cm^{-2}. [PbS]M:- *1.20×10^{-2}; + 2.728×10^{-2}; ● 4.463×10^{-2}; O 7.391×10^{-2}.

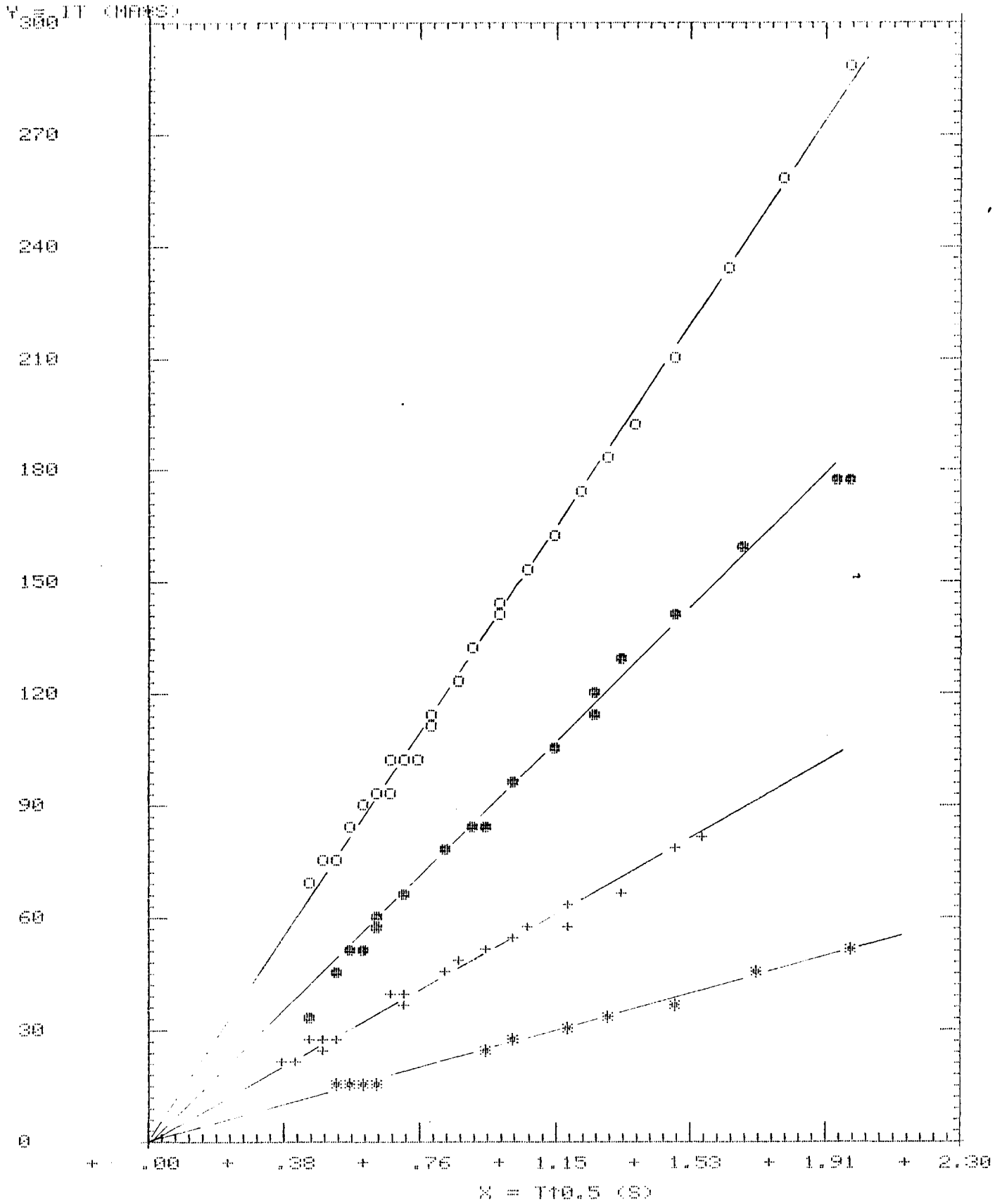


FIGURE NUMBER 6.3.34: A plot of $I\tau$ vs $\tau^{\frac{1}{2}}$ for the oxidation of PbS at a Pt flag electrode in the $PbCl_2$-KCl-NaCl ternary melt at 417°C. Area = 0.72 cm^2; [PbS]M:- *1.200×10^{-2} + 2.728×10^{-2}; ● 4.463×10^{-2}; O 7.39×10^{-2}.

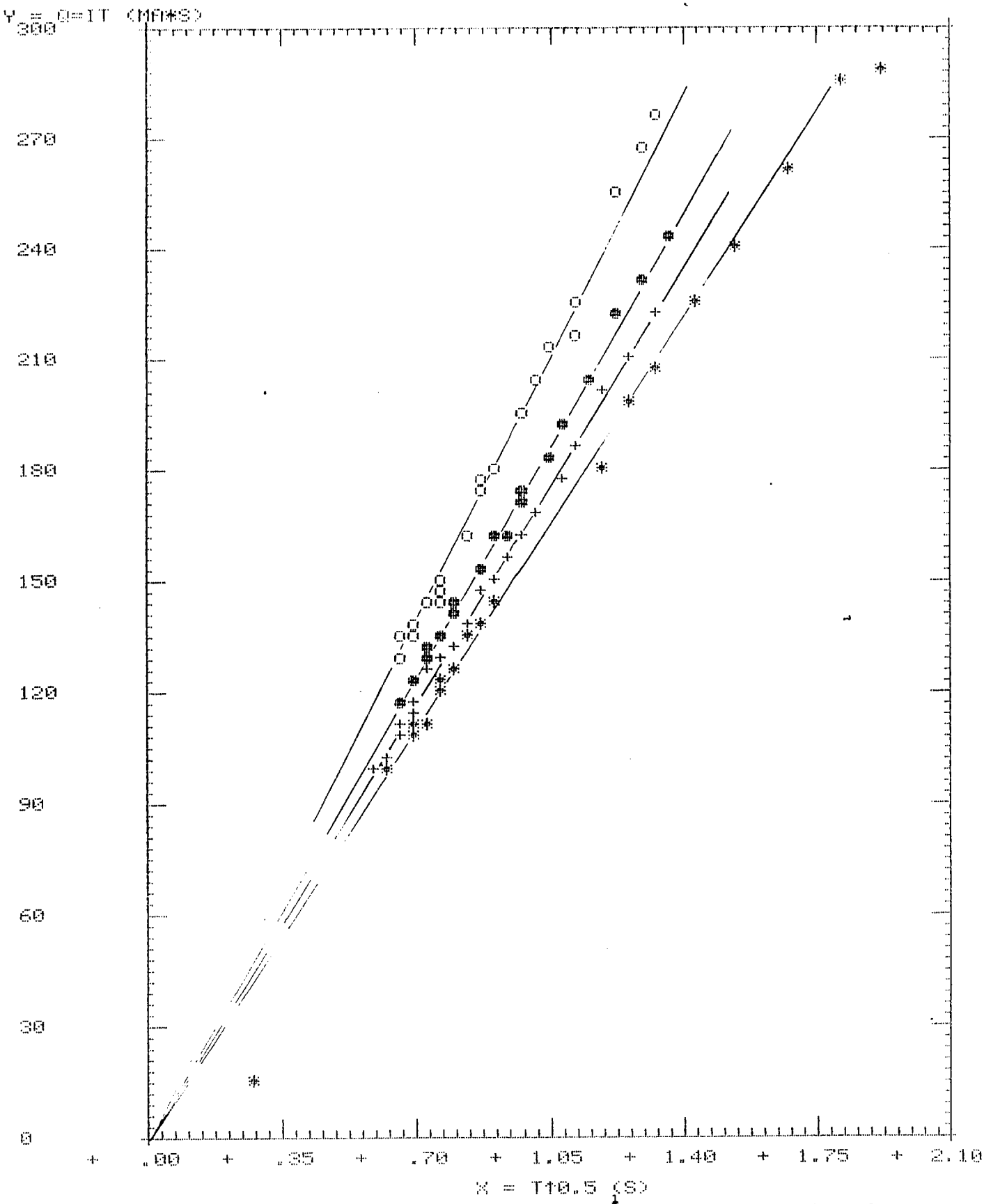


FIGURE NUMBER 6.4.35: A plot of $I\tau$ vs $\tau^{\frac{1}{2}}$ for the oxidisation of PbS at a Pt electrode at various temperatures. Solvent = $PbCl_2$-KCl-NaCl: area = 0.72 cm^2; * 431°C; + 450°C; ● 464°C; O 487°C.

$$\tau_1 \left[\left(\frac{n_1 + n_2}{n_1}\right)^2 - 1\right] = \tau_2$$

from which

$$\left(\frac{n_1 + n_2}{n_1}\right)^{"} = 8.375$$

Thus with a $n_1/n_2 = 0.5$, a $\tau_2/\tau = 8.0$ is predicted, which is very close to the observed value considering the low resolution of τ_1.

6.5 Discussion

The results obtained for the oxidation of the sulphide ion will be discussed in two parts. Firstly the results obtained at the carbon based electrodes which may be considered to be inert electrodes, and secondly the results obtained at the metal electrodes gold and platinum will be discussed. In contrast to that of the carbon-based electrodes the reactivity of gold and platinum with sulphur may lead to the formation of semiconducting films of PtS and AuS, the ease of formation being given by the thermodynamic free energy (ΔG) values. The calculated ΔG values for the formation of PtS, PtS_2 and AuS from the data provided by Mills (67) for a temperature of 450°C are given below:

$$Pt(s) + \tfrac{1}{2}S_2(g) \rightleftharpoons PtS(s) \qquad \Delta G^\circ = -17.86 \text{ Kcal/mole}$$

$$Pt(s) + S_2(g) \rightleftharpoons PtS_2(s) \qquad \Delta G^\circ = -23.42 \text{ Kcal/mole}$$

$$PtS(s) + \tfrac{1}{2}S_2(g) \rightleftharpoons PtS_2(s) \qquad \Delta G^\circ = -5.56 \text{ Kcal/mole}$$

$$Au(s) + \tfrac{1}{2}S_2(g) \rightleftharpoons AuS(g) \qquad \Delta G = +52.97 \text{ Kcal/mole}$$

The above values indicate that the formation of platimum sulphides may readily occur and this is indeed substantiated from electrochemical studies (177). The formation of AuS is however thermodynamically unfavourable according to Mills (67); no solid gold sulphides have been reported in the literature, although AuS species have been detected in mass spectroscopy

studies. However it may be reasonable to suggest the formation of AuS intermediates at an electrode surface during an electrochemical perturbation.

Prior to discussing the results in detail it is of interest to comment upon the effect of a post-chemical dissolution reaction upon the voltammetric response. There is strong evidence in the literature to suggest that electrogenerated sulphur may react with the sulphide ion to form electroactive polymeric sulphide species (170) according to the general reaction scheme

$$S_n + S^{2-} \rightarrow S^{2-}_{n+1}$$

Skylas and Welch, for example, have given some evidence for this reaction in a $PbCl_2$-KCl melt (189) as has Weaver in the LiCl-KCl melt (177) in which sulphur itself is known to be insoluble (176). If a dissolution reaction occurs then the following voltammetric behaviour may be expected:

(a) $Q_A > Q_C$ for the formation of the initial surface sulphur (sulphide) film, and it may be afunction of the sweep rate ν, and the anodic switching potential E^a_λ. At high ν, Q_C may tend to become equal to Q_A if the dissolving species have insufficient time to diffuse appreciably into the solution. At low sweep rate however, Q_A will generally tend to be greater than Q_C.

(b) When Q_C/Q_A is measured as a function of E^a_λ, $Q_C/Q_A = 1$ in the double layer region or if the sulphur (sulphide) film formed is virtually insoluble in the solution. At intermediate potentials $Q_C/Q_A < 1$ if the film formation is followed by a dissolution reaction.

(c) The formation of a soluble electroactive species may result in additional reduction waves in the return

scan. The chemical stability of these species determines the scan rate at which the extra waves may be observed.

However the predicted response of (a) and (b) above may also occur as a result of the physical removal of the film by, for example, a physical dissolution process.

Carbon

The cyclic voltammetric results for S^{2-} oxidation and reduction of carbon-based electrodes has indicated a single main process to occur. At low PbS concentrations the position on the potential axis was the same as that obtained using the $PbCl_2$-KCl melt and may therefore be attributed to the same overall reaction, i.e.

$$S^{2-} \rightarrow S + 2e$$

The absence of any additional reduction waves indicates that the sulphur product does not back react with the S^{2-} present in solution to form reducible polysulphide species. This observation is in contrast to those results obtained by Skylas and Welch (189) for the $PbCl_2$-NaCl melt.

The results obtained show that the oxidation of S^{2-} is diffusion-controlled. This is substantiated from the linear I_p^a-$\nu^{\frac{1}{2}}$ plots (Fig. 5.24), linear I_p^a-$t^{-\frac{1}{2}}$ chronoamperometric plots and, under galvanostatic conditions, by the applicability of Sand's equation, i.e. linear $\tau^{\frac{1}{2}}$ vs 1/I plots, Figs. 5.2.15 and 5.2.17. The more sensitive galvanostatic $i\tau$ vs i plots were found to be linear (Figs. 5.2.16 and 5.2.18) with extrapolated zero intercepts at both vitreous carbon and graphite electrodes thus inferring the absence of any adsorption process, the presence of the latter being manifested by a positive $i\tau$ intercept. The absence of any adsorption or double layer effects under potentiostatic conditions is evidenced from the plot of the anodic charge Q^A vs $\nu^{-\frac{1}{2}}$ (Fig. 5.28) with an extrapolated

zero intercept according to the equation (249):

$$Q^A = k' \nu^{-\frac{1}{2}} + Q_{ads} + Q_{film} + Q_{DL}$$

where k' is a sweep rate independent constant.

However, a consideration of the voltammetric behaviour upon increasing scan rate and in particular as the bulk PbS concentration was increased shows both the oxidation and reduction waves to become extended (Fig. 6.2.2). A shift and flattening effect upon the cyclic voltammetric response with increasing scan rate may occur as a result of a solution ohmic drop. As a consequence of the latter neither the true peak potential $E_{p,true}$ nor the true potential sweep rate ν_{true} are the same as that applied to the cell, i.e.

$$E_{p,true} = E - IR_{\Omega}$$

and

$$\nu_{true} = = R_{\Omega} (dI/dt)$$

where I is the total current flowing and R the resistance of the solution. The sweep rate dependency upon the voltammetric response of a charge transfer reaction with uncompensated resistance leads to a linear E_p vs $\ell n \nu$ dependency (250).

The voltammetric results obtained in this present study show that both the peak anodic current I_p^a, the peak anodic potential E_p^a and the half-peak width are linearly dependent upon $\nu^{\frac{1}{2}}$.

Although as was mentioned above the I_p^a vs $\nu^{\frac{1}{2}}$ relation may be used as a criterion for diffusion control, other mechanisms may give the same dependency. Thus, for example, film formation and growth under low field conditions limited by ion migration through the film results in the relation

$$i = (\frac{2nF}{V_m})^{\frac{1}{2}} \nu^{\frac{1}{2}}$$

However, considering the further $\nu^{\frac{1}{2}}$ dependency of the potential functions E_p^a (Fig. 6.2.9) and $E_p - E_{p/2}$ (Fig. 6.2.10), the electron transfer reaction cannot be considered as simple reversible or irreversible processes. For the former mechanism E_p^a is independent of ν and for the latter case E_p^a is dependent upon $\ell n\nu$ (19). In both cases $E_p - E_{p/2}$ is constant.

The only mechanism known to the author which theoretically predicts the observed behaviour is that for film formation under ohmic resistance control (251). The theoretical analysis derived and experimentally substantiated by Calandra et al (251) assumes a Mueller type passivity model in which two types of layer growth occur. Initially a solid layer of low conductivity forms at constant thickness and extends across the electrode surface until only small pores in the layer remain; the film subsequently thickens with a constant pore area. Thus the insoluble film starts to crystallize out at certain points and extends outwards over the electrode surface as a layer of uniform thickness δ. The resistance of the pores R' threading the layer is given by:

$$R' = \frac{\delta}{k_s A_o (1-\theta)}$$

where k_s is the specific conductivity of the electrolyte solution in the pore, A_o the electrode area and δ the surface coverage. The current flowing as a result of an applied potential, E, is given by:

$$E = I(R' + R_o)$$

where R_o is the resistance of the cell without film formation, thus

$$I = \frac{E}{R_o + \frac{\delta}{k_s A_o (1-\theta)}}$$

If one next considers the simple fast electrode reaction

$$S + X^- \qquad X(S) + e$$

involving the formation of an insoluble species X of low electrical conductivity on the electrode surface, then when a potential sweep, i.e. $\nu = dE/dT$ is applied both E and θ change with time. If it is assumed that δ is sweep rate independent then the current is given by the equation:

$$I_p = \left(\frac{nF\gamma kA_o}{M}\right)^{\frac{1}{2}} (1 - \theta_p)\nu^{\frac{1}{2}}$$

and

$$E_p = \left[R_o + \frac{\delta}{k\, A_o(1-\theta_p)}\right] \left(\frac{kA_o M}{nF\gamma\delta^2}\right)^{\frac{1}{2}} (1-\theta_p)\nu^{\frac{1}{2}}$$

The voltammetric results are in reasonable agreement with the above equations, although no current intercepts are predicted. Howerver it is known that positive current intercepts may occur as a result of a chemical (nucleation process) in the absence of a change in potential with time (252), some supportive evidence of linear I_p -$\nu^{\frac{1}{2}}$ relations with positive intercepts has been given by Conway et al (253) for the formation of AgO and Ag_2O porous films.

In general the mechanism for the spreading of an insoluble layer over the electrode surface may involve three fundamental steps:

(1) Electrochemical reaction at the uncovered metal surface to form an adsorbed oxidised species.

(2) Surface diffusion of this to the periphery of a spreading insoluble patch.

(3) Incorporation into the spreading patch.

If the first step is rate controlling then the rate is proportional to the uncovered area, but if the last step is rate controlling then the rate is proportional to the length of the edge of the growing patch. A transient peak is expected in the potentiostatic response but not in the galvanostatic

response. Surface diffusion control relates to the average distance between a discharge site and the edge of a patch and no transient peak is predicted (254).

The galvanostatic and potentiostatic transients obtained in the present study did not show any evidence of any peaks. This is particularly true of the I-t transients although many experiments were conducted in an attempt to find typical nucleation and growth transients. On the whole typical diffusion control potentiostatic and galvanostatic plots were obtained thus indicating,on the basis of the above points, either electron transfer or surface diffusion but not lattice incorporation to be the rate determining step. Some of the I-t transients obtained, particularly those at high PbS contents and high overpotentials were found to be virtually constant after the initial current decay due to the double layer charging and this would be more consistent with the Mueller passivity type of mechanism.

Further evidence for the formation of an insulating sulphur film was obtained from the very slow potentiodynamic scans. The resultant I-E curve (Fig. 6.2.12) exhibits the classical shape expected for the formation of an insulating film such as may be obtained in corrosion studies for example. The current for the process continues to increase until the surface coverage, θ, of the insulating product equals unity. Thus the electrode surface is blocked to further electron transfer and hence the current decreases to very low levels. The kinetic theory of inhibition and passivation in electrochemical reactions has been given in depth by Gilroy and Conway (255). The shift in the reduction peak potential towards more cathodic potentials may also be related to the reduction of an insoluble insulating film (251).

The reduction I-t transients obtained (Fig. 6.2.13) are very unusual. The current transients do not exhibit any peak as may occur for the reduction of, for example, silver oxides (252), nor do they show any

significant diffusion contribution. The curves show (Fig. 6.2.13) an initially large current which remains virtually constant with time before rapidly falling to zero, the time at which the current decays being dependent upon the anodic charge. Similar curves for the reduction of sulphur at a vitreous carbon electrode in a $PbCl_2$-KCl melt have been obtained by du Guibert et al (191) and, indeed, have been substantiated by this work (see Chapter 5). The former authors found similar curves to be obtained upon the oxidation of a reduced Ni film in the same electrolyte (191).

The low charge ratios of the voltammetric reduction to oxidation process, i.e. $Q^C/A^A < 1$ (Fig. 6.2.7), clearly indicates that some of the sulphur product is being removed prior to reduction. The absence of any additional voltammetric reduction peaks suggests that the formation of stable, reducible polysulphide species is not occurring. However, sulphur has been shown to be quite soluble in this melt within the temperature range ~420-500°C with solubility values of 1-10 x 10^{-4} mole S/cm^3, see Chapter 7. It is further known that sulphur exhibits a very high vapour pressure at these temperatures, thus the low charge ratios, i.e. charge efficiencies, may be explained in terms of either sulphur dissolving into the melt or loss through vapourisation. At low scan rates both of these mechanisms will contribute to the small Q^C/Q^A and I_p^c/I_p^a values. As the scan rate is increased the effectiveness of these two processes becomes smaller. Similar plots to those obtained have been determined for the formation of an insoluble film followed by a chemical dissolution reaction (253). A value of $Q^C/Q^a = 1$ will only be obtained if the sulphur film is virtually insoluble in the melt.

The galvanostatic transient obtained as a result of low applied current densities revealed some interesting detail. Thus at low temperatures and PbS concentration a linear E-t region may be observed prior to the main oxidation transition wave (Fig. 6.2.19). The presence of the constant dE/dt region was clearly demonstrated to be dependent upon the initial condition

of the electrode surface (Fig. 6.2.21). It is tentatively suggested that this phenomenon is related to an initial nucleation stage. Nucleation and growth phenomenon are well known to be highly sensitive to the condition of the electrodes substrate and that surface microroughness and the presence of any adsorbed species may alter the electrochemical response. It is interesting to note that the constant dE/dt transients were only observed at the very smooth vitreous carbon electrode rather than on the rough graphite one. The energy required to form nuclei will be much greater on the former electrode and indeed fewer nucleation sites would be available. If the constant dE/dt transition could be attributed to a surface phenomenon then it may be analysed according to a pseudo-capacitance model, i.e. $C_s = i/[dE/dt]$, a constant C_s value would, for example, be expected for a pure coulombic, i.e. adsorption type process. However it was shown (Fig. 6.2.20) that the value of C_s decreases with increasing current desntiy and that it was to some extent concentration dependent. A similar decrease in C_s with increasing current density has been obtained for the nucleation of oxide films upon bismuth in aqueous solutions (254). No physical reason for this decrease can be made.

The state of an electrode surface may be conveniently examined by open-circuit decay E-t transients after galvanostatic charging (256). The results obtained in this study show two distinct types of behaviour (Fig. 6.2.23). For a given current density, at low overpotentials, a normal exponential decrease in $E_{O.C}$ with t occurs (Fig. 6.2.24). Analysis of the transients shows linear E_{OC} (fall) vs log t_{decay} plots which conform to the equation (257):

$$E = K + b \log (t + \theta)$$

where K and b are constants and θ is an adjustable parameter. The slope of the dE/dlog t_{decay} plot being approximately linearly dependent upon the

initial potential, i.e. E at t_{decay} = 0 (Fig. 6.2.25). However as the overpotential is increased to beyond 0.4V (w.r.t Ag^+/Ag), upon switching the current off a sudden drop in potential occurs in a typical resistance mode, the extent of the voltage drop being dependent upon the anodic charge Q^a which hence may infer the existence of a surface film. Subsequently a linear dE_{OC}/dt region is observed (Fig. 6.2.23), both the time and the value of the slope over which this region extends being dependent upon either the overpotential or the charge passed. Finally the open-circuit potential decays with log t_{decay}. To the author's knowledge only two types of surface phenomenon may give rise to a constant dE_{OC}/dt Region.

(1) As a consequence of an adsorbed species via a Temkin type isotherm (258).

(2) As a result of the dissolution of a porous film (259).

The high overpotential and charge passed infer that process (1) above is unlikely, the constant dE_{OC}/dt region would therefore be consistent with the idea of the formation of a porous sulphur film followed by a physical dissolution process. Similar open-circuit plots have been obtained for the dissolution of porous oxide films of Aℓ (260) and Zn (261).

Platinum and Gold

The voltammetric behaviour for the oxidation of S^{2-} at Au and Pt electrodes has clearly shown the presence of two anodic processes which may be resolved at low PbS concentrations and low temperatures. The observed response at these two electrodes is quite different to those obtained at carbon-based substrates. The nature of process A, i.e. the pre-wave was found to be dependent upon the electrode substrate. The high reactivity of Pt and Au with sulphur to form the metal sulphides together with the observed difference in the voltammetric response on these substrates may infer a nucleation and growth of a metal sulphide film prior to the main

sulphide oxidation process. Indeed it is known that anodic peaks are formed as a result of the process of spreading of, for example, oxide nuclei to cover the electrode surface (262). The existence of multiple peaks may be interpreted as the nucleation and spreading of successive layers (263). A simplified view of the latter model should result in the charge in each peak corresponding to a monolayer charge. A consideration of simple nucleation theory shows that the formation of a film or indeed of a monolayer will occur at less negative potentials than that of the equilibrium potential for the main redox reaction.

However, before discussing the results in detail it is worth noting that several alternative mechanisms may be invoked to explain the existence of the two oxidation waves. The first and most obvious mechanism involves a *consecutive electron transfer reaction which* may be represented by the general scheme:

$$A^{x-} \rightleftharpoons A^{(x+1)-} + e$$

$$A^{(x+1)-} \rightleftharpoons A + e$$

The above mechanism would be expected to occur at all bulk PbS concentrations and to yield a constant peak current ratio, this being dependent upon the ratio of the number of electrons involved in each reaction (19). Furthermore the voltammetric response should be virtually independent of the electrode substrate. The above mechanism is not in accord with the results obtained.

A second mechanism which may be invoked involves the presence of two anodically active species in solution. The general reaction scheme describes the system:

$$A^{x-} \rightleftharpoons A + xe \qquad E_1$$

$$B^{y-} \rightleftharpoons B + ye \qquad E_2$$

Two situations may arise to give the above scheme. First, one of the two electron transfer reactions may result from the presence of an electroactive impurity species. However no 'common' anionic impurity species was found to correspond to process A (see Chapter 9) and furthermore it is unlikely that the resultant voltammetric wave would be so dependent upon the nature of the electrode substrate. The second situation may arise from the presence of two anodically active sulphur species. An equilibrium between the two species corresponding to a redox reaction and thus a poised open-circuit potential would result at an inert electrode. The addition of Na_2S containing sulphur as an impurity to a LiCℓ-KCℓ solvent resulted in the redox reaction $2S^{2-} \overset{2e}{\rightleftharpoons} S_2^{2-}$ (177). No poised open-circuit potentials were measured during these investigations, thus the above mechanism does not operate in the present system.

The more anodic of the two oxidation processes occurs at the same potential and exhibits, in general, the same voltammetric morphology on both electrodes and indeed compares well with the result obtained at the carbon-based electrodes. Thus process B must correspond to the same oxidation/reduction process and is attributed to the formation of sulphur. The morphology of the voltammetric I-E curve for process B and the $I_p^c/I_p^a > 1$ values signify the mechanism to be one of the deposition and stripping of an insoluble product. The oxidation process at both electrodes was shown to be diffusion-controlled by the linear I_p^a vs $\nu^{\frac{1}{2}}$ plots (Figs. 6.3.2 and 6.4.2), the linear I vs $t^{-\frac{1}{2}}$ (Fig. 6.4.31) and the linear chronopotentiometric Sand's plots, i.e. $\tau^{\frac{1}{2}}$ vs 1/i (Fig. 6.4.34). The latter results did not reveal the presence of any associated coulombic processes, i.e. adsorption which yields positive $i\tau$ intercepts (42). The decrease in the current parameter $I_p^a/\nu^{\frac{1}{2}}$ with increasing sweep rate particularly in the low sweep rate region may be diagnostic of a following chemical reaction. The low charge ratios measured and the trend in the current ratio I_p^c/I_p^a with increasing sweep rate would initially support the above hypothesis. However, as

mentioned in the above discussion section for the carbon electrodes, sulphur exhibits a relatively high solubility in this melt and indeed has a high vapour presence. Thus at low sweep rates both processes act to remove the sulphur product and hence a very low current and charge ratio is obtained. As the sweep rate is increased further the two 'dissolution' mechanisms become less important and the charge ratio should tend to unity.

The effect of increasing the anodic switching potential E_λ^a (Figs. 6.3.10 and 6.4.18),shows that sulphur deposition does not substantially occur until a potential very close to the E_p^a value is reached. As E_λ^a is increased beyond E_p^a then a greater amount of sulphur is deposited and presumably a greater degree of polymerisation occurs. At the gold electrode it is clear from Fig. 6.3.10 that the potential at which film reduction commences is independent of the amount of deposited sulphur. However the potential at which the stripping of the deposit is completed is dependent upon E_λ^a and hence Q_T^a and indeed shifts towards more cathodic potentials, (Figs. 6.3.10 and 6.4.18). The peak potentials for both the oxidation E_p^a and reduction E_p^c processes remain constant with increasing sweep rate over the range 0.02-0.4 V/s. The small peak separation and the constancy of E_p^a with sweep rate indicate the process to be highly reversible. The shift in peak potential with the bulk concentration for an insoluble product is given by the equation (264):

$$E_p = E_o - 2.303 \frac{RT}{nF} \log(\gamma_R C_R) + 1.1 \frac{RT}{nF}$$

The various potentials measured, both for process A and B at both electrodes are in accord with the above relation (Figs. 6.3.6 and 6.4.4) and indeed the slopes for each of the potentials are approximately the same at 0.06-0.07V. A value of 0.069V for a 2-electron process is predicted at 417°C. Thus the number of electrons involved in each process is two.

Consider now the electrochemical behaviour of the pre-wave or process A.

At the gold electrode the cyclic voltammetry shows that no reverse wave is associated with this oxidation wave (Fig. 6.3.7). The absence of a reverse wave may be a consequence of the irreversibility of the electron transfer reaction, however a predicted shift in the forward peak potential (E_p^a) should be linear with increasing $\ell n\nu$ (19). The observed independence of E_p^a of sweep rate does not substantiate an irreversible electron transfer mechanism. The absence of a reverse wave may be explained in terms of the instability of the proposed AuS film. The peak current for process A was found to be linearly dependent upon $\nu^{\frac{1}{2}}$,(Figs. 6.3.8 and 6.4.10), and the corresponding charge to be linearly dependent upon $\nu^{-\frac{1}{2}}$ (Fig. 6.3.9) both criteria confirming diffusion control.

At the Pt electrode a well defined reduction peak was associated with process A. The influence of increasing the surface coverage or 'build-up' of the proposed PtS film may be observed by increasing the forward E_λ^a potential through process A (Fig. 6.4.5). The increase in E_λ^a causes the whole of the reverse wave to shift towards more cathodic potentials, the shift in E_p^c being linearly dependent upon E_λ^a. The effect of increasing scan rate clearly shows process A to be diffusion controlled according to the linear I_p^a vs $\nu^{\frac{1}{2}}$ plots (Fig. 6.4.10). This is further confirmed by the chronoamperometric $I\text{-}t^{-\frac{1}{2}}$ results (Fig. 6.4.31). The peak potential exhibits a slight shift with increasing sweep rate although this is within the experimental precision. It is thus inferred that the reaction is quite reversible. This is further substantiated by the small peak separation value $\sim$0.25V. It is notable that the ratio of the two peak currents for this process I_p^c/I_p^a equals unity (as measured from i = 0). However the charge ratio Q^c/Q_T^a is less than unity thus indicating that either (a) the reaction product has been removed, or (b) that only a portion of the product is reduced.

The latter is supported by the combined constant potential electrolysis and cyclic voltammetric wave form studies (Fig. 6.4.13 and Table 6.4.6). The reduction process also exhibits diffusion controlled behaviour.

The discussion of the results for process A has thus far indicated that the process is diffusion controlled and in no case is a linear relation corresponding to a direct reduction or formation of a monolayer indicated (265). The charge values for the formation of the presumed sulphide film are much in excess of the value for a monolayer $\sim$700 $\mu C/cm^2$ (177), as found in most other galvanostatic and controlled-potential investigations (266). Thus if a crystalline film of PtS is formed then the $I_p - \nu^{\frac{1}{2}}$ relations may infer that solid state diffusion controls both the growth and reduction of the PtS phase under potentiostatic conditions. The presence of solid-state diffusion may be inferred from the independence of I_p values of stirring rate. In the case of monolayer formation and reduction, the current peaks are predicted to be linearly dependent upon ν, corresponding to a constant adsorption pseudo-capacitance, C_s, at a given potential ($i = C_s\ dV/dt$). The peak arises in such cases simply because in the positive direction the surface is eventually blocked by the species being electrochemically adsorbed, while in the negative direction the rate of monolayer reduction initially increases due to the increasingly negative potential but the reduction current must eventually fall with continuing increase of potential as the surface layer is consumed. In the case of Pt and possibly Au sulphides further electrochemical reaction may occur because of the semiconducting properties of the metal sulphides, thus the surface does not become blocked.

The effect of process B upon the reduction process may be clearly observed by increasing E_λ^a beyond the peak potential for process A (Fig. 6.4.18). It is noted that the reduction of process A increases with increasing anodic charge thus indicating that the film continues to thicken as further sulphur is deposited on the electrode.

As further sulphur is deposited the potential at which the main reduction process occurs shifts towards more positive values and reaches a constant value of 0.41V. Both the peak reduction potential and the potential at which reduction is complete shift towards more cathodic potentials.

The interrelation between the two processes may be observed by employing a switching potential $E^a_\lambda > E^a_o/B)$ and examining the effect of increasing sweep rate and E^a_λ. The gradually increasing value of Q^c_T/Q^a_T with increasing sweep rate suggests that a greater proportion of the total anodic charge is captured upon reversing the scan, however the charge ratio remains quite low, i.e. < 0.5. Fig. 6.4.22 shows that the main reduction wave for sulphur on Pt does not exhibit diffusion control although a greater degree of linearity (I^c_p vs $\nu^{\frac{1}{2}}$) occurs as E^a_λ is increased. The ratio of the two cathodic peak currents shows that no simple relation between the two exists, i.e. $I^c_p(A)/I^c_p(B) \neq$ constant ν. (Fig. 6.4.23). As the amount of anodic charge is increased via an increase in E^a_λ the $I^c_p(A)/I^c_p(B)$ ratio decreases (Fig. 6.4.23), thus indicating that the reduction procss A is not significantly enhanced by the sulphur product. The relative cathodic charge ratios show a similar trend (Fig. 6.2.24).

Both the two anodic peaks and the reduction peak current for process B exhibit diffusion control over the temperature range 417-530°C (Figs. 6.4.25 and 6.4.26). A plot of log I_p vs 1/T K shows that an Arrhenius type relation is obeyed by the two oxidation waves but not by the cathodic wave (Fig. 6.4.28). The relation between the respective charges for processes A and B with increasing temperature (Fig. 6.4.29) shows that the total anodic charge increases in an exponential manner with increasing temperature and that the charge for sulphur deposition follows a similar trend. The charge for process A shows a very slight increase with increasing temperature. The decrease in the cathodic charge clearly shows that as the temperature is

increased the amount of reducible product at the electrode or within the diffusion layer decreases. This must be attributed to the physical removal of the sulphur product.

The I-t transients obtained at both Pt and Au electrodes always exhibited diffusion control and under no circumstances ~~was~~ were typical nucleation and growth transients obtained (262). Thus if one infers PtS formation then on the basis of the general mechanisms outlined on page 263 then either electron transfer or surface diffusion but not lattice incorporation is the rate determining step.

CHAPTER 7

THE ELECTROCHEMISTRY OF DISSOLVED SULPHUR GAS IN THE $PbCl_2$ - KCl - NaCl EUTECTIC MELT

7.1 Introduction

A knowledge of the solubility and resultant electrochemistry of sulphur gas in lead chloride-based melts is an obvious pre-requisite to a fuller understanding of the oxidation and subsequent reduction of the sulphide ion in these melts.

Initial attempts were made to repeat the work of Skyllas and Welch who estimated the solubility of sulphur in PbS-$PbCl_2$-NaCl melts by the addition of sulphur pellets. The addition of sulphur pellets to either pure $PbCl_2$-KCl or $PbCl_2$-KCl-NaCl melts with and without additions of PbS over the temperature range 417-440°C were not successful. Considerable vapourisation of the sulphur occurred resulting in the rapid attack of all metallic components of the cell. Even after arranging for suitable protection from the sulphur the solutions were not stable for sufficient time in which to gather electrochemical information.

The experimental technique adopted was to use a small entirely enclosed cell situated in the hot zone of the furnace in which a separate beaker held a quantity of liquid sulphur, see section 4.1.3. Consequently the only sulphur in contact with the melt was as a direct result of the sulphur vapour pressure. The system may be represented by:

$$S_{(l)} \rightleftharpoons \tfrac{1}{2}S_{2(g)} \rightleftharpoons \tfrac{1}{2}S_{2(g)(\text{in solution})}$$

The vapour pressure of the sulphur may only be changed by a corresponding increase in temperature of the cell. The melt employed was the $PbCl_2$-KCl-NaCl ternary eutectic melt; a sealed planar vitreous carbon

working electrode was used.

7.2 Results

The $PbCl_2$-KCl-NaCl salt was initially melted at 414°C after which a period of two hours was allowed for equilibrium to be attained prior to initiating electrochemical measurements. During the slow and very careful melting period, the brown sulphur liquid pool was clearly observed. Brown gaseous sulphur could also be seen to be permeating the solid salt. Once molten the melt was a dark brown colour rather than the intense yellow colour of the pure $PbCl_2$-based melts.

Unfortunately the design of the cell does not allow for an initial voltammetric evaluation of the melt purity. However melt from the same 'batch' as that used in this experiment was found to be of acceptable electrochemical purity. Thus one may be confident that the melt employed was free of electroactive impurities.

An initial voltammogram obtained at the vitreous carbon electrode after the two hour equilibrium period is shown in Fig. 7.1. A single reduction wave with a peak potential of 0.3V was observed with a corresponding oxidation wave at 0.45V. No further reduction processes were observed up to the limiting Pb^{2+} reduction potential. The voltammetric response was found to be highly variable as a consequence of this and also from the fact that the sulphur gas penetrated the voids in the solid eutectic powder prior to melting. Therefore the system was allowed to equilibriate for a further 18 hours. A considerable improvement in the reproducibility of the voltammograms resulted. Fig. 7.2 shows a series of voltammograms obtained indicating the typical reproducibility of the system. The I-E curves were recorded at 5 minute intervals. Fig. 7.3 shows that upon cycling the reduction peak current decreases and the peak potential shifts towards more positive potentials. The anodic response was very reproducible.

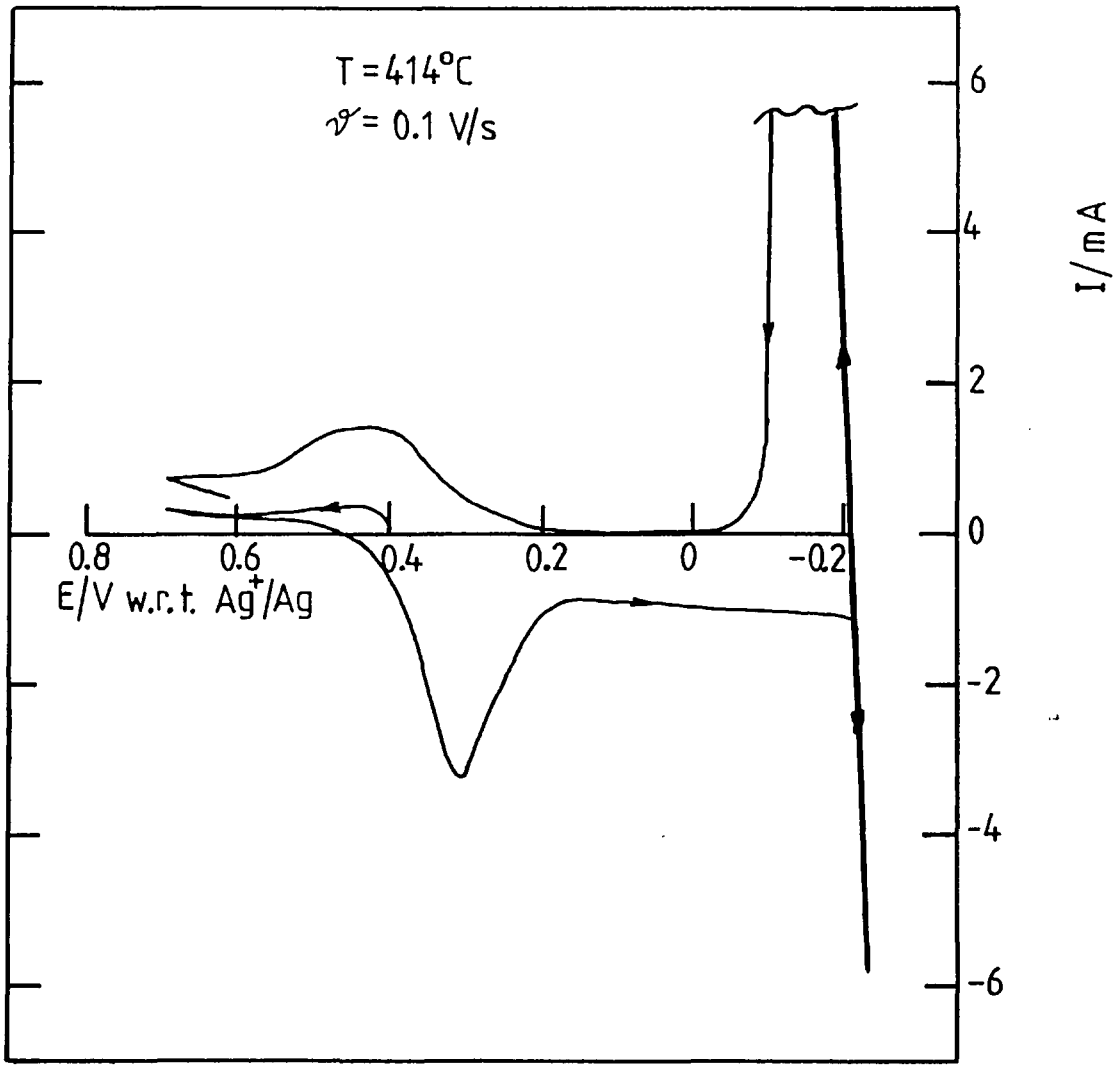


Fig. 7.1: An initial voltammogram obtained for the reduction of dissolved sulphur gas in a $PbCl_2$-KCl-NaCl ternary eutectic melt at 414°C. Electrode: vitreous carbon; area = 0.0855 cm^2.

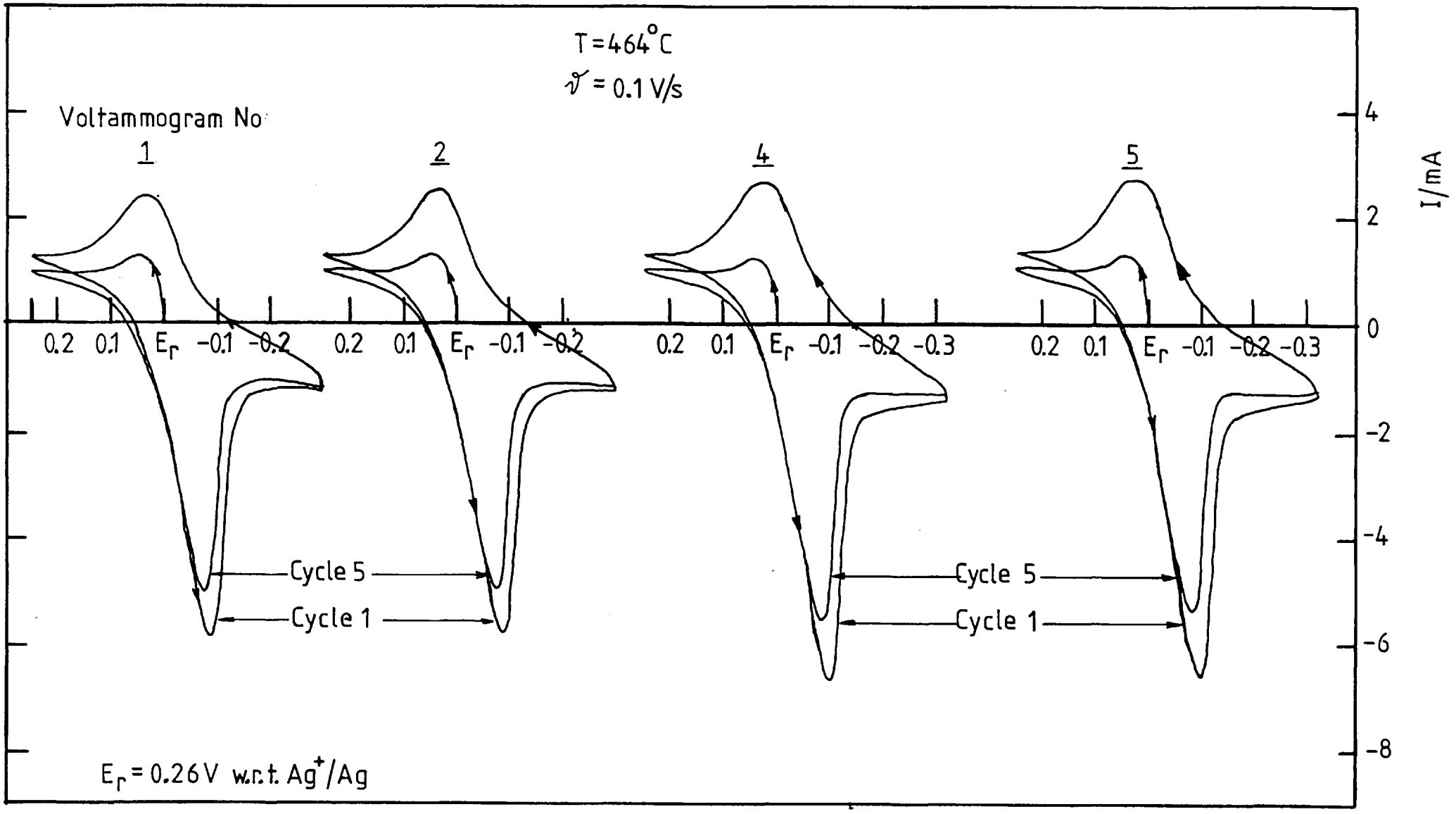


fig. 7.2: A series of typical sweep voltammogram detailed for the reduction and oxidation of dissolved sulphur gas at a vitreous carbon electrode. Voltammogram 1 obtained after 2 hours equilibrium at temperature; subsequent I-E curves were obtained after 3 minute intervals.

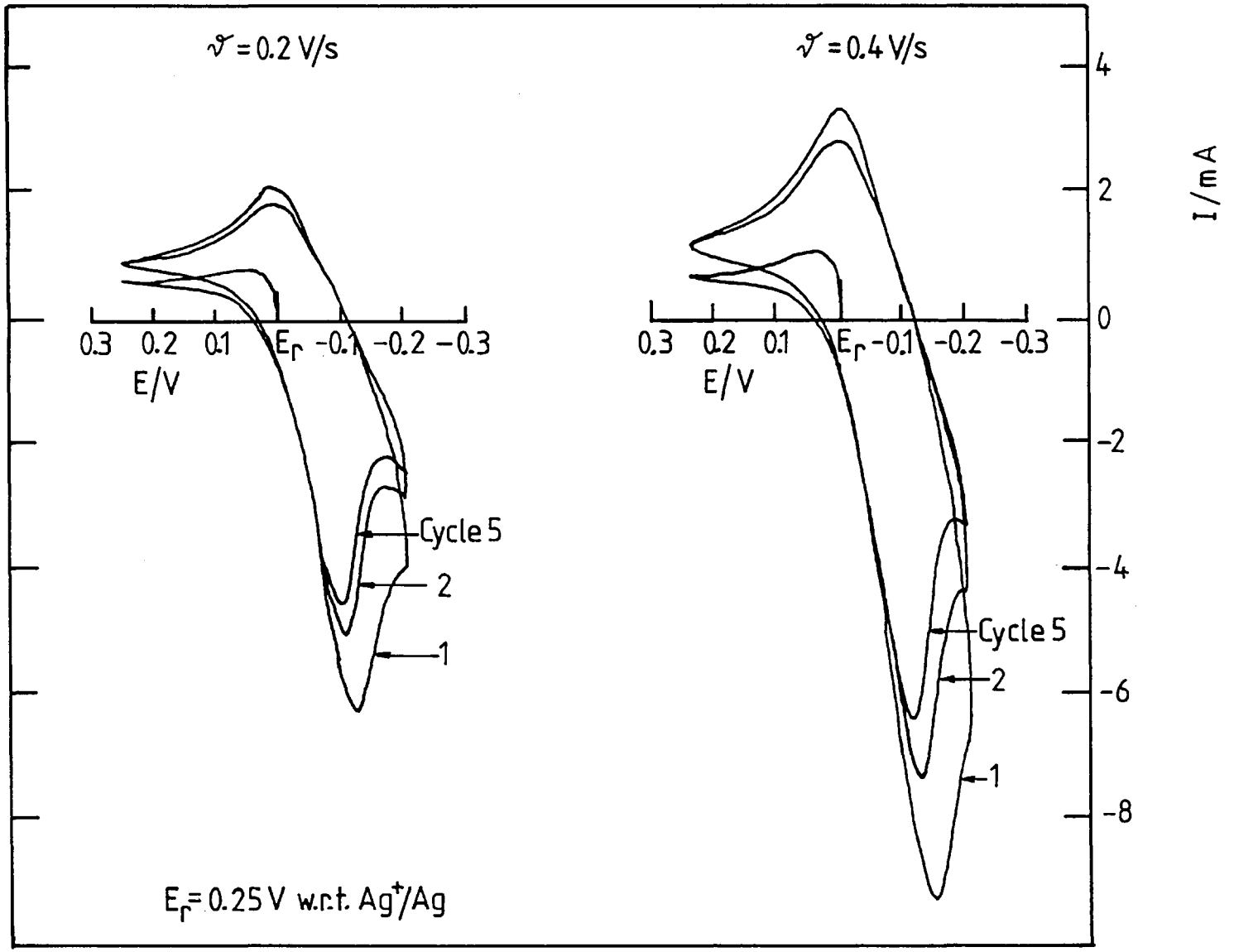


Fig. 7.3: Effect of scan rate on the voltammetric behaviour of dissolved sulphur in the $PbCl_2$-KCl-NaCl eutectic. The effect of continuous cycling is also shown. T = 414°C.

The results of increasing scan rate at a temperature of 414°C are shown in Fig. 7.3 and Table 7.1 in which the results of voltammograms Nos. 1 and 5 and cycles 1 and 5 have been analysed. Clearly as a consequence of the irreproducibility of the response care must obviously be exercised as to which I-E curves are to be analysed. The first voltammogram and cycle No. 1 should directly represent the concentration of sulphur in the melt, however it was this cycle which was the least reproducible. The fifth voltammogram was found to be the most reproducible.

Fig. 7.4 shows the cathodic peak current I_p^c to increase with sweep rate and although there exists a considerable scatter in the results and Randles-Sevcik I_p^c vs $\nu^{\frac{1}{2}}$ relation may be discerned at the higher scan rates.

Table 7.2 shows the effect of increasing temperature upon the cyclic voltammetric parameters. Fig. 7.5 shows the results of the 5th voltammogram in which the peak current I_p^c decreases approximately linearly with increasing 1/T°K. However upon increasing the cell temperature a corresponding change in partial pressure of sulphur occurs and hence the concentration of dissolved sulphur changes. Fig. 7.6 shows the relation between $I_p^c T^{\frac{1}{2}}$ and $P_{S_2}^{\frac{1}{2}}$. The latter was calculated from the formula obtained by Baker [53], i.e.

$$\log P_{S_2}(\text{atm}) = 6.00282 - 31584.42T^{-1} - 2.23934 \times 10^{-3}T + 1.14662 \times 10^{-6}T^2$$

Clearly the peak current is not quite linearly dependent upon the $P_{S_2}^{\frac{1}{2}}$. Tables 7.3 and 7.4 show the calculated values of the concentration of gaseous sulphur dissolved in the melt as a function of increasing temperature. The values were calculated from the Randles-Sevcik equation for a soluble reactant and product assuming n = 2 and a value for the diffusion coefficient. Table 7.3 assumes $D_S = D_{S^{2-}}$ and a value of

TABLE 7.1

The effect of sweep rate upon the voltammetric parameters for the reduction and oxidation of dissolved sulphur in the $PbCl_2$-KCl-NaCl eutectic melt at 414°C.

Voltammogram 1										
Cycle 1						Cycle 5				
V v/s	Ip^c mA	$Ip^a EIp^c$	Ep^c V*	Ep^a V*	$Ep^c-Ep/2$ mV	Ip^c mA	Ip^a/Ip^c	Ep^c V*	Ep^a V*	$Ep^c-Ep/2^a$ mV
0.05	5.0	0.724	0.05	0.23	50	5.0	0.60	0.13	0.23	50
0.1	8.4	0.61	0.115	0.22	100	6.6	0.69	0.11	0.21	60
0.15	6.1	0.73	0.115	0.25	70	4.7	0.77	0.15	0.25	40
0.2	6.5	0.75	0.11	0.25	65	4.6	0.75	0.15	0.25	40
0.3	8.6	0.76	0.1	0.25	80	5.7	0.76	0.14	0.25	60
0.4	11.2	0.76	0.1	0.25	80	7.1	0.74	0.14	0.25	40
				Voltammogram 5						
0.05	5.5	0.52	0.14	0.25	50	4.5	0.65	0.14	0.25	50
0.1	7.1	0.57	0.12	0.24	60	5.8	0.60	0.15	0.24	50
0.15	5.5	0.68	0.13	0.25	60	4.1	0.78	0.16	0.25	50
0.2	6.2	0.72	0.13	0.25	60	4.4	0.80	0.15	0.25	60
0.3	8.0	0.73	0.12	0.25	65	5.5	0.77	0.15	0.25	55
0.4	9.3	0.76	0.11	0.25	80	6.4	0.74	0.14	0.25	60

+ The first voltammogram recorded

* E/v w.r.t. Ag^+/Ag

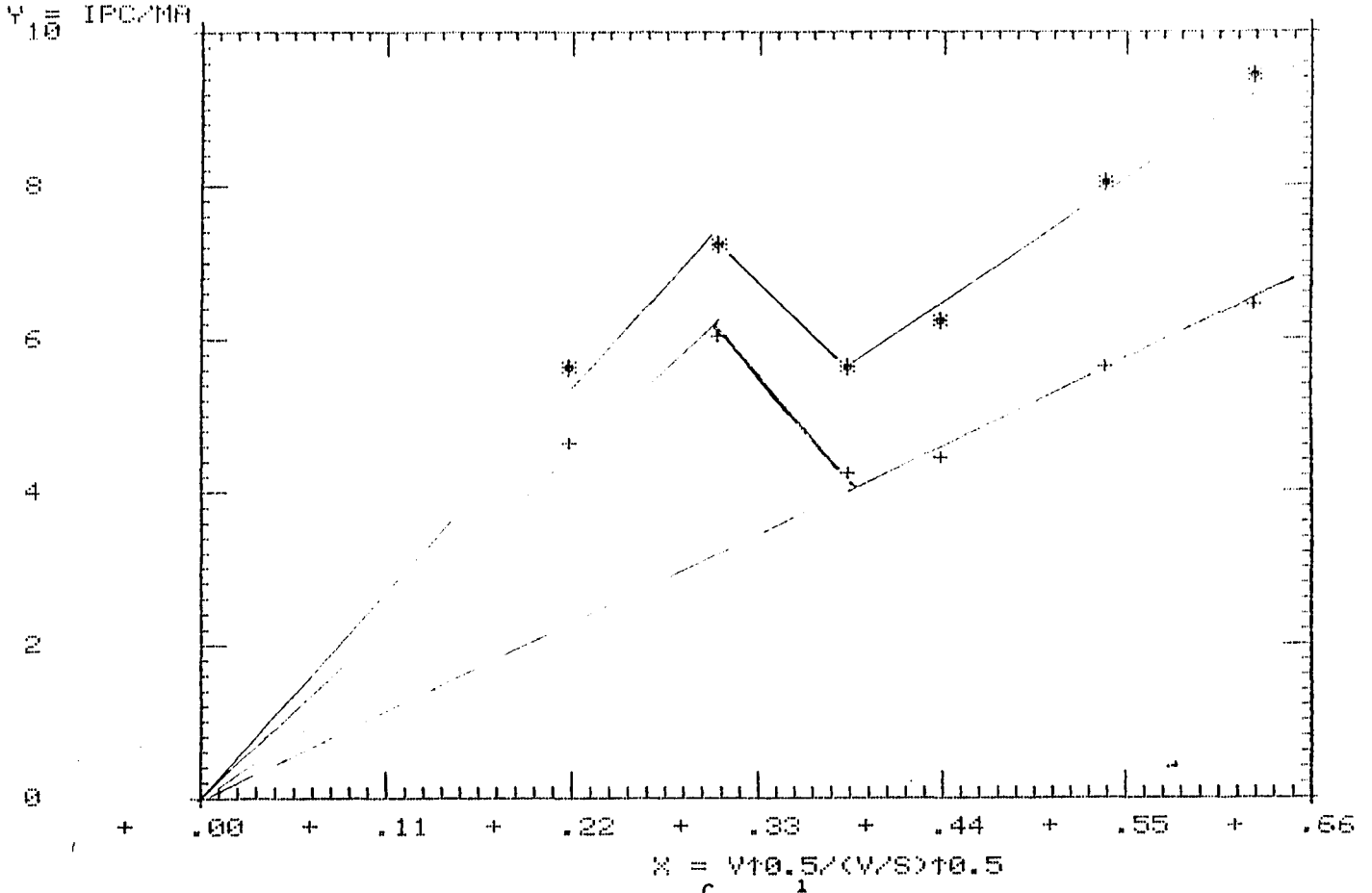


FIGURE NUMBER 7.4: A plot of I_p^c vs $\nu^{\frac{1}{2}}$ for the reduction of dissolved sulphur gas. Solvent = $PbCl_2$ - KCl- NaCl ternary eutectic. Electrode: vitreous carbon; area = 0.0855 cm^2. Fifth voltammogram : * Cycle 1: + cycle 5.

TABLE 7.2

The effect of increasing temperature and hence pS_2 upon the voltammetric parameter for the reduction of gaseous sulphur in the $PbCl_2$-KCl-NaCl melt at a sweep rate of 0.1v/s. Electrode = vitreous carbon ; Area = 0.0855 cm^2.

Voltammogram 1											
		Cycle 1					Cycle 5				
T ^oK	pS_2 atm	Ip^c mA	Ip^a/Ip^c	Ep^c V	Ep^a V	Ep^a-Ep/2 mV	Ip^c mA	Ip^a/Ip^c	Ep^c V	Ep^a V	Ep^a-Ep/2 mV
716	0.957	5.8	0.61	0.17	0.29	60	5.0	0.67	0.18	0.29	50
737	1.2934	6.6	0.64	0.22	0.35	60	6.2	0.66	0.22	0.35	70
753	1.6091	11.25	0.56	0.2	0.36	70	13.0	0.49	0.2	0.36	70
772	2.063	13.0	0.49	0.22	0.37	70	14.5	0.52	0.2	0.37	70
				Voltammogram 5							
716	0.957	6.5	0.63	0.15	0.25	70	5.3	0.72	0.17	0.25	50
737	1.2934	8.7	0.57	0.21	0.35	70	8.0	0.60	0.21	0.35	60
753	1.6091	14.25	0.50	0.19	0.34	80	13.75	0.51	0.19	0.34	75
772	2.063	25.5	-	0.14	0.36	100	22.0	-	0.18	0.36	80

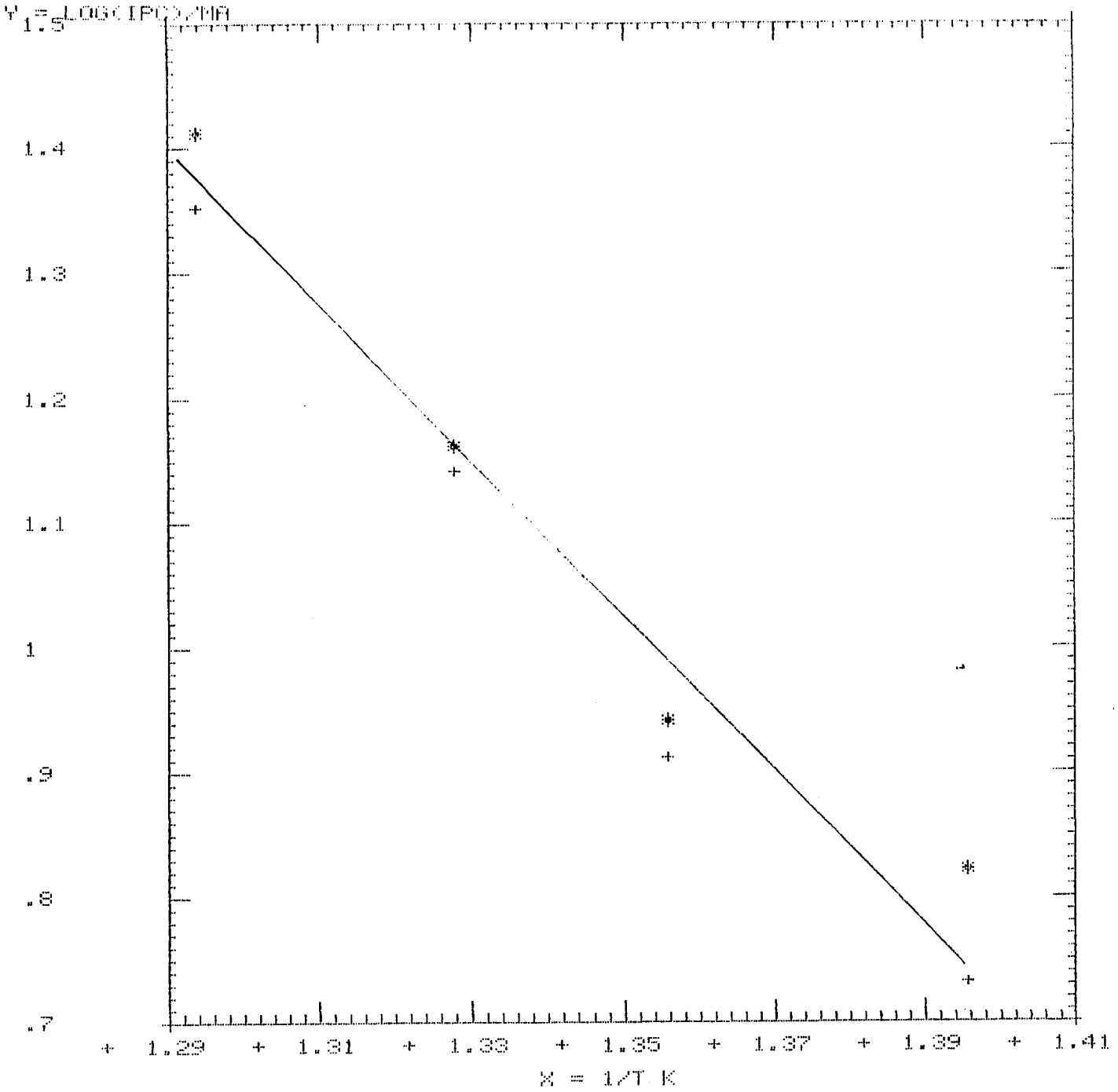


FIGURE NUMBER 7.5: An Arrhenius plot for the reduction of dissolved sulphur in the $PbCl_2$ - KCl- NaCl ternary eutectic melt. Electrode: vitreous carbon; area = 0.855 cm^2.

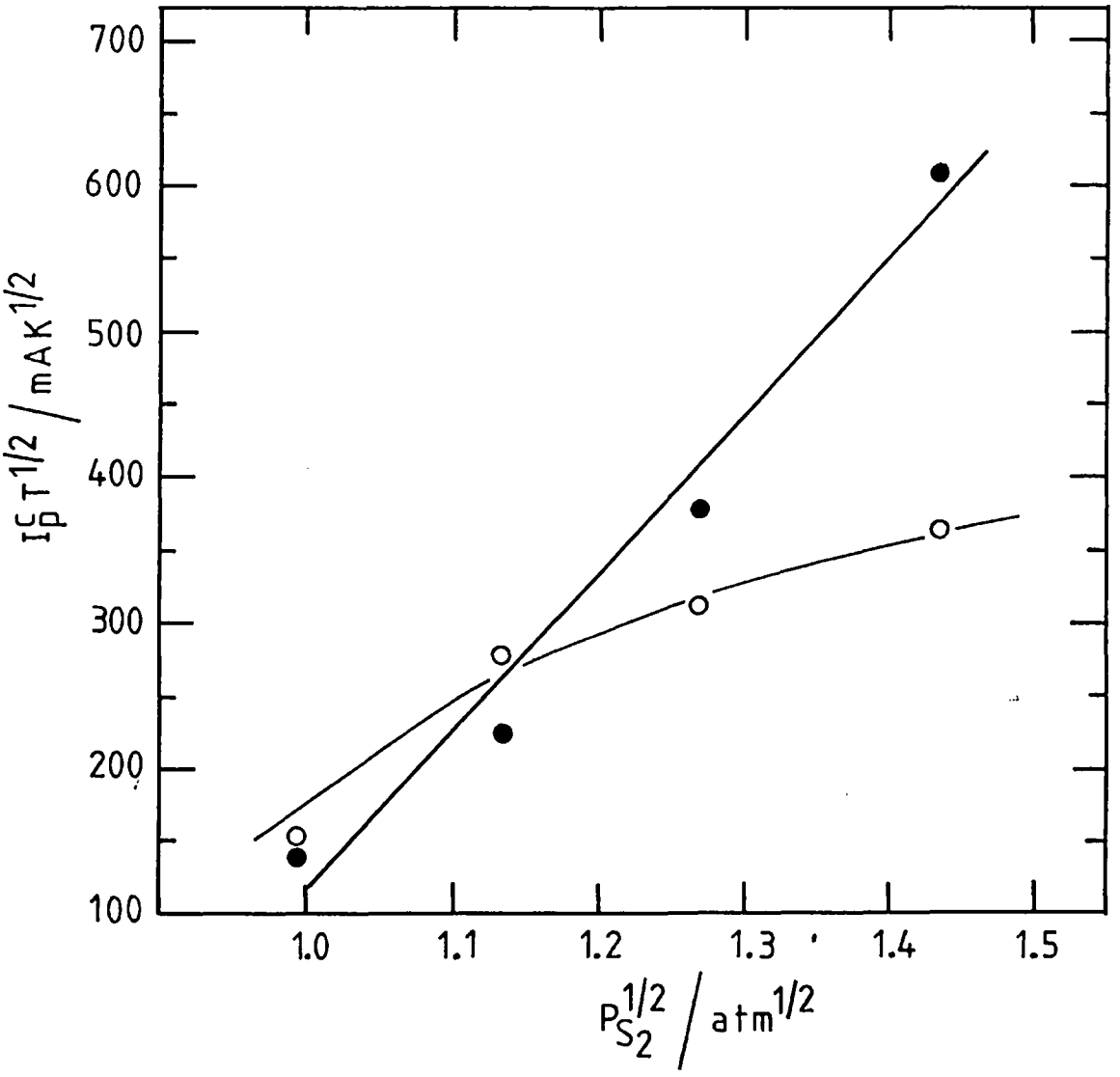


Fig. 7.6: The effect of increasing the partial pressure of sulphur gas upon the peak current for sulphur reduction.
Electrode = vitreous carbon; area = 0.0855 cm^2;
solvent = $PbC\ell_2$ - KCℓ- NaCℓ.

O Voltammogram 1, Cycle 1

● Voltammogram 5, Cycle 5

TABLE 7.3

Calculated values of the solubility of gaseous sulphur in the $PbCl_2$-KCl-NaCl ternary melt as a function of temperature. Assuming n = 2 and D = 3 x $10^{-6}cm^2/s$.

T^oK	Voltammogram 1		Voltammogram 5	
	Cycle 1	Cycle 5	Cycle 1	Cycle 5
716	2.494 x 10^{-4}	2.150 x 10^{-4}	2.795 x 10^{-4}	2.279 x 10^{-4}
737	2.879 x 10^{-4}	2.705 x 10^{-4}	3.796 x 10^{-4}	3.490 x 10^{-4}
753	4.961 x 10^{-4}	5.7327 x 10^{-4}	6.284 x 10^{-4}	6.063 x 10^{-4}
772	5.805 x 10^{-4}	6.474 x 10^{-4}	11.386 x 10^{-4}	9.823 x 10^{-4}

TABLE 7.4

Calculated values of the solubility of gaseous sulphur in the $PbCl_2$-KCl-NaCl ternary melt as a function of temperature. Assuming n = 2 and D = 2 x $10^{-5}cm^2/s$.

T^oK	Voltammogram 1		Voltammogram 5	
	Cycle 1	Cycle 5	Cycle 1	Cycle 5
716	9.659 x 10^{-5}	8.327 x 10^{-5}	1.0825 x 10^{-4}	8.827 x 10^{-5}
737	1.115 x 10^{-4}	1.048 x 10^{-4}	1.469 x 10^{-4}	1.352 x 10^{-4}
753	1.921 x 10^{-4}	2.223 x 10^{-4}	2.4337 x 10^{-4}	2.348 x 10^{-4}
772	2.2481 x 10^{-4}	2.5075 x 10^{-4}	4.441 x 10^{-4}	3.804 x 10^{-4}

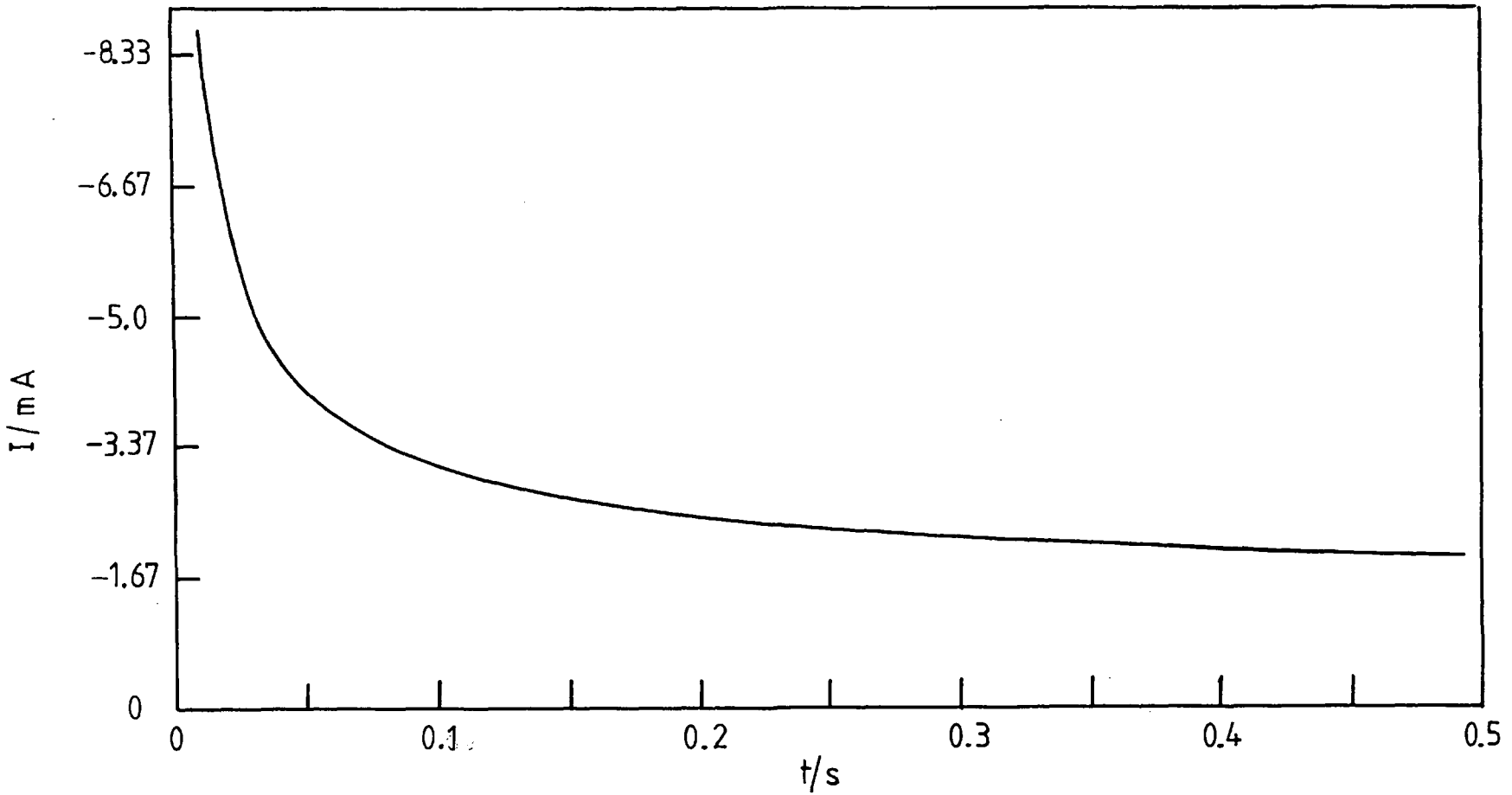


Fig. 7.7: An I-t transient obtained for the reduction of dissolved sulphur gas at a vitreous carbon electrode showing typical 'diffusion control' behaviour. T = 414°C.

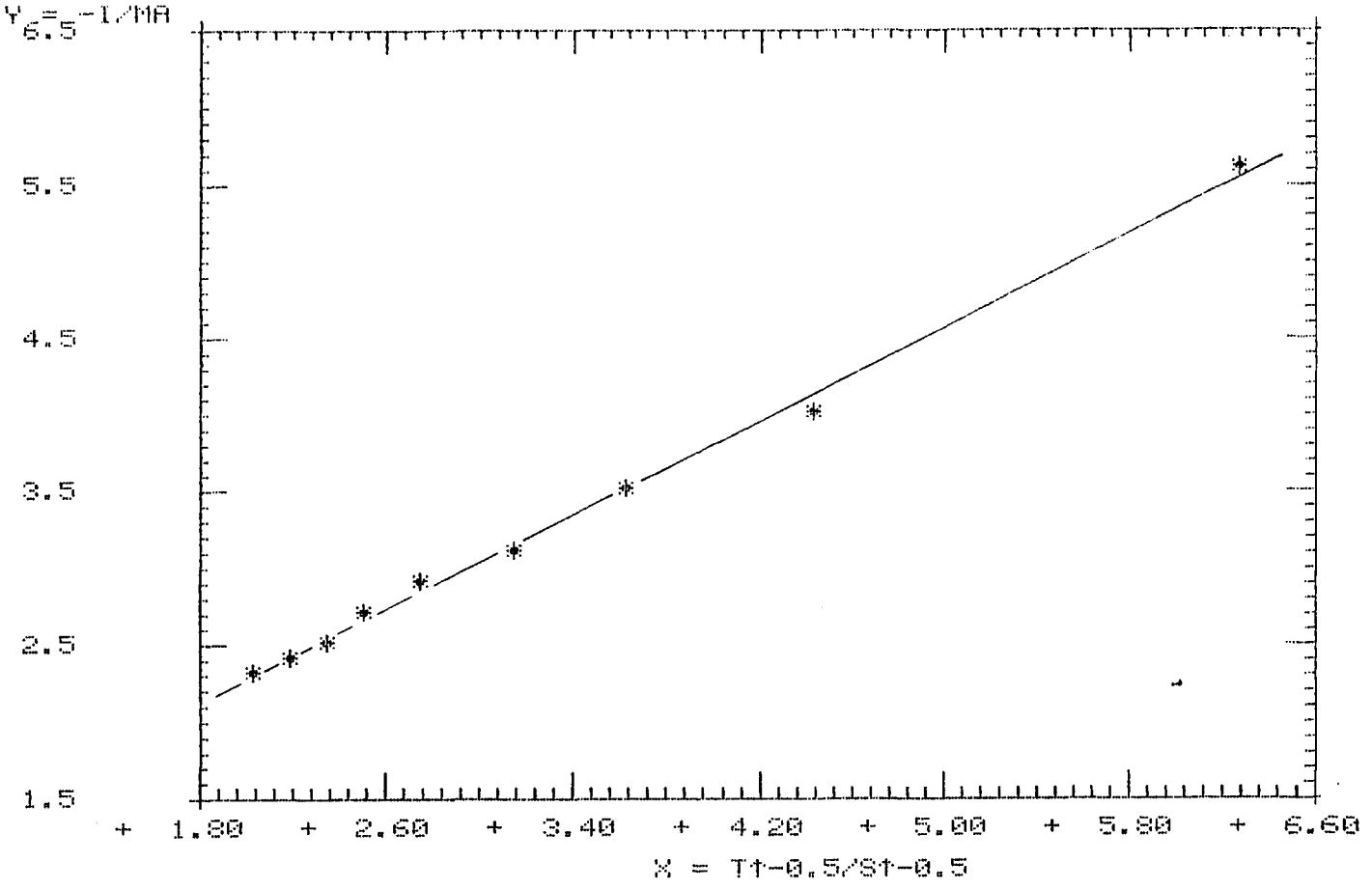


FIGURE NUMBER 7.8: A plot of I vs $t^{-\frac{1}{2}}$ for the reduction of dissolved sulphur in the $PbCl_2$-KCl-NaCl ternary eutectic melt at 414 °C.

Electrode: vitreous carbon; area = 0.0855 cm^2.

3×10^{-6} cm^2/S was used whereas Table 7.4 employs a more reasonable $D = 2 \times 10^{-5}$ cm^2/S value for molten salt systems. The results show that the concentration of dissolved sulphur increases with increasing temperature and hence P_{S_2} with values of the order of $2 - 9 \times 10^{-4}$ mole S/cm^3 assuming $D = 3 \times 10^{-6}$ cm^2/S over the temperature range 716-772°K.

A typical I-t transient obtained for the reduction of sulphur is shown in Fig. 7.7. The current decays linearly with $t^{-\frac{1}{2}}$ as would be expected for a diffusion-controlled process (Fig. 7.8).

7.3 Discussion

The voltammetric examination of the molten $PbCl_2$-KCl-NaCl salt containing dissolved sulphur gas clearly indicated a single reduction wave up to the limiting Pb^{2+} reduction potential. The reduction process may be directly attributed to the electroreduction of sulphur. The results obtained further support the evidence of the single reduction wave obtained for electrochemically formed sulphur obtained during the oxidation of PbS-containing solutions, see Chapters 5 and 6. The overall evidence obtained from these studies suggests that the S^{2-} ion is much more stable in $PbCl_2$-based melts than in the LiCl-KCl eutectic melt where further reduction to form polysulphide ions occurs, see Chapter 8. An attempt to ascertain the reduction mechanism via the cyclic voltammetric technique was not successful due to the relative irreproducibility of the response. This variance may be attributed to the difficulty which the sulphur solute species has to re-establish the original equilibrium concentration profile after the voltammetric perturbation. However from the very roughly linear increase in peak current with increasing $\nu^{\frac{1}{2}}$ a diffusion-controlled process may be inferred. This is more reliably confirmed from the linear $I\text{-}t^{-\frac{1}{2}}$ plot.

The primary objective of this experiment was to obtain a measure of the saturation solubility of sulphur gas in $PbCl_2$-based melt and further to determine the influence of the partial pressure of the gas phase.

Previous workers [190] estimated the saturation solubility of sulphur to be 2.3×10^{-4} mole S/cm^3 in a PbS-PbCℓ$_2$-NaCℓ (2.4×10^{-3} mole PbS/cm^3) melt at 430°C and 5.4×10^{-5} mole S/cm^3 in a 1.2×10^{-3} mole PbS/cm^3 solution. These authors found that upon adding sulphur pellets to the PbS-PbCℓ$_2$-NaCℓ solution a further additional reduction transition time was observed at a vitreous carbon electrode which was directly attributed to the reduction of sulphur. The saturation solubility was computed from the maximum transition time τ which was obtained upon continuous addition of sulphur. However the technique of adding sulphur pellets via a capillary tube even at a temperature of 430°C leads to the continuous vapourisation of sulphur from the melt. It is, therefore, unlikely that a true saturation solubility of sulphur can be obtained using this procedure.

In any explicit evaluation of gas solubility in a melt both the partial pressure of the gas phase and temperature must be included. The techniques and experimental arrangement required to vary the partial pressure of sulphur at any particular temperature has been fully analysed and perfected by the Flengas group [170]. However the apparatus required is very complex and was not applied in this present study. The experimental technique employed here relies upon the fact that the saturation pressure of gaseous sulphur in the cell is fixed by the equilibrium reaction:

$$S(\ell) \overset{K}{\rightleftharpoons} \tfrac{1}{2} S_2(g)$$

$$K = -RT \log P_{S_2}^{\frac{1}{2}}$$

The value of the equilibrium constant K and hence P_{S_2} is dependent upon the temperature of the system. The above equilibrium reaction assumes the gaseous sulphur species to be S_2, although it is well know that an equilibrium distribution of sulphur species (S_n, n = 2-8) occurs within the gas phase, see Section 3.2.2. Thus the true pressure of sulphur may be represented by:

$$P_S = \sum_{i=2}^{8} P_i$$

The ΔG° functions for the equilibrium

$$\frac{i}{2}\ S_2(g) \rightleftharpoons S_i(g)$$

have been given by Eriksson and Tegman [55]. However within the temperature range employed in this experiment the S_2 species is expected to be the most dominant. Thus the dissolved sulphur gas consists primarily of the S_2 species although a distribution of other S_n (n = 3-8) is most likely.

Since an 'all enclosed' cell design has been employed the results obtained reflect a truer equilibrium and hence saturation condition. The computed values of the saturation solubility of sulphur in the pure $PbCl_2$-KCl-NaCl melt are slightly higher, but of the same magnitude to those obtained by Skylas and Welch [190] in PbS-containing solutions. One would expect a greater solubility in PbS melts since both a physical and chemical dissolution mechanism is implied.

The increase in sulphur solubility with increasing P_{S_2} is shown (Fig. 7.6) as a plot of $I_p^c T^{\frac{1}{2}}$ vs $P_{S_2}^{\frac{1}{2}}$. The value of I_p^c is dependent upon both temperature and concentration of solute species and is expressed through the Randles Sercik equation, i.e.

$$I_p^c = \frac{0.42\ n^{3/2} F^{3/2} A\ \nu^{\frac{1}{2}} C}{R^{\frac{1}{2}} T^{\frac{1}{2}}}$$

The peak current may be normalised with respect to temperature by plotting the parameter $I_p^c T^{\frac{1}{2}}$. The concentration C_S may to a first approximation be related to the partial pressure of sulphur gas by Henry's law, i.e.

$$C_S = H(T)\ P_{S_2}^{\frac{1}{2}}$$

where H(T) is the Henrian constant.

An approximately linear relation between $I_p^c T^{\frac{1}{2}}$ vs $P_{S_2}^{\frac{1}{2}}$ was obtained for the fifth cycle of the fifth voltammogram. A large discrepancy occurs between the above relation and that for the initial cycle obtained at each temperature. However, allowing for the relatively large scatter obtained from the voltammograms a reasonably linear plot of $I_p^c T^{\frac{1}{2}}$ vs $P_{S_2}^{\frac{1}{2}}$ was obtained, thus confirming the principle of the cell design.

The computed values of C_S are much higher than one would expect for a 'pure' physical dissolution mechanism. For example, the solubilities of inert gases in alkali halides are of the order of 10^{-7} moles/cm^3. Reactive gases, i.e. exhibiting a chemical dissolution mechanism on the other hand exhibit larger solubilities and a very wide range of values may be obtained depending upon the system. Typical examples may be cited, e.g. 1.33×10^{-7} moles $C\ell_2$/cm^3 in KCℓ at 823°C to 12.80×10^{-5}mole HF/cm^3 in NaF (0.195) - ZrF_4 and of course chemical synthesis reactions may occur, e.g. $TiC\ell_4(g) + 2NaC\ell(\ell) \rightleftharpoons Na_2TiC\ell_6$ (s) [267].

A word of caution should, however, be added concerning the possibility of an experimental artefact when using a cell of this design. Gaseous solubility in molten salts may, as was outlined above, be described as either 'chemical' or physical and in some systems both types may be present [267]. A physical solubility arises from the concept that the molten salt structure contains voids or 'holes'. The measured solubilities of, for example, inert ~~cycles~~ gases in alkali halides are in good agreement with the values predicted from 'hole' theories [267] even though many assumptions are made in the latter theories. The present experimental arrangement used an initially powdered salt and there exists therefore a large voidage fraction into which sulphur gas may permeate prior to the melting of the salt. It is, therefore, feasible that excess sulphur gas may become physically entrapped in the liquid salt and thus contribute to a higher C_S value. During the experiment some very gentle shaking of the cell and a prolonged

equilibrium time was sued in an attempt to eliminate, as far as possible, the above condition. Obviously the effect of voidage may be eliminated by the use of a solid mass of salt.

CHAPTER 8

THE ELECTROCHEMISTRY OF POLYSULPHIDE CONTAINING SOLUTIONS

8.1 Introduction

The aim of the work reported here was to electrochemically characterise $PbCl_2$-based melts containing various polysulphide ions, i.e. S_n^{2-} (n = 2-6,8) using the techniques of cyclic voltammetry and chronoamperometry. Sulphur is known to chemically react with the sulphide ion to yield polysulphide ions according to the general reaction:

$$S^{2-} + \frac{(n-1)}{2} S_2(g) \rightleftharpoons S_n^{2-} \quad (n = 2\text{-}6,8)$$

Indeed the above reaction is the basis for the synthesis of, for example, alkali metal polysulphides. It is clear therefore that electrochemically generated sulphur may back-react with the S^{2-}-containing solution to yield reducible polysulphide ions.

The polysulphides employed in this present study were those of Na_2S_2, Na_2S_4 and Na_2S_5. The compounds were prepared by heating stoichiometric quantities of dry Na_2S and S according to the method of Tegman (58), see section 4.6.

Initially pellets of the polysulphide compounds were added to the purified $PbCl_2$-KCl (77-23 m/o) eutecic at 460°C. Decomposition of all the polysulphides occurred immediately with the evolution of gaseous sulphur. As a result the metal parts of the cell (i.e. electrode contacts) were attacked and as a consequence the 'run' was terminated. Further experiments were undertaken using the $PbCl_2$-KCl-NaCl ternary eutectic melt, initially at 440°C. Again the polysulphides decomposed yielding sulphur gas. However adequate protection of the electrodes allowed some useful data to be

collected. The 'runs' were again terminated after prolonged attack of the metal parts by the sulphur gas.

Upon adding the polysulphides, dark precipitates were initially formed and the solution within the vicinity of the particles became green in colour. However upon prolonged Ar bubbling the green colouration disappeared and the sulphur gas removed from the system. The collection of electrochemical data was usually limited to a 2 hour period after the complete removal of the sulphur gas.

The voltammetric response obtained at a vitreous carbon electrode was exactly the same for all of the polysulphides added. Thus to avoid unnecessary repetition only the results for the polysulphide Na_2S_4 will be given in detail.

Cyclic voltammograms were obtained as a function of increasing sweep rate (0.02 - 0.4 V/s) and polysulphide concentration, i.e. 1.496×10^{-2} - 6.21×10^{-2} mole Na_2S_2/Kg; 5.69×10^{-3} - 1.76×10^{-2} mole Na_2S_4/Kg and 7.564×10^{-3} - 3.10×10^{-2} mole Na_2S_5/Kg. A sealed planar vitreous carbon electrode was used.

The measured open circuit potential of the inert electrode was found to vary in a random manner after each polysulphide addition, thus indicating the absence of any redox poising reactions in solution.

8.2 Results

8.2.1 Cyclic Voltammetry

Fig. 8.1 shows a typical voltammogram obtained at a vitreous carbon electrode after the complete removal of sulphur gas from the solution. The upper switching potential was limited to +0.6V wrt Ag^+/Ag. The voltammogram clearly shows the presence of a single oxidation wave occurring at a peak potential of $E_p^a = 0.4V$. A single corresponding reduction wave occurs at $E_p^c \cong 0.33V$. The morphology of the I-E curves are typical of that expected for the deposition and stripping of an insoluble product.

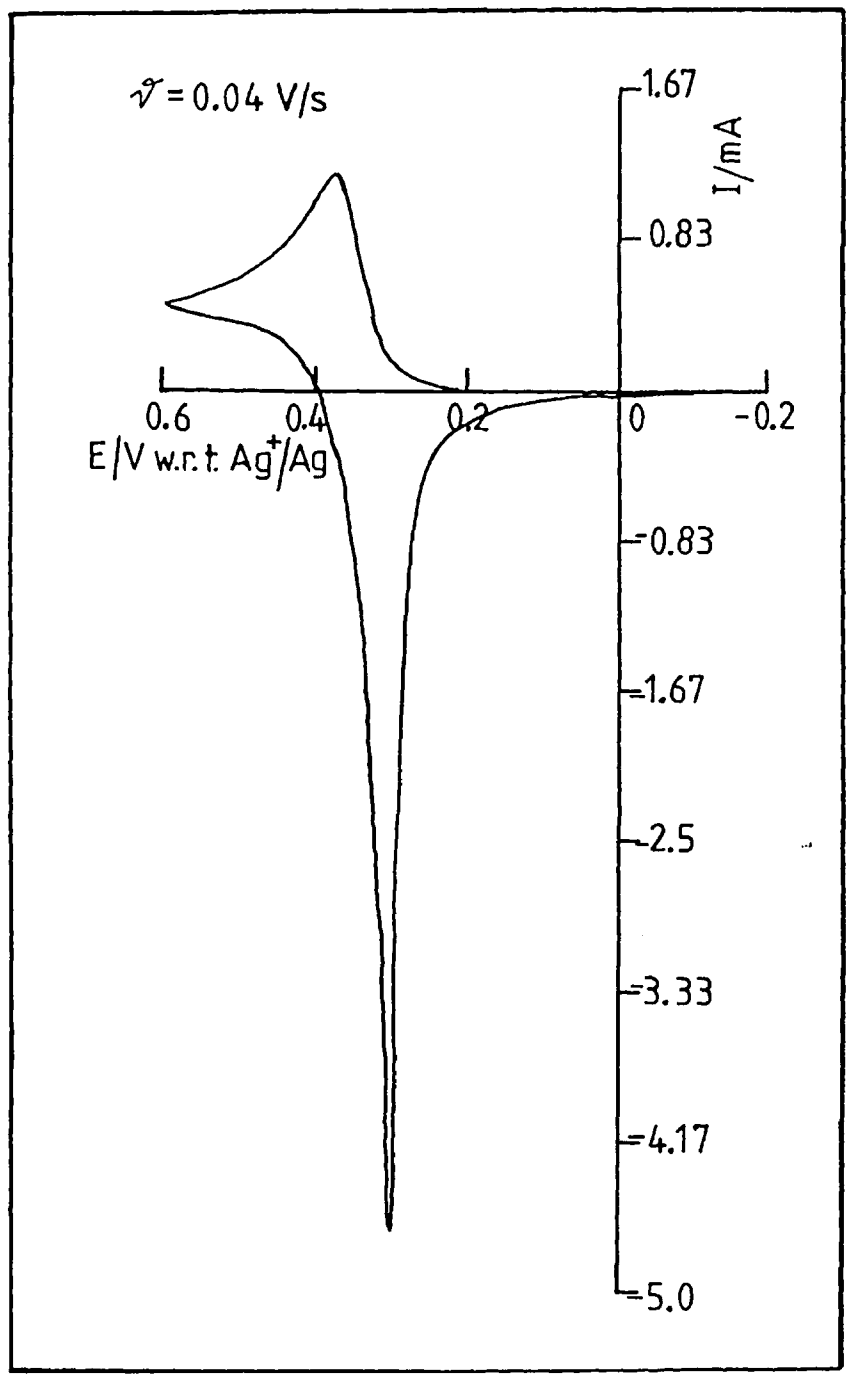


Fig. 8.1: A cyclic voltammogram obtained at a vitreous carbon electrode in an initial solution of Na_2S_4 in the $PbCl_2$-KCl-NaCl melt. $[Na_2S_4] = 1.26 \times 10^{-2}$ mole/Kg T = 440°C. Electrode area = 0.0855 cm^2.

TABLE 8.1

The effect of increasing sweep rate upon the cyclic voltammetric parameters for an initial 5.691×10^{-3} mole Na_2S_4/Kg in the ternary $PbCl_2$-KCl-NaCl melt at 440°C. Electrode = vitreous carbon; Area = 0.0855 cm^2.

V v/s	Ip^a mA	$Ip^a/v^{\frac{1}{2}}$	Ip^c/Ip^a	Ep^a V	Ep^c V	ΔE V	Ep^a-Ep/2 V
0.02	0.425	3.01	3.47	0.4	0.335	0.065	0.05
0.04	0.575	2.88	3.22	0.4	0.330	0.06	0.05
0.06	0.666	2.72	3.38	0.4	0.330	0.06	0.05
0.08	0.766	2.71	3.27	0.4	0.330	0.06	0.05
0.10	0.833	2.64	3.28	0.4	0.335	0.065	0.05
0.15	1.00	2.58	3.19	0.4	0.330	0.06	0.05
0.20	1.21	2.70	3.01	0.4	0.330	0.06	0.05
0.25	1.33	2.67	2.98	0.4	0.330	0.06	0.05
0.30	1.50	2.74	2.84	0.4	0.330	0.06	0.05
0.35	1.60	2.71	2.81	0.4	0.330	0.06	0.05
0.40	1.75	2.77	2.70	0.4	0.325	0.075	0.05

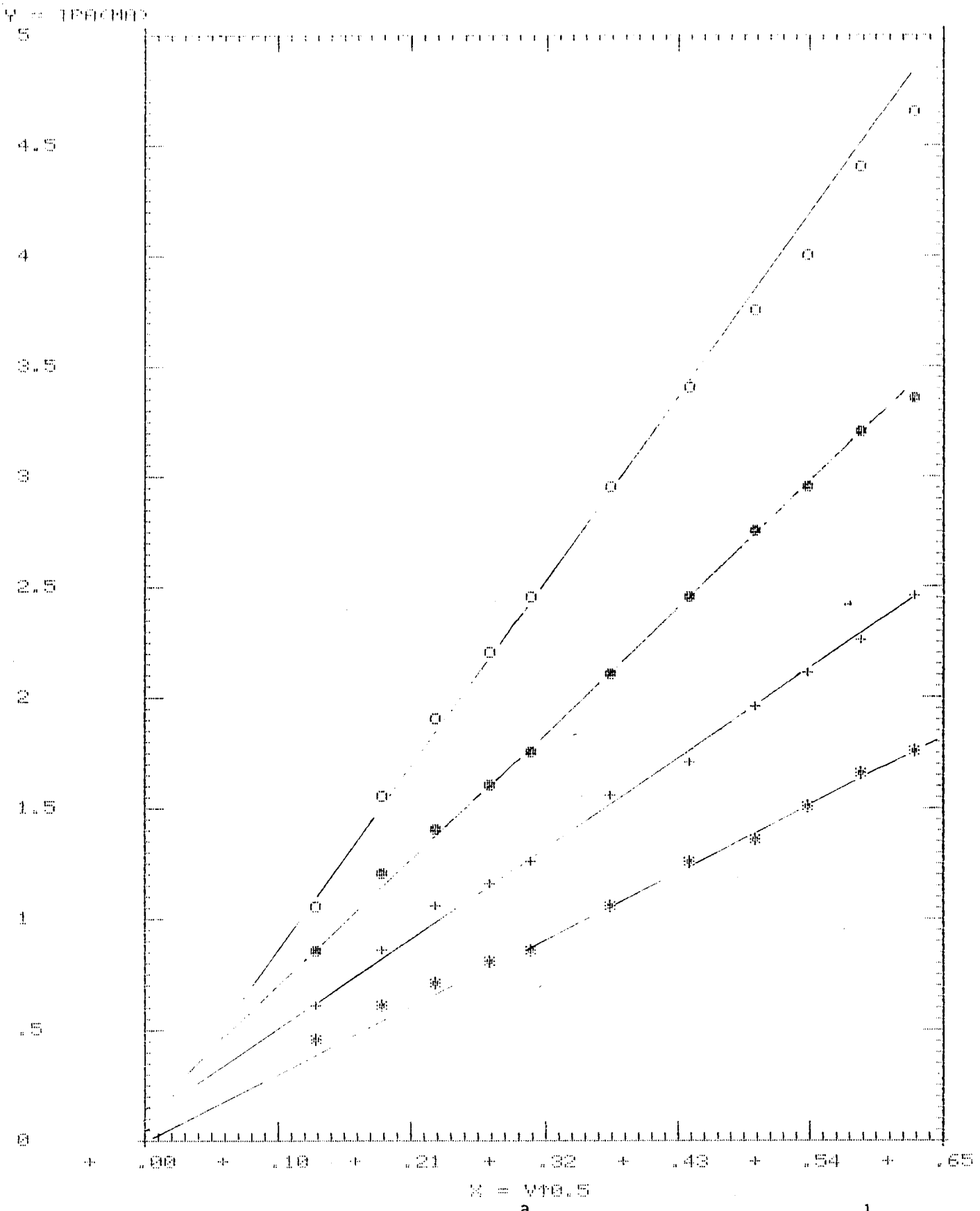


FIGURE NUMBER 8.2: A plot of I_p^a as a function of (sweep rate)$^{\frac{1}{2}}$. For an initial solution of Na_2S_4 in the $PbCl_2$-KCl-NaCl melt. * = 5.69×10^{-3}M; + = 9.07×10^{-3}M; ● = 1.69×10^{-2}M; O = 2.19×10^{-2}M.

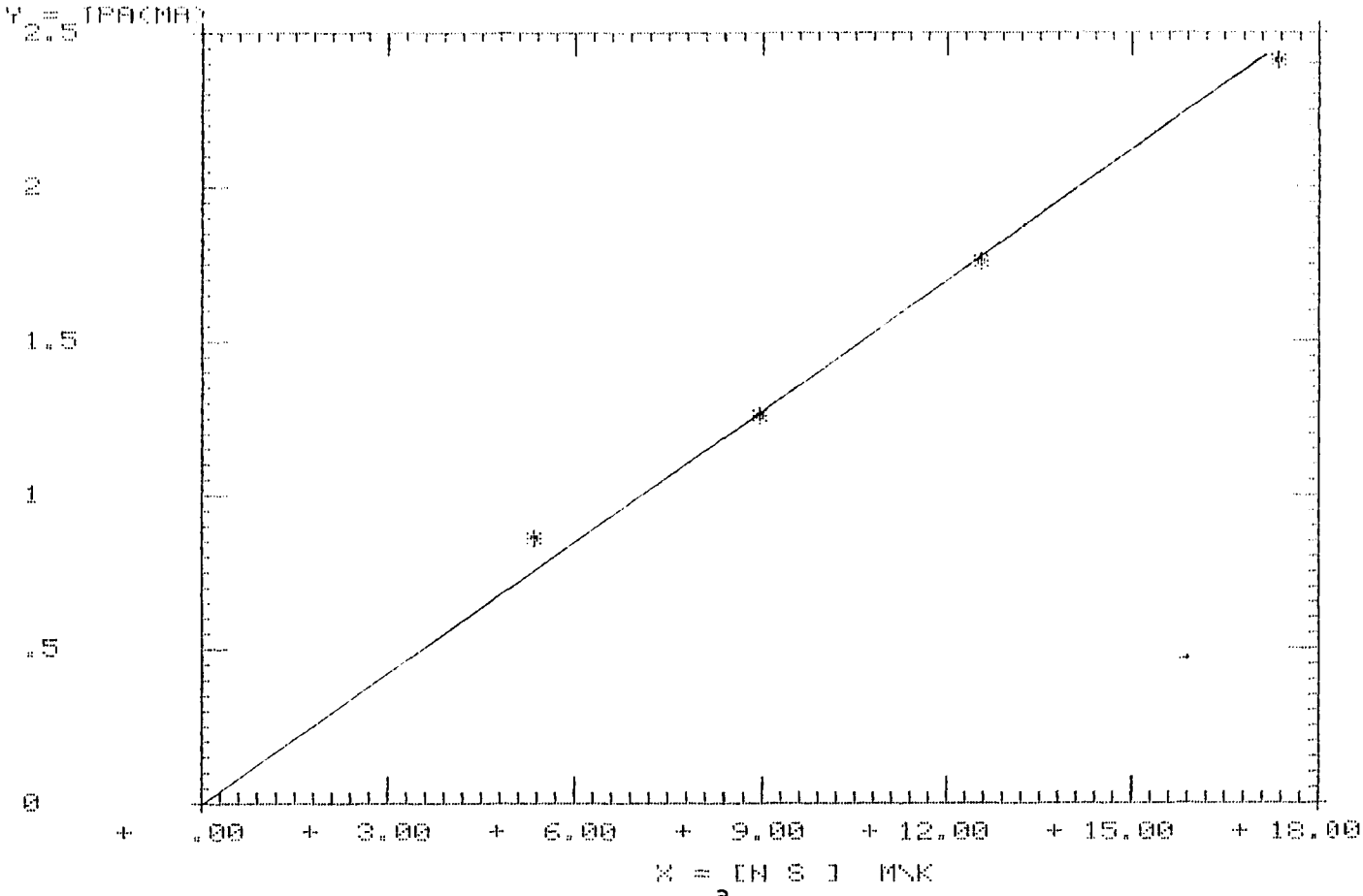


FIGURE NUMBER 8.3: A plot of I_p^a vs Na_2S_4 concentration for a sweep rate of 0.1 V/s. Solvent = $PbC\ell_2$-$KC\ell$-$NaC\ell$; temperature = 440°C; electrode = vitreous carbon; area = 0.0855 cm^2.

The effect of increasing scan rate upon the voltammetric parameters is given in Table 8.1 for an initial Na_2S_4 concentration of 5.691×10^{-3} mole/Kg. Fig. 8.2 shows the oxidation peak current to increase linearly with increasing (sweep rate)$^{\frac{1}{2}}$ with zero current intercepts. The more sensitive current function $I_p^a/\nu^{\frac{1}{2}}$ remains virtually constant with increasing sweep rate thus inferring the absence of any kinetic or chemical complication to the electron transfer stop. The ratio of the reverse to forward peak currents, i.e. I_p^c/I_p^a was found to be much greater than unity as calculated from the modified Nicholson equation (18). The latter result confirms the oxidation product to be of an insoluble nature. The peak potentials E_p^a and E_p^c remain constant with increasing sweep rate with values of 0.4V and 0.33V respectively. Thus the peak separation $E = E_p^a - E_p^c$ remains constant with increasing sweep rate as does the half peak width $(E_p^a - E_{p/2})$ with values of 70 mV and 50 mV respectively.

The effect of increasing the initial Na_2S_4 concentration upon the anodic peak current is shown in Fig. 8.3. The peak current I_p^a increases linearly with increasing Na_2S_4 concentration with an extrapolated zero intercept.

8.2.2 Chronoamperometry

A typical I-t response as a result of a small (0.5s) constant potential pulse is shown in Fig. 8.4, and the analysed results in Table 8.2. Fig. 8.5 clearly shows that the current I^a decreases linearly with decreasing $t^{-\frac{1}{2}}$ and hence obeys the Cottrell equation, i.e.

$$I = nFC \left(\frac{D}{\pi t}\right)^{\frac{1}{2}}$$

The product $It^{\frac{1}{2}}$ remains constant throughout the current decay.

No peaks in the I-t transients were observed at any applied potential which could be attributed to a nucleation and growth phenomenon.

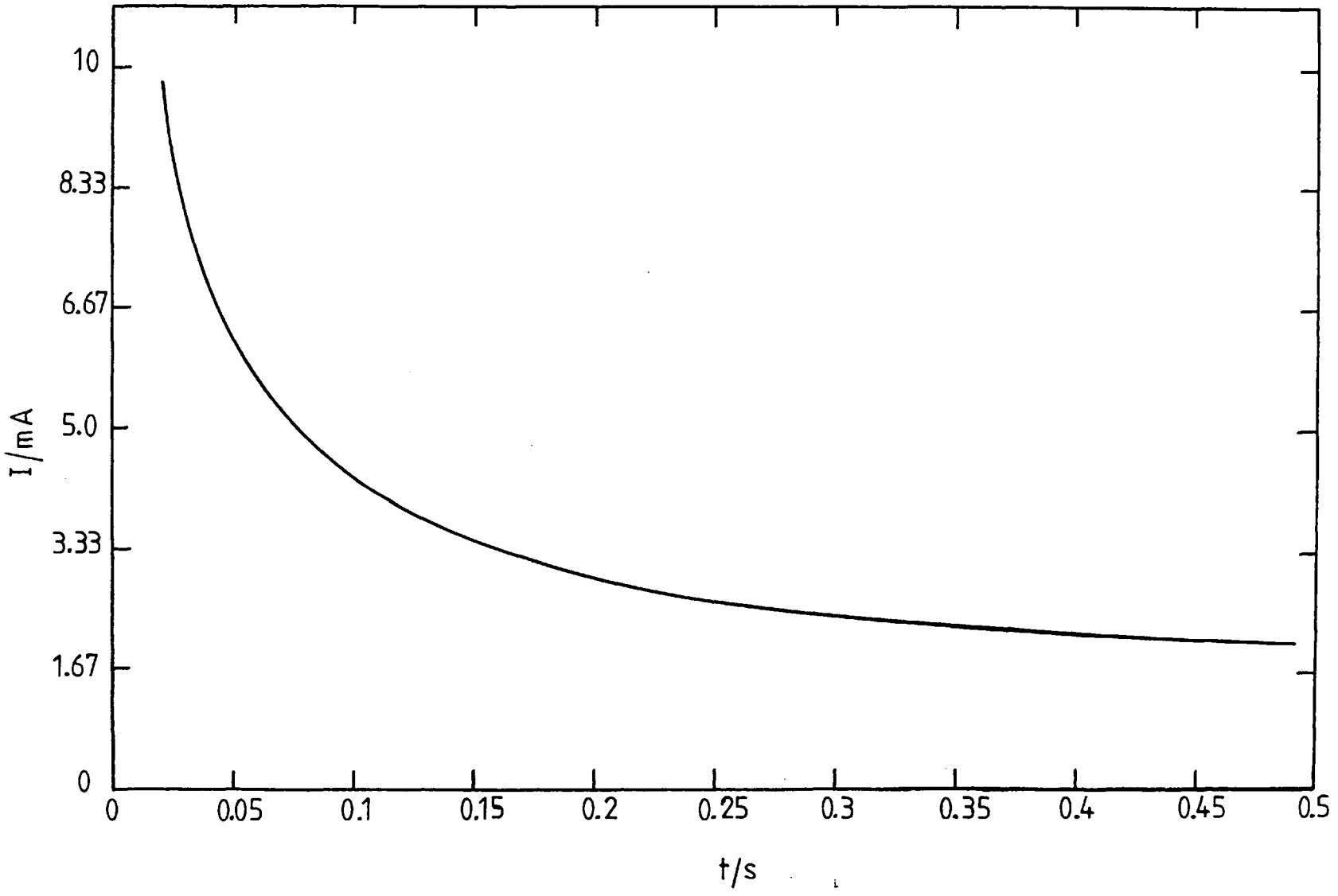


Fig. 8.4: A typical I-t response obtained at a vitreous carbon electrode for the oxidation of an initial solution of 1.76×10^{-2} mole Na_2S_4/Kg. Solvent = $PbC\ell_2$-KCℓ-NaCℓ. Temperature 440°C; area = 0.0855 cm^2; E = 0.45V wrt Ag^+/Ag.

TABLE 8.2

The results obtained from an I-t transient for the oxidation of an initial solution of 1.76×10^{-2} mole Na_2S_4/Kg at 440°C. E = +0.4V wrt Ag^+/Ag. Electrode = vitreous carbon; Area = 0.0855 cm^2.

I^a mA	t (s)	$t^{-\frac{1}{2}}$ $s^{-\frac{1}{2}}$	$It^{\frac{1}{2}}$ $mAs^{\frac{1}{2}}$
5.75	0.05	4.472	1.286
4.0	0.10	3.162	1.265
3.25	0.15	2.582	1.259
2.75	0.2	2.236	1.230
2.458	0.25	2.00	1.230
2.375	0.30	1.826	1.301
2.208	0.35	1.690	1.306
2.08	0.4	1.581	1.318
1.958	0.45	1.491	1.314

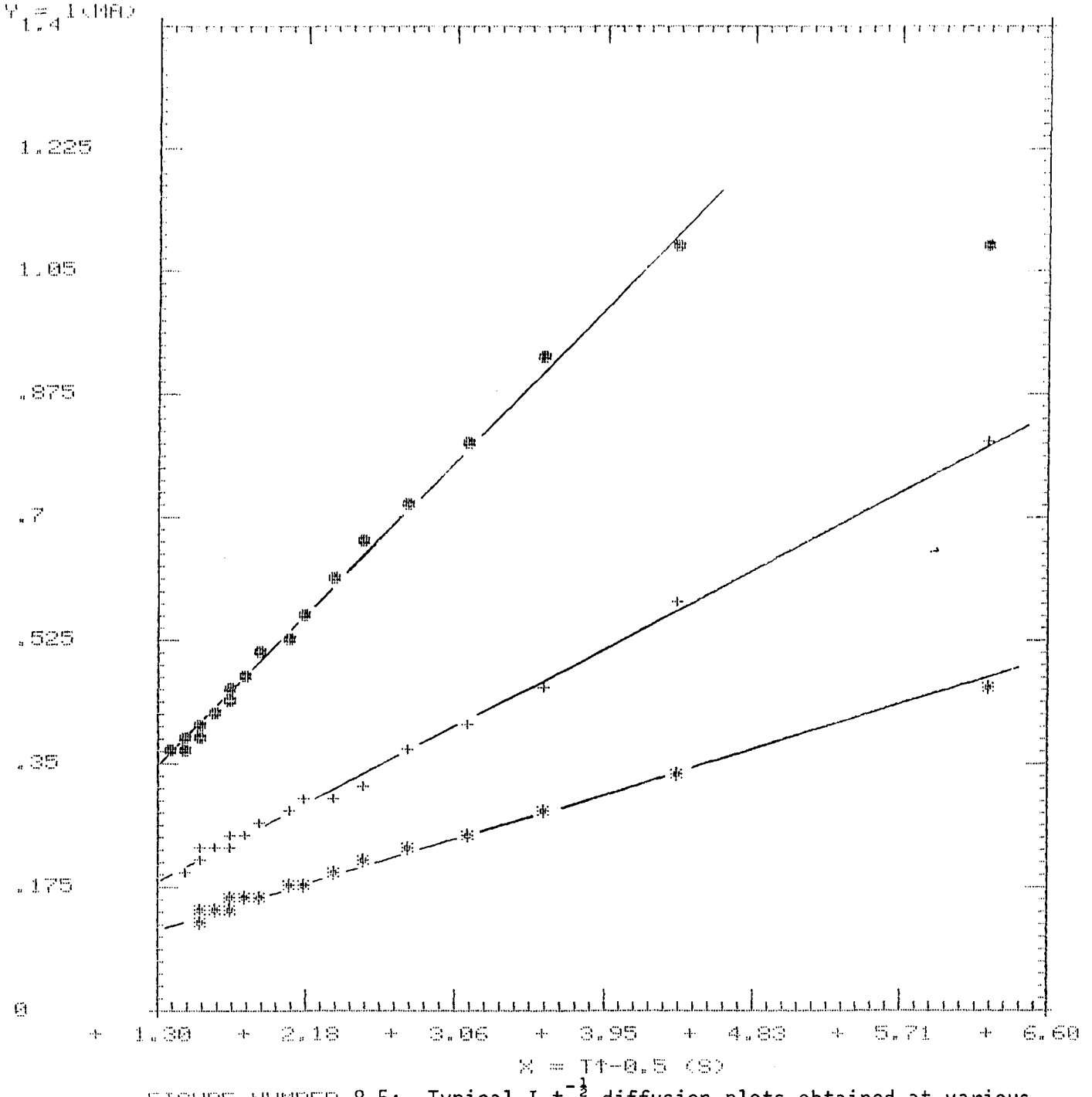


FIGURE NUMBER 8.5: Typical $I\text{-}t^{-\frac{1}{2}}$ diffusion plots obtained at various applied potentials.
⋆ E = 0.28V wrt Ag^+/A; + E = 0.3V; ● E = 0.35V.
$[Na_2S_4]$ = 1.76 x 10^{-2} mole/Kg; Solvent = $PbCl_2$-KCl-NaCl; electrode = vitreous carbon; area = 0.0855 cm^2; T = 440°C.

8.3 Discussion

The results have shown that alkali metal polysulphides decompose when added to $PbC\ell_2$-based melts, the most probable reaction being:

$$Na_2S_n \rightarrow Na_2S_{(soln)} + \frac{n-1}{2} S_2(g)$$

However the free energy values for the above reaction calculated from the data given by Tegman (268) are quite positive, i.e. Na_2S_2 ΔG_r = + 41.3 KJ/mole, Na_2S_4 ΔG_r = +91.5 kJ/mole and Na_2S_5 ΔG_r = +101.9 KJ/mole at T = 723K. The above decomposition reaction goes to completion because of the removal of gaseous sulphur from the system.

The voltammetric response of the resultant solutions compares very well with those obtained from PbS containing solutions at the same temperature, thus inferring the presence of the S^{2-} ion. However a notable difference between the two sets of I-E curves is the absence of a pre-wave on the present voltammograms. The general shape of the I-E curve suggests the deposition and stripping of an insoluble product and is confirmed by the $I_p^c/I_p^a > 1$ values. The insoluble product is presumably S. The oxidation wave conforms to the Randles Sevcik equation, i.e. I_p^a increasing linearly with both increasing $\nu^{\frac{1}{2}}$ and concentration (both exhibit extrapolated zero current intercepts) and this clearly shows the process to be diffusion-controlled. Further confirmation is obtained from the I-t response and the Cottrell equation. The very small potential peak separation, i.e. E = 0.07V indicates the electron transfer step to be highly reversible. The number of electrons (n) involved in the oxidation process may be obtained from the half peak width value, i.e. $E_p^a - E_{p/2}$. Using the appropriate equation for an insoluble product (19):

$$E_p^a - E_{p/2} = 0.77\ RT/nF$$

an n = 1 is obtained.

The n value calculated by this means is clearly inconsistent with the proposed mechanism

$$S^{2-} \rightarrow S + 2\varepsilon$$

Unfortunately the n value was not confirmed by an exhaustive controlled potential electrolysis.

The work of Cleaver et al (147) has similarly demonstrated the decomposition of sodium polysulphides to occur when they were added to a LiCℓ-KCℓ eutectic melt at 420°C yielding sulphur gas. The same authors concluded that Na_2S was completely insoluble in the LiCℓ-KCℓ melt. However Cleaver et al (147) found that the addition of $Na_2S_{2.2}$ led to stable solutions for a sufficient period to allow the collection of voltammetric information. The cyclic voltammograms obtained at a gold electrode revealed two oxidation and reduction processes. The more anodic of the two oxidation waves was demonstrated to be due to the deposition and stripping of insoluble sulphur. The less anodic wave was determined to be a n = 1 process and by comparison with their results obtained in the KSCN melt this was attributed to the reaction:

$$S_2^{2-} \longrightarrow S_2^{-} + \varepsilon'$$

Both oxidation and reduction waves were found to be diffusion controlled and a $D = 5.7 \times 10^{-5}$ cm^2/s was calculated for the disulphide ion.

CHAPTER 9

IDENTIFICATION OF ANIONIC IMPURITIES IN THE $PbCl_2$-KCl EUTECTIC MELT

9.1 Introduction

During the electrochemical examination of PbS-$PbCl_2$-KCl solutions a pre-wave associated with the main S^{2-} oxidation wave was noted. It was subsequently decided to determine if the presence of the pre-wave could be directly attributed to any anionic impurity species. The impurity compounds studied were PbO, PbO_2 and $PbSO_4$ over the corresponding concentration ranges 4.31×10^{-5} - 1.90×10^{-4} mole PbO/cm^3, 3.61×10^{-5} - 1.74×10^{-4} mole PbO_2/cm^3 and 5.29×10^{-5} - 1.91×10^{-4} mole $PbSO_4/cm^3$ respectively. The solvent melt was the $PbCl_2$-KCl (77-23 m/o) eutectic at 450°C; a planar vitreous carbon electrode was used.

9.2 PbO and PbO_2 Solute

9.2.1 Results

Both PbO and PbO_2 pellets were found to dissolve rapidly in the solvent. A voltammetric examination of the resultant solutions showed the same response for both types of solute species. Fig. 9.2.1 shows a typical I-E curve obtained. A single oxidation wave with a peak potential of $\sim$0.9V w.r.t. Ag^+/Ag was observed and no corresponding reduction wave was obtained within the available potential window of the solvent or within the range of scan-rates employed (0.02-0.4 V/s). A precise electrochemical evaluation of the oxidation process was hampered by the irreproducibility of the voltammetric response; see for example Fig. 9.2.2. The influence of increasing scan rate is shown in Fig. 9.2.3 and some approximate voltammetric parameters are given in Table 9.2.1 below.

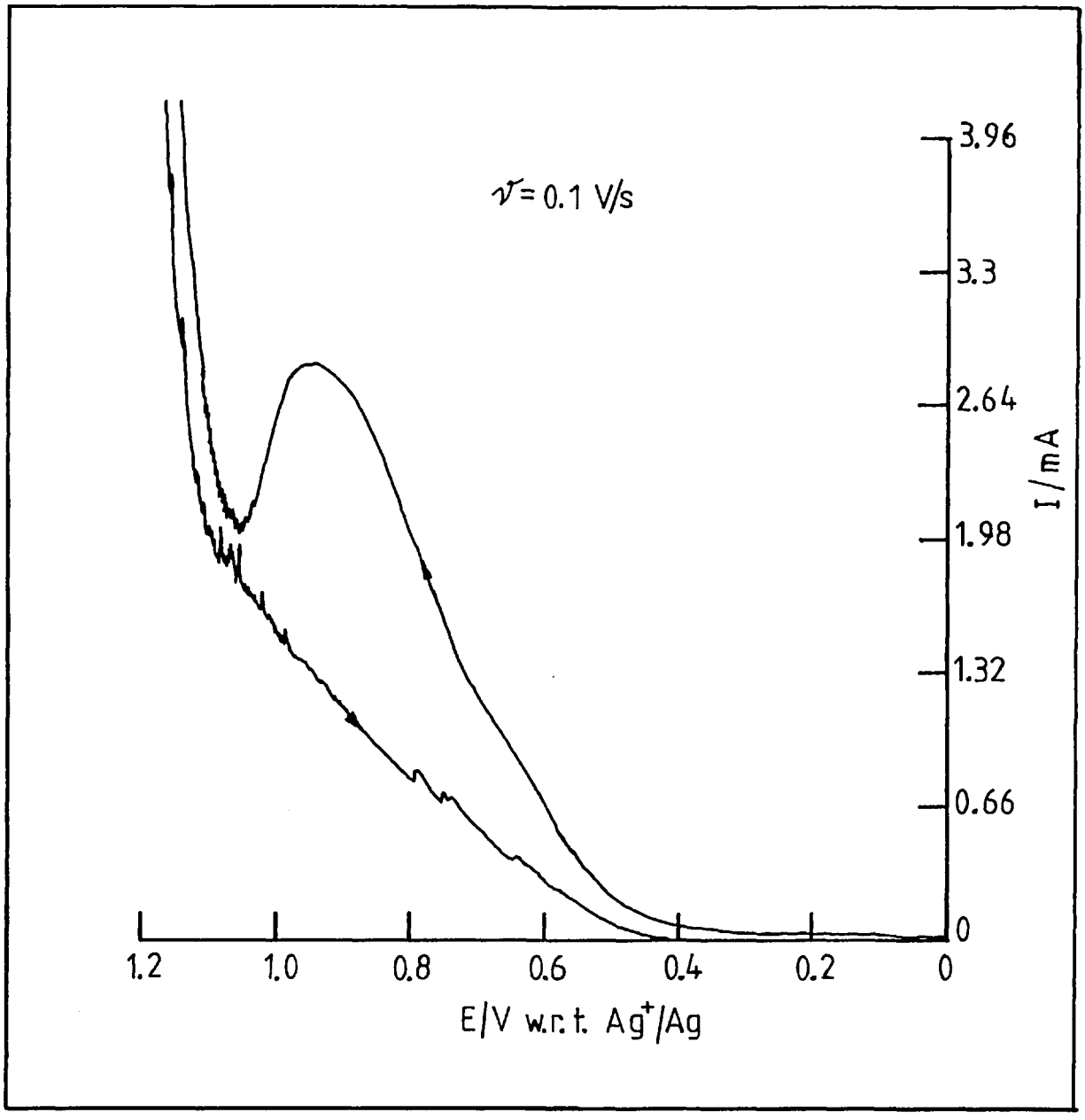


Fig. 9.2.1: A cyclic voltammogram for the oxidation of PbO in the $PbCl_2$-KCl (77-23 m/o) melt at 450°C.
[PbO] = 8.17×10^{-5} mole $/cm^3$; electrode = vitreous carbon; area = 0.0855 cm^2.

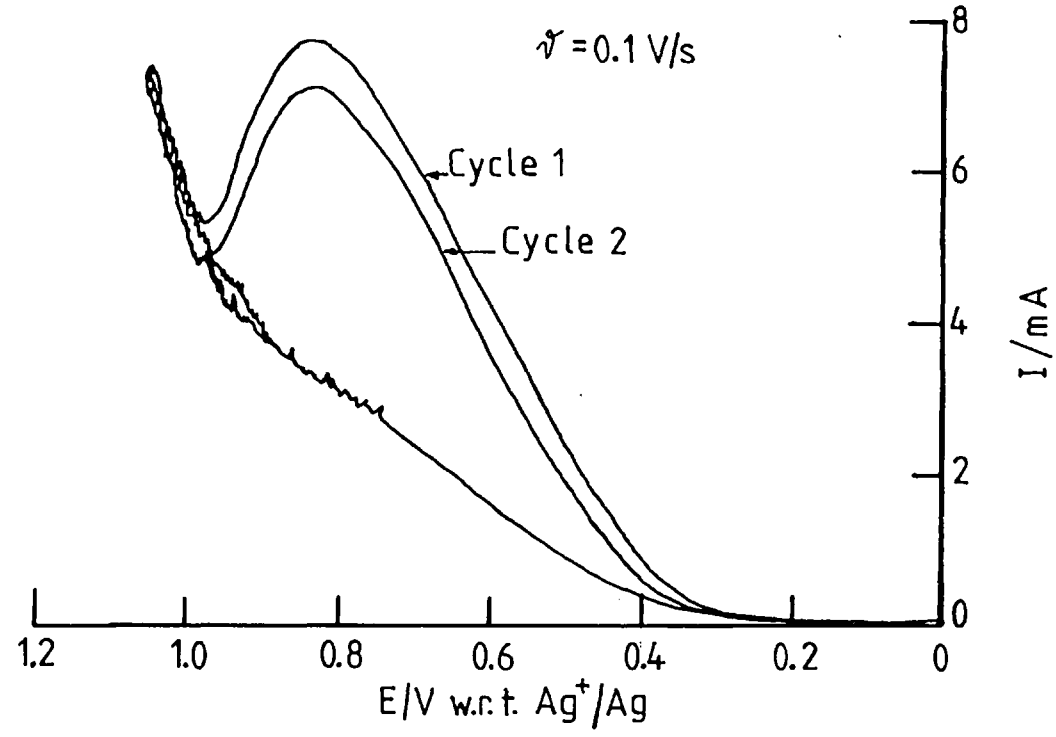


Fig. 9.2.2: The influence of cycling on the voltammetric response for O^{2-} oxidation.
[PbO] = 1.90 x 10^{-4} mole/cm^3. T = 450°C; solvent = $PbCl_2$-KCl; electrode = vitreous carbon; area = 0.0855 cm^2.

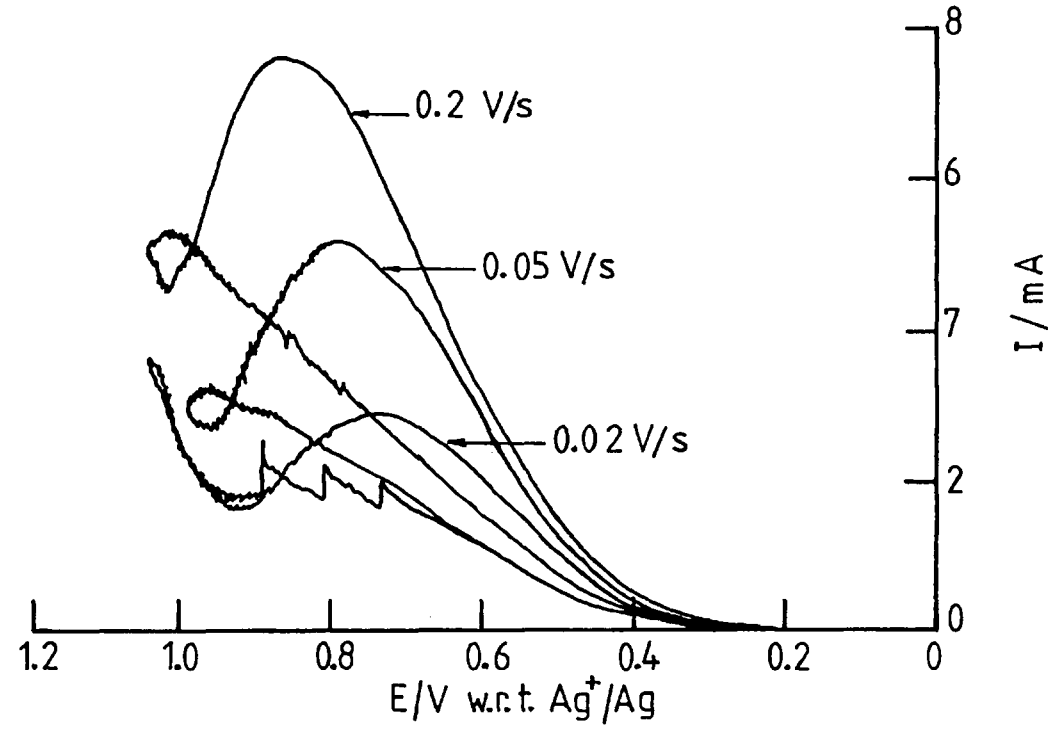


Fig. 9.2.3: The influence of increasing scan rate upon the oxidation of O^{2-} at a vitreous carbon electrode.
[PbO] = 1.90 x 10^{-4} mole/cm^3; solvent = $PbCl_2$-KCl; T = 450°C; area = 0.0855 cm^2.

TABLE 9.2.2.

The influence of PbO and PbO_2 concentration upon the voltammetric parameters. Sweep rate = 0.1V/S. Electrode = Vitreous Carbon Area = 0.0855 cm^2

C mole/cm^3	Ip^a mA	Ep^a V	Ep^a-Ep/Z^a mV
PbO 4.31×10^{-5}	1.3	1.05	300
PbO 8.17×10^{-5}	2.87	0.95	220
PbO 1.34×10^{-4}	4.08	0.90	210
PbO 1.90×10^{-4}	5.7	0.87	210
PbO_2 3.61×10^{-5}	0.3	0.94	240
PbO_2 7.98×10^{-5}	0.3	0.92	230
PbO_2 1.27×10^{-4}	2.2	0.94	250
PbO_2 1.74×10^{-4}	3.9	0.935	250
"			

Table 9.2.1: The influence of increasing scan rate (ν) upon the oxidation of PbO in the $PbCl_2$-KCl (77-23 m/o) melt at 450°C. [PbO] = 1.9×10^{-4} mole/cm^3; electrode = vitreous carbon; area = 0.0855 cm^2.

ν V/s	I_p^a mA	$I_p^a/\nu^{\frac{1}{2}}$ mA $V^{-\frac{1}{2}}$ $S^{\frac{1}{2}}$	E_p^a V	$E_p^a - E_{p/2}^a$ mV
0.02	2.9	20.51	0.73	200
0.05	5.15	23.03	0.79	200
0.15	7.6	19.62	0.87	230
0.20	6.85	15.32	0.9	255
0.30	8.1	14.79	0.94	260

It is noted that the peak potential E_p^a shifts anodic with increasing scan rate which possibly indicates an irreversible electron transfer step. The variation of the peak current value and the half-peak width may be due to the irreproducibility of the voltammograms.

The influence of increasing solute concentration upon the voltammetric parameters is given in Table 9.2.2 for a scan rate of 0.1 V/s. The results correspond to the initial cycle.

9.2.2 Discussion

Lead oxide (PbO) is known to be highly soluble in $PbCl_2$ and indeed the phase diagram indicates a solubility of ~20 m/o PbO at 450°C (269). Thus PbO may be a significant impurity element in any inadequately purified $PbCl_2$ based electrolyte. Furthermore, the $PbCl_2$-KCl (77-23 m/o) melt has been shown to dissolve many metal oxides to a significant degree (193). Thus Plichon and de Guibert (193) determined the solubilities of BaO, CaO, CdO, Ag_2O, MnO and Cu_2O to be > m/o at 440°C and those of SnO_2, CoO and NiO to be $< 10^{-2}$ M. The metal oxide Cr_2O_3 was found to be totally insoluble in this melt. The slow scan (5 mV s^{-1}) voltammetric response at a vitreous carbon

electrode of PbO-$PbCl_2$-KCl solutions obtained by the same authors showed a single very broad wave to occur at ~1.2V w.r.t. Pb^{2}/Pb. This is in agreement with the results presented here. The number of electrons involved in the oxidation process was determined as n = 2 (per mole PbO) via constant potential electrolysis. The overall reaction scheme

$$2O^{2-} + C(s) \rightarrow CO_2(g) + 4\varepsilon'$$

was proposed.

It is interesting to note that the voltammetric response for both PbO and PbO_2 solutes was the same (at least to within the experimental precision obtained in these experiments). The decomposition reaction

$$PbO_2(s) \rightarrow PbO(s) + \tfrac{1}{2}O_2(g)$$

has a free energy of $\Delta G = -5.333$ Kcal/mole at 450°C (723K) and this probably explains this observation. Solutions containing both PbO and PbO_2 did not result in any redox poising reactions, which could be attributed to the above reaction. However, these experiments were conducted under an atmosphere of purified Ar and thus any gaseous O_2 formed would have been displaced. No further experiments were undertaken using PO_2 atmospheres.

The results obtained within this brief study are not sufficient to provide any reliable mechanistic information. Indeed the sole purpose was to identify the oxidation waves due to PbO and PbO_2 solutes, the peak potentials for which occur at much more positive potentials than that for the S^{2-}/S oxidation.

9.3 $PbSO_4$ Solute

9.3.1 Results

The addition of $PbSO_4$ pellets to the purified solvent initially results in a very 'cloudy' solution which cleared upon prolonged Ar agitation. No insoluble species was observed. A voltammetric examination of the resultant

solution at 450°C did not reveal any electroactive species to be present in the melt. The I-E curves were exactly the same as those obtained in the pure solvent melt. The $PbCl_2$-$PbSO_4$ phase diagram (269) shows that at a temperature of 500°C the solubility of $PbSO_4$ is approximately 10 m/o. A further experiment at 530°C similarly showed the absence of any electroactive species.

The addition of 1.91×10^{-4} mole $PbSO_4/cm^3$ to a PbS-$PbCl_2$-KCl solution (5.414×10^{-5} mole PbS/cm^3) at 450°C did not in any way change the voltammetric charadteristics of the S^{2-}/S reaction.

9.3.2 Discussion

The voltammetric examination of $PbSO_4$-containing solutions has shown the SO_4^{2-} anion to be electrochemically inactive within the potential range of the $PbCl_2$-KCl solvent at temperatures of 450°C and 530°C.

Pure sulphate melts are known to undergo anodic decomposition of inert electrodes to form sulphur trioxide and oxygen (270-274). However the results obtained in the present study do not agree with those of Rempell (275) who reported the SO_4^{2-} ion to be oxidised (and hence electrochemically active) at a potential less positive than that for chlorine evolution in the NaCl-KCl melt. This may be explained by a comparison of the thermodynamic decomposition potentials for the reactions:

$$PbCl_2 \rightarrow Pb(l) + Cl_2(g) \qquad \Delta G_{773} = 58.486 \text{ Kcal/mole}$$

and

$$PbSO_4(s) \rightarrow Pb(l) + SO_3(g) + \tfrac{1}{2}O_2(g) \quad \Delta G_{773} = 74.074 \text{ Kcal/mole}$$

Using the relation $\Delta G = -nFE$, the calculated decomposition potentials for $PbCl_2$ and $PbSO_4$ are 1.268V and 1.606V respectively. Thus the anodic decomposition of $PbSO_4$ will not occur within the potential window of $PbCl_2$ unless a very significant depolarisation reaction occurs. Several authors

have concluded that the SO_4^{2-} anion is cathodically inactive in the LiCℓ-KCℓ melt (270-276), although Senderoff [277] and Woodwall (278) found that the SO_4^{2-} anion could be reduced via a two electron, diffusion-controlled process. Legey, (279) observed that the addition of SO_4^{2-} to a 1.44×10^{-2} molar Cr^{3+} solution did not affect the chronopotentiometric response for chromium deposition. Similarly Tran Kim Hoa (207) showed that the addition of $PbSO_4$ did not affect the Pb^{2+}/Pb chronopotentiometric response although the low current efficiencies were explained in terms of secondary reactions occurring between the Pb metal and $PbSO_4$.

Burrows and Hills (280) have suggested that the corrosion of many metals in melts containing SO_4^{2-} may be enhanced by the presence of SO_3 as a consequence of the reaction

$$SO_4^{2-} \longrightarrow SO_3 + O^{2-}$$

The equilibrium of the above reaction is clearly dependent upon the solubility of the metal oxide formed and indeed some supporting evidence has been given by Kochergin et al for the increased corrosion of iron in $ZnSO_4$-containing baths (281).

In the case of $PbSO_4$, the high solubility of PbO should enhance the reaction

$$PbSO_4 \longrightarrow PbO + SO_3$$

However an estimated ΔG for the above is quite positive, i.e. $\Delta G = + 40.39$ Kcal/mole at 773K, thus indicating the $PbSO_4$ to be a stable compound. Legey has further reviewed and investigated the techniques available for the removal of the SO_3^{2-} anion from melts (279).

CHAPTER 10

RELATED STUDIES

CONTACT ANGLE MEASUREMENTS

10.1 Introduction

A knowledge of the wetting characteristics of solvent electrolytes upon electrode substrates is very pertinent to an understanding of gas evolving electrodes, both from the technological and fundamental points of view. In particular the design of more efficient anode structures with a consequent improvement in the overall electrolytic process may result from a detailed description of the physico-chemical properties of the three phase boundary. Consequently a series of experiments was undertaken to measure the contact angle of liquid $PbCl_2$-alkali halide based melts upon various commercially available graphite materials. The effect of both increasing PbS concentration and temperature was studied. The types of substrates employed and a brief description of their properties and usage are given in Table 10.1.

10.2 Results

The measured contact angles for droplets of the purified solvents $PbCl_2$, $PbCl_2$-KCl and $PbCl_2$-KCl-NaCl at the temperatures of 501°C, 450°C and 400°C are given in Table 10.2. All the pure solvents are observed to wet the vitreous carbon substrate, i.e. $\theta < 90°$. For the particular case of $PbCl_2$, non-wetting ($\theta > 90°$) occurs on all the graphite substrates except EYA110. For the ternary eutectic melt non-wetting occurs on all the substrates except EYA4 at both temperatures of 400°C and 450°C. The binary melt wetted the substrates EYA4 and EYA9 but did not wet EYA110, CYA9 and boron nitride. The influence upon the contact angle of the addition of PbS to the melts $PbCl_2$-KCl-NaCl, $PbCl_2$-KCl and $PbCl_2$ is shown in Tables 10.3,

TABLE 10.1

General data for the graphites employed as contact angle substrates. EYA grades: ash less than 0.1%.

CYA9: A general purpose ungraphitized fine grained carbon graphite which can be used under oxidizing conditions to 250°C. It is a strong form of carbon with high electrical resistance and thermal conductivity.

EYA9: Is the graphitized counterpart of CYA9. It tends to have a higher hardness, strength and electrical resistance, good thermal conductivity and oxidation rates.

EYA110: Is a highly developed electro-graphite which has a good resistance to oxidation and good thermal conductivity. It is used mainly in metallurgical applications due to its fine grain structure.

EYA4: Is a medium textured highly graphitic material, having lower hardness and strength properties than commercial hard carbons. With comparatively low electrical resistance and good thermal conductivity.

TABLE 10.2

The measured contact angles of droplets of pure solvent melts upon carbon substrates.

	Pure Solvent Melt.			
Substrates	$PbCl_2$ 501°C	$PbCl_2$-KCl 450°C	$PbCl_2$-KCl-NaCl 400°C	$PbCl_2$-KCl-NaCl 450°C
VC	17.0	37.5	48.75	45.8
EYA4	100.5	48.5	21.0	23.0
CYA9	118.5	112.5	114.0	123.5
EYA9	93.0	82.75	108.0	106.75
EYA110	49.0	129.0	97.5	98.0
BN	105.0	122.0	-	70.0

VC = Vitreous Carbon: BN = Boron Nitride

TABLE 10.3

Contact Angle as a function of PbS concentration in the $PbCl_2$-KCl-NaCl eutectic melt.

	$PbCl_2$-KCl-NaCl + $X^{m}/_{o}$ PbS 450°C				
Substrate	$0^{m}/_{o}$	$2^{m}/_{o}$	$4^{m}/_{o}$	$6^{m}/_{o}$	$8^{m}/_{o}$
VC	45.8	0	0	0	0
CYA9	123.5	72.5	40	77.5	44.5
EYA110	98.0	42	39	44.25	35.5

	$PbCl_2$-KCl-NaCl + $X^{m}/_{o}$ PbS 500°C				
Substrate	$0^{m}/_{o}$	$2^{m}/_{o}$	$4^{m}/_{o}$	$6^{m}/_{o}$	$8^{m}/_{o}$
VC	-	0	0	0	0
CYA9	-	74.25	37.5	94	49.5
CYA110	-	45.5	42	49.75	37.0

TABLE 10.4

Contact Angles as a function of PbS concentration in the $PbCl_2$-KCl eutectic melt.

	$PbCl_2$-KCl + $X^{m}/_{o}$ PbS 450°C				
Substrate	$0^{m}/_{o}$	$2^{m}/_{o}$	$4^{m}/_{o}$	$6^{m}/_{o}$	$8^{m}/_{o}$
VC	37.5	0	17.5	0	0
CYA9	112.5	92.5	45	37.5	18.25
EYA110	129	38.25	41	52	46.5

	$PbCl_2$-KCl + $X^{m}/_{o}$ PbS 500°C				
Substrate	$0^{m}/_{o}$	$2^{m}/_{o}$	$4^{m}/_{o}$	$6^{m}/_{o}$	$8^{m}/_{o}$
VC	-	0	30	0	0
CYA9	-	88.5	56	35.5	12.75
EYA10	-	45	42	54.3	44.5

TABLE 10.5

Contact angles as a function of PbS concentration in the $PbCl_2$ melt at 501°C.

	$PbCl_2$ + X m/o PbS 501°C				
Substrate	0 m/o	5 m/o	10 m/o	15 m/o	20 m/o
VC	17.0	0	0	18.25	16.5
CYA9	118.5	87.5	16.5	101.75	106.
EYA110	49	61	91	14	38.5

10.4 and 10.5 respectively. In all cases the addition of lead sulphide to the solvent melt resulted in complete wetting ($\theta = 0$) of the vitreous carbon substrate. The addition of PbS to the melts $PbC\ell_2$-KCℓ and $PbC\ell_2$-KCℓ-NaCℓ results in the melting of all the substrates although no statistically meaningful trend was noted, the exception being the CYA9 graphite which shows a decrease in θ with increasing PbS concentration added to be binary eutectic salt. The addition of PbS to the pure $PbC\ell_2$ melt at 501°C does not result in any specific change in contact angle. On the vitreous carbon substrate θ values < 20°C were obtained whereas contact angles on the EYA110 substrate indicated wetting behaviour and on the CYA9 non-wetting.

10.3 Discussion

Fig. 10.1 shows the equilibrium shape of a drop of liquid on a solid surface. The liquid drop is in equilibrium as a consequence of the interaction of three boundary forces, γ_{LG} the interfacial energy between liquid and gas, γ_{SG} the interfacial energy between solid and gas, and γ_{SL} the interfacial energy between solid and liquid. The three forces are related to the contact angle, θ, by the Young Dupré equation (282):

$$\gamma_{SG} - \gamma_{SL} = \gamma_{LG} \cos \theta$$

If θ is less than 90° then the liquid wets the solid and if $\theta = 0$ then complete wetting occurs and the liquid spreads over the solid surface at a rate dependent upon the liquid viscosity and the surface roughness. When $\theta > 90°$ no wetting occurs.

The surface free energy of a solid and hence the values of γ_{SL}, γ_{SG} are very sensitive to both the physical and chemical states of the solid surface. Even the smoothest surfaces contain microscopic imperfections, i.e. a surface roughness (r) which affects the value of θ. Wenzel (283) has

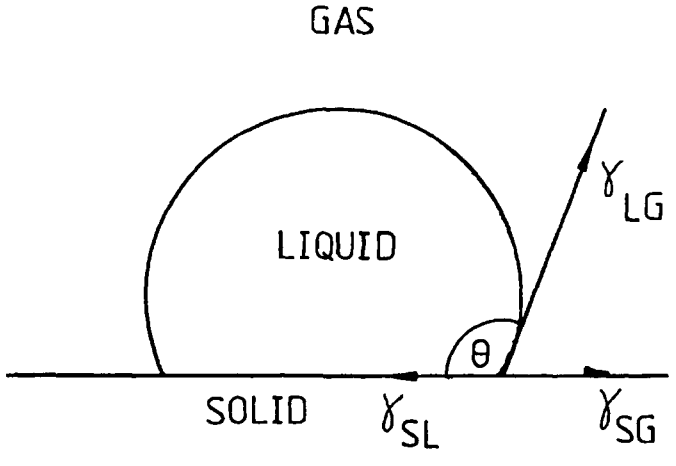


Fig. 10.1: A diagramatic representation of a liquid drop on a solid substrate. The system is in mechanical equilibrium as a result of the interaction between the boundary forces γ_{LG}, γ_{SG} and γ_{SL}.

shown that the true contact angle θ may be calculated from the measured contact angle 'θ' and the surface roughness (r) by the equation

$$f = \frac{\cos \theta}{\cos' \theta}$$

Adsorbed species on the surface also act to decrease the surface free energy and hence affect θ (284). The solid substrates chosen in this study reflect the type of electrode materials that have been used in the electrochemical studies, and those which are commercially available would most probably be used as industrial anode materials. The photographs given in Chapter 5 give an indication of the surface roughnesses exhibited by some of these materials. The results have shown that for a pure solvent melt non-wetting occurs on all the graphite substrates except EYA4 and wetting occurs at the vitreous carbon electrode. However upon adding $PbS_{\perp}$ to the eledtrolytes a significant decrease in the contact angle occurs. At the vitreous carbon electrode complete melting occurs, i.e. θ= 0, the graphite substrates generally yielding θ values less than 90°. The overall decrease in contact angle with the addition ofPbS to the solvent which occurs for all solvent/substrate combinations must indicate that the effect is a real one. Thus the lowering effect cannot simply be attributed to differences in the initial substrate interfacial free energies as a consequence of the cleaning procedure or of local surface roughness. Nevertheless, the cleaning procedure of graphite fibres has been shown to be very critical with regard to the contact angles of sulphur droplets. Thus for example a non-chemically treated substrate may yield θ values of ∿90°, whereas chemically treated fibres showed complete wetting (245). The further influence of adsorbed organic compounds is considered to be very small at a temperature of 400°C + .

For a given three phase system in which the $\gamma_{S/G}$ value remains constant, then a decrease in θ must be associated with a decrease of either

or (most probably) both $\gamma_{S/L}$ and $\gamma_{L/G}$. A very tentative reason may be the adsorption of sulphide ions at the s/ℓ and/or ℓ/g interfaces leading to an overall decrease in θ.

Hall has investigated in some depth the effect of electrode polarisation upon the wettability of liquid sulphur droplets upon a vitreous carbon electrode in both KSCN and the LiCℓ-KCℓ electrolytes (245). The contact angle was found to change from ∿30° to +160° over the potential range 0 → - 1.6V wrt Pt/Pt [11]. He also found that the large change in θ was not due to a change in the s/ℓ or the g/ℓ interfacial tensions. The large increase in the free energy of the carbon/sulphur interface upon cathodic polarisation was though to be due to a coulombic repulsion between the negatively charged electrode and the negatively charged long chain polymeric species adsorbed on the bulk liquid sulphur interface.

CONCLUSIONS

(1) Electrochemical investigation of the sulphide ion (PbS) in the binary $PbC\ell_2$-$KC\ell$(77-23 m/o) eutectic melt over the temperature range 440-530°C at carbon electrodes (vitreous carbon and spec-pure graphite) has revealed two primary oxidation processes to occur within the available potential window. These reactions may be represented by the equations:

(a) $S^{2-}_{(soln)} \rightleftharpoons \frac{1}{2}S_2 + 2e'$ $\quad E^a_p = 0.45V$

(b) $2S + 2C\ell^- \rightarrow S_2C\ell_2(g) + 2e'$ $\quad E^a_p = 0.95V$

At temperatures <~460°C, reaction (1) was found to be highly reversible with a reduction wave at $E^c_p = 0.33V$. Using the techniques of cyclic voltammetry and chronoamperometry, reaction (1) was determined to be diffusion controlled. The diffusion coefficient for the sulphide ion calculated from the Randles Sevcik equation were found to decrease with increasing PbS concentration, i.e. $D = 2.1 \times 10^{-6}$ cm^2/s at 4.51×10^{-2} mole PbS/ℓ to $D = 1.19 \times 10^{-6}$ at 1.573×10^{-1} mole PbS/ℓ assuming n = 2 and an insoluble reaction product. This was tentatively explained in terms of PbS dimer formation.

The voltammetric response did not reveal the presence or formation of reducible polysulphide species. At temperatures <~460°C the morphology of the voltammograms was consistent with the formation and stripping of an insoluble product. However extensive investigations using I-t transients did not reveal the presence of any nucleation and growth phenomena. The low voltammetric charge efficiency obtained was explained in terms of the dissolution of sulphur in the solvent.

At higher temperatures, sulphur gas evolution was verified from the voltammetric response and the formation of condensed sulphur on

the cool parts of the cell after prolonged electrolysis. Some evidence for the existence of an 'anode effect' was obtained under steady-state conditions although this effect was quite irreproducible. A possible kinetic scheme describing sulphur gas evolution was made on the basis of the observed Tafel slopes.

(2) The oxidation of PbS in a $PbCl_2$-KCl-NaCl eutetic melt was examined electrochemically at a temperature of 417°C. The use of this melt enabled a lower operating temperature to be employed and thus the possibility of sulphur/sulphide film formation could be examined. Two electrode systems were employed (a) non-reactive carbon electrodes and (b) reactive platinum and gold electrodes. All three electrode systems were electrochemically characterised.

At the carbon based electrodes unusual cyclic voltammograms were obtained. The I-E curves were found to be extended with both an increase in sweep rate and bulk PbS concentration. Although, on the basis of the voltammetric current functions a diffusion controlled process was inferred, analysis of all the parameters revealed the presence of the formation of an insoluble film under ohmic resistance control. The results were found to agree reasonably well with those predicted theoretically. Further evidence for possible film formation was gained from the chronopotentiometric and open circuit decay results.

The results obtained at the reactive platinum and gold electrodes were found to be complex. At both electrodes two oxidation waves were obtained at peak potentials of $E_p^a(A) = 0.3V$ and $E_p^a(B) = 0.4V$. At the gold electrode no reverse wave was associated with process A and indeed this oxidation wave was manifested as a 'shoulder' to the main anodic process. Both oxidation processes occurring at the gold

electrode were found to be diffusion controlled and the more anodic process to be highly reversible.

At the Pt electrode process it was found to be a quite distinct and separate wave with a reduction wave at $E_p^c(A) = 0.09V$. This reduction wave was only observed in very dilute solutions at $T > \sim 430°C$. Again analysis of the electrochemical responses was found to be diffusion controlled.

The results obtained at the reactive electrodes were interpreted in terms of the formation and growth of a sulphide film or intermediate via a diffusion controlled process. No evidence for any monolayer or adsorption type process(es) was obtained.

(3) The addition of the sodium polysulphides Na_2S_2, Na_2S_4 and Na_2S_5 to either the $PbCl_2$-KCl or the $PbCl_2$-KCl-NaCl eutectic melts at $T \geq 460°C$ were found to completely decompose. Addition of the polysulphides to the ternary melt at 440°C similarly underwent decomposition forming a stable S^{2-} containing solution according to the reaction

$$Na_2S_n \rightarrow Na_2S_{(soln)} + \frac{n-1}{2} S_2 (g)$$

Electrochemical characterisation of the resultant solutions was in good agreement with those obtained for the sulphide ion in the binary melt at the same temperature. These results substantiate the earlier electrochemical conclusions that the polysulphide ion is not stable in this melt.

(4) Attempts to obtain electrochemical information concerning the solubility of sulphur in $PbCl_2$-MCl melts by the addition of

sulphur pellets was not successful. However the use of an 'all-enclosed' cell design enabled qualitative information to be gained. Using this cell, a single reduction wave for the dissolved sulphur was obtained up to the solvent limit. The voltammetric peak height was found to be highly sensitive to cycling and on the whole irreproducible results were obtained. However the reduction of dissolved sulphur was found to be diffusion controlled. The peak height was found to increase with the partial pressure of sulphur ($p_{S_2}^{\frac{1}{2}}$).

The calculated solubilities of sulphur in the $PbCl_2$-KCl-NaCl eutectic over the temperature range 716-772K was found to vary between 8.827×10^{-5} - 3.804×10^{-4} mole S/cm^3 assuming an n = 2 process and a $D = 2 \times 10^{-5}$ cm^2/s. The results are in good agreement with previous workers.

(5) The possibility of anionic impurities was assessed. Thus the electrochemical characterisation of the species PbO, PbO_2 and $PbSO_4$ was undertaken using cyclic voltammetry. Both the oxides PbO and PbO_2 were found to dissolve rapidly in the $PbCl_2$-KCl solvent. The I-E curves for both species were identical; yielding a single oxidation wave at $E_p^a \cong 0.95V$. No corresponding reduction wave was observed. The overall oxidation process was found to be diffusion controlled.

The $PbSO_4$ solute was found to be soluble in the melt although electrochemically inactive within the potential window available. This conclusion is in agreement with the calculated thermodynamic potentials.

(6) A brief study of the melting characteristics of the solvent melts $PbCl_2$, $PbCl_2$-KCl and $PbCl_2$-KCl-NaCl on various polished carbon substrates was evaluated over the temperature range 400-500°C. On the vitreous carbon substrate, all the pure melts were found to wet the substrate yielding contact angle between 17-50°. On the graphite electrodes a $\theta > 90°$, i.e. non-wetting, was obtained. The results of adding PbS to the solvents over the range 0-8 $^{m}/o$ resulted in a significant decrease in the contact angle. No statistically meaningful variation was noted with increasing concentration. On the vitreous carbon substrate complete wetting generally occurred, i.e. $\theta = 0$.

APPENDIX 1

The most comprehensive data on sulphur vapour comes from the mass spectrometric studies of Berkowitz and Marquart [54]. Their results show in graphical form the equilibrium constants relating the various partial pressures as functions of temperature. These generate the following six independent equations:

(1) $3\log P_{S_2} - 2 \log P_{S3} = -6.00 \times 10^3 T^{-1} + 8.50$

(2) $2\log P_{S_2} - \log P_{S4} = -5.73 \times 10^3 T^{-1} + 6.49$

(3) $\log P_{S_5} - 5/8 \log P_{S_8} = -1.22 \times 10^3 T^{-1} + 1.52$

(4) $\log P_{S_6} - 3/4 \log P_{S_8} = -1.22 \times 10^3 T^{-1} + 1.52$

(5) $\log P_{S_7} - 7/8 \log P_{S_8} = -1.16 \times 10^3 T^{-1} + 1.55$

(6) $4\log P_{S_2} - \log P_{S_8} = -20.9 \times 10^3 T^{-1} + 23.6$

REFERENCES

1. Rosenqvist, T., "Principles of Extractive Metallurgy", McGraw-Hill Co., (1974).

2. Pehlke, R.D., "Unit Processes of Extractive Metallurgy", Elsevier, New York, (1973).

3. Biswas, A.K. and Davenport, W.G., "Extractive Metallurgy of Cu", International Series on Materials Science and Technology, V20, D.W. Hopkins, Ed., Pergamon Press, (1976).

4. "Second Progress Report on Recent Advances in Extraction Metallurgy", J. Mackowiak, Ed., in International Metals Review, 21, 118 (1976)

5. "Advances in Extractive Metallurgy", Proc. Symp. I.M.M. London, (1967).

6. See for example, Trans. I.M.M. and J. Metals.

7. Friedman, L.J. and Rinckhoff, J.B., A.I.M.E. Annual Meeting, Atlanta, Georgia, March (1977).

8. "Background Information for New Source Performance Standards. Primary Cu, Zn and Pb Smelters", EPA-450/2-74-002a, October (1976).

9. Mathews et al., "SO_2 Control Processes for Non-Ferrous Smelters", PB-251-409, Jan. (1976).

10. Cigan, J.M. and Catterill, C.H., eds. in "Extractive Metallurgy of Pb and Zn", A.I.M.E. World Symposium on Mining and Metallurgy of Pb and Zn, A.I.M.E., New York (1970).

11. Cigan, J.M., Mackey, T.S. and O'Keefe, T.J., eds. "Lead, Zinc, Tin '80'", TMS-AIME World Symposium on Metallurgy and Environmental Control. The Metallurgical Society of AIME, Warrendale, Pennsylvania (1980).

12. Castle, D.M., J. Metals 30 (Jan.), 30 (1978).

13. MacDonald, B.I. and Weiss, M., J. Metals 30 (Jan.), 24 (1978).

14. Muller, E., "Smelting of Lead Concentrates by the Kirert Process", Enzmettal 29 (1976).

15. Chaudburic, K.B. and Melcher, G., C.I.M. Bull. 71 (1978).

16. Friedman, L.J., J. Metals, 33 (March), 44 (1981).

17. Delahay, P., "New Instrumental Methods in Electrochemistry", New York, Intersience (1954).

18. Adams, R.N., "Electrochemistry at Solid Electrodes", New York, M. Dekker (1969).

19. Weissberger, A. and Rossiter, B.W., "Physical Methods of Chemistry. Part IIA, Electrochemical Methods", New York, Wiley-Interscience (1971).

20. Paunovic, M., J. Electroanal. Chem. 14, 447 (1967).

21. Reinmuth, W.H., Anal. Chem. 33, 322 (1961).

22. Davies, D.G., J. Electroanal. Chem. 14, 447 (1967).

23. Nicholson, R.S. and Shain, T., Anal. Chem. 36 706 (1964).

24. Mamantov, G., Manning, D.L. and Dale, J.M., J. Electroanal. Chem. 9, 253 (1965).

25. Matsuda, H. and Ayabe, Y., Z. Electrochem. 59, 494 (1955).

26. Nicholson, R.S., Anal. Chem. 37, 1351 (1965).

27. Nicholson, R.S. and Shain, T., Anal. Chem. 37, 178 (1965).

28. Mastragostino, M., Nadjo, L. and Saveant, J.M., Electrochim. Acta 13, 721 (1968).

29. Andrieux, C.P., Nadjo, L. and Saveant, J.M., J. Electroanal. Chem. 26, 147 (1970).

30. Shuman, M.S., Anal. Chem. 42, 521 (1960).

31. Saveant, J.M. and Vianello, E., Compt. Rend 256, 2597 (1963).

32. Saveant, J.M. and Vianello, E., Electrochim. Acta 10, 905 (1965).

33. Saveant, J.M. and Vianello, E., Electrochim. Acta 12, 1545 (1967).

34. Shuman, M.S., Anal. Chem. 41, 142 (1969).

35. Nicholson, R.S., Anal. Chem. 37, 667 (1965).

36. Olmstead, M.L., Hamilton, R.C. and Nicholson, R.S., Anal. Chem. 41 260 (1969).

37. Polcyn, D.S. and Shain, I., Anal. Chem. 38, 70 (1966).

38. Wopschall, R.S. and Shain, I., Anal. Chem. 39, 1514 (1967).

39. Dudley, P.G., M. Phil. Thesis, University of London (1979).

40. Davis, D.G., "Electroanalytical Chemistry", V1, A.J. Bard Ed., Marcel Dekker, New York, 1966, pp. 157-196.

41. Lingane, P.T., Critical Rev. Anal. Chem. 1, 587 (1971).

42. Murray, R.W., in reference [19], pp. 592-616.

43. Reinmuth, W.H., Anal. Chem. 32, 1514 (1960).

44. Testa, A.C. and Reinmith, W.H., Anal. Chem. 33, 1320 (1961).

45. Mamantov, G., Papoff, P. and Delahay, P., J. Am. Chem. Soc. 79, 4034 (1957).

46. Torsi, G., Fung, K.W., Begun, G.M. and Mamantov, G., Inorg. Chem. 10, 2285 (1971).

47. Delimarskii, Yu K. and Markov, B.F., "Electrochemistry of Fused Salts", The Sigma Press, Washington D.C. (1961).

48. Fung, K.W. and Mamantov, G., "Comprehensive Analytical Chemistry", C.L. Wilson and D.W. Wilson Eds., Elsevier, Amsterdam, New York.

49. Laitinen, H.A., Pure Appl. Chem. 15 227 (1967).

50. Meyer, B., ed: "Elemental Sulphur : Chemistry and Physics", New York, Interscience (1965).

51. West, W.A. and Menzies, A.W.C., J. Phys. Chem. 33, 1929, p. 1880.

52. Rau, H., Kutty, T.R.N. and Guedes de Carvalho, J.R.F., J. Chem. Thermodyn. 5, 291 (1973).

53. Baker, E.H., Trans. Instn. Min. Metall. (Sect.C) 80 C93 (1971).

54. Berkowitz, J. and Marquart, J.R., J. Chem. Phys. 39, 275 (1963).

55. Eriksson, G. and Tegman, R., Chimica Scripta 10, 45 (1976).

56. Cleaver, B., Davies, A.J. and Hames, M.D., Electrochim. Acta 18 719 (1973).

57. Cleaver, B. and Davies, J.A., Electrochim. Acta 18, 727 (1973).

58. Rosen, E. and Tegman, R., Chem. Scripta 2, 239 (1972).

59. Cleaver, B. and Davies, A.J., Electrochim. Acta 18, 741 (1973).

60. Wells, A.F., "Structural Inorganic Chemistry", 4th Edition, Clarendon Press, Ocford (1975).

61. Evans, R.C., "Crystal Chemistry", Cambridge University Press, London (1964).

62. Pauling, L., "The Nature of the Chemical Bond", 3rd Edition, Cornell University Press (1960).

63. Ross, V., "Geochemistry, Minearalogy and Crystal Structure of Sulphides", Econ. Geol. 52, 755 (1957).

64. Azaroff, L.V. and Brophy, J.J., "Electronic Processes in Materials", McGraw-Hill, New York (1963).

65. Shuey, R.T., "Semiconducting Ore Minerals", Developments in Economic Geology No-4, Elsevier, Amsterdam.

66. Vaughan, D.J. and Craig, J.R., "Mineral Chemistry of Metal Sulphides", Cambridge University Press (1978).

67. Mills, K.C., "Thermodynamic Data for Inorganic Sulphides, Selenides and Tellurides", Butterworths, London (1974).

68. Ramsdell, L.S., Am. Mineral 10, 281 (1925).

69. Bloem, J., Philips Res. Rept. 11, 273 (1956).

70. Bleom, J. and Kröger, F.A., Z. Phys. Chem. N.F. 7, 1 (1956).

71. Samura, G.A. and Drickamer, H.G., J. Chem. Phys. 37, 1159 (1962).

72. Jellinek, F., Chpt. 19 in "Inorganic Sulphur Chemistry", G. Nickless Ed., Elsevier, Amsterdam, 1968.

73. Pauling, L. and Brockway, L.O., Z. Kristallogr. 82, 188 (1932).

74. Pauling, L., Z. Kristallogr. 84, 10 (1934).

75. Bouchard, R.J. et al., Inorg. Chem. 7, 2208 (1968).

76. Grillot, E., Bull. Soc. Chim. France, 39 (1951).

77. Aminoff, G., Z. Kristallogr. 58, 203 (1923).

78. Fuller, M.L., Phil. Mag. 8, 658 (1928).

79. Kjekshins, A. and Pearson, W.B., Solid State Chem. 1, 83 (1964).

80. Wickman, F.E. and Smith, D.K., Am. Mineral 55, 1843 (1970).

81. Berry, L.A., Am. Mineral 39, 504 (1954).

82. Wadsley, A.D., "Inorganic non-stoichiometric cmpds" in Non-Stoichiometric Cmpds, L. Mandelcorn ed., Academic Press, New York, pp. 99-209 (1964).

83. Anderson, J.C., Bull. Soc. Chim. Fr., 2203 (1969).

84. Fender, B.E.F., M.T.P. International Review of Science, Inorganic Chemistry Series 1, 10 243

85. Jellinek, F., M.T.P. International Review of Science, Inorganic Chemistry Series 1, 5 (1972), Butterworth, London.

86. Dalven, R., Infrared Phys. 9, 141 (1969).

87. Zemel, J.N., Jensen, J.D. and Schoolar, R.B., Phys. Rev. 140 A330-A342 (1965).

88. Kravchenko, A.F., Timchenko, A. Kh. and Godovikov, A.A., Doklady Akad. Nauk SSSR 167 74 (1966).

89. Cheroff, G. and Keller, S.P., Phys. Rev. 111, 98 (1958).

90. Fok, M.V., Sov. Phys., Solid State 5, 1085 (1963).

91. Samara, G.A. and Drikamar, H.G., J. Phys. Chem. Solids 23, 457 (1962).

92. Morehead, F.F. and Fowler, A.B., J. Electrochem. Soc. 109, 688 (1962).

93. Morehead, F.F., J. Electrochem. Soc. 110, 285 (1963).

94. Spokes, E.M. and Mitchell, D.R., Min. Eng. 60, 373 (1959).

95. Brummage, W.H., Yarger, C.R. and Lin, C.L., Phys. Rev. 113, 765 (1964).

96. Kegs, J.D. et al., Can. Mineral 9, 453 (1968).

97. Hastings, J.M., Elliott, N. and Corliss, L.M., Phys. Rev. 115, 13 (1959).

98. Kautz, R.L., Dresselhaus, M.S., Adler, D. and Linz, A., Phys. Rev. 6B, 2078 (1972).

99. Schwarz, E.J. and Vaughan, D.J., J. Geomag Geoelec. 24, 441 (1972).

100. Sparks, J.J. and Komoto, T., Rev. Mod. Phys. 40, 752 (1968).

101. Blander, M., Ed., "Molten Salt Chemistry", Interscience Publishers, New York, 1964.

102. Sundheim, B.R., Ed., "Fused Salts", McGraw-Hill, New York (1964).

103. McDonald, I.R. and Singer, K., Chem. Brit. 9, 54 (1973).

104. Bloom, H., "The Chemistry of Molten Salts", W.A. Benjamin, New York, (1967).

105. Mamantov, G., "Molten Salts: Characterization and Analysis", Marcel Dekker, New York (1969).

106. Braunstien, J., Mamantov, G. and Smith, G.P., Eds., "Advances in Molten Salt Chemistry", Vol. 1, Plenum Press, New York (1971).

107. Petrucci, S., Ed., "Ionic Interactions", Vol. 1, Academic Press, New York (1971).

108. Janz, G.J., "Molten Salts Handbook", Academic Press, New York (1967).

109. Forland, T., Grjotheim, K., Motzfeld, K. and Urnes, S., Eds., "Selected Topics in High Temperature Chemistry", Universitetstorlaget, Oslow (1966).

110. Ann. N.Y. Acad. Sci. 22, 759-1098 (1960).

111. Kleppa, O.J., Ann. Rev. Phys. Chem. 16, 187 (1965).

112. Lumsden, J., "Thermodynamics in Molten Salt Mixtures", Academic Press, New York, New York (1966).

113. Inman, D., Graves, A.D. and Sethi, R.S., in "Electrochemistry", Vol. 1, A Specialist Periodical Report, The Chemical Society, London (1970).

114. Janz, G.J. and Reeves, R.D., in "Advances in Electrochemistry and Electrochemical Engineering", Vol. 5, G.W. Tobias, Ed., Interscience Publishes, New York (1967).

115. Petrucci, S., Ed., "Ionic Interactions", Vol. II, Academic Press, New York (1971).

116. Gruen, D.M., Quart. Rev. 19, 349 (1965).

117. Delimarskii, Yu. K. and Markov, B.F., "Electrochemistry of Fused Salts", The Sigma Press, Washington, D.C. (1961).

118. Fung, K.W. and Mamantov, G., "Advances in Molten Salt Chemistry", Vol. 2, Braunstein, J., Mamantov, G. and Smith, G.P., Eds., Plenum Press, New York, (1973), pp. 199-254.

119. Inman, D., Graves, A.D. and Nobile, A.A., "Electrochemistry", Vol. 2, A Specialist Periodical Report, The Chemical Society, London (1972).

120. Laity, R.W. in "Reference Electrodes", Ives, D.J.G. and Janz, G.J., Eds., Academic Press, New York (1961), pp. 524-606.

121. Alabysher, A.F., Lantratov, M.F. and Moracherskii, A.G., "Reference Electrodes for Fused Salts", English Translation, The Sigma Press, Washington, DC (1965).

122. Rossotti, H., Ed., "Chemical Applications of Potentiometry", D. Van Nostrand Co. Ltd., London (1969), pp. 176-194.

123. Graves, A.D., Hills, G.J. and Inman, D., "Advances in Electrochemistry and Electrochemical Engineering", Vol.5, Delahag, P., Ed., Interscience Publishers, New York (1966), p. 117.

124. Charlot, G. and Tremillon, B., Translated by P.T. Harrey "Chemical Reactions in Solvents and Melts", Pergamon Press (1969).

125. Reddy, T.B., Electrochem. Technol. 1, 325 (1963).

126. Bockris, J. O'M., White, J.L. and Mackenzie, J.D., Eds., "Physico Chemical Measurements at High Temperatures", Butterworths, London (1959).

127. Corbett, J.D. and Duke, F.R., "Techniques of Inorganic Chemistry", Vol. 1, Jonassen, H.B. and Weissberger, A., Eds., Interscience Publishers, New York (1963), pp. 103-156.

128. Bailey, R.A. and Janz, G.J., "The Chemistry of Nonaqueous Solvents", Vol.1, Lagowski, J.J., Ed., Academic Press, New York (1961), pp. 291-371.

129. Flengas, S.N. and Kucharski, A.S., Canadian J. Chemistry 49, 3971 (1971).

130. Lux, H.Z., Electrochem. 45, 303 (1939).

131. Flood, H. and Forland, J., Acta Chem. Scand. 1, 592 (1947).

132. Pearson, R.G., J. Am. Chem. Soc. 85, 3533 (1963).

133. Marcus, Y., Isreal J. Chem. 10, 659 (1972).

134. Greenberg, J., Sundheim, B.R. and Gruen, D.M., J. Chem. Phys. 29, 461 (1958).

135. Lux, H. and Anslinger, H., Chem. Ber. 94, 1161 (1961).

136. Bodewig, F.G. and Plambeck, J.A., J. Electrochem. Soc. 117, 904 (1970).

137. Bodewig, F.G. and Plambeck, J.A., J. Electrochem. Sco. 116, 607 (1969).

138. Giggenbach, W., J. Inorg. Nucl. Chem. 30, 3189 (1968).

139. Giggenbach, W., Inorg. Chem. 10, 1308 (1971).

140. Gruen, D.M., McBeth, R.L. and Zielen, A.J., J. Am. Chem. Soc. 93, 6691 (1971).

141. Martin, R.P., Doub., W.H. Jr., Roberts, J.L. and Sawyer, D.T., Inorg. Chem. 12, 1921 (1973).

142. Giggenbach, W., J. Chem. Soc. (D) 729 (1973)

143. Huglen, R., Poulsen, F.W., Mamantov, G. and Marassi, R., Inorg. Nucl. Chem. Letters 14, 167 (1978).

144. Liu, C.H., Zielen, A.J. and Gruen, D.M., J. Electrochem. Soc. 120, 67 (1973).

145. Saboungi, M.L., Marr, J.J. and Blander, M., J. Electrochem. Soc. 125, 1567 (1978).

146. Saboungi, M.L., Marr, J.J. and Blander, M., Trans. A.I.M.E. 10B, 477 (1979).

147. Cleaver, B., Davies, A.J. and Schriffrin, D.J., Electrochim. Acta 18, 747 (1973).

148. Brookes, H., in "Ionic Liquids", D. Inman and D.G. Lovering, Plenum Press, New York, 1981.

149. Bell, M.C. and Flengas, S.N., J. Electrochem. Soc. 111, 569, 1440 (1964).

150. Blachnik, R. and Kahleyss, H., Thermochimica Acta 3, 145 (1971).

151. Thompson,W.T. and Flengas, S.N., Can. J. Chem. 46, 1611 (1968).

152. Blachnik, R. and Kudermann, G., Z. Naturforsch 286, 1 (1973).

153. Chang, S.K. and Toguri, J.M., J. Chem. Thermodynamics 7, 423 (1975).

154. Bell, M.C. and Flengas, S.N., J. Electrochem. Soc. 111, 575 (1964).

155. Bell, M.C. and Flengas, S.W., J. Electrochem. Soc. 113, 27 (1966).

156. Bell, M.C. and Flengas, S.W., J. Electrochem. Soc. 113, 31 (1966).

157. Pelton, A.D. and Flengas, S.W., Can. J. Chem. 48, 2016 (1970).

158. Garbee, A.K. and Flengas, S.N., J. Electrochem. Soc. 119, 613 (1972).

159. Truthe, W., Z. Anorg. Chem. 76, 161 (1912).

160. Grantham, L. and Yosim, S., J. Chem. Phys. 45, 1192 (1966).

161. Sakai, K., J. Chem. Soc. Japan 75, 182 (1954).

162. Yang, L., Pound, G. and Derge, G., Trans. AIME 206, 783 (1956).

163. Gerischer, H., Z. Elektrochem. 54, 540 (1950).

164. Allen, P.L., Hickling, A., Trans. Far. Soc. 53, 1626 (1957).

165. Armstrong, R.D., Porter, D.F., Thirsk, H.R., J. Phys. Chem. 72, 2300 (1968).

166. Loucka, T., J. Electroanal. Chem. 36, 355 (1972).

167. Selis, S.M., Electrochim Acta 15, 1285 (1970).

168. South, K.D., Sudworth, J.L. and Gibson, J.G., J. Electrochem. Soc. 119, 554 (1972).

169. Ludwig, F.A., Tischer, R.P., Aikens, D.A. and Fung, K.W., Extended Abs. No. 386, 147th Meeting, The Electrochem. Soc., May (1975).

170. Tischer, R.P. and Ludwig, F.A. in "Advances in Electrochemistry and Electrochemical Engineering", V10, C.W. Tobias and H. Gerisher, Eds., Interscience, New York (1977).

171. Delarue, G., Soc. Chim. France, Bull 906, 1654 (1960).

172. Adamo, F. and Kennedy, J.H., J. Electrochem. Soc. 119, 1518 (1972).

173. Birk, J.R. and Steunenberg, R.K., Advances in Chemistry Series, American Chemical Society, Washington D.C., No. 140, p.186 (1975).

174. Kam, K.W. and Johnson, K.E., J. Electroanal. Chem. 115, 53 (1980).

175. Raleigh, D.O., White, J.T. and Ogdon, C.A., J. Electrochem. Soc., 126, 1087 (1979.

176. Bernard, J.P.,de Haan, A. and Van der Poorten, Compt. Read. Ser. C. 276, 587 (1973).

177. Inman, D. and Weaver, M.J., Electrochim Acta 20, 929 (1975).

178. Tremillon, B. and Letisse, G., J. Electroanal. Chem. 17, 371 (1968).

179. Torsi, G. and Mamantov, G., Inorg. Chem. 10, 1900 (1971).

180. Torsi, G. and Mamantov, G., Inorg. Chem. 11, 1439 (1972).

181. Fannin, A.A., King, L.A. and Seegmiller, T.W., J. Electrochem. Soc. 119, 801 (1972).

182. Boxall, L.G., Jones, H.L. and Osteryoung, R.A., J. Electrochem. Soc. 120, 223 (1973).

183. Marassi, R., Mamantov, G. and Chambers, J.Q., Inorg. Nucl. Chem. Letters 11, 245 (1975).

184. Marassi, R., Mamantov, G., Matsunaga, M., Springer, S.E. and Wianx, J.P., J. Electrochem. Soc. 126, 231 (1979).

185. Paulsen, K.A. and Osteryoung, R.A., J. Am. Chem. Soc. 98, 6866 (1976).

186. Mamantov, G., Marassi, R. and Chambers, J.Q., J. Electrochem. Soc. 123, 1128 (1976).

187. Robinson, J., Gilbert, B. and Osteryoung, R.A., Inorg. Chem. 16, 3040 (1977).

188. Welch, B.J. and King, P.L. in "Physical Chemistry of Process Metallurgy : the Richardson Conference", The Institution of Mining and Metallurgy (1974).

189. Skyllas, M. and Welch, B.J., Electrochim. Acta 23, 1157 (1978).

190. Skyllas-Kazacos, M. and Welch, B.J., Electrochim. Acta 25, 179 (1980).

191. de Guibert, A., Plichon, V. and Badoz-Lambling, J., J. Electrochem. Soc. 126, 1902 (1979).

192. Lelievre, D., de Guibert, A. and Plichon, V., Extended Abstracts, 30th Meeting, International Society of Electrochemistry, Trondhiem, Norway, p. 231 (1979).

193. de Guibert, A. and Plichon, V., J. Electroanal. Chem. 90, 399 (1979).

194. Plichon, V., de Guibert, A. and Moscardo-Levelut, M.N., in "Ionic Liquids", D. Inman and D.G. Lovering, Eds., Plenum Press, New York, 1981.

195. Skeaff, J.M., J. Institution of Mining and Metallurgy, London, Section C, C71 (1980).

196. Townsend, C.P., D.R.P. Pat. 182478 (1906).

197. Gibson, A.R. and Robson, S., British Patent 448328 (1934).

198. Richardson, J.B., Trans. Instn. Min. Met. 46, 339 (1936).

199. Gibson, A.R., 5th Monthly Report, The National Smelting Co. Ltd., 30.6.1933.

200. Angel, G. and Garnum, E., Tek. Tid. 75, 279 (1945).

201. Sawamoto, H. and Saito, T., J. Mining Inst. Japan 68, 555 (1952).

202. Winterhager, H. and Kammel, R., Z. Erzbergban u. Metallhütenw 9 , 97 (1956).

203. Yangase, T., Suginohara, Y. and Kyono, I., Denki Kagaku 36, 129 (1968).

204. King, P.L. and Welch, B.J., J. Appl. Electrochem. 2, 23 (1972).

205. Welch, B.J., King, P.L. and Jenkins, R.A., Scand. J. Metall. 1, 49 (1972).

206. King, P.L. and Welch, B.J., Proc. Anstralas. Inst. Min. Metall. 246, 7 (1973).

207. Tran Kim Hoa and Welch, B.J., J. Appl. Electrochem. 3, 45 (1973).

208. Starliper, A.G. and Kenworthy, H., U.S. Bur. of Mines, Rept. Investigations, No. 6554.

209. Hoar, T.P. and Ward, R.G., Trans. Inst. Mining Met. C, p. 393, May (1958).

210. Haver, F.P., Uchida, K. and Wong, M.M., U.S. Bur. of Mines, Rept. of Investigations, Inv. No. 7185 (1969).

211. Colom, F. and De la Cruz, M., Electrochim Acta 14, 217 (1969).

212. Inman, D. and White, S.H., J. Appl. Electrochemistry 8, 375 (1978).

213. Inman, D. and Williams, D.E., "Future Prospects for Electrodepositing Metals from High-Temperature Inorganic Melts", in Electrochemistry - The Past Thirty Years and the Next Thirty Years, Bloom, H. and Gutmann, F., Eds., Plenum Press, New York (1976).

214. Spencer, R., Ph.D. Thesis, University of London (1970).

215. Warren, F., Ph.D. Thesis, University of London (1976).

216. Viré, S., Ph.D. Thesis, University of London (1982).

217. White, S.H., in "Ionic Liquids", D. Inman and D.G. Lovering, Eds., Plenum Press, New York (1981).

218. Höy-Peterson, N., J. of Metals, p.43, April (1969).

219. Watanabe, N. and Asane, , J. Electrochem. Soc. Japan 34, 107 (1971).

220. Thonstad, J., Nordmo, F. and Rodseth, J.K., Electrochim. Acta 19, 761 (1974).

221. Snow, R.J. and Welch, B.J., Austral. Inst. Min. Met. Proceed. 221, 43 (1967).

222. Angerstein-Kozlowska, H. and Conway, B.E., J. Electroanal. Chem. 95, 1 (1979).

223. Vetter, K.J., "Electrochemical Kinetics", Academic Press, 1967.

224. Triaca, W.E., Solomons, C. and Bockris, J.O'M., Electrochim. Acta 13, 1949 (1968).

225. Parsons, R., Trans. Faraday Soc. 54, 1053 (1958).

226. Bockris, J.O'M., J. Phys. Chem. 24, 817 (1956).

227. Conway, B.E., "Electrode Processes", Ronald (1965).

228. Janssen, L.J.J. and Hoogland, J.G., Electrochim. Acta. 15, 1667 (1970).

229. Tunold, R., Bo, H.M., Paulsen, K.A. and Yttredal, J.O., Electrochim. Acta 16, 2101 (1971).

230. Piontelli, R., Electrochim. Metall. 1, 1 (1966).

231. Drossbach, P., Hashino, T., Krahl, P. and Pfeiffer, W., Chemie-Ing-Techn. 33, 84 (1961).

232. Elchardus, E., C.r. hebd. Séanc. Acad. Sci., Paris 206, 460 (1938).

233. Vajna, A., Allumino 20, 29 (1951).

234. Krohn, C.H., Thesis, N.H.T. Trondheim (1963).

235. Henning, G., J. Chem. Phys. 20, 1443 (1952).

236. Rüdorf, W., Hoffmann, K., Rüdorff, G., Endell, J. and Ruess, G., Z. Anorg. Chem. 256, 126 (1948).

237. Shibata, S., Electrochim. Acta 23, 619 (1978).

238. Shibata, S., Denki Kagaku 44, 709 (1976).

239. Vogt, H., Electrochim. Acta 25, 527 (1980).

240. Mazza, B., Pedeferri, P. and Re, G., Electrochim. Acta 23, 87 (1978).

241. Gessler, I., Dissertation, T.H. Müchen (1967).

242. Drossbach, P. and Krahl, P., Z. Elektrochem. 62, 178 (1958).

243. Lippmann, G., Ann. Phys. Chem.149, 547 (1873).

244. Möller, H.G., Ann. Phys. 25, 725 (1908).

245. Hall, S.M., Ph.D. Thesis, Southampton University, 1980.

246. Fritz, W., Phys. Z. 36, 379 (1935).

247. Stephan, K. and Vogt, H., Electrochim. Acta 24, 11 (1979).

248. Reinmuth, W.H., Anal. Chem. 33, 485 (1961).

249. Osteryoung, R.A., Lauer, G. and Anson, F.C., J. Electrochem. Soc. 110, 926 (1963).

250. De Tacconi, N.R., Calandra, A.J. and Arvia, A.J., Electrochim. Acta 18, 571 (1973).

251. Calandra, A.J., De Tacconi, N.R., Pereiro, R. and Arvia, A.J., Electrochim. Acta 19, 901 (1974).

252. Fleischman, M., Lax, D.J. and Thirsk, H.R., Trans. Faraday Soc. 64, 3137 (1968).

253. Thak, B.V., Perkins, R.S., Kozlowska, H.A. and Conway, B.E., Electrochim Acta 17, 1447 (1972).

254. Williams, D.E. and Wright, G.A., Electrochim. Acta 21, 1 (1976).

255. Gilroy, D. and Conway, B.E., J. Phys. Chem. 69, 1259 (1965).

256. Conway, B.E. and Bourgault, P.L., Trans. Faraday Soc. 58 (1962)

257. Weaver, M.J., Ph.D. Thesis, London University (1972).

258. Gileadi, E., Kirowa-Eisner, E. and Penciner, J., "Interfacial Electrochemistry: An Experimental Approach", Addison-Wesley, Reading Massachusetts (1975).

259. Diggle, J.W., in "Oxides and Oxide Films", V2, J.W. Diggle, Ed., Marcel Dekker, New York, p. 281 (1973).

260. Diggle, J.W., Research diploma thesis, Royal Institute of Chemistry, London (1966).

261. Brummer, S.B. and Makrides, A.C., J. Electrochem. Soc. 111, 1122 (1964).

262. Vermilyea, D.A., in "Adv. Electrochem. electrochem. Engng." 3, 211, P. Delahay, Ed., Interscience, New York (1963).

263. Bewick, A., Fleischmann, M. and Thirsk, H.R., Trans. Faraday Soc. 58, 2200 (1962).

264. Berzons, T. and Delahay, P., J. Am. Chem. Soc. 75, 555 (1953).

265. Stonehart, P., Kozlowska, H.A. and Conway, B.E., Proc. Roy. Soc., London A310, 541 (1969).

266. Dirske, T.P. and de Vires, D.B., J. Phys. Chem. 63, 107 (1959).

267. Flengas, S.N. and Block-Bolten, A., in "Advances in Molten Salt Chemistry", V2, J. Braunstein, G. Mamantov and G.P. Smith, Eds., p. 27, Plenum Press, New York (1973).

268. Tegman, R., Chemica Scripta 9, 158 (1976).

269. Levin, E.M., Robbins, C.R. and MCMurdie, H.F., "Phase Diagrams for Ceramists", Reser. Ed. (1964).

270. Burrows, B. and Hills, G.J., Electrochim. Acta 15, 445 (1970).

271. Flood, H. and Forland, T.,Disc. Far. Soc. 1, 302 (1947).

272. Liu, C.H., J. Phys. Chem. 66, 164 (1962).

273. Johnson, K.E. and Laitinen, H.A., J. Electrochem. Soc. 110, 314 (1963).

274. Ariva, A.J., Calandra, A.J. and Videla, H.A., Electrochim. Acta 13, 167 (1968).

275. Rempel, S.I. and Malkova, E.M., Zh. Prikl. Khim. 25, 558 (1952).

276. Wrench, D.M. and Inman, D., Electrochim. Acta 12, 1601 (1967).

277. Senderoff, S., Klopp, E.M. and Kronenberg, M.L., Quart. Tech. Prog. Rep. 8 and 9, Contract NORD 18240 (1960).

278. Woodall, B. quoted by Laitinen, H., Talanta 12, 1237 (1965).

279. Legey, J.C.L., Ph.D. Thesis, University of London (1973).

280. Burrows, B.W. and Hills, G.J., J. Inst. Fuel, April 168 (1966).

281. Kochergin, V.P. et al., "Fis. Khim. Rasplavlen. Solei i Shlakov", Akad. Nauk SSSR Ural'sk. Filial, Inst. Elektrokhim., Tr. Vses. Soveshch, Sverdlovsk 215 (1960).

282. Adamson, A.W., "The Physical Chemistry of Surfaces", Interscience Publishers, New York (1967).

283. Wenzel, R.N., Ind. Eng. Chem. 28, 988 (1936).

284. Aveyard, R. and Haydon, D.A., "An Introduction to the Principles of Surface Chemistry", Cambridge University Press (1973).

284. Uchida, I., Urushibata, H. and Toshima, S., J. Electroanal. Chem., 96, 45 (1975).

285. Gupta, N.K., Rev. Sci. Instrum., 42, 1368 (1971).

286. Inman, D., Ph.D. Thesis, London University, 1957.

287. Rosén, E. and Tegman, R., Acta Chem. Scand. 25, 3329 (1971).

ACKNOWLEDGEMENTS

The author would like to express his thanks to the Warren Spring Laboratories for supplying financial support which made this work possible. He would also like to express his appreciation to his supervisor, Dr. D. Inman for his guidance and encouragement throughout the work. In particular for his support during the author's stay at Imperial College.

Many thanks are also due to Dr. Duan Shuzhen for her help during part of this work and to Mr. R. Rudkin for his technical assistance.

Thanks also to Mr. G. Hicks for his glassblowing expertise and his willingness to help.

Finally the author would like to express his appreciation to Mr. C. Winter (W.S.L.) for his encouragement and friendship during this work.